

PhD Thesis

Hadron interactions and cosmic strings from lattice simulations

Jorge Juan Baeza Ballesteros

Programa de Doctorado en Física - 3126
Valencia, July 2024



VNIVERSITAT
ID VALÈNCIA

Supervisors:

Pilar Hernández Gamazo
Daniel García Figueroa

arXiv:2410.20996v1 [hep-lat] 28 Oct 2024



VNIVERSITAT
DE VALÈNCIA

Hadron interactions and cosmic strings from lattice simulations

PhD Thesis by

Jorge Juan Baeza Ballesteros

IFIC - Universitat de València - CSIC
Departament de Física Teòrica
Programa de Doctorado en Física - 3126

Under the supervision of

**M Pilar Hernández Gamazo
Daniel García Figueroa**

Valencia, July 2024

Agradecimientos

Cuando pienso que ya han pasado cuatro años desde que comenzó esta aventura por el mundo de la física, siento una mezcla de sorpresa y melancolía. Parece que fue ayer cuando empezó y, sin embargo, he vivido un sinnúmero de experiencias y adquirido una infinidad de conocimientos. A lo largo de este camino, muchas personas me han acompañado, sin las cuales no me habría sido posible llegar hasta aquí.

A Pilar y Dani, mis directores, quienes me han guiado en este viaje y me han enseñado a pensar como un verdadero científico, quienes han estado ahí para aconsejarme cuando necesitaba ayuda y para mostrarme lo divertida que puede ser la investigación, quienes me han dado libertad para estudiar nuevas ideas y me han apoyado siempre. Pilar, me has transmitido esa visión crítica que es tan importante para un científico y siempre me has animado a explorar nuevos horizontes, sin dejar de preocuparte por mi progreso. Dani, de ti he aprendido la importancia de fijarme en los detalles y, al mismo tiempo, no perder de vista la relevancia global de cada resultado. A los dos os estoy enormemente agradecido, y echaré realmente de menos ser vuestro estudiante de doctorado.

A Fernando, que ha sido un mentor para mí todos estos años y sin quien posiblemente este viaje nunca habría tenido lugar. Aún recuerdo cuando me contaste de qué iba la investigación en lattice. Ese fue, posiblemente, el punto de partida de mi camino como científico. Desde que nos conocemos siempre has estado ahí para darme consejos, no solo en el plano científico, sino también en el personal. Muchas gracias.

A Max, Steve, Raúl, André y Mark, por hacerme sentir a gusto en todos mis viajes, por proponerme nuevas ideas y enseñarme a plantear los problemas desde únicas perspectivas. Jamás olvidaré todo lo que he aprendido con vosotros y los buenos momentos que he vivido alrededor del mundo.

Al resto de mis colaboradores: Hans, Mattias, Tomáš, Joanes, Ed y Andrea, con quienes he descubierto un sinfín de nuevos enfoques desde los que enfrentarme a los diferentes obstáculos que aparecen en el mundo de la ciencia.

A mis compañeros de SOM, especialmente a David y Nico, por todos los buenos momentos en el IFIC y fuera de él.

A mis padres, mis hermanos y mi abuela, que siempre han estado ahí para apoyarme y aconsejarme. Gracias a vosotros he crecido hasta ser quien soy.

Por último, a Lucía, que me ha acompañado durante todo este viaje, que ha estado a mi lado desde mucho antes que comenzara y que seguirá ahí en todas las aventuras venideras. Me has dado ánimo cuando lo necesitaba, distracción cuando no era capaz relajarme y cariño cuando me sentía perdido. Has escuchado atentamente mil historias sobre mi trabajo y me has aconsejado sobre cómo afrontar cada nuevo día. Sin ti no habría llegado hasta donde estoy hoy.

Muchas gracias a todos por estar a mi lado y por haberme acompañado en esta divertida aventura.

Valencia, julio 2024

List of publications

This doctoral thesis is based on the following publications and works in preparation, listed in the order they appear in the dissertation:

- [1] J. Baeza-Ballesteros, P. Hernández and F. Romero-López, *A lattice study of $\pi\pi$ scattering at large N_c* , JHEP 06 (2022) 049.
- [2] J. Baeza-Ballesteros, P. Hernández and F. Romero-López, *Meson-meson scattering at large N_c* , 2024 (in preparation).
- [3] J. Baeza-Ballesteros, J. Bijnens, T. Husek, F. Romero-López, S. R. Sharpe and M. Sjö, *The isospin-3 three-particle K -matrix at NLO in ChPT*, JHEP 05 (2023) 187.
- [4] J. Baeza-Ballesteros, J. Bijnens, T. Husek, F. Romero-López, S. R. Sharpe and M. Sjö, *The three-pion K -matrix at NLO in ChPT*, JHEP 03 (2024) 048.
- [5] J. Baeza-Ballesteros and M. T. Hansen, *Two- and three-particle scattering in the (1+1)-dimensional $O(3)$ non-linear sigma model*, 2024 (in preparation).
- [6] J. Baeza-Ballesteros, E. J. Copeland, D. G. Figueroa and J. Lizarraga, *Gravitational wave emission from a cosmic string loop: Global case*, Phys. Rev. D 110 (2024) 043522.
- [7] J. Baeza-Ballesteros, E. J. Copeland, D. G. Figueroa and J. Lizarraga, *Gravitational Wave Emission from a Cosmic String Loop, II: Local Case*, 2024 (submitted to Phys. Rev. Lett.).

The research presented also appeared in conference proceedings:

- [8] J. Baeza-Ballesteros, P. Hernández and F. Romero-López, *$\pi\pi$ scattering at Large N_c* , PoS LATTICE2021 (2022) 309.
- [9] J. Baeza-Ballesteros and M. T. Hansen, *Two- and three-particle scattering in the (1+1)-dimensional $O(3)$ non-linear sigma model*, PoS LATTICE2022 (2023) 050.
- [10] J. Baeza-Ballesteros, P. Hernández and F. Romero-López, *Progress in meson-meson scattering at large N_c* , PoS LATTICE2023 (2024) 059.

The author has also participated in the development of the *CosmoLattice* package:

- [11] J. Baeza-Ballesteros, D. G. Figueroa, A. Florio and N. Loayza Romero, *CosmoLattice Technical Note II: Gravitational Waves*, 2022.
- [12] J. Baeza-Ballesteros, D. G. Figueroa and N. Loayza Romero, *CosmoLattice Technical Note III: Gravitational Waves from $U(1)$ gauge theories*, 2023.

Finally, other published works to which the author contributed, that are not presented in this dissertation, are:

- [13] J. Baeza-Ballesteros, A. Donini and S. Nadal-Gisbert, *Dynamical measurements of deviations from Newton's $1/r^2$ law*, Eur. Phys. J. C 82 (2022) 154.
- [14] J. Baeza-Ballesteros, A. Donini, G. Molina-Terriza, F. Monrabal and A. Simón, *Towards a realistic setup for a dynamical measurement of deviations from Newton's $1/r^2$ law: the impact of air viscosity*, Eur. Phys. J. C 84 (2024) 596

Abbreviations and conventions

Throughout this dissertation, we made use of a number of abbreviations. They are summarized below, separated in two groups depending on whether they appear in the first or the second part of this doctoral thesis:

Part I - Hadron interactions from lattice QCD

BH	Bull's head	NLO	Next-to-leading order
ChPT	Chiral perturbation theory	NNLO	Next-to-next-to-leading order
CMF	Center-of-mass frame	OPE	One-particle exchange
df	Divergence free	pNGB	Pseudo-Nambu-Goldstone bosons
DD	Doublet-doublet	PV	Principal value
DS	Doublet-singlet	RChT	Resonant chiral theory
dof	Degrees of freedom	QC	Quantization condition
EFT	Effective field theory	QCD	Quantum chromodynamics
ERE	Effective range expansion	QED	Quantum electrodynamics
GEVP	Generalized eigenvalue problem	RFT	Relativistic field theory
IAM	Inverse amplitude method	SM	Standard model
irrep	Irreducible representations	<i>s</i> -OPE	<i>s</i> -channel one-particle exchange
LEC	Low-energy constant	SD	Singlet-doublet
LO	Leading order	SS	Singlet-singlet
NGB	Nambu-Goldstone bosons		

Part II - Cosmic string loops from lattice simulations

CMB	Cosmic microwave background	NG	Nambu-Goto
FLRW	Friedmann-Lemaître -Robertson-Walker	RD	Radiation domination
GW	Gravitational wave	TT	Transverse-traceless
GWB	Gravitational wave background	UV	Ultraviolet
IR	Infrared	VOS	Velocity-dependent one-scale

As of conventions, we work in natural units ($c = \hbar = 1$) and use the mostly-minus signature for the metric. This means that the metric of Minkowski spacetime is $g_{\mu\nu} = \text{diag}(+1, -1, -1, -1)$. When indicating components of Minkowski vectors, we use Greek indices to refer to all its components, while Latin indices refer only to the spacial ones. We assume repeated indices in equations are summed over, unless otherwise stated. Also, spacial vectors are indicated using bold variables.

When considering matrix quantities describing scattering processes, in general, column indices refer to the initial state, while row indices correspond to the final state. Similarly, arguments related to the final state are indicated first than those related to the initial state, and time flows from right to left in Feynman diagrams.

Lastly, we use NLO to refer only to the correction to the LO, rather than the full LO+NLO result. An analogous criteria is also used to denote higher orders in perturbation theory.

Preface

Field theory is the basic framework to describe high-energy physics. The Standard Model of particle physics is the paradigmatic example of a quantum field theory, which is the synthesis of quantum mechanics and special relativity. It describes three of the fundamental forces of nature—the electromagnetic, the weak and the strong forces—and has been successful at describing fundamental phenomena at an astonishing level of precision. Certain phenomena of the early universe can also be described by field theories, such as inflation, phase transitions and cosmic defects. In many cases, due to large occupation numbers, these phenomena can be investigated using classical-field-theory techniques.

In many regimes, quantum and classical field theories can be described by means of analytical techniques. Within the Standard Model, this is for example the case of quantum electrodynamics, which describes the electromagnetic interactions. The small size of the fine structure coupling, $e^2/4\pi \approx 1/137$, allows for a perturbative expansion in powers of this quantity. Many processes occurring during the history of our universe can also be investigated analytically, by treating fluctuations of the metric or the matter fields as small perturbations.

However, the use of analytical techniques to study field theories is not always feasible. In the case of quantum chromodynamics (QCD), the theory that describes the strong interaction, the phenomenon of asymptotic freedom prevents perturbative techniques from being applicable at low energies, where the strong coupling grows large. This precludes analytical predictions, for instance, of the hadron spectrum. This is particularly true in relation to the existence and properties of resonances, which are hadronic states that only exist virtually during scattering processes. A longstanding question is whether QCD can predict the presence of such particles, which requires the use of non-perturbative techniques.

Analytical methods also fail to describe non-perturbative and non-linear phenomena that may take place in the early universe. This is, for instance, the case of particle production during and after inflation and also the case of the observable signatures of early-universe processes, such as the emission of gravitational waves (GWs). Making reliable predictions of these phenomena is of vital importance in view of current and projected GWs experiments. The detection of a background of GWs emitted by processes taking place during the early universe will open the door to the study of high-energy physics at scales well above those reachable by ground-based accelerators. However, a correct interpretation of a possible signal depends on reliable theoretical predictions, which in turn requires of alternative techniques to capture the non-linear dynamics.

The most successful approach to investigate beyond-analytical regimes in quantum and classical field theories is the use of lattice techniques. These are based on the formulation of the field theory on a discretized and finite volume, which allows to obtain predictions from numerical simulations. In the case of QCD, Monte Carlo methods allow to evaluate the path integral and extract information about physical observables, such as hadron masses or multiparticle scattering amplitudes. Regarding early-universe phenomena, the evolution of matter fields and the emission of GWs can be determined from the numerical solution of the equations of motion.



This doctoral thesis is devoted to the study of hadron scattering in QCD and the emission of particles and GWs from cosmic string loops that may arise in the early universe, using numerical lattice simulations. The dissertation consists of ten chapters, organized in two independent parts.

Part I focuses on the study of two- and three-hadron scattering using lattice QCD techniques, complemented by analytical results from chiral perturbation theory and the large N_c limit. The fundamentals of QCD are introduced in chapter 1, where lattice QCD, effective field theories and the large N_c limit are also discussed. The basics of multiparticle scattering are introduced in chapter 2, with special emphasis on the quantization conditions that permit to study such processes in a finite volume.

The following five chapters present the results of my doctoral work on lattice QCD. They can be grouped in three separate lines of research. Chapters 3 and 4 deal with the investigation of the N_c dependence of meson-meson scattering observables, and are mainly based on ref. [1] and ongoing work [2]. Chapters 5 and 6 focus on the study of three-pion interactions using chiral perturbation theory. More concretely, they summarize the results

from refs. [3, 4], where we determined the three-pion K -matrix up to next-to-leading order in chiral perturbation theory. Finally, chapter 7 is devoted to the study of two- and three-particle interactions in the $O(3)$ non-linear sigma model, commonly used as a toy model of QCD, with the aim of testing the relativistic-field-theory three-particle finite-volume formalism [5].

Part II of this thesis is dedicated to the study of the dynamics and GW emission from cosmic string loops using classical-field-theory lattice simulations. Chapter 8 introduces the basics of classical field theory in an expanding universe, and explains how lattice simulations can be used to study the non-linear field dynamics, as well as the associated GW emission. Chapters 9 and 10 are focused on the application of these techniques to characterize the evolution and GW emission of decaying cosmic string loops. In particular, these two chapters present, respectively, the results from ref. [6] for the case of global loops, and results from ref. [7] for local loops.

Contents

Agradecimientos	i
List of publications	iii
Abbreviations and conventions	v
Preface	vii
I Hadron interactions from lattice QCD	1
1 Hadrons and quantum chromodynamics	3
1.1 Quantum chromodynamics	4
1.1.1 Asymptotic freedom and confinement	7
1.1.2 Chiral symmetry and the hadron spectrum	9
1.2 QCD on the lattice	12
1.2.1 The QCD lattice action	14
1.2.2 Computing correlation functions	17
1.2.3 Physical observables from lattice correlators	19
1.2.4 Thermal effects	22
1.3 The 't Hooft limit of QCD	24
1.3.1 Ordinary hadrons at large N_c	25
1.3.2 Tetraquarks at large N_c	27
1.4 Effective field theories	27
1.4.1 Chiral Perturbation Theory	28
1.4.2 ChPT at large N_c	31

2	Hadron interactions	35
2.1	Particle scattering in infinite volume	36
2.1.1	Two-particle scattering	37
2.1.2	Three-particle scattering	39
2.2	Meson interactions from ChPT	42
2.2.1	Two-pion scattering in ChPT	43
2.2.2	Three-pion scattering at LO in ChPT	44
2.3	Particle scattering from the lattice	47
2.3.1	Two-particle quantization condition	48
2.3.2	Three-particle quantization condition	51
3	Pion-pion scattering near threshold at large N_c	55
3.1	Pion-pion scattering in $N_f = 4$ QCD	56
3.1.1	Pion-pion scattering at large N_c	57
3.1.2	Pion-pion scattering in $SU(N_f)$ ChPT	59
3.1.3	Pion-pion scattering in $U(N_f)$ ChPT	61
3.2	Lattice setup	64
3.2.1	Extraction of finite-volume energies	67
3.3	Results for pion-pion scattering	68
3.3.1	Convergence of the threshold expansion	68
3.3.2	Discretization effects	71
3.4	Matching to ChPT	74
3.4.1	Fitting procedure	74
3.4.2	Fits to ChPT	75
3.4.3	Discussion and comparison to previous literature	77
3.5	Conclusions	81
4	Meson-meson scattering at large N_c	83
4.1	Lattice setup	84
4.1.1	Set of interpolating operators	84
4.1.2	Computation of correlation functions	89
4.2	Finite-volume energy spectra	90
4.3	Extraction of infinite-volume scattering amplitudes	100
4.4	Conclusions	106

5	The isospin-three three-pion K-matrix at NLO in ChPT	109
5.1	Relating \mathcal{M}_3 to $\mathcal{K}_{\text{df},3}$ at NLO in ChPT	110
5.2	Computation of $\mathcal{K}_{\text{df},3}$ at NLO	113
5.2.1	Preliminaries to the computation	114
5.2.2	The subtracted OPE contribution	115
5.2.3	The non-OPE contribution	119
5.2.4	The bull's head subtraction contribution	122
5.2.5	Numerical evaluation	126
5.3	Results for $\mathcal{K}_{\text{df},3}$	127
5.3.1	Comparison to lattice results	128
5.3.2	Range of validity of the threshold expansion	131
5.4	Conclusions	133
6	The three-pion K-matrix at NLO in ChPT	135
6.1	$\mathcal{K}_{\text{df},3}$ for general isospin	136
6.1.1	The flavor space	136
6.1.2	Building blocks of the integral equations	138
6.1.3	Relating \mathbf{M}_3 to $\mathbf{K}_{\text{df},3}$	140
6.1.4	Threshold expansion of $\mathbf{K}_{\text{df},3}$	141
6.2	Computation of $\mathbf{K}_{\text{df},3}$	144
6.2.1	The subtracted-OPE contribution	144
6.2.2	The s -channel OPE contribution	147
6.2.3	The non-OPE contribution	148
6.2.4	The BH subtraction	148
6.3	Results for $\mathbf{K}_{\text{df},3}$	151
6.4	Conclusions	155
7	Two- and three-particle scattering in the $O(3)$ model	159
7.1	The (1+1)-dimensional $O(3)$ non-linear sigma model	160
7.1.1	The integrable S -matrix	161
7.1.2	Two- and three-particle S -matrix	164
7.2	QCs in 1+1 dimensions	166
7.2.1	Two-particle formalism	166
7.2.2	RFT Three-particle formalism	167

7.3	Lattice setup	170
7.3.1	Single- and three-cluster algorithms	170
7.3.2	Two- and three-particle correlation functions	173
7.3.3	Lattice simulations	175
7.4	Results for finite-volume energies	176
7.5	Comparison to analytical predictions	180
7.5.1	Two-particle energies	180
7.5.2	Three-particle energies	180
7.6	Conclusions	188

II Cosmic strings loops from lattice simulations 191

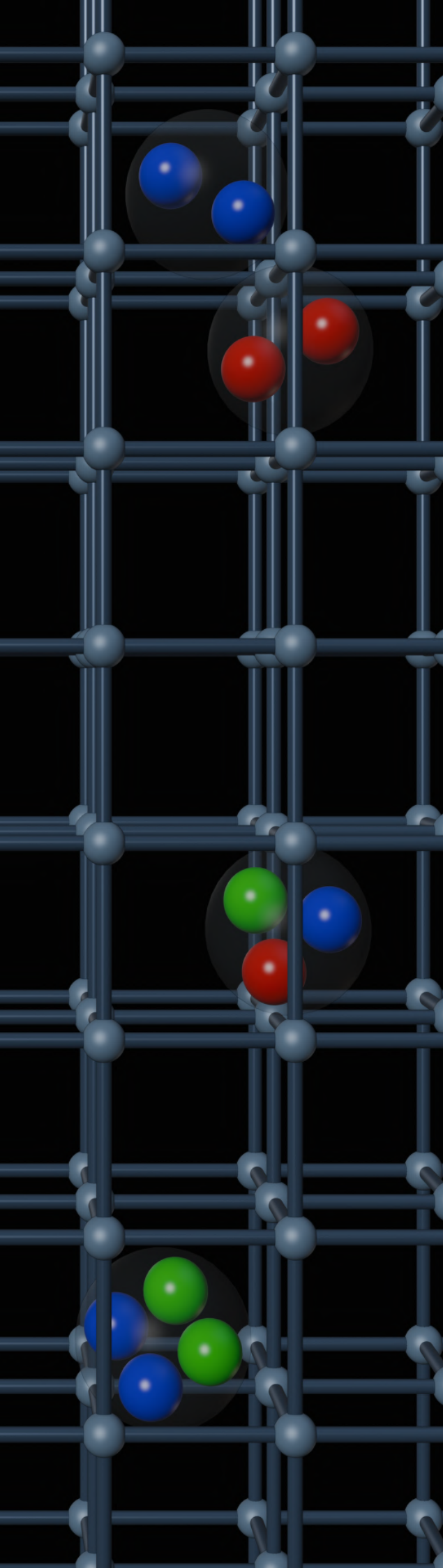
8 Lattice techniques for cosmology 193

8.1	The expanding universe	194
8.1.1	Field-theory description	195
8.2	Classical field theory on the lattice	198
8.2.1	Lattice definition and Fourier transform	198
8.2.2	A dimensionless discretized model	201
8.2.3	Solving the field dynamics	203
8.3	Emission of gravitational waves	204
8.3.1	Simulating the emission of GWs	206

9 GW emission from cosmic string loops: global case 209

9.1	Global cosmic strings in the early universe	210
9.1.1	The QCD axion	212
9.1.2	Analytical solutions for cosmic strings	213
9.1.3	The Nambu-Goto approximation	215
9.2	Lattice simulations of global strings	217
9.2.1	Global-string observables	217
9.2.2	Generation of network loops	221
9.2.3	Generation of artificial loops	225
9.3	Results	229
9.3.1	Loop decay into particles	229
9.3.2	Particle emission	234
9.3.3	GW emission	235
9.4	Conclusion	240

10 GW emission from cosmic string loops: local case	243
10.1 The Abelian-Higgs model	244
10.1.1 Infinite string solution	246
10.2 Lattice simulations of local strings	248
10.2.1 Local-string observables	248
10.2.2 Generation of network loops	250
10.2.3 Generation of artificial loops of type I	253
10.2.4 Generation of artificial loops of type II	256
10.3 Results	258
10.3.1 Particle emission from network loops	258
10.3.2 Particle emission from artificial strings	261
10.3.3 GW emission	266
10.4 Conclusions	271
Conclusions and outlook	273
Resumen	279
Bibliography	295



Part I

Hadron Interactions from Lattice QCD

*Tu voz pudo enternecerme,
tu presencia suspenderme,
y tu respeto turbarme.
¿Quién eres? Que aunque yo aquí
tan poco del mundo sé, [...].*

*La vida es sueño
Calderón de la Barca*

1 Hadrons and quantum chromodynamics

The strong interaction is one of the four fundamental forces of nature. Its name comes from its strength: it is responsible for binding protons and neutrons in atomic nuclei, vastly overcoming the effect of electric repulsion. Quantum chromodynamics (QCD) is the quantum field theory that describes the strong force, and combined with the theory of electroweak interactions, conforms the Standard Model of particle physics.

The tale of the strong interaction is now almost a century long.¹ It started back in 1935 when Yukawa first proposed it as a new force responsible for binding protons and neutrons in atomic nuclei [16]. He predicted that this force would be mediated by some massive particles, which he named mesons, of a mass around 100 MeV. In 1947, the π meson was discovered [17], earning him a Nobel Prize in physics two years later.

Following this finding, a myriad of new subatomic particles were discovered in particle accelerators in the 1950s and 1960s, which were initially thought to be fundamental. It was soon realized by Gell-Mann [18] and Ne'eman [19] independently that these particles could be organized in simple geometrical patterns according to their isospin, strange and charm quantum numbers, in what was called the *Eightfold way*. This classification lead Gell-Mann and Zweig to propose the quark model [20, 21] according to which all known subatomic particles were indeed composed of other more fundamental spin-1/2 ones, the quarks, q . They distinguished two types of composite particles, also known as *hadrons*: *mesons*, formed by a quark and an antiquark, $\bar{q}q$, and *baryons*, composed of three quarks, qqq .

¹See for example ref. [15] for a detailed history of strong interactions.

The quark model found rapid success, as it made possible to predict the existence of new hadrons that were observed in experiment shortly after [22, 23]. The model also implied that, if quarks were to obey Pauli statistics, they should have an additional quantum number, which was named *color* [24–26]. This led to the proposal of QCD as the fundamental theory governing strong interactions [27]. As will be explained in this chapter, this is a non-Abelian $SU(3)$ gauge theory with quarks and gluons as fundamental particles. These particles, however, can not be found as isolated states in nature. Due to the properties of asymptotic freedom and confinement, only colorless hadrons are observed.

Fifty years after the proposal of QCD, it is still one of the most active fields of study within high energy physics. On the theory side, confinement and asymptotic freedom preclude the application of standard perturbative methods to study the hadron spectrum of QCD. Still, other alternative approaches exist, such as lattice QCD, the 't Hooft limit or the use of effective field theories, that make it possible to investigate the low-energy regime of QCD. On the experimental side, new composite particles are continuously being discovered and characterized. During the last decades some new states have been observed with properties that cannot be explained by a meson or baryon structure, but are expected to have a more exotic nature, such as tetraquarks [28–34], composed of two quarks and two antiquarks, $\bar{q}q\bar{q}q$.

In this chapter the basics of QCD are reviewed, together with some of the most successful techniques that allow one to study its low-energy regime. In sec. 1.1, the theory of strong interactions is introduced and some of its main features are discussed. Sec. 1.2 presents the lattice regularization of QCD, arguably the most successful first-principles approach to its low-energy regime. Finally, in secs. 1.3 and 1.4 two other techniques are considered: the limit of large number of colors and chiral perturbation theory, respectively.

1.1 Quantum chromodynamics

Quantum chromodynamics is the quantum field theory that describes the strong interactions between quarks and gluons. It is a non-Abelian gauge theory based on a $SU(N_c)$ Lie group, where N_c is the number of colors, which is the charge associated to the strong interaction. In nature, it can take three different values, $N_c = 3$: red, green and blue.

The matter content of the theory are quarks and gluons. Quarks are represented by spin-1/2 fermion fields, $q(x)$, which transform under the fundamental irreducible representation (irrep) of $SU(N_c)$ (while antiquarks, $\bar{q}(x)$, transform in the antifundamental one). They contain both spin and

color indices, which are left implicit. In nature, quarks appear in $N_f = 6$ different flavors (up, down, strange, charm, bottom and top), which are distinguished by their couplings to the Higgs field.

The second component of QCD are gluons, the mediators of the strong force. They are represented by a gauge field, $A_\mu(x)$, which transforms under the adjoint representation of the color group. This field can be expressed as a linear combination of the generators of the $\mathfrak{su}(N_c)$ Lie algebra—the Gell-Mann matrices, t^a —with real coefficients, $A_\mu = A_\mu^a t^a$, where the color indices are left implicit.

The dynamics of quarks and gluons are described by the QCD action,

$$S_{\text{QCD}}[q, \bar{q}, A] = \int d^4x \mathcal{L}_{\text{QCD}}[q, \bar{q}, A], \quad (1.1)$$

where the Lagrangian² is integrated over the whole Minkowski spacetime, $x = (t, \mathbf{x})$. The Lagrangian density of QCD can be separated in two parts,

$$\mathcal{L}_{\text{QCD}}[q, \bar{q}, A] = \mathcal{L}_{\text{F}}[q, \bar{q}, A] + \mathcal{L}_{\text{G}}[A]. \quad (1.2)$$

The first one contains all the fermionic terms, including their coupling to gluons,

$$\mathcal{L}_{\text{F}}[q, \bar{q}, A] = \sum_{f=1}^{N_f} \bar{q}_f (i\gamma_\mu D^\mu - m_f) q_f, \quad (1.3)$$

where γ_μ are the Dirac gamma matrices, $\bar{q} = q^\dagger \gamma_0$, m_f is the bare quark mass for flavor f , and

$$D_\mu = \partial_\mu - igA_\mu, \quad (1.4)$$

is the covariant derivative, with g the gauge coupling that characterizes the strength of the interactions between quarks and gluons. Note that we have written eq. (1.3) as a sum over an arbitrary number of flavors, N_f . While $N_f = 6$ in nature, it is convenient to keep the dependence on N_f explicit.

The second term of eq. (1.2) contains the kinetic term for the gauge field and its self-interactions. It takes the simple form

$$\mathcal{L}_{\text{G}}[A] = -\frac{1}{2} \text{tr} [F_{\mu\nu} F^{\mu\nu}], \quad (1.5)$$

where the trace runs over the color indices and $F_{\mu\nu} = F_{\mu\nu}^a t^a$, with

$$F_{\mu\nu}^a = \partial_\mu A_\nu^a - \partial_\nu A_\mu^a + if^{abc} A_\mu^b A_\nu^c, \quad (1.6)$$

is the field-strength tensor of the gauge field. Here we have introduced the structure constants of the $\mathfrak{su}(N_c)$ algebra, f^{abc} defined from

$$[t^a, t^b] = if^{abc} t^c. \quad (1.7)$$

²We will abuse language and refer to the Lagrangian density simply as the Lagrangian.

As $SU(3)$ is a non-Abelian group, $f^{abc} \neq 0$ and so the QCD Lagrangian contains cubic and quartic self-interaction vertices for the gluon.

The action in eq. (1.1) is invariant under local gauge transformations,

$$\begin{aligned} q(x) &\rightarrow \Omega(x)q(x), \\ A_\mu(x) &\rightarrow \Omega(x)A_\mu(x)\Omega(x)^\dagger + \frac{i}{g}\partial_\mu\Omega(x)\Omega(x)^\dagger, \end{aligned} \quad (1.8)$$

where $\Omega(x) \in SU(3)$. In addition, the QCD action is invariant under CP transformations, where C refers to charge conjugation and P to parity inversions. These two discrete symmetries act on the quark and gluon fields,

$$\begin{aligned} q(t, \mathbf{x}) &\xrightarrow{P} \gamma_0 q(t, -\mathbf{x}), & q(t, \mathbf{x}) &\xrightarrow{C} C^{-1} \bar{q}^\top(t, \mathbf{x}), \\ \bar{q}(t, \mathbf{x}) &\xrightarrow{P} \bar{q}(t, -\mathbf{x}) \gamma_0, & \bar{q}(t, \mathbf{x}) &\xrightarrow{C} -q^\top(t, \mathbf{x}) C, \\ A_0(t, \mathbf{x}) &\xrightarrow{P} A_0(t, -\mathbf{x}), & A_0(t, \mathbf{x}) &\xrightarrow{C} -A_0^\top(t, \mathbf{x}), \\ A_i(t, \mathbf{x}) &\xrightarrow{P} -A_i(t, -\mathbf{x}), & A_i(t, \mathbf{x}) &\xrightarrow{C} -A_i^\top(t, \mathbf{x}), \end{aligned} \quad (1.9)$$

where X^\top denotes the transpose matrix of X , and C is a matrix acting on spin indices defined implicitly via the relation $C\gamma_\mu C^{-1} = -\gamma_\mu^\top$.

It is possible to include one further term in the QCD Lagrangian in eq. (1.2) which, while allowed by gauge symmetry, does not preserve CP invariance. This is the so called θ -term,

$$\mathcal{L}_\theta[A] = -\theta \frac{g^2 N_f}{32\pi^2} \text{tr} [F_{\mu\nu} \tilde{F}^{\mu\nu}], \quad (1.10)$$

where $\tilde{F}^{\mu\nu} = \epsilon^{\mu\nu\rho\sigma} F_{\rho\sigma}$ is the dual tensor of the field-strength tensor and θ is an unknown phase. This term can be written as a total derivative, and so does not contribute to perturbation theory at any order. Still, its integral over the whole spacetime takes an integer value, known as the *topological charge*. Gauge configurations are classified in topological sectors, which contribute to QCD observables beyond perturbation theory.

In addition, as already mentioned, a non-zero θ parameter implies the violation of the CP symmetry by the strong interactions. In particular, a neutron dipole moment would be induced. The experimental measurement of this observable make it possible to constrain $\theta < 10^{-10}$ [35, 36]. The small size of the measured θ angle is known as the *strong CP problem*. During the years, many different proposals have been made to solve it. One of the most interesting ones is the inclusion of a new spontaneously broken $U(1)$ symmetry—the *Peccei-Quinn symmetry* [37, 38]—with its corresponding

Goldstone boson—the *axion*—, as this new particle would also represents a dark matter candidate [39]. This hypothetical mechanism is discussed in the context of its cosmological implications in sec. 9.1.1.

1.1.1 Asymptotic freedom and confinement

At first glance, QCD seems very similar to the theory of electromagnetism, quantum electrodynamics (QED). The only differences in the QCD action are the trace over color indices in eq. (1.5) and the last term in eq. (1.6), which vanishes in QED. Still, the two theories are like night and day.

A characteristic property of quantum field theories is the *running* of the couplings, this is, the fact that the interaction couplings depend on the scale at which physics are probed. The coupling constant of QED, related to the electric charge of the electron e , is small at low energies or large scales, $e^2/4\pi \sim 1/137$, and grows with the energy. This implies that QED can be studied with standard perturbative techniques. In contrast, the coupling constant of QCD decreases at small scales, i.e., $g(\Lambda) \rightarrow 0$ as $\Lambda \rightarrow \infty$, and becomes large at low energies. Thus, the low-energy properties of QCD cannot be understood in perturbation theory.

This characteristic property of QCD is known as *asymptotic freedom* [40, 41], and gives rise to the rich phenomenology of the strong interaction. One of its main implications is the fact that QCD can be studied perturbatively at high energies, where the coupling is small. In particular one can use perturbation theory to determine the running of the strong coupling at high energies. The beta function has been computed up to five loops in perturbation theory [42, 43]. At one-loop order it reads [40, 41],

$$\beta(\alpha_s) = \mu \frac{d\alpha_s}{d\mu} = -\frac{\alpha_s^2}{2\pi} \beta_0 + \mathcal{O}(\alpha_s^4), \quad (1.11)$$

with

$$\beta_0 = \frac{11}{3}N_c - \frac{2}{3}N_f, \quad (1.12)$$

where $\alpha_s = g^2/4\pi$. The one-loop result for the beta function is universal, this is, does not depend on the regularization (this is also true for the two-loop-order result).

From this result, one can observe that the theory is asymptotically free, with $\beta(\alpha_s) < 0$, as long as $N_c \leq 2N_f/11$. This condition is well satisfied in nature, where $N_c = 3$ and $N_f = 6$. The result for the beta function allows one to determine a low-energy scale, Λ_{QCD} , at which the QCD coupling becomes infinite,

$$\Lambda_{\text{QCD}} = \Lambda_{\text{UV}} \exp \left[-\frac{4\pi}{\alpha_s(\Lambda_{\text{UV}})} \right], \quad (1.13)$$

where Λ_{UV} is some reference high-energy scale. Using experimental results, one can estimate $\Lambda_{\text{QCD}} \approx 300 \text{ MeV}$.

This scale separates the high- and low-energy regimes of QCD. At high energies, α_s becomes small and QCD turns into a weakly interacting theory, in which quarks and gluons behave as quasi-free particles. This occurs for example in heavy-ion collisions and the early universe, where a quark-gluon plasma is formed [44]. In this regime, perturbation theory has been successfully used to make accurate predictions, which are in agreement to experimental results [34].

For energies below Λ_{QCD} , interactions are very strong, leading to the phenomenon of *confinement*. Quarks and gluons do not exist in isolation, but instead form composite particles, the hadrons, which can only appear in nature as colorless states that transform under the singlet representation of the color group. In the quark model, hadrons can either be mesons, composed of a quark and an antiquark with the same color, or baryons formed of three quarks of different colors. Other possibly exotic hadrons, such as tetraquarks, pentaquarks or hybrid states have also been found in experiment [28, 30–34]. The mass of these composite states does not originate from the mass of its composing quarks (which only amounts for $\sim 1\%$ of the mass in the case of the proton, for instance), but rather from the energy of the strong interaction itself. The strong force is thus responsible for the majority of the (visible) mass of the universe.

In the low-energy regime, contrary to high energies, perturbation theory fails and one is forced to look for alternative approaches to QCD. During the last decades, many different techniques have been developed, which have shown different levels of predicting capability. In this chapter, we discuss three of them: the lattice regularization of QCD, the large N_c limit and effective field theories, which are the main tools guiding the first part of this doctoral dissertation.

Before moving on, it is worth emphasizing that the proof of asymptotic freedom and confinement shown in this section is based on perturbative arguments. A fully non-perturbative demonstration has not been carried out, and a rigorous proof is one of the holy grails of mathematics [45]. Still, a vast amount of experimental data has been gathered during the last decades, showing convincing evidence of these properties.

1.1.2 Chiral symmetry and the hadron spectrum

To explain how quarks combine into hadrons and why these hadrons organize into the geometric patterns predicted by the quark model, we need to introduce one last approximate symmetry of QCD, *chiral symmetry*, and how it is spontaneously broken at low energies. We consider first the massless limit of QCD, in which the fermion Lagrangian reads,

$$\mathcal{L}_F = \sum_{f=1}^{N_f} \bar{q}_f i\gamma_\mu (\partial_\mu - igA^\mu) q_f. \quad (1.14)$$

In this limit, QCD is invariant under the following global vector and axial transformations,

$$G = \text{SU}(N_f)_V \times \text{SU}(N_f)_A \times \text{U}(1)_V \times \text{U}(1)_A, \quad (1.15)$$

which defines the chiral symmetry group. This acts on quark fields as

$$\begin{aligned} q &\xrightarrow{\text{SU}(N_f)_V} \exp(i\alpha_V^a t^a) q, & q &\xrightarrow{\text{U}(1)_V} \exp(i\alpha_V) q, \\ q &\xrightarrow{\text{SU}(N_f)_A} \exp(i\gamma_5 \alpha_A^a t^a) q, & q &\xrightarrow{\text{U}(1)_A} \exp(i\gamma_5 \alpha_V) q. \end{aligned} \quad (1.16)$$

where $\gamma_5 = i\gamma_0\gamma_1\gamma_2\gamma_3$, t_a here are the generators of the $\text{SU}(N_f)$ group acting in flavor space and quark fields are to be understood as a vector in the space of all flavors. While these transformation properties are reminiscent of gauge transformations shown in eq. (1.8), now we are considering global transformations, and so $\alpha_{A,V}^a$ and $\alpha_{A,V}$ are constants independent of the spacetime coordinates. The invariance of massless QCD under chiral transformations implies that a quark mass term cannot be generated by quantum corrections, and so quark masses only renormalize multiplicatively.

At low energies, however, chiral symmetry is not realized. An axial $\text{SU}(N_f)$ transformation would map a hadron to another one of opposite chirality, and so the hadron spectrum will be composed of pairs of mass-degenerate particles, which are not observed in nature. The reality is that chiral symmetry is spontaneously broken below the QCD scale to its vector component,

$$G \longrightarrow H = \text{SU}(N_f)_V \times \text{U}(1)_V, \quad (1.17)$$

with an order parameter given by the quark condensate,

$$\Sigma = \langle 0 | \bar{q}q | 0 \rangle \sim \Lambda_{\text{QCD}} \neq 0. \quad (1.18)$$

The $\text{U}(1)$ part of the unbroken symmetry group corresponds to the baryon number,³ while $\text{SU}(N_f)_V$ corresponds to the so called *isospin symmetry*. Low-lying hadrons organize into different irreps of the latter, with definite isospin

³Note that baryon number, B , is not conserved in the electroweak sector of the Standard Model. Still, $B - L$ remains a global symmetry, where L is the lepton number.

quantum numbers, as discussed later. These refer to total isospin, its third component, as well as strangeness and charmness.

According to Goldstone theorem [46–48], a spontaneously broken continuous symmetry implies the existence of massless particles, known as Nambu-Goldstone bosons (NGB), in a number equal to that of the generators of the broken group. In the case of chiral symmetry, these particles are the pseudoscalar mesons, generated by acting on the vacuum with the Noether charges of the $SU(N_f)_A$ symmetry. At the classical level, there is also another boson—the η' —associated to the $U(1)_A$ broken symmetry. However, as we will discuss below, this symmetry is additionally broken by quantum effects, i.e., it is anomalous [49, 50].

Before that, we consider massive quarks. Adding a mass term to eq. (1.14) explicitly breaks chiral symmetry. However, not all quarks have the same mass. In the case of up and down quarks, their masses are very similar and much smaller than Λ_{QCD} , this is, $m_u \approx m_d \ll \Lambda_{\text{QCD}}$. If we focus on $N_f = 2$ QCD, chiral symmetry is approximately realized. Hadrons are still organized according to the isospin irreps and pseudoscalar mesons (the pions, π) are associated to the spontaneous breaking of $SU(2)_A$. Now, however, they are massive pseudo-Nambu Goldstone bosons (pNGB), with a mass

$$M_\pi^2 \sim m_{u,d} \Lambda_{\text{QCD}}. \quad (1.19)$$

which is still much smaller than that of other hadrons, such as the proton, $M_\pi \approx 135 \text{ MeV} \ll M_p \approx 935 \text{ MeV}$. Thus, chiral symmetry is key to understand the lightness of the pions in nature.

If one considers the strange quark, similar arguments also apply, as $m_s < \Lambda_{\text{QCD}}$. However, in this case the effects breaking chiral symmetry are larger and, as a result, the pseudoscalar mesons containing a strange quark (the kaons, K) are more massive than the pions, $M_K = 435 \text{ MeV}$. In the case of heavier quarks, such as the charm or the bottom, these argument does not hold, as $m_c, m_b > \Lambda_{\text{QCD}}$. However, if one considers a hypothetical scenario in which there are N_f light quarks, the conclusions presented here would still hold. This is the base of one of the main research works presented in this doctoral thesis—see chapters 3 and 4.

We can now come back to the $U(1)_A$ symmetry, which is broken by the chiral anomaly [51–53]. The corresponding Noether current, \mathcal{J}_A^μ is not conserved, but couples to the topological charge of QCD,

$$\partial_\mu \mathcal{J}_A^\mu = -N_f \frac{g^2}{16\pi^2} \text{tr} [F_{\mu\nu} \tilde{F}^{\mu\nu}], \quad (1.20)$$

which can also be derived from the change in the measure of the path integral under a $U(1)_A$ transformation [54].

The anomalous breaking of the $U(1)_A$ symmetry implies that the associated pNGB, the η' particle, is much more massive than the other pseudoscalar mesons [55] with a mass $M_{\eta'} = 910$ MeV. In the limit of large number of colors—see sec. 1.3—Witten and Veneziano derived a relation between the mass of the η' and that of the pions [56, 57], the so-called *Witten-Veneziano formula*,

$$M_{\eta'}^2 = 2M_K^2 - M_\eta^2 + \frac{2N_f}{F_\pi^2} \chi_{\text{top}}, \quad (1.21)$$

where F_π is the pion decay constant⁴, M_η is the mass of the η meson and χ_{top} is the topological susceptibility of the pure gauge theory. This is defined as an integral of the two-point function of the topological charge operator over the whole spacetime, evaluated in the pure Yang-Mills theory ($N_f = 0$),

$$\chi_{\text{top}} = \int d^4x \langle q(x)q(0) \rangle_{N_f=0}, \quad (1.22)$$

where $q(x)$ is the topological charge operator,

$$q(x) = \frac{g}{32\pi^2 N_c} \text{Tr} [F_{\mu\nu} \tilde{F}^{\mu\nu}]. \quad (1.23)$$

As already mentioned, hadrons are classified in multiplets that correspond to the different irreps of the approximate $SU(N_f)_V$ isospin symmetry. From eq. (1.16), it is clear that quarks transform in the fundamental irrep of the isospin group, while antiquarks transform in the antifundamental irrep. Hadrons are thus classified in the different irreps arising from the combination of quarks and antiquarks forming color singlets. Consider for example the real-world case with $N_f = 3$. Mesons are composed by a quark and an antiquark and so they form an octet and a singlet,

$$3 \otimes \bar{3} = 8 \oplus 1, \quad (1.24)$$

where each irrep is labelled by its dimension and the overline refers to the antifundamental representation. In the case of pseudoscalar mesons, the octet is the Eightfold way [18, 19] and the singlet corresponds to the η' . This classification is also valid for other mesons formed of a quark and an antiquark, such as vector mesons. In the case of baryons, composed by three quarks, we get a singlet, two octets and a decuplet,

$$3 \otimes 3 \otimes 3 = 10 \oplus 8 \oplus 8 \oplus 1. \quad (1.25)$$

The proton and the neutron lie in one of the octets, while other baryons, such as the Δ baryons and the Ω^- lie in the decuplet. This classification is the theoretical basis underlying the quark model.

⁴We use the convention in which $F_\pi \approx 92.3$ MeV in the real world.

1.2 QCD on the lattice

In QCD, as in any other quantum field theory, predictions of physical observables are extracted from the computation of expectation values of gauge-invariant operators. These can be determined using the path integral formalism, based on Feynman's approach to quantum mechanics [58]. The expectation value of some operator O is computed as an integral over all possible field configurations,

$$\langle O[q, \bar{q}, A] \rangle = \frac{1}{\mathcal{Z}} \int \mathcal{D}q \mathcal{D}\bar{q} \mathcal{D}A O[q, \bar{q}, A] e^{iS_{\text{QCD}}[q, \bar{q}, A]}, \quad (1.26)$$

where $\mathcal{Z} = \langle \mathbb{1} \rangle$ is the partition function and S_{QCD} is the QCD action from eq. (1.1).

The path-integral formalism provides a method to determine any physical observable. However, its practical utility is limited by its degree of complexity. In many cases, physical predictions are obtained using perturbation theory, which is based on an asymptotic expansion in the interaction couplings. However, as we have seen in sec. 1.1.1, this is not an option for QCD at low energies.

The formulation of QCD on a discrete spacetime, better known as *lattice QCD*, is an alternative approach to the theory of strong interactions that makes it possible to compute expectation values of the form of eq. (1.26) by numerical methods. It was first proposed by Kenneth Wilson in the 1970s [59, 60], and has become the main approach to study the low-energy regime of QCD. For a detailed introduction to the topic see, for example, ref. [61].

Lattice QCD relies on the computation of the path integral in a finite volume and Euclidean time via the discretization of the spacetime, that turns the infinite-dimensional path integral into a finite-dimensional one. Typically, we work with lattices of the form

$$\Lambda \in \{a(n_0, n_1, n_2, n_3) \mid n_\mu \in \mathbb{Z}, 0 \leq n_0 < T/a, 0 \leq n_i < L/a\}, \quad (1.27)$$

where L and T are the space and time extents of the lattice, and a is the lattice spacing, which also acts as a ultraviolet regulator of the theory. After rotating to Euclidean time, $t_E = -it$, and working in the all-plus Euclidean metric, $g_{\mu\nu} = \text{diag}(+1, +1, +1, +1)$, eq. (1.26) takes the form

$$\langle O[q, \bar{q}, A] \rangle = \int \left[\prod_{x \in \Lambda} dq(x) d\bar{q}(x) dA(x) \right] O_E[q, \bar{q}, A] \frac{1}{\mathcal{Z}} e^{-S_{\text{QCD}}^{E,a}[q, \bar{q}, A]}, \quad (1.28)$$

where $S_{\text{QCD}}^{E,a}$ denotes the discretized Euclidean QCD action—see sec. 1.2.1—and O_E indicates the Euclidean-time operator. The use of a finite volume

also has the implication that the values of momenta allowed in the lattice are quantized, with their particular form depending on the choice of boundary. In the most common case of periodic boundary conditions, the allowed three-momenta are

$$\mathbf{k} = \frac{2\pi}{L} \mathbf{n}, \quad (1.29)$$

where $\mathbf{n} \in \mathbb{Z}^3$.

A direct evaluation of eq. (1.28) would still require of the computation of a large number of nested integrals. The introduction of an Euclidean time makes the exponential factor real, which can then be interpreted as a probability distribution, with normalization \mathcal{Z} . This allows the evaluation of the path integral using Markov chain Monte Carlo techniques [62, 63],

$$\langle O[q, \bar{q}, A] \rangle = \frac{1}{N_{\text{conf}}} \sum_{i=1}^{N_{\text{conf}}} O[q_i, \bar{q}_i, A_i] + \mathcal{O}(N_{\text{conf}}^{-1/2}), \quad (1.30)$$

where the sum is performed over a number, N_{conf} , of field configurations, $\{q_i, \bar{q}_i, A_i\}$, distributed according to the probability distribution

$$\mathcal{P}\{q, \bar{q}, A\} \sim \frac{1}{\mathcal{Z}} \exp(-S_{\text{QCD}}^{\text{E},a}[q, \bar{q}, A]). \quad (1.31)$$

Field configurations following this distribution are generated using different techniques. At the present time, hybrid Monte Carlo algorithm is the state of the art for QCD computations [64]. In practice, generating configurations and subsequently computing observables is computationally very expensive and requires of the use of high-performance computing.

The use of sampling techniques implies that numerical results have a statistical uncertainty that can be, in principle, systematically improved by increasing statistics. On the other hand, the systematic error introduced by a finite lattice spacing or the finite volume can be reduced by extrapolations to the continuum or to infinite volume, respectively. A systematic uncertainty is unavoidable in these extrapolations and should be carefully quantified. It is usually said that lattice QCD is systematically improvable.

Finally, it is worth mentioning that computations on the lattice are not restricted to real-world QCD. The use of lattice techniques allows one to vary parameters of the theory. For example, one can consider unphysical quark masses—typical lattice simulations are performed at heavier-than-physical pion mass due to a cheaper computational cost—or different number of flavors. It also makes it possible to simulate other theories such as simple toy models or possible theories beyond the Standard Model. In the work presented in this dissertation, we exploit this possibility, using the lattice to study QCD as a function of the number of colors—see chapters 3 and 4—and to explore the (1+1)-dimensional $O(3)$ non-linear sigma model as a toy model for QCD—see chapter 7.

1.2.1 The QCD lattice action

The choice of a discretized action and operators plays a major role in lattice computations. It determines the symmetries of the discretized theory, and also has an impact on the size of discretization corrections. While these can be accounted for with a continuum extrapolation, one wants to ensure the systematic error induced by such extrapolation is as small as possible.

The simplest choice of a discretized QCD action is that of Wilson [59]. To guarantee gauge invariance, the $\mathfrak{su}(3)$ -valued A_μ fields are substituted by $SU(3)$ -valued *link variables*, $U_\mu = \exp(iagA_\mu)$. These are the parallel transporters between two adjacent point in the lattice. The Wilson gauge action is

$$S_G[U] = \frac{\beta}{N_c} \sum_{x \in \Lambda} \sum_{\mu < \nu} \text{Tr}[1 - \text{Re } P_{\mu\nu}(x)], \quad (1.32)$$

where $\beta = 2N_c/g^2$ and $P_{\mu\nu}(x)$ is the smallest Wilson loop, the *plaquette*,

$$P_{\mu\nu}(x) = U_\mu(x)U_\nu(x + a\hat{\mu})U_\mu(x + a\hat{\nu})^\dagger U_\nu(x)^\dagger, \quad (1.33)$$

where $\hat{\mu}$ is the unit vector in the μ direction, and similarly for $\hat{\nu}$. The action in eq. (1.32) is equivalent to the continuum one in eq. (1.5), up to errors of order $\mathcal{O}(a^2)$.

The fermionic Wilson action is given by

$$S_F[q, \bar{q}, U] = a^4 \sum_{x, y \in \Lambda} \bar{q}(x) D_W(x, y) q(y), \quad (1.34)$$

where $D_W(x, y)$ is the Wilson-Dirac operator,

$$D_W(x, y) = \left(m_f + \frac{4r}{a} \right) \delta_{xy} - \frac{1}{2a} \sum_{\mu} \left(\frac{r}{2} - \gamma_\mu \right) U_\mu(x) \delta_{x+a\hat{\mu}, y} + \left(\frac{r}{2} + \gamma_\mu \right) U_\mu^\dagger(x + a\hat{\mu}) \delta_{x-a\hat{\mu}, y}, \quad (1.35)$$

where r is a real constant. This action recovers the continuum one in the $a \rightarrow 0$ limit, although this discretization is not directly obtained from substituting the continuum covariant derivatives by gauge-transported finite differences. Instead, one also includes a $-(ra/2)\bar{q}\nabla^2 q$ operator, known as the Wilson term. The impact of this term can be seen from the quark propagator in the gauge-free case ($g = 0$),

$$D_{W, \text{free}}^{-1}(x, y) = S_{\text{free}}(x, y) = \frac{1}{L^3 T} \sum_k S_{\text{free}}(k) e^{ik(x-y)}, \quad (1.36)$$

with

$$S_{\text{free}}(k) = \frac{m_f + \frac{r}{2}\hat{k}^2 - i\gamma_\mu \bar{k}^\mu}{\left(m_f + \frac{r}{2}\hat{k}^2 \right)^2 + \bar{k}^2}, \quad (1.37)$$

where $\hat{k}_\mu = 2 \sin(k_\mu/2)$ and $\bar{k}_\mu = \sin k_\mu$. Without the Wilson term, $r = 0$, the propagator has poles not only at the center of the first Brillouin zone, $k = 0$, but also at the edges, where any $k_\mu = \pi/a$. This implies that the continuum theory describes $16 = 2^d$ fermions instead of one [65], where $d = 4$ is the number of spacetime dimensions. The fermion-doubling problem is solved by the addition of the Wilson term. Typically, $r = 1$ is chosen in lattice simulations.

However, the addition of the Wilson term breaks chiral symmetry. This implies that discretization errors in eq. (1.34) are $\mathcal{O}(a)$, and also that the quark masses renormalize additively. On general grounds, the Nielsen-Ninomiya no-go theorem [66, 67] states that it is not possible to find a local discrete Dirac operator with no doublers that respects continuum chiral symmetry.

Other fermion discretization have also been proposed to deal with the lack of chiral symmetry. These include staggered fermions [68], which possess an additional taste symmetry, domain-wall fermions [69], defined on a five-dimensional lattice, and non-local overlap fermions, which satisfy an exact modified chiral symmetry [70].

Improved actions

To perform a controlled continuum extrapolation, one needs discretization effects to be small. This can be reached by going to very fine and computationally expensive lattices, but also by redefining the lattice action and operators so that cutoff effects appear only at higher orders. These are the so-called *improved actions and operators*, and play a major role in reducing discretization effects, especially for the fermion action.

A systematic method to reduce discretization effects is the *Symanzik improvement program* [71, 72]. The key idea is to include a complete set of higher-dimensional terms in the definition of the lattice action and operators, which vanish in the continuum. Tuning the coefficients of these terms allows one to systematically subtract cutoff corrections of order a , a^2 and so on.

In the case of the fermion Wilson action in eq. (1.34), $\mathcal{O}(a)$ improvement can be obtained by adding a single dimension-five operator, known as the clover term [73],

$$S_{\text{F}}^{\text{imp}} = S_{\text{F}} + c_{\text{sw}} a^5 \sum_{x \in \Lambda} \sum_{\mu < \nu} \bar{q}(x) \frac{1}{2} \sigma_{\mu\nu} F_{\mu\nu}^{\text{clover}}(x) q(x), \quad (1.38)$$

where $\sigma_{\mu\nu} = [\gamma_\mu, \gamma_\nu]/2i$, $F_{\mu\nu}^{\text{clover}}$ is a clover-discretized version of the gauge field-strength tensor and c_{sw} is the Sheikholeslami-Wohlert coefficient. Note

that in order to guarantee $\mathcal{O}(a^2)$ corrections, the value of c_{sw} needs to be finely tuned. It can also be computed using lattice perturbation theory [74, 75]. For the standard Wilson action, its value is

$$c_{\text{sw}} = 1 + 0.2659g^2 + \mathcal{O}(g^4). \quad (1.39)$$

However, this perturbative result only ensures that the discretization effect can be at most $\mathcal{O}(ag)$. Full $\mathcal{O}(a^2)$ improvement requires a non-perturbative tuning of c_{sw} [76–78]. In addition, one has to complement these changes of the action with a suitable modification of the operators [79].

In the case of the gauge action, eq. (1.32) only presents $\mathcal{O}(a^2)$ corrections. Still, it is possible to reduce the observed size of these effects by the addition of dimension-six operators. Some versions of the improved action are the Lüscher-Weisz [80] or the Iwasaki [81, 82] gauge actions, which include terms corresponding to other types of Wilson loops bigger than the plaquette, such as rectangles, saddles or clovers.

In parallel to the Symanzik improvement, other methods also help at reducing discretization effects. This is the case of a using a *twisted mass* [83]—see ref. [84] for a review. In the case of an even number of degenerate quarks of mass m , the twisted mass is implemented by changing the bare quark mass,

$$m\mathbb{1} \rightarrow m\mathbb{1} + i\mu\gamma_5 T, \quad (1.40)$$

where T is a diagonal traceless matrix acting in flavor space with diagonal entries equal to ± 1 , and m and μ are the bare real and twisted masses, respectively. In the continuum this modification can be undone by a chiral rotation of the quark fields. However, in a discrete theory that does not preserve chiral symmetry, the modification leads to an alternative regularization.

A relevant case of a twisted action is that of maximal twist [85]. This is achieved when the renormalized real quark mass becomes zero, which can be checked numerically from the partially-conserved axial current. The twisted mass then plays the role of the quark mass. In this limit, $\mathcal{O}(a^2)$ improvement is achieved for some observables and the vector current is protected against renormalization, which allows one to numerically determine the pion decay constant from the correlator of two bare pseudoscalar currents.

The main disadvantage of using a twisted mass is that it explicitly breaks parity and isospin symmetry. This means pseudoscalar mesons become non-degenerate even in the case of degenerate quark masses. Although cutoff effects are $\mathcal{O}(a^2)$, they have been shown to become very large in certain cases [86, 87]. These effects can be reduced by further including a clover term in the action [88]—see eq. (1.38).

1.2.2 Computing correlation functions

Once a lattice action is chosen, a chain of correlated configurations can be generated and used to compute the desired expectation values. Typically, these are the correlation function, or correlators, of products of operators defined at different time slices, $O = O(t_1)O(t_2)\dots$. In this dissertation, we focus on two-point correlation functions, in which operators are defined at two times slices, called the *source* and the *sink*.

From the correlators, physical observables can be determined with some statistical error. To obtain the best estimate of this error, one needs to take into account the autocorrelations between field configurations [89]. A simpler alternative, which we use for the work presented in this dissertation, is to average correlated configurations into blocks which are assumed to be uncorrelated, and then use bootstrap [90] or jackknife resampling [91] for the analysis. Note that, in this case, one must explicitly check that the result is not affected by the block size.

How the correlation function is computed on each configuration depends on the operators themselves. In the case of purely gluonic operators, as well as for operators in scalar theories, one just evaluates the operators at different times, and computes the correlation function from their product.

When considering fermions, fermionic variables are first integrated over to rewrite the correlation function in terms of the fermion propagator, $S(x, y)$ [92]. As an example, let's consider a single π^+ interpolating operator with three-momentum \mathbf{p} ,

$$\pi^+(t, \mathbf{p}) = \sum_{\mathbf{x}} e^{-i\mathbf{p}\mathbf{x}} \bar{d}(t, \mathbf{x}) \gamma_5 u(t, \mathbf{x}), \quad (1.41)$$

where the sum is performed over all lattice sites at fixed time slice. The single-pion correlator can then be computed as

$$\langle \pi^+(t, \mathbf{p}) \pi^+(0, \mathbf{p})^\dagger \rangle = \sum_{\mathbf{x}, \mathbf{y}} e^{i\mathbf{p}(\mathbf{y}-\mathbf{x})} \langle \text{Tr}[S(\mathbf{y}, \mathbf{x}) S^\dagger(\mathbf{y}, \mathbf{x})] \rangle, \quad (1.42)$$

where $x = (0, \mathbf{x})$ and $y = (t, \mathbf{y})$ denote lattice sites, the trace runs over the color and spin indices, and we have used γ_5 -hermiticity⁵ to rewrite the right-hand side. Evaluating this correlator in a given configuration exactly would require to know $S(x, y)$ for all x and y , which is not possible, as the Dirac operator possess $\mathcal{O}(10^{10})$ rows and columns.

To circumvent this limitation, one computes the inverse of the Dirac operator acting on some chosen source vector, $\psi(x)$, by solving the system

⁵ $\gamma_5 S(x, y) \gamma_5 = S^\dagger(y, x)$.

of linear equations

$$\sum_{y,z} D(x,y)S(y,z)\psi(z) = \psi(x). \quad (1.43)$$

This usually involves some preconditioner [93, 94] that alleviates the computational cost and then the iterative application of some Krylov solver [95–97] until the desired precision is achieved.

The choice of source plays a central role in the computation of the correlation functions. In the example of the single pion, the simplest option is to use a point source. This means setting a single entry of ψ to one, associated to a fixed lattice site, color and spin. The computation of the desired correlation functions is achieved by combining several sources with other spin and color. Momentum can be selected by doing a Fourier transform in the sink coordinate, which corresponds to performing only the sum over \mathbf{y} in eq. (1.42). The statistical error of this observable can later be reduced by repeating the computation for different point sources at several lattice sites, for example over a coarse sublattice [98].

Another option, only valid for meson operators, is to use *stochastic sources* [99–101]. In this case, the components of ψ are either set to zero or to some random noise, $\xi(x)$, which enforces the correct sum over the source position, spin and color up to stochastic noise,

$$\xi_{s_1 c_1}(x_1)\xi_{s_2 c_2}(x_2)^\dagger = \delta_{x_1, x_2}\delta_{s_1, s_2}\delta_{c_1, c_2} + \mathcal{O}(N^{-1/2}). \quad (1.44)$$

where N is the number of non-zero elements of ψ . One possibility is to set the random noise in color and space, for a fixed time and spin, $\xi_c^i(\mathbf{x})$. This are the so-called *time- and spin-diluted stochastic sources*. The computation is repeated for several stochastic sources on each configuration to reduce the stochastic noise. For example, using time- and spin-diluted stochastic sources, the correlator function of a pion at rest takes the form

$$\langle \pi^+(t)\pi^+(0)^\dagger \rangle = \sum_{i=1}^N \sum_{c_1, c_2} \sum_{\mathbf{x}_1, \mathbf{x}_2, \mathbf{y}} \left\langle \text{Tr} \left\{ S(y, x_1)\xi_{c_1}^i(\mathbf{x}_1)S \left[(y, x_2)\xi_{c_2}^i(\mathbf{x}_2) \right]^\dagger \right\} \right\rangle, \quad (1.45)$$

where the spin indices are left implicit and both x_1 and x_2 have $t = 0$ time coordinate. In this expression, i labels different realizations of the stochastic noise, highlighting the need to average over several independent sources to obtain a sensible result.

The use of stochastic sources also makes it possible to project to definite momentum the operators at source. This can be achieved by multiplying each noise element of the source vectors by a Fourier factor, $\xi^{\mathbf{p}}(x) = e^{i\mathbf{p}x}\xi(x)$. After multiplying two noise vectors,

$$\xi_{s_1 c_1}^{\mathbf{p}_1}(x_1)^\dagger \xi_{s_2 c_2}^{\mathbf{p}_2}(x_2) = e^{i\mathbf{x}_1(\mathbf{p}_2 - \mathbf{p}_1)}\delta_{x_1, x_2}\delta_{s_1, s_2}\delta_{c_1, c_2} + \mathcal{O}(N^{-1/2}). \quad (1.46)$$

which is the Fourier factor of a meson with three-momentum $\mathbf{p} = \mathbf{p}_2 - \mathbf{p}_1$. Naively, this requires to invert the Dirac operator for each value of the quark momentum. However for computations that aim to study operators with several momenta, one can reduce the number of required inversions by wisely choosing the quark momenta so that all the desired meson momenta can be reconstructed.

A more sophisticated option is to use smeared sources [102–104], or the eigenvalues of the Laplacian or Heaviside operator of three-dimensionally smeared fields [105, 106]. This latter possibility is commonly known as *distillation*.

1.2.3 Physical observables from lattice correlators

From the Euclidean correlation functions computed in a finite volume, we can determine finite-volume energies and matrix elements. If we focus on two-point correlation functions, their spectral decomposition takes the form

$$\langle O(t)O^\dagger(0) \rangle = \frac{1}{\mathcal{Z}} \text{Tr} \left[e^{-tH} O(t) O^\dagger(0) \right] = \sum_n |\langle 0|O(0)|n \rangle|^2 e^{-E_n|t|}, \quad (1.47)$$

where H is the Hamiltonian operator and $\mathcal{Z} = \text{Tr}[e^{-tH}]$ is the partition function. In the last step, we have considered, for simplicity, infinite time extent, $T \rightarrow \infty$ and used time-translation invariance to set the source at $t = 0$. The sum is performed over all states $|n\rangle$ in the Fock space of the theory, with energy E_n . Most of these states, however, have different quantum numbers from the studied operator, and so do not overlap onto it, $O(0)|n\rangle = 0$. Note that set of all states in the theory is discrete, due to the theory being defined in a finite volume. Typically, one furthermore assumes that the states with non-zero overlap are non-degenerate.

If the correlation function could be determined for any Euclidean time with infinite precision, it would be possible to determine the real-time correlation functions by analytic continuation. However, as we only possess a finite number of noisy data points, this becomes an ill-posed problem. Still, the energies and matrix elements appearing in the spectral decomposition are physical quantities, provided the operators are properly renormalized.

The values of these energies and matrix elements can be determined from fitting the lattice results. The fit is performed at late enough times, $t/a \gg 1$, so that only the lowest-lying states survive, but early enough so that statistical noise is small [107, 108]. Typically, the fit function is a single or a sum of exponentials. The fit is repeated for several fit ranges and the results are obtained from the ranges that show a plateau in the fitted results.

The time range is typically chosen by visual inspection. Recently, it has also become common to use weights based on Bayesian arguments [109–111] to average the results from different fit ranges. The set of results to average can be those obtained for all possible fits, or only a subset that are found to lie close to the plateau. In the first case, one expects that the averaged result coincides with the plateau.

The use of Bayesian weights allows one to obtain the final mean result as a weighted average and the final variance as the combination of a statistical and a systematic contributions. For example, let $\{a_i\}$ be the results for some quantity for different fit ranges, with variances $\{\sigma_{a,i}^2\}$ and corresponding weights $\{w_i\}$. The weighted mean is

$$\langle a \rangle = \sum_i a_i w_i, \quad (1.48)$$

while the total variance becomes

$$\sigma_a^2 = \sigma_{a,\text{stat}}^2 + \sigma_{a,\text{syst}}^2, \quad (1.49)$$

where the statistical and systematic contributions to the variance are, respectively,

$$\begin{aligned} \sigma_{a,\text{stat}}^2 &= \sum_i \sigma_{a,i}^2, \\ \sigma_{a,\text{syst}}^2 &= \sum_i a_i^2 w_i - \left(\sum_i a_i w_i \right)^2. \end{aligned} \quad (1.50)$$

The simplest weight choice is

$$w_i \propto \exp \left[-\frac{1}{2} \left(\chi_i^2 - 2N_i + 2N_{\text{par}} \right) \right], \quad (1.51)$$

where χ_i^2 is the chi-square of the fit of sample i , N_i is the number of fitted points and N_{par} the number of parameters in the fit function. Note that this method also makes it possible to compare between different fit functions.

One of the obstacles in the extraction of finite-volume energies and matrix elements is that, in principle, all states of the Fock space contribute to the spectral decomposition. However, the operators can be chosen to minimize the number of states contributing. For example, one can use some operator having the same transformation properties under C and P as the state of interest. Also, one typically projects to definite total momentum.

One also wants to define operators having the correct spin and angular momentum quantum numbers. However, the lattice itself breaks rotation invariance. Instead, the finite-volume theory has a discrete cubic symmetry, and operators can be projected into irreps, Λ , of the cubic group or of the

relevant little group in case of non-zero total momentum, \mathcal{G} . This is done using the formula [112, 113],

$$O^{\Lambda\lambda}(t) \propto \sum_{R \in \mathcal{G}} \Gamma_{\lambda\lambda}^{(\Lambda)}(R) U_R O(t) U_R^\dagger, \quad (1.52)$$

where R denotes the elements of \mathcal{G} , U_R is the operator that applies the transformation R to O and $\Gamma^{(\Lambda)}(R)$ is the representation of R in the irrep Λ . The index λ indicates the component in those irreps that have more than one dimension, and is not summed over in eq. (1.52). Note that each irrep Λ contains contributions coming from different total angular momenta [112–114].

Another of the limitations in the extraction of finite-volume results comes from using a single operator. In this case, one can only reliably extract the energies of the lowest lying state and the fit range is limited by excited-state contamination. This problem can be sorted out by computing the matrix of correlators between a set of operators, $\{O_i\}_{i=1}^N$,

$$C_{ij}(t) = \langle O_i(t) O_j^\dagger(0) \rangle. \quad (1.53)$$

This can then be used to solve a generalized eigenvalue problem (GEVP) [114, 115],

$$C(t)v_n = \lambda_n(t, t_0)C(t_0)v_n. \quad (1.54)$$

The eigenvalues of the GEVP are in general of the form

$$\lambda_n \propto e^{-E_n(t-t_0)} \left\{ 1 + \mathcal{O} \left[e^{-(E_m-E_n)t} \right] \right\}, \quad (1.55)$$

where E_n indicates the n -th lowest finite-volume energy. Corrections to this asymptotic behaviour, as indicated, depend on the energy separation between energy levels [114]. However, if one solves the GEVP with $t \leq 2t_0$, these correction are dominated by the distance to the $N + 1$ state [115],

$$\lambda_n \propto e^{-E_n(t-t_0)} + \mathcal{O} \left[e^{-(E_{N+1}-E_n)t} \right]. \quad (1.56)$$

The eigenvectors, on the other hand, are related to the overlaps of the operators onto the different states,

$$C(t_0)v_n = Z_n^i e^{-E_n t_0}, \quad (1.57)$$

where $Z_n^i = \langle 0 | O_i(0) | n \rangle$.

The finite-volume energies and matrix elements extracted from correlation functions can be used to constrain physical observables. In some cases, they are themselves very close to quantities of interest that can be measured experimentally. For example, if $O(t)$ is a single-pion operator with zero total

momentum, the lowest energy is the finite-volume pion mass. From an all-order perturbation theory study [116], it is known to be equal to its infinite-volume counterparts up to exponentially-suppressed volume corrections. In the case of the pion mass, these volume effects are known from chiral perturbation theory, which is introduced in sec. 1.4.1, and can be subtracted. At leading order [117, 118],

$$M_\pi(L) = M_\pi \left[1 + \frac{1}{2N_f} \frac{M_\pi^2}{(4\pi F_\pi)^2} g_1(M_\pi L) \right] + \dots, \quad (1.58)$$

with

$$g(x) = \sum_{\mathbf{n} \in \mathbb{Z}^3} \frac{4}{|\mathbf{n}|x} K_1(|\mathbf{n}|x), \quad (1.59)$$

where $K_1(x)$ is the modified Bessel function of the second kind, which decays exponentially for $x \gg 1$. Similar results also exist for the pion decay constant [118, 119]. In the practice, several lattice computation are performed at different volumes and these perturbative results are used as an ansatz for infinite-volume extrapolations.

In other cases, however, finite-volume quantities are not directly related to physical observables. This is the case, for example, of multiparticle processes. Scattering amplitudes and decay widths are intrinsically real-time quantities defined in infinite volume, and so do not have an analogue in the Euclidean finite volume. Still, it is possible to constrain them using the finite-volume energy spectrum. The formalisms that make it possible to do so in the case of two- and three-particle systems is discussed in detail in sec. 2.3 and plays a central role in the work presented in this dissertation.

1.2.4 Thermal effects

In realistic simulations the time extent of the lattice is not infinite. It is not always possible to use lattices with $M_\pi T \gg 1$, and so one needs to take finite- T effects into account. These are the so-called *thermal effects*. For finite T , we can write the spectral decomposition as

$$C(t) = \langle O(t)O(0)^\dagger \rangle = \frac{1}{\mathcal{Z}} \text{Tr} \left[e^{-TH} O(t) O^\dagger(0) \right] = \frac{1}{\mathcal{Z}} \sum_{n,m} |Z_{nm}|^2 e^{-E_n T} e^{(E_n - E_m)t}, \quad (1.60)$$

where $\mathcal{Z} = \text{Tr}[\exp(-TH)]$ is the partition function, H is the Hamiltonian operator and $Z_{nm} = \langle n|O(0)|m \rangle$. Compared to eq. (1.47), the sum now runs over all possible pairs of states (n, m) , which leads to many new terms in

the sum. If we assume Hermitian operators that have no vacuum quantum numbers, these terms can be classified in two groups.

First, there are terms in which one of the states is the vacuum, this is, $|n\rangle = |0\rangle$ or $|m\rangle = |0\rangle$. These correspond, respectively, to forward and backward propagation of the physical states of interest. The combined contribution to the correlation function takes the form

$$C_{m=0}(t) \supset \frac{1}{Z} \sum_n |Z_{n0}|^2 e^{-E_n T/2} \cosh \left[E_n \left(t - \frac{T}{2} \right) \right]. \quad (1.61)$$

These contributions are analogous to those in eq. (1.47), but appear with a different functional dependence on the energies. Still, if these were the only terms present one could use the techniques presented in the previous section, including the GEVP, to extract the finite-volume energies, with the only difference being the use of a distinct fit function, i.e., a hyperbolic cosine instead of an exponential.

The second set of terms in eq. (1.60) are those for which both $n, m \neq 0$. These terms depend on the energy difference of two states, none of which is the state of interest. For example, if we are interested in two-particle states, the dominant contamination is related to single-particle states. If we assume one of these terms dominates, depending on some energy difference ΔE , and neglect the backpropagating contamination discussed above, the correlation function takes the form

$$C(t) = \sum_n |Z_{n0}|^2 e^{-E_n t} + B e^{-\Delta E t}, \quad (1.62)$$

where B is some unspecified amplitude. This contamination can be removed by performing a weight-shifting [112],

$$C(t) \rightarrow C(t) - e^{\Delta E} C(t+1). \quad (1.63)$$

Multiplying the correlator by the exponential factor shifts the time dependence of the last term in eq. (1.62), so that one can completely cancel it by computing the variation of the correlator. We note that this method can be extended to the case in which backpropagating thermal effects are also considered, although this sometimes needs of some approximations. This is discussed in sec. 4.2.

1.3 The 't Hooft limit of QCD

The *'t Hooft* or *large N_c limit* of QCD is an alternative approach to the low-energy regime of strong interactions [120]. It is the limit in which the number of colors is taken to infinity, $N_c \rightarrow \infty$, while the number of quark flavors is kept constant, $N_f = \text{const}$. The limit constitutes a simplification of the theory of strong interactions that keeps most of its non-perturbative features and allows one to make predictions as a power series in $1/N_c$. For a review on the 't Hooft limit—see ref. [121].

To define a sensible $1/N_c$ expansion, the coupling constant of QCD is rescaled, $g \rightarrow g/\sqrt{N_c}$. The β -function becomes

$$\beta(\alpha_s) = \mu \frac{d\alpha_s}{d\mu} = -\frac{\alpha_s^2}{2\pi} \left(\frac{11}{3} - \frac{2}{3} \frac{N_f}{N_c} \right) + \mathcal{O}(\alpha_s^3), \quad (1.64)$$

so $\beta(\alpha_s) < 0$ at large N_c , and so the large N_c theory is asymptotically free. This also means that we expect the theory to be confining at low energies. Indeed, QCD becomes a theory of non-interacting narrow resonances and glueballs at large N_c [120, 122, 123].

The large N_c limit makes it possible to characterize the N_c and N_f dependence of physical observables, and can also be used to make qualitative and some quantitative predictions of hadron physics. However, quantitative predictions are not possible beyond leading order in N_c , since subleading N_c corrections are hard to estimate analytically. The lattice regularization provides with a tool to study them from first principles by simulating at different N_c —see ref. [124] for a recent review. Studying these effects, in the context of two-mesons systems, has been one of the main focuses of my doctoral work—see chapters 3 and 4.

The N_c and N_f dependence of physical observables can be derived from the study of Feynman diagrams, rewritten using 't Hooft double-line notation that makes the color propagation explicit. The quark propagator is kept as a single directed line, while gluon propagators are substituted by two lines with opposite orientation.⁶ Interactions vertices are transformed in accordance—see fig. 1.1. The N_c and N_f dependence of vacuum diagrams can then be determined. Each color loop amounts to a factor of N_c , each coupling constant introduces a factor of $1/\sqrt{N_c}$ and finally each internal quark loop adds a factor of N_f . The scaling of a disconnected diagram is the product of the scaling of each separate connected piece.

⁶This substitution is based on the $U(N_c)$ gluon propagator. However, the difference between $U(N_c)$ and $SU(N_c)$ is in general $\mathcal{O}(N_c^{-2})$.

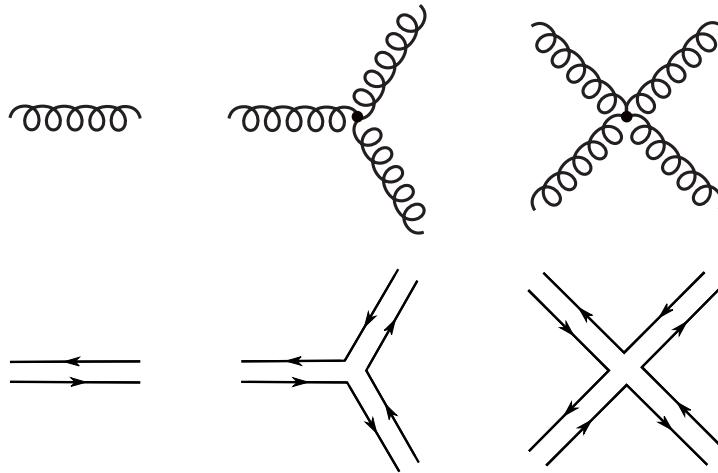


Figure 1.1. Schematic representation of the gluon propagator and self-interacting vertices in the standard (top row) and double-line (bottom row) notation.

The N_c counting can be given a geometric interpretation. Diagrams drawn using the double-line notation can be regarded as surfaces. Color loops represent polygons which are glued together by the gluon propagators, and quark loops, both internal and external, can be regarded as the boundaries of this surface. The N_c dependence of a given vacuum diagram is then N_c^χ , where χ is the Euler character of the surface. This number can be computed from the number of vertices, V , edges, E , and faces, F , of the surface, $\chi = V - E + F$. The leading order contributions originate from planar diagrams. Purely gluonic ones scale as $\mathcal{O}(N_c^2)$, and those containing quarks are $\mathcal{O}(N_c)$. It is commonly said that the 't Hooft limit of QCD is a limit of planar diagrams.

Alternative large N_c limits of QCD also exist. These include the Veneziano limit [57], in which $N_c \rightarrow \infty$ while keeping the ratio N_f/N_c constant, and a variation of the 't Hooft limit in which quarks are kept in the antifundamental irrep of $SU(N_c)$, that is isomorphic to the fundamental irrep for $N_c = 3$ [125–128]. The latter is relevant due to its relation to string theories [129, 130]. Moreover, the large N_c limit has also been used to study other theories, such as (1+1)-dimensional QCD [131] or QCD in the limit of heavy quarks [122], in which it makes quantitative computations. possible

1.3.1 Ordinary hadrons at large N_c

The nature and interactions of hadrons can be studied using the 't Hooft limit. With the large N_c counting introduced above, one can determine the N_c scaling of the chiral condensate,

$$\Sigma = -\langle \bar{q}(x)q(x) \rangle \propto N_c. \quad (1.65)$$

Therefore, spontaneous chiral symmetry breaking holds at large N_c , and a low-lying spectrum of pseudoscalar mesons arises as the corresponding pNGB.

We can study the correlation function of mesons. Meson operators are fermion bilinears,

$$O_M(x) = \frac{1}{\sqrt{N_c}} \bar{q}(x) \Gamma T q(x), \quad (1.66)$$

where Γ is some combination of Dirac gamma matrices and T is some matrix in flavor space. The $\sqrt{N_c}$ normalization ensures that the meson correlator is of order unity, and so the mass of the mesons remains independent of N_c , $M_M \propto \mathcal{O}(N_c^0)$. One can in general study a connected n -meson correlation function,

$$\langle O_M(x_1) \dots O_M(x_n) \rangle_{\text{conn}} \sim N_c^{1-n/2}. \quad (1.67)$$

From this result, multiple conclusions can be extracted. First, the pion decay constant, defined as the two-point function of the axial current, scales as $F_\pi^2 \propto \mathcal{O}(N_c)$. Second, scattering processes are suppressed with N_c . In particular, the two-meson scattering amplitude scales as $\mathcal{M}_2 \propto \mathcal{O}(N_c^{-1})$. Similarly, decay amplitudes that originate from three-point functions, are suppressed as $N_c^{-1/2}$. One concludes that at large N_c , QCD becomes a non-interacting theory of infinite stable resonances [120, 122, 123].⁷ Similar arguments also hold for glueballs.

It is interesting to comment on the singlet meson. At large N_c the axial anomaly is suppressed as $\mathcal{O}(N_f/N_c)$, and so the spontaneous chiral symmetry breaking pattern in eq. (1.17) becomes

$$G = \text{U}(N_f)_V \times \text{U}(N_f)_A \longrightarrow H = \text{U}(N_f)_V. \quad (1.68)$$

Thus, at large N_c the singlet mesons become mass-degenerate with the remaining mesons. In the case of pseudoscalar mesons, this can be observed by looking at eq. (1.21). After the $g \rightarrow g/\sqrt{N_c}$ substitution and taking $N_c \rightarrow \infty$, the η' mesons becomes degenerate with the rest of pseudoscalars.

The 't Hooft limit can also be used to study baryons. Contrary to mesons, the number of composing quarks of baryons grows with N_c , as one needs to combine N_c quarks to create a color singlet. Thus, baryon masses grow as $M_B \propto \mathcal{O}(N_c)$. Still, one can define large N_c counting rules for baryon correlation functions, with predictive power in the baryon sector [122, 132–136].

⁷The fact that the number of resonance must be infinite can be seen from studying the logarithmic running of QCD correlation functions [121].

1.3.2 Tetraquarks at large N_c

Finally, we can comment about exotic tetraquark states at large N_c . The traditional picture, based on the views of Witten [122] and Coleman [123], is that these states do not exist in the 't Hooft limit. Their argument was based on the factorization property, according to which correlation functions of singlet operators factorize at large N_c ,

$$\langle O_1 O_2 \rangle = \langle O_1 \rangle \langle O_2 \rangle + \mathcal{O}(N_c^{-1}). \quad (1.69)$$

For example, in the case of tetraquarks, the correlation function of two local tetraquark operators, $\langle (\bar{q}q)^2 (\bar{q}q)^2 \rangle$, would decompose in the correlation functions of two non-interacting mesons.

This argument, however, was put in doubt by Weinberg [137]. The connected and the disconnected parts of the four-quark operator correlation function may describe different phenomena, and one is not necessarily a subleading correction to the other. While the disconnected part represents two non-interacting mesons at large N_c , tetraquarks could still arise from poles in the connected part, even if it is suppressed in N_c . Therefore, it is not possible to rule out the existence of tetraquarks at large N_c and, if they were present, their decay width would scale as $\Gamma \sim 1/N_c$, just as ordinary resonances.

This last point was later revisited in ref. [138], where it was shown that the scaling of Γ would depend on the flavor composition of the tetraquark. In particular, it was argued that open-flavor tetraquarks (those which do not contain a quark-antiquark pair of the same flavor), should scale as $\Gamma \sim 1/N_c^2$. This result was also discussed in ref. [139], in which they further argued against the existence of these states in the large N_c limit. The authors of this last reference also studied the existence of tetraquarks in the large N_c limit with quarks in the antifundamental irrep [140]. In this case, they managed to prove their existence with $\Gamma \sim 1/N_c^2$. One of the objectives of the work presented in this dissertation is to study the possible existence of these resonances for varying N_c using lattice simulations—see chapter 4.

1.4 Effective field theories

Another widely used technique to describe QCD at low energies is that of effective field theories (EFTs). EFTs are quantum field theories that describe the dynamics of those states in a theory with masses below some cutoff scale, Λ , at energies $E \ll \Lambda$. Even if the theory contains heavier states in the spectrum, their effect at these low energies appears in the form of

higher-dimensional operators. EFTs are therefore non-renormalizable, but are predictive at fixed order in E/Λ .

The EFT Lagrangian is the most general Lagrangian consistent with the symmetries of the underlying theory, with which one is able to determine [141] “the most general matrix elements consistent with Lorentz invariance, quantum mechanics, unitarity, cluster decomposition and the assumed symmetries.” The Lagrangian thus contains an infinite number of terms which appear multiplied by some unknown coefficients, known as *Wilson coefficients* or *low energy constants* (LECs). Despite having an infinite number of terms, EFTs still have predictive power. The operators in the Lagrangian can be organized depending on their energy dimension, so they contribute to processes at different orders in E/Λ . While this limits us to a finite precision, as more and more terms are needed to increase the accuracy of the result, EFTs are able to provide realistic predictions which can be compared against experiment.

The use of EFTs is widely extended in theoretical physics. Fermi’s theory has been used to describe weak decays [142] and the Euler-Heisenberg’s Lagrangian allows one to describe low-energy electron-photon scattering [143]. EFTs are even used to treat the Standard Model as the low-energy limit of a more fundamental high-energy theory, the so-called Standard Model EFT [144]. In this thesis, we focus on the paradigmatic chiral perturbation theory [141, 145–147], that describes the low-energy regime of QCD in terms of the lightest pseudoscalar mesons—see refs. [148, 149] for reviews. We also explain how this theory can be modified to study the large N_c limit of QCD. Further extensions exist that include baryons [150, 151], heavy mesons [152] and even the effect of a lattice spacing and a twisted mass [86, 153, 154] for application in lattice QCD.

1.4.1 Chiral Perturbation Theory

Chiral perturbation theory (ChPT) is an EFT that describes the low-energy regime of QCD in terms of the lightest non-singlet multiplet of pseudoscalar mesons. The ChPT Lagrangian is the most general CP -invariant Lagrangian consistent with spontaneous chiral symmetry breaking, see eq. (1.17). The basic building block of the ChPT Lagrangian is a representative element of the coset space, G/H , where the coordinates on this space represent the pNGB of the theory. A typical parametrization of this object is given in terms of the $N_f \times N_f$ unitary matrix,

$$U(x) = \exp \left[i \frac{\phi(x)}{F} \right], \quad (1.70)$$

where F is the bare pion decay constant and ϕ is a traceless matrix containing the pseudoscalar mesons. For example, for $N_f = 3$, it reads

$$\phi \equiv \begin{pmatrix} \pi^0 + \frac{1}{\sqrt{3}}\eta & -\sqrt{2}\pi^+ & -\sqrt{2}K^+ \\ \sqrt{2}\pi^- & -\pi^0 + \frac{1}{\sqrt{3}}\eta & -\sqrt{2}K^0 \\ \sqrt{2}K^- & \sqrt{2}\bar{K}^0 & -\frac{2}{\sqrt{3}}\eta \end{pmatrix}. \quad (1.71)$$

Under a chiral transformation, $U(x)$ transforms non-linearly,

$$U(x) \rightarrow RU(x)L^\dagger, \quad (1.72)$$

where $L, R \in \text{SU}(N_f)$. This construction intrinsically reproduces the consequences of spontaneous chiral symmetry breaking. The ground state of the theory, $U_0 = \mathbb{1}$, is invariant under the unbroken group, that corresponds to vector transformations with $R = L$, but not under axial-vector ones, with $L = R^\dagger$.

The most general chirally-invariant effective Lagrangian that can be build with the matrix $U(x)$ contains an infinite number of terms, which can be ordered in increasing powers of momentum, or, in other words, of the number of derivatives.⁸ At lowest order, the Lagrangian is

$$\mathcal{L}_2 = \frac{F^2}{4} \text{Tr} [\partial_\mu U^\dagger \partial^\mu U], \quad (1.73)$$

where the prefactor is chosen to ensure that kinetic terms for the mesons have the correct normalization. Expanding in terms of the pion field, one obtains

$$\mathcal{L} = \frac{1}{2} \partial_\mu \pi^0 \partial^\mu \pi^0 + \partial_\mu \pi^+ \partial^\mu \pi^- + \dots \quad (1.74)$$

Here, ... represents all the remaining terms from the expansion. These are an infinite number of interaction operators, involving all even powers of the pion field. This lowest-order Lagrangian thus makes it possible to describe interactions between any number of pNGB at tree level in terms of a single parameter, F .

Up to this point, we have constructed an EFT for massless mesons. However, we would like to include the explicit breaking of chiral symmetry, and so the quark and meson masses. These are introduced in ChPT via a coupling to an external scalar classical field. Consider the mass term of the quarks in the QCD Lagrangian—see eq. (1.3)—as a spurious field, χ , that transforms under chiral transformations as

$$\chi \rightarrow R\chi L^\dagger, \quad (1.75)$$

⁸Note that the number of derivatives is always even due to parity conservation.

so that the mass term in the Lagrangian is chirally invariant. Then, we can build the EFT including this new spurious field, which is taken to be a constant diagonal matrix containing the quark masses. For example, $\chi = \text{diag}(m_u, m_d, m_s)$ for $N_f = 3$.

A similar method makes it possible to include couplings to external pseudoscalar, vector and axial classical background fields, which can be used to study electromagnetic and weak interactions. In particular, an analysis of the axial current in the EFT allows one to identify F as the pion decay constant, F_π , in the chiral limit. These external fields are also needed to define the Noether currents in the effective theory and the corresponding form factors.

The addition of quark masses requires a consistent power counting. In ChPT, the quark mass is taken to be of the same order as the pion mass squared and the momentum squared,

$$\mathcal{O}(\delta) \sim \mathcal{O}(m_q) \sim \mathcal{O}(p^2) \sim \mathcal{O}(M_\pi^2), \quad (1.76)$$

where δ denotes the expansion parameter. Then, the most general Lagrangian at lowest order now contains a second term,

$$\mathcal{L}_2 = \frac{F^2}{4} \text{Tr} [\partial_\mu U^\dagger \partial^\mu U] + \frac{BF^2}{2} \text{Tr} [\chi U^\dagger + \chi^\dagger U], \quad (1.77)$$

where B is a LEC related to the chiral condensate. Expanding the Lagrangian in terms of the pion fields, one gets the new terms

$$\mathcal{L}_2 \supset -\frac{1}{2}(m_u + m_d)B\pi^0\pi^0 + (m_u + m_d)B\pi^+\pi^- + \dots \quad (1.78)$$

from which the pion mass can be identified,

$$M_\pi^2 = B(m_u + m_d), \quad (1.79)$$

and justifies the power counting in eq. (1.76). We note that the actual range of applicability of ChPT depends on how this small scale compares to the high energy scale at which we recover QCD. Typically, one takes Λ to be the mass of the lowest-lying resonance, the $\rho(770)$, or uses a scale related to the pion decay constant, $4\pi F_\pi$. The latter is usually more convenient to compare against lattice computations, as then low energy observables are a function of

$$\xi = \frac{M_\pi^2}{(4\pi F_\pi)^2}, \quad (1.80)$$

commonly known as the *chiral parameter*.

To perform computations beyond leading order (LO), higher order Lagrangian terms need to be included. At next-to-leading order (NLO), one-loop diagrams from \mathcal{L}_2 induce divergencies that can only be reabsorbed

by operators of higher order [155]. The fourth-order Lagrangian contains a larger number of terms. If one only considers purely mesonic operators, there are 9 different terms for generic N_f ,

$$\mathcal{L}_4 = \sum_{i=0}^8 L_i(\mu) O_i[U(x), \chi, \partial_\mu]. \quad (1.81)$$

Owing to the Cayley-Hamilton theorem [156–158], the number of independent operators is reduced to 8 for $N_f = 3$ and to 4 for $N_f = 2$. Renormalized LECs, L_i^r , are defined after absorbing all one-loop divergencies. Note that LECs depend on the scale of the computation, μ . Their value at two different scales μ_1 and μ_2 is related by

$$L_i^r(\mu_2) = L_i^r(\mu_1) + \frac{\Gamma_i}{16\pi^2} \log\left(\frac{\mu_1}{\mu_2}\right), \quad (1.82)$$

where Γ_i are rational constants [146]. In the $N_f = 2$ case, it is typical to define some scale-independent LECs, $\bar{\ell}_i$, via

$$\ell_i^r(\mu) = \frac{\gamma_i}{32\pi^2} \left[\bar{\ell}_i + \log\frac{M_{\pi,\text{phys}}^2}{\mu^2} \right], \quad (1.83)$$

where ℓ_i^r and γ_i is the usual notation to denote the $N_f = 2$ LECs and their Γ -constants, respectively, and $M_{\pi,\text{phys}} \approx 139.57$ MeV is the physical pion mass.⁹

1.4.2 ChPT at large N_c

ChPT admits an extension to study meson interactions at large N_c [147, 159–165]. Recall from sec. 1.3 that in this limit, the spontaneous symmetry breaking pattern of chiral symmetry changes to that of eq. (1.68). The singlet mesons becomes another pNGB and needs to be included into the ChPT meson matrix,

$$\tilde{U}(x) = U(x) \exp\left(i \frac{\sqrt{2}\eta'(x)}{\sqrt{N_f}F}\right). \quad (1.84)$$

In addition, N_c and the η' mass are included in the power counting scheme,

$$\mathcal{O}(\delta) \sim \mathcal{O}(N_c^{-1}) \sim \mathcal{O}(M_{\eta'}^2). \quad (1.85)$$

⁹We will explicitly denote the physical pion mass and physical decay constant as $M_{\pi,\text{phys}}$ and $F_{\pi,\text{phys}}$, respectively, to distinguish them from their counterparts at non-physical quark masses, which is the typical scenario in lattice simulations.

This affects the order at which terms appear in the effective Lagrangian as LECs accompanying each operator scale as N_c^{1-r} , with r the number of flavor traces in the operator in question.

With this two modifications, one can construct the most general effective Lagrangian. The lowest order Lagrangian now has one additional term,

$$\mathcal{L}_2 = \frac{F^2}{4} \text{Tr} [\partial_\mu \tilde{U}^\dagger \partial^\mu \tilde{U}] + \frac{BF^2}{2} \text{Tr} [\chi \tilde{U}^\dagger + \chi^\dagger \tilde{U}] + \frac{F^2}{4N_f} M_0^2 X^2, \quad (1.86)$$

where $X(x) = \log \det \tilde{U} + \theta$, with θ the QCD vacuum angle. From this Lagrangian, we observe $F_\pi^2 \sim \mathcal{O}(N_c)$ while $B, \chi_{\text{top}} \sim \mathcal{O}(N_c^0)$. Moreover, this Lagrangian makes it possible to recover the Witten-Veneziano formula, eq. (1.21), provided the new low-energy coupling obeys, $M_0^2 = 2N_f \chi_{\text{top}}/N_c$.

In large N_c ChPT, terms analogous to those in eq. (1.81) get split in two different orders of the chiral expansion according to the scaling with N_c of the respective LECs. For $N_f \geq 4$ one has [121]

$$\mathcal{O}(N_c) : L_0, L_3, L_5, L_8, \quad \mathcal{O}(N_c^0) : L_1, L_2, L_4, L_6, L_7. \quad (1.87)$$

Thus, at NLO only tree diagrams including the $\mathcal{O}(N_c)$ LECs need to be considered, while those with $\mathcal{O}(N_c^0)$ LECs first enter at next-to-next-to-leading order (NNLO), together with one-loop diagrams from \mathcal{L}_2 . New operators involving the η' also appear at higher-order Lagrangians—see ref. [165].

Different phenomenological approaches have tried to determine the leading N_c dependence of the LECs. This is the case of the resonant chiral theory [166], in which ChPT is matched to a theory including heavy resonances and the LECs result from the exchange of these particles. The actual values of the LECs depend on the features of the assumed spectrum, as well as on the imposition of different positivity bounds.

Before concluding, two comments are in place. First, determining the N_c scaling of the LECs for $N_f = 2$ and 3 is not so straightforward. Due to Cayley-Hamilton relations, some two-trace operators have enhanced N_c dependence. For example, at $N_f = 3$, both L_1 and L_2 scale as N_c and only the combination $L_1 - 2L_2$ is $\mathcal{O}(N_c^0)$ [121].

Second, although we use the same notation to denote the $SU(N_f)$ and $U(N_f)$ LECs, they do not take the same values. Nevertheless, it is possible to match both theories by integrating out the η' . Assuming N_f degenerate quark flavors, one finds [167, 168]

$$\begin{aligned}
[L_6]_{\text{SU}(N_f)} &= [L_6]_{\text{U}(N_f)} + \frac{1}{16N_f^2(4\pi)^2}(\lambda_0 - 1), \\
[L_7]_{\text{SU}(N_f)} &= [L_7]_{\text{U}(N_f)} - \frac{F_\pi^2}{16N_f M_0^2}, \\
[L_8]_{\text{SU}(N_f)} &= [L_8]_{\text{U}(N_f)} - \frac{\lambda_0}{8N_f(4\pi)^2},
\end{aligned} \tag{1.88}$$

where $\lambda_0 = \log(M_0^2/\mu^2)$. We note that the values of the $\text{SU}(N_f)$ LECs depend implicitly on N_f . Thus, quantities computed in traditional ChPT cannot be expanded in the standard way in the large N_c limit, only with positive powers of N_f . In addition, in the $\text{SU}(N_f)$ theory, L_7 presents an enhanced dependence on the number of colors, $[L_7]_{\text{SU}(N_f)} \sim \mathcal{O}(N_c^2)$ [167].

2 Hadron interactions

QCD stands out from other quantum field theories due to its richness. At low energies, the phenomena of asymptotic freedom and confinement make a vast spectrum of hadrons emerge. The Particle Data Group [34] summarizes the properties of all experimentally observed hadrons. These include mesons, baryons, and other observed states that are suspected to have more a more exotic structure.

In spite of their large number, almost every hadron is unstable and cannot be directly observed in experiment. Even in the absence of electroweak interactions, most hadrons would rapidly decay into lighter ones, having a lifespan of less than 10^{-22} seconds in many cases. The properties of these unstable particles are instead inferred from the interactions of their byproducts.

The short lifetime of many hadrons make the study of their properties from QCD incredibly challenging. The lattice, meanwhile, is in principle precluded from the study of real-time infinite-volume processes, as is the case of hadron interactions or decays.

In this chapter, we discuss how hadron interactions can be studied using ChPT and lattice QCD. In sec. 2.1 we introduce the main concepts used to describe two- and three-particle scattering. We then explain, in sec. 2.2, how ChPT can be used to study interactions of pseudoscalar mesons and how it can be modified to allow for the presence of resonances. Finally, sec. 2.3 explains the two- and three-particle finite-volume formalisms, that allow one to constrain infinite-volume scattering observables from the finite-volume multiparticle energy spectrum determined in lattice QCD computations.

2.1 Particle scattering in infinite volume

Experimentally, particle interactions can only be probed indirectly. The paradigmatic particle-physics experiment characterizes interactions between particles by studying the properties of the initial (ingoing) and final (outgoing) asymptotic states. Particles in both the initial and final states are assumed to be separated enough that they can be considered non-interacting. The process in which the particles of some initial state interact, leading to a different final one is known as a *scattering process*.

Theoretically, ingoing and outgoing states are defined asymptotically as a set of free non-interacting particles in the infinite past and future, respectively. We refer to these two states as $|i\rangle$ and $|f\rangle$, in this same order. The scattering matrix, or S -matrix, is defined as the matrix containing the transition probabilities between any two states of a given theory,

$$S_{fi} = \langle f|i\rangle. \quad (2.1)$$

Therefore, it encodes all physical information that can be extracted from the quantum field theory. Due to conservation of probability, the S -matrix is unitary, $SS^\dagger = \mathbb{1}$.

Usually, one is interested in the non-trivial part of the scattering matrix, known as the scattering amplitude, \mathcal{M} . If we consider a Lorentz invariant theory, as is the case of QCD, we define

$$S_{fi} = \delta_{fi} + i(2\pi)^4 \delta^{(4)}(P_f - P_i) \mathcal{M}_{fi}, \quad (2.2)$$

where P_i and P_f refer to the total four-momentum of the initial and final states, respectively.

The analytic properties of the S -matrix play an essential role in the understanding of the underlying physics [169]. When considered as a function of the *center-of-mass frame* (CMF) energy, the S -matrix contains branch cuts on the real axis, with branching points at the thresholds of multiparticle states. In addition, it also contains isolated poles.

In the S -matrix, single-particle states appear as poles at some value of the energy in the CMF, E^* . Stable states correspond to poles on the real axis of the first Riemann sheet, and are either single hadrons, such as nucleons, or *bound states* that appear close to some multiparticle threshold, such as the deuteron. These states can exist asymptotically.

In addition, we have unstable states, which represent the majority of hadrons. These do not form part of the Fock space of QCD and cannot be defined asymptotically. Instead, their properties are inferred from the

scattering of stable states. In the S -matrix, unstable states correspond to poles on the second Riemann sheet. If the pole lies in the lower complex plane, $E^* = M - i\Gamma/2$, the particle is known as a *resonance*, with mass M and decay width Γ . This is for example the case of the $\rho(770)$ resonance. If the pole instead lies on the real axis below some multiparticle threshold, $E^* = M$, the state is known as a *virtual bound state*.

2.1.1 Two-particle scattering

We now consider two-particle interactions, and focus on the case in which all particles have equal mass m . Let $\{k_1, k_2\}$ and $\{p_1, p_2\}$ be the ingoing and outgoing momenta of the particles in the initial and final states, respectively. The total momenta is then $P = k_1 + k_2 = p_1 + p_2$. These are all on shell, this is, they obey the relativistic dispersion relation, $p_a^2 = k_a^2 = m^2$. The two-particle scattering amplitude can then be written as a function of the Mandelstam variables,

$$s = (k_1 + k_2)^2, \quad t = (k_1 - p_1)^2, \quad u = (k_1 - p_2)^2. \quad (2.3)$$

These are related as

$$s + t + u = 4m^2, \quad (2.4)$$

and so the two-particle scattering amplitude, \mathcal{M}_2 , can be written as a function of only two independent variables.¹ These variables are usually chosen to be s , related to the CMF energy, $s = E^{*2}$, and the scattering angle between the initial- and final-state particles three-momenta, θ , defined from

$$t = -4q_2^{*2} \sin^2 \frac{\theta}{2}, \quad (2.5)$$

where $q_2^* = \sqrt{s/4 - m^2}$ is the magnitude of the relative three-momentum in the CMF.

In rotational-invariant theories, as is the case of QCD, it is common to project \mathcal{M}_2 to definite angular momentum,

$$\mathcal{M}_2(s, \theta) = \sum_{\ell', m'} \sum_{\ell, m} 4\pi Y_{\ell' m'}^*(\theta) Y_{\ell m}(\theta) \delta_{\ell' \ell} \delta_{m' m} \mathcal{M}_{2, \ell}(s). \quad (2.6)$$

Here ℓ and m are the total angular momentum and the corresponding azimuthal component of the initial state, and primed quantities refer to the

¹This result stands from the difference between the number of free momenta components of the initial and final states and the number of generators of the Poincaré group, $12 - 10 = 2$.

final state. Note that for rotational invariant theories \mathcal{M}_2 does not depend on the azimuthal angular momentum.

For a given partial wave, the unitarity property of the S -matrix leads to constraints on the imaginary part of the scattering amplitude,

$$\rho(s)|\mathcal{M}_{2,\ell}(s)|^2 = \text{Im } \mathcal{M}_{2,\ell}(s), \quad (2.7)$$

where we have introduced the two-particle phase-space factor,

$$\rho(s) = \frac{q_2^*}{16\pi s}. \quad (2.8)$$

Eq. (2.7) is known as the *optical theorem*, and characterizes the analytic structure of $\mathcal{M}_{2,\ell}$. It makes it possible to separate $\mathcal{M}_{2,\ell}$ as

$$\mathcal{M}_{2,\ell}^{-1} = \mathcal{K}_{2,\ell}^{-1}(s) - i\rho(s), \quad (2.9)$$

where \mathcal{K}_2 is the two-particle K -matrix. Its components are meromorphic functions that take real values for physical kinematics (i.e., for $s > 0$). Eqs. (2.7) and (2.9) also make clear the presence of a square-root branch cut in the two-particle scattering amplitude, which has a kinematic origin.

From $\mathcal{K}_{2,\ell}$, one can define the scattering phase shift, δ_ℓ , that connects with quantum-mechanical scattering theory,

$$\mathcal{K}_{2,\ell}^{-1}(s) = \rho(s) \cot \delta_\ell(s). \quad (2.10)$$

Close to threshold it is typical to expand the phase shift using an *effective-range expansion* (ERE),

$$q_2^{*2\ell+1} \cot \delta_\ell(s) = \frac{1}{a_\ell} + r_\ell \frac{q_2^{*2}}{2} + \dots \quad (2.11)$$

where a_ℓ is known as the *scattering length* (although only a_0 has dimension of length) and r_ℓ is the *effective range*. Note that we are using the convention for the scattering length that is positive for attractive interactions and negative for repulsive ones. The powers of q_2^* on the left-hand-side of eq. (2.11) are required to ensure \mathcal{K}_2 is smooth at threshold, and so high partial waves are suppressed close to threshold. This is vital in making the study of multiparticle systems on the lattice viable—see sec. 2.3.1.

If a bound state is present close to a s -wave two-particle threshold, the effective range and effective length provide information about the nature of the state. Weinberg's criterium [170, 171] relates the probability of a bound state being a compact particle or a molecular state to its field renormalization factor, that can be computed as

$$Z = 1 - \left[1 - \frac{2r_0}{a_0} \right]^{-1/2}. \quad (2.12)$$

A value of Z close to unity indicates a state of compact nature, while a small value of Z would point towards a hadronic molecule.

2.1.2 Three-particle scattering

In the three-particle case, the description of a scattering process is more complicated. We let $\{k_1, k_2, k_3\}$ and $\{p_1, p_2, p_3\}$ be the momenta of the three particles in the initial and final state, respectively, and $P = k_1 + k_2 + k_3 = p_1 + p_2 + p_3$ the total momenta.

The three-particle scattering amplitude, \mathcal{M}_3 , can be written as a function of eight independent variables. However, in the line of the relativistic-field-theory (RFT) three-particle finite-volume formalism, to be introduced in sec. 2.3.2, we describe it redundantly in terms of 11 kinematic variables. These are the CMF energy, E^* , and five variables characterizing each of the initial and the final states. The dependence on E^* is kept implicit.

The three particles in the initial and final state are typically separated in an *interacting pair* or *dimer*, and a *spectator*. Each state is described with the three-momentum of the spectator, \mathbf{k} and \mathbf{p} for the initial and final state, respectively, together with the direction of the relative momentum of the dimer particles in their CMF, denoted by $\hat{\mathbf{a}}_k$ and $\hat{\mathbf{a}}_p$ for the initial and final dimer, in this same order.²

Scattering quantities are typically projected to into partial waves of the dimers. For example, the three-particle scattering amplitude is projected as

$$\mathcal{M}_3(\mathbf{p}, \hat{\mathbf{a}}_p^*; \mathbf{k}, \hat{\mathbf{a}}_k^*) = \sum_{\ell' m'} \sum_{\ell m} 4\pi Y_{\ell' m'}^*(\hat{\mathbf{a}}_p^*) \mathcal{M}_3(\mathbf{p}, \mathbf{k})_{\ell' m'; \ell m} Y_{\ell m}(\hat{\mathbf{a}}_k^*), \quad (2.13)$$

We note that the partial-wave-projected three-particle scattering amplitude still depends on 11 variables, which are the three-momenta of the initial and final spectator, \mathbf{k} and \mathbf{p} , the angular momentum indices of the initial and final dimer, (ℓ, m) and (ℓ', m') , and the total energy, E^* .

It is common in the context of the formalism, for legibility, to leave the angular momentum indices implicit. Thus, $\mathcal{M}_3(\mathbf{p}, \mathbf{k})$ refers to the three-particle scattering amplitude projected to the partial waves of both the initial and final spectator. This same conventions are also kept for other quantities, for example, the scattering amplitude of the dimer or the corresponding phase space. We stress that, instead of indicating that these quantities depend on the Mandelstam variables of the corresponding dimer, we typically keep the three-momentum of the associated spectator as the argument. For instance, $\mathcal{M}_2(\mathbf{k})$ has to be understood as the partial-wave projected two-particle scattering amplitude of the dimer, $\mathcal{M}_2(\mathbf{k}) \equiv \mathcal{M}_{2, \ell}(s)$, with $s = (P - k_3)^2$ and $k = (\sqrt{\mathbf{k}^2 + m^2}, \mathbf{k}^2)$. This same notation holds for the phase space factor, defined in eq. (2.8), this is, we use $\rho(\mathbf{k}) \equiv \rho(s)$.

²We use momentum subscripts to indicate that a quantity is defined in the CMF of the dimer associated to an spectator with that momentum.

As in the case of two particles, the analytic structure of \mathcal{M}_3 is constrained by the unitarity of the S -matrix. One can rewrite \mathcal{M}_3 as a function of both \mathcal{M}_2 , as pairwise scattering can happen within a three particle system, and a three-particle K -matrix that contains the information about short-range three-particle interactions. The definition of this quantity, however, is not unique and requires a prescription to separate successive two-particle scattering from short-range three-particle interactions. We here follow the approach of the RFT formalism [172, 173], in which a non-divergent or *divergence-free* (df) three-particle K -matrix is defined, called $\mathcal{K}_{\text{df},3}$. We also focus, for now, on the case of identical particles.

The first step to define $\mathcal{K}_{\text{df},3}$ is to remove possible divergences from \mathcal{M}_3 that originate from successive two particle interactions [174–177]. The divergence-free three-particle scattering amplitude is introduced as,

$$\mathcal{M}_{\text{df},3}(\mathbf{p}, \mathbf{k}) = \mathcal{M}_3(\mathbf{p}, \mathbf{k}) - \mathcal{S} \left\{ \mathcal{D}^{(\text{u,u})}(\mathbf{p}, \mathbf{k}) \right\}. \quad (2.14)$$

Here \mathcal{S} indicates symmetrization over all nine possible assignments of initial and final momenta, and $\mathcal{D}^{(\text{u,u})}$ is the unsymmetrized subtraction term. This term satisfies an integral equation,

$$\mathcal{D}^{(\text{u,u})}(\mathbf{p}, \mathbf{k}) = -\mathcal{M}_2(\mathbf{p})G^\infty(\mathbf{p}, \mathbf{k})\mathcal{M}_2(\mathbf{k}) - \int_r \mathcal{M}_2(\mathbf{p})G^\infty(\mathbf{p}, \mathbf{r})\mathcal{D}^{(\text{u,u})}(\mathbf{r}, \mathbf{k}). \quad (2.15)$$

where, recall, $\mathcal{M}_2(\mathbf{q})$ denotes the partial-wave-projected scattering amplitude of a dimer associated to an spectator with three-momentum \mathbf{q} . Also we define $\int_r \equiv \int d^3r/[2\omega_r(2\pi)^3]$, with $\omega_r = \sqrt{\mathbf{r}^2 + m^2}$, and

$$G^\infty(\mathbf{p}, \mathbf{k})_{\ell' m'; \ell m} = \left(\frac{k_p^*}{q_{2,p}^*} \right)^{\ell'} \frac{4\pi Y_{\ell' m'}(\hat{\mathbf{k}}_p^*) H(x_p) H(x_k) Y_{\ell m}^*(\hat{\mathbf{p}}_k^*)}{b_{pk}^2 - m^2 + i\epsilon} \left(\frac{p_k^*}{q_{2,k}^*} \right)^\ell. \quad (2.16)$$

Here, $b_{pk} = P - p - k$, with $k = (\omega_k, \mathbf{k})$ and $p = (\omega_p, \mathbf{p})$, p_k^* refers to the magnitude of \mathbf{p} on the CMF of the pair associated with spectator of momentum k , $q_{2,k}^* = |\hat{\mathbf{a}}_k^*|$, and similarly for k_p^* and $q_{2,p}^*$, respectively. Finally $H(x)$ is any smooth cutoff function that vanishes for $x \leq 0$ and is equal to unity for $x \geq 1$, with $x_q = (P - q)^2/4m^2$. The dependence on this arbitrary function sets a scheme, making $\mathcal{K}_{\text{df},3}$ scheme-dependent. A typical choice for $0 < x < 1$ is [172]

$$H(x) = \exp \left[-\frac{1}{x} \exp \left(-\frac{1}{1-x} \right) \right]. \quad (2.17)$$

After eliminating the divergences in \mathcal{M}_3 , $\mathcal{K}_{\text{df},3}$ is obtained from another integral equation,

$$\mathcal{M}_{\text{df},3}(\mathbf{p}, \mathbf{k}) = \mathcal{S} \left\{ \int_s \int_r \mathcal{L}^{(\text{u,u})}(\mathbf{p}, \mathbf{s}) \mathcal{T}(\mathbf{s}, \mathbf{r}) \mathcal{R}^{(\text{u,u})}(\mathbf{r}, \mathbf{k}) \right\}, \quad (2.18)$$

where

$$\mathcal{L}^{(u,u)}(\mathbf{p}, \mathbf{k}) = \left[\frac{1}{3} + i\mathcal{M}_2(\mathbf{p})\rho(\mathbf{p}) \right] \bar{\delta}(\mathbf{p} - \mathbf{k}) + i\mathcal{D}^{(u,u)}(\mathbf{p}, \mathbf{k})\rho(\mathbf{k}), \quad (2.19)$$

$$\mathcal{R}^{(u,u)}(\mathbf{p}, \mathbf{k}) = \bar{\delta}(\mathbf{p} - \mathbf{k}) \left[\frac{1}{3} + i\rho(\mathbf{p})\mathcal{M}_2(\mathbf{p}) \right] + i\rho(\mathbf{p})\mathcal{D}^{(u,u)}(\mathbf{p}, \mathbf{k}), \quad (2.20)$$

with $\bar{\delta}(\mathbf{p} - \mathbf{k}) \equiv 2\omega_k(2\pi)^3\delta^{(3)}(\mathbf{p} - \mathbf{k})$, and

$$\mathcal{T}(\mathbf{p}, \mathbf{k}) = \mathcal{K}_{\text{df},3}(\mathbf{p}, \mathbf{k}) - \int_{\mathbf{s}} \int_{\mathbf{r}} \mathcal{K}_{\text{df},3}(\mathbf{p}, \mathbf{s})\rho(\mathbf{s})\mathcal{L}^{(u,u)}(\mathbf{s}, \mathbf{r})\mathcal{T}(\mathbf{r}, \mathbf{k}). \quad (2.21)$$

Eq. (2.18) separates the divergence-free amplitude into three factors. Both \mathcal{L} and \mathcal{R} , often called *decorators*, depend only on the two-particle scattering amplitude. Their role here is to remove from $\mathcal{M}_{\text{df},3}$ the effect of long-range pairwise interactions happening before or after short-range three-particle interactions take place. The remaining factor, \mathcal{T} , contains the effect of these three-particle interactions. It is given by an integral equation, eq. (2.21), which includes a factor of \mathcal{L} , that represents possible long-range pairwise processes that can take place between successive short-range three-particle interactions. We finally note that, when solving this last equation, one must enforce $\mathcal{K}_{\text{df},3}$ to be symmetric under particle exchange. The study of the solutions of the integral equations relating $\mathcal{K}_{\text{df},3}$ to \mathcal{M}_3 is an active field of study [178–180].

As in the case of the two-particle K -matrix, $\mathcal{K}_{\text{df},3}$ can be expanded about threshold. As it is a function of a larger number of kinematical variables, more than one term can appear at each order in the threshold expansion. In the case of three identical particles of mass m , these terms must be invariant under any permutations of the particle in the initial and final states, as well as under the exchange of the initial and final states themselves. Up to quadratic order it contains five different terms [181],

$$M_\pi^2\mathcal{K}_{\text{df},3} = \mathcal{K}_0 + \mathcal{K}_1\Delta + \mathcal{K}_2\Delta^2 + \mathcal{K}_A\Delta_A + \mathcal{K}_B\Delta_B + \mathcal{O}(\Delta^3), \quad (2.22)$$

where

$$\Delta = \frac{P^2 - 9m^2}{9m^2}, \quad \Delta_A = \sum_i (\Delta_i^2 + \Delta_i'^2) - \Delta^2, \quad \Delta_B = \sum_{i,j} \tilde{t}_{ij} - \Delta^2. \quad (2.23)$$

Here, we have defined

$$\tilde{t}_{ij} = \frac{(p_i - k_j)^2}{9m^2}, \quad \Delta_i = \frac{(P - k_i) - 4m^2}{9m^2}, \quad \Delta_i' = \frac{(P - p_i) - 4m^2}{9m^2}. \quad (2.24)$$

Note that these quantities are not all independent—see ref. [181].

In general, one can determine the number of terms that appear at some order in the threshold expansion of $\mathcal{K}_{\text{df},3}$ using group-theory argument. For three mass-degenerate non-identical particles the allowed operators should transform under some irrep of the $G = (S_3 \times S'_3) \times Z_2$ group, where $S_3^{(\prime)}$ is the permutation group with three elements, acting on the momenta of the initial (final) state, and Z_2 refers to exchange of the initial and final states. This is discussed in detail in app. B of ref. [4].

2.2 Meson interactions from ChPT

ChPT provides a tool to describe interactions between mesons using an effective Lagrangian, as explained in sec. 1.4.1. If we consider isospin symmetry to be exact, pseudoscalar mesons organize in multiplets of the isospin group, $SU(N_f)$ —see sec. 1.1.2. What is more, interactions between multiple mesons can be classified in scattering channels, which correspond to different irreps of this same group. This means that both the initial and final scattering states lie on the same irrep, and so the scattering amplitude is (block-)diagonal in isospin.

Consider the simple $N_f = 2$ case. The pseudoscalar mesons are the pions, $\{\pi^+, \pi^0, \pi^-\}$, which form an isospin triplet with total isospin $I_\pi = 1$. Scattering of two pions can happen in three scattering channels,

$$3 \otimes 3 = 5 \oplus 3 \oplus 1, \quad (2.25)$$

corresponding to total isospin $I_{\pi\pi} = 2, 1$ and 0 , respectively. Isospin is conserved in scattering processes, and so the two-particle scattering amplitude is diagonal in isospin.

In the case of three pions, one first combines two of them into two-pion scattering channels and then adds the third particle [182],

$$3 \otimes 3 \otimes 3 = (5 \oplus 3 \oplus 1) \otimes 3 = 7 \oplus (5 \oplus 5) \oplus (3 \oplus 3 \oplus 3) \oplus 1. \quad (2.26)$$

The combination of three isospin-one particles leads to seven different irreps, which can be organized into four scattering channels, corresponding to three-particle isospin $I_{\pi\pi\pi} = 3, 2, 1$ and 0 .

The $I_{\pi\pi\pi} = 2$ and 1 irreps have non-zero multiplicity. Typically, each copy is characterized by the isospin of the two-particle subsystem from which the three-pion irrep was created. These are also the possible isospin in which pairwise interactions can happen within each channel. In the case of the $I_{\pi\pi\pi} = 2$ channel, pion-pion interactions can happen with $I_{\pi\pi} = 2$ and 1 , while for $I_{\pi\pi\pi} = 1$ all three two-particle channels are allowed. Note however,

that the scattering amplitude is not diagonal in these subchannels, and so they mix. In the $I_{\pi\pi\pi} = 3$ and $I_{\pi\pi\pi} = 0$ channels, on the other hand, pairwise interactions can only happen with $I_{\pi\pi} = 2$ and 1, respectively.

2.2.1 Two-pion scattering in ChPT

ChPT can be used to obtain prediction for the pion-pion scattering amplitude. For the maximal isospin channel, the LO result is [141]

$$\mathcal{M}_2^{I_{\pi\pi}=2, \text{LO}} = \frac{1}{F_\pi^2} (2M_\pi^2 - s). \quad (2.27)$$

The scattering amplitude and the effective range obey

$$a_0^{I_{\pi\pi}=2} = -\frac{M_\pi^2}{16\pi^2 F_\pi^2}, \quad M_\pi^2 a_0^{I_{\pi\pi}=2} r_0^{I_{\pi\pi}=2} = -3. \quad (2.28)$$

These results, especially that for $a_0^{I_{\pi\pi}=2}$, lead to very good agreement with experimental observations [183]. Higher-order results, which are known up to NNLO [146, 184], only amount to some minor corrections. Note however, this is not true for every scattering amplitude. In some cases, NLO correction can be large, even bigger than the LO result. We will see an example of this when studying the three-pion K -matrix in chapters 5 and 6.

One of the limitations of ChPT, as we have already commented, is that it leads to scattering amplitudes that contain no poles. This limits its range of applicability to energies below that of the lowest lying resonance. One option to circumvent this hindrance is the introduction of additional fields in the chiral Lagrangian representing these resonances [166, 185]. This is the base of the resonant chiral theory, that allows one to determine the value of the LECs from integrating out these additional degree of freedom.

Another compelling alternative is the inverse amplitude method (IAM) [186–190]. The basis of this technique are the perturbative expansion of the partial-wave projected scattering amplitude,

$$\mathcal{M}_{2,\ell} \approx \mathcal{M}_{2,\ell}^{(0)} + \mathcal{M}_{2,\ell}^{(1)} + \mathcal{O}(\delta^2), \quad (2.29)$$

and the observation that, when working at some fixed order in the chiral expansion, unitarity conditions are only satisfied perturbatively,

$$\text{Im}\mathcal{M}_{2,\ell}^{(0)} = 0, \quad \text{Im}\mathcal{M}_{2,\ell}^{(1)} = \rho\mathcal{M}_{2,\ell}^{(0)2}. \quad (2.30)$$

This can be combined with dispersion relations to solve for the scattering amplitude. One obtains a result that satisfies perturbative unitarity exactly,

$$\mathcal{M}_{2,\ell} \approx \frac{\mathcal{M}_{2,\ell}^{(0)2}}{\mathcal{M}_{2,\ell}^{(0)} - \mathcal{M}_{2,\ell}^{(1)}}. \quad (2.31)$$

At low energies, the standard ChPT expansion is recovered. However, it differs from the standard approach starting at $\mathcal{O}(\delta^2)$. This implies that the numerical values of the LECs in the unitarized theory will be similar, yet different, from those in standard ChPT [186, 188, 190]. Note this procedure can be extended to include higher orders in the perturbative expansion [190].

The amplitudes obtained with the IAM may present resonant poles, and so can be used to describe scattering processes in channels containing a resonant state, without the need of including them explicitly in the chiral Lagrangian. For example, the IAM has been used to fit experimental data from meson scattering [188], and also, in combination with large N_c arguments, to study the dependence of resonances with N_c [191–193].

2.2.2 Three-pion scattering at LO in ChPT

Three-pion scattering can too be described using ChPT, and scattering amplitudes are known up to NLO [194–196]. These amplitudes can be separated in several parts, according to the topology of the Feynman diagrams that contribute to each of them. Here we focus on the maximal isospin case, $I_{\pi\pi\pi} = 3$, at LO. The NLO case is studied in chapter 5 and the remaining isospin channels are considered in chapter 6. The isospin-three three-particle scattering amplitude, at LO, can be divided into two parts, corresponding to the two Feynman diagrams represented in fig. 2.1.

The first part is the so-called *one-particle exchange* (OPE) amplitude, $\mathcal{M}_3^{\text{LO,OPE}}$, which contains one-particle reducible diagrams that represent two consecutive pairwise interactions. The amplitude is given by the Feynman diagram in fig. 2.1a, after symmetrizing over the initial and final momenta. For a the choice of the interacting pair in fig. 2.1a, the unsymmetrized OPE amplitude is

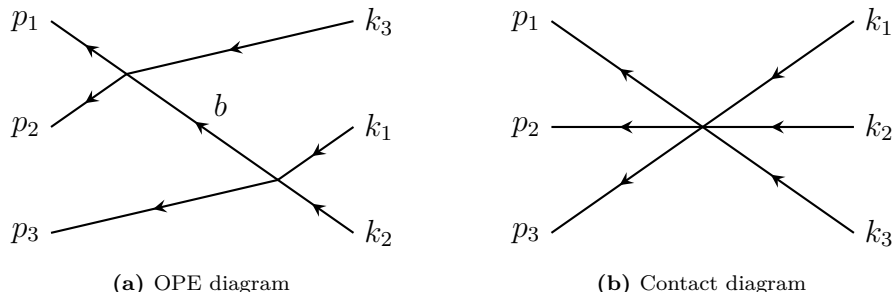


Figure 2.1. Feynman diagrams contributing to \mathcal{M}_3 at LO for maximal isospin. For diagram (a), there are eight additional diagrams corresponding to the symmetrization of initial and final momenta. In all cases, time flows from right to left.

$$\mathcal{M}_3^{(u,u)\text{LO,OPE}}(\mathbf{p}_3, \mathbf{k}_3) = -\mathcal{M}_{2,\text{off}}^{\text{LO}}(\mathbf{p}_3) \frac{1}{b^2 - M_\pi^2 + i\epsilon} \mathcal{M}_{2,\text{off}}^{\text{LO}}(\mathbf{k}_3), \quad (2.32)$$

where $\mathcal{M}_{2,\text{off}}^{\text{LO}}$ is the LO two-particle amplitude in which one of the external particles is left off-shell, and $b = P - k_3 - p_3$ is the momentum of the exchanged particle, which is the off-shell one. We recall that we indicate as the argument of the partial-wave-projected two-particle amplitude of dimer the three-momentum of the corresponding spectator and leave the angular momentum indices implicit. At LO, $\mathcal{M}_{2,\text{off}}$ is purely s -wave. For example, for the initial state it takes the form

$$\mathcal{M}_{2,\text{off}}^{\text{LO}}(\mathbf{k}_3) = \frac{1}{F_\pi^2} (t + u - 2M_\pi^2) = \frac{1}{F_\pi^2} [(2M_\pi^2 - s) + (b^2 - M_\pi^2)], \quad (2.33)$$

where we have used the Mandelstam variables corresponding to the initial dimer,

$$s = (k_1 + k_2)^2, \quad t = (k_1 - p_3)^2, \quad u = (k_2 - p_3)^2. \quad (2.34)$$

The off-shellness is introduced in the amplitude via the relation

$$s + t + u = 3M_\pi^2 - b^2. \quad (2.35)$$

corresponding to the case in which the off-shell momentum has the same spacial components as its on-shell counterpart, but does not obey the on-shell dispersion relation, $b^2 \neq M_\pi^2$. The total OPE amplitude is recovered from symmetrizing $\mathcal{M}_3^{(u,u)\text{LO,OPE}}$ over all different assignments of momenta.

The second part of the $I_{\pi\pi\pi} = 3$ amplitude is the non-OPE part, that contains all the remaining diagrams that are one-particle irreducible. At LO, this is just the diagram in fig. 2.1b,

$$\mathcal{M}_3^{\text{LO,non-OPE}} = \frac{1}{F_\pi^4} (-4P^2 + 18M_\pi^2). \quad (2.36)$$

The total amplitude is then the sum of the two parts

$$\mathcal{M}_3^{\text{LO}} = \mathcal{M}_3^{\text{LO,OPE}} + \mathcal{M}_3^{\text{LO,non-OPE}}. \quad (2.37)$$

Note, however, that this separation is arbitrary. The OPE contribution is defined from eq. (2.32), but one is free to modify the off-shell part in eq. (2.33), given there by the term proportional to $b^2 - M_\pi^2$. The non-OPE part is the remainder of the full amplitude. The choice of a different parametrization of the pion fields may also lead to a different off-shell convention.

Using the results for $\mathcal{M}_3^{\text{LO}}$, it is possible to obtain predictions for the isospin-three three-pion K -matrix at LO in ChPT [3, 194]. While in general

$\mathcal{K}_{\text{df},3}$ is obtained from \mathcal{M}_3 via integral equations, these can be reduced to algebraic relations when working at fixed order in perturbation theory.

Although in ChPT contributions are normally ordered as a power series in the pion mass and the momentum squared, here it is easier to study the powers of $1/F_\pi^2$. The scattering amplitudes are then $\mathcal{M}_2^{\text{LO}} = \mathcal{O}(1/F_\pi^2)$ and $\mathcal{M}_3^{\text{LO}} = \mathcal{O}(1/F_\pi^4)$. The subtraction needed to obtain the divergence-free amplitude can be obtained from eq. (2.15). At LO, since $G^\infty = \mathcal{O}(1)$,

$$\mathcal{D}^{(\text{u,u})\text{LO}}(\mathbf{p}, \mathbf{k}) = -\mathcal{M}_2^{\text{LO}}(\mathbf{p})G^\infty(\mathbf{p}, \mathbf{k})\mathcal{M}_2^{\text{LO}}(\mathbf{k}). \quad (2.38)$$

so that the divergence-free amplitude becomes

$$\mathcal{M}_{\text{df},3}^{\text{LO}}(\mathbf{p}, \mathbf{k}) = \mathcal{M}_3^{\text{LO}}(\mathbf{p}, \mathbf{k}) - \mathcal{S} \left\{ \mathcal{D}^{(\text{u,u})\text{LO}}(\mathbf{p}, \mathbf{k}) \right\}, \quad (2.39)$$

Note that in eq. (2.38) two-pion amplitudes are on-shell. This term removes the divergencies arising when the exchanged particle in $\mathcal{M}_3^{\text{LO,OPE}}$ goes on shell. The LO non-OPE part, by contrast, does not need any subtraction.

In the $I_{\pi\pi\pi} = 3$ channel pairwise interactions only happen with $I_{\pi\pi} = 2$. At LO, the two-particle isospin-two amplitude is purely s -wave, and so we can substitute $G^\infty(\mathbf{p}, \mathbf{k}) = G_{ss}^\infty(\mathbf{p}, \mathbf{k})$, where

$$G_{ss}^\infty(\mathbf{p}, \mathbf{k})_{\ell'm';\ell m} \equiv \delta_{\ell'0}\delta_{m'0}\delta_{\ell 0}\delta_{m 0} \frac{H(x_p)H(x_k)}{b_{pk}^2 - M_\pi^2 + i\epsilon}. \quad (2.40)$$

We can also set the cutoff functions to one, since all momenta in the subtraction in eq. (2.38) are on-shell.

To compute $\mathcal{M}_{\text{df},3}^{\text{LO}}$ it is convenient to separate $\mathcal{M}_3^{\text{LO}}$ into an OPE and a non-OPE part,

$$\mathcal{M}_{\text{df},3}^{\text{LO}}(\mathbf{p}, \mathbf{k}) = \mathcal{M}_3^{\text{LO,non-OPE}}(\mathbf{p}, \mathbf{k}) + \mathcal{S} \left\{ \mathcal{M}_3^{(\text{u,u})\text{LO,OPE}}(\mathbf{p}, \mathbf{k}) - \mathcal{D}^{(\text{u,u})\text{LO}}(\mathbf{p}, \mathbf{k}) \right\}. \quad (2.41)$$

The second term on the right-hand side is the divergence-free OPE amplitude. For the momenta assignment in fig. 2.1a, its unsymmetrized version is,

$$\mathcal{M}_{\text{df},3}^{(\text{u,u}),\text{LO,OPE}}(\mathbf{p}_3, \mathbf{k}_3) = \frac{1}{F_\pi^4} \left[2p_1 \cdot p_2 + 2k_1 \cdot k_2 - (b^2 - M_\pi^2) \right]. \quad (2.42)$$

After symmetrizing, one can combine with the non-OPE result in eq. (2.36) to obtain,

$$\mathcal{M}_{\text{df},3}^{\text{LO}}(\mathbf{p}, \mathbf{k}) = \frac{M_\pi^2}{F_\pi^4} (18 + 27\Delta), \quad (2.43)$$

where Δ is defined in eq. (2.23).

The final step to compute the three-particle K -matrix is to use eq. (2.21), that relates the divergence-free amplitude to $\mathcal{K}_{\text{df},3}$. Both \mathcal{L} and \mathcal{R} , given in eqs. (2.19) and (2.20), start at $\mathcal{O}(1)$,

$$\mathcal{L}^{(\text{u,u})\text{LO}}(\mathbf{p}, \mathbf{k}) = \mathcal{R}^{(\text{u,u})\text{LO}}(\mathbf{p}, \mathbf{k}) = \frac{1}{3}\bar{\delta}(\mathbf{p} - \mathbf{k}), \quad (2.44)$$

and so $\mathcal{T}^{\text{LO}} = \mathcal{O}(1/F_\pi^4)$, since it has the same order as $\mathcal{M}_{\text{df},3}$. From eq. (2.21), this implies $\mathcal{K}_{\text{df},3}^{\text{LO}} = \mathcal{O}(1/F_\pi^4)$, while the second term on the right-hand side is $\mathcal{O}(1/F_\pi^8)$. Thus, $\mathcal{T}^{\text{LO}} = \mathcal{K}_{\text{df},3}^{\text{LO}}$.

We can finally put this into eq. (2.21) combined with the results in eq. (2.44) to finally get

$$\mathcal{M}_{\text{df},3}^{\text{LO}} = \mathcal{S} \left\{ \frac{\mathcal{K}_{\text{df},3}^{\text{LO}}}{9} \right\} = \mathcal{K}_{\text{df},3}^{\text{LO}}, \quad (2.45)$$

where the symmetrization yields a factor of nine since $\mathcal{K}_{\text{df},3}$ is symmetric, by definition, in the $I_{\pi\pi\pi} = 3$ channel. Thus, we find

$$M_\pi^2 \mathcal{K}_{\text{df},3}^{\text{LO}} = \frac{M_\pi^4}{F_\pi^4} (18 + 27\Delta). \quad (2.46)$$

From this result, we can identify the coefficients of the threshold expansion in eq. (2.22), finding $\mathcal{K}_0 = 18 (M_\pi/F_\pi)^4$ and $\mathcal{K}_1 = 27 (M_\pi/F_\pi)^4$. These results at LO have been compared against lattice results, finding a large discrepancy. In chapter 5 we study the size of NLO corrections, finding they are large and lead to much better agreement between ChPT and the lattice.

2.3 Particle scattering from the lattice

At first glance, the study of multiparticle interactions using lattice techniques may seem impossible. Scattering is a real-time process between asymptotic states in which particles are very far from each other, while lattice computations are performed in Euclidean time and a finite volume, where such asymptotic states cannot be defined. Using lattice simulations, we can only compute correlation functions, from which finite-volume energies can be extracted, as explained in sec. 1.2.2.

However, from the finite-volume energies of multiparticle states one can extract information about the interactions between the asymptotic states of the theory. After all, both scattering amplitudes and the finite-volume energy spectrum are determined by the same Lagrangian. The relation between both is given by the so-called *quantization conditions* (QCs), which have been developed for systems of both two- [197, 198] and three-particles [172, 173].

QCs are obtained from studying the relation between finite- and infinite-volume correlators. In finite volume, the correlator takes the form in eq. (1.47). One can Fourier-transform the Euclidean time coordinate to Euclidean energy and then rotate it back to Minkowski energy, obtaining

$$C_L(E) = \sum_n \frac{2iE_n |Z_n|^2}{E^2 - E_n^2}, \quad (2.47)$$

where we include a subscript “ L ” to indicate we are referring to the finite-volume correlator. The finite volume correlator thus presents simple poles at the finite-volume energies, E_n , with purely imaginary residues with a positive imaginary part. The QCs exploit this feature, by relating the finite-volume correlator to its infinite-volume counterpart, plus some corrections that depend on the scattering amplitudes and are singular at the finite-volume energies.

Other alternative approaches to study multiparticle interactions on the lattice also exist. Two well-known examples are the HAL QCD method, which makes use of multiparticle potentials computed from spacial correlation functions to solve Schrödinger’s equation [199–202], and a recent technique that aims at extracting scattering amplitudes directly from the finite-volume correlator [203].

2.3.1 Two-particle quantization condition

The two-particle QC was first proposed for systems of two identical scalar particles in a seminal work by Lüscher [197, 198], and has since been extended to any possible two-particle process [204–212]. This includes higher partial waves, moving frames, coupled channels and arbitrary spin and masses.

The starting point of the formalism is expressing the finite-volume correlation function as an all-orders expansion in perturbation theory, which is assumed to converge to the full theory. In the elastic energy region, the diagrams can be rewritten as a succession of smooth kernels—the *Bethe-Salpeter kernels*—that contain all diagrams that are two-particle irreducible in the s -channel, joined by two-particle s -channel loops that are evaluated in finite volume—see fig. 2.2. Using Poisson summation [213], it can be proved that the Bethe-Salpeter kernel is equal to its infinite-volume counterpart up to exponentially suppressed volume effects,³ which are neglected. Two-particle s -channel loops are equal to their infinite-volume version plus an extra sum-minus-integral correction, which contains power-law finite volume effects arising when an intermediate two-particle state goes on shell.

³Technically, these corrections fall faster than any power law.

$$C_2(E) = C_{2,0} + \text{[diagram 1]} + \text{[diagram 2]} + \dots$$

Figure 2.2. Schematic representation of the two-particle correlation function. Circles represent the Bethe-Salpeter kernels and squares are the operator insertions, while $C_{2,0}$ contains all diagrams with no two-particle s -channel loop.

After summing all the diagrams, the two-particle finite-volume correlator becomes

$$C_{2,L}(P) = C_{2,\infty}(P) - A_2(P) \frac{i}{F^{-1}(P, L) + \mathcal{K}_2(E)} B_2(P), \quad (2.48)$$

where $A_2(E)$ and $B_2(E)$ are related to two-particle irreducible diagrams in the s -channel containing operator insertions, $C_\infty(P)$ is the infinite-volume correlation function, and F is the aforementioned sum-minus-integral correction. The latter is a finite-volume geometric factor that only depends on the total momentum and the size of the lattice. In the case of two identical scalar particles, it takes the form

$$F(P, L)^{\ell' m'; \ell m} = \left[\frac{1}{L^3} \sum_{\mathbf{k}} -\text{PV} \int \frac{d^3 k}{(2\pi)^3} \right] \frac{4\pi Y_{\ell' m'}(\hat{\mathbf{k}}^*) Y_{\ell m}^*(\hat{\mathbf{k}}^*)}{8\omega_{\mathbf{k}} \omega_{P\mathbf{k}} (E - \omega_{\mathbf{k}} - \omega_{P\mathbf{k}})} \left(\frac{k^*}{q_2^*} \right)^{\ell' + \ell}, \quad (2.49)$$

where exponentially suppressed volume effects are neglected. Here, $Y_{\ell m}$ are the spherical harmonics, q_2^* is the magnitude of the back-to-back momentum in the CMF, \mathbf{k}^* is the \mathbf{k} vector boosted to that frame, and we define the energies

$$\omega_{\mathbf{k}} = \sqrt{\mathbf{k}^2 + m^2}, \quad \omega_{P\mathbf{k}} = \sqrt{(\mathbf{P} - \mathbf{k})^2 + m^2}. \quad (2.50)$$

Finally, the sum in eq. (2.49) is performed over all momenta allowed in the finite volume—see eq. (1.29). Note that the pole in the integral is regulated using the principal-value (PV) prescription—see ref. [214] for details on this prescription, and refs. [209, 212, 215] for an efficient way to evaluate F .

The main implication of this result is that, since all $C_{2,\infty}$, A_2 and B_2 are smooth, the poles in the finite-volume correlator originate from zeros in the denominator of the last term. The energies at which these poles arise, which in turn are the finite-volume energies, are the solutions of the two-particle quantization condition,

$$\det[F^{-1}(P, L) + \mathcal{K}_2(E)] = 0. \quad (2.51)$$

Using this condition, finite-volume energies can be used to constrain infinite-volume scattering observables.

Some comments are in place. All the elements appearing in the quantization condition are matrices in angular momentum. This means F and \mathcal{K}_2 are, a priori, infinite dimensional. In the practice, they can be truncated at some maximum partial wave, ℓ_{\max} , since the contribution to the scattering amplitude near threshold is suppressed for large ℓ —see eq. (2.11). Also, whereas \mathcal{K}_2 is diagonal, F mixes different partial waves, since rotational symmetry is broken in a cubic box. If one works instead in the basis of irreps of the cubic group or the corresponding little group, F becomes block diagonal, and only a subset of partial waves are mixed—see refs. [113, 198].

Although not appearing explicitly in the QC, the A_2 and B_2 factors in eq. (2.48) play an important yet subtle role. They project out those states on which the chosen operators have zero overlap, and so the determinant only runs over the relevant states. For example, if one is studying $\pi\pi$ scattering in the $I_{\pi\pi} = 2$ channel, p -channel elements of F do not enter the quantization condition.

Finally, the applicability of eqs. (2.48) and (2.51) is restricted to the elastic region. For higher energies, intermediate states with three or more particles could go on-shell, leading to additional power-law finite-volume effects. For a system of two particles of mass m , the elastic region is, in general, $m < E^* < 3m$, but the range is increased to $0 < E^* < 4m$ with \mathbb{Z}_2 symmetry. Note that the formalism has been extended above the $3m$ barrier with the three-particle quantization condition—see sec. 2.3.2—and below the lower m limit with the explicit consideration of one-particle exchange in the t - and u -channel [216–218].

In some simple cases, it is possible to transform eq. (2.51) into an algebraic equation. For example, if we consider two identical particles of mass m and only consider s -wave interactions, the two-particle QC takes the form

$$k \cot \delta_0 = \frac{2}{\gamma L \pi^{1/2}} \mathcal{Z}_{00}^P \left(\frac{q^* L}{2\pi} \right), \quad (2.52)$$

where γ is the boost factor to the center-of-mass frame and \mathcal{Z} is the generalized Lüscher zeta function [197, 198, 205].

In the limit of large L , eq. (2.51) can be expanded to obtain a relation between the energy shift, defined as the difference between the interacting and the free energy, $\Delta E = E - E_{\text{free}}$, and the scattering parameters. In the case of the ground state, $\Delta E_{\text{thr}} = E_{\text{thr}} - 2m$ is related to the parameters in the ERE expansion, given in eq. (2.11),

$$\begin{aligned} \Delta E_{\text{thr}} = & -\frac{4\pi a_0}{mL^3} \left[1 + \left(\frac{a_0}{\pi L}\right) \mathcal{I} + \left(\frac{a_0}{\pi L}\right)^2 (\mathcal{I}^2 - \mathcal{J}) \right. \\ & \left. - \left(\frac{a_0}{\pi L}\right)^3 (-\mathcal{I}^3 + 3\mathcal{I}\mathcal{J} - \mathcal{K}) + \frac{2\pi r_0 a_0^2}{L^3} + \frac{\pi a_0}{m^2 L^3} \right] + \mathcal{O}(L^{-7}), \end{aligned} \quad (2.53)$$

where $\mathcal{I} = -8.9136\dots$, $\mathcal{J} = 16.5323\dots$ and $\mathcal{K} = 8.4019$ are numerical constants [219]. The leading term in this relation was first obtained in ref. [220] for a model of hard spheres. The general quantum-field-theory result up to $\mathcal{O}(L^{-5})$ was worked out in ref. [197], while the $\mathcal{O}(L^{-6})$ correction, in which relativistic effects first appear, was computed in ref. [221]. Note that this expansion is only expected to converge when $|a_0/L| \ll 1$. Similar relations also exist for excited states and for systems of more than two particles [219, 221–225].

2.3.2 Three-particle quantization condition

The two-particle formalism is limited to energies below the lowest three-particle threshold. This limits its capability to study the hadron spectrum, as many resonances are known to mainly decay into three or more particles [34]. During the last decade, three different versions of a three-particle QC have been developed to overcome this limitation: the RFT approach [172, 173], the finite-volume unitarity approach [226, 227] and the non-relativistic effective-field-theory approach [228, 229].

The first formalism to be developed was the RFT formalism, which has been generalized to systems including two-to-three processes [230], two-particle resonances [231], non-identical [182] and non-degenerate [232–234] particles, three spin-1/2 particles [235], and certain cases of coupled channels [236]. The other two formalisms were proposed at a later date and have seen less development. Note that all of them have been shown to be equivalent in the limits where they can be compared [237, 238].

In this dissertation, we focus on the RFT formalism, and discuss here the case of three-identical particles. The standard derivation of the QC is based on an all-order skeleton expansion similar to the one used for two-particles—see ref. [239] for an alternative approach based on time-ordered perturbation theory. The three-particle finite-volume correlator is related to its infinite-volume counterpart as

$$C_{3,L}(P) = C_{3,\infty}(P) + A_3(P) \frac{i}{F_3^{-1}(\mathcal{K}_2, P, L) + \mathcal{K}_{\text{df},3}(E)} B_3(P). \quad (2.54)$$

Here $\mathcal{K}_{\text{df},3}$ is the three-particle divergence-free K -matrix, related to \mathcal{M}_3 via the integral equations introduced in sec. 2.1.2, F_3 is a geometric factor

defined below that depends not only on the size of the box but also on two-particle interactions, $C_{3,\infty}$ is the infinite-volume correlator, and A_3 and B_3 are smooth factors related to three-particle operator insertions, that play an analogous role to A_2 and B_2 in the two-particle case.

Following the description made in sec. 2.1.2, three-particle states are characterized with $(\mathbf{k}\ell m)$ indices, where ℓ and m refer to the angular momentum of the dimer, and \mathbf{k} is the three-momentum of the spectator, which takes discrete values on the finite volume—see eq. (1.29). F_3 takes the form,

$$F_3 = \frac{1}{3}\tilde{F} + \tilde{F} \frac{1}{\tilde{\mathcal{K}}_2^{-1} - (\tilde{F} + G)} \tilde{F}. \quad (2.55)$$

In this equation, \tilde{F} and $\tilde{\mathcal{K}}_2$ are modified versions of the geometric factor from the two-particle quantization condition, F , and two-particle K -matrix, \mathcal{K}_2 , respectively. The former originates from two-particle loops, diagrammatically represented in fig. 2.3a, and contains power-law finite volume effects. It is diagonal on the spectator momenta but not on the angular momentum indices,

$$\begin{aligned} \tilde{F}(P, L)_{\mathbf{p}\ell'm'; \mathbf{k}\ell m} &= \delta_{\mathbf{p}\mathbf{k}} H(x_k) \left[\frac{1}{L^3} \sum_{\mathbf{a}} -\text{PV} \int \frac{d^3 a}{(2\pi)^3} \right] \\ &\times \frac{4\pi Y_{\ell'm'}(\hat{\mathbf{a}}^*) Y_{\ell m}^*(\hat{\mathbf{a}}^*) H(x_a) H(x_{ka})}{8\omega_a \omega_{ka} (E - \omega_k - \omega_a - \omega_{ka})} \left(\frac{k^*}{q_k^*} \right)^{\ell'+\ell}, \end{aligned} \quad (2.56)$$

where $\omega_{ka} = \sqrt{m^2 + (P - k - a)^2}$ and $x_{ka} = (P - k - a)^2/4m^2$, and other variables are introduced in sec. 2.1.2. On the other hand, $\tilde{\mathcal{K}}_2$ is diagonal in all the indices (here left implicit),

$$(\tilde{\mathcal{K}}_2)^{-1} = \mathcal{K}_2^{-1} + \rho(k)[1 - H(k)]. \quad (2.57)$$

Finally, G is related to other type of power-law finite-volume effects coming from OPE-like diagrams, like that in fig. 2.3b,

$$\begin{aligned} G(P, L)_{\mathbf{p}\ell'm'; \mathbf{k}\ell m} &= \\ &\frac{1}{4\omega_k \omega_p L^3} \left(\frac{k_p^*}{q_{2,p}^*} \right)^{\ell'} \frac{4\pi Y_{\ell'm'}(\hat{\mathbf{k}}_p^*) H(x_p) H(x_k) Y_{\ell m}^*(\hat{\mathbf{p}}_k^*)}{b^2 - m^2} \left(\frac{p_k^*}{q_{2,k}^*} \right)^{\ell}, \end{aligned} \quad (2.58)$$

In this equation, kinematical variables follow analogous definitions to those presented in sec. 2.1.2. The same holds true for the cutoff function, which in this case plays a twofold role. By removing high spectator momenta, situations in which the interacting pair energy would be on the left-hand cut, invalidating the formalism, are prevented. Also, it allows one to truncate the matrices at some \mathbf{k}_{max} , which is combined with truncation in angular momentum.

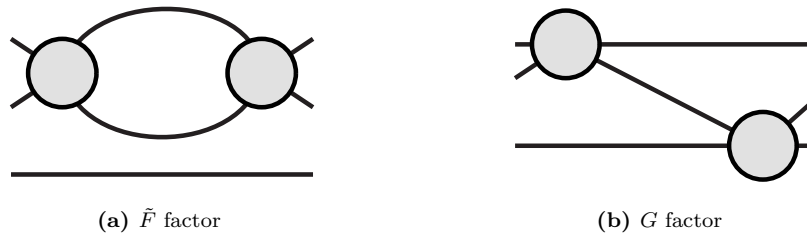


Figure 2.3. Diagrammatic representation of the factors appearing in the three-particle RFT formalism that lead to finite-volume power-law effects. Each line correspond to one particle and gray circles are Bethe-Salpeter kernels.

As in the case of the two-particle QC, three-particle energies lie at the zeros of the denominator in eq. (2.54), leading to the three-particle QC,

$$\det[F_3^{-1}(\mathcal{K}_2; P, L) + \mathcal{K}_{\text{df},3}(P)] = 0. \quad (2.59)$$

This QC has a range of applicability that is limited, for general theories, to energies $2m < E^* < 4m$. In the case of interactions with \mathbb{Z}_2 symmetry, as is the case of pions if isospin-breaking corrections are neglected, this range is extended to $m < E^* < 5m$.

The QC in eq. (2.59) simplifies in the so-called isotropic approximation, in which only s -wave interactions are considered and $\mathcal{K}_{\text{df},3}$ is assumed to be only a function of the total energy, E . In this limit, eq. (2.59) becomes

$$F_3^{\text{iso}}(E^*) = \langle 1 | F_3 | 1 \rangle = -\frac{1}{\mathcal{K}_{\text{df},3}^{\text{iso}}(E^*)}, \quad (2.60)$$

where $|1\rangle$ is a vector with ones in all the entries. This limit was explored numerically in ref. [240]. A threshold expansion for the ground state energy shift has also been worked out in the context of the RFT formalism [241], and has been analytically tested in a simple scalar theory [221, 242].

Before concluding, we comment on the generalization of the RFT formalism to general three-pion isospin [182]. While in the maximal isospin case the three pions can be treated as identical and eq. (2.59) can be applied, this is not true for the remaining channels. To properly include all channels, all elements in eq. (2.54) are promoted to 7×7 matrices, which are block diagonal in three-pion isospin channels, but not in the two-particle subchannels within each three-particle isospin. The non-zero entries of \tilde{F} , \tilde{K}_2 and G are equal to those in eqs. (2.56) to (2.58), respectively, multiplied by some numerical factors related to Clebsh-Gordan coefficients. Moreover, $\mathcal{K}_{\text{df},3}$ obeys different symmetries under particle exchange. For example, while $\mathcal{K}_{\text{df},3}$ is symmetric under particle exchange in the $I_{\pi\pi\pi} = 3$ channel, it becomes fully antisymmetric for $I_{\pi\pi\pi} = 0$. These different transformation properties imply new forms of the threshold expansion, which are presented in sec. 6.1.4.

3 Pion-pion scattering near threshold at large N_c

The large N_c limit of QCD, introduced in sec. 1.3, has proven to have predictive power in the non-perturbative regime of the theory, and has been used by many phenomenological approaches to the low-energy regime of QCD—see ref. [121] for a review. In some cases, however, large N_c predictions fail to reproduce experimental results. An example of this is the well-known $\Delta I = 1/2$ puzzle [243–249]. Large N_c predictions for the $K \rightarrow \pi\pi$ process predict a ratio $A_2/A_0 = \sqrt{2}$ between the decay amplitude into two pions in the isospin-two and -zero channels. This result, however, completely disagrees with experimental measurements, $(A_2/A_0)_{\text{exp}} \approx 22.4$.

The lattice regularization makes it possible to quantify such corrections by directly simulating at several values of N_c . In this context, lattice techniques have been mainly used to study the hadron and glueball spectrum, as well as weak matrix elements, such as those involved in the $\Delta I = 1/2$ rule [250–260]—see ref. [124] for a recent review. Indeed, large subleading N_c corrections have been found in the case of non-leptonic kaon decays [257, 259]. Lattice simulations also open the door to answer other timely questions, such as the possible existence of tetraquarks at large N_c , discussed in sec. 1.3.2.

In this chapter, the results from refs. [1, 8] are summarized, in which we investigate the scattering of two pseudoscalar mesons as a function of N_c . We work with $N_f = 4$ degenerate quark flavors, meaning all up, down, strange and charm quarks have the same mass. We consider $N_c = 3 - 6$ and $M_\pi \approx 360 - 590$ MeV, and focus on two scattering channels. The same setup has previously been used in ref. [258] to study the N_c scaling of pion masses and decay constants, and in ref. [259] to investigate the $\Delta I = 1/2$ puzzle.

Using lattice simulations, we measure two-particle finite-volume energies near threshold. In particular, we use Lüscher’s formalism to match our

results to ChPT predictions including the η' , which we compute for the first time. From the matching of the lattice results and ChPT we study the N_c dependence of the relevant LECs from first principles.

This chapter is organized as follows. In sec. 3.1 we describe how the scattering of two pseudoscalar mesons in a theory with $N_f = 4$ can be classified in different isospin channels. We also use the large N_c limit and ChPT to obtain analytical predictions for the processes of interest. The lattice setup is presented in sec. 3.2, followed by lattice results in sec. 3.3. In sec. 3.4 we present the results of the fits to ChPT, and compare them to previous literature. The main conclusions of this work can be found in sec. 3.5.

3.1 Pion-pion scattering in $N_f = 4$ QCD

In a theory with $N_f = 4$ degenerate light quark flavors, spontaneous chiral symmetry breaking leaves an exact $SU(4)$ isospin symmetry. The lightest pseudoscalar mesons appear as a 15-dimensional multiplet, plus a singlet representing the η' particle,

$$4 \otimes 4 = 15 \oplus 1. \quad (3.1)$$

The multiplet includes all pseudoscalar π , K , D , D_s and η mesons. Since all of them are degenerate in this scenario, we will refer to them generically as pions.

Two-pion scattering organizes in different scattering channels, corresponding to irreps of the isospin group. For $N_f = 4$, there is a total of seven scattering channels [261],

$$15 \otimes 15 = 84 \oplus 45 \oplus 45 \oplus 20 \oplus 15 \oplus 15 \oplus 1. \quad (3.2)$$

This same number of irreps holds for any $N_f \geq 4$, while it reduces to six for $N_f = 3$ and three for $N_f = 2$ —see sec. 2.2.1.

In this work, we focus on two of these scattering channels, which contain s -wave interactions and can be studied in the lattice without the need to compute quark propagators between two lattice sites with the same time coordinate. These are the 84- and the 20-dimensional irreps. The former is symmetric in quarks and antiquarks, and is equivalent to the $I_{\pi\pi} = 2$ channel of two-flavor QCD. We refer to it as the SS channel. The 20-dimensional irrep is antisymmetric in both quarks and antiquarks, and only exists for $N_f \geq 4$. We call it the AA channel. Representative states of each of these channels are, respectively, $|\pi^+\pi^+\rangle$ and $|D_s^+\pi^+\rangle - |D^+K^+\rangle$. Note that both

channels contain states with four distinct quark flavors. Throughout this chapter, we denote a generic irrep using a $R \in \{SS, AA\}$ label.

The 45-dimensional irreps—which are degenerate, as one is the conjugate of the other—can also be studied in the lattice without the need of equal-time quark propagators. However, they only contain odd partial waves, and so their scattering amplitude vanishes at threshold. These channels are studied in chapter 4 as a function of the center-of-mass energy.

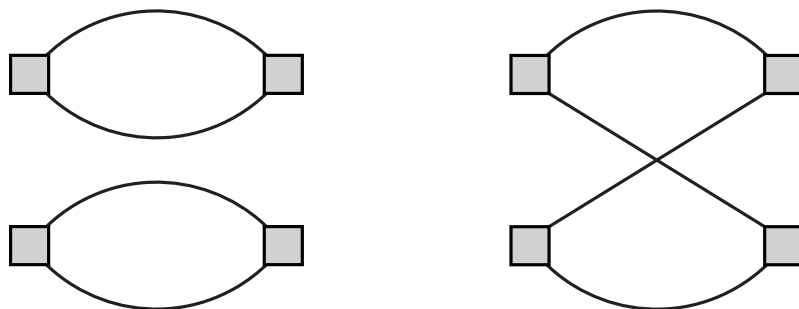
3.1.1 Pion-pion scattering at large N_c

The N_c and N_f scaling of the scattering amplitudes of the SS and AA channels can be determined from a perturbative analysis of the correlation functions. For both channels, these can be computed as a linear combination of two terms, corresponding to two topologies of the Wick contractions,

$$C_{SS} = 2(D - C), \quad C_{AA} = 2(D + C), \quad (3.3)$$

where D and C stand for the disconnected and connected contractions, respectively. They are diagrammatically represented in fig. 3.1 and are explicitly expressed in eq. (3.30) in terms of quark propagators.

One can determine the N_c and N_f scaling of these correlation functions. This requires to include possible gluon lines and internal quark loops to the diagrams in fig. 3.1 and to use the large N_c counting rules presented in sec. 1.3. Diagrams with no additional quark or gluon lines contribute to the leading terms. The D diagram, shown in fig. 3.1a, contains two color loops, and so is $\mathcal{O}(1)$, while the C diagram in fig. 3.1b is $\mathcal{O}(N_c^{-1})$, as it contains a single color loop. Note that both diagrams contain four insertions of pion



(a) Disconnected (D) diagram, $\mathcal{O}(N_c^2)$

(b) Connected (C) diagram, $\mathcal{O}(N_c)$

Figure 3.1. Diagrammatic representation of those Wick contractions contributing to the SS and AA channels. Solid lines are quark propagators, while the squares represent pion insertions.

operators, which we normalize with a $N_c^{-1/2}$ factor. Including internal gluon lines in each disconnected piece of D or in C does not affect this scaling, and so such diagrams also contribute to the leading N_c term.

From this result, one can determine the leading N_c dependence of other scattering observables. For example, the scattering length, defined in eq. (2.11) can be expressed in terms of correlations functions of zero-momentum pions as

$$M_\pi a_0^R \propto \frac{C_R - C_\pi^2}{C_\pi^2}, \quad (3.4)$$

where $C_\pi \sim \mathcal{O}(1)$ is the single-pion propagator and, recall, $R \in \{SS, AA\}$ indicates some general two-pion channel. The single-pion propagator corresponds to one of the two disconnected pieces in fig. 3.1a, and its scaling was explicitly expressed in eq. (1.67). Note that it has the same topology as C , and so they have the same large N_c scaling.

The subtraction in the numerator of eq. (3.4) implies that disconnected pieces in D do not contribute to the scattering length. Non-factorizable contributions from D correspond to subleading diagrams in which at least two gluons are exchanged between the two quark loops, and so are at most $\mathcal{O}(N_c^{-2})$ —see, for example, fig. 3.2a. The leading contribution to the scattering length thus comes from C , which is $\mathcal{O}(N_c^{-1})$. Subleading corrections to this contraction come from diagrams exchanging a planar gluon that include an internal quark loop, and so scale as $\mathcal{O}(N_f/N_c^2)$ —see fig. 3.2b.

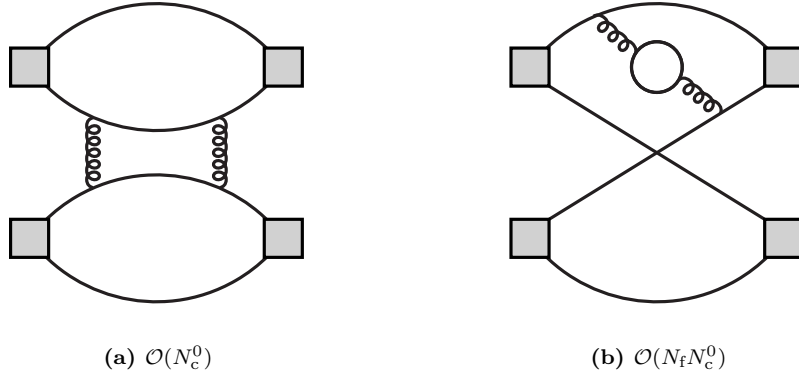


Figure 3.2. Subleading N_c diagrams contributing to the Wick contractions in fig. 3.1. Grey squares represent pion insertions, solid lines are quark propagators and curly lines represent gluons.

All this discussion can be summarized as follow,

$$\begin{aligned} C &= \frac{1}{N_c} \left(a + b \frac{N_f}{N_c} \right) + \mathcal{O}(N_c^{-3}), \\ D - C_\pi^2 &= \frac{c}{N_c^2} + \mathcal{O}(N_c^{-3}), \\ C_\pi &= \frac{1}{N_c} \left(d + e \frac{N_f}{N_c} \right) + \mathcal{O}(N_c^{-3}), \end{aligned} \quad (3.5)$$

where $a - e$ are numerical constants independent of N_c and N_f , naturally expected to be $\mathcal{O}(1)$. Combining these results with eqs. (3.3) and (3.4), one derives

$$M_\pi a_0^R = \pm \frac{1}{N_c} \left(\tilde{a} + \tilde{b} \frac{N_f}{N_c} \mp \tilde{c} \frac{1}{N_c} \right) + \mathcal{O}(N_c^{-3}), \quad (3.6)$$

where $\tilde{a} - \tilde{c}$ are linear combination of $a - e$ and the upper (lower) signs correspond to the SS (AA) channels. Thus, large N_c arguments predict that one channel should be attractive (i.e., has positive scattering length), while the other is repulsive (negative scattering length), at least if subleading corrections are not abnormally large. Note that this same scaling is also predicted for other scattering quantities, such as the scattering amplitudes.

3.1.2 Pion-pion scattering in $\overline{\text{SU}}(N_f)$ ChPT

Scattering of two pions in a theory with N_f degenerate quarks can be described using standard ChPT, based on the $\text{SU}(N_f)$ isospin group—see sec. 1.4.1. Results for the scattering amplitudes are known up to NNLO [261]. For the SS and AA channel, LO amplitudes are independent of N_f ,

$$\mathcal{M}_2^{SS,LO} = -\mathcal{M}_2^{AA,LO} = \frac{1}{F_\pi^2} (2M_\pi^2 - s). \quad (3.7)$$

Using these results, the s -wave scattering lengths and effective ranges can be determined,

$$M_\pi a_0^{SS} = -M_\pi a_0^{AA} = -\frac{M_\pi^2}{16\pi^2 F_\pi^2}, \quad M_\pi^2 a_0^R r_0^R = -3. \quad (3.8)$$

As anticipated, the results for the SS channel are equal to that for the $I_{\pi\pi} = 2$ channel presented in eq. (2.27) for $N_f = 2$. Note that LO ChPT predicts scattering lengths of opposite signs for the SS and AA channels, as expected from large N_c arguments. At LO, the SS channel is predicted to be repulsive at threshold, while the AA channel is expected to be attractive. Both scattering lengths also scale as $\mathcal{O}(N_c^{-1})$, since $F_\pi \sim \mathcal{O}(N_c^{1/2})$, in agreement with eq. (3.6).

At NLO, the amplitudes depend on linear combinations of the LECs from the fourth-order chiral Lagrangian in eq. (1.81). The NLO s -wave amplitudes—which do not include the LO results—read

$$\begin{aligned}
\frac{F_\pi^4}{M_\pi^4} \mathcal{M}_{2,0}^{SS,\text{NLO}} &= 32L_{SS} + 32q^2 L'_{SS} + \frac{128}{3} q^4 L''_{SS} \\
&+ \frac{1}{4\pi^2} \left[-1 - \frac{1}{N_f^2} + \frac{1}{N_f} + q^2 \left(-3 - \frac{N_f}{18} \right) + q^4 \left(-\frac{10}{3} - \frac{11N_f}{27} \right) \right] \\
&+ \frac{1}{4\pi^2} \left[-1 - \frac{1}{N_f^2} + \frac{1}{N_f} + q^2 \left(-3 - \frac{N_f}{6} \right) + q^4 \left(-\frac{10}{3} - \frac{5N_f}{9} \right) \right] \ln \frac{M_\pi^2}{\mu^2} \quad (3.9) \\
&+ (2 + 8q^2 + 8q^4) \bar{J}(s) + F_{SS}(q^2),
\end{aligned}$$

$$\begin{aligned}
\frac{F_\pi^4}{M_\pi^4} \mathcal{M}_{2,0}^{AA,\text{NLO}} &= -32L_{AA} + 32q^2 L'_{AA} + \frac{128}{3} q^4 L''_{AA} \\
&+ \frac{1}{4\pi^2} \left[-1 - \frac{1}{N_f^2} - \frac{1}{N_f} + q^2 \left(-3 + \frac{N_f}{18} \right) + q^4 \left(-\frac{10}{3} + \frac{11N_f}{27} \right) \right] \\
&+ \frac{1}{4\pi^2} \left[-1 - \frac{1}{N_f^2} - \frac{1}{N_f} + q^2 \left(-3 + \frac{N_f}{6} \right) + q^4 \left(-\frac{10}{3} + \frac{5N_f}{9} \right) \right] \ln \frac{M_\pi^2}{\mu^2} \quad (3.10) \\
&+ (2 + 8q^2 + 8q^4) \bar{J}(s) + F_{AA}(q^2).
\end{aligned}$$

Here $\bar{J}(x)$ is a loop integral—see refs. [149, 262]—and $q = q_2^*/M_\pi$ is the magnitude of the relative momentum normalized by the pion mass,

$$q = \sqrt{\frac{s}{4M_\pi^2} - 1}. \quad (3.11)$$

We have also defined the following functions, which need to be evaluated numerically,

$$\begin{aligned}
F_{SS}(q^2) &= \int_{-1}^1 \left[1 + \frac{2}{N_f^2} - \frac{2}{N_f} + \frac{2N_f}{3} + q^2 \left(2 + \frac{4N_f}{3} - 2x \right) \right. \\
&\quad \left. + q^4 \left(2 + N_f - 4x - \frac{4N_f x}{3} + 2x^2 + \frac{N_f x^2}{3} \right) \right] \bar{J}[t(x)] dx, \quad (3.12)
\end{aligned}$$

$$\begin{aligned}
F_{AA}(q^2) &= \int_{-1}^1 \left[1 + \frac{2}{N_f^2} + \frac{2}{N_f} - \frac{2N_f}{3} + q^2 \left(2 - \frac{4N_f}{3} - 2x \right) \right. \\
&\quad \left. + q^4 \left(2 - N_f - 4x + \frac{4N_f x}{3} + 2x^2 - \frac{N_f x^2}{3} \right) \right] \bar{J}[t(x)] dx, \quad (3.13)
\end{aligned}$$

with $t(x) = -2q_2^{*2}(1-x)$. Finally, we have defined the following linear combinations of LECs from the \mathcal{L}_4 Lagrangian in eq. (1.81),

$$\begin{aligned}
L_{SS} &= L_0 + 2L_1 + 2L_2 + L_3 - 2L_4 - L_5 + 2L_6 + L_8, \\
L'_{SS} &= 4L_0 + 4L_1 + 6L_2 + 2L_3 - 2L_4 - L_5, \\
L''_{SS} &= 3L_0 + 2L_1 + 4L_2 + L_3,
\end{aligned} \tag{3.14}$$

$$\begin{aligned}
L_{AA} &= L_0 - 2L_1 - 2L_2 + L_3 + 2L_4 - L_5 - 2L_6 + L_8, \\
L'_{AA} &= -4L_0 + 4L_1 + 6L_2 - 2L_3 - 2L_4 + L_5, \\
L''_{AA} &= -3L_0 + 2L_1 + 4L_2 - L_3.
\end{aligned} \tag{3.15}$$

These results can be used to determine the scattering lengths, given in eqs. (2.7) and (2.8) of ref. [1], and other scattering observables.

The amplitudes in eqs. (3.7), (3.9), and (3.10) are expected to scale with N_c as given in eq. (3.6). As we have seen, this holds for LO terms, and is also straightforward to check for NLO terms without LECs. This means it must also hold for the LEC terms, as expected from eq. (1.87). The combinations in eqs. (3.14) and (3.15) can thus be parametrized as a power series in N_c , with common large N_c for both channels. For example, we write

$$L_R = N_c L^{(0)} + L_R^{(1)} + \mathcal{O}(N_c^{-1}), \tag{3.16}$$

and similarly for L'_R and L''_R . The scaling with N_f however, is not so clear. The chiral logarithms in eqs. (3.9) and (3.10) depend explicitly on inverse powers of N_f , which are not expected from large N_c arguments. This does not mean the large N_c limit breaks, but is a consequence of considering the wrong effective theory. This N_f dependence is compensated by an analogous implicit dependence of the LECs. To consistently apply ChPT in the large N_c limit, one needs to include the singlet meson, the η' , which becomes degenerate with the pions. The symmetry group is therefore $U(N_f)$ instead of $SU(N_f)$, as we consider in the following.

3.1.3 Pion-pion scattering in $U(N_f)$ ChPT

At large N_c , the η' meson becomes degenerate with pions, and so needs to be included in the low-energy EFT. This is the basis of large N_c or $U(N_f)$ ChPT, introduced in sec. 1.4.2. The implicit N_f dependence of the LECs in the $SU(N_f)$ theory is a result of integrating out this particle.

While several quantities have been computed in $U(N_f)$ ChPT, this is not the case for meson scattering amplitudes, that we determined for the first time in ref. [1]. At LO, scattering amplitudes are equivalent to those in eq. (3.7). Contributions at NLO in the counting of large N_c ChPT, eqs. (1.76)

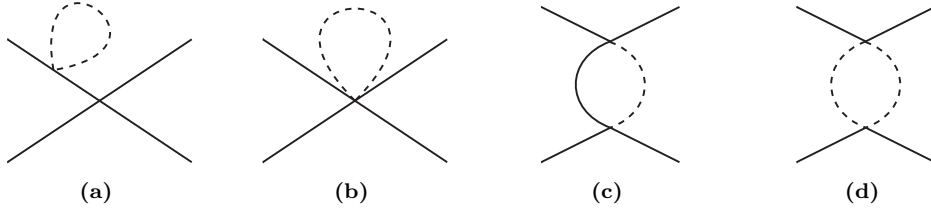


Figure 3.3. Additional one-loop Feynman diagrams needed to study two-pion scattering in the SS and AA channels in large N_c ChPT. Solid lines depict pions, while dotted ones represent the η' .

and (1.85), are given by tree-level diagrams including $\mathcal{O}(N_c)$ LECs. However, NLO is in general insufficient, and one needs to go to NNLO.

At NNLO, loop diagrams start to contribute and effects from the η' meson need to be included, represented in fig. 3.3. In addition, one also needs to consider tree-level diagrams with two insertions of $\mathcal{O}(N_c)$ LECs. Overall, the full amplitudes up to NNLO can be computed as

$$\left[\mathcal{M}_2^{R,\text{NNLO}}\right]_{\text{U}(N_f)} = \left[\mathcal{M}_2^{R,\text{NLO}}\right]_{\text{SU}(N_f)} + \mathcal{M}_K + \Delta Z_{\eta'}^2 \mathcal{M}_{\text{LO}} + \mathcal{M}_{\eta'}^{\text{loop}}, \quad (3.17)$$

where $\Delta Z_{\eta'}^2$ represents the additional mass renormalization due to η' loops—diagram 3.3a—and $\mathcal{M}_{\eta'}^{\text{loop}}$ includes the contributions from diagrams 3.3b, 3.3c and 3.3d. Finally, \mathcal{M}_K accounts to tree level diagrams with products of two $\mathcal{O}(N_c)$ LECs.

The full scattering amplitudes up to NNLO in large N_c ChPT are

$$\begin{aligned} \left[\mathcal{M}_2^{SS,\text{NNLO}}\right]_{\text{U}(N_f)} &= \left[\mathcal{M}_2^{SS,\text{NLO}}\right]_{\text{SU}(N_f)} + \left(\frac{M_\pi^2}{F_\pi^2}\right)^3 \left[K_{SS} + q^2 K'_{SS}\right] \\ &\quad - \frac{2M_\pi^4}{F_\pi^4 N_f} \left(1 - \frac{2}{N_f}\right) B_1(t) - \frac{2M_\pi^4}{F_\pi^4 N_f^2} B_2(t) + (t \leftrightarrow u), \end{aligned} \quad (3.18)$$

$$\begin{aligned} \left[\mathcal{M}_2^{AA,\text{NNLO}}\right]_{\text{U}(N_f)} &= \left[\mathcal{M}_2^{AA,\text{NLO}}\right]_{\text{SU}(N_f)} - \left(\frac{M_\pi^2}{F_\pi^2}\right)^3 \left[K_{AA} + q^2 K'_{AA}\right] \\ &\quad + \frac{2M_\pi^4}{F_\pi^4 N_f} \left(1 + \frac{2}{N_f}\right) B_1(t) - \frac{2M_\pi^4}{F_\pi^4 N_f^2} B_2(t) + (t \leftrightarrow u), \end{aligned} \quad (3.19)$$

where $B_1(x)$ and $B_2(x)$ are loop integrals corresponding to diagrams 3.3c and 3.3d, respectively,

$$\begin{aligned} B_1(z) &= \frac{1}{(4\pi)^2} \left\{ \frac{1}{M_{\eta'}^2 - M_\pi^2} \left(M_{\eta'}^2 \log \frac{M_{\eta'}^2}{\mu^2} - M_\pi^2 \log \frac{M_\pi^2}{\mu^2} \right) \right. \\ &\quad \left. + \int_0^1 \log \left[\frac{M_\pi^2 x + M_{\eta'}^2 (1-x) - x(1-x)z}{M_\pi^2 x + M_{\eta'}^2 (1-x)} \right] dx \right\}, \end{aligned} \quad (3.20)$$

$$B_2(z) = \frac{1}{(4\pi)^2} + \frac{1}{(4\pi)^2} \log \frac{M_{\eta'}^2}{\mu^2} - \bar{J} \left(z \frac{M_\pi}{M_{\eta'}^2} \right), \quad (3.21)$$

with $M_{\eta'}$ given by the Witten-Veneziano formula in eq. (1.21). Also, we have introduced K_R and K'_R , which are products of $\mathcal{O}(N_c)$ LECs. For example, we have

$$K_{SS} = K_{AA} = \left[128(L_8 - 2L_5)^2 \right]_{\mathcal{O}(N_c^2)}, \quad (3.22)$$

where $[\dots]_{\mathcal{O}(N_c^2)}$ refers to the leading $\mathcal{O}(N_c^2)$ contribution. Moreover, note that although the linear combinations of LECs appearing in $[\mathcal{M}_2^{R,\text{NLO}}]_{\text{SU}(N_f)}$ take the same form as in eqs. (3.14) and (3.15), their numeric values may differ between the $\text{SU}(N_f)$ and the $\text{U}(N_f)$ theories.

Taking the large N_c limit, $M_{\eta'} \rightarrow M_\pi$, one can check the $1/N_f$ factors appearing in the chiral logarithms cancel and the expected large N_c scaling from eq. (3.6) is recovered. This same scaling must hold for the LEC terms, which can be parametrized as

$$[L_R]_{\text{U}(N_f)} = N_c L^{(0)} + N_f L_c^{(1)} \mp L_a^{(1)} + \mathcal{O}(N_c^{-1}), \quad (3.23)$$

where, again, the upper and lower signs correspond to the SS and AA channels, respectively. The correlated and anticorrelated terms, $L_c^{(1)}$ and $L_a^{(1)}$ are independent of N_f . Comparing to eqs. (3.14) and (3.15), we note

$$\begin{aligned} L_0 + L_3 - L_5 + L_8 &= N_c L^{(0)} + N_f L_c^{(1)} + \mathcal{O}(N_c^{-1}), \\ 2L_1 + 2L_2 - 2L_4 + 2L_6 &= L_a^{(1)} + \mathcal{O}(N_c^{-1}). \end{aligned} \quad (3.24)$$

Equivalent arguments hold for L'_R and L''_R , as well as for K_R and K'_R . Note that higher order N_c corrections only contribute at higher order in the power counting in eq. (1.85), and so truncating at this order is natural in $\text{U}(N_f)$ ChPT.

We can also match $\text{U}(N_f)$ and $\text{SU}(N_f)$ ChPT in the $M_{\eta'} \gg M_\pi$ limit, obtaining a relation between the LECs in the two theories, as shown in eq. (1.88). For example, for the $L_R^{(1)}$ terms in eq. (3.16), we get

$$\begin{aligned} [L_{SS}^{(1)}]_{\text{SU}(N_f)} &= [L_{SS}^{(1)}]_{\text{U}(N_f)} - \frac{1}{8N_f^2(4\pi)^2} (N_f \lambda_0 - \lambda_0 + 1), \\ [L_{AA}^{(1)}]_{\text{SU}(N_f)} &= [L_{AA}^{(1)}]_{\text{U}(N_f)} + \frac{1}{8N_f^2(4\pi)^2} (1 - N_f \lambda_0 - \lambda_0), \end{aligned} \quad (3.25)$$

with $\lambda_0 = \log(M_0^2/\mu^2)$ and $M_0^2 = M_{\eta'}^2 - M_\pi^2$. This relation sheds light on the origin of the implicit $1/N_f$ and $1/N_f^2$ dependence of the $\text{SU}(N_f)$ LECs.

3.2 Lattice setup

We study pion-pion scattering in the SS and AA channels using lattice simulations with $N_c = 3 - 6$. In all cases, we consider several values of the pion mass, $M_\pi = 360 - 590$ MeV. Simulations are performed with the HiRep code [263, 264] and we work with a lattice setup analogous to that of refs. [258, 259]. Configurations are generated using the Iwasaki gauge action with $N_f = 4$ flavors of dynamical clover-improved Wilson fermions. The value of c_{sw} is determined from one-loop $N_c = 3$ results [75] boosted by the plaquette, which is kept constant for all N_c according to its expected leading N_c dependence [258].

In this work, we compute the relevant correlation functions using two different regularizations in the valence sector: a unitary setup with the same action for sea and valence fermions, and a mixed-action setup [265] with maximally-twisted clover-improved fermions for the valence quarks. In the latter case we tune the bare twisted mass, $a\mu_0$, to ensure the valence pion mass, M_π^v , matches its sea value, M_π^s , computed in the unitary setup. The use of maximally-twisted fermions allows us to achieve automatic $\mathcal{O}(a)$ improvement, and also to determine F_π without the need of renormalization constants [84],

$$F_\pi = \frac{\sqrt{2}\mu_0 \langle 0 | \bar{q} \gamma_5 q | \pi \rangle}{M_\pi}. \quad (3.26)$$

In addition, the combination of both regularizations is useful to study discretization effects, as physical observables must agree in the continuum limit.

A summary of the parameters used in the simulations is presented in table 3.1, and in table 3.2 we summarize our results for single-pion quantities. Pion masses and decay constants are extracted from single-pion correlators, and are corrected to account for finite-volume effects estimated from ChPT—see eq. (1.58). We have also determined the physical lattice spacing of the simulations—see ref. [258] for details. The “A” ensembles have $a = 0.075(2)$ fm and had previously been used in refs. [258, 259]. On the other hand, the “B” and “C” ensembles, generated for this work, have $a = 0.065(2)$ fm and $a = 0.059(2)$ fm, respectively. Assuming $\mathcal{O}(a^2)$ scaling, the finest ensembles should present $\sim 40\%$ smaller cutoff effects than the coarsest ones.

Ensemble	$L^3 \times T$	β	c_{sw}	am^s	am^v	$a\mu_0$
3A10	$20^3 \times 36$			-0.4040	-0.4214	0.01107
3A11	$24^3 \times 48$			-0.4040	-0.4214	0.01107
3A20	$24^3 \times 48$	1.778	1.69	-0.4060	-0.4196	0.00781
3A30	$24^3 \times 48$			-0.4070	-0.4187	0.00632
3A40	$32^3 \times 60$			-0.4080	-0.4163	0.00513
3B10	$24^3 \times 48$	1.820	1.66	-0.3915	-0.4035	0.00825
3B20	$32^3 \times 60$			-0.3946	-0.4011	0.00431
3C10	$24^3 \times 48$	1.850	1.64	-0.3817	-0.3934	0.00870
3C20	$32^3 \times 60$			-0.3847	-0.3921	0.00512
4A10	$20^3 \times 36$			-0.3735	-0.4163	0.00513
4A20	$24^3 \times 48$	3.570	1.69	-0.3752	-0.3865	0.00844
4A30	$24^3 \times 48$			-0.3760	-0.3865	0.00778
4A40	$32^3 \times 60$			-0.3780	-0.3851	0.00546
5A10	$20^3 \times 36$			-0.3458	-0.3611	0.01225
5A20	$24^3 \times 48$	5.969	1.69	-0.3490	-0.3611	0.00906
5A30	$24^3 \times 48$			-0.3500	-0.3607	0.00824
5A40	$32^3 \times 60$			-0.3530	-0.3596	0.00509
6A10	$20^3 \times 36$			-0.3260	-0.3415	0.01298
6A20	$24^3 \times 48$	8.974	1.69	-0.3300	-0.3414	0.00956
6A30	$24^3 \times 48$			-0.3311	-0.3414	0.00803
6A40	$32^3 \times 60$			-0.3340	-0.3409	0.00542

Table 3.1. Summary of ensemble parameters used in this work. L and T indicate the number of points in the spatial and temporal extent of the lattices, respectively, β is the gauge coupling, c_{sw} is the Sheikholeslami-Wohlert coefficient, and am^s is the bare mass of the Dirac operator in the sea sector. Finally, am^v and $a\mu_0$ are bare mass and the bare twisted mass used in the mixed-action setup, in this same order.

Ensemble	aM_π^s	aM_π^v	aF_π	ξ
3A10	0.222(3)	0.2211(23)	0.0449(4)	0.154(6)
3A11	0.2150(15)	0.2185(10)	0.0452(3)	0.148(3)
3A20	0.1853(13)	0.1830(8)	0.0409(3)	0.1267(25)
3A30	0.1611(16)	0.1616(8)	0.0378(3)	0.1157(25)
3A40	0.1419(10)	0.1423(6)	0.03577(14)	0.1003(14)
3B10	0.1751(11)	0.1764(9)	0.03626(23)	0.150(3)
3B20	0.1189(8)	0.1221(6)	0.03121(13)	0.0969(16)
3C10	0.1756(18)	0.1759(18)	0.0336(4)	0.174(7)
3C20	0.1308(13)	0.1289(12)	0.02866(24)	0.128(4)
4A10	0.2044(13)	0.2035(15)	0.0521(4)	0.0968(25)
4A20	0.1805(8)	0.1799(6)	0.05103(16)	0.0787(9)
4A30	0.1707(7)	0.1730(5)	0.04952(19)	0.0773(9)
4A40	0.1399(8)	0.1419(8)	0.0464(3)	0.0593(12)
5A10	0.2125(11)	0.2126(8)	0.06154(22)	0.0756(10)
5A20	0.1803(6)	0.1798(5)	0.05846(24)	0.0599(6)
5A30	0.1707(6)	0.1715(6)	0.0570(3)	0.0573(9)
5A40	0.1331(5)	0.1330(4)	0.05306(15)	0.0398(3)
6A10	0.2147(7)	0.2142(6)	0.06874(21)	0.0615(6)
6A20	0.1798(6)	0.1802(4)	0.06582(21)	0.0475(4)
6A30	0.1685(7)	0.1666(5)	0.06324(23)	0.0439(5)
6A40	0.1353(3)	0.1347(5)	0.05950(13)	0.0324(3)

Table 3.2. Results for the pion mass for the unitary and mixed-action setups (M_π^s and M_π^v , respectively), the pion decay constant, F_π , and the chiral parameter, ξ , as defined in eq. (1.80). All quantities have their leading finite-volume effects corrected—see eq. (1.58).

3.2.1 Extraction of finite-volume energies

Two-pion ground-state energies are determined from two-point correlation functions,

$$C_R(t) = \langle O_R(t) O_R^\dagger(t) \rangle, \quad (3.27)$$

where we define two-pion operators for the channels of interest,

$$\begin{aligned} O_{SS}(t) &= \pi^+(t) \pi^+(t), \\ O_{AA}(t) &= \frac{1}{\sqrt{2}} \left[\pi^+(t) D_s^+(t) - K^+(t) D^+(t) \right]. \end{aligned} \quad (3.28)$$

Single-pion interpolators in these operators are projected to zero momentum. For example,

$$\pi^+(t) = \sum_i \bar{d}(\mathbf{x}, t) \gamma_5 u(\mathbf{x}, t), \quad (3.29)$$

and similarly for K^+ , D^+ and D_s^+ , with the corresponding quark flavors [34]. As shown in eq. (3.3), the correlation functions can be computed as a linear combination of the disconnected and the connected Wick contractions. On the lattice, these are evaluated, respectively, as

$$\begin{aligned} D(t) &= \sum_{\mathbf{y}_1, \mathbf{y}_2} \sum_{\mathbf{x}_1, \mathbf{x}_2} \langle \text{Tr}[S^\dagger(\mathbf{y}_1, x_1) S(\mathbf{y}_1, x_1)] \text{Tr}[S^\dagger(\mathbf{y}_2, x_2) S(\mathbf{y}_2, x_2)] \rangle, \\ C(t) &= \sum_{\mathbf{y}_1, \mathbf{y}_2} \sum_{\mathbf{x}_1, \mathbf{x}_2} \langle \text{Tr}[S^\dagger(\mathbf{y}_2, x_1) S(\mathbf{y}_1, x_1) S^\dagger(\mathbf{y}_1, x_2) S(\mathbf{y}_2, x_2)] \rangle, \end{aligned} \quad (3.30)$$

where $x_i = (0, \mathbf{x}_i)$ and $y_i = (t, \mathbf{y}_i)$. We evaluate these contractions using time- and spin-diluted stochastic sources with $\mathbb{Z}_2 \times \mathbb{Z}_2$ noise, and make use of time-translation invariance to average over multiple equivalent locations of the source and the sink.

From the correlation functions, we are able to extract the ground-state energies. We take thermal effects into account, which become relevant around $t \sim T/2$ —see sec. 1.2.4. Taking into account backwards propagation and that the leading thermal effects are time independent for zero total momentum, the two-pion correlation function asymptotically looks like

$$C_R(t) = A_R \cosh[E_R(t - T/2)] + B_R, \quad (3.31)$$

where A_R and B_R are positive constants related to matrix elements of the two-pion interpolating operators, and E_R is the corresponding two-pion energy. Instead of directly fitting the correlators, we consider the ratio [266, 267]

$$R(t) = \frac{C_R(t+1) - C_R(t-1)}{C_\pi^2(t+1) - C_\pi^2(t-1)}, \quad (3.32)$$

which eliminates the constant noise and has been empirically seen to reduce excited-states contamination [268, 269]. At late times, the ratio behaves as

$$R(t) = K_R [\cosh(\Delta E_R t') + \sinh(\Delta E_R t') \coth(2M_\pi t')] , \quad (3.33)$$

where $\Delta E_R = E_R - 2M_\pi$ is the energy shift, $t' = t - T/2$ and K_R is a normalization constant that depends on the channel.

We extract the finite-volume energy shift from fits to eq. (3.33), fixing M_π to the value obtained from fitting the single-pion correlator and taking into account correlations between different times slices. Errors are determined using bootstrap, averaging the configurations on blocks several times larger than the autocorrelation time. We observe that our results are unaffected by the choice of the block size. Fits of the correlators are performed over the range $t \in [t_{\min}, T/2 - 1]$ and are repeated for several t_{\min} . The energy shift is determined where the results show a plateau, which we determine by visual inspection. Our results for the mixed-action setup are shown in table 3.3.

3.3 Results for pion-pion scattering

Using the finite-volume energies, we determine the scattering lengths using the threshold expansion, given in eq. (2.53). The results at $\mathcal{O}(L^{-5})$ are presented in table 3.3, noting that the scattering lengths are roughly of the same magnitude for both channels with opposite signs. This agrees with expectations from the large N_c limit and ChPT, and indicates the SS channel is repulsive, while the AA channel is attractive.

In fig. 3.4 we compare the scattering length against the LO prediction from ChPT, given in eq. (3.8). We observe good agreement for the SS channel, indicating that higher-order corrections are small. For the AA , on the other hand, such corrections seem sizable, although still smaller than the LO for the masses studied.

3.3.1 Convergence of the threshold expansion

The threshold expansion in eq. (2.53) is a priori only valid for $|a_0/L| \ll 1$, and so the truncation at $\mathcal{O}(L^{-5})$ may introduce a non-negligible systematic error if $|a_0/L| \sim 1$. To estimate the size of such systematic errors, we compare results obtained at $\mathcal{O}(L^{-5})$ and $\mathcal{O}(L^{-6})$ using the mixed-action setup. For the $\mathcal{O}(L^{-6})$ case, we use an estimate for the effective range based on LO predictions from ChPT, $M_\pi^2 a_0^R r_0^R = -3$.

Ensemble	$\Delta E_{SS}/M_\pi$	$M_\pi a_0^{SS}$	$\Delta E_{AA}/M_\pi$	$M_\pi a_0^{AA}$
3A10	0.100(4)	-0.494(17)	-0.075(4)	0.73(4)
3A11	0.0495(17)	-0.442(13)	-0.0458(13)	0.72(3)
3A20	0.082(4)	-0.416(14)	-0.063(3)	0.57(4)
3A30	0.114(4)	-0.392(11)	-0.082(7)	0.52(5)
3A40	0.0532(20)	-0.324(11)	-0.050(3)	0.49(3)
3B10	0.104(3)	-0.456(9)	-0.093(3)	0.81(3)
3B20	0.087(3)	-0.324(10)	-0.064(3)	0.390(24)
3C10	0.120(6)	-0.503(19)	-0.117(5)	1.02(4)
3C20	0.111(9)	-0.45(3)	-0.082(4)	0.64(4)
4A10	0.0825(25)	-0.345(9)	-0.063(3)	0.445(25)
4A20	0.0473(14)	-0.255(6)	-0.0410(15)	0.319(15)
4A30	0.0529(14)	-0.252(6)	-0.0456(23)	0.317(20)
4A40	0.0269(13)	-0.179(9)	-0.0276(11)	0.236(11)
5A10	0.0507(11)	-0.259(4)	-0.0469(10)	0.356(10)
5A20	0.0342(11)	-0.192(6)	-0.0334(7)	0.250(6)
5A30	0.0381(12)	-0.186(6)	-0.0323(15)	0.206(11)
5A40	0.0235(10)	-0.132(6)	-0.0209(13)	0.141(9)
6A10	0.0402(15)	-0.217(7)	-0.0393(9)	0.295(8)
6A20	0.0290(13)	-0.167(6)	-0.0261(6)	0.189(5)
6A30	0.0301(16)	-0.139(7)	-0.0308(16)	0.177(11)
6A40	0.0171(5)	-0.102(3)	-0.0172(10)	0.118(7)

Table 3.3. Results for the two-pion energy shifts, $\Delta E_R = E_R - 2M_\pi$, for the SS and AA channels obtained in the mixed-action setup, together with the corresponding scattering lengths computed using eq. (2.53) to $\mathcal{O}(L^{-5})$.

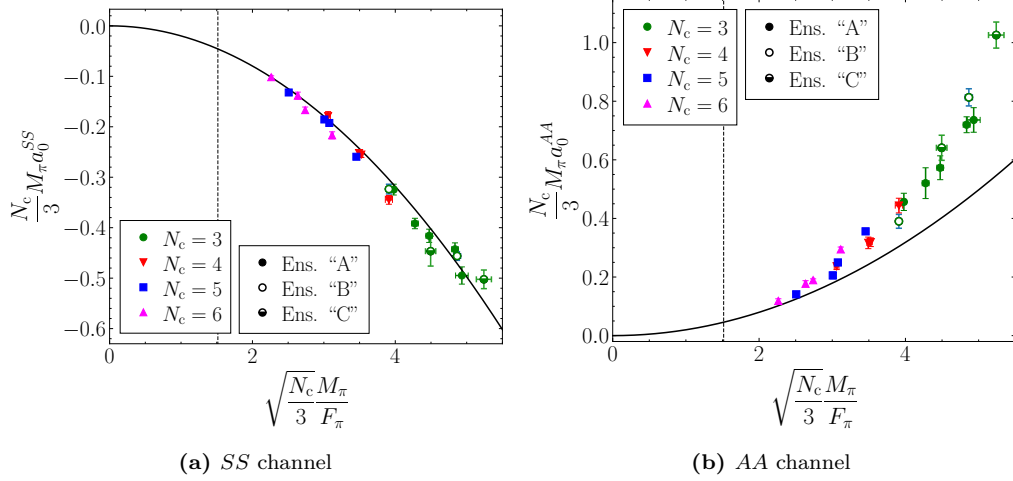


Figure 3.4. Results for the s -wave scattering length obtained using the threshold expansion to $\mathcal{O}(L^{-5})$, together with LO ChPT predictions. Both axes are multiplied by a factor that eliminates leading N_c dependencies. The physical point is indicated with a vertical dashed line.

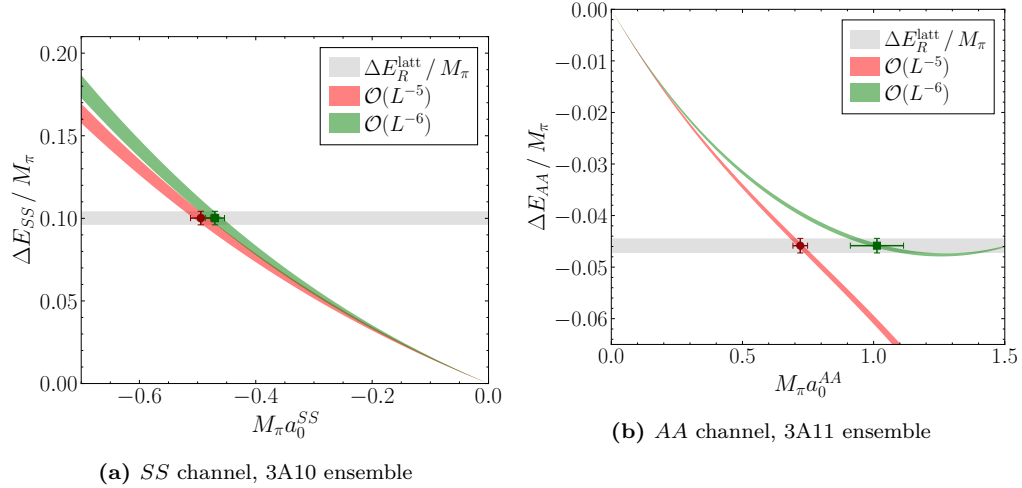


Figure 3.5. Results for the scattering length obtained using the threshold expansion in eq. (2.53) up to $\mathcal{O}(L^{-5})$ (red) and $\mathcal{O}(L^{-6})$ (green). The gray band is the energy shift from the lattice, ΔE_R^{latt} and the points are the corresponding determinations of the scattering length.

For the SS channel, both orders produce very similar results, with discrepancies smaller than one standard deviation. In fig. 3.5a this comparison is shown for the 3A10 ensemble. The gray horizontal band is the lattice result for ΔE_{SS} , while the green and red bands represent the right-hand side of eq. (2.53) up to $\mathcal{O}(L^{-5})$ and $\mathcal{O}(L^{-6})$, respectively, with a width coming from the error of $M_\pi L$.

The case of the AA channel is more complicated. For ensembles with small ξ we observe reasonable agreement. However, this is not the case at larger ξ , and we even reach the case in which the expansion at $\mathcal{O}(L^{-6})$ does not reproduce the finite-volume energy shift for any value of a_0^{AA} . In fig. 3.5b we show the same comparison as before for the 3A11 ensemble, with the same color code. We observe how the convergence of the asymptotic expansion fails, with the $\mathcal{O}(L^{-6})$ case barely yielding a result for the scattering length.

From this comparison, we conclude that some of our ensembles lie in a regime where the threshold expansion is not valid, and so may be affected by uncontrolled systematic effects. To circumvent this problematic, we make use of the full finite-volume formalism, given in eq. (2.52) for single-channel s -wave interactions, in the remaining of this study.

3.3.2 Discretization effects

Discretization effects are small for isospin-two pion-pion interactions [270], while examples are known from the baryon sector in which they are significant [271]. We studied their impact in our observables considering the $N_c = 3$ ensembles, which are available at different lattice spacings, and compare results obtained for the two fermion regularizations, which should be equal in the continuum. The ratio between the results for the energy shift is shown in fig. 3.6, where the superscripts “unit” and “mixed” refer to the unitary and the mixed-action setups, respectively. In the SS channel, we observe no significant cutoff effects, while large discrepancies are visible in the AA channel, that seem to decrease for finer lattices. This is, to our knowledge, the first time large cutoff effects have been observed in the context of meson-meson scattering.

To study the impact of discretization effects in the AA channel in both regularizations, we perform a continuum extrapolation for $q \cot \delta_0$, computed using eq. (2.52). We recall that δ_0 is the s -wave scattering phase shift and we have defined $q = q_2^*/M_\pi$, with q_2^* the relative momentum in the CMF.

The continuum extrapolation must be performed along a line of constant physics. In our context, this is characterized by the value of ξ and the relative CM momentum, q . Since our ensembles at different lattice spacing do not

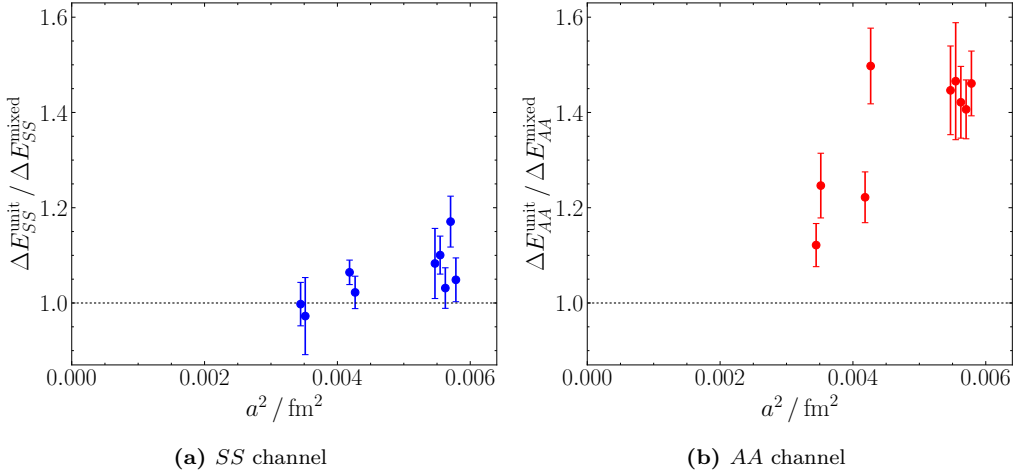


Figure 3.6. Ratio between the results for the energy shifts computed using a unitary and a mixed-action lattice setup, as a function of the lattice spacing. Results are only shown for $N_c = 3$ ensembles.

lie on the same line of constant physics, we need to interpolate/extrapolate to some reference value, $(q_{\text{ref}}^2, \xi_{\text{ref}})$, to perform a continuum extrapolation.

We proceed as follows. First, for every $N_c = 3$ ensemble and both the unitary and the mixed-action result, we shift $q \cot \delta_0$ to $q_{\text{ref}}^2 = -0.08$ using the ERE, eq. (2.11), to order $\mathcal{O}(q^2)$. For the effective range, we use a prior based on LO ChPT—see eq. (3.8)—with a conservative width, $M_\pi^2 r_0^{AA} a_0^{AA} \in [-5, -1]$. This prior introduces some systematic error in the shifted results, but this is usually much smaller than the original statistical error. Next, we interpolate linearly to $\xi_{\text{ref}} = 0.14$ at fixed lattice spacing. We use three ensembles for the interpolation in the “A” case, as depicted in fig. 3.7, and both ensembles available for the “B” and “C” cases.

The results for both regularizations at fixed $(q_{\text{ref}}^2, \xi_{\text{ref}})$ are used to perform a continuum extrapolation, shown in fig. 3.8. Our results are consistent with a universal continuum limit, and the expected $\mathcal{O}(a)$ improvement is observed in both regularizations, since they seem to approach the continuum limit as $\mathcal{O}(a^2)$. Similar conclusions also hold for other choices of $(q_{\text{ref}}^2, \xi_{\text{ref}})$.

We decide to include these discretization effects explicitly in the scattering amplitudes, which we modify as

$$\mathcal{M}_2^{AA, \text{latt}} = \mathcal{M}_2^{AA, \text{cont}} + 32\pi^2 a^2 \xi W, \quad (3.34)$$

where “latt” and “cont” superscripts refer to lattice and continuum quantities, respectively. This modification is motivated by an extension of ChPT that includes the effect of the lattice spacing and a twisted mass—see app. B from ref. [1] for details on this computation in our particular setup. In this effective theory, W is a linear combination of new LECs and is expected to

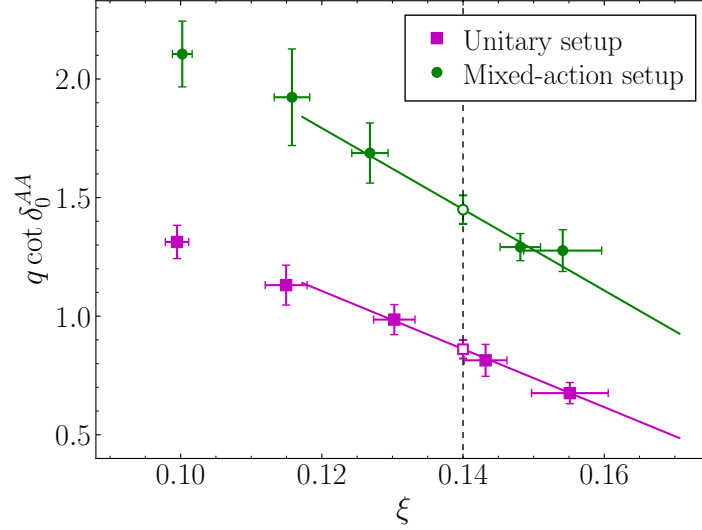


Figure 3.7. Linear interpolation of $q \cot \delta_0$ to the reference value $\xi_{\text{ref}} = 0.14$ (dashed line) for the “3A” ensembles at $q_{\text{ref}}^2 = -0.08$. We show the results for the unitary (magenta squares) and the mixed-action (green dots) setups, and depict the result as an empty point. Only the three closest points are used for the interpolation.

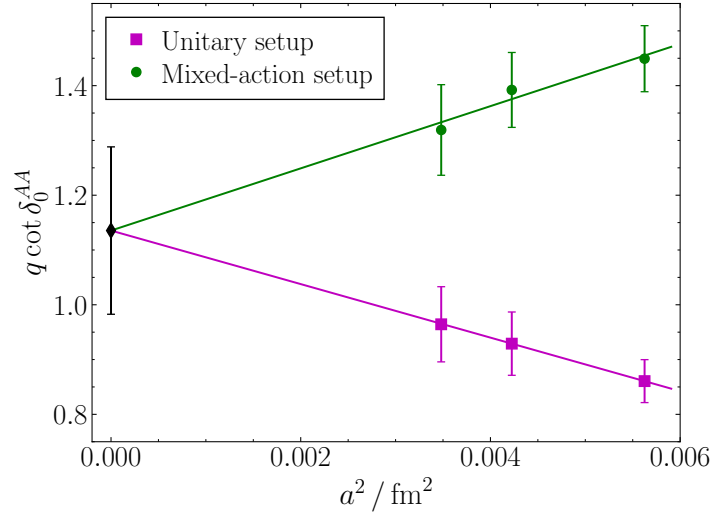


Figure 3.8. Constrained continuum extrapolation of $q \cot \delta_0$ computed from a unitary (magenta squares) and a mixed-action (green dots) setups at $(q_{\text{ref}}^2, \xi_{\text{ref}}) = (-0.08, 0.14)$. The continuum results is shown as a black diamond.

be independent of N_c at leading order, $W \sim \mathcal{O}(N_c^0)$. The results from this effective theory, however, do not explain why discretization effects are larger in the AA channel, compared to the SS one. It is probably a consequence of the particular numerical values of the LECs in this effective theory.

For the phase shift, eq. (3.34) translates to

$$q \cot \delta_0^{\text{AA,latt}} = q \cot \delta_0^{\text{AA,cont}} \left(1 - \frac{32\pi^2 a^2 \xi W}{\mathcal{M}_{2,0}^{\text{AA,LO}}} \right). \quad (3.35)$$

This expression is used to fit the results at finite lattice spacing for both regularizations imposing a common continuum limit. For the remaining of this work, we make use of the mixed-action setup. For that case, the continuum extrapolation allows us to determine

$$W_{\text{mixed}} = -42(29) \text{ fm}^{-2}, \quad (3.36)$$

which we use as an extra input when matching the AA channel to ChPT.

3.4 Matching to ChPT

Given a scattering amplitude, Lüscher's formalism allows one to obtain predictions of the corresponding finite-volume energies that can be matched to lattice results, constraining the parameters in the scattering amplitudes. In this section, we use the two-particle formalism to match our lattice results to SU(4) and U(4) ChPT predictions, given in eqs. (3.9), (3.10), (3.18), and (3.19), and constrain the N_c dependence of the LECs. In the AA channel, we include cutoff effects as indicated in eq. (3.34).

3.4.1 Fitting procedure

To evaluate the ChPT predictions of the scattering amplitudes, we choose a value for the renormalization scale related to $4\pi F_\pi$ with no the leading N_c dependence,

$$\mu^2 = \frac{3}{N_c} (4\pi F_\pi)^2. \quad (3.37)$$

Also, we use a value of $M_{\eta'}$ given by the Witten-Veneziano relation, eq. (1.21),

$$\frac{M_{\eta'}^2}{(4\pi F_\pi)^2} = \xi + \frac{a_0}{N_c^2}, \quad (3.38)$$

where $a_0 \approx 6.5$ is determined using the topological susceptibility from ref. [272]. Finally, we set those LECs that appear in the amplitudes multiplied

by some power of the momentum— L'_R , L''_R and K'_R —to zero. We have checked that, as our results are close to threshold, we are mostly insensitive to the values of these LECs. Using the results for the amplitudes, we can obtain predictions for the finite-volume energies using Lüscher's formalism. For the evaluation of Lüscher's theta function we use the implementation from refs. [273, 274].

Due to non-negligible correlations between the finite-volume energies and ξ , an ordinary least-squares fit is not suitable for matching our results to ChPT. Instead, we use York regression [275] and define the χ^2 as

$$\chi^2 = \min_{\delta_i} [\mathbf{R}^T V^{-1} \mathbf{R}], \quad (3.39)$$

where \mathbf{R} is a vector containing our data with a specific form that depends on the channel of interest and V is the corresponding covariance matrix. For example, for a fit to the SS channel, \mathbf{R} is composed by a succession of tuples $\mathbf{R}_i = (f(x_i + \delta_i) - y_i, \delta_i)$, where δ_i are real numbers which are minimized and i labels each ensemble. Here, $x_i = \xi_i$, $y_i = E_{R,i}$ are our lattice results for the chiral parameter and finite-volume energies and f are the ChPT predictions for the latter, obtained using the finite-volume formalisms, as described above. In this example, V is block-diagonal, as ensembles are independent.

We also consider more complicated fits. For fits to the AA channel, we constrain the W factor in eq. (3.34). We include in \mathbf{R} the result for W from eq. (3.36) as a prior, and its correlations to the $N_c = 3$ ensembles in V , which is thus no longer block diagonal. We also perform simultaneous fits to both SS and AA channels, in which the tuples are enlarged

$$\mathbf{R}_i = (f^{SS}(x_i + \delta_i) - y_i^{SS}, f^{AA}(x_i + \delta_i) - y_i^{AA}, \delta_i). \quad (3.40)$$

Note we do not consider the error from $M_\pi L$ for the fits, as they are much smaller than the errors in ξ and we have found them to have a negligible effect.

3.4.2 Fits to ChPT

We first work at fixed N_c and fit each channel separately to SU(4) ChPT up to NLO and U(4) ChPT up to NNLO. We determine the values of L_R from the fits, as well as K_R and W for fits to U(4) ChPT and the AA channel, respectively. Results are shown in table 3.4 for the SS channel and table 3.5 for the AA channel. For the SS channel, we observe that ChPT fails to describe the lattice results for the heaviest masses, and we opt not to include the $N_c = 3$ ensembles with $\xi \gtrsim 0.14$ in the fits. For fits to the

N_c	SU(4) ChPT		U(4) ChPT		
	$L_{SS} \times 10^3$	χ^2 / dof	$L_{SS} \times 10^3$	$K_{SS} \times 10^3$	χ^2 / dof
3	-1.85(7)	1.8/4	-2.5(7)	-0.5(6)	1.6/3
4	-1.79(8)	3.0/3	-0.9(8)	1.3(1.0)	0.1/2
5	-1.83(11)	2.3/3	-2.2(6)	-0.3(9)	2.3/2
6	-2.10(16)	3.8/3	-1.7(8)	1.2(1.7)	2.8/2

Table 3.4. Results of fits of ΔE_{SS} to SU(4) and U(4) ChPT at fixed N_c . $N_c = 3$ ensembles with $\xi \gtrsim 0.14$ are not fitted.

N_c	SU(4) ChPT			U(4) ChPT			
	$L_{AA} \times 10^3$	W/fm^{-2}	χ^2 / dof	$L_{AA} \times 10^3$	$K_{AA} \times 10^3$	W/fm^{-2}	χ^2 / dof
3	-2.4(5)	-72(17)	23.4/8	1.7(1.3)	2.2(7)	-39(23)	12.8/7
4	-1.8(1.2)	-45(30)	1.2/3	-1.1(2.7)	0.5(2.3)	-41(32)	1.2/2
5	-4.2(1.1)	-75(22)	8.5/3	1.2(2.8)	5.6(2.7)	-41(32)	3.9/2
6	-5.4(1.5)	-72(24)	5.4/3	0.1(3.2)	6.6(3.3)	-39(33)	1.6/2

Table 3.5. Results of fits ΔE_{AA} to SU(4) and U(4) ChPT at fixed N_c .

AA channel, on the other hand, we use the W result in eq. (3.36) as an additional prior.

The results for L_R are represented in figs. 3.9a and 3.9b. We observe that both in the SU(4) and the U(4) theories they are well described by a leading and a subleading N_c dependence—see eq. (3.16). However, only the U(4) result reproduces the expected common large N_c behavior of both channels. Linear fits are performed separately for each channel in fig. 3.9a, while in fig. 3.9b a common large N_c limit is imposed.

A similar study is presented in fig. 3.9c for K_R determined from fits to U(4) ChPT. This quantity should only include a leading N_c dependence at the order we work, which should be equal in both channels—see eq. (3.22). We observe the fit results for each channel are consistent with a single $\mathcal{O}(N_c^2)$ term, but this is not equal for both channels. A universal large N_c limit is only reproduced if subleading N_c corrections are included.

We next perform fits including all N_c to both SU(4) and U(4) theories for both channels. We parametrize L_R as in eq. (3.16) and include only a

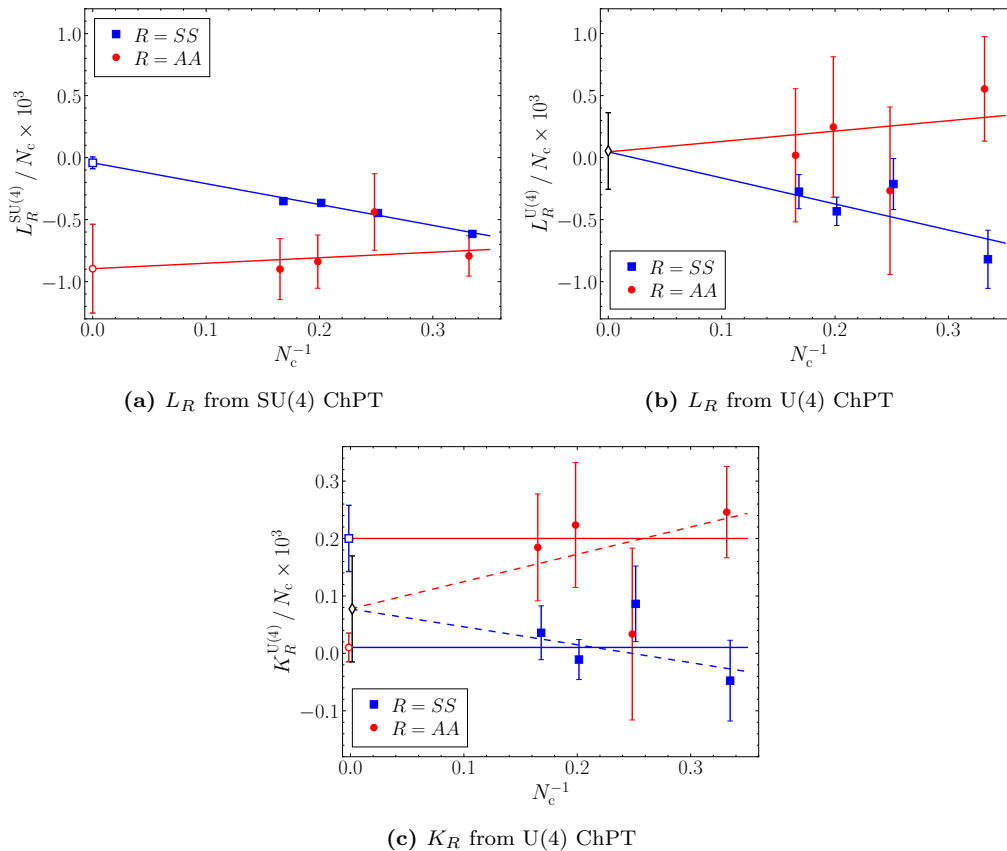


Figure 3.9. Top: Results for the LECs from fits to ChPT at fixed N_c for the SS (blue squares) and AA (red dots) channels. The lines are fits to eq. (3.16), and the empty points are the large N_c prediction. In the U(4) theory, we have imposed a common large N_c result for both channels. **Bottom:** Results for K_R from fits to U(4) ChPT for the SS (blue squares) and AA (red dots) channels. The points are fitted to a different constant for each channel (solid lines) and to a constrained linear dependence (dashed lines).

$\mathcal{O}(N_c^2)$ term for K_R , this is, $K_R = N_c^2 K_R^{(0)}$. Results for separate fits to each channel are summarized in table 3.6. Note that the results for $L^{(0)}$ are only compatible for the U(4) fit, which also leads to smaller values of the χ^2 . We finally perform a simultaneous fit of both channels to U(4) ChPT. We impose a common large N_c limit for L_R , but keep the K_R terms different. The results are presented in table 3.7 and are illustrated in fig. 3.10.

3.4.3 Discussion and comparison to previous literature

From the results of the global fit of both channels to U(4) ChPT, given in table 3.7, we observe that the leading N_c contribution to the LECs, $L^{(0)}$, is anomalously small. In addition, using eqs. (3.23) and (3.24), we can determine the N_f dependence of the subleading term,

Channel	Fit	$L^{(0)} \times 10^3$	$L_R^{(1)} \times 10^3$	$K_R^{(0)} \times 10^5$	W/fm^{-2}	χ^2/dof
SS	SU(4)	-0.04(1.3)	-1.70(18)	—	—	12.8/15
	U(4)	-0.01(7)	-1.78(20)	1.2(2.5)	—	12.2/14
AA	SU(4)	-1.22(19)	0.8(4)	—	-94(15)	38.5/19
	U(4)	-0.1(4)	1.8(4)	21(5)	-32(23)	22.5/18

Table 3.6. Fit results to SU(4) and U(4) ChPT for both the SS and AA channels.

$L^{(0)} \times 10^3$	$L_{SS}^{(1)} \times 10^3$	$L_{AA}^{(1)} \times 10^3$	$K_{SS}^{(0)} \times 10^5$	$K_{AA}^{(0)} \times 10^5$	W/fm^{-2}	χ^2/dof
-0.02(8)	-1.79(19)	1.7(4)	0.8(2.2)	22(3)	-31(9)	35.6/33

Table 3.7. Results from a simultaneous fit of both the AA and SS channels to U(4) ChPT, imposing a common large N_c limit for L_R . The goodness of the fit is illustrated in fig. 3.9.

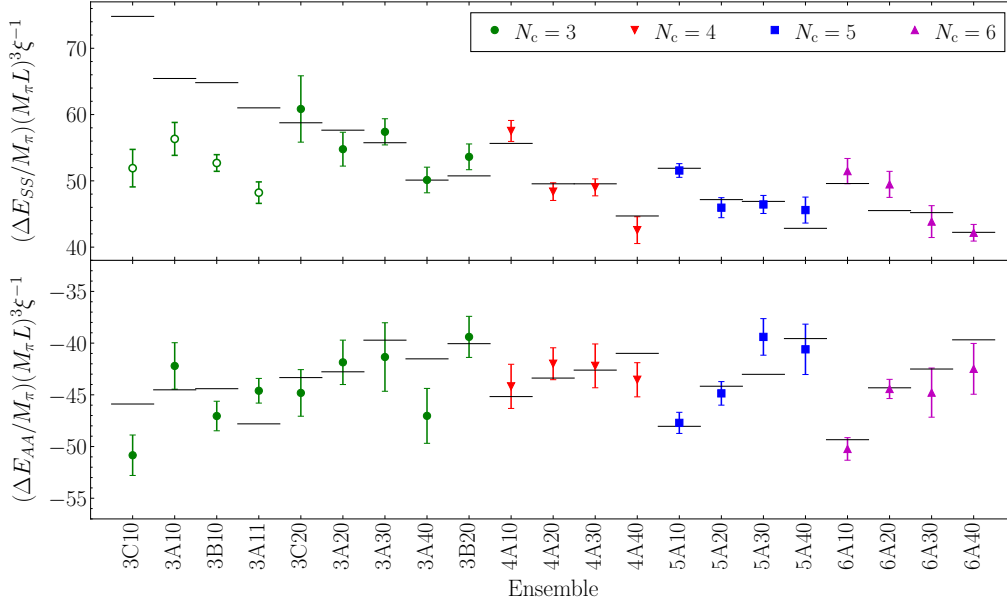


Figure 3.10. Results of a simultaneous chiral and N_c fit to U(4) ChPT predictions of both the SS (top) and AA (bottom) channels. Points represent our lattice results multiplied by a factor that eliminates leading chiral and N_c dependencies, and horizontal lines are the best fit predictions from U(4) ChPT, as summarized in table 3.7. Empty points in the SS channel are not fitted. Within each color, ξ decreases from left to right.

$$\begin{aligned}
L_0 + L_3 - L_5 + L_8 &= -0.02(8)N_c - 0.01(5)N_f + \mathcal{O}(N_c^{-1}), \\
L_1 + L_2 - L_4 + L_6 &= -0.88(10) + \mathcal{O}(N_c^{-1}).
\end{aligned}
\tag{3.41}$$

A striking result is that the leading N_c term is suppressed compared to subleading corrections, which dominates at low values of N_c . It also seems that the subleading term proportional to N_f is much smaller than that independent of the number of colors. However, note that these coefficients are scale-dependent, and this situation changes for other choices of the renormalization scale—see eq. (1.82).

Our results can be compared to predictions obtained in the resonant chiral theory (RChT) [166, 276, 277], in which the LECs at large N_c are saturated by the contributions obtained from integrating out low-lying resonances. In the single-resonance approximation, one obtains the same result for both the SS and the AA channel, $L_R^{\text{RChT}} = -0.07 \cdot N_c$ [276]. This agrees with our $U(4)$ result at large N_c , but fails at $N_c = 3$, where subleading effects dominate.

The SS channel results for $N_c = 3$ can moreover be compared to results available in the literature for the isospin-two channel with $N_f < 4$. To do so, we first determine L_{SS} for the desired N_f , using eq. (3.41). Then, we use eq. (3.25) to translate our results to the $SU(N_f)$ theory and, finally, we change the renormalization scale to the one used in the literature.¹ Our ensembles have $\mu = 1.40(12)$ GeV, determined averaging the quantity in eq. (3.38) over all ensembles. We quote separately the error related to the change of scale.

For $N_f = 3$ we compare to results for the LECs coming from fits to experimental data. These are presented at the mass of the $\rho(770)$ resonance, $\mu = M_\rho = 0.77$ GeV,

$$\begin{aligned}
L_{I_{\pi\pi=2}}^{N_c=3, N_f=3} &= -1.14(22)_{\text{stat}}(11)_\mu \times 10^{-3} \text{ this work,} \\
L_{I_{\pi\pi=2}}^{N_c=3, N_f=3} &= -0.9(1.5) \times 10^{-3} \quad \text{ref. [279] (table 1, col. 2),} \\
L_{I_{\pi\pi=2}}^{N_c=3, N_f=3} &= -0.7(3.2) \times 10^{-3} \quad \text{ref. [147],}
\end{aligned}
\tag{3.42}$$

where the error in the last two is computed from adding in quadrature the error of the separate LECs contributing.

We also compare to lattice results for $N_f = 2$ at a scale $\mu = \sqrt{2}F_{\pi, \text{phys}} \approx 130.2$ MeV [183]. For $N_f = 2$, one typically quotes the quantity

$$\ell_{I_{\pi\pi=2}} = 512\pi^2 L_{SS}^{N_c=3, N_f=2}. \tag{3.43}$$

¹Note that the running of the LECs is different between the $SU(N_f)$ [278] and $U(N_f)$ [165] theories.

We obtain

$$\begin{aligned}
 \ell_{I_{\pi\pi=2}} &= 4.3(1.2)_{\text{stat}}(0.5)_{\mu}, && \text{this work,} \\
 \ell_{I_{\pi\pi=2}} &= 4.65(0.85)_{\text{stat}}(1.07)_{\text{sys}} && \text{ref. [267] ,} \\
 \ell_{I_{\pi\pi=2}} &= 3.79(0.61)_{\text{stat}} \left(\begin{smallmatrix} +1.34 \\ -0.11 \end{smallmatrix} \right)_{\text{sys}} && \text{ref. [270] ,}
 \end{aligned}
 \tag{3.44}$$

where the results in refs. [267, 270] separately quote statistical and systematic errors.

The AA channel cannot be compared to experimental results as it only exists for $N_f \geq 4$. However, this channel shows attractive interactions and so one could wonder if it might present a resonant state that may be interpreted as a tetraquark. LHCb has recently reported on the finding of several tetraquark states. These include the $T_{c\bar{s}0}^0(2900)$ in the mass spectrum of $D^- K^+$ [30, 31], and the $T_{c\bar{s}0}^{++}(2900)$ and $T_{c\bar{s}0}^0(2900)$ in the mass spectrum of $D_s^+ \pi^+$ and $D_s^+ \pi^-$ [32, 33], respectively. In a theory with $N_f = 4$ degenerate quarks, all the aforementioned states would have the same flavor, spin and parity quantum numbers of the AA channel.

To explore the possible existence of such a state at higher center-of-mass energy, we use the inverse amplitude method, described in sec. 2.2.1. In fig. 3.11, we represent the phase shift of the unitarized amplitude in the $U(4)$ theory at fixed $\xi = 0.1$ and $N_c = 3$, computed from eq. (3.19). We use our best-fit results from table 3.7 for L_{AA} and K_{AA} , and let L'_{AA} and L''_{AA} be zero, with errors of the size of L_{AA} . We also set $K'_{AA} = 0$. From this analysis, we

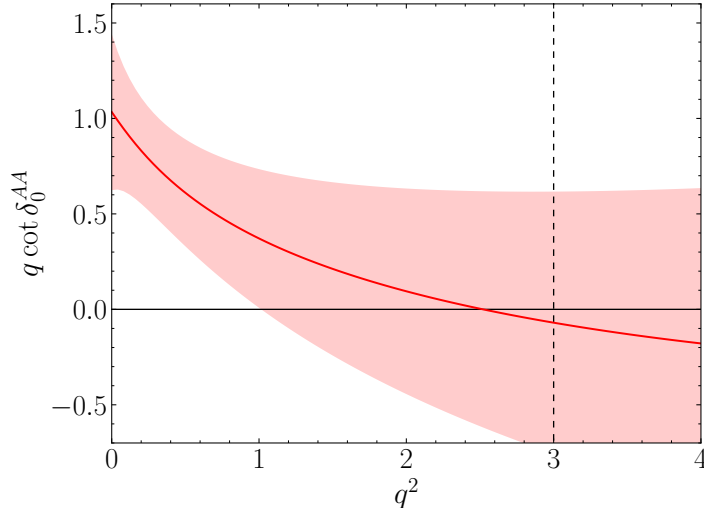


Figure 3.11. Unitarized result for $q \cot \delta_0$ for the AA channel obtained applying the inverse amplitude method to the $U(N_f)$ ChPT amplitude in eq. (3.19), with values of the parameters as defined in the text. We observe a change of sign, indicating the possible presence of a tetraquark resonance.

conclude it is plausible that a tetraquark resonance is present in this channel, as indicated by $q \cot \delta_0$ crossing the horizontal axis from above. Note that while the LEC values differ between standard and unitarized ChPT, this difference is small and should not affect our qualitative conclusions.

3.5 Conclusions

In this chapter, we have presented the results from refs. [1, 8], in which pion-pion interactions near threshold are studied for varying number of colors, N_c . We have used a theory with $N_f = 4$ degenerate quark flavors, and focused on two different scattering channels: the SS channel, which is analogous to the $I_{\pi\pi} = 2$ channel of two-flavor QCD, and the AA channel, which is attractive and only exists for $N_f \geq 4$.

Running lattice simulations with $N_c = 3 - 6$ and $M_\pi = 360 - 590$ MeV, we have determined the ground-state finite-volume energies for both channels of interest. The computations have been performed using two different regularizations of valence fermions: a unitary setup with Wilson fermions, and a mixed-action setup with a twisted mass in the valence quarks. By comparing both, which must coincide in the continuum, we have identified large discretization effects in the AA sector, which are constrained by comparing results at various lattice spacing.

Using the two-particle finite-volume formalism, we have matched our results to ChPT, finding that the correct large N_c behavior is only reproduced by $U(N_f)$ ChPT predictions, which we have calculated up to NNLO. From this comparison, the leading and subleading N_c dependence of the relevant LECs have been constrained. The results indicate that the leading coefficient in the N_c is abnormally small compared to subleading corrections.

One of the most interesting observations of this work is the attractive nature of the AA channel. An exploratory study based on the inverse amplitude method suggests the possible existence of a tetraquark resonance at higher center-of-mass energies in this channel, which could be related to some experimental findings of tetraquark states in the LHCb experiment [30–33]. In the next chapter, ongoing work in this direction is presented, in which we focus on the study of meson-meson interactions as a function of energy. One of our main goals is to explore the possible presence of a tetraquark state in the AA channel, which may open the door to study the nature of tetraquark states as a function of the number of colors.

4 Meson-meson scattering at large N_c

The possible existence of tetraquarks in the large N_c limit has been a topic of controversy during the last decade—see sec. 1.3.2. Traditionally, such states were thought not to exist at large N_c [122, 123], but recent arguments pointed in the opposite direction [137–139]. Lattice QCD provides us with a tool to shed light on this question from first principles, by simulating QCD with varying number of colors. In particular, the setup presented in chapter 3—with $N_f = 4$ degenerate light quark flavors—represents an interesting playground to explore the existence of tetraquarks at large N_c .

In a theory with $N_f = 4$ degenerate quark flavors, meson interactions happen in seven scattering channels—see sec. 3.1. Of particular interest for the search of tetraquarks is the AA channel, which only exists for $N_f \geq 4$. It presents attractive interactions at low energies, and a study based on unitarized ChPT, presented in sec. 3.4.3, suggests that this channel may contain a resonance. Due to its flavor quantum number—some of its states have four open flavors—such a resonance would undoubtedly be a tetraquark.

The possible existence of a tetraquark in this channel is further supported by recent experimental findings. During the last year, LHCb has reported on the discovery of different tetraquark resonances. These include the $T_{cs0}^0(2900)$, observed in the mass spectrum of D^-K^+ [30, 31], and the $T_{c\bar{s}}^{++}(2900)$ and the $T_{c\bar{s}}^0(2900)$, found in the mass spectra of $D_s^+\pi^+$ and $D_s^+\pi^-$ [32, 33], respectively. While in real-world QCD these states are expected to be part of two separate isospin triplets, they would all share the quantum numbers of the AA channel in a theory with $N_f = 4$ degenerate flavors. It is worth mentioning that all these states have phenomenologically been described as vector-meson molecules [280], since their masses lie close to the D^*K^* and $D_s^*\rho$ thresholds.

Another interesting experimental finding is that of the $T_{c\bar{s}1}^0$ vector tetraquark, observed in the mass spectrum of D^-K^+ [30, 31]. In our model, this particle would be part of the 45 dimensional irreps, known as the AS and SA channels. These two irreps are related by charge conjugation and so share the same scattering amplitude. We thus only consider the AS channel from here on.

This chapter presents some results on the N_c dependence of meson-meson interactions for energies up to the four-pion threshold [2, 10]. In particular, we use the $N_f = 4$ setup presented in chapter 3, and focus on the SS , AA and AS channels. We analyze meson-meson interactions as a function of the energy below the four-pion threshold, and explore the possible presence of tetraquark states in the AA and AS channels.

The chapter is organized as follows. In sec. 4.1, the lattice setup used for this study is described, with particular emphasis on the set of operators used to compute the correlation functions. In sec. 4.2, we explain how finite-volume energies are determined and present our results for the finite-volume spectra of all three channels for varying N_c . In sec. 4.3 the two-particle quantization condition is used to constrain the scattering phase shifts, and we study their dependence on the number of colors. We end with a brief conclusion in sec. 4.4.

4.1 Lattice setup

To study meson-meson interactions as a function of N_c , we use replicas of the 3A11, 4A10, 5A10 and 6A10 ensembles—see table 3.1 for a summary of the simulation parameters—and consider a unitary setup with clover-improved Wilson fermions. These ensembles have $N_c = 3 - 6$, as indicated by the first digit in their name, and share a very similar heavier-than-physical pion mass, $M_\pi \approx 590$ MeV, and lattice spacing, $a = 0.075$ fm. Lattice simulations are performed with the HiRep code [263, 264], as done for the work presented in chapter 3.

4.1.1 Set of interpolating operators

The study of meson-meson scattering on the lattice requires the determination of the two-particle finite-volume energy spectrum for the energy range of interest. As Lüscher's quantization condition is limited to energies at which only two-particle states can go on-shell, we are restricted to work

below any three- or four particle elastic regime.¹ In our case, this roughly corresponds to energies below the four-pion inelastic threshold, $E_{4\pi} = 4M_\pi$.²

To reliably determine all finite-volume energies, as was explained in sec. 1.2.3, one needs to compute a matrix of correlation functions,

$$C_{ij}(t) = \langle O_i(t)O_j^\dagger(0) \rangle, \quad (4.1)$$

for a sufficiently large set of operators, $\{O_i\}$. This set must contain operators having significant overlap onto all the finite-volume states expected in the energy range of interest. For example, if one expects a resonant state to appear in the scattering process, the inclusion of an interpolating single-particle operator with the quantum numbers of such state may be necessary to properly determine the finite-volume spectrum [281].

For our work, we consider three types of interpolating operators, working at various values of the total three-momentum, \mathbf{P} . We use two types of two-meson operators, with the form of two pions, $\pi\pi$, or two vector mesons, $\rho\rho$, which are complemented by local tetraquark operators, T . The inclusion of $\rho\rho$ operators is required since in our ensemble vector mesons are stable bound states, with a mass $M_\rho \lesssim 2M_\pi$ —see table 4.1—and so states of two vector mesons may lie below the four-pion threshold. It is also useful in the search for tetraquarks, since it has been argued [280] that the tetraquarks of interest could be molecular states of two vector mesons.

The starting point to construct two-particle interpolating operators are single-meson operators. These are constructed as quark-bilinears projected to definite three-momentum \mathbf{p} ,

$$O_M(\mathbf{p}, \Gamma; t) = \sum_{\mathbf{x}} \bar{q}_{f_1}(\mathbf{x}; t) \Gamma q_{f_2}(\mathbf{x}; t) e^{-i\mathbf{p}\mathbf{x}}, \quad (4.2)$$

Here, Γ is a matrix in Dirac space that characterizes the intrinsic transformation properties of the meson under rotations, parity and charge conjugation. Also, momentum projection is performed summing over the set of all lattice sites with fixed time coordinate t . Note the two fermions are allowed to have different flavors, f_1 and f_2 , which we use to project to definite isospin.

Single-particle operators with zero total momentum are used to determine the mass of pseudoscalar ($\Gamma = \gamma_5$, to which we refer as π), scalar ($\Gamma = \mathbb{1}$, a_0), vector ($\Gamma = \gamma_i$, ρ) and axial ($\Gamma = \gamma_5\gamma_i$, a_1) non-singlet mesons. The results are summarized in table 4.1 for all four ensembles. Note that these results only give an accurate result for the pion mass. Other mesons have a

¹A formalism that allows one to study three-to-two processes exists—see ref. [230]—but we restrict ourselves to the two particle sector.

²As we will see below, in our ensembles vector mesons are stable, and so the $\rho\pi\pi$ threshold lies slightly below that of four pions.

Ensemble	$\Gamma = \gamma_5 (aM_\pi)$	$\Gamma = \gamma_i (aM_\rho)$	$\Gamma = \mathbb{1} (aM_{a_0})$	$\Gamma = \gamma_5 \gamma_i (aM_{a_1})$
3A11	0.2130(7)	0.355(4)	0.430(15)	0.45(3)
4A10	0.2026(6)	0.396(8)	0.409(24)	0.55(3)
5A10	0.2131(5)	0.403(4)	0.405(14)	0.590(12)
6A10	0.2169(5)	0.417(4)	0.412(10)	0.608(14)

Table 4.1. Masses in lattice units of different types of non-singlet mesons, characterized by different choices of Γ in eq. (4.2). The results are determined from the single particle correlator, neglecting interactions with multiparticle states.

non-zero overlap into two-particle states and so an exhaustive determination of their masses should come from a variational analysis that includes mixing with multiparticle states. Nevertheless, this approximate result shows that $\rho\rho$ operators must be included in the set of operators, as such states will appear close below the four-pion threshold. Operators of two axial or scalar mesons, on the other hand, need not be included. We note that in the case of pions and vector mesons, we also determine the one-particle correlation functions at non-zero momentum, needed to compute ratios as presented in eq. (4.22).

Interpolating operators of two particles are build as the product of two single-meson operators,

$$\begin{aligned}
(\pi\pi)(\mathbf{p}_1, \mathbf{p}_2) &= O_M(\mathbf{p}_1, \gamma_5)O_M(\mathbf{p}_2, \gamma_5), \\
(\rho_i\rho_j)(\mathbf{p}_1, \mathbf{p}_2) &= O_M(\mathbf{p}_1, \gamma_i)O_M(\mathbf{p}_2, \gamma_j),
\end{aligned} \tag{4.3}$$

where $\mathbf{P} = \mathbf{p}_1 + \mathbf{p}_2$. To study the scattering of two mesons, these operators are projected to definite flavor channel, as well as to irreps of the cubic group (for $\mathbf{P} = 0$) or the relevant little group (for $\mathbf{P} \neq 0$). For simplicity, we refer generically to the latter irreps as *cubic-group irreps*. Note that flavor and cubic-group projections can be performed independently: the former only involves quark flavors, while the latter concerns momenta and spin.

The projection to flavor irreps determines the different Wick contractions contributing to the correlation function. For example, we consider pion-pion operators of the form

$$\begin{aligned}
(\pi\pi)^{SS}(\mathbf{p}_1, \mathbf{p}_2) &= \pi^+(\mathbf{p}_1)D_s^+(\mathbf{p}_2) + K^+(\mathbf{p}_1)D^+(\mathbf{p}_2) + (\mathbf{p}_1, \leftrightarrow \mathbf{p}_2), \\
(\pi\pi)^{AA}(\mathbf{p}_1, \mathbf{p}_2) &= \pi^+(\mathbf{p}_1)D_s^+(\mathbf{p}_2) - K^+(\mathbf{p}_1)D^+(\mathbf{p}_2) + (\mathbf{p}_1, \leftrightarrow \mathbf{p}_2), \\
(\pi\pi)^{AS}(\mathbf{p}_1, \mathbf{p}_2) &= \pi^+(\mathbf{p}_1)D_s^+(\mathbf{p}_2) + K^+(\mathbf{p}_1)D^+(\mathbf{p}_2) - (\mathbf{p}_1 \leftrightarrow \mathbf{p}_2),
\end{aligned} \tag{4.4}$$

and similarly for $\rho\rho$ operators, using the respective vector mesons (ρ , K^* , D^* and D_s^*). These states can be used to determine the form of the correlation function, presented in sec. 4.1.2 below. Note that the SS and AA states are even under particle exchange, while the AS is odd. This implies the former two channels only contain even partial waves, while the latter contains odd partial waves.

Projection to definite cubic-group irreps is performed following eq. (1.52). This is simple for two-pion states, as one basically only needs to take into account possible momenta combinations, but becomes cumbersome for two vector-mesons. The reason is that, as their name indicates, vector mesons possess an additional vector index. This means that for some given \mathbf{p}_1 and \mathbf{p}_2 , nine different combinations of the vector indices i and j in $\rho\rho$ operators are possible—see the second line of eq. (4.3). Thus, for a fixed non-interacting energy—defined as the sum of the single-meson energy associated to each of these particles, $E^{\text{free}} = E_{M,\mathbf{p}_1} + E_{M,\mathbf{p}_2}$ —several different projections may exist to one same irrep. For example, if we consider the $\mathbf{P} = (0, 1, 1)$ frame with $|\mathbf{p}_1|^2 = 0$ and $|\mathbf{p}_2|^2 = 2$, three different $\rho\rho$ operators transform under the A_1 irrep,

$$\begin{aligned} (\rho\rho)_1 &= \rho_2([0, 0, 0])\rho_3([0, 1, 1]) + \rho_3([0, 0, 0])\rho_2([0, 1, 1]), \\ (\rho\rho)_2 &= \rho_2([0, 0, 0])\rho_2([0, 1, 1]) + \rho_3([0, 0, 0])\rho_3([0, 1, 1]), \\ (\rho\rho)_3 &= \rho_1([0, 0, 0])\rho_1([0, 1, 1]), \end{aligned} \tag{4.5}$$

where the numbers in square brackets are the three-momenta, which we express in this chapter in units of $2\pi/L$, with L the lattice side.

To systematically determine all $\rho\rho$ operators in each cubic-group irrep, we initially consider all possible operators with the same non-interacting energy, to which eq. (1.52) is applied. The resulting projected operators are not all linearly independent, and so we need to determine a maximal set of linearly independent ones. We note that, while it is possible to construct two-vector-meson operators in almost all cubic-group irreps, we only focus on irreps containing pion-pion s -wave interactions for the SS and AA , and p -wave interactions for the AS channels, respectively. The number of operators considered in each irrep is shown in table 4.2.

Two-particle operators are complemented by local tetraquark operators, which may be required to correctly determine the finite-volume energy spectrum if tetraquark states are present. These operators are constructed from the local product of two quark bilinears, projected to definite total momentum,

Irrep	SS and AA channels			AS channel		
	$\pi\pi$	$\rho\rho$	T	$\pi\pi$	$\rho\rho$	T
$A_1^+(0)$	5	6	5	–	–	–
$T_1^-(0)$	–	–	–	4	8	2
$A_1(1)$	5	9	7	5	9	2
$E(1)$	–	–	–	3	13	2
$A_1(2)$	8	18	9	6	12	2
$B_1(2)$	–	–	–	4	15	2
$B_2(2)$	–	–	–	6	16	2
$A_1(3)$	5	7	7	5	7	2
$E(1)$	–	–	–	5	12	2
$A_1(4)$	5	8	7	2	3	2
$E(1)$	–	–	–	3	9	2

Table 4.2. Number of operator of operators of each type used in each isospin channel and cubic-group irrep. The number in parenthesis indicates $|\mathbf{P}|^2$ in units of $2\pi/L$. We note that operators in E and T_1^+ irreps have multiplicity two and three, respectively.

$$\begin{aligned}
T_{\Gamma_1, \Gamma_2}(\mathbf{P}, t) &= \sum_{\mathbf{x}} T_{\Gamma_1 \Gamma_2}(x) e^{-i\mathbf{P}\mathbf{x}} \\
&= \sum_{\mathbf{x}} \bar{q}_{f_1}(x) \Gamma_1 q_{f_2}(x) \bar{q}_{f_3}(x) \Gamma_2 q_{f_4}(x) e^{-i\mathbf{P}\mathbf{x}}, \quad (4.6)
\end{aligned}$$

where $x = (t, \mathbf{x})$. We consider several combinations $\{\Gamma_1, \Gamma_2\}$ for both scalar and vector channels, having the spin, J , parity, P and charge conjugation, C , quantum numbers of interest. In particular, we use

$$\begin{aligned}
J^{PC} = 0^{++} &: \{\gamma_5, \gamma_5\}, \{\gamma_5 \gamma_0, \gamma_5 \gamma_0\}, \{\mathbb{1}, \mathbb{1}\}, \{\gamma_i, \gamma_j\}, \{\gamma_5 \gamma_i, \gamma_5 \gamma_i\}, \\
J^{PC} = 1^{-+} &: \{i\gamma_5, \gamma_5 \gamma_i\}, \{\gamma_5 \gamma_0, \gamma_5 \gamma_i\}.
\end{aligned} \quad (4.7)$$

Note the i factor in the first combination of the 1^{-+} tetraquark. This is required to ensure the operator is correctly hermitian, and so the correlation matrix obeys $C^*(t) = C(T - t)$, with T the time extent of the lattice, that we use to average our numerical results.

Tetraquark operators are also projected to flavor irreps, in analogy to eq. (4.4), and to definite cubic-group irreps using eq. (1.52). The total number of tetraquark operators considered for this work for each channel and irrep is presented in table 4.2

4.1.2 Computation of correlation functions

The correlation functions in the channels of interest can be computed as a linear combination of the connected and disconnected Wick contractions, diagrammatically shown in fig. 3.1, using different combinations of momenta and Dirac structures. We can write

$$\begin{aligned} C^{SS}(t) &= D_1 + D_2 - C_1 - C_2, \\ C^{AA}(t) &= D_1 + D_2 + C_1 + C_2, \\ C^{AS}(t) &= D_1 - D_2 - C_1 + C_2, \end{aligned} \quad (4.8)$$

where we have introduced

$$\begin{aligned} D_1 &= D(\mathbf{p}_1, \Gamma'_1, \mathbf{p}_2, \Gamma'_2; \mathbf{k}_1, \Gamma_1, \mathbf{k}_2, \Gamma_2), \\ D_2 &= D(\mathbf{p}_2, \Gamma'_2, \mathbf{p}_1, \Gamma'_1; \mathbf{k}_1, \Gamma_1, \mathbf{k}_2, \Gamma_2), \\ C_1 &= C(\mathbf{p}_1, \Gamma'_1, \mathbf{p}_2, \Gamma'_2; \mathbf{k}_1, \Gamma_1, \mathbf{k}_2, \Gamma_2), \\ C_2 &= C(\mathbf{p}_2, \Gamma'_2, \mathbf{p}_1, \Gamma'_1; \mathbf{k}_1, \Gamma_1, \mathbf{k}_2, \Gamma_2). \end{aligned} \quad (4.9)$$

Here $(\mathbf{k}_1, \mathbf{k}_2)$ and $(\mathbf{p}_1, \mathbf{p}_2)$ are the momenta of the initial- and final-state particles, respectively, with $\mathbf{P} = \mathbf{k}_1 + \mathbf{k}_2 = \mathbf{p}_1 + \mathbf{p}_2$, while (Γ_1, Γ_2) and (Γ'_1, Γ'_2) are the corresponding Dirac matrices. The connected and disconnected contractions take the general form, respectively,

$$\begin{aligned} D_1 &= \sum_{\mathbf{x}_1, \mathbf{x}_2} \sum_{\mathbf{y}_1, \mathbf{y}_2} e^{-i(\mathbf{p}_1 \mathbf{y}_1 + \mathbf{p}_2 \mathbf{y}_2)} e^{i(\mathbf{k}_1 \mathbf{x}_1 + \mathbf{k}_2 \mathbf{x}_2)} \Theta(\mathbf{x}_1, \mathbf{x}_2) \Theta(\mathbf{y}_1, \mathbf{y}_2) \\ &\quad \times \langle \text{Tr} [\hat{\Gamma}'_1 S(\mathbf{y}_1, \mathbf{x}_1) \tilde{\Gamma}'_1 S^\dagger(\mathbf{y}_1, \mathbf{x}_1)] \text{Tr} [\hat{\Gamma}'_2 S(\mathbf{y}_2, \mathbf{x}_2) \tilde{\Gamma}'_2 S^\dagger(\mathbf{y}_2, \mathbf{x}_2)] \rangle, \end{aligned} \quad (4.10)$$

$$\begin{aligned} C_1 &= \sum_{\mathbf{x}_1, \mathbf{x}_2} \sum_{\mathbf{y}_1, \mathbf{y}_2} e^{-i(\mathbf{p}_1 \mathbf{y}_1 + \mathbf{p}_2 \mathbf{y}_2)} e^{i(\mathbf{k}_1 \mathbf{x}_1 + \mathbf{k}_2 \mathbf{x}_2)} \Theta(\mathbf{x}_1, \mathbf{x}_2) \Theta(\mathbf{y}_1, \mathbf{y}_2) \\ &\quad \times \langle \text{Tr} [\hat{\Gamma}'_2 S(\mathbf{y}_2, \mathbf{x}_1) \tilde{\Gamma}'_1 S^\dagger(\mathbf{y}_1, \mathbf{x}_1) \hat{\Gamma}'_1 S(\mathbf{y}_1, \mathbf{x}_2) \tilde{\Gamma}'_2 S^\dagger(\mathbf{y}_2, \mathbf{x}_2)] \rangle, \end{aligned} \quad (4.11)$$

where we define $\hat{\Gamma} = \gamma_5 \Gamma$ and $\tilde{\Gamma} = \gamma_0 \Gamma^\dagger \gamma_0 \gamma_5$, and $\langle \dots \rangle$ indicates ensemble average. We have also introduced functions that generalize these contractions to both two-particle and tetraquark operators. For the initial state, we use

$$\Theta(\mathbf{x}_1, \mathbf{x}_2) = \begin{cases} 1 & \text{Two-particle operator at source,} \\ \delta_{\mathbf{x}_1, \mathbf{x}_2} & \text{Tetraquark operator at source,} \end{cases} \quad (4.12)$$

and similarly for the final-state operator and $\Theta(\mathbf{y}_1, \mathbf{y}_2)$.

To evaluate the correlation functions we use different techniques for each type of operator at source. At sink, on the other hand, we project to definite momentum summing over the whole lattice. Correlation functions with two mesons at source are computed using time- and spin-diluted $\mathbb{Z}_2 \times \mathbb{Z}_2$ stochastic sources, and are averaged by repeating the computations on 36 different time slices for each configuration. On the other hand, correlation functions with a tetraquark operator at source are first computed using point sources localized in a sparse spacial lattice,

$$\Lambda_S(t) = \{(t, s_1 + dn_1, s_2 + dn_2, s_3 + dn_3) \mid n_i \in \mathbb{Z}, 0 \leq n_i < L/d, 0 \leq s_i < d\}, \quad (4.13)$$

where $s_i \in \mathbb{Z}$ are some randomly chosen offsets. The results are later projected to definite total momentum summing only over this sparse lattice,

$$T_{\text{sp}}(\mathbf{P}) = \sum_{\mathbf{x} \in \Lambda_S(t)} T(\mathbf{x}) e^{-i\mathbf{P}\mathbf{x}}. \quad (4.14)$$

We use a step $d = 4$ for all our ensembles, and repeat the computation for two time slices separated by half of the lattice time extent, with different random offsets s_i .

After computing the matrix of correlation functions, we use the relations $C(t) = C^\dagger(t)$ and $C(T - t) = C^*(t)$ to average the numerical results. For all operators considered here, the matrix of correlators in the SS and AA channels is purely real. Thus, we set the imaginary part of our lattice results to zero, as it is just a numerical artifact of the use of stochastic sources for meson-meson operators. By contrast, the correlation function for the AS channel is expected to be complex-valued. Still we empirically observe that, in general, the imaginary part of two-meson correlation functions to be much smaller than the real part.

4.2 Finite-volume energy spectra

Using the matrix of correlators, $C(t)$, it is possible to determine the finite-volume energy spectrum beyond the ground state. This requires the application of variational methods, such as the GEVP—see eq. (1.54). The applicability of this technique, however, relies on the assumption that no thermal pollution is present. The only exception to this is the case of real correlation functions, for which backwards propagation can be allowed—see eq. (1.61).

In our ensembles, general thermal pollution is present. As discussed in sec. 1.2.4, our correlators are expected to have the general form in eq. (1.60). For example, the real part looks like

$$\text{Re } C(t) = \sum_n A_n \cosh(E_n t') + \sum_{m,n} B_{nm} \cosh(\Delta E_{mn}^{\text{th}} t'), \quad (4.15)$$

where $\tilde{t} = t - T/2$, and A_n and B_{mn} are related to the correlator matrix elements, while the imaginary part is analogous with hyperbolic sine functions instead of hyperbolic cosines. In eq. (4.15), the first sum contains the two-particle energies that we want to determine, while the second contains thermal effects that depend on an energy difference. For example, the dominant thermal pollution is related to the energy difference between two single-meson states,

$$\Delta E_{mn}^{\text{th}} \approx E_{M,\mathbf{q}_1} - E_{M,\mathbf{q}_2}, \quad (4.16)$$

for momenta such that $\mathbf{P} = \mathbf{q}_1 - \mathbf{q}_2$. The presence of this second term spoils the application of the GEVP, as it prevents the variational approach from converging close to the center of the lattice, where thermal effects may dominate the correlation function.

To mitigate this effect, we use an extension of the shift-reweighting procedure presented in eq. (1.63) that takes into account that our correlation function behaves as a sum of hyperbolic functions rather than of exponentials. This is, we take into account backwards propagation in the correlator. We assume that a two-pion term dominates the second sum of eq. (4.15), with energy $\Delta E^{\text{th}} = E_{\pi,\mathbf{p}_1} - E_{\pi,\mathbf{p}_2}$, and approximately eliminate it by redefining the correlator

$$\tilde{C}(t) = \frac{1}{2} \left\{ \frac{\cosh(\Delta E^{\text{th}} t')}{\cosh[\Delta E^{\text{th}}(t'_+)]} C(t+1) - \frac{\cosh(\Delta E^{\text{th}} t)}{\cosh[\Delta E^{\text{th}}(t'_-)]} C(t-1) \right\}, \quad (4.17)$$

with $t'_\pm = t' \pm 1$. The energies used to eliminate the thermal effects, $E_{\pi,\mathbf{p}}^{\text{free}}$, are single-pion energies computed using the continuum dispersion relation,

$$E_{\pi,\mathbf{p}}^{\text{free}} = \sqrt{\mathbf{p}^2 + M_\pi^2}. \quad (4.18)$$

for different choices of the single-particle momenta, as shown in table 4.3. In the case of the rest, $[0, 1, 1]$ and $[0, 0, 2]$ frames, this simply amounts to computing the derivative of the matrix of correlators.

The procedure presented above removes dominant thermal effects in the real part of the matrix of correlators, but not in the imaginary part. Thus, it completely eliminates the corresponding thermal contaminations for the SS and AA channels, but not for the AS case, which contains a non-zero imaginary part. However, we empirically observe the imaginary part of the AS channel correlators to be, in general, much smaller than its real counterpart, and so we expect this procedure to largely soften the effect of thermal pollution also in this channel.

After getting rid of the leading thermal effects, we use $\tilde{C}(t)$ to solve a GEVP. In particular, we use the *single-pivot procedure*, in which the GEVP

\mathbf{P}	$ \mathbf{p}_1 ^2$	$ \mathbf{p}_2 ^2$
[0, 0, 0]	0	0
[0, 0, 1]	1	0
[0, 1, 1]	1	1
[1, 1, 1]	2	1
[0, 0, 2]	1	1

Table 4.3. Magnitude of the single particle momenta used to perform the shift-reweighting technique in eq. (4.17) that approximately eliminates leading thermal effects. Momenta are indicated in units of $2\pi/L$.

is only solved for the mean of the correlator at a single time $t_d > t_0$,

$$\tilde{C}(t_d)v_n(t_0, t_d) = \lambda(t_0, t_d)\tilde{C}(t_0)v_n(t_0, t_d). \quad (4.19)$$

Then, the resulting matrix of eigenvectors is used to rotate $\tilde{C}(t)$ for all times and samples. In other words, the matrix of eigenvectors determined from the GEVP in eq. (4.19) is used to uniquely define operators that have maximum overlap into a single finite-volume state. We note this procedure is numerically very stable. For our analysis, we use $(t_0, t_d) = (3, 5)$.

Another option is the so-called *rolling-pivot approach*, in which the GEVP is solved for all t in the mean of the correlator, and the eigenvectors at each t are used to rotate $C(t)$ on each sample. We find that the application of this method leads to comparable results.

Note that a priori the applicability of the GEVP to our matrices of correlators may seem incorrect, since we are defining different tetraquark operators at source and sink. At source, we use sparse operators, introduced in eq. (4.14), while we sum over all lattice sites at sink. This means that the matrix elements $\langle 0|T_{\text{sp}}|n\rangle$ and $\langle 0|T|n\rangle$ are in general different. While both the sparse and the non-sparse operators have equal matrix elements for those state on which both overlap, the former operator also has non-zero overlaps with states having total momenta of the form $\mathbf{P} + 2\pi\mathbf{n}/dL$, for $\mathbf{n} \in \mathbb{Z}^3$. However, the A_n coefficient appearing in the spectral decomposition of the correlator—see eq. (4.15)—is the product of that matrix element and the one corresponding to the final-state operator, which does not overlap with those states. For example, if both the initial and the final state operators are a tetraquark,

$$A_n = \langle 0|T(0)|n\rangle\langle n|T_{\text{sp}}|0\rangle, \quad (4.20)$$

and similarly for any two-particle final operator. Thus, $A_n = 0$ for those states on which the final-state operator does not overlap. By projecting

over the whole lattice in the final states, we prevent possible excited-state contamination associated to the sparse operators.

The eigenvalues of the GEVP provide us with information about the overlap of the different operators with each finite-volume state. One can define the relative overlap of state $|n\rangle$ with the operator O_i as

$$\mathcal{Z}_{ni} = \frac{\langle 0|O_i|n\rangle}{\sum_j \langle 0|O_j|n\rangle}. \quad (4.21)$$

An example of the relative overlaps is shown in fig. 4.1 for a reduced set of states and operators in the rest-frame A_1^+ irrep for the AA channel with $N_c = 3$. Each panel presents the relative overlaps of one state into the different operators. We observe that, in general, finite-volume states have maximum overlap onto the operator with the closest associated free energy. For example, in the case of the $\pi(1)\pi(1)$ operator, where the number in parenthesis is the magnitude squared of the pion momentum, this would be two times the energy of a pion with $|\mathbf{p}| = 1$. Also, we note that the $n = 2$ state is predominantly a $\rho\rho$ state. Finally, no state has a dominant overlap into the tetraquark operator, which indicates that our states are all predominantly two-particle states. However, pion-pion operators seem to have a non-negligible overlap onto it, indicating that their inclusion into the operator base may help to better determine the pion-pion spectrum.

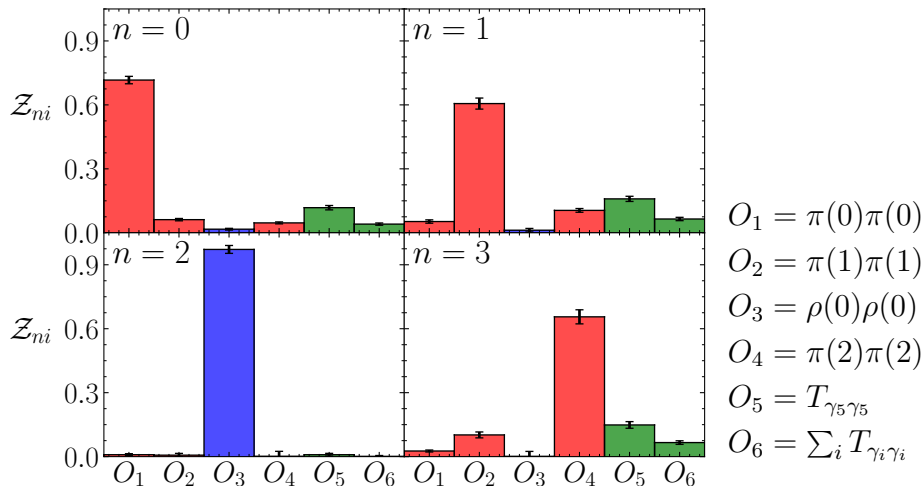


Figure 4.1. Relative overlaps of the lowest-lying finite-volume states, $|n\rangle$, with the operators used to solve the GEVP—see eq. (4.21), for the rest-frame A_1^+ irrep for the AA channel with $N_c = 3$. Different colors correspond to different types of operators: $\pi\pi$ (red), $\rho\rho$ (blue) and local tetraquarks (green). Numbers in parenthesis indicate the magnitude squared of the single-particle momentum, in units of $(2\pi/L)^2$.

The eigenvalues of the GEVP are used to extract the lowest lying finite-volume energies, E_n . To improve this determination, we define ratios generalizing the method presented in eq. (3.32) to moving frames and excited states. Using the relative overlaps in eq. (4.21), we assign each eigenvalue to a different operator onto which the corresponding state has maximum overlap. For those eigenvalues associated to a two-meson operator of the form, $O_M(\mathbf{k}_1)O_M(\mathbf{k}_2)$, we define the following ratio,

$$R(t) = \frac{\tilde{C}(t)}{\partial_0[C_{M,\mathbf{k}_1}(t)C_{M,\mathbf{k}_2}(t)]}, \quad (4.22)$$

where $C_{M,\mathbf{k}}$ refers to the single-meson correlation function for species $M \in \{\pi, \rho\}$ with momentum \mathbf{k} . This ratio is fitted assuming single- and two-particle correlation functions to be dominated by a single state. The single-particle correlator is approximated by

$$C_{M,\mathbf{k}}(t) = A \cosh\left(E_{M,\mathbf{k}}^{\text{latt}} t'\right), \quad (4.23)$$

where $E_{M,\mathbf{k}}^{\text{latt}}$ is the energy resulting from fitting the single-particle correlator $C_{M,\mathbf{k}}(t)$ and A is some unknown amplitude. The two-particle correlation function is given in general in eq. (4.15). If we consider a single state, and neglect thermal effects that are removed with eq. (4.17), we can set $B_{nm} = A_{n \neq 1} = 0$ and approximate,

$$C(t) = A_1 \cosh\left(E_{\text{int}}^{\text{latt}} t'\right). \quad (4.24)$$

This form of the two-particle correlator is introduced in eq. (4.17) to define $\tilde{C}(t)$, which is used in eq. (4.22) to define the fit function. The fit allows us to determine the finite-volume energy shift, defined as,

$$\Delta E_{\text{int}} = E_{\text{int}}^{\text{latt}} - E_{M,\mathbf{k}_1}^{\text{latt}} - E_{M,\mathbf{k}_2}^{\text{latt}}. \quad (4.25)$$

The total energy is finally reconstructed as

$$E_{\text{int}} = \Delta E_{\text{int}} + E_{M,\mathbf{k}_1}^{\text{free}} + E_{M,\mathbf{k}_2}^{\text{free}}, \quad (4.26)$$

where $E_{M,\mathbf{k}}^{\text{free}}$ is the single-meson energy computed using the continuum dispersion relation, eq. (4.18). This definition of the finite-volume energy using the continuum dispersion relation, rather than the energies determined from the lattice, has empirically been shown to reduce discretization effects on the determination of the finite-volume energies [269, 282, 283].

This fit to eq. (4.22) is repeated for several fit ranges, $t \in [t_{\text{min}}, t_{\text{max}}]$, varying both the lower and the upper limit. The final results are obtained averaging the results in a range where they are observed to plateau, using the weights presented in eq. (1.51). An example of such determination is

presented in fig. 4.2, and the complete results, obtained using the full basis of operators, are shown in figs. 4.3 to 4.5, for the SS , AA and AS channels, in this same order. We also indicate in each case, the non-interacting $\pi\pi$ and $\rho\rho$ energies (solid and dashed black lines, respectively) and the some of the most relevant inelastic thresholds for each channel (gray dotted and dashed-dotted lines). A full summary of all the threshold relevant for each channel is presented in fig. 4.6, computed using the meson masses in table 4.1.

Finally, we have studied the effect of varying the types of operators used to determine the matrix of correlation functions. The energy spectra of the AA channel for $N_c = 3$ obtained for different choices of the operator set are presented in fig. 4.7. We observe how the inclusion of $\rho\rho$ operators leads to the determination of a large number of new energy-levels, related to states of two vector mesons. However, it has a minimal impact on states of two-pions. Similarly, further considering tetraquark operators also has an almost negligible effect on pion-pion states. Only for some excited states, the additional operators help in reducing the error.

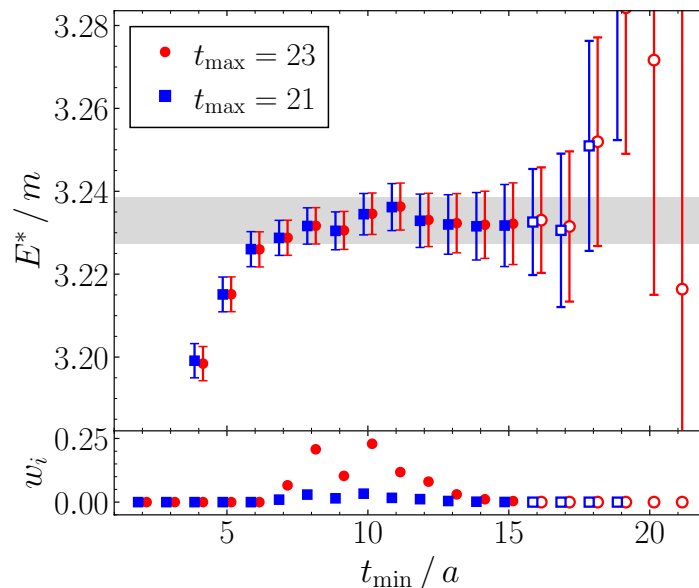


Figure 4.2. Best-fit results to eq. (4.22) for the ground-state energy in the $\mathbf{P} = [0, 0, 1]$ frame of the AA channel with $N_c = 3$, for different values of t_{\min} and two choices of t_{\max} . The final result (gray band) is obtained by averaging the results using the weights from eq. (1.51), in the bottom panel. Empty points are manually excluded from the average.

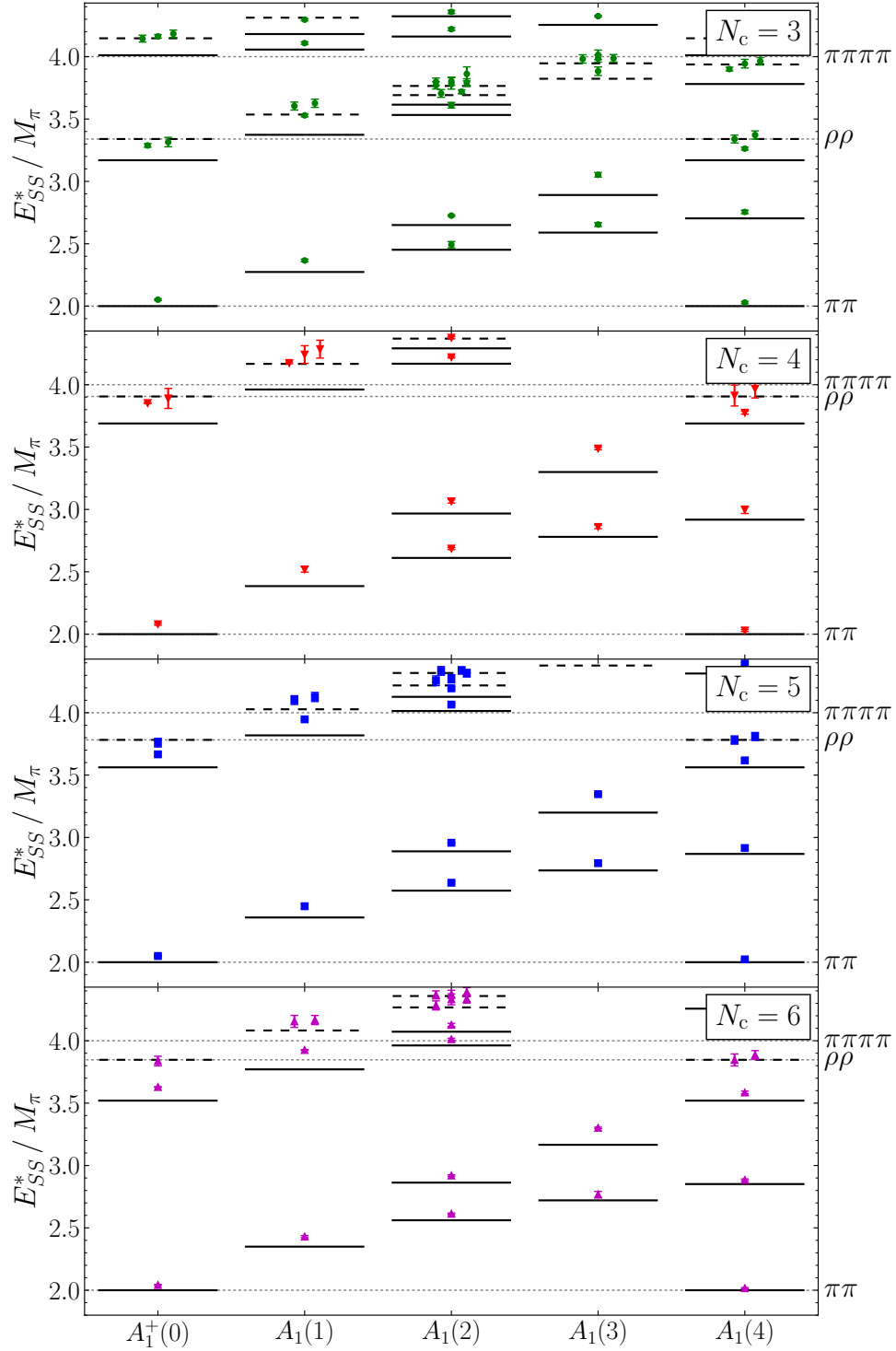


Figure 4.3. Finite-volume spectra for the SS channel, extracted using the full set of operators. Each panel corresponds to a different N_c and each column represents a different irrep of the cubic group and momentum frame, with $|\mathbf{P}|^2$ indicated in parenthesis. Horizontal solid and dashed segments indicate non-interacting $\pi\pi$ and $\rho\rho$ energies, respectively, while gray dashes lines are relevant inelastic thresholds—see fig. 4.6 for a full list.

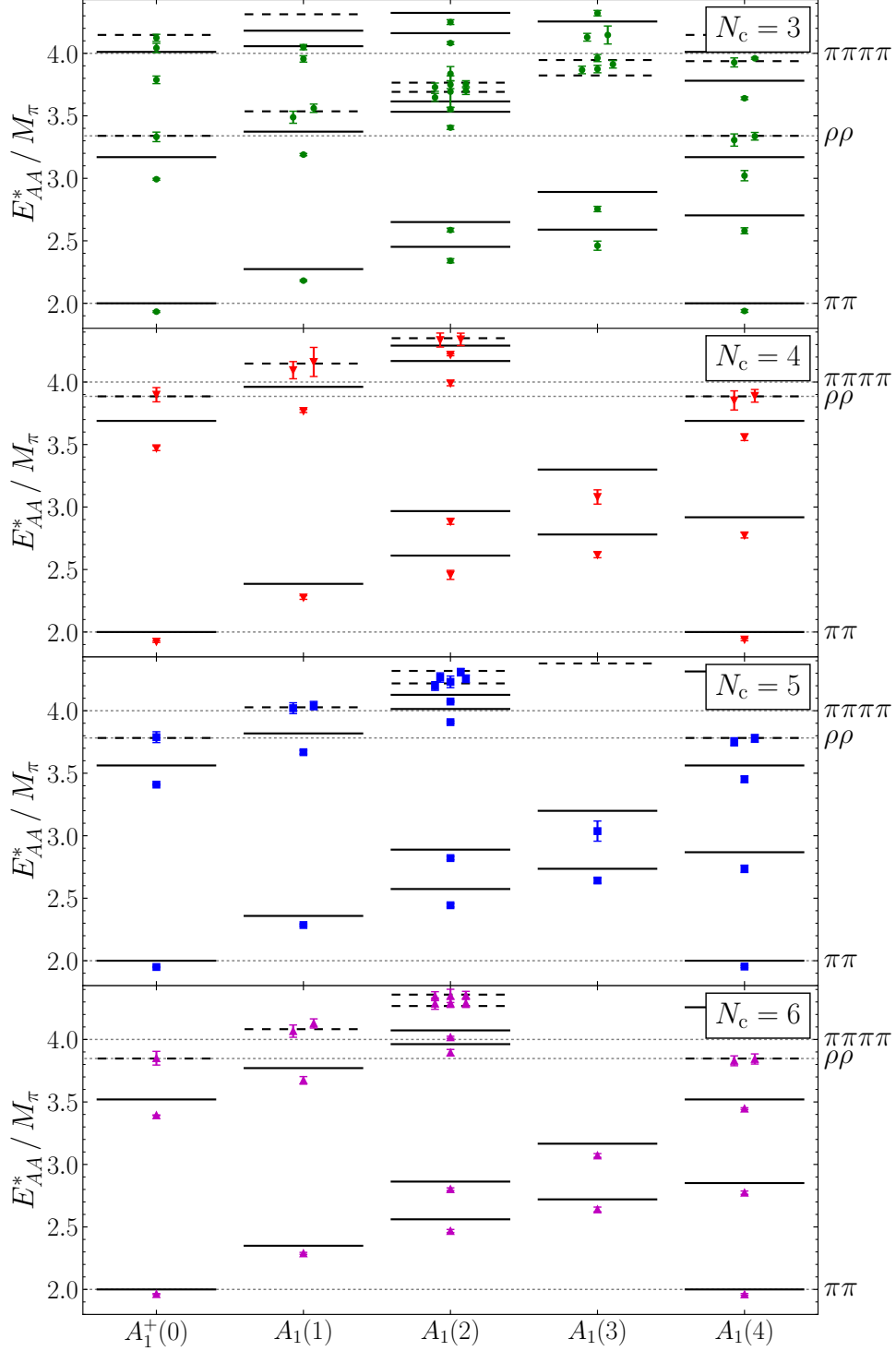


Figure 4.4. Same as fig. 4.3 for the AA channel.

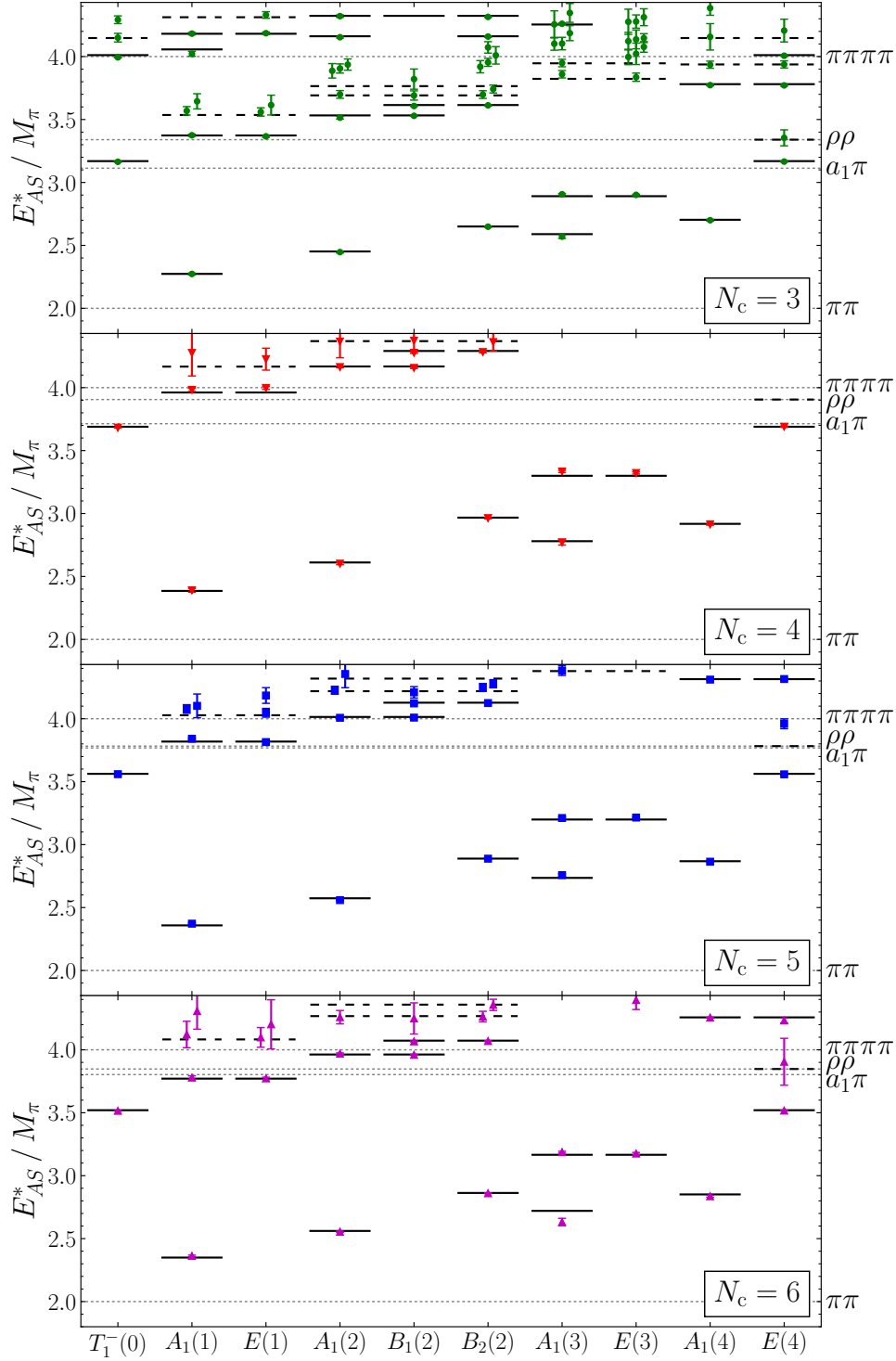


Figure 4.5. Same as fig. 4.3 for the AS channel.

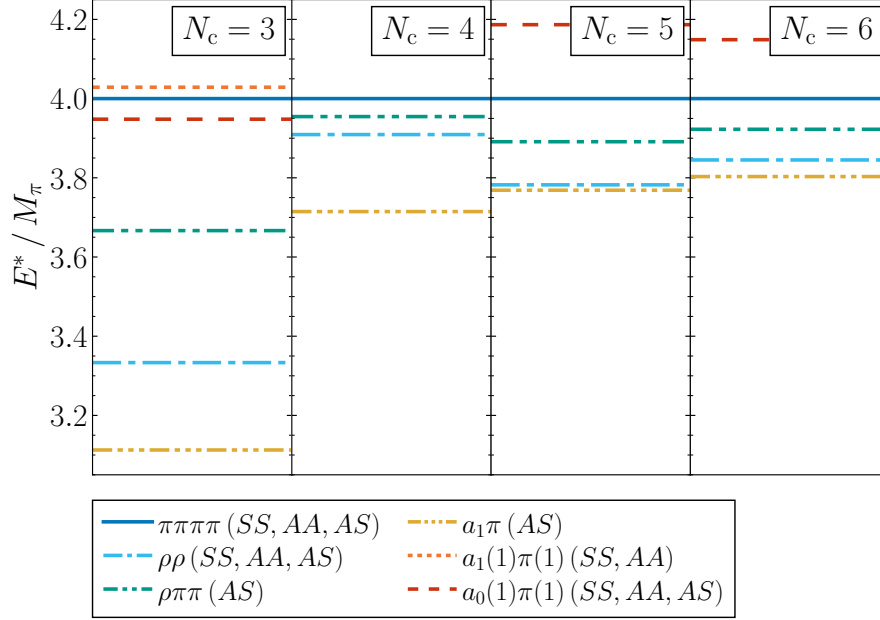


Figure 4.6. Relevant inelastic threshold in our ensembles, computed using the meson masses in table 4.1. We indicate in which channels these threshold are present in the figure legend.

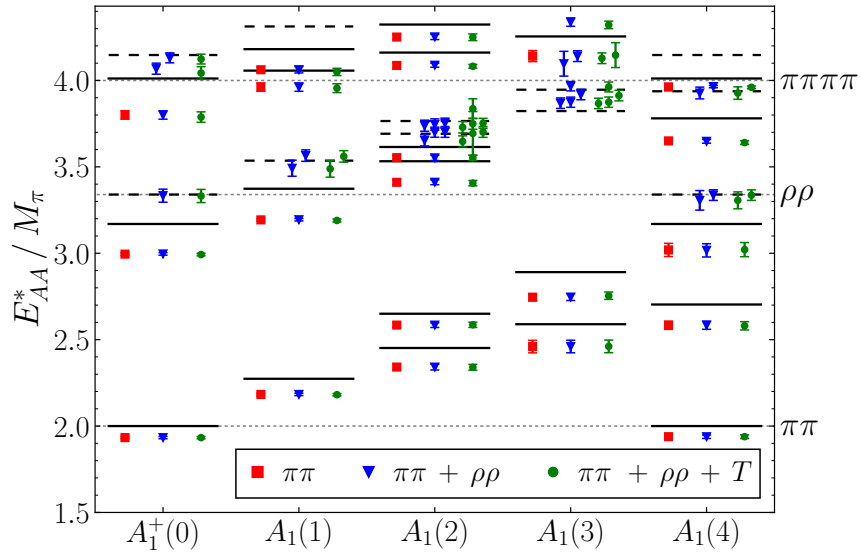


Figure 4.7. Results for the finite-volume spectrum of the AA channel for $N_c = 3$ extracted using different choices of the operator set, as indicated in the figure legend.

4.3 Extraction of infinite-volume scattering amplitudes

Finite-volume energies can be used to constrain the infinite-volume scattering observables, using the two-particle quantization condition introduced in sec. 2.3.1. In this chapter, we present results for pion-pion interactions. This means we restrict our analysis to those finite-volume states that have a maximum relative overlap into pion-pion operators. We also only focus on the lowest partial waves in each channel. Furthermore, we consider all the states below the four-pion threshold, neglecting interactions with $\rho\rho$ and $\rho\pi\pi$ states, that we expect to be very small.

In the case of the SS and AA channel, which contain only even partial waves, the quantization condition reduces to the algebraic relation given in eq. (2.52) if only s wave is considered. In the case of the AS channel, that contains odd partial waves, the QC can also be simplified if only p wave is taken into account. Its form, however, depends on the particular cubic-group irrep and momentum frame—see refs. [281, 284, 285]. For example, in the case of the A_1 and E irreps of the $\mathbf{P} = [0, 0, 1]$ frame, it takes the form

$$\begin{aligned} q_2^* \cot \delta_1^{A_1(1)} &= \frac{2}{\gamma L \pi^{1/2}} \left[\mathcal{Z}_{00}^{\mathbf{P}}(\tilde{q}) + \frac{2}{\sqrt{5}q^2} \mathcal{Z}_{20}^{\mathbf{P}}(\tilde{q}) \right], \\ q_2^* \cot \delta_1^{E(1)} &= \frac{2}{\gamma L \pi^{1/2}} \left[\mathcal{Z}_{00}^{\mathbf{P}}(\tilde{q}) - \frac{1}{\sqrt{5}q^2} \mathcal{Z}_{20}^{\mathbf{P}}(\tilde{q}) \right], \end{aligned} \quad (4.27)$$

where we have defined $\tilde{q} = q_2^* L / 2\pi$, with q_2^* is the magnitude of the relative momentum in the center-of-mass frame.

Using these simplified forms of the QC, we are able to extract a result for the scattering phase shift from each finite-volume energy level. The results are presented in figs. 4.8 to 4.10 for the SS , AA and AS channels, respectively. We also indicate as vertical dashed lines the most relevant inelastic thresholds, computed using the lightest vector meson masses value among all ensembles, corresponding to the 3A11 ensemble. Note that in the AS channel we additionally indicate the $a_1\pi$ threshold, where a_1 is the axial non-singlet meson, as this state may couple to two pions in odd partial waves. Other thresholds, are not indicated for legibility, but can be determined from the results in table 4.1 and fig. 4.6.

For both the SS (fig. 4.8) and AA (fig. 4.9) channels, we observe that the phase shift grows in magnitude rapidly above threshold, but depends weakly on the energy above $k^2 \gtrsim M_\pi^2$. The result for the SS channel is negative, indicating repulsive interactions, while that of the AA channel is positive, thus interactions are attractive. We note also that, for both

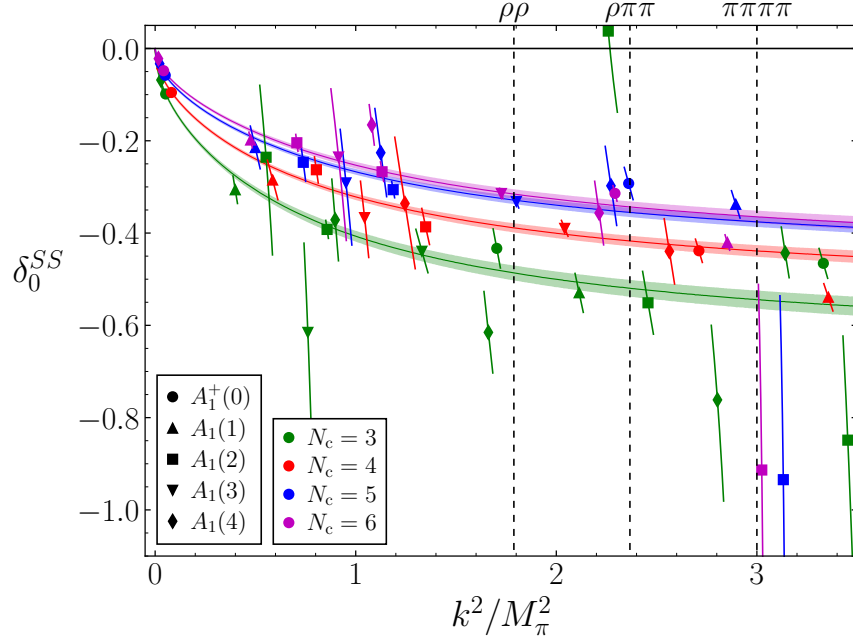


Figure 4.8. Results of the s -wave phase shift for the SS channel, determined for different N_c and cubic group irreps, as indicated in the figure legends. Shaded regions indicate the best-fit results to a modified ERE—see eq. (4.28).

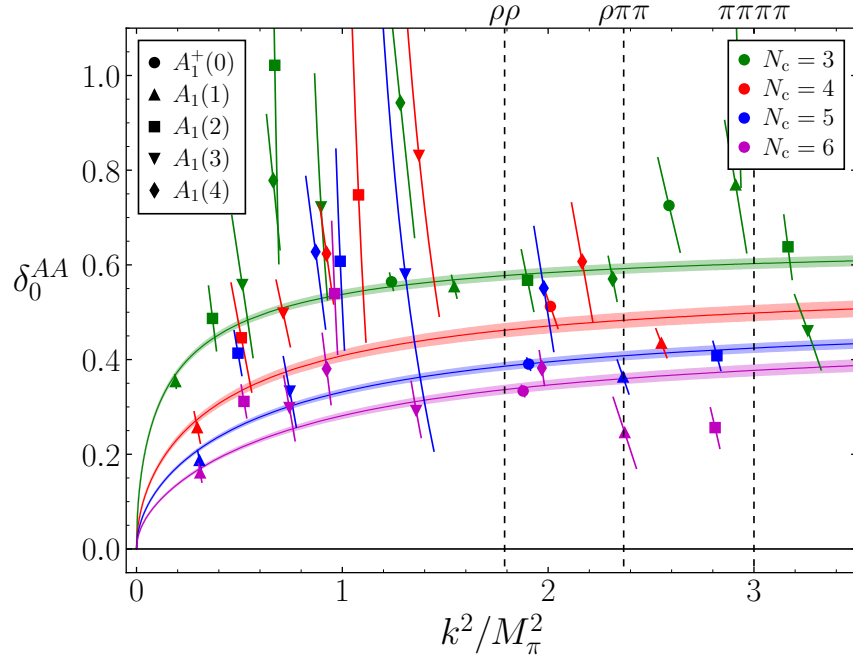


Figure 4.9. Same as fig. 4.8 for the AA channel.

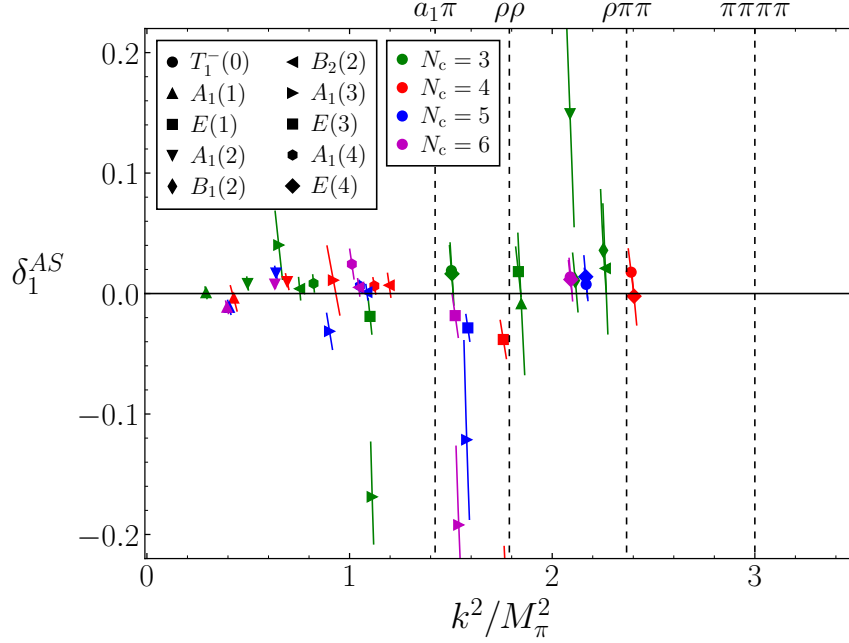


Figure 4.10. Results of the p -wave phase shift for the AS channel determined for different N_c and cubic group irreps, as indicated in the figure legends.

channels, the phase shift, and so the strength of the interactions decreases with N_c , as expected from large N_c arguments. For the AS channel (fig. 4.10), in contrast, the scattering phase shift remains small throughout the elastic region, indicating that interactions in this channel are very weak. This is consistent with ChPT expectations, which predict the scattering amplitude for this channel to only start at NLO—see ref. [261].

We can use the QC to constrain the infinite-volume scattering amplitudes. Given some parametrization of the amplitude one can obtain a prediction for the finite volume energies. These predictions can be matched to the lattice results to determine the parameters of the amplitude.

We perform fits of our lattice results for the SS and AA channels to a modified ERE [286, 287],

$$q_2^* \cot \delta_0 = \frac{E^* M_\pi}{E^{*2} - 2z^2} \left[B_0 + B_1 \frac{q_2^{*2}}{M_\pi^2} \right], \quad (4.28)$$

where B_i and z are parameters to be determined. This is a modification of the standard effective-range expansion in eq. (2.11), that includes the E^* kinematical factor in front and a denominator that reproduces the so-called Adler-zero [288, 289], this is, the fact that ChPT predicts the scattering amplitude to have a zero below threshold. We note that the parameters of

the modified ERE can be related to those of the standard ERE expanding close to threshold,

$$M_\pi a_0 = \frac{1}{B_0}, \quad M_\pi^2 r_0 a_0 = 2 \frac{B_1}{B_0} - 3, \quad (4.29)$$

where we have used the LO ChPT prediction, $z = M_\pi$.

In table 4.4, we show the results of these fits at fixed N_c , in which we set $z = M_\pi$. For $N_c = 3$ we have also tried other alternative fits with more free parameters, such as fitting z or one additional higher-order coefficient, but observed no significant improvement in the description of the lattice results.

From these fits, we are able to extract information of the scattering length and effective range of the two channels, using the relations in eq. (4.29). The results are represented in fig. 4.11 and summarized in table 4.5. The results for the scattering length are divided by the LO ChPT prediction—see eq. (3.8)—which removes leading N_c dependencies and we also expect to alleviate mass dependencies. These LO predictions are computed using the results for the pion decay constant computed for these ensembles in ref. [1]—see table 3.2. Finally, we also indicate in fig. 4.11 the LO ChPT prediction with horizontal dashed lines.

Using these results, we perform an extrapolation to large N_c . We observe that in all cases the $N_c = 4 - 6$ data is well reproduced by a linear relation that includes leading and subleading N_c terms. However, it seems that $1/N_c^2$ effects are significant for $N_c = 3$, which we thus do not include for the linear

Channel	N_c	B_0	B_1	χ^2 / dof
<i>SS</i>	3	-2.38(4)	-2.55(21)	10.1/10 = 0.85
	4	-3.09(8)	-3.28(19)	6.1/8 = 0.76
	5	-3.93(9)	-3.81(23)	7.9/8 = 0.98
	6	-4.37(4)	-3.84(22)	13.5/8 = 1.68
<i>AA</i>	3	0.927(15)	2.63(9)	28.7/14 = 2.05
	4	1.79(5)	3.12(19)	24.1/10 = 2.41
	5	2.53(6)	3.63(17)	30.2/10 = 3.02
	6	3.37(7)	3.94(20)	29.1/10 = 2.91

Table 4.4. Results from the fits of the finite-volume energies to predictions from a modified ERE with $z = M_\pi$ fixed, as given in eq. (4.28). Fits are performed for each channel and value of N_c separately.

Channel	N_c	$M\pi a_0 / M_\pi a_0^{\text{LO}}$	χ^2 / dof	$M_\pi^2 a_0 r_0$	χ^2 / dof
SS	3	0.953(16)	—	-0.85(18)	—
	4	1.075(26)	—	-0.88(16)	—
	5	1.065(24)	—	-1.06(14)	—
	6	1.155(10)	—	-1.24(10)	—
	∞	1.34(5)	4.7/1 = 4.7	-2.0(5)	0.05/1 = 0.05
AA	3	2.44(4)	—	2.67(22)	—
	4	1.86(5)	—	0.50(22)	—
	5	1.67(4)	—	-0.13(15)	—
	6	1.50(3)	—	-0.66(14)	—
	∞	0.78(14)	0.08/1 = 0.08	-3.0(7)	0.13/1 = 0.13
$SS+AA$	∞	1.40(15)	5.3/3 = 1.77	-2.2(1.0)	1.7/3 = 0.57

Table 4.5. Results for the scattering length, divided by LO ChPT predictions from eq. (3.8), and the effective range for both SS and AA channels, determined from the results in table 4.4 using eq. (4.29). We also show the large N_c results obtained from a linear extrapolation of the $N_c = 4 - 6$ results for each channel separately, as well as from a constrained quadratic extrapolation of all N_c for both channels combined.

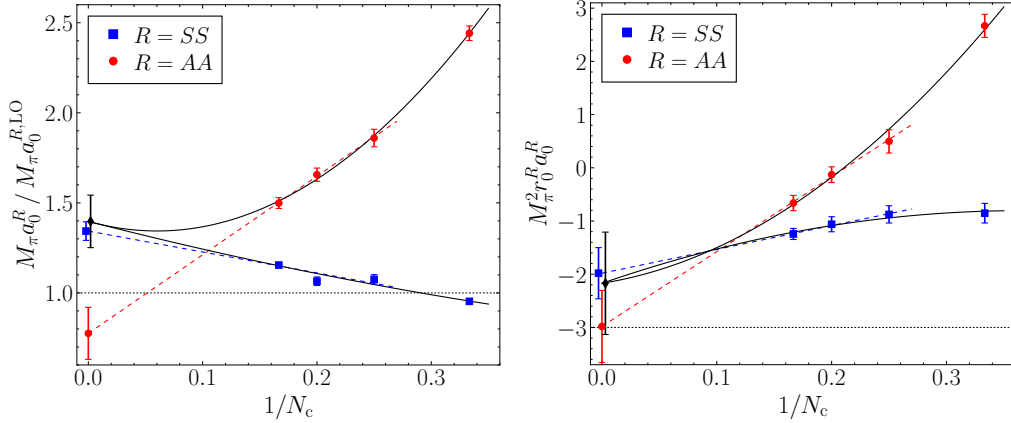


Figure 4.11. Results for the scattering length divided by LO ChPT predictions (left)—see eq. (3.8)—and for the scattering range (right), for both the SS and AA channels. These are determined from the results of a fit to a modified effective range expansion, see eq. (4.29). Results for $N_c = 4 - 6$ are fitted to a linear relation (dashed lines) to extrapolate to the large N_c limit. We also indicate the result of a constrained large N_c extrapolation for all $N_c = 3 - 6$ results and including up to $\mathcal{O}(N_c^{-2})$ corrections (solid lines).

extrapolations. The results of the fit are represented as dashed lines in fig. 4.11, and the extrapolated predictions are presented in table 4.5 as a solid line.

These large N_c results, however, are not consistent with large N_c expectations which predict the large N_c limit of the two quantities represented in fig. 4.11 to be equal for both channels—see, for example, eq. (3.6). We have found, however, that our results, including those with $N_c = 3$, are consistent with a common large N_c limit if $1/N_c^2$ effects are included. This fit, performed with a constrained large N_c limit, is also presented in fig. 4.11.

Both for $M_\pi a_0^R$ and $M_\pi^2 a_0^R r_0^R$, we observe that subleading N_c effects are larger for the AA channel than for the SS one. From the point of view of ChPT, these subleading effects are dominated by the chiral logarithms and other LEC-independent terms—see for example eqs. (3.9) and (3.10). In the AA channel, all such terms appear with the same sign, and so add up in the final contribution. In the SS channel, on the other hand, different terms have different signs, and the total result is smaller.

We find the large N_c result for the effective range to be consistent with the LO ChPT prediction, which is itself $\mathcal{O}(N_c^0)$. By contrast, there is a larger difference between large N_c results and LO ChPT for the scattering length. In the large N_c limit, subleading chiral corrections appear as a polynomial in the chiral parameter, $\xi = M_\pi^2/(4\pi F_\pi)^2$, with the coefficients being products of $\mathcal{O}(N_c)$ LECs. In our case, the chiral parameter is rather large, and so large chiral corrections could be expected.

Furthermore, while we observe no evidence of any pion-pion resonance in the AA channel above threshold, the fir results for $N_c = 3$ are compatible with the presence of a virtual tetraquark bound state at $E_{\text{bound}}/M_\pi = 1.741(13)$. This corresponds to a below-threshold pole in the scattering matrix on the real energy axis of the second Riemann sheet, given by the condition

$$q_2^* \cot \delta_0 - \sqrt{-q_2^{*2}} = 0, \quad (4.30)$$

as illustrated with a star in fig. 4.12. Using the results for the scattering length and effective range in table 4.4, and eq. (2.12), we can determine the renormalization factor of the associated state, $Z = 0.577(13)$. According to Weinberg's criterium in sec. 2.1.1, this quantity is related to the possibility of the state being compact or a hadronic molecule. In particular, $Z = 1$ would indicate a purely compact state, while $Z = 0$ corresponds to molecules. In our case, the observed virtual bound state seems to have both a compact and a molecular component. A strong confirmation of the existence of this bound state, however, requires to study its presence with respect to the use of different parametrizations of the scattering amplitude. We finally note that no such state is found for the remaining N_c .

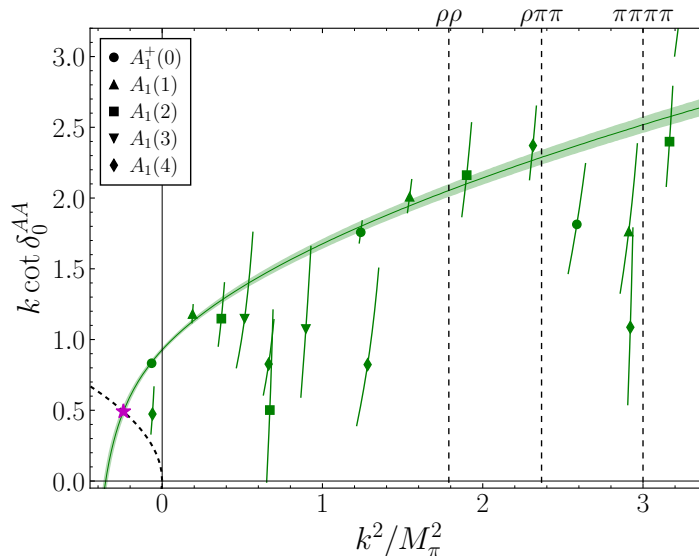


Figure 4.12. Scattering phase shift for the AA channel with $N_c = 3$, together with the best-fit results to a modified ERE—see eq. (4.28). We observe the presence of a virtual bound state, given by the solution to eq. (4.30), indicated by a star.

4.4 Conclusions

In this chapter, results on the study of meson-meson scattering as a function of the number of colors, N_c , have been presented [2, 10]. We work in a theory with $N_f = 4$ degenerate quark flavor, and focus on three different scattering channels: the SS channel, which is analogous to the isospin-two channel of two-flavor QCD, the AA channel which only exists for $N_f \geq 4$, and the AS channel, that contain odd partial waves. The latter two are particularly interesting, since they have the quantum numbers which some recently found tetraquarks would be expected to have in a $N_f = 4$ world.

We have determined the finite-volume spectrum of all three channels for different momentum frames and cubic-group irreps, using two-particle operators with the form of two pions or two vector mesons, complemented by local tetraquark operators. For the SS and AA channels, we have used the quantization condition to constrain the pion-pion scattering amplitude, and characterized the N_c scaling of the scattering length and effective range, finding that they are compatible with the expected large N_c limit only if $\mathcal{O}(N_c^{-2})$ corrections are allowed. We have also observed evidence of a virtual bound state in the AA channel for $N_c = 3$, at an energy $E_{\text{bound}}/M_\pi = 1.741(13)$. For the AS channel, on the other hand, we have found very weak interactions, which are consistent with ChPT, that predicts a zero scattering amplitude at LO.

The work presented in this chapter constitutes a further step in the study of subleading N_c effects in meson-meson scattering. Using the results presented in this chapter, we expect to constrain the N_c scaling of different combinations of LECs from ChPT, complementing the results presented in chapter 3. Also, further investigation is needed regarding the found virtual bound state in the AA channel. In particular, its existence needs to be well-established by using several parametrizations of the scattering amplitudes, and also analyzing possible effects from higher partial waves and mixing with vector-meson states. It would also be compelling to analyze the dependence of this state on the quark mass, which could shed some light into the tetraquark resonances found experimentally.

5 The isospin-three three-pion K -matrix at NLO in ChPT

The study of multiparticle interactions on the lattice is an active field of research—see refs. [290–293] for recent reviews. Many two-particle systems have been analyzed in detail during the last decades, including a large number of two-meson systems, and also some meson-baryon and baryon-baryon examples. In the three particle case, the RFT finite-volume formalism, presented in sec. 2.3.2, allows to study many three-particle processes. Its practical use, however, has been mainly focused on three-meson systems at maximal isospin [194, 268, 294–302].

One of the most studied system is that of three pions at maximal isospin, $\pi^+\pi^+\pi^+$. A priori, one would expect ChPT to provide an accurate description of the system near threshold. At least, this is the case in the two-particle world, in which the two-pion scattering lengths are in very good agreement with LO ChPT [270, 303, 304]. In the case of three pions, however, it was observed in refs. [194, 301] that lattice results for the three-pion divergence-free K -matrix, $\mathcal{K}_{\text{df},3}$, show a significant deviation from LO ChPT predictions, presented in sec. 2.2.2. This discrepancy could be due to systematic effects neglected in the lattice determinations of $\mathcal{K}_{\text{df},3}$, or arise because of large higher-order ChPT corrections.

In this chapter, the results from ref. [3] are presented, in which NLO ChPT contributions to the $I_{\pi\pi\pi} = 3$ K -matrix were determined, starting from the three-pion NLO amplitudes from refs. [195, 196]. As in the case of LO, the integral equations relating \mathcal{M}_3 to $\mathcal{K}_{\text{df},3}$ reduce to an algebraic relation when working at NLO. This relation is presented in sec. 5.1 and is later used to determine the isospin-three $\mathcal{K}_{\text{df},3}$ up to quadratic order in the threshold expansion: the details of the computation are detailed in sec. 5.2 and the results are summarized in sec. 5.3. The conclusions of this work are presented in sec. 5.4.

5.1 Relating \mathcal{M}_3 to $\mathcal{K}_{\text{df},3}$ at NLO in ChPT

The three-particle divergence-free K -matrix is related to the three-particle scattering amplitude, \mathcal{M}_3 , by integral equations, introduced in sec. 2.1.2. When working at fixed order in ChPT, these equations reduce to linear algebraic relations, as presented in sec. 2.2.2 at LO. We now extend this relation to NLO. We note that by NLO we refer only to the next-to-leading order contribution, rather than to a complete LO+NLO result.

We recall that three-particle states can be kinematically described in two ways. In refs. [195, 196], scattering amplitudes are presented as a function of the momenta of all three initial- and final-state particles. We refer to these as $\{k_1, k_2, k_3\}$ and $\{p_1, p_2, p_3\}$, respectively, with $P = k_1 + k_2 + k_3 = p_1 + p_2 + p_3$ the total momentum.¹

On the other hand, the integral equations defining $\mathcal{K}_{\text{df},3}$ use the typical parametrization of the RFT formalism, which we now summarize. In this, a three-particle state is separated in a spectator and a two-particle dimer, and is described by the three-momentum of the spectator and the direction of the relative momentum of the dimer in its CMF. These quantities are called \mathbf{k} and $\hat{\mathbf{a}}_k^*$ for the initial state, and \mathbf{p} and $\hat{\mathbf{a}}_p'^*$ for the final one, respectively. Typically, observables are projected to partial waves of the initial and final dimer. This means that, in general, scattering quantities are a function of the three-momenta of the initial and final spectators, \mathbf{k} and \mathbf{p} , the angular-momentum indices of both states, (ℓ, m) and (ℓ', m') , and the total energy in the center-of-mass frame of the three particles, E^* . In general, we leave the angular momentum indices, as well as the dependence on E^* , implicit. For example, the three-particle amplitude projected to the partial waves of both initial and final dimer is indicated as $\mathcal{M}_3(\mathbf{p}, \mathbf{k})$.

We stress that this same choice of arguments is maintained for two-particle quantities. For example, the two-particle scattering amplitude of the initial dimer, projected to the corresponding partial wave of this dimer, is indicated as $\mathcal{M}_2(\mathbf{k})$. We note that this quantity depends on the Mandelstam variables of the initial dimer, $\mathcal{M}_2(\mathbf{k}) = \mathcal{M}_{2,\ell}(s)$, with $s = (P - k)^2$ and k the on-shell momentum of the initial spectator.

Note the relation between both parametrizations of the kinematic variables of three-particle states is not fixed. Instead, all possible assignments of external momenta to the spectator and dimer usually need to be considered and combined in the determination of $\mathcal{K}_{\text{df},3}$. In the case of the $I_{\pi\pi\pi} = 3$ channel, one needs to symmetrize over all these possible combinations.

¹In reality, refs. [195, 196] consider all six momenta incoming, but these two options can be trivially related by changing the sign of the final-state momenta.

We now derive the relation between \mathcal{M}_3 and $\mathcal{K}_{\text{df},3}$ for three pions at maximal isospin at NLO in ChPT, the corresponding relation at LO was presented in sec. 2.2.2. Recall this relation is obtained by studying the integral equations presented in sec. 2.1.2 as a power series in $1/F_\pi^2$. The scattering amplitudes at LO scale as $\mathcal{M}_2^{\text{LO}} = \mathcal{O}(1/F_\pi^2)$ and $\mathcal{M}_3^{\text{LO}} = \mathcal{O}(1/F_\pi^4)$, while at NLO they are $\mathcal{M}_2^{\text{NLO}} = \mathcal{O}(1/F_\pi^4)$ and $\mathcal{M}_3^{\text{NLO}} = \mathcal{O}(1/F_\pi^6)$.

We first focus on the determination of the divergence-free amplitude at NLO, $\mathcal{M}_{\text{df},3}^{\text{NLO}}$. Recall that at LO the unsymmetrized subtraction term in eq. (2.15) takes the form

$$\mathcal{D}^{(\text{u,u})\text{LO}}(\mathbf{p}, \mathbf{k}) = -\mathcal{M}_2^{\text{LO}}(\mathbf{p})G^\infty(\mathbf{p}, \mathbf{k})\mathcal{M}_2^{\text{LO}}(\mathbf{k}), \quad (5.1)$$

where G^∞ is defined in eq. (2.16). At NLO, the subtraction term becomes,

$$\begin{aligned} \mathcal{D}^{(\text{u,u})\text{NLO}}(\mathbf{p}, \mathbf{k}) &= -\mathcal{M}_2^{\text{LO}}(\mathbf{p})G^\infty(\mathbf{p}, \mathbf{k})\mathcal{M}_2^{\text{NLO}}(\mathbf{k}) \\ &\quad -\mathcal{M}_2^{\text{NLO}}(\mathbf{p})G^\infty(\mathbf{p}, \mathbf{k})\mathcal{M}_2^{\text{LO}}(\mathbf{k}) \\ &\quad + \int_{\mathbf{r}} \mathcal{M}_2^{\text{LO}}(\mathbf{p})G^\infty(\mathbf{p}, \mathbf{r})\mathcal{M}_2^{\text{LO}}(\mathbf{r})G^\infty(\mathbf{r}, \mathbf{k})\mathcal{M}_2^{\text{LO}}(\mathbf{k}), \end{aligned} \quad (5.2)$$

where we recall $\int_{\mathbf{r}} = \int d^3r/[2\omega_r(2\pi)^3]$, with $\omega_r = \sqrt{M_\pi^2 + \mathbf{r}^2}$.

In the case of the $I_{\pi\pi\pi} = 3$ channel, we can substitute $G^\infty \rightarrow G_{ss}^\infty$, given in eq. (2.40), in the last line on eq. (5.2), as $\mathcal{M}_2^{\text{LO}}$ is purely s -wave, see eq. (2.27). On the other hand, $\mathcal{M}_2^{\text{NLO}}$ contains all even partial waves, and such substitution is not possible on the other terms. The divergence-free amplitude is defined after subtracting,

$$\mathcal{M}_{\text{df},3}^{\text{NLO}}(\mathbf{p}, \mathbf{k}) = \mathcal{M}_3^{\text{NLO}}(\mathbf{p}, \mathbf{k}) - \mathcal{S} \left\{ \mathcal{D}^{(\text{u,u}),\text{NLO}}(\mathbf{p}, \mathbf{k}) \right\}, \quad (5.3)$$

where \mathcal{S} denotes symmetrization over the initial and final momenta.

The divergence-free amplitude is related to $\mathcal{K}_{\text{df},3}$ by an integral equation, that we reproduce here,

$$\mathcal{M}_{\text{df},3}(\mathbf{p}, \mathbf{k}) = \mathcal{S} \left\{ \int_{\mathbf{s}} \int_{\mathbf{r}} \mathcal{L}^{(\text{u,u})}(\mathbf{p}, \mathbf{s})\mathcal{T}(\mathbf{s}, \mathbf{r})\mathcal{R}^{(\text{u,u})}(\mathbf{r}, \mathbf{k}) \right\}, \quad (5.4)$$

where we recall that \mathcal{S} indicates that the quantity between brackets needs to be symmetrized over all permutations of momenta in the initial and final state, and \mathcal{L} and \mathcal{R} are decorators defined in eqs. (2.19) and (2.20). At LO and NLO in ChPT, they take the form

$$\begin{aligned} \mathcal{L}^{(\text{u,u})\text{LO}}(\mathbf{p}, \mathbf{k}) &= \mathcal{R}^{(\text{u,u})\text{LO}}(\mathbf{p}, \mathbf{k}) = \frac{1}{3}\bar{\delta}(\mathbf{p} - \mathbf{k}), \\ \mathcal{L}^{(\text{u,u})\text{NLO}}(\mathbf{p}, \mathbf{k}) &= \mathcal{R}^{(\text{u,u})\text{NLO}}(\mathbf{p}, \mathbf{k}) = i\mathcal{M}_2^{\text{LO}}(\mathbf{k})\rho(\mathbf{k})\bar{\delta}(\mathbf{p} - \mathbf{k}), \end{aligned} \quad (5.5)$$

where recall $\bar{\delta}(\mathbf{p} - \mathbf{k}) \equiv 2\omega_k(2\pi)^3\delta^{(3)}(\mathbf{p} - \mathbf{k})$. Combining the results in eq. (5.5) into eq. (5.4) allows us to rewrite the latter as an algebraic relation,

$$\mathcal{M}_{\text{df},3}(\mathbf{p}, \mathbf{k}) = \mathcal{S} \left\{ \frac{1}{3} \mathcal{T}^{\text{LO}}(\mathbf{p}, \mathbf{k}) \rho(\mathbf{k}) \mathcal{M}_2^{\text{LO}}(\mathbf{k}) + \frac{1}{3} \mathcal{M}_2^{\text{LO}}(\mathbf{p}) \rho(\mathbf{p}) \mathcal{T}^{\text{LO}}(\mathbf{p}, \mathbf{k}) + \frac{1}{9} \mathcal{T}^{\text{NLO}}(\mathbf{p}, \mathbf{k}) \right\}. \quad (5.6)$$

From here, it is clear that $\mathcal{T}^{\text{NLO}} = \mathcal{O}(1/F_\pi^6)$.

The \mathcal{T} variable is related to $\mathcal{K}_{\text{df},3}$ via the integral equation

$$\mathcal{T}(\mathbf{p}, \mathbf{k}) = \mathcal{K}_{\text{df},3}(\mathbf{p}, \mathbf{k}) - \int_s \int_r \mathcal{K}_{\text{df},3}(\mathbf{p}, \mathbf{s}) \rho(\mathbf{s}) \mathcal{L}^{(\text{u,u})}(\mathbf{s}, \mathbf{r}) \mathcal{T}(\mathbf{r}, \mathbf{k}). \quad (5.7)$$

Recalling $\mathcal{T}^{\text{LO}} = \mathcal{K}_{\text{df},3}^{\text{LO}} = \mathcal{O}(1/F_\pi^4)$, one finds that the last term on the right hand side of eq. (5.7) is $\mathcal{O}(1/F_\pi^8)$, and so can be neglected at the order we are working, meaning $\mathcal{T}^{\text{NLO}} = \mathcal{K}_{\text{df},3}^{\text{NLO}}$, in analogy to LO.

Finally, combining all these results into eq. (5.6), we find

$$\mathcal{M}_{\text{df},3}^{\text{NLO}}(\mathbf{p}, \mathbf{k}) = \mathcal{K}_{\text{df},3}^{\text{NLO}}(\mathbf{p}, \mathbf{k}) + \frac{i}{3} \mathcal{S} \left\{ \mathcal{K}_{\text{df},3}^{\text{LO}}(\mathbf{p}, \mathbf{k}) \rho(\mathbf{k}) \mathcal{M}_2^{\text{LO}}(\mathbf{k}) + \mathcal{M}_2^{\text{LO}}(\mathbf{p}) \rho(\mathbf{p}) \mathcal{K}_{\text{df},3}^{\text{LO}}(\mathbf{p}, \mathbf{k}) \right\}, \quad (5.8)$$

where we have used that $\mathcal{K}_{\text{df},3}^{\text{NLO}}$ is symmetric by definition, and so the symmetrization generates a factor of nine. If we further use the LO result for the three-particle K -matrix, given in eq. (2.45), $\mathcal{K}_{\text{df},3}^{\text{LO}} = \mathcal{M}_{\text{df},3}^{\text{LO}}$, this equation can be rewritten as

$$\mathcal{K}_{\text{df},3}^{\text{NLO}}(\mathbf{p}, \mathbf{k}) = \mathcal{M}_{\text{df},3}^{\text{NLO}}(\mathbf{p}, \mathbf{k}) - \frac{i}{3} \mathcal{S} \left\{ \mathcal{M}_{\text{df},3}^{\text{LO}}(\mathbf{p}, \mathbf{k}) \rho(\mathbf{k}) \mathcal{M}_2^{\text{LO}}(\mathbf{k}) + \mathcal{M}_2^{\text{LO}}(\mathbf{p}) \rho(\mathbf{p}) \mathcal{M}_{\text{df},3}^{\text{LO}}(\mathbf{p}, \mathbf{k}) \right\}. \quad (5.9)$$

The terms in brackets on the right hand side of eq. (5.9) are purely imaginary for physical kinematics, as $\mathcal{M}_2^{\text{LO}}$, $\mathcal{M}_3^{\text{LO}}$ and ρ are all real. In contrast, $\mathcal{K}_{\text{df},3}$ is purely real. Therefore, one can simplify this relation

$$\mathcal{K}_{\text{df},3}^{\text{NLO}} = \text{Re} \mathcal{M}_{\text{df},3}^{\text{NLO}}. \quad (5.10)$$

The cancellation of the imaginary parts in eq. (5.9) can then be used as a cross-check of the formalism. Such analysis is presented in app. E of ref. [3].

5.2 Computation of $\mathcal{K}_{\text{df},3}$ at NLO

As we have shown, determining $\mathcal{K}_{\text{df},3}$ at NLO in ChPT just requires to determine the real part of the divergence-free NLO amplitude. In the $I_{\pi\pi\pi} = 3$ channel, the computation can be divided in three parts, each of which with different particularities. We write,

$$\mathcal{K}_{\text{df},3}^{\text{NLO}} = \text{Re}\mathcal{M}_{\text{df},3}^{\text{NLO}} = \text{Re}\left\{\mathcal{M}_3^{\text{NLO,OPE}} - \mathcal{D}^{\text{NLO,OPE}}\right\} + \text{Re}\mathcal{M}_3^{\text{NLO,non-OPE}} - \text{Re}\mathcal{D}^{\text{BH}}, \quad (5.11)$$

which is schematically represented in fig. 5.1. The first term on the right-hand side is called the one-particle exchange (OPE) part of the amplitude, $\mathcal{M}_3^{\text{NLO,OPE}}$, together with the corresponding subtraction, $\mathcal{D}^{\text{NLO,OPE}}$, given by the first two lines of eq. (5.2). The remaining of the amplitude is the non-OPE part, $\mathcal{M}_3^{\text{NLO,non-OPE}}$. It also requires a subtraction term, called the bull-head (BH) subtraction, \mathcal{D}^{BH} , corresponding to the last line in eq. (5.2). Note that the real part of the non-OPE amplitude is smooth, and so is the real part of the BH subtraction. Thus both can be evaluated independently, which is not true for the imaginary parts. Finally, recall that this division into

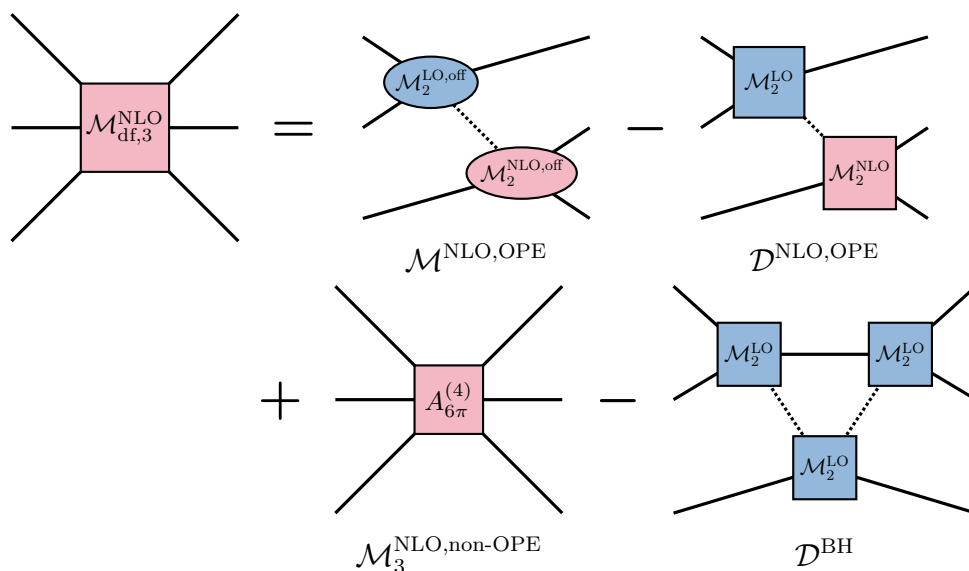


Figure 5.1. Schematic representation of eq. (5.11). Solid and dotted lines represent on- and off-shell pions, respectively. Similarly, amplitudes in square boxes are fully on-shell, while those in ovals have one leg off-shell. Blue and pink colors correspond to LO and NLO, in this same order. Finally, $A_{6\pi}^{(4)}$ is the non-OPE part of the NLO amplitude, given in ref. [195].

different pieces is unphysical, as it depends on the off-shell convention—see sec. 2.2.2 for a detailed discussion.

The computation of these three different terms will be presented in the remainder of this section. All of them can be determined almost analytically, the only numerical contribution comes from the BH subtraction, where the cutoff function, $H(x)$, plays a role. We first present in sec. 5.2.1 some preliminary results which are used throughout the computation. The details for the OPE, non-OPE and BH subtraction are then presented in secs. 5.2.2 to 5.2.4, in this same order. Finally, in sec. 5.2.5 we comment on some numerical approaches used to cross-check the analytical results.

5.2.1 Preliminaries to the computation

The main goal of this work is to determine the threshold expansion of $\mathcal{K}_{\text{df},3}$ up to quadratic order. The standard form of this expansion was presented in eq. (2.22),

$$M_\pi^2 \mathcal{K}_{\text{df},3} = \mathcal{K}_0 + \mathcal{K}_1 \Delta + \mathcal{K}_2 \Delta^2 + \mathcal{K}_A \Delta_A + \mathcal{K}_B \Delta_B + \mathcal{O}(\Delta^3), \quad (5.12)$$

where Δ , Δ_A and Δ_B are defined in eq. (2.23). However, $\mathcal{K}_{\text{df},3}$ can also be expanded about threshold in other ways, which are useful throughout the computation presented in this chapter.

One alternative is to use kinematical variables that can be expressed in terms of \tilde{t}_{ij} variables, defined in eq. (2.24). For example, we can write

$$M_\pi^2 \mathcal{K}_{\text{df},3} = c_0 + c_1 \mathcal{Q}_0 + c_2 \mathcal{Q}_1 + c_3 \mathcal{Q}_2 + c_4 \mathcal{Q}_3 + \mathcal{O}(\Delta^3), \quad (5.13)$$

with kinematic operators,

$$\begin{aligned} \mathcal{Q}_0 &\equiv \mathcal{S}[\tilde{t}_{11}] &&= -2\Delta, \\ \mathcal{Q}_1 &\equiv \mathcal{S}[\tilde{t}_{11}\tilde{t}_{11}] &&= \Delta^2 + \Delta_B, \\ \mathcal{Q}_2 &\equiv \mathcal{S}[\tilde{t}_{11}\tilde{t}_{12} + \tilde{t}_{11}\tilde{t}_{21}] &&= \frac{1}{2}(2\Delta^2 + \Delta_A - 2\Delta_B), \\ \mathcal{Q}_3 &\equiv \mathcal{S}[\tilde{t}_{11}\tilde{t}_{22} + \tilde{t}_{21}\tilde{t}_{12}] &&= \frac{1}{2}(2\Delta^2 - \Delta_A + \Delta_B). \end{aligned} \quad (5.14)$$

where we have indicated the relations to those operators in eq. (5.12). From here one can find a relation between the coefficients in both expressions. For example, $\mathcal{K}_1 = -2c_1$.

Another option is to consider an unsymmetrized K -matrix, $\mathcal{K}_{\text{df},3}^{(\text{u,u})}$, from which $\mathcal{K}_{\text{df},3}$ can be recovered after symmetrization, this is,

$$\mathcal{K}_{\text{df},3} = \mathcal{S} \left\{ \mathcal{K}_{\text{df},3}^{(\text{u,u})} \right\} \quad (5.15)$$

Under particle exchange $\mathcal{K}_{\text{df},3}^{(\text{u,u})}$ has the same symmetries as a three-particle system with one particle different from the other two. The corresponding threshold expansion, which was first worked out in ref. [233], takes the following form

$$\begin{aligned} M_\pi^2 \mathcal{K}_{\text{df},3}^{(\text{u,u})} = & c'_0 + c'_1 \Delta + c'_2 \Delta_3^{\text{S}} + c'_3 \tilde{t}_{33} \\ & + c'_4 \Delta^2 + c'_5 \Delta \Delta_3^{\text{S}} + c'_6 \Delta \tilde{t}_{33} + c'_7 \Delta_3 \Delta'_3 + c'_8 (\Delta_3^{\text{S}})^2 + c'_9 \Delta_3^{\text{S}} \tilde{t}_{33} + c'_{10} \tilde{t}_{33}^2 \\ & + c'_{11} \mathcal{Q}_{--} + c'_{12} \mathcal{Q}_{+-} + c'_{13} \mathcal{Q}_{3-} + c'_{14} \mathcal{Q}_{tu} + \mathcal{O}(\Delta^3), \end{aligned} \quad (5.16)$$

where Δ_3 and Δ'_3 are defined in eq. (2.24), and we have introduced $\Delta_3^{\text{S}} = \Delta_3 + \Delta'_3$. Here, \mathcal{Q}_X are operators that contribute to non-zero partial waves [3]. The only one of interest for this work is

$$\mathcal{Q}_{tu} = \tilde{t}_{13} \tilde{t}_{23} + \tilde{t}_{31} \tilde{t}_{32}. \quad (5.17)$$

One can symmetrize the initial and final momenta to recover $\mathcal{K}_{\text{df},3}$ and relate the coefficients in eq. (5.16) to those in eq. (5.12). For example, we find

$$\mathcal{K}_{\text{B}} = c'_{10} + 9c'_{11} + 3c'_{12} - 6c'_{13} - c'_{14}. \quad (5.18)$$

5.2.2 The subtracted OPE contribution

We first focus on the subtracted OPE contribution. This comes from diagrams such as those shown in fig. 5.2, together with the subtraction of divergencies that arise when the exchanged particle, of momentum $b = P - p_3 - k_3$, goes on-shell. This contribution can be determined analytically only after this subtraction is included.

To determine the OPE contribution to $\mathcal{K}_{\text{df},3}$ at NLO, we first determine the OPE contribution to the unsymmetrized K -matrix, $\mathcal{K}_{\text{df},3}^{(\text{u,u}),\text{OPE}}$. We consider the case in which the initial and final spectator have momentum k_3 and p_3 , respectively, and later symmetrize the result. The unsymmetrized divergence-free amplitude takes the form

$$\mathcal{M}_{\text{df},3}^{(\text{u,u})\text{NLO},\text{OPE}}(\mathbf{p}_3, \mathbf{k}_3) = \mathcal{M}_3^{(\text{u,u})\text{NLO},\text{OPE}}(\mathbf{p}_3, \mathbf{k}_3) - \mathcal{D}^{(\text{u,u})\text{NLO},\text{OPE}}(\mathbf{p}_3, \mathbf{k}_3), \quad (5.19)$$

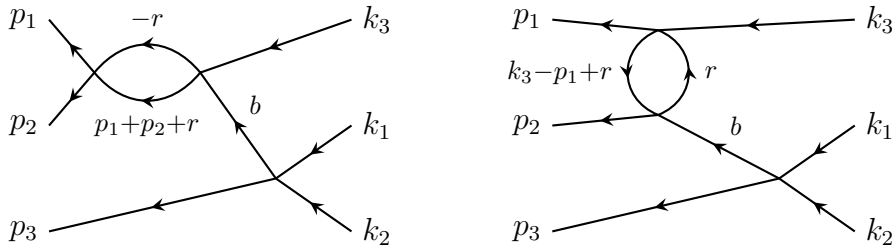


Figure 5.2. Examples of OPE NLO diagrams. In this case, $b = P - k_3 - p_3$.

where the unsymmetrized amplitude and subtraction term are

$$\mathcal{M}_3^{(\text{u,u})\text{NLO,OPE}}(\mathbf{p}_3, \mathbf{k}_3) = -\mathcal{M}_{2,\text{off}}^{\text{NLO}}(\mathbf{p}_3) \frac{1}{\bar{b}^2 + i\epsilon} \mathcal{M}_{2,\text{off}}^{\text{LO}}(\mathbf{k}_3)_{+\leftrightarrow}, \quad (5.20)$$

$$\mathcal{D}^{(\text{u,u})\text{NLO,OPE}}(\mathbf{p}_3, \mathbf{k}_3) = -\mathcal{M}_2^{\text{NLO}}(\mathbf{p}_3) G^\infty(\mathbf{p}_3, \mathbf{k}_3) \mathcal{M}_2^{\text{LO}}(\mathbf{k}_3)_{+\leftrightarrow}. \quad (5.21)$$

Here \leftrightarrow denotes exchange between the LO and NLO amplitudes and we define $\bar{b}^2 \equiv b^2 - M_\pi^2$.

For the subsequent analysis, it is convenient to express the two-particle amplitudes, before projecting to partial waves, as a function of Mandelstam variables of the interacting pair. For example, we use $\mathcal{M}_2(\bar{s}, t, u)$ to refer to the scattering amplitude of the initial dimer, where we define

$$\bar{s} = (k_1 + k_2)^2 - 4M_\pi^2, \quad t = (k_1 - p_3)^2, \quad u = (k_2 - p_3)^2, \quad (5.22)$$

all of which vanish at threshold. Analogous definitions hold for the final state, distinguished by primed variables. We note that, when off-shell, these variables obey the simple relation

$$\bar{s} + t + u = \bar{s}' + t' + u' = \bar{b}^2, \quad (5.23)$$

with $\bar{b}^2 = 0$ on shell. We also note that we can set $\epsilon = 0$ in eq. (5.20) and in the G^∞ factor in eq. (5.21), defined in eq. (2.16), as the divergence that the $i\epsilon$ term regulates is canceled by the subtraction. Also, as the LO amplitude is real and we are only interested in the real part of $\mathcal{M}_{\text{df},3}$, we can just work with the real part of the NLO result. Finally note that the cutoff factors in G^∞ can be set to unity, as external particles are always on-shell.

The starting point to evaluate eqs. (5.19) to (5.21) are the LO and NLO off-shell two-pion isospin-two amplitudes. These take the general form,

$$F_\pi^4 \mathcal{M}_{2,\text{off}}(\bar{s}, t, u) = A_{4\pi}(t, u, s) + A_{4\pi}(u, s, t), \quad (5.24)$$

where $A_{4\pi}$ is the four-pion amplitude [195]. At LO, it takes the form,

$$F_\pi^2 A_{4\pi}^{(2)}(s, t, u) = s - M_\pi^2, \quad (5.25)$$

while at NLO,

$$\begin{aligned} F_\pi^4 A_{4\pi}^{(4)}(s, t, u) &= (t - u)^2 \left(-\frac{5}{36}\kappa - \frac{1}{6}L + \frac{1}{2}\ell_2^r \right) \\ &+ M_\pi^2 s \left(-\frac{2}{9}\kappa - \frac{2}{9}L - 8\ell_1^r + 2\ell_4^r \right) + s^2 \left(-\frac{7}{12}\kappa - \frac{1}{2}L + 2\ell_1^r + \frac{1}{2}\ell_2^r \right) \\ &+ M_\pi^4 \left(\frac{13}{20}\kappa + \frac{7}{6}L + 8\ell_1^r + 2\ell_3^r - 2\ell_4^r \right) + \bar{J}(s) \left(\frac{1}{2}s^2 - \frac{1}{2}M_\pi^4 \right) \\ &+ \left[\frac{1}{6}\bar{J}(t)(2t^2 - 10M_\pi^2 t - 4M_\pi^2 s + st + 14M_\pi^4) + (t \leftrightarrow u) \right]. \end{aligned} \quad (5.26)$$

Here $\kappa = 1/16\pi^2$, $L = \kappa \log(M_\pi^2/\mu^2)$, with μ the renormalization scale, ℓ_i^r are the $N_f = 2$ LECs introduced in sec. 1.4.1, and \bar{J} are loop integrals [149, 262]. Note that the LO amplitude only contains s -wave, while the NLO one contains all even partial waves. However, when working at quadratic order in the threshold expansion, only $\ell = 0, 2$ need to be considered.

The first step is to expand the off-shell amplitudes about threshold, including terms up to cubic order. The LO amplitude is easily found to be

$$F_\pi^2 \mathcal{M}_{2,\text{off}}^{\text{LO}}(\bar{s}, t, u) = -2M_\pi^2 - \bar{s} + \bar{b}^2. \quad (5.27)$$

The NLO amplitude, on the other hand, requires expanding the \bar{J} functions. Neglecting imaginary parts, one finds

$$\frac{1}{\kappa} \text{Re} \bar{J}(4M_\pi^2 + \bar{s}) = 2 - \frac{1}{2} \frac{\bar{s}}{M_\pi^2} + \frac{1}{12} \frac{\bar{s}^2}{M_\pi^4} - \frac{1}{60} \frac{\bar{s}^3}{M_\pi^6} + \mathcal{O}(\bar{s}^4), \quad (5.28)$$

$$\frac{1}{\kappa} \bar{J}(t) = \frac{1}{6} \frac{t}{M_\pi^2} + \frac{1}{60} \frac{t^2}{M_\pi^4} + \frac{1}{420} \frac{t^3}{M_\pi^6} + \mathcal{O}(t^4). \quad (5.29)$$

The off-shell amplitude then takes the schematic form

$$\begin{aligned} F_\pi^4 \text{Re} \mathcal{M}_{2,\text{off}}^{\text{NLO}}(\bar{s}, t, u) &= e_0 M_\pi^4 + e_1 M_\pi^2 \bar{s} + e_2 \bar{s}^2 + e_3 M_\pi^2 \bar{b}^2 + e_4 \bar{s} \bar{b}^2 \\ &+ e_5 (\bar{b}^2)^2 + e_{tu} tu + e_6 \frac{\bar{s}^2 \bar{b}^2}{M_\pi^2} + e_7 \frac{\bar{s} (\bar{b}^2)^2}{M_\pi^2} + e_8 \frac{(\bar{b}^2)^3}{M_\pi^6} + \tilde{e}_{tu} \frac{(\bar{b}^2 - \bar{s})}{M_\pi^6} tu + \dots, \end{aligned} \quad (5.30)$$

where e_i are constants depending on κ , L and the LECs, and ... indicates higher order terms.

Next, we separate the NLO amplitude into different partial waves, needed to compute the subtraction term. Most of the terms in eq. (5.30) only contribute to s -wave, the only exception being those containing tu factors, which also contribute to d -wave. This factor can be decomposed as

$$tu = \frac{1}{4} (\bar{s} - \bar{b}^2)^2 - 4(\mathbf{a}_k^* \cdot \mathbf{p}_k^*)^2, \quad (5.31)$$

where \mathbf{a}_k^* and \mathbf{p}_k^* are the three momenta \mathbf{k}_1 and \mathbf{p}_3 boosted to the CMF of the initial-state dimer. Using the addition theorem of spherical harmonics [305], one can decompose

$$(\mathbf{a}_k^* \cdot \mathbf{p}_k^*)^2 = q_{2,k}^{*2} p_k^{*2} \left[\frac{8\pi}{15} \sum_m Y_{2m}^*(\hat{\mathbf{a}}_k^*) Y_{2m}(\hat{\mathbf{p}}_k^*) + \frac{1}{3} \right], \quad (5.32)$$

where we have introduced the magnitudes of \mathbf{a}_k^* and \mathbf{p}_k^* , which can be expanded about threshold,

$$\begin{aligned} |\mathbf{a}_k^*|^2 &= q_{2,k}^{*2} = \frac{1}{4} \bar{s}, \\ p_k^{*2} &= \frac{(s - \bar{b}^2)^2}{4s} - M_\pi^2 = \frac{1}{4} \bar{s} - \frac{1}{2} \bar{b}^2 + \frac{1}{16} (\bar{b}^2)^2 + \dots \end{aligned} \quad (5.33)$$

From here, one can decompose the off-shell tu term into s - and d -wave parts,

$$\begin{aligned}
 [tu]_s &= \frac{1}{4}(\bar{s} - \bar{b}^2)^2 - \frac{4}{3}q_{2,k}^{*2}p_k^{*2}, \\
 [tu]_d &= q_{2,k}^{*2}p_k^{*2} \frac{8\pi}{15} \sum_m Y_{2m}^*(\hat{\mathbf{a}}_k^*) Y_{2m}(\hat{\mathbf{p}}_k^*).
 \end{aligned} \tag{5.34}$$

Analogous results hold for the final-state $t'u'$ term.

The contribution from the s -wave part of the NLO amplitude to $\mathcal{K}_{\text{df},3}^{(\text{u,u}),\text{NLO}}$ is now easy to evaluate. We can set G^∞ to $G_{ss}^\infty = 1/\bar{b}^2$ and separate the relevant LO and NLO off-shell amplitudes as an on-shell part and a term proportional to \bar{b}^2 ,

$$\mathcal{M}_{2,\text{off}} = \mathcal{M}_2 + \bar{b}^2 \delta \mathcal{M}_2. \tag{5.35}$$

Then, one finds

$$\begin{aligned}
 F_\pi^6 \mathcal{K}_{\text{df},3}^{(\text{u,u}),\text{NLO, OPE},s} &= -\mathcal{M}_2^{\text{NLO}} \delta \mathcal{M}_2^{\text{LO}} \\
 &\quad - \delta \mathcal{M}_2^{\text{NLO}} \mathcal{M}_2^{\text{LO}} - \delta \mathcal{M}_2^{\text{NLO}} \delta \mathcal{M}_2^{\text{LO}} + \leftrightarrow.
 \end{aligned} \tag{5.36}$$

Substituting the results in eq. (5.30), one can rewrite this in terms of the operators in eq. (5.16), obtaining the unsymmetrized K -matrix.

The contribution from the d -wave part of the NLO amplitude requires the use of G_{20}^∞ and G_{02}^∞ , which include a barrier factor. Note these correspond to the $G_{\ell\ell}^\infty$ factor when one of the two dimers is d wave—see eq. (2.16). For example, if the d -wave interaction happens for the initial dimer ($\ell = 2$), the barrier factor takes the form $G_{02}^\infty \propto (p_k^{*2}/q_{2,k}^{*2})^2$. From eqs. (5.30) and (5.34), and recalling that $p_k^{*2} = q_{2,k}^{*2}$ on shell, one notes,

$$[tu]_{d,\text{on}} \left(\frac{p_k^{*2}}{q_{2,k}^{*2}} \right)^2 = [tu]_{d,\text{off}}. \tag{5.37}$$

This means the barrier factor in G^∞ converts the on-shell tu factor to its off-shell counterpart.

For the term with e_{tu} coefficient in eq. (5.30), this implies that the subtraction picks up the difference between the off- and on-shell values of the LO amplitude,

$$F_\pi^6 \mathcal{K}_{\text{df},3}^{(\text{u,u}),\text{NLO, OPE},d} \supset -\delta \mathcal{M}_2^{\text{LO}} e_{tu} ([tu]_{d,\text{off}} + [t'u']_{d,\text{off}}). \tag{5.38}$$

To convert to the basis in eq. (5.16), one substitutes

$$[tu]_d = tu - [tu]_s. \tag{5.39}$$

The first term directly contributes to \mathcal{Q}_{tu} in eq. (5.16), while the second, given in eq. (5.34), only contributes to s -wave coefficients.

Slightly more complicated is the term with \tilde{e}_{tu} in eq. (5.30), as one needs to consider $\bar{s}^2[tu]_d$ and $\bar{b}^2[tu]_d$ separately. The former follows the same lines as the $[tu]_d$ factor above, while the latter is off-shell by definition, and so has no associated subtraction term. The result is just given by substituting into eq. (5.20) and keeping only the terms in the LO amplitude that are independent of momenta, $\mathcal{M}^{\text{LO}} = 2/F_\pi^2 + \dots$,

$$F_\pi^6 \mathcal{K}_{\text{df},3}^{(\text{u,u})\text{NLO,OPE},d} \supset -2\tilde{e}_{tu} ([tu]_{d,\text{off}} + [t'u']_{d,\text{off}}). \quad (5.40)$$

Again, by using eq. (5.39) it is possible to determine the contribution to the different terms of the expansion in eq. (5.16).

The subtracted-OPE contribution to $\mathcal{K}_{\text{df},3}$ at NLO is finally obtained after symmetrization of $\mathcal{K}_{\text{df},3}^{(\text{u,u})\text{OPE,NLO}}$. Combining the s - and d -wave contributions, we find,

$$\begin{aligned} \frac{F_\pi^6}{M_\pi^6} \mathcal{K}_0^{\text{NLO,OPE}} &= 25\kappa + 78L - 72(8\ell_1^r + 6\ell_2^r + \ell_3^r - 2\ell_4^r), \\ \frac{F_\pi^6}{M_\pi^6} \mathcal{K}_1^{\text{NLO,OPE}} &= \frac{6831}{20}\kappa + 372L - 18(74\ell_1^r + 67\ell_2^r - 14\ell_4^r), \\ \frac{F_\pi^6}{M_\pi^6} \mathcal{K}_2^{\text{NLO,OPE}} &= \frac{230481}{280}\kappa + 576L - 108(10\ell_1^r + 11\ell_2^r), \\ \frac{F_\pi^6}{M_\pi^6} \mathcal{K}_A^{\text{NLO,OPE}} &= -\frac{53199}{560}\kappa + 45L + \frac{27}{2}(14\ell_1^r - 17\ell_2^r), \\ \frac{F_\pi^6}{M_\pi^6} \mathcal{K}_B^{\text{NLO,OPE}} &= \frac{54171}{140}\kappa + 216L - 324(2\ell_1^r + \ell_2^r). \end{aligned} \quad (5.41)$$

5.2.3 The non-OPE contribution

The contribution from the non-OPE part of the NLO amplitude is more straightforward to compute, as it can be treated independently of the subtraction. For the three-pion $I_{\pi\pi\pi} = 3$ channel, it takes the form

$$\begin{aligned} \mathcal{M}_3^{\text{NLO,non-OPE}} &= \\ &A_{6\pi}^{(4)}(k_1, -p_1, k_2, -p_2, k_3, -p_3) + A_{6\pi}^{(4)}(k_1, -p_2, k_2, -p_1, k_3, -p_3) \\ &+ A_{6\pi}^{(4)}(k_1, -p_1, k_2, -p_3, k_3, -p_2) + A_{6\pi}^{(4)}(k_1, -p_2, k_2, -p_3, k_3, -p_1) \\ &+ A_{6\pi}^{(4)}(k_1, -p_3, k_2, -p_1, k_3, -p_2) + A_{6\pi}^{(4)}(k_1, -p_3, k_2, -p_2, k_3, -p_1), \end{aligned} \quad (5.42)$$

where $A_{6\pi}^{(4)}(q_1, q_2, q_3, q_4, q_5, q_6)$ is the six-pion amplitude at NLO defined in eq. (35) of ref. [195] with all momenta ingoing. This amplitude can be decomposed into different terms,

$$A_{6\pi}^{(4)} = A_\pi + A_L + A_l + A_J + A_C, \quad (5.43)$$

each of which can be separately expanded around threshold. To identify the corresponding contributions to the coefficients in eq. (5.12), we rewrite first the expanded amplitudes in terms of the operators in eq. (5.13), and then relate them to the standard form of the expansion.

A_π , A_L and A_l contain terms proportional to κ , L and ℓ_i^r , and are by construction quadratic polynomials in products of the momenta. Thus, no expansion is needed, and the contributions to each coefficient in eq. (5.12) are straightforward to identify. The A_J part contains $\bar{J}(q^2)$ functions, that need to be expanded up to quadratic order either about threshold, $q^2 = 4M_\pi^2$, or about $q^2 = 0$, using eq. (5.28).

The last term, A_C , contains C functions. These are related to triangle loop integrals arising in diagrams of the form of those shown in fig. 5.3, and depend on three pairs of momenta. As the real part of the amplitude is finite, it can be determined using a naive principal-value prescription [306].

The C functions need to be expanded in two different cases, which we exemplify here for the simplest C function, called C_0 . We note the same techniques also hold for other C functions, which contain powers of momentum in the denominator. In the Feynman-parameter representation, C_0 takes the form

$$C_0 = -\kappa \int_0^1 dx dy dz \frac{\delta(1-x-y-z)}{M_\pi^2 - xyq_1^2 - yzq_2^2 - zxq_3^2}, \quad (5.44)$$

where q_1 , q_2 and q_3 are the total incoming momenta into each vertex of the triangle loop.

The first expansion occurs in the case all three q_i^2 small. This happens when the initial/final momenta enter the with the same topology as fig. 5.3b.

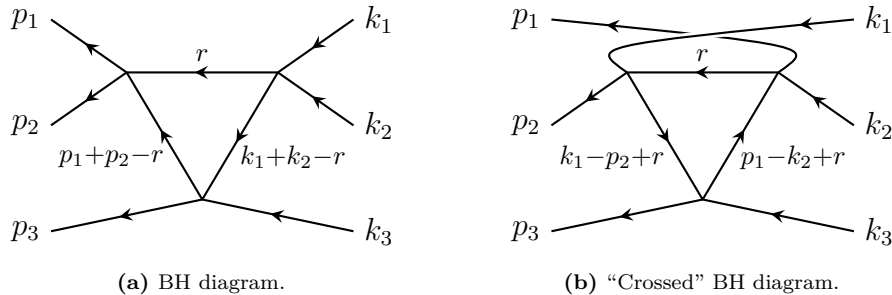


Figure 5.3. Two configurations of the triangle-loop diagram that contribute to the isospin-three scattering amplitude. In total, 15 diagrams with the triangle topology contribute, of which nine correspond to the configuration (a) and six to (b). Note that only the former requires subtraction, given in eqs. (5.50) and (5.51).

In that particular example $q_1 = k_2 - p_1$, $q_2 = k_1 - p_2$ and $q_3 = k_3 - p_3$. The Feynman-parameter integral can be evaluated after expanding the denominator, obtaining,

$$\begin{aligned} \frac{C_0}{\kappa} = & -\frac{1}{2M_\pi^2} - \frac{1}{24M_\pi^4} (q_1^2 + q_2^2 + q_3^2) \\ & - \frac{1}{180M_\pi^6} (q_1^4 + q_2^4 + q_3^4 + q_1^2 q_2^2 + q_2^2 q_3^2 + q_1^2 q_3^2) + \dots \end{aligned} \quad (5.45)$$

Note that in this case the integral is finite, and we do not need any prescription to regulate divergencies.

The second expansion case originates from diagrams of the form of fig. 5.3a, in which $q_1 = k_1 + k_2$, $q_2 = -p_1 - p_2$ and $q_3 = k_3 - p_3$. In this case, the threshold expansion corresponds to q_3^2 small and both q_1^2 and q_2^2 close to $4M_\pi^2$. This is equivalent to having small $\bar{s}_1 = q_1^2 - 4M_\pi^2$ and $\bar{s}_2 = q_2^2 - 4M_\pi^2$. In terms of these variables, the C integral can be rewritten as

$$C_0 = -\kappa \int_0^1 dx dy dz \frac{\delta(1-x-y-z)}{M_\pi^2(1-2y)^2 - xy\bar{s}_1 - yz\bar{s}_2 - zxq_3^2}. \quad (5.46)$$

As before, we first expand the denominator and then perform the Feynman integrals. These are trivial in the case of x and z , but the result for the y integral is divergent. We know that the real part is finite about threshold, and so can compute it using a principal-value (PV) prescription that discards the imaginary part. Integrals having singularities in the integration path are averaged over contours surrounding the singularity from above and below. For example,

$$\begin{aligned} \text{PV} \int_0^1 dz \frac{1}{(1-2y)^n} &= \frac{1}{2} \text{PV} \int_{-1}^1 dv \frac{1}{v^n} \\ &= \frac{1}{4} \int_\pi^0 e^{-in\theta} de^{i\theta} + \frac{1}{4} \int_\pi^0 e^{in\theta} de^{-i\theta} = \begin{cases} 0 & n \text{ odd,} \\ -1/(n-1) & n \text{ even.} \end{cases} \end{aligned} \quad (5.47)$$

This allows us to obtain

$$\begin{aligned} \frac{C_0}{\kappa} = & \frac{1}{2M_\pi^2} + \frac{1}{M_\pi^4} \left(\frac{5}{72} q_3^2 - \frac{1}{24} \bar{s}_1 - \frac{1}{24} \bar{s}_2 \right) \\ & + \frac{1}{M_\pi^6} \left[\frac{2}{225} q_3^4 - \frac{1}{90} q_3^2 (\bar{s}_1 + \bar{s}_2) + \frac{1}{180} (\bar{s}_1^2 + \bar{s}_2^2 + \bar{s}_1 \bar{s}_2) \right] + \dots \end{aligned} \quad (5.48)$$

After expanding all C functions about the relevant values, one can follow the same procedure as for the other terms in $A_{6\pi}^{(4)}$ to determine the contribution to the different coefficients in the threshold expansion.

Adding the contributions to $\mathcal{K}_{\text{df},3}^{\text{NLO,non-OPE}}$ from all terms in eq. (5.43), we obtain

$$\begin{aligned}
 \frac{F_\pi^6}{M_\pi^6} \mathcal{K}_0^{\text{NLO,non-OPE}} &= 14\kappa + 33L + 36(8\ell_1^r + \ell_3^r - 2\ell_4^r), \\
 \frac{F_\pi^6}{M_\pi^6} \mathcal{K}_1^{\text{NLO,non-OPE}} &= -\frac{35}{2}\kappa + 12L + 36(20\ell_1^r + \ell_2^r - 4\ell_4^r), \\
 \frac{F_\pi^6}{M_\pi^6} \mathcal{K}_2^{\text{NLO,non-OPE}} &= -\frac{9747}{50}\kappa - 216L + 324(2\ell_1^r + \ell_2^r), \\
 \frac{F_\pi^6}{M_\pi^6} \mathcal{K}_A^{\text{NLO,non-OPE}} &= \frac{576}{5}\kappa - 54L - 81(2\ell_1^r - 3\ell_2^r), \\
 \frac{F_\pi^6}{M_\pi^6} \mathcal{K}_B^{\text{NLO,non-OPE}} &= -\frac{13797}{50}\kappa - 162L + 243(2\ell_1^r + \ell_2^r).
 \end{aligned} \tag{5.49}$$

5.2.4 The bull's head subtraction contribution

The last term contributing to $\mathcal{K}_{\text{df},3}^{\text{NLO}}$ is the BH part of the subtraction, which cancels divergencies arising from diagrams of the form of fig. 5.3a when any of the loop particles goes on shell. Note these divergencies appear in the imaginary part, and so the real part of the subtraction is finite. However, while an expansion about threshold of this real part can be performed, its coefficients involve integrals including the cutoff function, $H(x)$, and so can only be computed numerically.

Consider first the unsymmetrized subtraction, given by the last line in eq. (5.2). For the momenta configuration in fig. 5.3a it takes the form

$$\mathcal{D}^{(\text{u,u})\text{BH}}(\mathbf{p}_3, \mathbf{k}_3) = -\frac{1}{F_\pi^6} (2p_1 \cdot p_2) I(\mathbf{p}_3, \mathbf{k}_3) (2k_1 \cdot k_2), \tag{5.50}$$

with

$$I(\mathbf{p}_3, \mathbf{k}_3) = \int_r \frac{H(x_r) [(P-r)^2 - 2M_\pi^2] H(x_r)}{[(p_+ - r)^2 - M_\pi^2 + i\epsilon] [(k_+ - r)^2 - M_\pi^2 + i\epsilon]}, \tag{5.51}$$

where $x_r = (P-r)^2/(4M_\pi^2)$ and we have substituted $G^\infty \rightarrow G_{ss}^\infty$, given in eq. (2.40), since $\mathcal{M}_2^{\text{LO}}$ is purely s -wave.

We work in the CMF of the three-particle system, $P = (E^*, 0)$, and set $d^3r = r^2 dr d\cos\theta d\phi$. To evaluate the angular integrals, we rewrite first

$$\begin{aligned}
 (p_+ - r)^2 - M_\pi^2 &= p_+^2 - 2p_+ \cdot r \\
 &= p_+^2 - 2E_{p_+} \omega_r + 2\mathbf{p}_+ \cdot \mathbf{r} \equiv 4M_\pi^2 - 4M_\pi \omega_r + \Delta_{p_+}, \tag{5.52}
 \end{aligned}$$

where $p_+ = (p_1 + p_2) = (E_{p_+}, \mathbf{p}_+)$ and we implicitly define Δ_{p_+} . Similarly, we expand $(k_+ - r)$ and define Δ_{k_+} . These quantities are both $\mathcal{O}(\sqrt{\Delta})$, and so we use them to expand the denominators about threshold,

$$I(\mathbf{p}_3, \mathbf{k}_3) = \int_r H^2(x_r) [E^{*2} - 2E^* \omega_r - M_\pi^2] \sum_{a,b=0}^{\infty} \frac{\Delta_{p_+}^a \Delta_{k_+}^b}{(4M_\pi^2 - 4M_\pi \omega_r)^{a+b+2}}, \quad (5.53)$$

where the sum can be truncated at some convenient order. The angular integrals can be performed using integrals of the form

$$\int d \cos \theta d\phi (\mathbf{p}_+ \cdot \mathbf{r})(\mathbf{k}_+ \cdot \mathbf{r}) = 4\pi \frac{r^2}{3} \mathbf{p}_+ \cdot \mathbf{k}_+, \quad (5.54)$$

and its generalizations [3].

At this point, one can expand the integrand about threshold, using $E = 3M_\pi \sqrt{1 + \Delta}$ and $x_r = (E^{*2} - 2E^* \omega_r + M_\pi^2)/4M_\pi$, and identify the contribution to the different coefficients of the unsymmetrized threshold expansion, given in eq. (5.16). This includes only terms with corresponding coefficients $c'_0 - c'_{10}$. Symmetrizing over the initial and final momenta allows us to obtain the results

$$\begin{aligned} \frac{F_\pi^6}{M_\pi^6} \mathcal{K}_0^{\text{NLO,BH}} &= \frac{27}{2} H_{0,0} - \frac{9}{4} H_{2,0}, \\ \frac{F_\pi^6}{M_\pi^6} \mathcal{K}_1^{\text{NLO,BH}} &= \frac{117}{4} H_{0,0} - \frac{21}{8} H_{2,0} + \frac{3}{4} H_{4,0} + \frac{189}{4} H_{0,1}, \\ \frac{F_\pi^6}{M_\pi^6} \mathcal{K}_2^{\text{NLO,BH}} &= \frac{243}{160} H_{0,0} + \frac{2241}{320} H_{2,0} - \frac{423}{160} H_{4,0} \\ &\quad - \frac{369}{1280} H_{6,0} + \frac{5751}{64} H_{0,1} + \frac{567}{8} H_{0,2}, \\ \frac{F_\pi^6}{M_\pi^6} \mathcal{K}_A^{\text{NLO,BH}} &= -\frac{891}{64} H_{0,0} + \frac{1161}{128} H_{2,0} - \frac{45}{64} H_{4,0} - \frac{9}{128} H_{6,0}, \\ \frac{F_\pi^6}{M_\pi^6} \mathcal{K}_B^{\text{NLO,BH}} &= -\frac{81}{320} H_{0,0} + \frac{297}{640} H_{2,0} + \frac{27}{160} H_{4,0} - \frac{27}{640} H_{6,0}. \end{aligned} \quad (5.55)$$

Here, $H_{m,n}$ are given by integrals of the form

$$H_{m,n} \equiv \frac{1}{\pi^2} \int_0^{1/\sqrt{3}} dz \frac{\sqrt{1+z^2}}{z^m} \frac{d^n}{dx^n} [H^2(x)]. \quad (5.56)$$

where $x = 1 - 3z^3$, so the integration limits correspond $x = 1$ and $x = 0$. These terms originate after expanding $H(x)$, defined in eq. (2.17), about threshold and rewriting the integrals using a variable z defined via $\omega_r = M_\pi(1 + 2z^2)$. These terms obey the recursion relation,

$$H_{m,n+1} + H_{m-2,n+1} = \frac{1}{6} [(2-m)H_{m,n} - (m+1)H_{m+2,n}] - \frac{1}{6} \left[(f'_{m-1}(z) + f'_{m+1}(z)) \frac{d^n}{dx^n} H^2(x) \right]_0^{1/\sqrt{3}}, \quad (5.57)$$

which has been used to simplify the results in eq. (5.55). The functions f_n are implicitly defined from

$$\frac{d}{dz} f_m(z) = \frac{1}{\pi^2} \frac{\sqrt{1+z^2}}{z^m}, \quad (5.58)$$

independently of the integration constant in $f_m(z)$. Note they are singular at $z = 0$ for $m > 0$.

Note that $H(x)$ is non analytic at $x = 0$ and $x = 1$. Thus, the expansion is of asymptotic nature, not properly capturing the energy dependence in the upper limit of the integral. However, the expansion still captures very accurately the threshold behavior of \mathcal{D}^{BH} . We comment on this below, and also study the convergence numerically in sec. 5.3.2, where we compare the threshold result up to quadratic order to the full $\mathcal{K}_{\text{df},3}$ evaluated numerically.

The evaluation of the $H_{m,n}$ factors in eq. (5.55) is troublesome. For $n = 0$ and $m > 0$, the integrand in eq. (5.56) presents a singularity in the lower endpoint, so a naive application of the PV prescription is not valid. Instead, one can use the Hadamard finite-part prescription to regulate it [307]. To do so, we first use integration by parts

$$H_{m,0} = f_m(z) H^2(x) \Big|_{z=0}^{z=1/\sqrt{3}} - \int_0^{1/\sqrt{3}} dz f_m(z) (-6z) \frac{d}{dx} H^2(x). \quad (5.59)$$

At $z = 0$ the first term on the right-hand side of eq. (5.59) is singular for $m > 0$, but not the second one since derivatives of H vanish exponentially as $z \rightarrow 0$. The $z \rightarrow 1/\sqrt{3}$ limit vanishes identically, since H and all its derivatives are zero in this case. The Hadamard finite part of $H_{m,0}$ is obtained by dropping the singular $z = 0$ term and evaluating the integral, which yields a finite result.

The applicability of Hadamard finite-part prescription is not clear a priori. Most traditional proofs rely on the analyticity of the integrand, which is not valid here since $H(x)$ is not analytic. However, ref. [308] presents a proofs that only requires smoothness of the integrands, which is satisfied in our case. It also requires $m > 1$, but the only integral not satisfying this condition is $H_{0,0}$, which is convergent. The application of the prescription also relies on $\text{Re}\mathcal{D}^{(u,u)\text{BH}}$ being finite, but this is the case since all divergencies in $\mathcal{M}_3^{(u,u)}$ appear in its imaginary part.

Note that the Hadamard finite-part prescription validates the Taylor expansion of $H(x)$ used to obtain eq. (5.56). The Taylor series converges

for $0 < x < 1$, but the convergence is extremely poor in the vicinity of the essential singularities at the endpoints. However, taking the Hadamard finite part in eq. (5.59), all remaining integrands contain derivatives of $H(x)$, which are exponentially suppressed near these endpoints. Thus, the result is insensitive to the regions where the convergence is poor.

There is one final simplification that can be done, which allows us to rewrite eq. (5.56) in terms of a fully analytical part plus some small cutoff-dependent correction that need to be evaluated numerically. The idea is to write $H(x) = 1 + \tilde{H}(x)$, so that

$$H_{m,n} = \tilde{H}_{m,n} + \delta_{n,0} \int_0^{1/\sqrt{3}} dz \frac{1}{\pi^2} \frac{\sqrt{1+z^2}}{z^m}, \quad (5.60)$$

where $\tilde{H}_{m,n}$ is obtained by substituting $H(x) \rightarrow \tilde{H}(x)$. The second term on the right-hand side can be evaluated analytically using the Hadamard finite part prescription. Choosing $f_0(0) = 0$ as the integration constant for f_0 , the result of the integral is simply $f_m(1/\sqrt{3})$. Eq. (5.57) can be rewritten for the $f_m \delta_{n,0}$ terms,

$$(m+1)f_{m+2}(z) + (m-2)f_m(z) = -(1+z^2)f'_{m+1}(z), \quad (5.61)$$

which can be used to determine all f_m in terms of κ and $f_0 = f_0(1/\sqrt{3}) = \frac{4}{3}\kappa(4 + 3 \log 3)$.

Using this procedure, the results for the threshold coefficients of $\mathcal{K}_{\text{df},3}^{\text{NLO,BH}}$ are simplified,

$$\begin{aligned} \frac{F_\pi^6}{M_\pi^6} \mathcal{K}_0^{\text{NLO,BH}} &= 96\kappa + 9f_0 + \mathcal{D}_0, \\ \frac{F_\pi^6}{M_\pi^6} \mathcal{K}_1^{\text{NLO,BH}} &= 296\kappa + 24f_0 + \mathcal{D}_1, \\ \frac{F_\pi^6}{M_\pi^6} \mathcal{K}_2^{\text{NLO,BH}} &= \frac{5661}{50}\kappa + \frac{621}{40}f_0 + \mathcal{D}_2, \\ \frac{F_\pi^6}{M_\pi^6} \mathcal{K}_A^{\text{NLO,BH}} &= -\frac{1764}{5}\kappa + \frac{135}{32}f_0 + \mathcal{D}_A, \\ \frac{F_\pi^6}{M_\pi^6} \mathcal{K}_B^{\text{NLO,BH}} &= -\frac{612}{25}\kappa + \frac{189}{160}f_0 + \mathcal{D}_B. \end{aligned} \quad (5.62)$$

Here \mathcal{D}_X are cutoff-depending numerical corrections coming from $\tilde{H}_{m,n}$, defined from the requirement that eq. (5.62) equals eq. (5.55). The values of the remainders, in the case of the standard cutoff in eq. (2.17) are presented in eq. (5.69). A study of their dependence on the choice of the cutoff function is presented in app. A of ref. [3]. We remark that eq. (5.62) cannot be directly obtained from eq. (5.55) by substituting $H_{m,n} \rightarrow f_m \delta_{n,0}$. Instead, one needs to perform this substitution before applying the simplifying relation given in eq. (5.57).

5.2.5 Numerical evaluation

The (almost) analytic results presented in the previous sections have been cross checked by direct numerical evaluation. The numeric results also allow us to test the convergence of the threshold expansion away from threshold, and to study the relative contributions from different partial waves, in the case of the subtracted OPE part. Such analysis are presented in sec. 5.3.2.

The numerical determination of the subtracted OPE is relatively simple. It requires to project the off- and on-shell two-pion amplitudes to partial waves, compute the subtraction with some finite ε in the exchanged-particle propagator, including the correct barrier factors, and add all the partial waves with the relevant spherical harmonics. The computation of $\mathcal{M}_{\text{df},3}^{\text{non-OPE}}$ is also straightforward, as one can use known results for the C functions in terms of dilogarithmic functions [262].

It is also possible to compute \mathcal{D}^{BH} numerically, although this presents more complications. One option is to directly evaluate eq. (5.51), but singularities in the integrand can lead to bad convergence. It is more convenient to first separate the integral into a convergent and a divergent part, and treat the latter one analytically, leaving it in a form that allows for easier numerical evaluation ref. [3].

The numerical computation of $\mathcal{K}_{\text{df},3}$ is performed for various chosen kinematical configurations. Each of these is a family of six on-shell four-momenta depending on a single parameter p that vanishes at threshold. We refer to each of these families as \mathcal{F}_a . The ones used in this work are summarized in table 5.1. Numerically evaluating $\mathcal{K}_{\text{df},3}$ for different values of p close to zero allows us determine the coefficients of a Taylor expansion of $\mathcal{K}_{\text{df},3}$ in p^2 as

$$\mathcal{K}_{\text{df},3}(\mathcal{F}_a) = c_0^a + c_1^a p^2 + c_2^a p^4 + \mathcal{O}(p^6). \quad (5.63)$$

a	$\mathbf{p}_1^{(a)}(p)$	$\mathbf{p}_2^{(a)}(p)$	$\mathbf{k}_1^{(a)}(p)$	$\mathbf{k}_2^{(a)}(p)$
1	$(p, 0, 0)$	$(-\frac{1}{2}p, \frac{\sqrt{3}}{2}p, 0)$	$(0, 0, -p)$	$(\frac{\sqrt{3}}{2}p, 0, \frac{1}{2}p)$
2	$(p, 0, 0)$	$(-\frac{1}{2}p, \frac{\sqrt{3}}{2}p, 0)$	$(-p, 0, 0)$	$(\frac{1}{2}p, \frac{\sqrt{3}}{2}p, 0)$
3	$(2p, 0, 0)$	$(-p, \frac{\sqrt{3}}{2}p, 0)$	$(0, 0, -2p)$	$(\frac{\sqrt{3}}{2}p, 0, p)$

Table 5.1. Momenta families used in the numerical evaluation of $\mathcal{K}_{\text{df},3}$, all with zero total momentum. We only quote the spacial part of the four-momenta, with the remaining element constrained by the on-shell relation, $p_i^2 = k_i^2 = M_\pi^2$. Also, \mathbf{k}_3 and \mathbf{p}_3 can be inferred from $\mathbf{P} = \mathbf{p}_1 + \mathbf{p}_2 + \mathbf{p}_3 = \mathbf{k}_1 + \mathbf{k}_2 + \mathbf{k}_3 = 0$.

If we consider the expansion of the kinematical operators appearing in the threshold expansion,

$$\begin{aligned}\Delta(\mathcal{F}_a) &= d_1^a p^2 + d_2^a p^4 + \mathcal{O}(p^6), \\ \Delta_A(\mathcal{F}_a) &= d_A^a p^4 + \mathcal{O}(p^6), \\ \Delta_B(\mathcal{F}_a) &= d_B^a p^4 + \mathcal{O}(p^6),\end{aligned}\tag{5.64}$$

one can note that a single family is sufficient to determine

$$\mathcal{K}_0 = c_0^a, \quad \mathcal{K}_1 = c_1^a/d_1^a.\tag{5.65}$$

For the quadratic-order coefficients, on the other hand, the results from three separate families need to be combined. One first constructs

$$Q = \begin{pmatrix} (d_1^{a_1})^2 & d_A^{a_1} & d_B^{a_1} \\ (d_1^{a_2})^2 & d_A^{a_2} & d_B^{a_2} \\ (d_1^{a_3})^2 & d_A^{a_3} & d_B^{a_3} \end{pmatrix}, \quad V = \begin{pmatrix} c_2^{a_1} - c_1^{a_1} d_2^{a_1}/d_1^{a_1} \\ c_2^{a_2} - c_1^{a_2} d_2^{a_2}/d_1^{a_2} \\ c_2^{a_3} - c_1^{a_3} d_2^{a_3}/d_1^{a_3} \end{pmatrix},\tag{5.66}$$

from which it is possible to obtain

$$\begin{pmatrix} \mathcal{K}_2 & \mathcal{K}_A & \mathcal{K}_B \end{pmatrix}^\top = Q^{-1}V.\tag{5.67}$$

5.3 Results for $\mathcal{K}_{\text{df},3}$

Combining the analytical results determined in sec. 5.2—see eqs. (5.41), (5.49), and (5.62)—and including the LO results from eq. (2.46), the coefficients of the full LO+NLO isospin-three three-pion K -matrix are

$$\begin{aligned}\mathcal{K}_0 &= \left(\frac{M_\pi}{F_\pi}\right)^4 18 + \left(\frac{M_\pi}{F_\pi}\right)^6 \left[-3\kappa(35 + 12 \log 3) - \mathcal{D}_0 + 111L + \ell_{(0)}^r \right], \\ \mathcal{K}_1 &= \left(\frac{M_\pi}{F_\pi}\right)^4 27 + \left(\frac{M_\pi}{F_\pi}\right)^6 \left[-\frac{\kappa}{20}(1999 + 1920 \log 3) - \mathcal{D}_1 + 384L + \ell_{(1)}^r \right], \\ \mathcal{K}_2 &= \left(\frac{M_\pi}{F_\pi}\right)^6 \left[\frac{207\kappa}{1400}(2923 - 420 \log 3) - \mathcal{D}_2 + 360L + \ell_{(2)}^r \right], \\ \mathcal{K}_A &= \left(\frac{M_\pi}{F_\pi}\right)^6 \left[\frac{9\kappa}{560}(21809 - 1050 \log 3) - \mathcal{D}_A - 9L + \ell_{(A)}^r \right], \\ \mathcal{K}_B &= \left(\frac{M_\pi}{F_\pi}\right)^6 \left[\frac{27\kappa}{1400}(6698 - 245 \log 3) - \mathcal{D}_B + 54L + \ell_{(B)}^r \right].\end{aligned}\tag{5.68}$$

Here \mathcal{D}_X are the only cutoff-dependent parts, which need to be evaluated numerically,

$$\begin{aligned} \mathcal{D}_0 &\approx -0.0563476589, & \mathcal{D}_1 &\approx 0.129589681, & \mathcal{D}_2 &\approx 0.432202370, \\ \mathcal{D}_A &\approx 9.07273890 \times 10^{-4}, & \mathcal{D}_B &\approx 1.62394747 \times 10^{-4}. \end{aligned} \quad (5.69)$$

Also, we have defined the following linear combinations of LECs,

$$\begin{aligned} \ell_{(0)}^r &= -288\ell_1^r - 432\ell_2^r - 36\ell_3^r + 72\ell_4^r, & \ell_{(1)}^r &= -612\ell_1^r - 1170\ell_2^r + 108\ell_4^r, \\ \ell_{(2)}^r &= -432\ell_1^r - 864\ell_2^r, & \ell_{(A)}^r &= 27\ell_1^r + \frac{27}{2}\ell_2^r, & \ell_{(B)}^r &= -162\ell_1^r - 81\ell_2^r. \end{aligned} \quad (5.70)$$

Note that, while both ℓ_i and L depend on the renormalization scale, μ , the complete results in eq. (5.68) are scale independent, and so is $\mathcal{K}_{\text{df},3}$.

5.3.1 Comparison to lattice results

The results in eq. (5.68) can be compared to lattice determinations of $\mathcal{K}_{\text{df},3}$. Different works have studied the system of three pions at maximal isospin using the RFT formalism [181, 268, 298, 301], finding similar qualitative disagreement with LO ChPT predictions. This discrepancy can be partially explained by NLO ChPT corrections. In particular, we focus our comparison on the results of ref. [301], in which \mathcal{K}_0 , \mathcal{K}_1 and \mathcal{K}_B are determined for pion masses of 200, 280 and 340 MeV.

We use the following values for the scale-independent LECs, which were introduced in eq. (1.83),

$$\bar{\ell}_1 = -0.4(6), \quad \bar{\ell}_2 = 4.3(1), \quad \bar{\ell}_3 = 3.07(64), \quad \bar{\ell}_4 = 4.02(45). \quad (5.71)$$

The values of $\bar{\ell}_1$ and $\bar{\ell}_2$ are determined by combining experiment, ChPT and dispersion relations [309], while $\bar{\ell}_3$ and $\bar{\ell}_4$ come from averaging results from $N_f = 2 + 1$ lattice simulations [183], based on refs. [310–314]. We also take into account the correlations between $\bar{\ell}_1$ and $\bar{\ell}_2$ using the covariance matrix from ref. [309],

$$\text{Cov}(\bar{\ell}_1, \bar{\ell}_2) = \begin{pmatrix} 0.35 & -0.033 \\ -0.033 & 0.012 \end{pmatrix}. \quad (5.72)$$

For the comparison, we choose μ so the results in eq. (5.68) depend only on M_π/F_π . This is achieved by taking $\mu = 4\pi F_\pi$ in L and approximating $\mu \approx 4\pi F_{\pi,\text{phys}}$ in the definition of $\bar{\ell}_i$ given in eq. (1.83). This different choice only affects the NNLO part, since F_π does not depend on M_π at LO, and

allows us to rewrite ChPT predictions only as a function of M_π/F_π . For example, \mathcal{K}_0 can be rewritten as

$$\mathcal{K}_0 = \left(\frac{M_\pi}{F_\pi}\right)^4 18 + \left(\frac{M_\pi}{F_\pi}\right)^6 \left[-3\kappa(35 + 12 \log 3) - \mathcal{D}_0 + 111\kappa \log \left(\frac{\xi}{\xi_{\text{phys}}} \right) + \kappa \bar{\ell}_{(0)} \right], \quad (5.73)$$

with $\bar{\ell}_{(0)} = -48\bar{\ell}_1 - 144\bar{\ell}_2 + 9\bar{\ell}_3 + 72\bar{\ell}_4$, $\xi \equiv M_\pi^2/(4\pi F_\pi)^2$ and $\xi_{\text{phys}} \equiv M_{\pi,\text{phys}}^2/(4\pi F_{\pi,\text{phys}})^2$.

In fig. 5.4, we compare the LO+NLO ChPT predictions for \mathcal{K}_0 and \mathcal{K}_1 to the lattice results. We also show the LO ChPT result for comparison. We observe how, in general, the discrepancy is reduced when NLO contributions are included. For \mathcal{K}_0 , it leads to smaller predictions that lie closer to the lattice results. For \mathcal{K}_1 , on the other hand, the corrections are large, leading to a change of sign with respect to LO for all but small pion masses. The LO+NLO results for $\mathcal{K}_{\text{df},3}$ have the same sign and lie close to the lattice data.

To interpret these findings, two different perspectives can be taken. One could argue that, in view of the size of NLO corrections, the chiral expansion converges poorly in the mass region where lattice results lie and so ChPT cannot be trusted. A more optimistic interpretation is that, for some reason, NLO corrections are larger than the LO results. This could be for example due to the presence of new diagrams, such as triangle loops in fig. 5.3.

In view of the agreement between lattice results and the ChPT prediction, it is instructive to study how well the values of the LECs in eq. (5.70) can be constrained. From a single-parameter fit to the lattice data, shown in fig. 5.4, we obtain,

$$\begin{aligned} \ell_{(0)}^r &= 1.55(11), & \chi^2/\text{dof} &= 2.93/2, \\ \ell_{(1)}^r &= 4.09(25), & \chi^2/\text{dof} &= 0.36/2, \end{aligned} \quad (5.74)$$

where we show the χ^2 of the fits and the corresponding number of degrees of freedom (dof). This results are to be compared to the phenomenological values, eq. (5.71),

$$\ell_{(0)}^r = 1.19(25), \quad \ell_{(1)}^r = 2.71(46). \quad (5.75)$$

The fits are shown in fig. 5.4.

In fig. 5.5 we show the NLO predictions for \mathcal{K}_2 , \mathcal{K}_A and \mathcal{K}_B . Note that all these vanish at LO in ChPT. In the case of \mathcal{K}_B , we compare to the lattice results from ref. [301]. We observe a similar situation as between \mathcal{K}_1 and

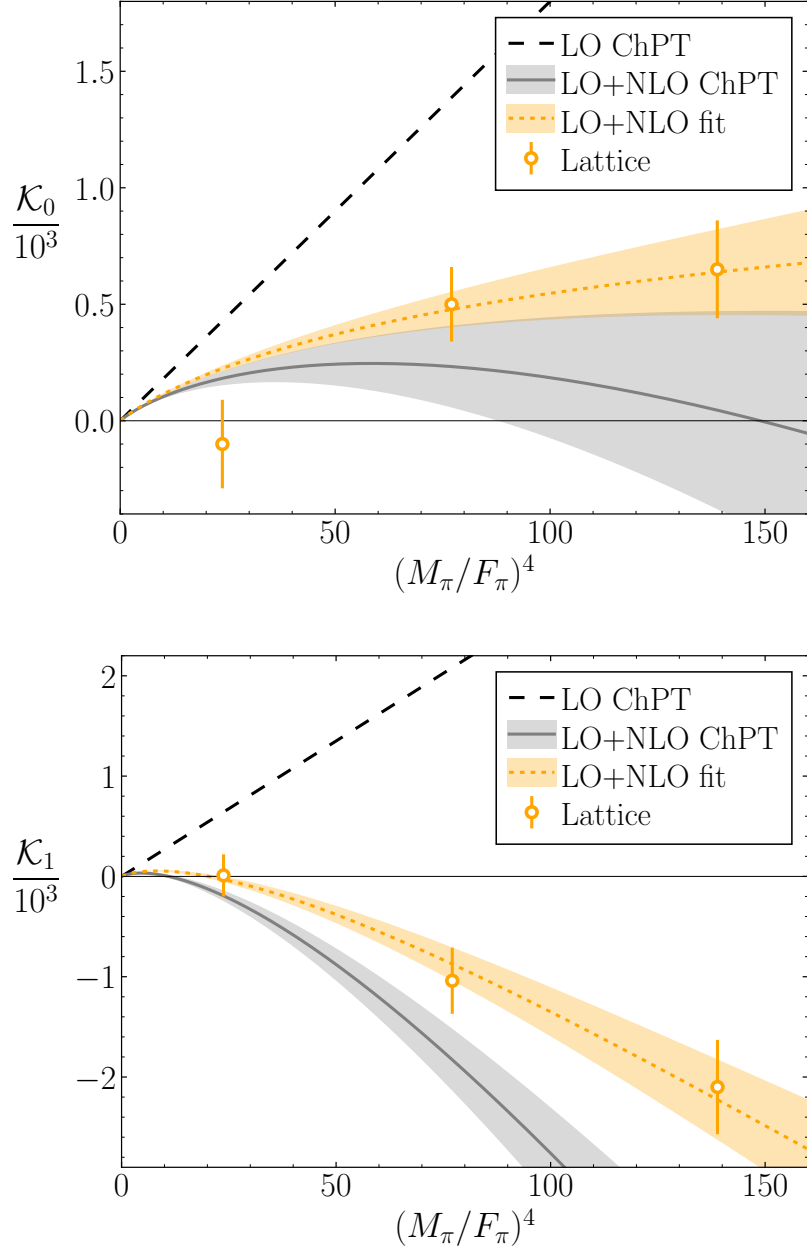


Figure 5.4. LO (dashed black line) and LO+NLO (grey line and band) ChPT predictions for \mathcal{K}_0 (top) and \mathcal{K}_1 (bottom) as functions of $(M_\pi/F_\pi)^4$, using LECs from refs. [183, 309] [see eq. (5.71)]. These predictions are compared to lattice results from ref. [301] (orange points). We also present the best fit to the lattice data (dotted orange line and band).

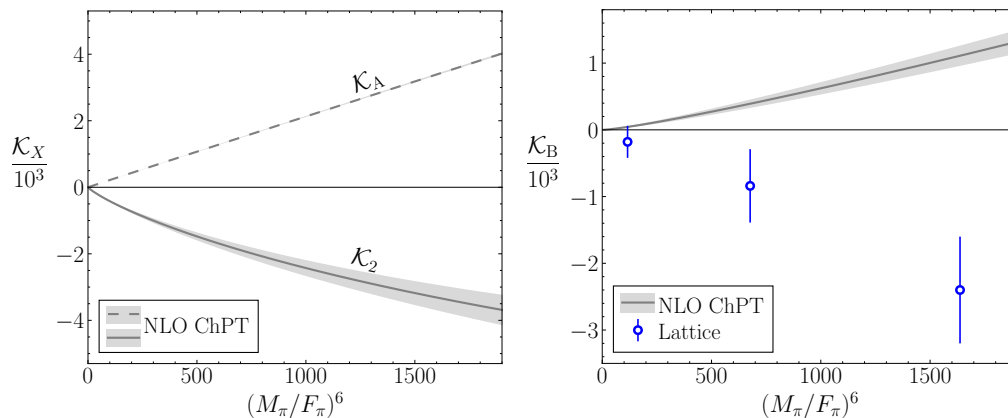


Figure 5.5. NLO ChPT predictions for \mathcal{K}_2 and \mathcal{K}_A (left), and \mathcal{K}_B (right) as functions of $(M_\pi/F_\pi)^6$, using LECs from refs. [183, 309] [see eq. (5.71)]. In the case of \mathcal{K}_B , we compare to lattice results from ref. [301] (blue points).

LO ChPT, with a large discrepancy between NLO predictions and lattice results of $\mathcal{K}_{\text{df},3}$, even showing opposite signs. It is possible that, similar to the \mathcal{K}_1 case, this discrepancy gets reduced by large NNLO corrections.

5.3.2 Range of validity of the threshold expansion

In lattice studies, the three-particle K -matrix is typically parametrized using a threshold expansion, which is assumed to be valid for all energies below the first inelastic threshold. In the three-pion case, this corresponds to CMF energies below the mass of five pions, $E^* < 5M_\pi$. We can use our results to test the actual convergence of the threshold expansion by comparing them to the full $\mathcal{K}_{\text{df},3}$ evaluated numerically using the techniques described in sec. 5.2.5. We here show the results for the first kinematical family in table 5.1, with other families leading to analogous conclusions.

In fig. 5.6 we show this comparison for the full $\mathcal{K}_{\text{df},3}$ for physical pion mass and $M_\pi = 340$ MeV, the heaviest value used in ref. [301]. In both cases, we observe reasonable agreement between the full and the expanded results up to the inelastic threshold, where the discrepancy is 10% and 20% for physical mass and $M_\pi = 340$ MeV, respectively. For the heavy pion mass, we present in fig. 5.7 a separate comparison for each of the terms in eq. (5.11). We observe good convergence for both the non-OPE and the BH subtraction part, at the 5% level in all the elastic regime, while the discrepancy is as big as 30% in the OPE part.

Finally, we also study the contribution of successive partial wave of the NLO amplitude to $\mathcal{K}_{\text{df},3}^{\text{OPE}}$. While the threshold expansion only contains s

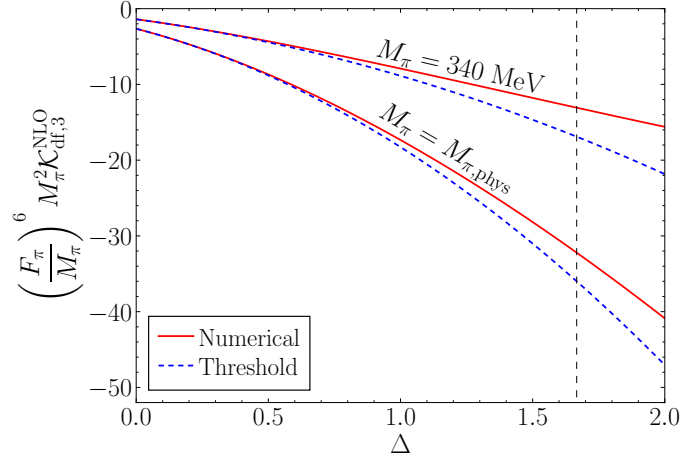


Figure 5.6. Comparison between numerical results and the threshold expansion for $\mathcal{K}_{\text{df},3}$, evaluated for the first momentum family in table 5.1. The comparison is presented for two pion masses, with $M_\pi = 340$ MeV corresponding to the heaviest pion mass used in ref. [301]. The dashed vertical line indicates the inelastic threshold at $E^* = 5M_\pi$.

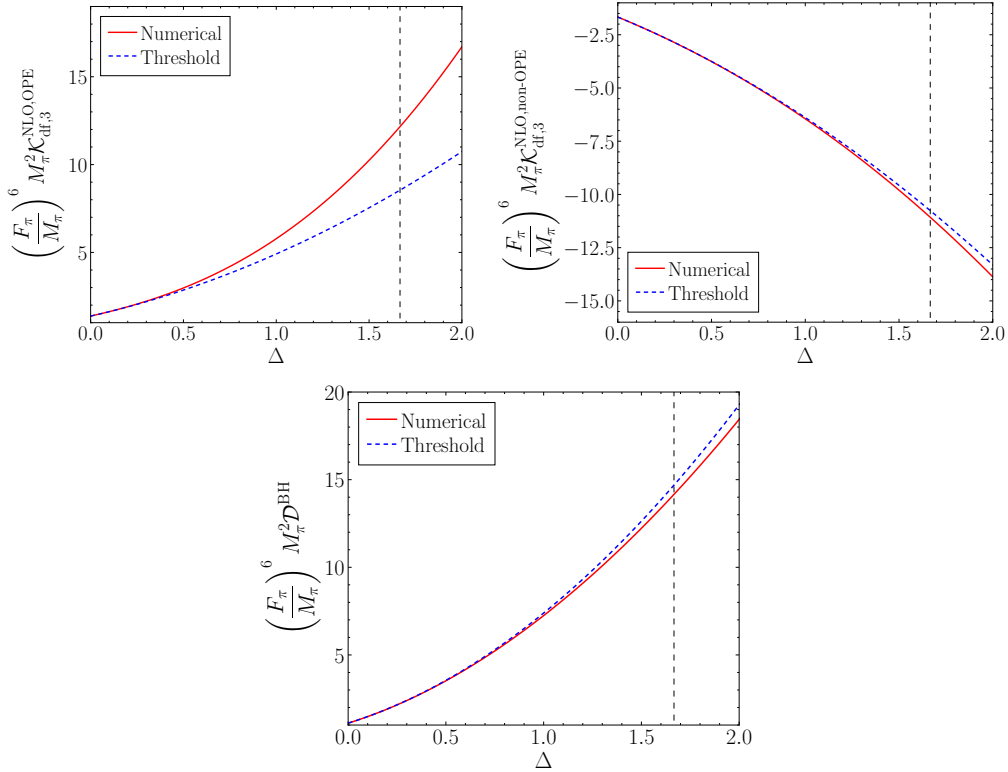


Figure 5.7. Comparison of the numerical and the threshold results for the different contributions to $\mathcal{K}_{\text{df},3}$ —see eq. (5.11)—evaluated for the first momentum family in table 5.1 for $M_\pi = 340$ MeV. The panels correspond to the OPE part (top left), non-OPE part (top right) and BH subtraction (bottom). The dashed vertical line indicates the inelastic threshold at $E^* = 5M_\pi$.

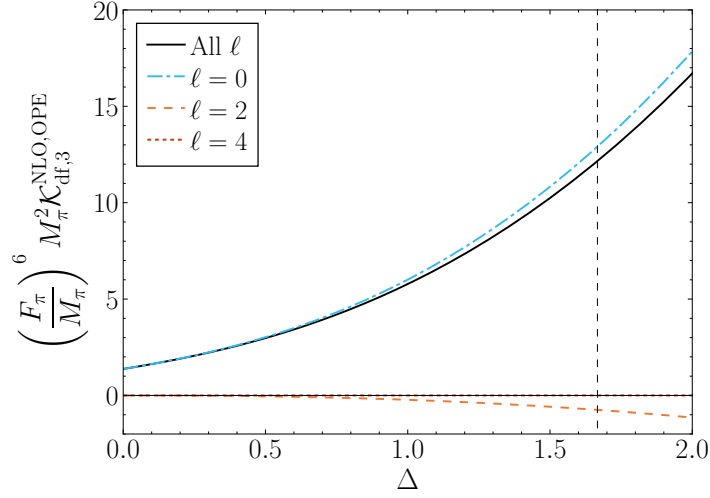


Figure 5.8. Comparison of contributions to $\mathcal{K}_{\text{df},3}^{\text{NLO,OPE}}$ from different partial waves of the NLO dimer amplitude, numerically evaluated for the first momentum family in table 5.1 with $M_\pi = 340$ MeV. The black line is the full result including all partial waves, and the vertical dashed line is the inelastic threshold. Contributions from $\ell \geq 4$ are negligible.

and d -waves, all even partial waves are present in the full result. However, as can be seen in fig. 5.8 where the contribution of the first three nonzero partial waves is shown for $M_\pi = 340$ MeV, there is rapid convergence with ℓ . For $\ell \geq 4$, the contribution turns out to be negligible in the elastic region. A similar result holds for lighter pion masses.

5.4 Conclusions

In this chapter the results from ref. [3] have been presented, in which the divergence-free K -matrix of three pions at maximal isospin was computed at NLO in ChPT, motivated by the observed discrepancies between lattice results for \mathcal{K}_0 and \mathcal{K}_1 and LO ChPT. Our main results are shown in eqs. (5.68) to (5.70). We have found that NLO corrections to these coefficients are indeed large and reduce the tension between lattice results and LO ChPT. This, however, may also be an indication that the convergence of the chiral expansion is rather poor for these quantities.

In this work we developed a series of techniques to determine $\mathcal{K}_{\text{df},3}$ at NLO in ChPT analytically, up to some cutoff-dependent corrections that need to be evaluated numerically. We found that at NLO in ChPT the integral equations relating \mathcal{M}_3 to $\mathcal{K}_{\text{df},3}$ simplify to a linear relation, $\mathcal{K}_{\text{df},3}^{\text{NLO}} = \text{Re}\mathcal{M}_3^{\text{NLO}}$, which can be separated into different non-singular contributions that we determined independently. This work opens the door to the computation

of $\mathcal{K}_{\text{df},3}$ in ChPT for more complex systems, such as that of three pions at non-maximal isospin [4], which are presented in the next chapter.

Finally, we have studied the convergence of the threshold expansion. We found good agreement between the expansion truncated at quadratic order and the full result, with corrections smaller than 20% in the elastic region, $E^* < 5M_\pi$. This gives confidence in the usage of a threshold expansion to parametrize $\mathcal{K}_{\text{df},3}$ when extracting it from numerical lattice simulations. We also analyzed the contributions from different dimer partial waves to the OPE part, concluding that partial waves with $\ell > 2$ are negligible.

6 The three-pion K -matrix at NLO in ChPT

Lattice studies of three particles have been mainly limited to pion and kaon states at maximal isospin [194, 268, 294–302]. However, it is expected that more complicated systems will be investigated in the early future. Of particular interest are systems of three pions at non-maximal isospin, in which some resonances can be found that only decay into three particles, such as the $\omega(782)$ resonance [34] in the isospin-zero channel.

In this chapter, the results from ref. [4] are presented, in which the three-pion K -matrix is determined up to NLO for all three-pion isospin channels. While the validity of ChPT at non-maximal isospin is limited by the presence of resonances,¹ these results can still prove useful to inspire parametrizations or put constraints on $\mathcal{K}_{\text{df},3}$ in the near-threshold energy region, and also contribute towards our understanding of the convergence of the chiral and threshold expansions.

The computation of $\mathcal{K}_{\text{df},3}$ for non-maximal isospin uses the same techniques developed for the isospin-three case presented in chapter 5, starting from the amplitudes in refs. [195, 196]. However, it includes some new complications. These are related to new kinematic structures in the threshold expansion of $\mathcal{K}_{\text{df},3}$ in the different isospin sectors, $3\pi \rightarrow \pi \rightarrow 3\pi$ diagrams for isospin one, and p -waves in some of the channels in both LO and NLO amplitudes.

This chapter is organized as follows. In sec. 6.1 we discuss how the integral equations relating \mathcal{M}_3 to $\mathcal{K}_{\text{df},3}$ —see sec. 2.1.2—are extended to include all isospin channels, and how they can be used to determine $\mathcal{K}_{\text{df},3}$ in

¹This is especially true for heavier-than-physical pion masses, for which resonances lie closer to the two- or three-pion threshold, since the mass of resonances has been found to depend only weakly on M_π [315].

ChPT. We also introduce in sec. 6.1.4 the threshold expansion of $\mathcal{K}_{\text{df},3}$ for the all isospin channels, which was first worked out in ref. [182]. The main steps of the computation of $\mathcal{K}_{\text{df},3}$ at LO and NLO are described in sec. 6.2. Finally, the results are presented in sec. 6.3, where we also comment on the convergence of the threshold expansion

6.1 $\mathcal{K}_{\text{df},3}$ for general isospin

6.1.1 The flavor space

Three-pion interactions classify in four different isospin channels, $I_{\pi\pi\pi} = 3, 2, 1$ and 0 —see sec. 2.2. Each of these channels has a different multiplicity, that corresponds to the different two-particle channels in which pairwise interactions can occur within the three-particle system. Both the $I_{\pi\pi\pi} = 3$ and $I_{\pi\pi\pi} = 0$ channels are one dimensional, as pairwise interactions only happen with two-particle isospin $I_{\pi\pi} = 2$ and $I_{\pi\pi} = 1$, respectively. The $I_{\pi\pi\pi} = 2$ channel is two dimensional, containing both $I_{\pi\pi} = 2$ and $I_{\pi\pi} = 1$. Finally, the $I_{\pi\pi\pi} = 1$ channel is three dimensional, and pairwise interactions occur in all three two-pion isospin channels.

The presence of different isospin channels implies that scattering quantities describing three-pion interactions are 7×7 matrices in flavor space—we neglect the third component of isospin, since interactions are diagonal in this quantum number. We indicate quantities that are matrices in flavor space using boldface font. For example, the general-isospin scattering amplitude is denoted as \mathbf{M}_3 , while $\mathbf{K}_{\text{df},3}$ is the three-pion K -matrix for all isospin.

The particular form of observables depends on the choice of basis for the flavor basis. In the case of single-pion quantities, two different basis are useful. The *charge basis*, $\{|\pi^+\rangle, |\pi^0\rangle, |\pi^-\rangle\}$, is composed of states of definite isospin, and so is suited for building multiparticle states. For the low-energy EFT computations, on the other hand, it is more common to use the *flavor basis*, $\{|i\rangle\}$, in which the pion matrix is defined as $|\phi\rangle = \sum_i \sigma_i |i\rangle$, with σ_i the Pauli matrices. These two basis are related as

$$|\pi^\pm\rangle = \mp \frac{|1\rangle \pm i|2\rangle}{\sqrt{2}}, \quad |\pi^0\rangle = |3\rangle, \quad (6.1)$$

where we use the Condon–Shortley sign convention [305].

Three-pion states are typically constructed combining single-pion states in the charge basis. Still, different basis of three-pion states can be chosen. One option is to work with states of definite three-particle isospin in which the flavor-space matrices become block-diagonal, with blocks of a size equal

to the multiplicity of each isospin channel. This choice still does not fully fix the basis, as states can be rotated within each isospin block. A typical option, related to the finite-volume quantization condition [182], is to choose three-particle states with definite two-particle isospin between the first two particles of the state. This is called the *isospin basis*,

$$|\pi\pi\pi\rangle_{\text{I}} = \begin{pmatrix} |\Pi\pi\rangle_3 \\ |\Pi\pi\rangle_2 \\ |\rho\pi\rangle_2 \\ |\Pi\pi\rangle_1 \\ |\rho\pi\rangle_1 \\ |\sigma\pi\rangle_1 \\ |\rho\pi\rangle_0 \end{pmatrix} = \begin{pmatrix} \frac{1}{\sqrt{5}} \left(|\Pi^+\pi^-\rangle + \sqrt{3}|\Pi^0\pi^0\rangle + |\Pi^-\pi^+\rangle \right) \\ \frac{1}{\sqrt{2}} \left(|\Pi^+\pi^-\rangle - |\Pi^-\pi^+\rangle \right) \\ \frac{1}{\sqrt{6}} \left(|\rho^+\pi^-\rangle + 2|\rho^0\pi^0\rangle + |\rho^-\pi^+\rangle \right) \\ \frac{1}{\sqrt{10}} \left(\sqrt{3}|\Pi^+\pi^-\rangle - 2|\Pi^0\pi^0\rangle + \sqrt{3}|\Pi^-\pi^+\rangle \right) \\ \frac{1}{\sqrt{2}} \left(|\rho^+\pi^-\rangle - |\rho^-\pi^+\rangle \right) \\ |\sigma\pi^0\rangle \\ \frac{1}{\sqrt{3}} \left(|\rho^+\pi^-\rangle - |\rho^0\pi^0\rangle + |\rho^-\pi^+\rangle \right) \end{pmatrix}, \quad (6.2)$$

where the subscript of the states on the left-hand side indicates their three-particle isospin. On the right-hand side we have defined the two-particle states with definite isospin,

$$\begin{aligned} |\Pi^0\rangle &= \frac{|\pi^+\pi^-\rangle + |\pi^-\pi^+\rangle + 2|\pi^0\pi^0\rangle}{\sqrt{6}}, & |\Pi^\pm\rangle &= \frac{|\pi^\pm\pi^0\rangle + |\pi^0\pi^\pm\rangle}{\sqrt{2}}, \\ |\rho^0\rangle &= \frac{|\pi^+\pi^-\rangle - |\pi^-\pi^+\rangle}{\sqrt{2}}, & |\rho^\pm\rangle &= \pm \frac{|\pi^\pm\pi^0\rangle - |\pi^0\pi^\pm\rangle}{\sqrt{2}}, \\ |\sigma\rangle &= \frac{|\pi^+\pi^-\rangle + |\pi^-\pi^+\rangle - |\pi^0\pi^0\rangle}{\sqrt{3}}, \end{aligned} \quad (6.3)$$

where the states in the top, central and bottom line have $I_{\pi\pi} = 2, 1$ and 0 , in this same order. Note that the name given to each state is reminiscent of the resonances present in each isospin channel. The $\rho(770)$ resonance appears in isospin-one pion-pion scattering, while the $\sigma(550)$ resonance is present in the isospin-zero channel.

An alternative basis that keeps the block structure is the *symmetric basis*. In this, the states within each isospin block are chosen to have definite transformation properties under the S_3 group, that describes permutations between the three pions. It is related to the isospin basis by a rotation of the $I_{\pi\pi\pi} = 1$ block,

$$|\pi\pi\pi\rangle_S = \begin{pmatrix} |\chi_s\rangle_3 \\ |\chi_1\rangle_2 \\ |\chi_2\rangle_2 \\ |\chi_s\rangle_1 \\ |\chi_1\rangle_1 \\ |\chi_2\rangle_1 \\ |\chi_a\rangle_0 \end{pmatrix} = \begin{pmatrix} |\Pi\pi\rangle_3 \\ |\Pi\pi\rangle_2 \\ |\rho\pi\rangle_2 \\ \frac{2}{3}|\Pi\pi\rangle_1 + \frac{\sqrt{5}}{3}|\sigma\pi\rangle_1 \\ -\frac{\sqrt{5}}{3}|\Pi\pi\rangle_1 + \frac{2}{3}|\sigma\pi\rangle_1 \\ |\rho\pi\rangle_1 \\ |\rho\pi\rangle_0 \end{pmatrix}. \quad (6.4)$$

Here $|\chi_s\rangle$ denotes a state that transforms under the one-dimensional trivial (symmetric) irrep of S_3 , $|\chi_a\rangle$ refers to a state transforming under the alternating (antisymmetric) irrep, and $\{|\chi_1\rangle, |\chi_2\rangle\}$ is a pair of states transforming under the two-dimensional standard irrep. Thus, states with $I_{\pi\pi\pi} = 3$ transform under the trivial irrep, those with $I_{\pi\pi\pi} = 2$ under the standard irrep, states with $I_{\pi\pi\pi} = 1$ under a direct sum of the trivial and the standard irreps, and $I_{\pi\pi\pi} = 0$ states under the alternating irrep.

To construct the elements of the quantization condition, ref. [182] makes use of a different basis composed of states with zero electric charge. This is known as the *charge basis*,

$$|\pi\pi\pi\rangle_C = \begin{pmatrix} |\pi^-\pi^0\pi^+\rangle \\ |\pi^0\pi^-\pi^+\rangle \\ |\pi^-\pi^+\pi^0\rangle \\ |\pi^0\pi^0\pi^0\rangle \\ |\pi^+\pi^-\pi^0\rangle \\ |\pi^0\pi^+\pi^-\rangle \\ |\pi^+\pi^0\pi^-\rangle \end{pmatrix}. \quad (6.5)$$

It is related to the isospin and symmetric basis by rotation—see ref. [4].

6.1.2 Building blocks of the integral equations

When extended to general isospin, the building blocks of the integral equations that relate the scattering amplitude to the divergence-free K -matrix—see sec. 2.1.2—become 7×7 matrices in flavor space. This is

the case of the two-particle amplitude that describes pairwise interactions between the first two particles of each state. In the charge basis, it is block diagonal,

$$\mathbf{M}_2 = \text{diag} \left(\mathbf{M}_2^+, \mathbf{M}_2^0, \mathbf{M}_2^- \right), \quad (6.6)$$

with blocks

$$\mathbf{M}_2^0 = \begin{pmatrix} A_{4\pi}(s) + A_{4\pi}(t) & -A_{4\pi}(s) & A_{4\pi}(s) + A_{4\pi}(u) \\ -A_{4\pi}(s) & A_{4\pi}(s) + A_{4\pi}(t) + A_{4\pi}(u) & -A_{4\pi}(s) \\ A_{4\pi}(s) + A_{4\pi}(u) & -A_{4\pi}(s) & A_{4\pi}(s) + A_{4\pi}(t) \end{pmatrix},$$

$$\mathbf{M}_2^+ = \mathbf{M}_2^- = \begin{pmatrix} A_{4\pi}(t) & A_{4\pi}(u) \\ A_{4\pi}(u) & A_{4\pi}(t) \end{pmatrix}, \quad (6.7)$$

where $A_{4\pi}$ is the four-pion amplitude in ChPT, given in eqs. (5.25) and (5.26) at LO and NLO, respectively. Here, we use $A_{4\pi}(s) = A_{4\pi}(s, t, u)$ as a shorthand notation, and similarly for $A_{4\pi}(t)$ and $A_{4\pi}(u)$, since $A_{4\pi}$ is symmetric in its last two arguments.

Similarly, the G^∞ factor becomes a 7×7 matrix,

$$\mathbf{G}_{\ell'\ell}^\infty = G_{\ell'\ell}^\infty \mathbf{T}_G, \quad (6.8)$$

where \mathbf{T}_G encodes the valid exchanges between the three-particle states, where the exchanged particle is the second one in the naming of the states. In the charge basis,

$$\mathbf{T}_G = \begin{pmatrix} \square & \square & \square & \square & \square & \square & \blacksquare \\ \square & \square & \square & \square & \blacksquare & \square & \square \\ \square & \square & \square & \square & \square & \blacksquare & \square \\ \square & \square & \square & \blacksquare & \square & \square & \square \\ \square & \blacksquare & \square & \square & \square & \square & \square \\ \square & \square & \blacksquare & \square & \square & \square & \square \\ \blacksquare & \square & \square & \square & \square & \square & \square \end{pmatrix}, \quad \square = 0, \quad \blacksquare = 1, \quad (6.9)$$

where we use squares rather than numbers for legibility. This same flavor structure can be used, in combination with eq. (6.6), to build the OPE part of the three-pion scattering amplitude—see eq. (6.32).

In addition to working with matrices in flavor space, the symmetrization appearing in eqs. (2.14) and (2.18) is modified to ensure the correct transformation properties under particle exchange, affecting momenta and flavor simultaneously. For example, the symmetrized divergence-free amplitude is defined from the unsymmetrized one as

$$\mathbf{M}_{\text{df},3} = \sum_{m=0}^2 \sum_{n=0}^2 \left(\mathbf{R}^m \right)^\top \mathbf{M}_{\text{df},3}^{(\text{u,u})} \left(R^m \{p_i\}, R^n \{k_i\} \right) \mathbf{R}^n, \quad (6.10)$$

where $R\{p_1, p_2, p_3\} = \{p_2, p_3, p_1\}$ is a cyclic permutation of the three momenta and \mathbf{R} is the representation of the permutation in the space of three pions. In the charge basis it reads,

$$\mathbf{R} = \begin{pmatrix} \square & \square & \square & \square & \blacksquare & \square & \square \\ \square & \square & \square & \square & \square & \square & \blacksquare \\ \square & \blacksquare & \square & \square & \square & \square & \square \\ \square & \square & \square & \blacksquare & \square & \square & \square \\ \square & \square & \square & \square & \square & \blacksquare & \square \\ \blacksquare & \square & \square & \square & \square & \square & \square \\ \square & \square & \blacksquare & \square & \square & \square & \square \end{pmatrix}, \quad \square = 0, \quad \blacksquare = 1. \quad (6.11)$$

This same symmetrization procedure applies to any other unsymmetrized quantity as well.

6.1.3 Relating \mathbf{M}_3 to $\mathbf{K}_{\text{df},3}$

As shown in secs. 2.2.2 and 5.1 for the isospin-three channel, the relation between \mathbf{M}_3 and $\mathbf{K}_{\text{df},3}$ becomes algebraic when working at LO and NLO in ChPT. At LO, the three-pion K -matrix is just the divergence-free amplitude,

$$\mathbf{K}_{\text{df},3}^{\text{LO}} = \mathbf{M}_{\text{df},3}^{\text{LO}}, \quad (6.12)$$

while at NLO,

$$\mathbf{K}_{\text{df},3}^{\text{NLO}} = \text{Re}\mathbf{M}_{\text{df},3}^{\text{NLO}}. \quad (6.13)$$

As done for the $I_{\pi\pi\pi} = 3$ case, it is convenient to subdivide the computation of the divergence-free amplitude in several parts. For the LO and NLO quantity, we write, respectively,

$$\mathbf{M}_{\text{df},3}^{\text{LO}} = \left(\mathbf{M}_{\text{df},3}^{\text{LO,OPE}} - \mathbf{D}^{\text{LO,OPE}} \right) + \mathbf{M}_{\text{df},3}^{\text{LO,s-OPE}} + \mathbf{M}_{\text{df},3}^{\text{LO,non-OPE}}, \quad (6.14)$$

$$\begin{aligned} \text{Re}\mathbf{M}_{\text{df},3}^{\text{NLO}} = & \left(\text{Re}\mathbf{M}_{\text{df},3}^{\text{NLO,OPE}} - \text{Re}\mathbf{D}^{\text{NLO,OPE}} \right) \\ & + \text{Re}\mathbf{M}_{\text{df},3}^{\text{NLO,s-OPE}} + \text{Re}\mathbf{M}_{\text{df},3}^{\text{NLO,non-OPE}} - \text{Re}\mathbf{D}^{\text{NLO,BH}}. \end{aligned} \quad (6.15)$$

Note this decomposition is very similar to that used for the $I_{\pi\pi\pi} = 3$ channels, diagrammatically represented in fig. 5.1 at NLO. The main novelty is the so-called *s-channel OPE* (*s-OPE*) contribution, $\mathbf{M}_{\text{df},3}^{\text{s-OPE}}$, diagrammatically represented in fig. 6.1. This is only present in the $I_{\pi\pi\pi} = 1$ channel, and is characterized by a single exchanged particle which carries all the momenta and isospin. The remaining terms in eq. (6.14) are the subtracted OPE, the non-OPE and the BH subtraction, in this same order, where the last one only appears at NLO. Each of the four contributions can be evaluated independently, as will be shown in sec. 6.2.

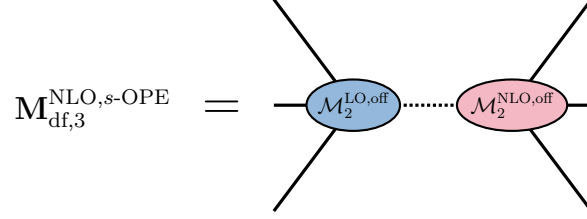


Figure 6.1. Schematic representation of the s -channel OPE diagram, which needs to be added to fig. 5.1 to compute $\mathbf{K}_{\text{df},3}$. It only contributes to the $I_{\pi\pi\pi} = 1$ channel. External pions are on-shell, while the intermediate one is always off-shell, represented with a dotted line. Also, the amplitudes, both the LO and the NLO ones, have one leg off-shell. One also needs to consider an additional diagram with the LO and NLO amplitudes exchanged.

6.1.4 Threshold expansion of $\mathbf{K}_{\text{df},3}$

Before moving to the computation of $\mathbf{K}_{\text{df},3}$, we discuss how it is expanded around threshold for the different isospin channels. These expansions were partially presented in ref. [182] for the first time. The result for three identical particles was presented in eq. (2.22). This applies to the $I_{\pi\pi\pi} = 3$ channel, since the corresponding pion states are symmetric under particle exchange. We reproduce it here for completion,

$$M_\pi^2 \mathbf{K}_{\text{df},3}^{I_{\pi\pi\pi}=3} = \mathcal{K}_0 + \mathcal{K}_1 \Delta + \mathcal{K}_2 \Delta^2 + \mathcal{K}_A \Delta_A + \mathcal{K}_B \Delta_B + \mathcal{O}(\Delta^3), \quad (6.16)$$

where Δ , Δ_A and Δ_B are defined in eq. (2.23). Note that, even if the $I_{\pi\pi\pi} = 3$ flavor space is one-dimensional, we keep the boldface notation.

States with non-maximal isospin, on the other hand, present different transformation properties under particle exchange, which characterize the possible kinematic operators that can appear in the expansion. In app. B of ref. [4], we computed the number of independent operators appearing up to cubic order in the expansion using group theoretical arguments. In this section, we summarize the form of said operators up to quadratic order in the $I_{\pi\pi\pi} = 2$ and 1 channels, and up to cubic order for $I_{\pi\pi\pi} = 0$.

The $I_{\pi\pi\pi} = 2$ channel involves a two-dimensional flavor space, with states transforming under the standard irrep of S_3 . Kinematic operators appearing in the threshold expansion are thus doublets transforming in this same irrep under particle exchange of either the initial or the final state.

Following ref. [182], we first introduce single-state doublets. At linear order in Δ we have, for the initial state,

$$\boldsymbol{\xi}^\mu = (\xi_1^\mu, \xi_2^\mu), \quad (6.17)$$

where

$$\xi_1 = \frac{2k_3 - k_1 - k_2}{\sqrt{6}M_\pi}, \quad \xi_2 = \frac{k_2 - k_1}{\sqrt{2}M_\pi}. \quad (6.18)$$

At quadratic order, one can construct two independent tensor doublets,

$$\xi(S)^{\mu\nu} = \frac{\xi^\mu P^\nu + \xi^\nu P^\mu}{M_\pi}, \quad (6.19)$$

$$\xi(\bar{S})^{\mu\nu} = (\xi_2^\mu \xi_2^\nu - \xi_1^\nu \xi_1^\mu, \xi_1^\mu \xi_2^\nu - \xi_2^\nu \xi_1^\mu), \quad (6.20)$$

and one scalar doublet,

$$\xi^{(2)} = (\xi_1^{(2)}, \xi_2^{(2)}) = -\frac{2}{9M_\pi} \xi^\mu P_\mu, \quad (6.21)$$

with

$$\xi_1^{(2)} = \frac{2\Delta_3 - \Delta_1 - \Delta_2}{\sqrt{6}}, \quad \xi_2^{(2)} = \frac{\Delta_2 - \Delta_1}{\sqrt{2}}. \quad (6.22)$$

Using these quantities and their final-state counterparts, one can write down four operators with the correct transformation properties,

$$\begin{aligned} \Xi_1 &\equiv \xi'^{\mu} \otimes \xi_{\mu}, \\ \Xi_2 &\equiv \xi'^{(2)} \otimes \xi^{(2)}, \\ \Xi_3 &\equiv \frac{1}{\sqrt{6}} [\xi'(\bar{S})^{\mu\nu} \otimes \xi(S)_{\mu\nu} + \xi'(S)^{\mu\nu} \otimes \xi(\bar{S})_{\mu\nu}], \\ \Xi_4 &\equiv \xi'(\bar{S})^{\mu\nu} \otimes \xi(\bar{S})_{\mu\nu}, \end{aligned} \quad (6.23)$$

where \otimes indicates tensor product. Combining them with Δ , we find that the threshold expansion of $\mathbf{K}_{\text{df},3}$ in the isospin-two channel is,

$$M_\pi^2 \mathbf{K}_{\text{df},3}^{I_{\pi\pi\pi}=2} = \left(\mathcal{K}_0^T + \mathcal{K}_1^T \Delta \right) \Xi_1 + \sum_{n=2,3,4} \mathcal{K}_n^T \Xi_n + \mathcal{O}(\Delta^3). \quad (6.24)$$

In the $I_{\pi\pi\pi} = 1$ channel, states transform under a direct sum of the standard and the trivial irrep of S_3 . It is convenient to work in the symmetric basis, given in eq. (6.4), putting the singlet as the first component.

$$\mathbf{K}_{\text{df},3}^{I_{\pi\pi\pi}=1} = \begin{pmatrix} \mathbf{K}_{\text{df},3}^{I_{\pi\pi\pi}=1,\text{SS}} & \mathbf{K}_{\text{df},3}^{I_{\pi\pi\pi}=1,\text{SD}} \\ \mathbf{K}_{\text{df},3}^{I_{\pi\pi\pi}=1,\text{DS}} & \mathbf{K}_{\text{df},3}^{I_{\pi\pi\pi}=1,\text{DD}} \end{pmatrix}. \quad (6.25)$$

The singlet-singlet (SS) term is equivalent to the $I_{\pi\pi\pi} = 3$ case, eq. (2.22),

$$M_\pi^2 \mathbf{K}_{\text{df},3}^{I_{\pi\pi\pi}=1,\text{SS}} = \mathcal{K}_0^{\text{SS}} + \mathcal{K}_1^{\text{SS}} \Delta + \mathcal{K}_2^{\text{SS}} \Delta^2 + \mathcal{K}_A^{\text{SS}} \Delta_A + \mathcal{K}_B^{\text{SS}} \Delta_B + \mathcal{O}(\Delta^3), \quad (6.26)$$

while the doublet-doublet (DD) is analogous to the $I_{\pi\pi\pi} = 2$, eq. (6.24),

$$M_\pi^2 \mathbf{K}_{\text{df},3}^{I_{\pi\pi\pi}=1,\text{DD}} = \left(\mathcal{K}_0^{\text{DD}} + \mathcal{K}_1^{\text{DD}} \Delta \right) \Xi_1 + \sum_{n=2,3,4} \mathcal{K}_n^{\text{DD}} \Xi_n + \mathcal{O}(\Delta^3). \quad (6.27)$$

The novelty are the operators entering the singlet-doublet (SD)—final-state singlet and an initial-state doublet—and doublet-singlet (DS) sectors. We consider the SD case, with analogous results holding for the DS. At linear order in Δ , only one kinematic operator exists, $\boldsymbol{\xi}^{(2)}$, defined in eq. (6.21). At quadratic order, we can construct four operators: $\Delta \boldsymbol{\xi}^{(2)}$ and $\boldsymbol{\xi}^{(4,n)} = (\xi_1^{(4,n)}, \xi_2^{(4,n)})$ for $n = 2, 3, 4$, where

$$\begin{aligned} \xi_1^{(4,2)} &= \frac{2\Delta_3^2 - \Delta_1^2 - \Delta_2^2}{\sqrt{6}}, & \xi_2^{(4,2)} &= \frac{\Delta_2^2 - \Delta_1^2}{\sqrt{2}}, \\ \xi_1^{(4,3)} &= \sum_i \frac{(\tilde{t}_{i1} + \tilde{t}_{i2})\tilde{t}_{i3} - 2\tilde{t}_{i1}\tilde{t}_{i2}}{\sqrt{6}}, & \xi_2^{(4,3)} &= \sum_i \frac{(\tilde{t}_{i2} - \tilde{t}_{i1})\tilde{t}_{i3}}{\sqrt{2}}, \\ \xi_1^{(4,4)} &= \sum_i \frac{2\tilde{t}_{i3}^2 - \tilde{t}_{i1}^2 - \tilde{t}_{i2}^2}{\sqrt{6}}, & \xi_2^{(4,4)} &= \sum_i \frac{\tilde{t}_{i2}^2 - \tilde{t}_{i1}^2}{\sqrt{2}}, \end{aligned} \quad (6.28)$$

where Δ_i and \tilde{t}_{ij} are defined in eq. (2.24). The threshold expansion of $\mathbf{K}_{\text{df},3}^{I_{\pi\pi\pi}=1,\text{SD}}$ is then

$$\frac{M_\pi^2}{\sqrt{30}} \mathbf{K}_{\text{df},3}^{I_{\pi\pi\pi}=1,\text{SD}} = \left(\mathcal{K}_0^{\text{SD}} + \mathcal{K}_1^{\text{SD}} \Delta \right) \boldsymbol{\xi}^{(2)} + \sum_{n=2,3,4} \mathcal{K}_n^{\text{SD}} \boldsymbol{\xi}^{(4,n)} + \mathcal{O}(\Delta^3), \quad (6.29)$$

where we have pulled out a factor of $\sqrt{30}$ for convenience. $\mathbf{K}_{\text{df},3}^{I_{\pi\pi\pi}=1,\text{DS}}$ is obtained by changing $k_i \leftrightarrow p_i$ and taking the transpose. Note, however, that due to time-reversal invariance of the K -matrix, the coefficients are equal in both SD and DS sectors, i.e., $\mathcal{K}_i^{\text{SD}} = \mathcal{K}_i^{\text{DS}}$.

Finally, the $I_{\pi\pi\pi} = 0$ channel is one dimensional in flavor space. States in this channel are totally antisymmetric under particle exchange, and so the operators entering the threshold expansion must also be antisymmetric under permutation of initial- and final-state particles. There is no such operator at constant or linear order in Δ , while we have a single operator at quadratic order and three independent ones at cubic order,

$$M_\pi^2 \mathbf{K}_{\text{df},3}^{I_{\pi\pi\pi}=0} = \left(\mathcal{K}_0^{\text{AS}} + \mathcal{K}_1^{\text{AS}} \Delta \right) \Delta_{\text{AS}}^{(2)} + \mathcal{K}_3^{\text{AS}} \Delta_{\text{AS}}^{(3)} + \mathcal{K}_4^{\text{AS}} \Delta_{\text{AS}}^{(4)} + \mathcal{O}(\Delta^4), \quad (6.30)$$

where the explicit form of the operators is

$$\begin{aligned} \Delta_{\text{AS}}^{(2)} &\equiv \sum_{\substack{i,j,k \\ m,n,r}} \epsilon_{ijk} \epsilon_{mnr} \tilde{t}_{im} \tilde{t}_{jn}, \\ \Delta_{\text{AS}}^{(3)} &\equiv \sum_{\substack{i,j,k \\ m,n,r}} \epsilon_{ijk} \epsilon_{mnr} \tilde{t}_{im} \tilde{t}_{jn} \tilde{t}_{kr}, \\ \Delta_{\text{AS}}^{(4)} &\equiv \sum_{\substack{i,j,k \\ m,n,r}} \epsilon_{ijk} \epsilon_{mnr} \tilde{t}_{im} \tilde{t}_{jn} (\tilde{t}_{im} + \tilde{t}_{jn}). \end{aligned} \quad (6.31)$$

6.2 Computation of $\mathbf{K}_{\text{df},3}$

The threshold-expansion coefficients of $\mathbf{K}_{\text{df},3}$ can be determined almost analytically, as was the case of the isospin-three channel presented in chapter 5. In this section, we explain the details of this computation at both LO and NLO in ChPT. We treat separately each of the terms in eqs. (6.14) and (6.15). The calculation is very similar to that of the $I_{\pi\pi\pi} = 3$ channel detailed in sec. 5.2, with a few changes and additional complications. The complete results at LO are presented in table 6.1 including the separate contribution of each term in eq. (6.14). The results at NLO are summarized in table 6.2 complemented by table 6.3, while the separate contribution from each term in eq. (6.15) can be found in ref. [4].

The computation of all the different contributions share some common lines, which in some cases differ from the methodology used in sec. 5.2. In all cases, all contributions are expanded about threshold and symmetrized when required in the charge basis. Moreover, the coefficients of the threshold expansion are only identified after symmetrization. This identification involves converting all products of momenta to \tilde{t}_{ij} variables, and then identifying the coefficients of the threshold expansion. At LO this can be done by inspection, but requires to solve a system of linear equations at higher order. Note this differs from the approach taken, for example, for the $I_{\pi\pi\pi} = 3$ OPE part in sec. 5.2.2, where the coefficients were worked out for the unsymmetrized K -matrix and then related to the symmetric result. However, the form of the expansion for the unsymmetrized K -matrix is not known at non-maximal isospin.

6.2.1 The subtracted-OPE contribution

The subtracted-OPE contribution can be computed in a similar fashion to the $I_{\pi\pi\pi} = 3$ channel, working first with unsymmetrized quantities. The unsymmetrized divergence-free OPE amplitude is,

$$\mathbf{M}_{\text{df},3}^{(\text{u,u}),\text{OPE}} = -\mathbf{M}_{2,\text{off}} \frac{\mathbf{T}_G}{b^2 + i\epsilon} \mathbf{M}_{2,\text{off}} + \sum_{\ell'\ell} \mathbf{M}_{2,\ell'} \mathbf{G}_{\ell'\ell}^\infty \mathbf{M}_{2,\ell}, \quad (6.32)$$

where \mathbf{M}_2 is given in eq. (6.6) and $\mathbf{G}_{\ell'\ell}^\infty$ in eq. (6.8). Here recall $\bar{b}^2 = b^2 - M_\pi^2$, where b is the momentum of the exchanged pion. Also $\mathbf{M}_{2,\text{off}}$ is the off-shell amplitude, with the external leg corresponding to the exchanged particle off-shell—see sec. 2.2.2. The on-shell amplitude is recovered by setting $\bar{b}^2 = 0$.

At LO, $\mathbf{M}_{\text{df},3}^{(\text{u,u}),\text{OPE}}$ is computed by substituting both \mathbf{M}_2 factors by the LO ChPT prediction. This takes the general form

$$\mathbf{M}_2^{\text{LO}} = \mathbf{k}_0 + \mathbf{k}_1 \bar{s} + \mathbf{k}_2(t+u) + \mathbf{k}_3(t-u), \quad (6.33)$$

where \mathbf{k}_i are 7×7 matrices of coefficients. The key difference to the $I_{\pi\pi\pi} = 3$ computation is that p -wave is present in this case. Thus, s - and p -waves need to be separated before performing the subtraction. At LO, this can be easily done taking the symmetric and antisymmetric parts, respectively,

$$\begin{aligned} \mathbf{M}_{2,s}(s,t,u) &= \mathbf{k}_0 + \mathbf{k}_2 \bar{s} + \mathbf{k}_2(t+u), \\ \mathbf{M}_{2,p}(s,t,u) &= \mathbf{k}_3(t-u). \end{aligned} \quad (6.34)$$

The subtraction for the s -wave part is straightforward to compute. For the p -wave, the addition theorem of spherical harmonics allows us to write

$$t-u = 4\mathbf{p}_k^* \cdot \mathbf{a}_k^* = 4p_k^* q_{2k}^* \left[\frac{4\pi}{3} \sum_m Y_{1m}^*(\hat{\mathbf{a}}_k^*) Y_{1m}(\hat{\mathbf{p}}_k^*) \right], \quad (6.35)$$

where recall p_k^* is the magnitude of the momentum of the final spectator in the CMF of the initial dimer, a_k^* is the relative CMF momentum of the particles in the dimer and $q_{2k}^* = |\mathbf{a}_k^*|$. An analogous relation also holds for the final state. As was the case of d -waves in eq. (5.37), the on- and off-shell $t-u$ terms are related by the barrier factors within \mathbf{G}^∞ ,

$$[t-u]_{\text{off}} = [t-u]_{\text{on}} \left(\frac{p_k^*}{q_{2k}^*} \right), \quad (6.36)$$

and similarly for the final state. At LO, this implies the full on-shell p -wave amplitude is set off shell by the barrier factor. This is not the case for the NLO case, which we consider below, where $t-u$ appears multiplied by other factors which may vanish on shell, such as \bar{b}^2 .

Taking eq. (6.36) into account, it is convenient to rewrite the off-shell amplitude,

$$\mathbf{M}_{2,\text{off}}^{\text{LO}} = \mathbf{M}_{2,s}^{\text{LO}} + \bar{b}^2 \delta\mathbf{M}_{2,s}^{\text{LO}} + \mathbf{M}_{2,p,\text{off}}^{\text{LO}}, \quad (6.37)$$

where s -wave contributions are separated into an on-shell and an off-shell part, given by the first and second term, respectively, while the last term is purely p -wave. Multiplying the last term by the barrier factor within \mathbf{G}^∞ , puts it on shell, and so eq. (6.32) becomes

$$\mathbf{M}_{\text{df},3}^{(\text{u,u}),\text{OPE,LO}} = -\delta\mathbf{M}_{2,s}^{\text{LO}} \mathbf{T}_G \mathbf{M}_{2,\text{off}}^{\text{LO}} - \mathbf{M}_{2,\text{off}}^{\text{LO}} \mathbf{T}_G \delta\mathbf{M}_{2,s}^{\text{LO}} + \bar{b}^2 \delta\mathbf{M}_{2,s}^{\text{LO}} \mathbf{T}_G \delta\mathbf{M}_{2,s}^{\text{LO}}. \quad (6.38)$$

The LO OPE contribution to the coefficients in the threshold expansion can be identified after substitution and symmetrization. The results are shown in table 6.1 in sec. 6.3.

We now turn to the NLO computation. The two-particle amplitude at NLO is obtained plugging eq. (5.26) into eq. (6.6). To compute the threshold expansion up to quadratic order, we need to expand this amplitude up to cubic order,

$$\begin{aligned}
\mathbf{M}_2^{\text{NLO}} = & \mathbf{a}_1 + \mathbf{b}_1 \bar{s} + \mathbf{b}_2(t+u) + \mathbf{b}_3(t-u) \\
& + \mathbf{c}_1 \bar{s}^2 + \mathbf{c}_2 \bar{s}(t+u) + \mathbf{c}_3 \bar{s}(t-u) + \mathbf{c}_4(t+u)^2 + \mathbf{c}_5(t+u)(t-u) + \mathbf{c}_6 tu \\
& + \mathbf{d}_1 \bar{s}^3 + \mathbf{d}_2 \bar{s}^2(t+u) + \mathbf{d}_3 \bar{s}^2(t-u) + \mathbf{d}_4 \bar{s}(t+u)^2 + \mathbf{d}_5 \bar{s}(t+u)(t-u) \\
& + \mathbf{d}_6 \bar{s} tu + \mathbf{d}_7(t+u)^3 + \mathbf{d}_8(t+u)^2(t-u) + \mathbf{d}_9(t+u)tu + \mathbf{d}_{10}(t-u)tu \\
& + \mathcal{O}(\bar{s}^4, t^4, u^4),
\end{aligned} \tag{6.39}$$

where \mathbf{a}_i , \mathbf{b}_i , \mathbf{c}_i and \mathbf{d}_i are 7×7 matrices of constant coefficients that depend on M_π , F_π and the LECs, ℓ_i . Note this requires expanding some \bar{J} functions—see eq. (5.28).

The NLO contribution to $\mathbf{K}_{\text{df},3}$ is obtained using eq. (6.32) considering the initial vertex at LO and the final one at NLO, and vice versa. The computation requires to separate the amplitude in different partial waves and to perform the subtraction, using eq. (6.36) and eq. (5.37) to absorb the barrier factors in p - and d -wave on-shell amplitudes, respectively. This computation can be divided in multiple parts, grouped according to their peculiarities. In most cases, the computation is straightforward, but in other cases some subtleties arise.

For instance, the terms with \mathbf{c}_5 , \mathbf{d}_5 and \mathbf{d}_8 are pure p -wave, and even after accounting for barrier factors some off-shell parts remain. More interesting is the term with \mathbf{d}_{10} coefficient. As it is of cubic order, it only contributes in combination to the LO \mathbf{k}_0 term, meaning only the off-shell part of the \mathbf{d}_{10} term survives the subtraction. This, however, contributes to both p and f waves ($\ell = 3$). Combining eqs. (5.31) and (6.35), and using the identity

$$(\hat{\mathbf{a}}_p^* \cdot \hat{\mathbf{k}}_p^*)^3 = q_{2,p}^* k^{*3} \left[\frac{3}{5} \frac{4\pi}{3} Y_{1m}^*(\hat{\mathbf{a}}_p^*) Y_{1m}(\hat{\mathbf{k}}_p^*) + \frac{2}{5} \frac{4\pi}{7} Y_{3m}^*(\hat{\mathbf{a}}_p^*) Y_{3m}(\hat{\mathbf{k}}_p^*) \right], \tag{6.40}$$

we can decompose $(t-u)tu$ into an p -wave and an f -wave part. The latter cancels completely, while the p -wave part looks as

$$[(t-u)tu]_p = \frac{1}{4} \left[(\bar{s} - \bar{b}^2)^2 - \frac{48}{5} q_{2,p}^{*2} k^{*2} \right] q_{2,p}^* k^* \frac{16\pi}{3} Y_{1m}^*(\hat{\mathbf{a}}_p^*) Y_{1m}(\hat{\mathbf{k}}_p^*). \tag{6.41}$$

The total contribution is finally obtained taking into account the p -wave barrier factor and subtracting.

Lastly, we can comment on the computation of the cubic order of $\mathbf{K}_{\text{df},3}^{I_{\pi\pi\pi}=0}$, as one may think that an expansion of $\mathbf{M}_2^{\text{NLO}}$ up to quartic order is required. However, the only two-particle isospin present in the $I_{\pi\pi\pi} = 0$ channel is $I_{\pi\pi} = 1$. At LO only the \mathbf{k}_3 term in eq. (6.34) contributes, while the only relevant terms at NLO are those with \mathbf{d}_3 , \mathbf{d}_5 , \mathbf{d}_8 and \mathbf{d}_{10} coefficients in eq. (6.39).

6.2.2 The s -channel OPE contribution

The second term in eqs. (6.14) and (6.15) is the s -channel OPE. This only occurs in the $I_{\pi\pi\pi} = 1$ channel and needs no subtraction since the exchanged particle is always off-shell for $E^* > 3M_\pi$, with momentum $b = P$. In the charge basis, the exchanged particle is a neutral pion, π^0 .

The s -channel OPE part of the amplitude can be always factorized as

$$\mathbf{M}_{\text{df},3}^{\text{s-OPE}} = -\mathbf{v}(p_1, p_2, p_3) \frac{1}{P^2 - M_\pi^2} \mathbf{v}^\dagger(k_1, k_2, k_3). \quad (6.42)$$

Here \mathbf{v} is a column vector containing the $\pi\pi\pi \rightarrow \pi^0$ amplitudes. In the charge basis, they can be computed from

$$\begin{aligned} F_\pi^2 \mathcal{M}_2[\pi^0(k_1)\pi^0(k_2)\pi^0(k_3) \rightarrow \pi^0(P)] &= A_{4\pi}(s) + A_{4\pi}(t) + A_{4\pi}(u), \\ F_\pi^2 \mathcal{M}_2[\pi^+(k_1)\pi^0(k_2)\pi^-(k_3) \rightarrow \pi^0(P)] &= -A_{4\pi}(t), \end{aligned} \quad (6.43)$$

plus permutations of the three-particle state. As for the OPE, LO contribution to $\mathbf{K}_{\text{df},3}^{I_{\pi\pi\pi}=1}$ are obtained when both vertices are LO, while the NLO contribution is obtained in the case one vertex is LO and the other is NLO, and vice versa.

In addition to the vertices, the computation of the coefficients of the threshold expansion requires expanding the propagator,

$$\frac{1}{P^2 - M_\pi^2} = \frac{1}{M_\pi^2(8 - 9\Delta)} = \frac{1}{8M_\pi^2} \left[1 - \frac{9}{8}\Delta + \frac{81}{64}\Delta^2 + \mathcal{O}(\Delta^3) \right]. \quad (6.44)$$

Note that this formally sets the radius of convergence of the threshold expansion to $|\Delta| < 9/8$. We analyze the implications of this limited convergence radius in sec. 6.3, where we compare exact numerical to threshold-expanded results of $\mathbf{K}_{\text{df},3}$. Also notice that the s -channel OPE is the only part of the amplitude which, at LO, contributes to terms of the threshold expansion beyond linear order. The separate results at LO are presented in table 6.1 in sec. 6.3.

6.2.3 The non-OPE contribution

The non-OPE amplitude is the remainder of the total three-particle amplitude after subtracting the OPE and s -OPE parts. As its real part is finite, its contribution to $\mathbf{K}_{\text{df},3}$ can be computed independently of the associated subtraction. At LO, this contribution can be evaluated in the charge basis using,

$$\begin{aligned}\mathcal{M}_3^{\text{LO,non-OPE}}[\pi^0\pi^0\pi^0 \rightarrow \pi^0\pi^0\pi^0] &= 27M_\pi^2, \\ \mathcal{M}_3^{\text{LO,non-OPE}}[\pi^0\pi^0\pi^0 \rightarrow \pi^+\pi^0\pi^-] &= 5M_\pi^2 - 3s'_{13} - t_{12} - t_{22} - t_{32}, \\ \mathcal{M}_3^{\text{LO,non-OPE}}[\pi^+\pi^0\pi^- \rightarrow \pi^+\pi^0\pi^-] &= -6M_\pi^2 + s_{13} + s'_{13} + t_{11} + 2t_{22} + t_{33},\end{aligned}\tag{6.45}$$

where $s_{ij} = (k_i + k_j)^2$, $s'_{ij} = (p_i + p_j)^2$ and $t_{ij} = (p_i - k_j)^2$. After rotating to the symmetric basis, the coefficients can be directly identified. They are summarized in table 6.1 in sec. 6.3.

At NLO, the amplitude can be easily computed in the charge basis using the results from ref. [195]. The general-isospin non-OPE amplitude at NLO includes some new types of C functions compared to the $I_{\pi\pi\pi} = 3$ case, but all of them can be expanded about threshold using the same techniques presented in sec. 5.2.3.

6.2.4 The BH subtraction

The BH subtraction only appears at NLO. It cancels divergencies happening in the non-OPE amplitude, associated to triangle diagrams as those in fig. 5.3. These divergencies happen in the imaginary part of the non-OPE amplitude, and so the real part of the subtraction is finite and can be computed independently of $\mathbf{M}_3^{\text{non-OPE}}$. As in sec. 5.2.4, the starting point is the unsymmetrized subtraction with the momentum assigned as in fig. 5.3a,

$$\mathbf{D}^{(\text{u,u}),\text{BH}}(\mathbf{p}_3, \mathbf{k}_3) = \int_r \mathbf{M}_2^{\text{LO}}(\mathbf{p}_3) \mathbf{G}^\infty(\mathbf{p}_3, \mathbf{r}) \mathbf{M}_2^{\text{LO}}(\mathbf{r}) \mathbf{G}^\infty(\mathbf{r}, \mathbf{k}_3) \mathbf{M}_2^{\text{LO}}(\mathbf{k}_3),\tag{6.46}$$

where recall $r = (\omega_r, \mathbf{r})$ is on-shell, with $\omega_r = \sqrt{\mathbf{r}^2 + M_\pi^2}$.

The main difference with the $I_{\pi\pi\pi} = 3$ computation is the presence of new kinematic structures and p -waves in the LO amplitudes. Before expanding, it is convenient to rewrite eq. (6.46) in terms of integrals that can be addressed with techniques similar to those presented in sec. 5.2.4. As a first step, we rewrite

$$\mathbf{D}^{(\text{u,u}),\text{BH}}(\mathbf{p}_3, \mathbf{k}_3) = \frac{1}{F_\pi^6} \int_r H^2(x_r) \mathbf{N}(\mathbf{p}_3, \mathbf{k}_3, \mathbf{r}) D^{-1}(\mathbf{p}_3, \mathbf{k}_3, \mathbf{r}).\tag{6.47}$$

Here, D is the same denominator as in eq. (5.51), equal for all initial- and final-states of the charge basis,

$$D(\mathbf{p}_3, \mathbf{k}_3, \mathbf{r}) = \left[(P - p_3 - r)^2 - M_\pi^2 + i\epsilon \right] \left[(P - k_3 - r)^2 - M_\pi^2 + i\epsilon \right]. \quad (6.48)$$

The numerator, \mathbf{N} , captures the isospin dependence. Its elements can be written as a product of three factors, $n_{ijk} \equiv n_i(p_3)n_j(r)n_k(k_3)$, with $i, j, k \in \{0, 1, 2\}$ —see ref. [4] for the exact expression. Each $n_i(q)$ incorporates the effect of one factor of $\mathbf{M}_2^{\text{LO}}(\mathbf{q})$ in eq. (6.46) and the associated barrier factors from \mathbf{G}^∞ , and depends on the momenta of the corresponding spectator. In particular, $n_0(q)$ is related to $A_{4\pi}(s_q)$, $n_1(q)$ from $A_{4\pi}(t_q) - A_{4\pi}(u_q)$, and $n_2(q)$ from $A_{4\pi}(t_q) + A_{4\pi}(u_q)$, where s_q, t_q and u_q are the on-shell Mandelstam variables of a dimer with spectator of momentum q .

Both $n_0(q)$ and $n_2(q)$ are s -wave, and so do not contain barrier factors. They are,

$$\begin{aligned} n_0(q) &= s_q - M_\pi^2, \\ n_2(q) &= t_q + u_q - M_\pi^2. \end{aligned} \quad (6.49)$$

By contrast, $n_1(q)$ is proportional to $t_q - u_q$. It contains p -waves and the corresponding barrier factors, and can be rewritten using eq. (6.36). This leaves a simple result when the spectator is an external particle that is on shell,

$$n_1(p_3) = -2(p_1 - p_2) \cdot r, \quad (6.50)$$

and similarly for $n_1(k_3)$. However, if the spectator has momentum r , a more lengthy development is required, which leaves

$$n_1(r) = 4 \left[\frac{p_3 \cdot (P - r) k_3 \cdot (P - r)}{(P - r)^2} - p_3 \cdot k_3 \right]. \quad (6.51)$$

Taking this decomposition into account, eq. (6.47) can be rewritten in terms of 27 integrals of the form

$$I_{ijk}(\mathbf{p}, \mathbf{k}) \equiv \frac{1}{F_\pi^6} \int_r H^2(x_r) n_{ijk}(\mathbf{p}, \mathbf{k}, \mathbf{r}) D^{-1}(\mathbf{p}, \mathbf{k}, \mathbf{r}), \quad i, j, k \in \{0, 1, 2\}, \quad (6.52)$$

corresponding to the 27 different possible numerators. To each of these integrals we can apply similar techniques to those in sec. 5.2.4, and expand them in terms of variables

$$H_{m,n,p} \equiv \frac{1}{\pi^2} \int_0^{1/\sqrt{3}} dz \frac{\sqrt{1+z^2}}{z^m x^p} \frac{d^n}{dx^n} [H^2(x)], \quad (6.53)$$

where recall $x = 1 - 3z^2$ and z is defined from $\omega_r = M_\pi(1 + 2z^2)$. The main difference to the $H_{m,n}$ functions in eq. (5.56) is the new p index relative to

the power of x in the denominator. This originates due to the $1/(P-r)^2$ factor in $n_1(r)$ —see eq. (6.51). These functions obey a recursive relation,

$$H_{m,n,p} = 3H_{m-2,n,p} + H_{m,n,p-1} = \frac{1}{3} \left(H_{m+2,n,p} - H_{m+2,n,p-1} \right), \quad (6.54)$$

in addition to eq. (5.57) for $p = 0$. Note that the $p = 0$ results are the $H_{m,n}$ functions used for the $I_{\pi\pi\pi} = 3$ channel in sec. 5.2.4.

To evaluate the integrals, we regularize them using the Hadamard finite-part prescription. For $n = 0$ we obtain

$$H_{m,0,p} = \int_0^{1/\sqrt{3}} dz \, 6z f_{m,p}(z) \frac{d}{dx} [H^2(x)], \quad (6.55)$$

where we define

$$\frac{d}{dz} f_{m,p}(x) = \frac{1}{\pi^2} \frac{\sqrt{1+z^2}}{z^m x^p}. \quad (6.56)$$

These results can be directly evaluated numerically. For $n \neq 0$, on the other hand, there is no need to use the Hadamard finite-part prescription. Derivatives of $H(x)$ are exponentially suppressed at the endpoints of the integral, which cancels the divergences there.

As in sec. 5.2.4, it is possible to obtain an analytic result by approximating $H(x) = 1$, in which case all $H_{m,n,0}$ are reduced to $f_{m,0}(1/\sqrt{3})\delta_{n,0}$. In reality, this approximation is more complicated for $H_{m,n,p}(x)$, as it does not converge for $p > 0$ due to a pole in the upper limit of eq. (6.53), at which $x = 0$. This divergence can also be regularized using the the Hadamard finite-part prescription, which is equivalent to dropping terms with $p > 0$. The complete result for $H_{m,n,p}$ can then be separated into this analytical approximation and a remainder, $\tilde{H}_{m,n,p}$,

$$H_{m,n,p} = \tilde{H}_{m,n,p} + f_{m,0}(1/\sqrt{3})\delta_{n,0}\delta_{p,0}. \quad (6.57)$$

Here $\tilde{H}_{m,n,p}$ is the only cutoff-dependent part, that vanishes for $H(x) = 1$, and needs to be evaluated numerically.

The complete contributions to the coefficients of the threshold expansion of $\mathbf{K}_{\text{df},3}$ can then be written as

$$\mathcal{K}_X = \mathcal{K}_X^{[\tilde{H}_{m,n,p}=0]} - \mathcal{D}_X, \quad (6.58)$$

where $\mathcal{K}_X^{[\tilde{H}_{m,n,p}=0]}$ can be expressed analytically, while \mathcal{D}_X needs to be evaluated numerically. Their values are listed in table 6.3. Typically, these numeric corrections are a small fraction of the full result. Note however, this is not always the case, as happens for the SS sector of the $I_{\pi\pi\pi} = 1$ channel.

6.3 Results for $\mathbf{K}_{\text{df},3}$

The complete results for $\mathbf{K}_{\text{df},3}$ are summarized in table 6.1 at LO, which also include the separate contribution from each term in eq. (6.14), and in table 6.2 at NLO, complemented by the cutoff-dependent remainders in table 6.3. These remainders are computed for the standard choice of the cutoff function, eq. (2.17). The full LO+NLO results are also shown in fig. 6.2 as a function of $(M_\pi/F_\pi)^2$, where we use the values of the LECs as given in eq. (5.71) and a renormalization scale $\mu = 4\pi F_\pi$, as done for example eq. (5.73). Note that the represented error bands (shaded regions) arise from the LECs, while we make no attempt at estimating higher-order corrections from ChPT. Some coefficients, moreover, do not have errors as they are independent of the LECs. Note the results for the $I_{\pi\pi\pi} = 3$ channel coincide with those presented in sec. 5.3, and we reproduce them here for completion.

We can compare LO to LO+NLO results for those coefficients for which the LO is non-zero. As was the case for the $I_{\pi\pi\pi} = 3$ channel, we in general observe bad convergence of the threshold expansion, with large corrections coming from NLO. This effect is thus generic for three-pion processes. Also note these corrections are larger at heavier-than-physical pion masses, while they are somehow smaller close to the physical point.

	\mathcal{K}_X	Total	$(F_\pi/M_\pi)^4 \times \mathcal{K}_X$		
			OPE	s -OPE	non-OPE
$I_{\pi\pi\pi} = 3$	\mathcal{K}_0	18	36	0	-18
	\mathcal{K}_1	27	63	0	-36
$I_{\pi\pi\pi} = 2$	\mathcal{K}_0^T	$\frac{9}{2}$	$\frac{21}{2}$	0	-6
	$\mathcal{K}_0^{\text{SS}}$	$-\frac{111}{8}$	-54	$-\frac{135}{8}$	57
	$\mathcal{K}_1^{\text{SS}}$	$-\frac{1137}{64}$	-27	$-\frac{945}{64}$	24
$I_{\pi\pi\pi} = 1$	$\mathcal{K}_2^{\text{SS}}$	$-\frac{135}{512}$	0	$-\frac{135}{512}$	0
	$\mathcal{K}_0^{\text{SD}}$	$-\frac{3}{8}$	-9	$-\frac{27}{8}$	12
	$\mathcal{K}_1^{\text{SD}}$	$\frac{27}{64}$	0	$\frac{27}{64}$	0
	$\mathcal{K}_0^{\text{DD}}$	$\frac{1}{2}$	$\frac{21}{2}$	0	-10
	$\mathcal{K}_2^{\text{DD}}$	$-\frac{81}{4}$	0	$-\frac{81}{4}$	0
$I_{\pi\pi\pi} = 0$	There are no $I_{\pi\pi\pi} = 0$ contributions at LO				

Table 6.1. LO ChPT results for $\mathbf{K}_{\text{df},3}$, together with the separate contributions from each term in eq. (6.14). There is no BH subtraction or cutoff dependence at this order.

\mathcal{K}_X	$(F_\pi/M_\pi)^6 \times \mathcal{K}_X^{[\tilde{H}_{m,n,p}=0]}$
\mathcal{K}_0	$-\kappa \left(105 + 36 \log 3 \right) + 111L - 288 \ell_1^r - 432 \ell_2^r - 36 \ell_3^r + 72 \ell_4^r$
\mathcal{K}_1	$-\kappa \left(\frac{1999}{20} + 96 \log 3 \right) + 384L - 612 \ell_1^r - 1170 \ell_2^r + 108 \ell_4^r$
\mathcal{K}_2	$\kappa \left(\frac{605061}{1400} - \frac{621}{10} \log 3 \right) + 360L - 432 \ell_1^r - 864 \ell_2^r$
\mathcal{K}_A	$\kappa \left(\frac{196281}{560} - \frac{135}{8} \log 3 \right) - 9L + 27 \ell_1^r + \frac{27}{2} \ell_2^r$
\mathcal{K}_B	$\kappa \left(\frac{90423}{700} - \frac{189}{40} \log 3 \right) + 54L - 162 \ell_1^r - 81 \ell_2^r$
\mathcal{K}_0^T	$-\kappa \left(\frac{59113}{3240} + \frac{1009}{144} \log 3 \right) - 90 \ell_1^r - 9 \ell_2^r + 18 \ell_4^r$
\mathcal{K}_1^T	$\kappa \left(\frac{9486697}{453600} - \frac{989}{480} \log 3 \right) + \frac{53}{2} L - \frac{195}{2} \ell_1^r - \frac{123}{4} \ell_2^r$
\mathcal{K}_2^T	$-\kappa \left(\frac{1248031}{7200} + \frac{5641}{320} \log 3 \right) - \frac{171}{2} L + \frac{837}{2} \ell_1^r + \frac{189}{4} \ell_2^r$
\mathcal{K}_3^T	$\kappa \left(\frac{23833}{33600} - \frac{317}{960} \log 3 \right) + \frac{27}{4} L - \frac{45}{4} \ell_1^r - \frac{117}{8} \ell_2^r$
\mathcal{K}_4^T	$\kappa \left(\frac{332981}{75600} - \frac{59}{960} \log 3 \right) + \frac{5}{3} L - 5 \ell_1^r - \frac{5}{2} \ell_2^r$
\mathcal{K}_0^{SS}	$-\kappa \left(\frac{1955}{8} + \frac{369}{4} \log 3 \right) - \frac{1237}{8} L + 342 \ell_1^r + 438 \ell_2^r - \frac{57}{2} \ell_3^r - \frac{111}{2} \ell_4^r$
\mathcal{K}_1^{SS}	$-\kappa \left(\frac{191089}{320} + \frac{993}{8} \log 3 \right) - \frac{24439}{64} L + \frac{2637}{4} \ell_1^r + \frac{4125}{4} \ell_2^r + \frac{45}{16} \ell_3^r - \frac{1137}{16} \ell_4^r$
\mathcal{K}_2^{SS}	$-\kappa \left(\frac{34274101}{89600} + \frac{33957}{320} \log 3 \right) - \frac{119505}{512} L + \frac{8811}{32} \ell_1^r + \frac{18027}{32} \ell_2^r - \frac{405}{128} \ell_3^r - \frac{135}{128} \ell_4^r$
\mathcal{K}_A^{SS}	$\kappa \left(\frac{1102239}{2240} - \frac{19575}{128} \log 3 \right) + \frac{273}{8} L - \frac{297}{4} \ell_1^r - \frac{261}{4} \ell_2^r$
\mathcal{K}_B^{SS}	$-\kappa \left(\frac{521271}{5600} + \frac{13419}{640} \log 3 \right) - 36L + 108 \ell_1^r + 54 \ell_2^r$
\mathcal{K}_0^{SD}	$\kappa \left(\frac{10853}{160} - \frac{255}{8} \log 3 \right) + \frac{23}{16} L + 36 \ell_1^r - \frac{39}{2} \ell_2^r - \frac{9}{4} \ell_3^r - \frac{3}{2} \ell_4^r$
\mathcal{K}_1^{SD}	$\kappa \left(\frac{643087}{8960} - \frac{3543}{64} \log 3 \right) - \frac{1647}{128} L + \frac{585}{8} \ell_1^r - \frac{9}{8} \ell_2^r + \frac{81}{32} \ell_3^r + \frac{27}{16} \ell_4^r$
\mathcal{K}_2^{SD}	$\kappa \left(\frac{166953}{2240} + \frac{513}{128} \log 3 \right) + \frac{21}{4} L - \frac{63}{4} \ell_2^r$
\mathcal{K}_3^{SD}	$\kappa \left(\frac{27783}{320} - \frac{3699}{128} \log 3 \right) + \frac{75}{4} L + \frac{81}{4} \ell_1^r - \frac{531}{8} \ell_2^r$
\mathcal{K}_4^{SD}	$\kappa \left(\frac{109539}{5600} - \frac{11097}{320} \log 3 \right) - \frac{39}{2} L + \frac{297}{4} \ell_1^r + \frac{171}{8} \ell_2^r$

Table 6.2. Full NLO results for $\mathcal{K}_{\text{df},3}$ up to quadratic order in the threshold expansion (cubic for $I_{\pi\pi\pi} = 0$). The cutoff-dependent remainders defined in eq. (6.58), \mathcal{D}_X , are not included. They are listed in table 6.3.

\mathcal{K}_X	$(F_\pi/M_\pi)^6 \times \mathcal{K}_X^{[\tilde{H}_{m,n,p}=0]}$
$\mathcal{K}_0^{\text{DD}}$	$\kappa\left(\frac{49121}{3240} + \frac{1259}{144}\log 3\right) + 28L - 54\ell_1^r - 63\ell_2^r + 2\ell_4^r$
$\mathcal{K}_1^{\text{DD}}$	$\kappa\left(\frac{11178103}{453600} + \frac{4279}{480}\log 3\right) + \frac{265}{6}L - \frac{149}{2}\ell_1^r - \frac{381}{4}\ell_2^r$
$\mathcal{K}_2^{\text{DD}}$	$\kappa\left(\frac{27345737}{50400} - \frac{11869}{320}\log 3\right) - \frac{123}{2}L + \frac{1251}{2}\ell_1^r + \frac{459}{4}\ell_2^r - 81\ell_4^r$
$\mathcal{K}_3^{\text{DD}}$	$\kappa\left(\frac{150229}{11200} + \frac{449}{320}\log 3\right) + \frac{45}{4}L - \frac{217}{12}\ell_1^r - \frac{593}{24}\ell_2^r$
$\mathcal{K}_4^{\text{DD}}$	$\kappa\left(\frac{212299}{75600} + \frac{83}{320}\log 3\right) + \frac{25}{9}L - \frac{7}{3}\ell_1^r - \frac{43}{6}\ell_2^r$
$\mathcal{K}_0^{\text{AS}}$	$\kappa\left(\frac{2721}{20} - \frac{81}{2}\log 3\right) - 162\ell_1^r + 81\ell_2^r$
$\mathcal{K}_1^{\text{AS}}$	$\kappa(132)$
$\mathcal{K}_3^{\text{AS}}$	$-\kappa\left(\frac{164673}{1120} - \frac{2187}{32}\log 3\right)$
$\mathcal{K}_4^{\text{AS}}$	$\kappa\left(\frac{28863}{448} - \frac{3645}{128}\log 3\right)$

Table 6.2 (cont.). Full NLO results for $\mathcal{K}_{\text{df},3}$ up to quadratic order in the threshold expansion (cubic for $I_{\pi\pi\pi} = 0$). The cutoff-dependent remainders defined in eq. (6.58), \mathcal{D}_X , are not included. They are listed in table 6.3.

\mathcal{D}_0	-0.056 347 6589	$\mathcal{D}_0^{\text{SS}}$	1.213 748 64
\mathcal{D}_1	0.129 589 681	$\mathcal{D}_1^{\text{SS}}$	4.737 727 30
\mathcal{D}_2	0.432 202 370	$\mathcal{D}_2^{\text{SS}}$	2.098 947 60
\mathcal{D}_A	0.000 907 273 890	$\mathcal{D}_A^{\text{SS}}$	-2.393 448 70
\mathcal{D}_B	0.000 162 394 747	$\mathcal{D}_B^{\text{SS}}$	-1.089 982 49
\mathcal{D}_0^{T}	-0.007 042 111 64	$\mathcal{D}_0^{\text{SD}}$	0.060 539 453 1
\mathcal{D}_1^{T}	-0.095 869 747 4	$\mathcal{D}_1^{\text{SD}}$	0.558 130 406
\mathcal{D}_2^{T}	-0.264 963 303	$\mathcal{D}_2^{\text{SD}}$	-0.105 910 881
\mathcal{D}_3^{T}	0.021 650 723 1	$\mathcal{D}_4^{\text{SD}}$	-0.135 426 533
\mathcal{D}_4^{T}	-0.001 531 207 94	$\mathcal{D}_4^{\text{SD}}$	-0.349 051 891
$\mathcal{D}_0^{\text{AS}}$	-0.301 063 917	$\mathcal{D}_0^{\text{DD}}$	0.048 482 775 8
$\mathcal{D}_1^{\text{AS}}$	0.881 880 013	$\mathcal{D}_1^{\text{DD}}$	-0.316 388 524
$\mathcal{D}_3^{\text{AS}}$	0.607 228 425	$\mathcal{D}_2^{\text{DD}}$	-1.906 375 12
$\mathcal{D}_4^{\text{AS}}$	-0.227 122 084	$\mathcal{D}_4^{\text{DD}}$	0.034 410 564 7
		$\mathcal{D}_4^{\text{DD}}$	-0.017 668 886 1

Table 6.3. Summary of the numerical cutoff-dependent remainders from the BH subtraction. They are computed using the standard cutoff in eq. (2.17).

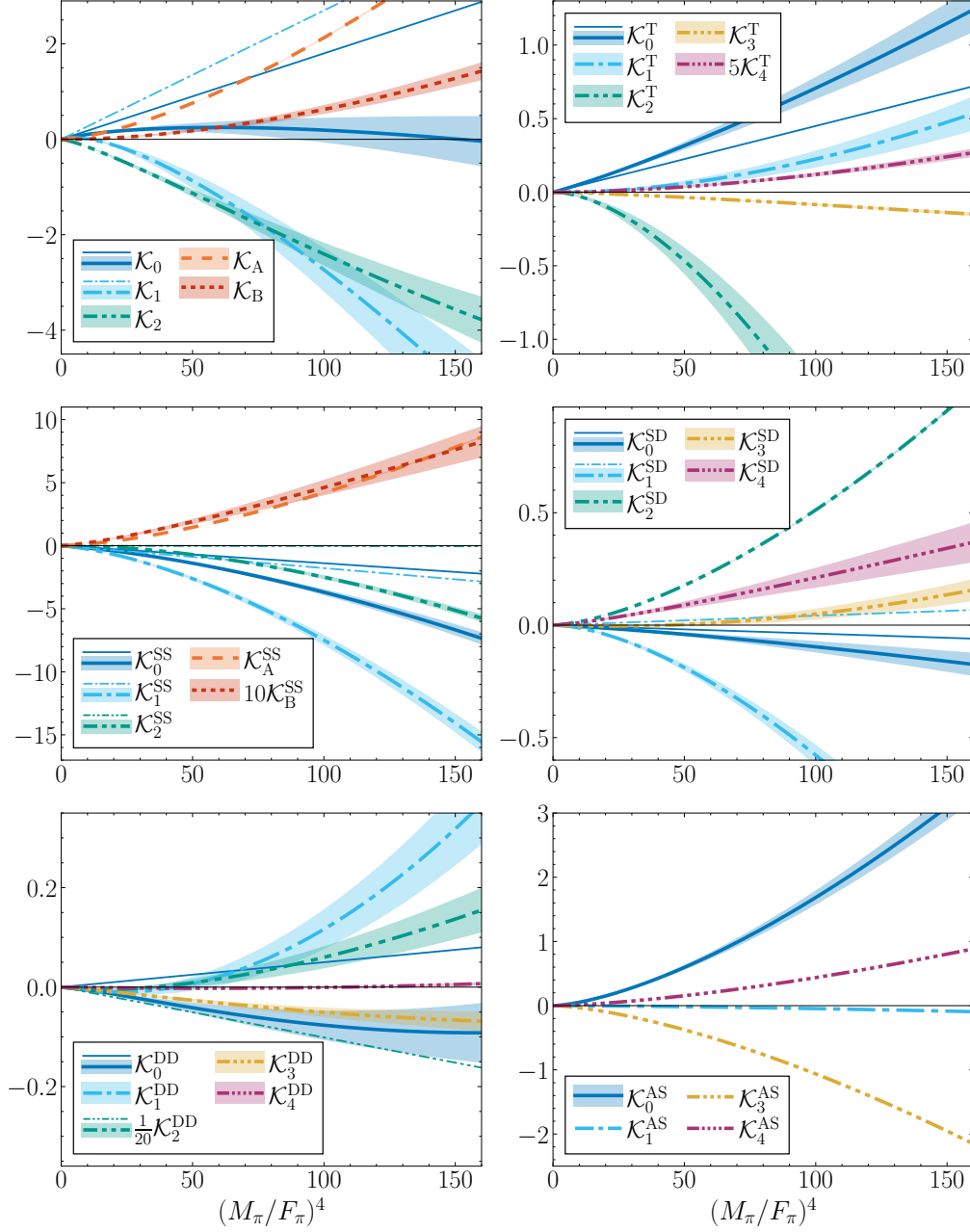


Figure 6.2. LO (thin lines) and LO+NLO (thick lines and bands) ChPT predictions for the threshold-expansion coefficients of $\mathcal{K}_{df,3}$ as a function of $(M_\pi/F_\pi)^4$, divided by a factor of 10^3 . Bands represent the uncertainties arising from the LECs—see eq. (5.73). Each panel corresponds to a different isospin and irrep of the permutation group, for the $I_{\pi\pi\pi} = 1$ channel. Some coefficients are rescaled for legibility. We note $\mathcal{K}_1^{\text{AS}}$, $\mathcal{K}_3^{\text{AS}}$ and $\mathcal{K}_4^{\text{AS}}$ have no error, as they are independent of the LECs.

We also study the convergence of the threshold expansion, comparing our threshold-expanded results to exact numeric determinations. This comparison is shown in fig. 6.3 for six of the 15 non-zero coefficients of $\mathbf{K}_{\text{df},3}$ in the symmetric basis. We take $M_\pi = 340$ MeV and use the momenta configuration,

$$\begin{aligned} \mathbf{k}_1 &= p(1, 0, 0), & \mathbf{p}_1 &= p\left(\frac{1}{2}, \frac{3}{4}, \frac{\sqrt{3}}{4}\right), \\ \mathbf{k}_2 &= p\left(-\frac{3}{4}, 1, 0\right), & \mathbf{p}_2 &= p\left(-\frac{\sqrt{3}}{2} - \frac{3}{8}, \frac{\sqrt{3}}{4} - \frac{9}{16}, -\frac{3\sqrt{3}}{16} + \frac{1}{4}\right), \\ \mathbf{k}_3 &= p\left(-\frac{1}{4}, -1, 0\right), & \mathbf{p}_3 &= p\left(\frac{\sqrt{3}}{2} - \frac{1}{8}, -\frac{\sqrt{3}}{4} - \frac{3}{16}, -\frac{\sqrt{3}}{16} - \frac{1}{4}\right), \end{aligned} \quad (6.59)$$

with p a real parameter. This configuration is asymmetric enough that all relevant elements in $\mathbf{K}_{\text{df},3}$ are non-zero.

We observe good convergence for all components up to $\Delta \lesssim 1$, and also that in many cases the convergence of the total result is better than that of the separate terms in eq. (6.15). Note that the formal limitation of the series to $|\Delta| < 8/9$, originating from the s -OPE contribution, does not seem to break the expansion. The s -OPE part is generally small and converges poorly (rather than diverging) above that limit. We found the non-presented elements of $\mathbf{K}_{\text{df},3}$ to show similar convergence, which is also true for other kinematical configurations and values of the pion mass.

Finally, we analyze the convergence of the NLO OPE part as higher partial waves of the NLO vertex are included. In fig. 6.4, we represent the contributions of different partial waves of the NLO two-particle amplitude to the OPE part of $\mathbf{K}_{\text{df},3}$ for the same six coefficients, kinematic configuration and pion mass used in fig. 6.3. We observe our result is dominated by the lowest partial waves, with negligible contributions above $\ell = 2$, the highest one captured by the threshold expansion.

6.4 Conclusions

In this chapter, the work from ref. [4] has been presented, in which the three-pion K -matrix was determined for general isospin up to NLO in ChPT. This generalized the work from ref. [3] presented in chapter 5. Our results show that NLO corrections are in general large compared to LO results, especially at heavier-than-physical pion mass. The bad convergence of the chiral expansion seems thus to be a generic feature of all three-pion isospin channels. On a more positive side, we found that the threshold expansion truncated at quadratic order provides a good description of the full K -matrix in the elastic region.

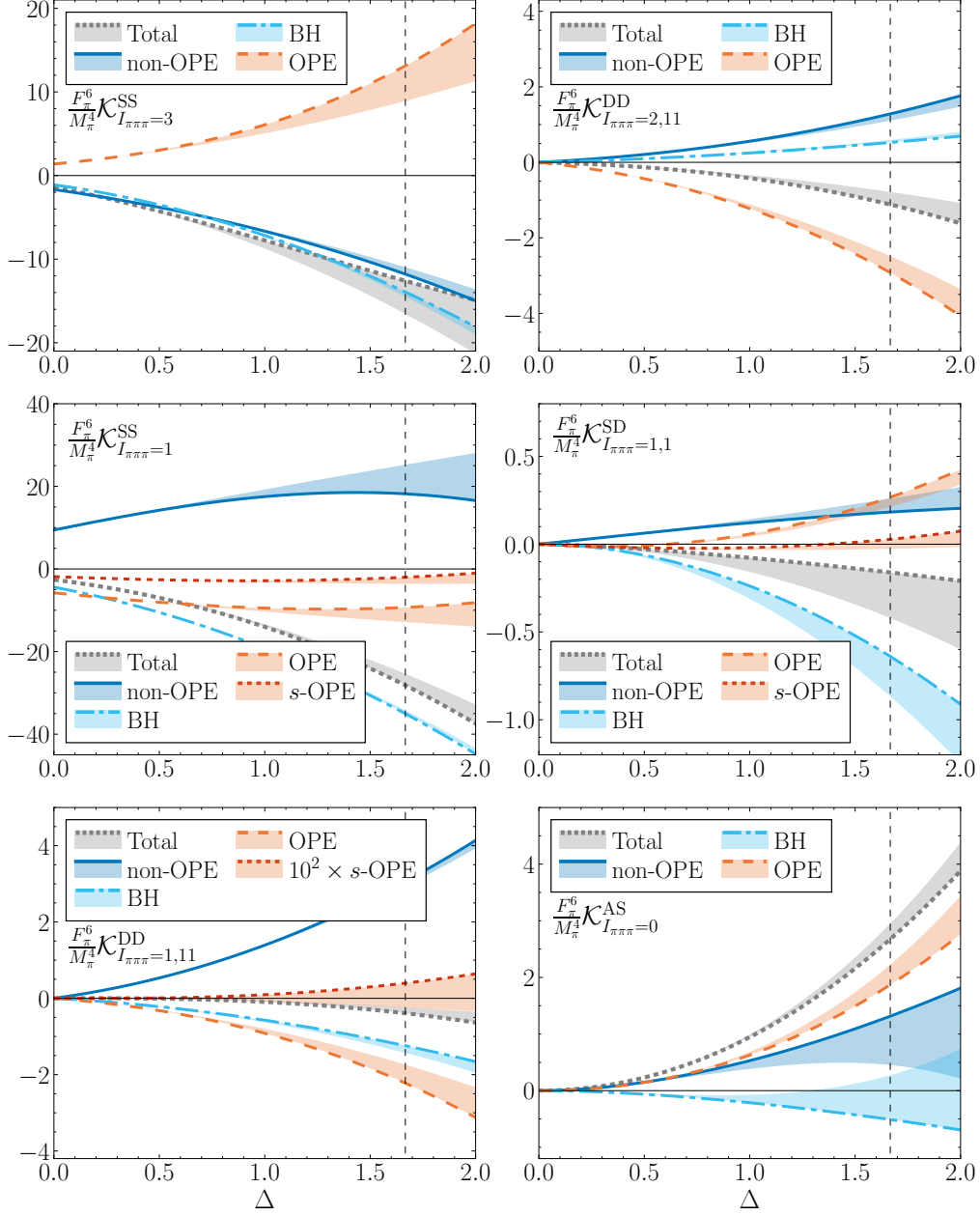


Figure 6.3. Convergence of the threshold expansion at $M_\pi = 340$ MeV, for various components of $\mathbf{K}_{\text{df},3}^{\text{NLO}}$ (LO is omitted) in the symmetric basis using the kinematic configuration in eq. (6.59). Results are represented for the total K -matrix as well as for the separate contributions according to eq. (6.15), where “BH” refers to $\mathbf{K}^{\text{BH}} = -\mathbf{D}^{\text{BH}}$. Lines represent the threshold expansion, and the width of the bands is the difference to the exact results, which thus correspond to the other end of the band. All values are divided by a factor 10^3 . Vertical lines represent the five-pion threshold.

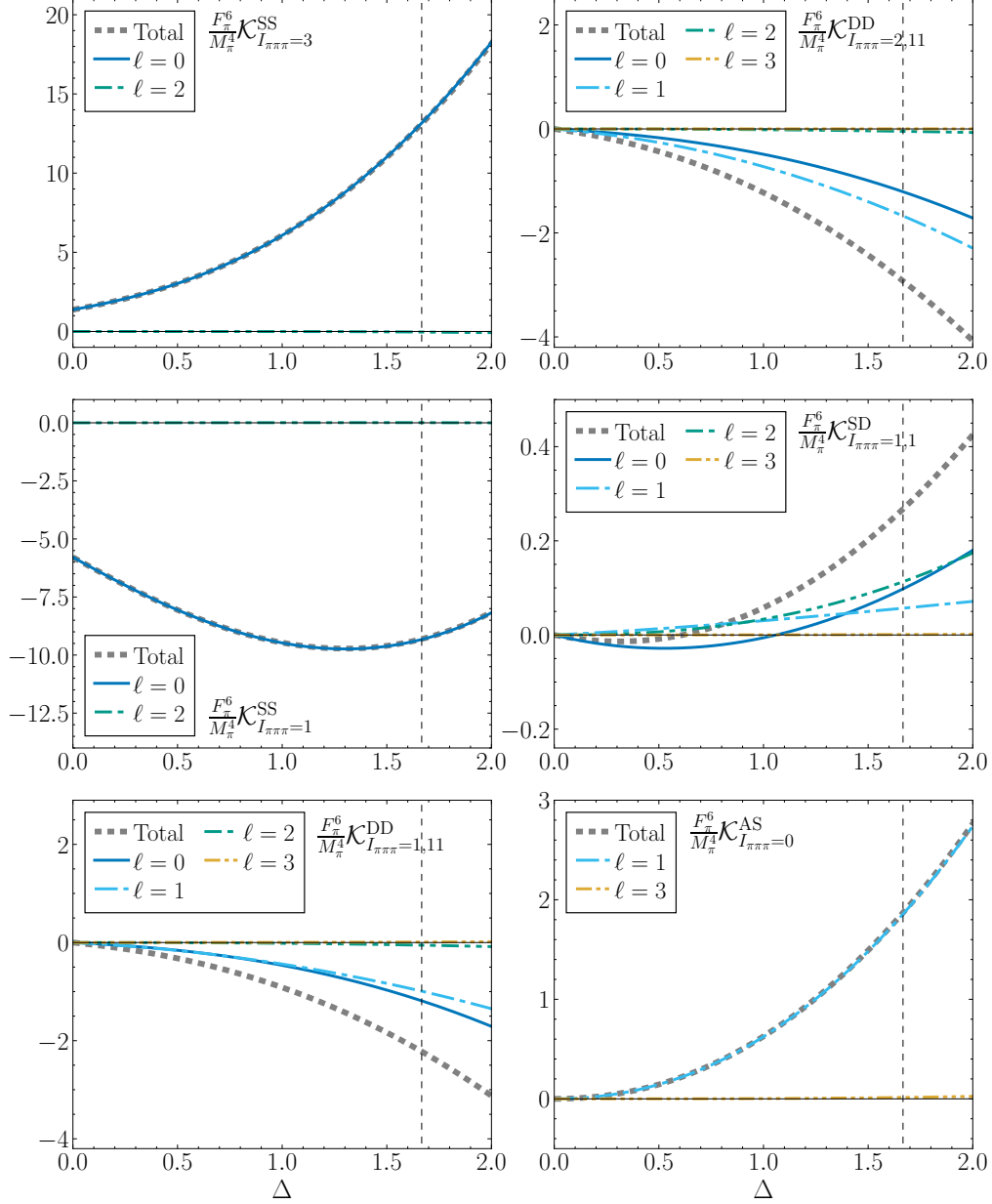


Figure 6.4. Comparison of contributions to $\mathbf{K}_{df,3}^{\text{NLO,OPE}}$ from different dimer partial waves in $\mathbf{M}_2^{\text{NLO}}$, evaluated numerically at $M_\pi = 340$ MeV using the kinematic configuration in eq. (6.59). All values are divided by a factor 10^3 . Partial waves that are identically zero, as well as the negligibly small $\ell > 3$, are omitted.

We expect that the results from this work will prove valuable in the future. In particular, it will be of major interest to compare them against future lattice results for three pions at non-maximal isospin. This work also opens the door to an extension to more complicated systems. An example of this could be systems of three kaons or pions and kaons, for which lattice results are already available [301, 302]. However, the NLO ChPT amplitudes would need to be worked out first.

7 Two- and three-particle scattering in the $O(3)$ model

The study of three-particle interactions on the lattice has undergone tremendous progress during the past decade. On the theoretical side, different formalisms have been developed. The relativistic-field-theory (RFT) approach, introduced in sec. 2.3.2, has been extended to a large number of three-particle systems, such as non-identical mesons, three nucleons or processes containing resonances. Its practical application to QCD, however, has been limited to states of three mesons at maximal isospin [194, 268, 298, 301, 302], which present very weak interactions. By contrast, the formalism has never been applied to a system for which analytical solutions are known—see however ref. [316] for an application to a scalar theory with a three-particle resonance.

A commonly used toy model for QCD is the (1+1)-dimensional $O(3)$ non-linear sigma model. It is an integrable model—i.e., it allows for analytic predictions of the scattering matrix—which presents very strong interactions. The model shares many of the non-perturbative features of QCD, such as asymptotic freedom and a low-energy spectrum of isospin-one particles. In addition, the lower dimensionality allows for cheap numerical computations. These characteristics make the $O(3)$ model ideal to investigate the RFT formalism, as lattice results could be compared against analytical predictions. Moreover, the strength of the interactions in this model makes it possible to explore a regime of the formalism which has not been studied before.

In this chapter, we present results on the study of two- and three-particle interactions in the (1+1)-dimensional $O(3)$ non-linear sigma model [5, 9]. In the two-particle sector, we focus on the isospin-two and -one channels, which we compare against analytical predictions. In the case of three particles we take a first step to test the RFT formalism. We determine the finite-volume energy spectra in the isospin-three, -two and -zero channels, and compare the

results against predictions made assuming a zero three-particle K -matrix, $\mathcal{K}_{\text{df},3} = 0$, using the RFT, that we have adapted to 1+1 dimensions.

The chapter is organized as follows. In sec. 7.1, we introduce the O(3) model and review the analytical results for the scattering matrix. The (1+1)-dimensional version of the two- and three-particle finite-volume formalisms is presented in sec. 7.2, followed by a description of the lattice techniques used to determine the finite-volume spectrum in sec. 7.3. Sec. 7.4 then presents our results for the two- and three-particle finite-volume energies, which we compare in sec. 7.5 to analytical predictions, setting $\mathcal{K}_{\text{df},3} = 0$ in the three-particle sector. We finalize with a short conclusion in sec. 7.6.

7.1 The (1+1)-dimensional O(3) non-linear sigma model

The (1+1)-dimensional O(3) non-linear sigma model—*O(3) model* from here on—has commonly served as a sandbox of QCD due to important qualitative similarities of the two theories. For example, it has been used to study the two-particle scattering formalism [114] and to test a novel technique to extract spectral functions from Euclidean correlators [317].

The Minkowski action for the O(3) model is

$$S[\boldsymbol{\sigma}] = \frac{\beta}{2} \int d^2x \partial_\mu \boldsymbol{\sigma}(x) \cdot \partial^\mu \boldsymbol{\sigma}(x), \quad (7.1)$$

where β is a dimensionless coupling constant, $x = (t, \mathbf{x})$ is a coordinate in the the (1+1)-dimensional Minkowski spacetime,¹ and $\boldsymbol{\sigma}$ is a three-component field of unit length, $\boldsymbol{\sigma}(x) \cdot \boldsymbol{\sigma}(x) = 1$, this is, $\boldsymbol{\sigma}(x) \in S^2$.

The O(3) model, like QCD, is asymptotically free and has a mass gap, m [318, 319]. In addition, it presents a global O(3) symmetry. Combined, these features imply a low energy spectrum consisting of three particles of mass m transforming in the fundamental representation of the $\mathfrak{o}(3)$ algebra. These properties have been proven in the large N limit of the O(N) model [320, 321], and are assumed to hold for all N .

While these features are shared by all O(N) models, the $N = 3$ case shows further similarities with two-flavor QCD. As commented, the O(3) model presents a low-lying spectrum of particles transforming under the fundamental irrep of $\mathfrak{o}(3)$, while two-flavor QCD has a SU(2) global isospin

¹We use boldface to indicate the spacial component of Minkowski vectors, even if there is only one spacial dimension, to distinguish from the full Minkowski vector.

symmetry and pions transform under the adjoint irrep of the associated Lie algebra. However, these two groups are isomorphic, $O(3) \cong SU(2)$, and also are the fundamental irrep of the $\mathfrak{o}(3)$ algebra and adjoint irrep of $\mathfrak{su}(2)$. Thus, like QCD, the $O(3)$ model presents a low-energy spectrum of isospin-one particles.

The presence of an isospin-one multiplet in the theory implies multiparticle states are organized in the same scattering channels as pions in QCD—see sec. 2.2. In particular, two-particle interactions can occur with two-particle isospin $I_{\sigma\sigma} = 2, 1$ and 0 , while three-particle scattering happens with three-particle isospin $I_{\sigma\sigma\sigma} = 3, 2, 1$ and 0 . Recall that the $I_{\sigma\sigma\sigma} = 2$ and $I_{\sigma\sigma\sigma} = 1$ channels have multiplicity two and three, respectively, which we characterize by the possible two-particle channels in which pairwise interactions can occur. These are the two-particle $I_{\sigma\sigma} = 2$ and $I_{\sigma\sigma} = 1$ channels for $I_{\sigma\sigma\sigma} = 2$, and all three two-particle channels for $I_{\sigma\sigma\sigma} = 1$ (this is, $I_{\sigma\sigma} = 2, 1$ and 0).

To study multiparticle interactions, it is key to understand the spacial symmetries of the (1+1)-dimensional theory. Due to the lower dimensionality, the Poincaré group is reduced to contain only three generators: two related to time and spatial translations, and another one related to relativistic boosts. There is however no generator related to spatial rotations, as there is only one single spacial dimension. Instead, the $SO(3)$ rotation group in 3+1 dimensions gets reduced to a discrete \mathbb{Z}_2 parity group.

This has important implications when studying scattering. In the (3+1)-dimensional world, interactions preserving rotation invariance are decomposed into different partial waves. In 1+1 dimensions, instead, scattering observables are separated into parity-odd and parity-even sectors. In the case of two-particles, this division is redundant, as each definite isospin contains only one sector. For example, two-particle isospin-two states which are even under particle exchange only contain parity-even interactions, while $I_{\sigma\sigma} = 1$ states are odd under particle exchange, and thus contain parity-odd interactions.

In the three-particle case, the situation is a bit more complicated as all channels can be projected to both parity sectors. This plays a major role in the application of the three-particle finite-volume formalism and the determination of lattice interpolating operators, since states with zero total momentum need to be projected to definite parity—see secs. 7.2.2 and 7.3.2.

7.1.1 The integrable S -matrix

Theories that allow for an analytical determination of the scattering S -matrix, usually based on the existence of an infinite number of symmetries,

are said to be *integrable*. Most known examples of integrable models live in 1+1 dimensions, such as the O(3) model. In contrast, it is believed that no interacting integrable theories exist in the (3+1)-dimensional world, since such a number of conservation laws would imply the absence of interactions.

The existence of an infinite number of conservation laws imposes very restrictive conditions into possible interactions in 1+1 dimensions. The main consequence is the property of *factorization* [318], which implies that the S -matrix of three or more particles factorizes into products of successive two-particle S -matrices. The infinite number of symmetries also implies no particle production, this is, that the number of particles is preserved [322], and that the initial and final sets of momenta are equal, with momenta only being reshuffled.

In the particular case of the O(3) model, the two-particle S -matrix is determined by combining factorization with unitarity and crossing symmetry. The result, which we present below, was first determined in refs. [323, 324], where the factorization property was assumed. The existence of an infinite number of non-local symmetries in the O(3) model was proven later in refs. [325–327].

Here, we briefly review the determination of the two-particle S -matrix from refs. [323, 324]. We let $\{k_1, k_2\}$ and $\{p_1, p_2\}$ be the momenta of the two particles in the initial and final states. Similarly, we denote the flavors of the two incoming particles as (a, b) and those of the two outgoing ones as (c, d) . Recall that states in the flavor basis, $\{|\sigma^1\rangle, |\sigma^2\rangle, |\sigma^3\rangle\}$ are related to those with definite isopin, $\{|\sigma^+\rangle, |\sigma^0\rangle, |\sigma^-\rangle\}$, by the relations analogous to those in eq. (6.1).

The factorizable S -matrix in the flavor basis takes the general form

$$S_{cd;ab}(p_1, p_2; k_1, k_2) = \delta^2(p_1 - k_1)\delta^2(p_2 - k_2) \times [\delta_{cd}\delta_{ab}\sigma_1(s) + \delta_{ca}\delta_{db}\sigma_2(s) + \delta_{da}\delta_{cb}\sigma_3(s)] , \quad (7.2)$$

where $s = (k_1 + k_2)^2$ is the usual Mandelstam variable. The σ_i factors are meromorphic functions that can be analytically determined from the properties of unitarity, crossing symmetry and factorization. It is common to work in terms of the relative rapidity of the two particles, $\theta = \theta_1 - \theta_2$, where θ_i is the rapidity of particle i ,

$$s = 2m^2(1 + \cosh \theta) . \quad (7.3)$$

This transforms physical values of s , $s > 4m^2$, into real values of θ , while values with $0 < s < 4m^2$ are mapped to the imaginary θ axis, with $0 < \text{Im}(\theta) < \pi$. Finally, values with $s < 0$ are turned to complex θ values with $\text{Im}(\theta) = \pi$ fixed and varying real part.

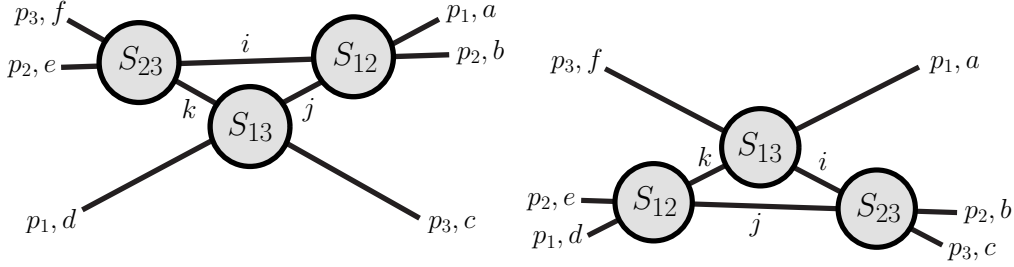


Figure 7.1. Diagrammatic representation of the two equivalent ways of computing the three-particle S -matrix in a factorizable theory. This equivalence leads to the Yang-Baxter equations, eq. (7.7). Note we have imposed that the final set of momenta is identical to the initial one, which is not true for the flavor indices. We use $S_{ab} = S(\theta_{ab})$, where θ_{ab} is the relative rapidity of particles a and b , and leave the flavor indices implicit.

Unitarity and crossing symmetry translate into the following conditions on the S -matrix, respectively,

$$S(\theta)S^\dagger(-\theta) = \mathbb{1}, \quad (7.4)$$

$$S(\theta) = S^\dagger(i\pi - \theta), \quad (7.5)$$

where the Hermitian conjugate of the S -matrix acts on initial- and final-state indices separately,

$$S_{cd;ab}^\dagger(p_1, p_2; k_1, k_2) = S_{dc;ba}(p_2, p_1; k_2, k_1). \quad (7.6)$$

These conditions are complemented by the so-called *Yang-Baxter equation* [328, 329], which incorporates the property of factorization. A multiparticle S -matrix is computed as a product of successive two-particle S -matrices and the final result must be independent of the order in which two-particle interactions occur. In the case of three-particles, this can happen in two ways, represented in fig. 7.1. If we label the three particles as “1”, “2” and “3”, and the initial and final flavor indices as $\{a, b, c\}$ and $\{d, e, f\}$, respectively, the Yang-Baxter equation looks like

$$\begin{aligned} S_{def;abc}^{3\text{-part}}(\theta_{12}, \theta_{23}, \theta_{31}) &= S_{ef,jk}(\theta_{23})S_{dk,ci}(\theta_{13})S_{ij;ab}(\theta_{12}) \\ &= S_{kf;aj}(\theta_{31})S_{de;ki}(\theta_{12})S_{ij;bc}(\theta_{23}), \end{aligned} \quad (7.7)$$

where sum over repeated i, j, k indices is implicit and θ_{nm} denotes the relative rapidity of particle n and m .

Eqs. (7.4), (7.5), and (7.7) can be translated into some conditions for the $\sigma_i(\theta)$ functions. The simplest solution to these equations is believed to correspond to the O(3) model,

$$\begin{aligned}
 \sigma_2(\theta) &= \frac{\theta(i\pi - \theta)}{(2\pi i - \theta)(i\pi + \theta)}, \\
 \sigma_1(\theta) &= -\frac{2\pi i}{\theta}\sigma_2(\theta), \\
 \sigma_3(\theta) &= -\frac{2\pi i}{i\pi - \theta}\sigma_2(\theta).
 \end{aligned} \tag{7.8}$$

In general, eqs. (7.4), (7.5), and (7.7) lead to a more general results, as σ_2 above may be multiplied by an arbitrary number of the so-called Castillejo-Dalitz-Dyson poles [330]. The result with one such pole is expected to correspond to the Gross-Neveu model [324, 331].

7.1.2 Two- and three-particle S -matrix

Using the analytic results for the S -matrix, one can obtain the scattering amplitude for the two- and three-particle channels of interest. The projection can be performed using one particular state of each channel, as the scattering amplitude is independent of the third component of isospin. For example, we can consider states with maximal third isospin component. In the isospin basis, they are,

$$\begin{aligned}
 |I_{\sigma\sigma} = 2\rangle &= |\sigma^+\sigma^+\rangle, \\
 |I_{\sigma\sigma} = 1\rangle &= \frac{1}{\sqrt{2}} (|\sigma^+\sigma^0\rangle - |\sigma^0\sigma^+\rangle), \\
 |I_{\sigma\sigma} = 0\rangle &= \frac{1}{2} (2|\sigma^0\sigma^0\rangle - |\sigma^+\sigma^-\rangle - |\sigma^-\sigma^+\rangle),
 \end{aligned} \tag{7.9}$$

where we leave the momentum dependence implicit.

The two-particle S -matrix for each isospin channel then takes the form

$$\begin{aligned}
 S_{I_{\sigma\sigma}=2}(\theta) &= \frac{\theta + 2\pi i}{\theta - 2\pi i}, \\
 S_{I_{\sigma\sigma}=1}(\theta) &= \frac{(\theta + 2\pi i)(\theta - i\pi)}{(\theta - 2\pi i)(\theta + i\pi)}, \\
 S_{I_{\sigma\sigma}=0}(\theta) &= \frac{\theta - i\pi}{\theta + i\pi}.
 \end{aligned} \tag{7.10}$$

From here, the scattering phase shift can be determined,

$$S_{I_{\sigma\sigma}}(\theta) = \exp[2i\delta_{I_{\sigma\sigma}}(\theta)]. \tag{7.11}$$

For all two-particle channels, the exact results for $\delta_{I_{\sigma\sigma}}$ are presented in fig. 7.2, as a function of the magnitude of the relative two-particle momentum, q_2^* .

Note that for all the channels, the phase shift decays logarithmically at large energies, as expected in an asymptotically-free theory.

These results also make it possible to determine the two-particle K -matrix, similarly to the (3+1)-dimensional case,

$$\mathcal{K}_{2,I_{\sigma\sigma}} = \rho(s) \cot \delta_{I_{\sigma\sigma}}(s), \quad (7.12)$$

where $\rho(s)$ is the phase space factor. In (1+1)-dimensions, it takes the form

$$\rho(s) = \frac{1}{8E^*q_2^*}, \quad (7.13)$$

where $E^* = \sqrt{s}$ is the total energy in the CMF frame.

The Yang-Baxter equation, eq. (7.7), also enables us to determine the three-particle S -matrix, which can then be projected to any channel of interest. For example, for the $I_{\sigma\sigma\sigma} = 3$ channel, one can use the state,

$$|I_{\sigma\sigma\sigma} = 3\rangle = |\sigma^+\sigma^+\sigma^+\rangle. \quad (7.14)$$

The S -matrix for this channel then is,

$$S_{I_{\sigma\sigma\sigma}=3}(\theta_{12}, \theta_{23}, \theta_{31}) = S_{I_{\sigma\sigma}=2}(\theta_{12})S_{I_{\sigma\sigma}=2}(\theta_{23})S_{I_{\sigma\sigma}=2}(\theta_{31}), \quad (7.15)$$

as one could have naively expected since pairwise interactions in this channel can only happen with $I_{\sigma\sigma} = 2$. This result can be used to determine the three-particle scattering amplitude, \mathcal{M}_3 , and the divergence-free K -matrix, $\mathcal{K}_{\text{df},3}$, using a (1+1)-dimensional version of the integral equations presented in sec. 2.1.2.

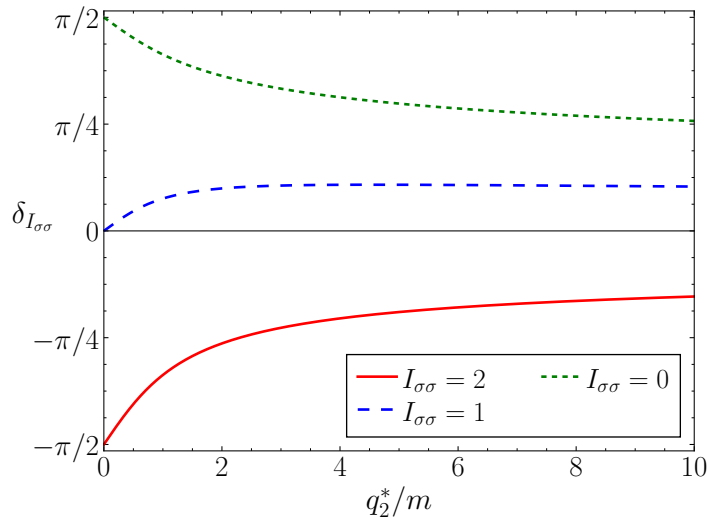


Figure 7.2. Analytic results for the two-particle scattering phase shift in all isospin channels. We focus on the $I_{\sigma\sigma} = 2$ and $I_{\sigma\sigma} = 1$ channels in this work.

7.2 QCs in 1+1 dimensions

Quantization conditions in 1+1 dimensions are derived in a similar way as their (3+1)-dimensional counterparts—see sec. 2.3. The main novelty is related to the absence of angular momentum. Spherical harmonics in eqs. (2.49), (2.56), and (2.58) are substituted by the corresponding functions in one dimension: the identity function for even parity ($p = 0$) and the sign function for odd parity ($p = 1$),

$$Y_p(\mathbf{q}) = \begin{cases} 1, & \text{even parity,} \\ \text{sign}(\mathbf{q}) = \mathbf{q}/|\mathbf{q}|, & \text{odd parity,} \end{cases} \quad (7.16)$$

where we indistinctly use \mathbf{q} to refer to the single-component spacial momentum vector and the component itself. In addition, infinite-volume integrals and finite-volume sums in eqs. (2.49) and (2.56) now run only over one spacial dimension. In the case of the finite volume and working with periodic boundary conditions, momenta sums run over the finite-volume set,

$$\mathbf{q} = \frac{2\pi}{L}\mathbf{n}, \quad (7.17)$$

where $\mathbf{n} \in \mathbb{Z}$ and L is the spacial size of the lattice.

7.2.1 Two-particle formalism

The two-particle formalism, introduced in sec. 2.3.1, is vastly simplified in the (1+1)-dimensional world [332]. The F geometric factor takes the form,

$$\tilde{F}(P, L)_{p'p} = \left[\frac{1}{L} \sum_{\mathbf{k}} -\text{PV} \int \frac{d\mathbf{k}}{2\pi} \right] \frac{Y_{p'}(\hat{\mathbf{k}}^*) Y_p^*(\hat{\mathbf{k}}^*)}{8\omega_{\mathbf{k}} \omega_{P\mathbf{k}} (E - \omega_{\mathbf{k}} - \omega_{P\mathbf{k}})} \left(\frac{k^*}{q_2^*} \right)^{p'+p}, \quad (7.18)$$

where, recall, $P = (E, \mathbf{P})$ is the total momentum, q_2^* is the magnitude of the relative momentum in the CMF and k^* is the magnitude of \mathbf{k} boosted to the CMF. Also, $\omega_{\mathbf{k}}$ and $\omega_{P\mathbf{k}}$ are defined in eq. (2.50), and p and p' denote the parity of the initial and final state, respectively.

A priori, this is a 2×2 matrix in parity space. However, note that $F_{01} = F_{10} = 0$ as they have an odd integrand. Moreover, $F_{00} = F_{11}$ up to exponentially suppressed volume effects, which we neglect. The remaining F_{00} coefficient can be analytically evaluated [332],

$$F(P, L)_{00} = \frac{\rho(s)}{2} \left\{ \cot \left[\frac{L\gamma(q_2^* + \omega_q^* \beta)}{2} \right] + \cot \left[\frac{L\gamma(q_2^* - \omega_q^* \beta)}{2} \right] \right\}. \quad (7.19)$$

Here, $\omega_q^* = E^*/2 = \sqrt{q_2^{*2} + m^2}$ is the single-particle energy in the CMF, with $E^* = \sqrt{s}$ the total energy in the CMF, and $\beta = \mathbf{P}/E$ and $\gamma = E/E^*$ are the boost factors to that frame.

The result in eq. (7.19) can be combined with eq. (7.12), so the two-particle QC, given in eq. (2.51), becomes an algebraic relation [332],

$$\cot \delta(s) + \frac{1}{2} \left\{ \cot \left[\frac{L\gamma(q_2^* + \omega_q^*\beta)}{2} \right] + \cot \left[\frac{L\gamma(q_2^* - \omega_q^*\beta)}{2} \right] \right\} = 0. \quad (7.20)$$

This QC was first worked out for $\mathbf{P} = 0$ in ref. [114], in which case it takes the simple form

$$2\delta(s) = -q_2^*L \pmod{2\pi}. \quad (7.21)$$

7.2.2 RFT Three-particle formalism

To study three-particle interactions in the $O(3)$ model, we adapt the RFT formalism to the (1+1)-dimensional world. Contrary to the two-particle case, the RFT formalism does not simplify to an algebraic relation in 1+1 dimensions, but is still a matrix equation of the form of eq. (2.59). Recall we describe three-particle states as composed of a spectator and a two-particle dimer. The different quantities appearing in the (1+1)-dimensional QC are matrices in the momenta of the initial and final spectator, as well as the parity—instead of its angular momentum—and the two-particle isospin of the dimer. As we have commented above, different two-particle channels project to a single parity sector, and so the last two indices are redundant.

The main two building blocks of the three-particle QC that need to be modified in 1+1 dimensions are \tilde{F} and G , introduced in eqs. (2.56) and (2.58), respectively. $\tilde{\mathcal{K}}_2$ takes the same form as in eq. (2.57), with the phase-space factor being that in eq. (7.13), while $\mathcal{K}_{\text{df},3}$ is still a dense matrix in all indices.

We consider first the case of three identical particles; the extension to general isospin will be discussed below. The (1+1)-dimensional \tilde{F} factor is defined in a very similar way to eq. (7.18), with the main difference being the appearance of some factors of the cutoff, $H(x)$, introduced in eq. (2.17)

$$F(P, L)_{\mathbf{k}'p', \mathbf{k}p} = \delta_{\mathbf{k}'\mathbf{k}} H(x_k) \left[\frac{1}{L} \sum_a -\text{PV} \int \frac{da}{2\pi} \right] \times \frac{Y_{p'}(\hat{\mathbf{a}}^*) Y_p^*(\hat{\mathbf{a}}^*) H(x_a) H(x_{ka})}{8\omega_k \omega_{Pk} (E - \omega_k - \omega_{Pk})} \left(\frac{a^*}{q_2^*} \right)^{p'+p}, \quad (7.22)$$

where recall \mathbf{a}^* indicates the momentum of one of the dimer particles in their CMF, a^* is the magnitude of this vector, and we define $x_a = (P - a)^2/4m^2$,

$x_k = (P - k)^2/4m^2$ and $x_{ka} = (P - k - a)^2/4m^2$. The two factors of H with \mathbf{a} -dependent arguments, however, take only values different from one for non-singular values of the integrand, and so setting them to one everywhere only introduces exponentially suppressed volume effects, that we neglect. Thus, we can use eq. (7.19) to write,

$$\tilde{F}(P, L)_{\mathbf{k}'p'; \mathbf{k}p} = \delta_{\mathbf{k}'\mathbf{k}} \delta_{p'p} H(x_k) F(P - k, L)_{00}. \quad (7.23)$$

The G factor is also modified, although its final form remains essentially the same as in 3+1 dimensions,

$$G(P, L)_{\mathbf{k}'p'; \mathbf{k}p} = \frac{1}{4\omega_k \omega_p L} \left(\frac{k_{k'}^*}{q_{2,k'}^*} \right)^{p'} \frac{Y_{p'}(\hat{\mathbf{k}}_{k'}^*) H(x_{k'}) H(x_k) Y_p(\hat{\mathbf{k}}_k^*)}{b^2 - m^2} \left(\frac{k_k'^*}{q_{2,k}^*} \right)^p, \quad (7.24)$$

where recall $k_{k'}^*$ refers to the magnitude of the spectator momentum, \mathbf{k} , in the rest frame of the dimer associated to a spectator of momentum \mathbf{k}' , and $q_{2,k}^*$ is the magnitude of the momentum of the interacting pair associated to a spectator of momentum \mathbf{k} in its CMF, and similarly for $k_k'^*$ and $q_{2,k'}^*$. Also $x_{k'}$ is defined similarly to x_k .

These quantities can be used to construct F_3 as in 3+1 dimensions—see eq. (2.55). The three-particle QC, eq. (2.59), makes it possible to either constrain the values of $\mathcal{K}_{\text{df},3}$ from the finite volume energies, or to predict the finite-volume spectrum from an analytic result of $\mathcal{K}_{\text{df},3}$.

A particularly useful exercise is the determination of the three-particle finite-volume spectrum assuming $\mathcal{K}_{\text{df},3} = 0$. In this case, the QC simplifies,

$$\det [\tilde{\mathcal{K}}_2^{-1} - \tilde{F} - G] = 0. \quad (7.25)$$

A comparison of such predictions, obtained using the scattering matrices in eq. (7.10), to lattice results for the finite-volume energies would provide insight on whether $\mathcal{K}_{\text{df},3} = 0$ in the O(3) model. A priori, one may believe this to be the case, as factorization implies three-particle scattering is the result of successive two-particle interactions. However, the integral equations relating the scattering amplitude to $\mathcal{K}_{\text{df},3}$ —see sec. 2.1.2—may not preserve the factorization property. This highlights the unphysical nature of $\mathcal{K}_{\text{df},3}$, as it may take non-zero values even in the absence of short-range three-particle interactions. This comparison is presented in sec. 7.5.2 below.

The extension of the RFT formalism to general isospin follows the same lines in 3+1 and 1+1 dimensions [182]. All variables of the formalism become matrices in flavor space, and we use boldface to refer to them. In the symmetric basis, defined in eq. (6.4), they are block diagonal in the different

isospin channels, each block having a size equal to the possible two-particle channels in which pairwise interactions can occur.

Both $\tilde{\mathbf{K}}_2$ and $\tilde{\mathbf{F}}$ are diagonal within each three-particle isospin block, with the latter taking the value corresponding to the two-particle isospin of the corresponding state. For example, in the $I_{\sigma\sigma\sigma} = 2$ channel,

$$\tilde{\mathbf{K}}_2^{I_{\sigma\sigma\sigma}=2} = \begin{pmatrix} \tilde{\mathcal{K}}_2^{I_{\sigma\sigma}=2} & 0 \\ 0 & \tilde{\mathcal{K}}_2^{I_{\sigma\sigma}=1} \end{pmatrix}. \quad (7.26)$$

The \mathbf{G} term, on the other hand, is a dense matrix within the block, with all its elements equal to eq. (7.24) multiplied by some factor related to Clebsch-Gordan coefficients. For the three channels on which we focus,

$$\mathbf{G}^{I_{\sigma\sigma\sigma}=3} = G = -\mathbf{G}^{I_{\sigma\sigma\sigma}=0}, \quad \mathbf{G}^{I_{\sigma\sigma\sigma}=2} = \frac{G}{2} \begin{pmatrix} -1 & -\sqrt{3} \\ -\sqrt{3} & 1 \end{pmatrix}, \quad (7.27)$$

Finally, $\mathbf{K}_{\text{df},3}$ is also dense within each block, and can be expanded around threshold for each three-particle isospin channel as presented in sec. 6.1.4.

Before moving on, a final comment is in order. When obtaining predictions for the finite-volume energies in the rest frame, $\mathbf{P} = 0$, one needs to separate between parity-even and parity-odd states. The building blocks in the QC can be block-diagonalized in these two sectors, which can therefore be studied separately.

Consider the basis of matrices in which the building blocks of the QC live, which is just the external product of two analogous basis for the initial and final state, defined for a fixed total energy. For the former, for example, such a base is composed of states $|\mathbf{k}, p\rangle$ with spectator momentum \mathbf{k} in the finite-volume set, eq. (7.17), and dimer parity p . Remember the parity of the dimer and its isospin are completely redundant, and so we do not indicate the latter one.

In the rest frame, the spectator momentum runs from $-\mathbf{k}_{\text{max}}$ to \mathbf{k}_{max} , where \mathbf{k}_{max} is the highest momentum such that $H(x_{k_{\text{max}}}) > 0$. States with $\mathbf{k} \neq 0$ can be grouped into pairs $(|-\mathbf{k}, p\rangle, |\mathbf{k}, p\rangle)^\top$, which can then be rotated to definite three-particle parity-even and -odd sectors,

$$\begin{pmatrix} |\mathbf{k}, \text{even}\rangle \\ |\mathbf{k}, \text{odd}\rangle \end{pmatrix} = \frac{1}{\sqrt{2}} \begin{pmatrix} 1 & (-1)^p \\ -1 & (-1)^p \end{pmatrix} \begin{pmatrix} |-\mathbf{k}, p\rangle \\ |\mathbf{k}, p\rangle \end{pmatrix}. \quad (7.28)$$

States with $\mathbf{k} = 0$ are intrinsically even or odd, depending on the parity of the dimer. For example, for the $I_{\sigma\sigma\sigma} = 3$ channel the $\mathbf{k} = 0$ state is even, as dimer interactions happen with $I_{\sigma\sigma} = 2$.

7.3 Lattice setup

Two- and three-particle finite-volume energies are determined using numerical lattice simulations. We employ the standard discretized Euclidean action,

$$S_E[\boldsymbol{\sigma}] = -\frac{\beta}{2} \sum_{x \in \Lambda} \sum_{\mu} \boldsymbol{\sigma}(x) \cdot \boldsymbol{\sigma}(x + a\hat{\boldsymbol{\mu}}), \quad (7.29)$$

where $x = (t, \mathbf{x})$ denotes a site of the (1+1)-dimensional lattice, Λ , with time and spacial extent T and L , respectively, and a is the lattice spacing. Also $\hat{\boldsymbol{\mu}}$ is a unit vector in the direction μ .

7.3.1 Single- and three-cluster algorithms

To generate configurations and evaluate single- and multi-particle correlation functions we use a cluster algorithm. This is a collective update algorithm applicable to spin systems that overcomes critical slowing down—this is, the exponential increase of autocorrelation times, especially in topological observables, as one approaches the continuum—and, when used to measure correlation functions, improves the signal to noise ratio [333–338]. It was first proposed in ref. [334] for a single cluster, and then generalized to two clusters in ref. [114] to study two-particle correlation functions. In this work, we further generalize it to three clusters to be able to investigate three-particle interactions.

Beginning with the single-cluster algorithm, consider a field configuration composed by a set of spins, $\boldsymbol{\sigma}(x) \in S^2$, in every lattice site, $x \in \Lambda$. To update the configuration, we choose a random unit vector $\mathbf{r} \in S^2$ and a “seed” lattice site. From this site, a cluster, C_r , is grown: for each site $x \in C_r$, we consider all of its non-cluster nearest neighbors, $y \notin C_r$, which are added to the cluster with probability,

$$p_{\text{add}} = 1 - \exp \{ \min [-2\beta\sigma_r(x)\sigma_r(y), 0] \}, \quad (7.30)$$

where $\sigma_r(x) = \mathbf{r} \cdot \boldsymbol{\sigma}(x)$. This process is repeated for each added site and non-rejected neighbors until all neighbors have been considered. Then, the configuration is updated by modifying all spins in C_r ,

$$\boldsymbol{\sigma}(x) \rightarrow \boldsymbol{\sigma}(x) - 2\sigma_r(x)\mathbf{r}. \quad (7.31)$$

The cluster can also be used to obtain improved estimators of single-particle correlation functions with reduced noise. The idea is to define

fixed-time interpolators with definite momentum by projecting only within the cluster,

$$\boldsymbol{\sigma}^{C_r}(t, \mathbf{p}) = \sum_{x \in C_r(t)} \boldsymbol{\sigma}(x) e^{i\mathbf{p}x}, \quad (7.32)$$

where $C_r(t)$ denotes all sites in C_r with time coordinate t . This field is then used to compute the desired result,

$$C_{2\text{pt}}(t, \mathbf{p}) = \langle \boldsymbol{\sigma}^{C_r}(t, \mathbf{p}) \cdot \boldsymbol{\sigma}^{C_r^*}(0, \mathbf{p}) \rangle = 3 \langle \sigma_r^{C_r}(t, \mathbf{p}) \sigma_r^{C_r^*}(0, \mathbf{p}) \rangle, \quad (7.33)$$

where we have used that the theory is invariant under global rotations of the spins. Here $\langle \cdot \rangle$ indicates that we average over multiple configurations, and also use time-translation invariance to average over multiple equivalent time separations. The single-particle correlation function with $\mathbf{p} = 0$ can then be used, for example, to extract the single particle mass, as explained in sec. 1.2.3.

It is worth discussing why the use of this algorithm improves the signal-to-noise ratio. To make it more clear, we consider an alternative update algorithm in which, instead of using one single cluster, we cover the full lattice with N_{cl} non-overlapping clusters, $C_{r,i}$, such that

$$\Lambda = \bigcup_{i=1}^{N_{\text{cl}}} C_{r,i}, \quad \bigcap_{i=1}^{N_{\text{cl}}} C_{r,i} = \emptyset. \quad (7.34)$$

These clusters are generated in succession using the same vector \mathbf{r} and “seed” sites chosen from the sites not belonging to any of the already generated clusters. The configuration is updated by flipping each of the cluster as in eq. (7.31) with probability 1/2. Thus, this process may lead to $2^{N_{\text{cl}}}$ possible updated configurations, all with the same probability.

Naively, the single-particle correlator is computed using single-particle operators projected over the whole time slice,

$$C_{2\text{pt}}(t, \mathbf{p}) = 3 \sum_{\mathbf{y} \in \Lambda(t)} \sum_{\mathbf{x} \in \Lambda(0)} e^{-i\mathbf{p}(\mathbf{x}-\mathbf{y})} \langle \sigma_r(\mathbf{y}) \sigma_r(\mathbf{x}) \rangle, \quad (7.35)$$

which is averaged over multiple realizations of the field. In particular, consider the average of over all $2^{N_{\text{cl}}}$ possible configurations resulting from the updating step described above. Within each cluster, σ_r has always the same sign, while spins in different clusters appear with equal and opposite signs an equal number of times in this set of configurations. Therefore, contributions where x and y belong to different clusters average to zero, and only lead to higher variances. In eq. (7.33), instead, we only sum over a single cluster, avoiding variance increases. The single-cluster algorithm is a simplification of this update process, in which we only generate and update one cluster, which is used to measure observables.

We note, however, that even for single-cluster observables there is still a grow in the uncertainty at long ranges. This responds to the finite-size of the clusters. Clusters grow up to a size of order the correlation length, m^{-1} , and non-zero measurements for longer time separations are scarce.

As one can observe from eq. (7.33), the single-cluster algorithm is suitable to study single-particle correlation functions, but not multiparticle states. In ref. [114], the algorithm was generalized to two clusters and in this work we extend it to three. The basic idea of the three-cluster algorithm is to choose three random orthonormal vectors, uniformly sampled from the unit sphere, $\mathbf{r}, \mathbf{u}, \mathbf{v} \in S^2$, so that $\mathbf{r}^2 = \mathbf{u}^2 = \mathbf{v}^2 = 1$ and $\mathbf{r} \cdot \mathbf{u} = \mathbf{u} \cdot \mathbf{v} = \mathbf{v} \cdot \mathbf{r} = 0$. After drawing the three vectors, one also randomly selects three (not-necessarily different) “seed” sites, which are used to grow three independent clusters, C_r, C_u and C_v , following the same procedure as in the single cluster case. The three cluster are allowed to overlap, and we also note that their growth does not interfere with each other, due to the orthogonality of the vectors. The clusters are finally updated following eq. (7.31) and used to measure cluster-improved versions of the correlation functions of interest.

Any of the three clusters alone can be used to measure the single-particle correlation functions as in eq. (7.33), while correlation functions of two and three particles require the use of two and three clusters, respectively. The relevant two- and three-particle correlation functions needed to study the channels of interest, called A_i ($i = 1, 2$) and B_j ($j = 1..6$), are presented in fig. 7.3. Two examples of how they are evaluated using the clusters are

$$\begin{aligned} A_3 &\propto \langle \sigma_r^{C_r}(\tau, \mathbf{p}_2) \sigma_u^{C_u}(\tau, \mathbf{p}_1) \sigma_u^{C_u*}(0, \mathbf{k}_2) \sigma_r^{C_r*}(0, \mathbf{k}_1) \rangle . \\ B_2 &\propto \langle \sigma_r^{C_r}(\tau, \mathbf{p}_3) \sigma_u^{C_u}(\tau, \mathbf{p}_2) \sigma_v^{C_v}(\tau, \mathbf{p}_1) \sigma_r^{C_r*}(0, \mathbf{k}_3) \sigma_v^{C_v*}(0, \mathbf{k}_2) \sigma_u^{C_u*}(0, \mathbf{k}_1) \rangle , \end{aligned} \quad (7.36)$$

where \mathbf{k}_i refers to the momenta of initial-state particles while \mathbf{p}_i refers to final state ones. The normalization of these correlation functions is not relevant for this work, as it does not affect the determination of the finite-volume energies. Note that none of the correlation functions computed in this work contains equal-time correlators. This means that their evaluation requires all two or three clusters to overlap in time. In the practice, the measurements need to be averaged over a large number of configurations. Correlation functions with equal-time contractions could be measured without this limitation, but they do not benefit from the noise reduction.

Finally, we highlight that the study of interactions of four or more particles in the O(3) model would not profit of the use of cluster-improved estimators. For this model, only three orthogonal directions can be defined and so one is limited to three independent clusters. One, however, could generalize the cluster algorithm for other O(N) models with $N > 3$.

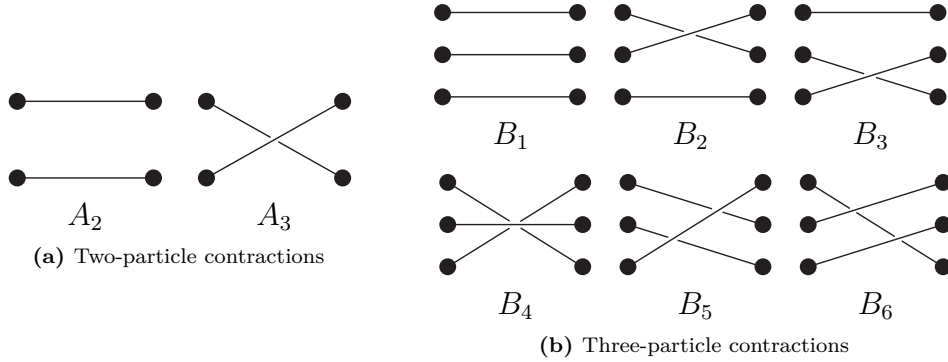


Figure 7.3. Diagrammatic representation of the Wick contractions needed for the computation of two- and three-particle correlation functions in this work. Initial and final states are represented at the right and left of the diagrams, respectively, and the corresponding momenta are $\{k_i\}$ and $\{p_i\}$, assigned to the vertices in order from top to bottom.

7.3.2 Two- and three-particle correlation functions

In this work, we focus on the isospin-two and -one channels for two particles and the isospin-three, -two and -zero channels for three particles. The corresponding correlations functions can be evaluated as a linear combination of different Wick contractions that contain no product of fields evaluated at equal times, represented diagrammatically in fig. 7.3. In the case of two particles,

$$\begin{aligned} C_{I_{\sigma\sigma}=2} &= A_2 - A_3, \\ C_{I_{\sigma\sigma}=1} &= A_2 + A_3. \end{aligned} \quad (7.37)$$

Three-particle correlation functions, on the other hand, are matrices in flavor space, with a multiplicity equal to that of the isospin channel. Isospin-three and -zero channels are one-dimensional, with correlation function

$$\begin{aligned} C_{I_{\sigma\sigma}=3} &= B_1 + B_2 + B_3 + B_4 + B_5 + B_6, \\ C_{I_{\sigma\sigma}=0} &= B_1 - B_2 - B_3 - B_4 + B_5 + B_6. \end{aligned} \quad (7.38)$$

The isospin-two channel, having multiplicity two, is more complicated. We work in the isospin basis, introduced in eq. (6.2), and let the two first particles of the states—the two upper dots in each state in fig. 7.3b—represent the dimer. The $I_{\sigma\sigma} = 2$ correlation function then takes the form

$$C_{I_{\sigma\sigma}=2} = \begin{pmatrix} C_{2,2} & C_{2,1} \\ C_{1,2} & C_{1,1} \end{pmatrix}, \quad (7.39)$$

where $C_{i,j}$ is the correlation function for a $I_{\sigma\sigma} = 2$ state where the initial and final dimer have two-particle isospin j and i , respectively,

$$\begin{aligned}
C_{2,2} &= B_1 + B_2 - \frac{1}{2}B_3 - \frac{1}{2}B_4 - \frac{1}{2}B_5 - \frac{1}{2}B_6, \\
C_{2,1} &= \frac{\sqrt{3}}{2} (B_3 - B_4 + B_5 - B_6), \\
C_{1,2} &= \frac{\sqrt{3}}{2} (B_3 - B_4 - B_5 + B_6), \\
C_{1,1} &= B_1 - B_2 + \frac{1}{2}B_3 + \frac{1}{2}B_4 - \frac{1}{2}B_5 - \frac{1}{2}B_6.
\end{aligned} \tag{7.40}$$

Note that, if one chooses the two last particles of the state to form the dimer, for example, the correlation function would be different, but will be related to the one in eq. (7.39) by a rotation of the basis.

To extract the finite-volume spectrum, we determine the correlation functions over a set of two- and three-particle operators characterized by different choices of momenta, $\sigma(\mathbf{q}_1)\sigma(\mathbf{q}_2)$ and $\sigma(\mathbf{q}_1)\sigma(\mathbf{q}_2)\sigma(\mathbf{q}_3)$, respectively. We consider total-momentum frames $\mathbf{P} = 0, 1, 2$ and 3 , in units of $2\pi/L$, and use all possible combinations of momenta so that the corresponding free energies in the CMF lie below $4m$ for two particles and $5m$ for three. Although no particle production occurs in the O(3) model, as discussed in sec. 7.1.1, we choose these values as our upper cutoffs. Therefore, we are only able to reliably extract the finite-volume energy below these limits.

Note that not every operator with arbitrary momenta can be projected to every isospin channel. In the case of two particles, operators with $\mathbf{q}_1 = \mathbf{q}_2$ do not project to the $I_{\sigma\sigma} = 1$ channel, which is antisymmetric under particle exchange. A similar thing happens in the three-particle isospin-zero channel, which is fully antisymmetric under particle exchange. In this case, only operators with all three momenta different have non-zero projection.

The $I_{\sigma\sigma} = 2$ case is more complicated, as it contains states in which the dimer has isospin two or one. Those states with all three momenta equal, $\mathbf{q}_1 = \mathbf{q}_2 = \mathbf{q}_3$, do not project to any of the two subchannels. States with two identical momenta only project to a single state. If $\mathbf{q}_1 = \mathbf{q}_2 \neq \mathbf{q}_3$, this is the state with an isospin-two dimer. Otherwise, both $I_{\sigma\sigma} = 2$ and $I_{\sigma\sigma} = 1$ states can be constructed, but turn out to be proportional once one takes into account the transformation properties of the states.

Finally, we can also comment on three-particle states with zero total momentum, which can be projected to even or odd parity, or both. In the isospin-three channel, all operators project to even parity, but only those having all three momenta different from zero project to the odd sector. In the isospin-zero channel, the contrary situation happens. Lastly, in the isospin-two channel all operators can be projected to both sectors.

7.3.3 Lattice simulations

Numerical simulations are performed using the `o3_cluster` code, an early version of which was shared with us by J. Bulava [339]. We generate a total of 12 ensembles, with four values of mL , each at three lattice spacings, corresponding to different choices of β . Both L and T are finely tuned to be able to extrapolate the finite-volume energies directly to the continuum. We set $mL > 6$ in all ensembles, so that exponentially suppressed finite-volume effects are negligible, and also $mT \sim 20.4$ to be safe of thermal effects. The parameters used for the simulations, together with the result for the single-particle masses, are presented in table 7.1 and summarized in fig. 7.4.

We generate $N_{\text{rep}} = 256, 512$ and 1024 replicas, for the coarsest, intermediate and finest ensembles, respectively. In all cases, the lattices are randomly initialized and we perform 12.8×10^6 thermalizing three-cluster updates. Following these, we measure the relevant correlation functions over $N_{\text{meas}} = 4 \times 10^6, 2 \times 10^6$ and 10^6 successive updates for the coarsest, intermediate and finest ensembles, respectively. Results are averaged over each replica, and we use jackknife for the analysis.

Ensemble	$L \times T$	β	am	mL
A1	140×463	1.63	0.0442101(28)	6.1894(4)
A2	242×801	1.72	0.0255795(13)	6.1902(3)
A3	353×1169	1.78	0.0175327(9)	6.1891(3)
B1	203×464	1.63	0.0441608(28)	8.9646(5)
B2	351×802	1.72	0.0255473(15)	8.9671(5)
B3	512×1170	1.78	0.0175109(9)	8.9656(5)
C1	280×464	1.63	0.0441573(25)	12.3640(7)
C2	484×802	1.72	0.0255503(13)	12.3664(6)
C3	706×1170	1.78	0.0175095(10)	12.3617(7)
D1	339×464	1.63	0.044159(3)	14.9699(10)
D2	586×802	1.72	0.0255486(16)	14.9715(9)
D3	855×1170	1.78	0.0175092(9)	14.9704(8)

Table 7.1. Summary of the parameters used for the lattice simulations, together with the results for the mass.

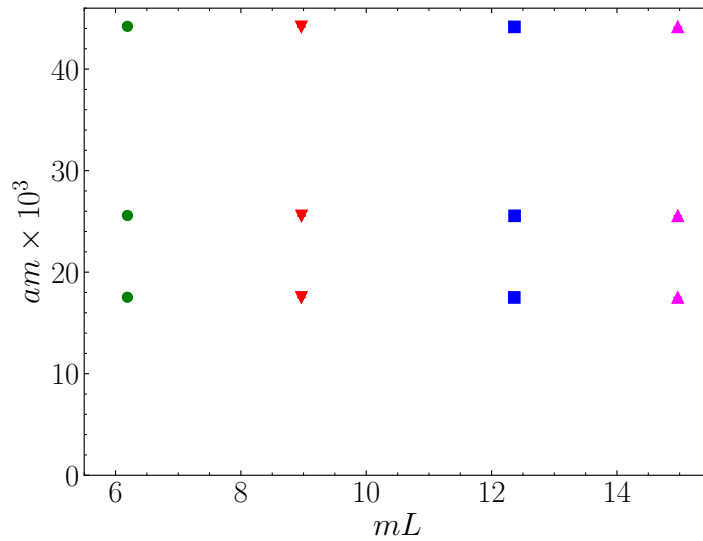


Figure 7.4. Summary of the simulations used in this work. All have $mT \approx 20.4$ to avoid thermal effects.

7.4 Results for finite-volume energies

Two- and three-particle matrices of correlators are used to solve a GEVP—see eq. (1.54)—using the single-pivot approach described in sec. 4.2. The resulting eigenvalues are fitted to a single exponential,

$$\lambda_n(t) = Ae^{-E_n t}, \quad (7.41)$$

to extract the finite-volume energies. This fit is repeated for different fit ranges, $t \in [t_{\min}, t_{\max}]$, with varying t_{\min} and fixed t_{\max} , and the results are averaged using the weights given in eq. (1.51). In most cases, the weighted average lies where the results show a plateau, although in some other cases we need to restrict the range over which t_{\min} is allowed to vary. Two examples of the fit results are shown in fig. 7.5. We observe that our results are stable under changes of t_{\max} , t_0 and t_d , introduced in eq. (4.19). This is shown in fig. 7.6 for the $I_{\sigma\sigma\sigma} = 3$ energies in the C1 ensemble, observing in general very minor variations.

We also study the stability of our results under a change on the set of operators used to compute the matrix of correlation functions. We observe a negligible dependence of the states of interest on the inclusion of operators with large associated free energy.

More interesting is to investigate, in the case of the $I_{\sigma\sigma\sigma} = 2$ channel, the effect of operators in which the dimer is projected to $I_{\sigma\sigma} = 2$ or $I_{\sigma\sigma} = 1$. In fig. 7.7, we compare the finite-volume energies obtained using the full

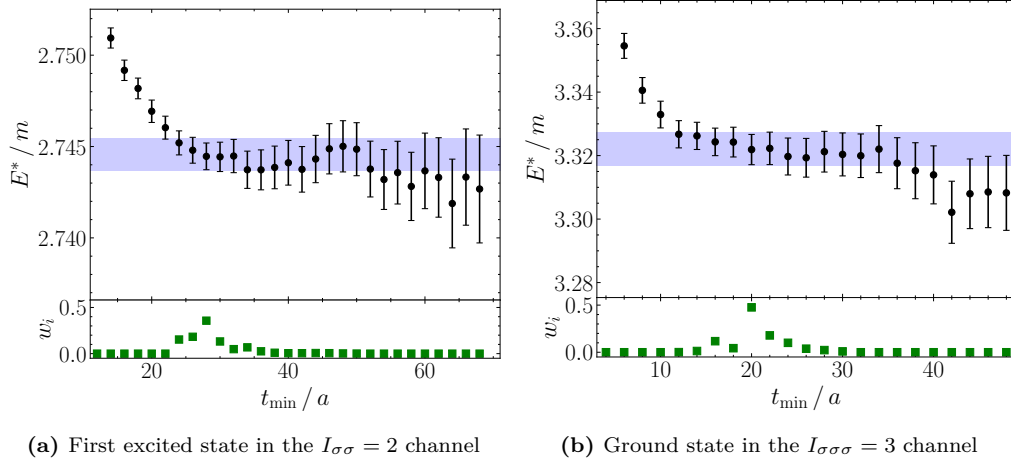


Figure 7.5. Best-fit results to a single exponential of one of the generalized eigenvalues, λ_n , of the correlation matrix of the two-particle isospin-two channel (left) and three-particle isospin-three channel (right). Both cases correspond to the rest-frame and the B1 ensemble. Fits are performed with varying t_{\min} and fixed t_{\max} and the final result is obtained by averaging the results using weights based on the Akaike Information Criterion—see eq. (1.51)—presented in the lower panels.

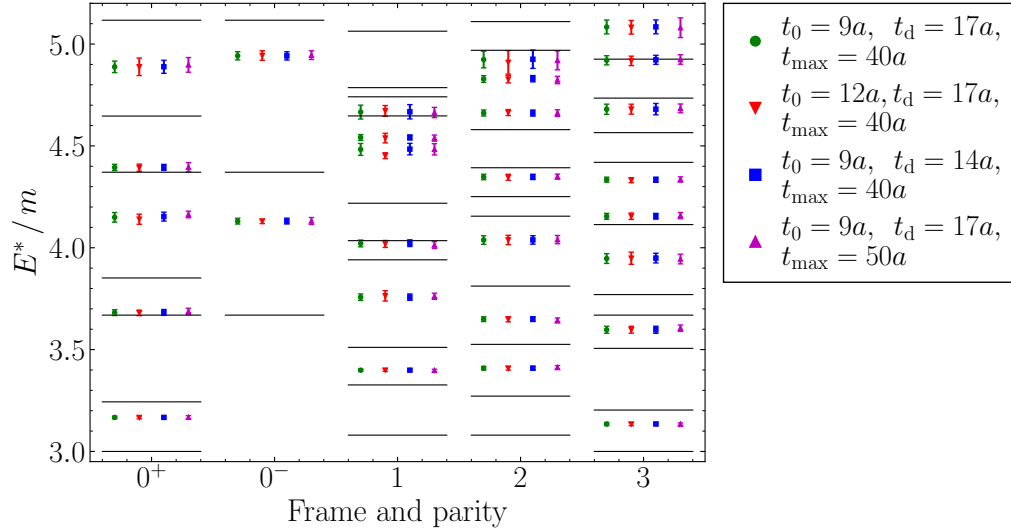


Figure 7.6. Comparison of the finite-volume energies for the $I_{\sigma\sigma\sigma} = 3$ channel in the C1 ensemble for different choices of the parameters used for the analysis. We observe variations differences between different choices of the parameters.

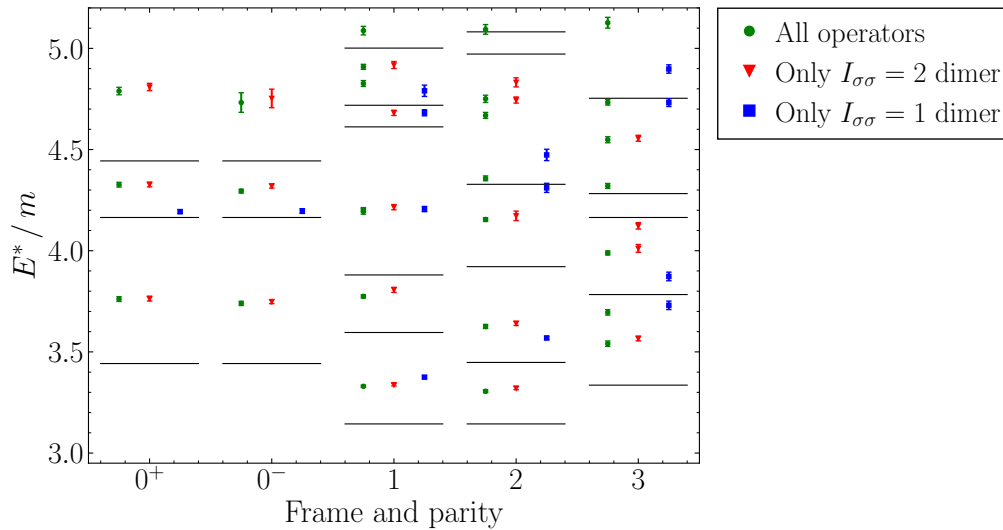


Figure 7.7. Comparison of the finite-volume energies for the $I_{\sigma\sigma\sigma} = 2$ channel in the B1 ensemble determined using different sets of operators to compute the matrix of correlators.

correlation matrices (green dots) to those that are obtained if we only use operators in which the dimer is in the isospin-two (red triangles) or isospin-one (blue squares) channel. We observe major differences between the determined spectra. This, however, was to be expected, as selecting the first two particles as the dimer is an arbitrary choice, and a difference selection would lead to operators that are linear combinations of the ones we use. Also note that the combined number of states obtained using only operators with $I_{\sigma\sigma} = 2$ or $I_{\sigma\sigma} = 1$ is larger than the set of states obtained with the full set of operators. This is due to the fact that, for some momenta combinations, operators defined from both values of $I_{\sigma\sigma}$ are proportional.

Using our finely-tuned ensembles, we extrapolate our results for the finite-volume energies directly to the continuum. The O(3) model is well-known to present large logarithmic discretization effects [340, 341]. These have been studied in detail and on-shell quantities, Q , such as finite-volume energies, are known to present the following asymptotic behavior,

$$Q(am) = Q(0) + C\beta^3(am)^2 \left[1 + \sum_{k=1}^{\infty} c_k \beta^k \right] + \mathcal{O}(a^4), \quad (7.42)$$

where C and $c_{\geq 3}$ depend on the particular observable, while c_1 and c_2 are universal for on-shell quantities, and can be computed from two- and three-loop integrals in lattice perturbation theory, respectively. For the standard action in eq. (7.29), they are [341]

$$c_1 = -1.13861509, \quad c_2 = -0.4881, \quad (7.43)$$

where the first is determined analytically, while the second is estimated numerically in ref. [341]. To extrapolate our results to the continuum, we consider only the $k = 1$ and $k = 2$ terms, and fit $Q(0)$ and C for each energy level, using the three available lattice spacings. Two examples of such extrapolations are shown in fig. 7.8.

Our results of the continuum-extrapolated two-particle finite-volume energies are shown in sec. 7.5 in fig. 7.9a and fig. 7.9b for the isospin-two and -one channels, respectively. The results for three particles are shown in fig. 7.12, fig. 7.13 and fig. 7.14 for $I_{\sigma\sigma\sigma} = 3, 2$ and 0 , in this same order. These figures also show the free energies and predictions obtained using the quantization conditions, as discussed in the next section.

Before moving on, though, it is worth commenting about the qualitative strength of the interactions in this model. Looking at the two-particle results in the $I_{\sigma\sigma} = 2$ channel, we observe that in many cases the energy shift with respect to the corresponding free energies is positive and of comparable size to the separation between consecutive free energies. This implies interactions are repulsive and very strong. The isospin-one-channel, on the other hand, is less strongly interacting and attractive.

These conclusions allow us to qualitatively understand the observed spectra in the three-particle case, which is dominated by pairwise interactions, with short-range three-particle interactions having small effect. In the $I_{\sigma\sigma\sigma} = 3$ channel, that contains only $I_{\sigma\sigma} = 2$ pairwise scattering, interactions are repulsive and so strong that finite-volume states have energy shifts larger than the separation between free states. The situation is similar in the

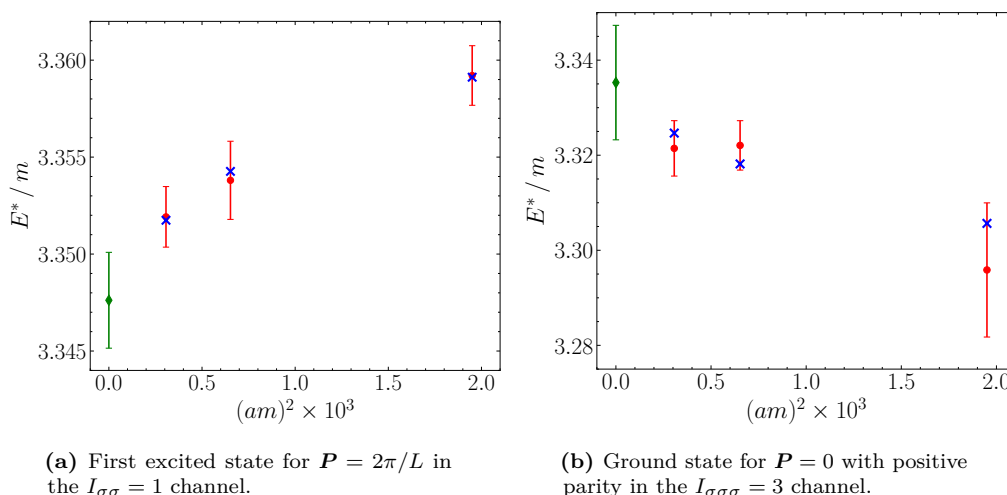


Figure 7.8. Example of continuum extrapolations of finite-volume energies in the B ensembles. Blue crosses represent the best-fit predictions from eq. (7.42) including only $k \leq 2$ terms.

$I_{\sigma\sigma} = 2$ channel, although the interaction strength seem to be somewhat smaller. Note however the presence of a larger number of states below $E^* = 5m$, due to the dimensionality of the channel. Finally, the $I_{\sigma\sigma\sigma} = 0$ shows attractive and not-so-strong interactions, which can be understood since pairwise interactions only happen with $I_{\sigma\sigma} = 1$.

7.5 Comparison to analytical predictions

7.5.1 Two-particle energies

Analytical results for two-particle finite-volume energies can be computed in the O(3) model using the two-particle QC introduced in sec. 7.2.1, together with the analytical predictions of the scattering phase shift in eqs. (7.10) and (7.11). These are shown as solid blue lines in figs. 7.9a and 7.9b, together with the continuum-extrapolated lattice results (red dots). We also indicate, as dashed lines, the non-interacting energies. Finally, note that no inelastic threshold is indicated, since particle production is forbidden in factorizable theories.

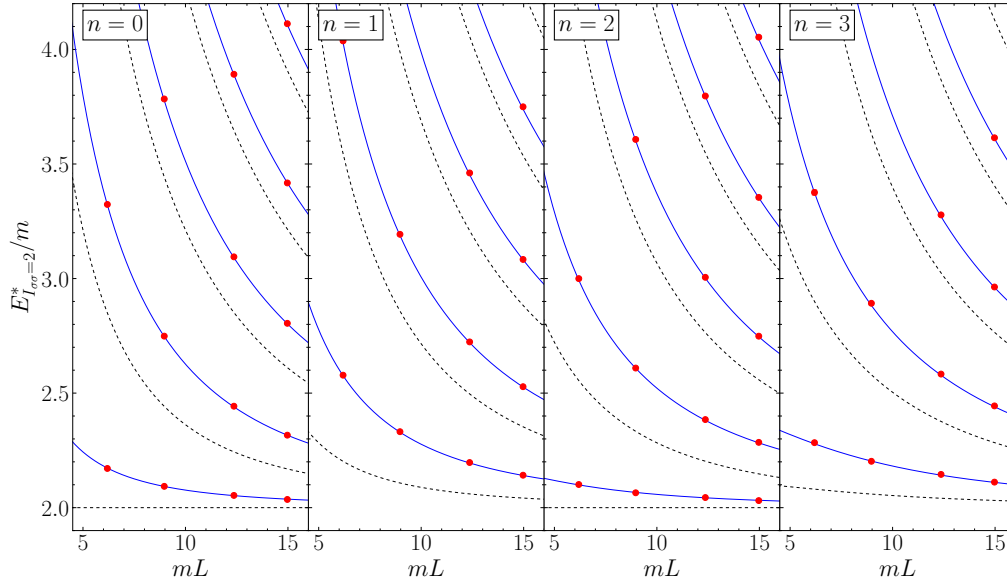
We observe very good agreement between lattice results and numerical predictions. We quantify this by computing the χ^2 between both,

$$\begin{aligned} \chi^2 / \text{dof} &= 54.6 / 47 = 1.16 && (I_{\sigma\sigma} = 2 \text{ channel}), \\ \chi^2 / \text{dof} &= 45.9 / 42 = 1.09 && (I_{\sigma\sigma} = 1 \text{ channel}). \end{aligned} \tag{7.44}$$

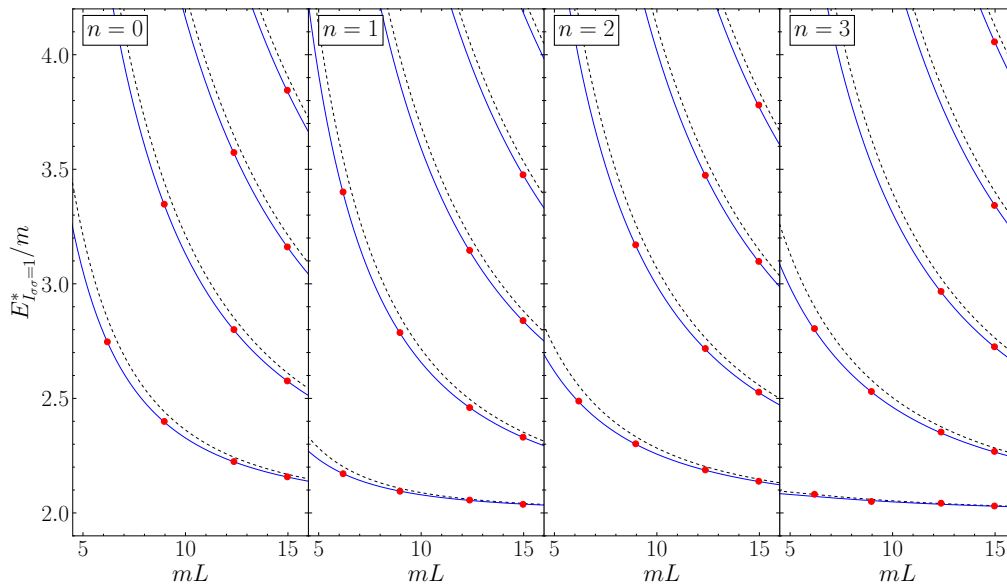
We stress these are not the results from a fit to the lattice, but instead a direct comparison between them and analytical expectations. We also note that states with $E^* > 4m$ are not considered to compute the χ^2 as their energies may not be well determined due to the scarcity of operators associated to free energies above this limit. These results root our confidence on the simulation and analysis procedure used, as described in secs. 7.3 and 7.4.

7.5.2 Three-particle energies

Analytical results for three particles could, a priori, be compared against analytical predictions. In the case of the RFT formalism, this would require first to analytically determine the three-particle K -matrix, $\mathcal{K}_{\text{df},3}$, solving a (1+1)-dimensional version of the integral equations introduced in sec. 2.1.2.



(a) $I_{\sigma\sigma} = 2$ channel



(b) $I_{\sigma\sigma} = 1$ channel

Figure 7.9. Results for the continuum-extrapolated finite-volume energies of two particles. Lattice results (red dots) are represented together with analytical predictions (solid blue lines) and non-interacting energies (dashed black lines). Each panel corresponds to a different momentum frame, with $\mathbf{P} = 2\pi n/L$.

In this work we take a first step in this direction, by comparing our lattice results against predictions obtained under the assumption that $\mathcal{K}_{\text{df},3} = 0$. A priori, this could seem like a reasonable assumption, since three-particle interactions in the O(3) model are the result of successive two-particle scattering. However, as we have already discussed, the factorization property is not preserved by the integral equations, and indeed, the definition of $\mathcal{K}_{\text{df},3}$ depends on the prescription used to remove the divergencies—in the case of the RFT formalism, the choice of the cutoff function. A comparison of the lattice results to $\mathcal{K}_{\text{df},3} = 0$ predictions will thus provide insight on to which extent $\mathcal{K}_{\text{df},3} \neq 0$, and with what statistical significance this can be claimed. Exploring the quantization condition in the simple $\mathcal{K}_{\text{df},3} = 0$ case also allows us to learn about the intricacies of the RFT formalism in a theory with very strong interactions. Recall the applications of the RFT formalism to QCD has been restricted to three-meson systems at maximal isospin, in which interactions are weak.

Obtaining analytical predictions of the finite-volume energies involves solving the QC. Under the assumption that $\mathcal{K}_{\text{df},3} = 0$, this reduces to finding all solutions to eq. (7.25) in the range of energies of interest, in this case $E^* \leq 5m$. A reliable option to use the eigenvalues, λ_n , of $\tilde{\mathcal{K}}_2^{-1} - \tilde{F} - G$. The finite-volume energies correspond to the location of the simple roots of any of the eigenvalues that cross zero from above [181]. We recall that the number of eigenvalues is equal to the size of the matrices in the QC, which is given by the number of possible spectator momenta in the finite-volume set so that $(P - k)^2 > 0$. Thus, the size of the matrices depends on the energy.

We face several complications while finding the solutions to the QC. One of them is related to the lower dimensionality of the system. At large mL , free energies are expected to approach threshold as $E^{\text{free}} \sim (mL)^{-2}$, while the finite-volume energy shifts scale as $\Delta E \sim (mL)^{-1}$ in one spacial dimension—it scales as $\Delta E \sim (mL)^{-3}$ in 3+1 dimensions, see for example eq. (2.53). This means that as one increases mL , interacting energies cross the free energies corresponding to higher states. At these crossing, some elements in \tilde{F} diverge, leading to numerical complications. Another difficulty arises when a solution lies just above from the opening of a new shell, this is, close to an energy where the size of the matrices in the QC is increased. In these cases, we find that the condition number of our matrices becomes large, leading again to numerical issues.

However, probably the most concerning problem we come across is the appearance of unphysical solutions. These show the correct physical properties expected from a solution to the QC, i.e., they are simple zeros of the eigenvalues that cross zero from above [181]. However, they decay faster than free energies with mL and do not converge to any value at large mL .

The full set of solution is presented for varying mL in fig. 7.10. Red lines correspond to the unphysical ones, while the physical ones are indicated as solid blue lines. We also represent the free energies in dashed black.

More interestingly, we find that the unphysical solutions disappear when we change the cutoff function. In fig. 7.10, we also present as blue dots the finite-volume energies obtained using a hard cutoff,

$$H_{\text{hard}}(x_k) = \Theta[(P - k)^2], \quad (7.45)$$

with Θ the Heaviside step function, instead of the standard choice in eq. (2.17), which we call here H_{std} for clarity. Using the hard cutoff, we observe no presence of the unphysical solutions, while the difference in the determination of physical energies is negligible. In fig. 7.11, we present the values of λ_n as a function of the energy for both cutoff choices for the positive-parity rest frame in the isospin-three channel using $mL = 10$. Additional solutions appear when the standard cutoff is used, at energies slightly above the opening of new matrix shells, denoted by the vertical dashed lines. We note that this effect is observed to happen in both the isospin-three and -two channels.

While the hard cutoff function is not smooth, we find it to work well numerically, and opted to use it to determine the predictions for the finite-volume energies. We note that it has already been used to explore analytical continuation of the solutions to the integral equations [179].

Predictions of the finite-volume energies computed using the two-particle amplitudes from eq. (7.10) and assuming $\mathcal{K}_{\text{df},3} = 0$ are presented as blue lines in figs. 7.12 to 7.14 for the isospin-three, -two and -zero channels, respectively. We also present the lattice results (red dots) and the non-interacting energies (black dashed lines). We observe how the finite-volume spectra are qualitatively well reproduced by $\mathcal{K}_{\text{df},3} = 0$ predictions, which only minor deviations.

To quantify the size of these differences, we compute the χ^2 between the predictions and the lattice results with $E^* < 5m$, as the set of operators used to compute correlation matrices only allow us to reliably extract the finite-volume spectrum up to this energy,

$$\begin{aligned} \chi^2 / \text{dof} &= 215.0 / 83 = 2.59 && (I_{\sigma\sigma\sigma} = 3 \text{ channel}), \\ \chi^2 / \text{dof} &= 602.7 / 152 = 3.96 && (I_{\sigma\sigma\sigma} = 2 \text{ channel}), \\ \chi^2 / \text{dof} &= 122.9 / 63 = 1.95 && (I_{\sigma\sigma\sigma} = 0 \text{ channel}). \end{aligned} \quad (7.46)$$

These results, while not showing a strong evidence of a non-zero $\mathcal{K}_{\text{df},3}$, point in that direction. We believe that the agreement with lattice results could

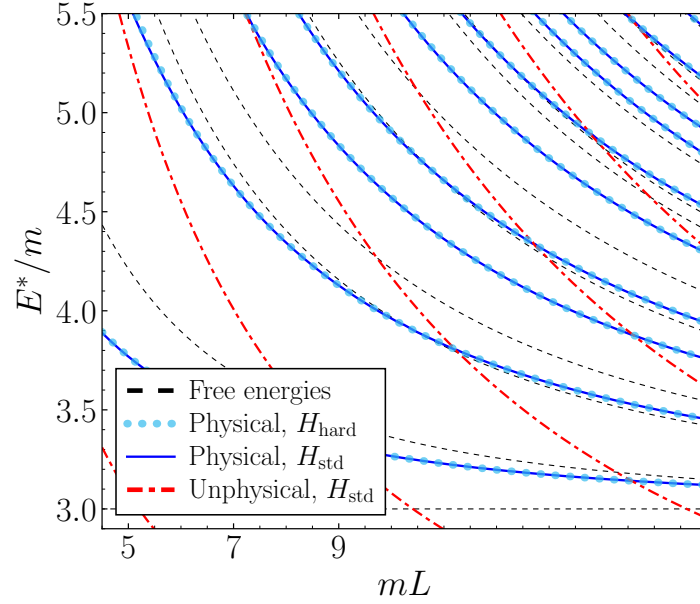


Figure 7.10. Results for the finite-volume energies assuming $\mathcal{K}_{\text{df},3} = 0$ for the $I_{\sigma\sigma\sigma} = 3$ channel in the rest frame with positive parity, obtained using two different cutoff functions. We observe the presence of unphysical solutions (red dashed lines) with the standard cutoff choice, eq. (2.17), which decay faster than expected and do not converge to threshold. Physical results (blue solid lines and dots), on the other hand, show negligible differences between the two cutoff choices.

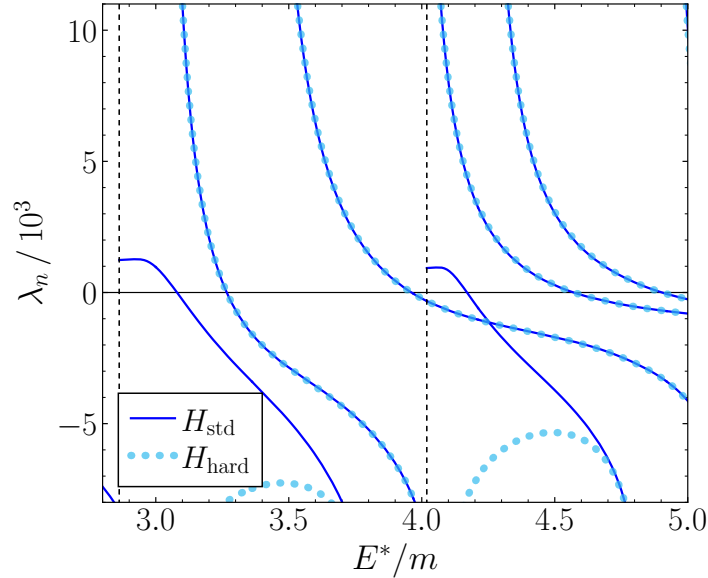


Figure 7.11. Eigenvalues of $\tilde{K}_2^{-1} - \tilde{F} - G$ for the $I_{\sigma\sigma\sigma} = 3$ channel rest frame with positive parity, for $mL = 10$, presented for the standard (blue solid lines) and the hard cutoff (blue dots). Vertical dashed lines indicate the energies at which the size of the matrix is increased.

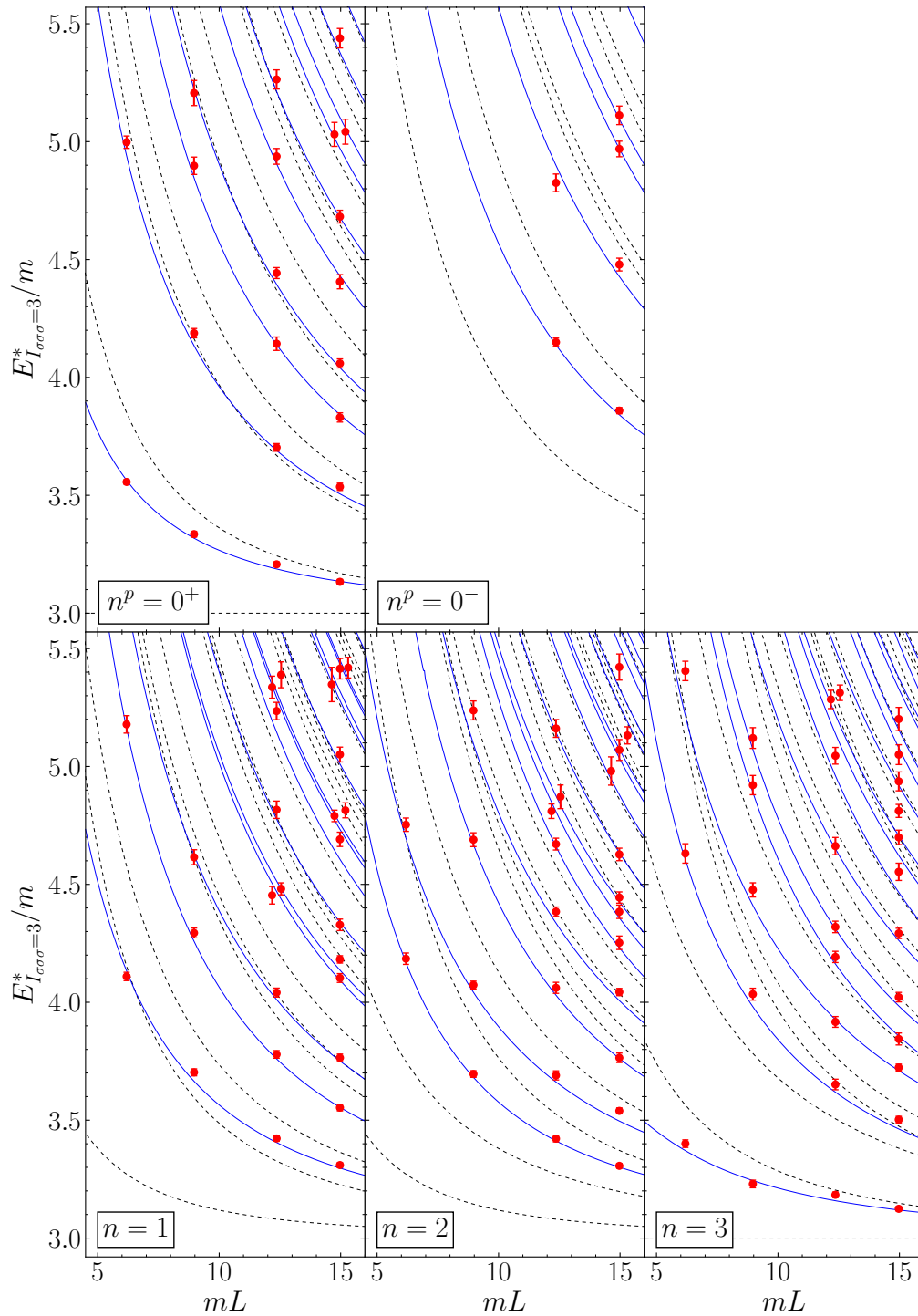


Figure 7.12. Results for the continuum-extrapolated finite-volume energies in the $I_{\sigma\sigma\sigma} = 3$ channel. Lattice results (red dots) are represented together with analytical predictions made assuming $\mathcal{K}_{\text{df},3} = 0$ and using the hard cutoff in eq. (7.45) (solid blue lines), and non-interacting energies (dashed black lines). Each panel corresponds to a different momentum frame, with $\mathbf{P} = 2\pi n/L$. We also present the two parity sectors, p , for the $n = 0$ case.

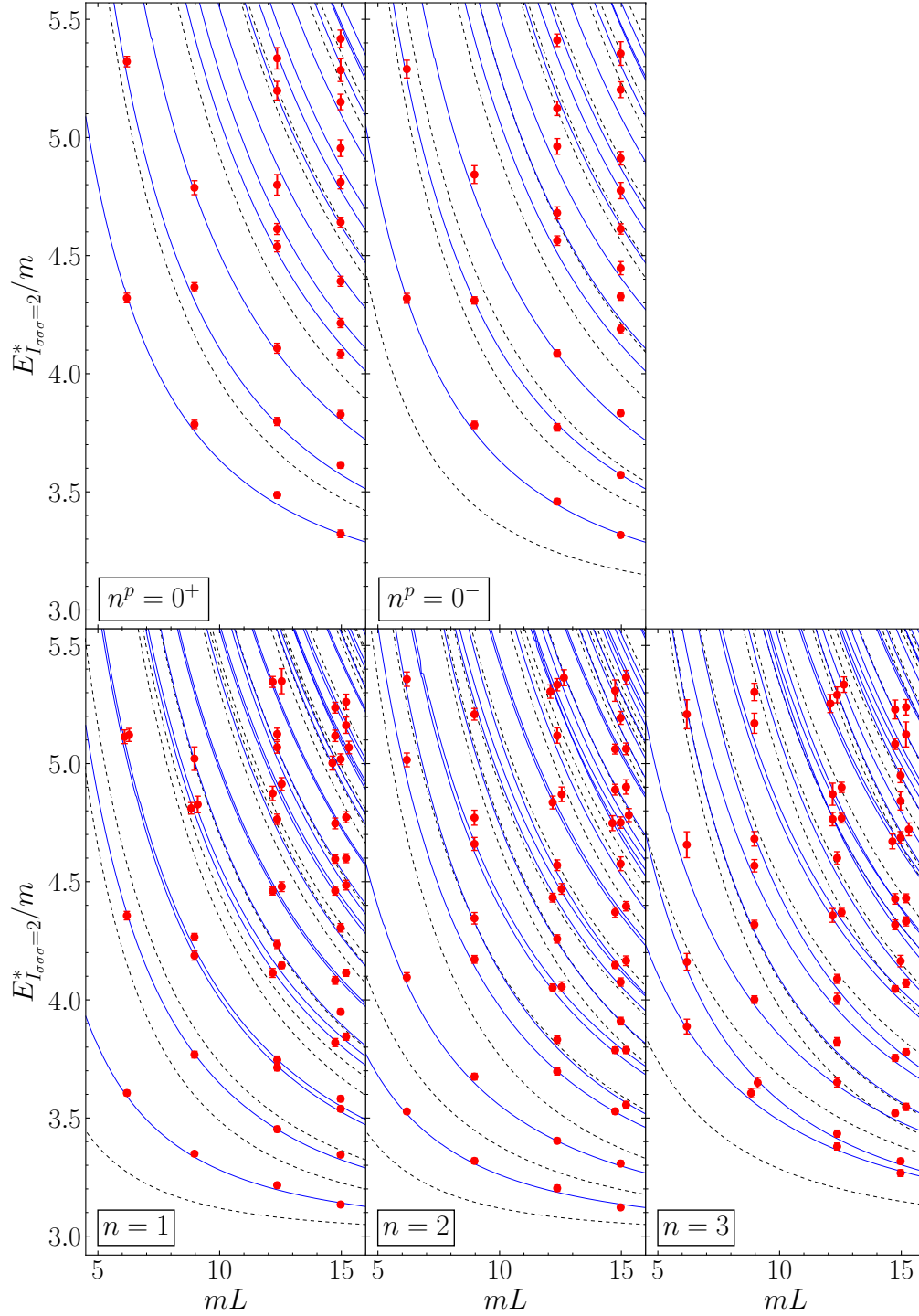


Figure 7.13. Same as fig. 7.12 for the $I_{\sigma\sigma} = 2$ channel.

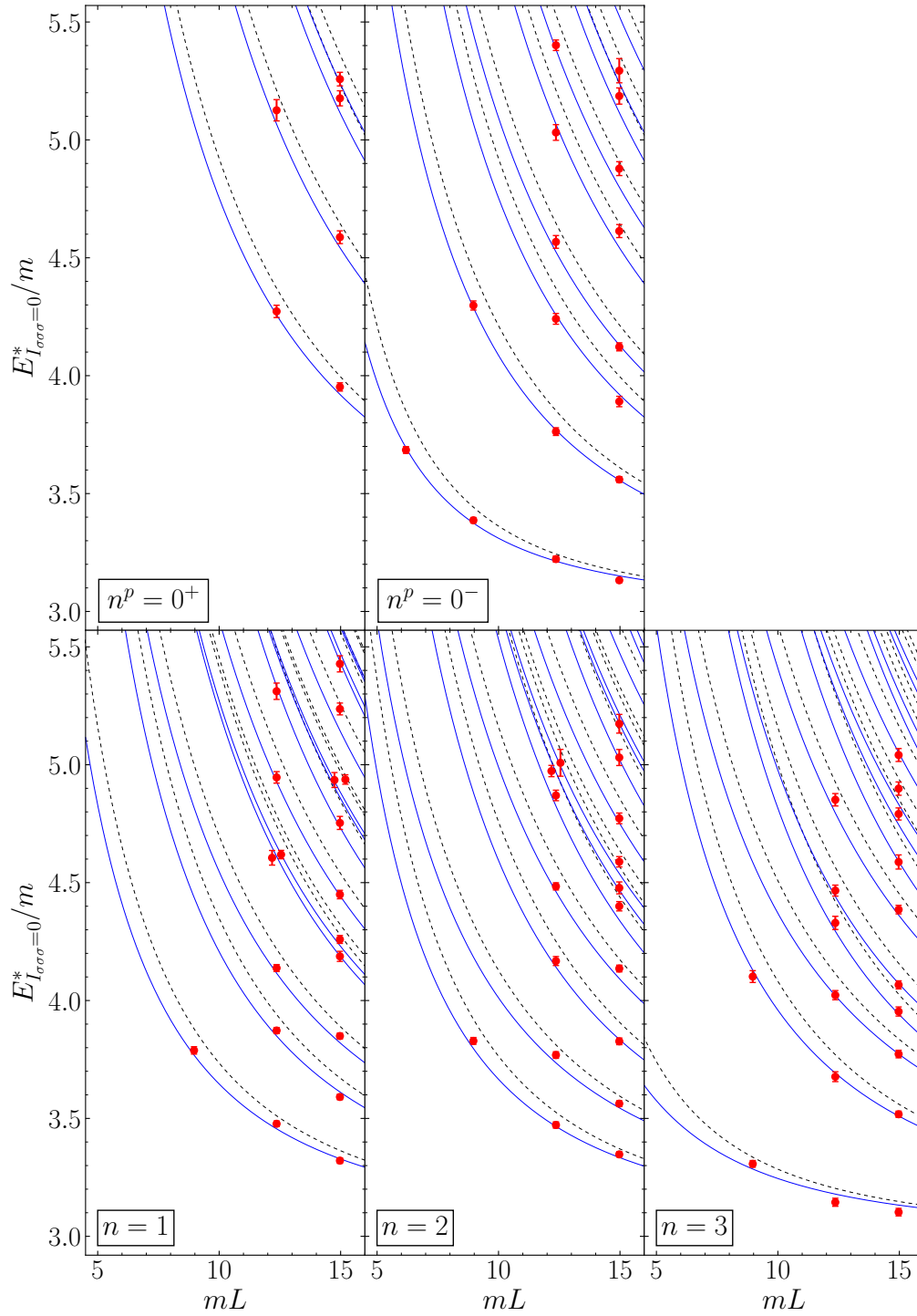


Figure 7.14. Same as fig. 7.12 for the $I_{\sigma\sigma} = 0$ channel.

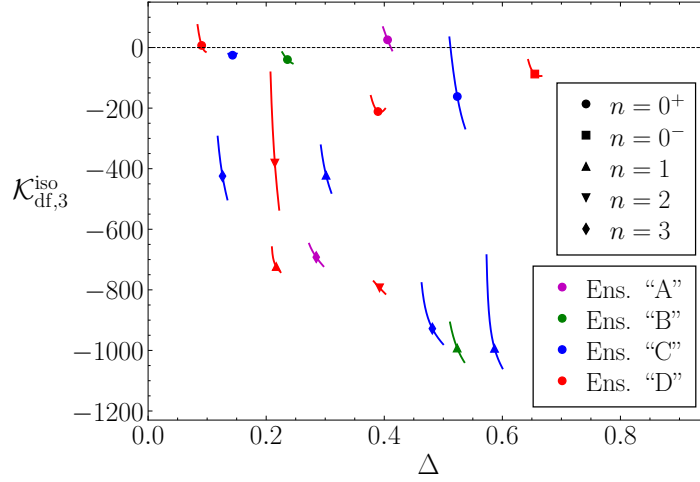


Figure 7.15. Results for the isotropic K -matrix in the $I_{\sigma\sigma\sigma} = 3$ channel, computed using the standard cutoff for those states with $E^* < 4m$.

be improved by allowing for a non-zero K -matrix, and especially by using an analytic determination of $\mathcal{K}_{df,3}$. The results from the comparison also evidence the difficulty of accurately determining $\mathcal{K}_{df,3}$ from lattice simulations. Since three-particle interactions are dominated by pairwise scattering, a precise determination of $\mathcal{K}_{df,3}$ requires of a vast level of precision in the finite-volume energies, well in the subpercent level.

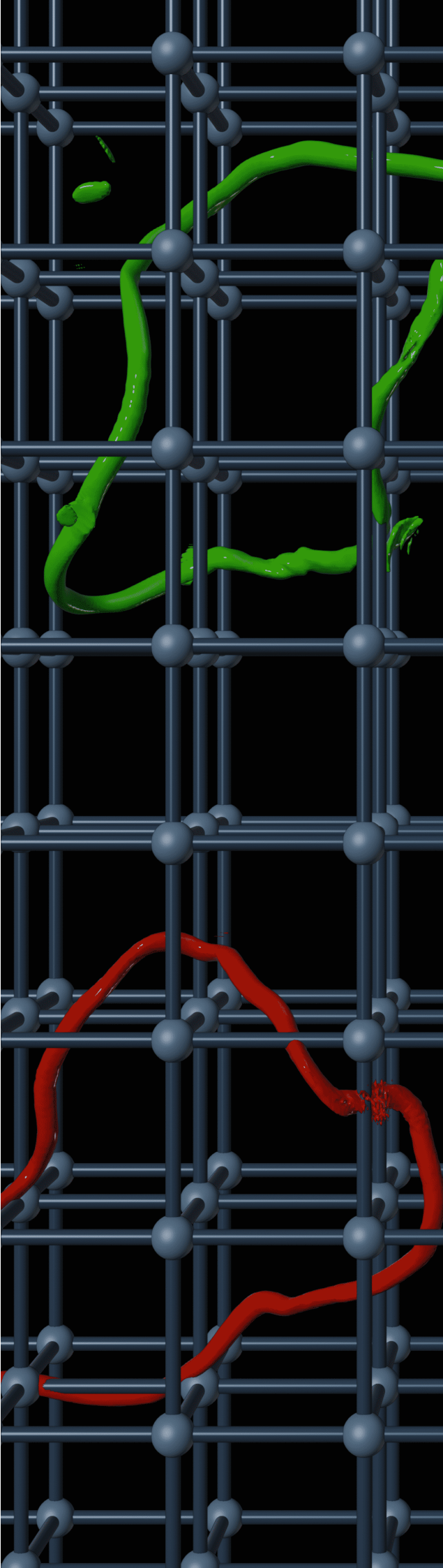
Finally, we compute the isotropic K -matrix, $\mathcal{K}_{df,3}^{\text{iso}}$, in the $I_{\sigma\sigma\sigma} = 3$ channel, following eq. (2.60). The results, computed only for states with $E^* < 4m$ and using the standard cutoff, are presented in fig. 7.15, as a function of $\Delta = (P^2 - 9m^2)/9m^2$. We observe how the points show a significant dispersion, with many of them taking values different from zero. This suggests that indeed $\mathcal{K}_{df,3} \neq 0$ in the O(3) model (otherwise all points would lie close to the $\mathcal{K}_{df,3}^{\text{iso}} = 0$ line) and also that the isotropic approximation does not properly reproduce the scattering K -matrix (since no trend is observed).

7.6 Conclusions

The O(3) model is commonly used as a toy model of QCD, as both theories share many features, such as asymptotic freedom and a low-energy spectrum of isospin-one particles. In addition, the O(3) model is integrable, allowing for analytical predictions of the scattering matrix. In this chapter, results on the study of two- and three-particle scattering in the O(3) model have been presented, with which we ultimately aim to test the RFT three-particle formalism by comparing lattice results to exact analytical predictions.

We have determined a large number of two- and three-particle finite-volume energies using a three-cluster generalization of the cluster update algorithm, working at four values of the physical volume at three lattice spacings each. Finite-volume energies have been directly extrapolated to the continuum by comparing the results at all three values of the lattice spacing. We have found very good agreement between lattice results for two-particle energies and analytical predictions. In the case of three-particles, we have compared our results to analytical determinations made under the assumption that $\mathcal{K}_{\text{df},3} = 0$, obtained using the RFT formalism, which we have extended to 1+1 dimensions. We have found that these predictions reproduce well the structure of the lattice results, but the discrepancy between analytical and lattice results suggests a non-zero K -matrix. We have also observed the presence of unphysical solutions to the QC, which appear only for some choices of the cutoff function.

The work presented in this chapter represents a first step towards a test of the three-particle QC, based on comparing lattice results to exact analytical predictions available in the $O(3)$ model. Following this work, we plan to use our results for the finite-volume energies to constrain the values of $\mathcal{K}_{\text{df},3}$. Eventually, we aim at comparing these to an analytical determination obtained from the factorizable S -matrix.



Part II

Cosmic String Loops from Lattice Simulations

*Mientras la ciencia a descubrir no alcance
las fuentes de la vida,
y en el mar o en el cielo haya un abismo
que al cálculo resista;
mientras la humanidad, siempre avanzando
no sepa a do camina;
mientras haya un misterio para el hombre,
¡habrá poesía!*

Rimas
Gustavo Adolfo Bécquer

8 Lattice techniques for cosmology

The history of the universe can be divided in two epochs, the early and the late universe, separated approximately when the cosmic microwave background (CMB) was released. Our knowledge of the early universe, especially of the very first second, is slim. The most accepted picture is that energies were reached well beyond the electroweak scale and, therefore, phenomena happening possibly involved physics beyond the Standard Model. This implies that the study of this very first moments of our universe is an open window to yet undiscovered particle physics.

Electromagnetic detectors, though, can only observe the universe after the release of the CMB. Certain processes that may occur in the first second of the universe are characterized by non-linear dynamics, and many of them are expected to emit gravitational waves that could be observed today as a stochastic background. Due to the weakness of the gravitational interaction, that background would retain information about the particle-physics process producing the gravitational radiation.

A proper interpretation of a potential measurement of primordial GWs, however, requires of accurate predictions. The non-linear nature of the phenomena that produce the GWs usually implies that analytical methods have limited applicability. Instead, to fully capture the non-linear dynamics, one is forced to rely on numerical computations.

In this chapter, we review the basics of field theory in an expanding background, and how it can be simulated on the lattice. Sec. 8.1 explains how non-linear phenomena in the early universe can be investigated using classical-field-theory techniques. Then, sec. 8.2 discusses how such processes can be simulated on the lattice, and how we do it in the *CosmoLattice* package. Finally, sec. 8.3 reviews how GWs are simulated on the lattice.

8.1 The expanding universe

The foundations of the standard cosmological model are the theory of general relativity and the *cosmological principle*. This principle states that, statistically, the universe is isotropic and homogeneous, this is, it is independent of direction and position. The cosmological principle constrains the metric of the universe, $g_{\mu\nu}$, to be the so-called *Friedmann-Lemaître-Robertson-Walker* (FLRW) *metric* [342]. Using spherical spatial coordinates, it takes the form

$$ds^2 = g_{\mu\nu}dx^\mu dx^\nu = dt^2 - a^2(t) \left[\frac{dr^2}{1+kr^2} + r^2(d\theta + \sin^2\theta d\phi^2) \right], \quad (8.1)$$

where $a(t)$ is the scale factor, that determines the time evolution of physical spacial distances, and k is the spatial curvature, that characterizes the geometry of the universe. It can be either positive, zero or negative, for a closed, flat and open universe, respectively. In the case of a flat universe, as is supported by observations, the metric can be rewritten in Cartesian coordinates as

$$ds^2 = dt^2 - a^2(t)(dx^2 + dy^2 + dz^2). \quad (8.2)$$

In some cases, it is convenient to conformally redefine the time coordinate to general α -time, η , defined from, $dt = a^\alpha(\eta)d\eta$, where α is some real parameter. In particular, $\alpha = 0$ corresponds to the standard *cosmic time*, while $\alpha = 1$ is the so-called *conformal time*, which we denote as τ . Throughout the remaining of this dissertation, we use the symbol $f' = df/d\eta$ to indicate derivative with respect to general α -time.

From Einstein field equations, one can obtain the evolution equations of the scale factor. These are the so-called *Friedmann equations* [343],

$$\mathcal{H}^2 = \left(\frac{a'}{a} \right)^2 = a^{2\alpha} \frac{\rho}{3m_p^2}, \quad (8.3)$$

$$\frac{a''}{a} = \frac{a^{2\alpha}}{6m_p^2} [(2\alpha - 1)\rho - 3p], \quad (8.4)$$

where ρ and p are the background energy density and pressure generated by the contents of the universe, $m_p = 1/\sqrt{8\pi G} \approx 2.44 \times 10^{18}$ GeV is the reduced Planck mass, with G the Newtonian constant of gravitation, and $\mathcal{H} = a'/a$ is the Hubble rate in α -time.

Based on the cosmological principle, the energy density and pressure of matter can be described as a perfect fluid that obeys a barotropic equation of state, $\rho = wp$, with w constant. In the case of radiation, non-relativistic

matter and vacuum energy, $w = 1/3, 0$ and -1 , in this same order. The Friedmann equations then lead to

$$a(\eta) = a_0 \left[1 + \frac{\mathcal{H}_0}{p} (\eta - \eta_0) \right]^r, \quad (8.5)$$

where

$$r = \frac{2}{3(1+w) - 2\alpha}, \quad (8.6)$$

and \mathcal{H}_0 and a_0 are the Hubble rate and scale factor at some reference time η_0 . At late enough time, $\eta \gg \mathcal{H}_0^{-1}$, the scale factor scales roughly as $a(\eta) \propto \eta^r$. For example, for a radiation-dominated universe, it grows linearly with conformal time, $a(\tau) \propto \tau$.

The standard cosmological model is successful at explaining many observed phenomena, but it has some shortcomings. One of the most notorious examples is the so-called *horizon problem*. According to the standard cosmology, the universe has a finite age, and so it should be divided in causally disconnected patches. Observationally, however, such patches have the same properties, in apparent contradiction with causality. Another unexplained aspect is the origin of the fluctuations that lead to the formation of structure.

All these problems are solved by the inclusion of an initial phase of accelerated expansion, $a'' > 0$, called *inflation* [344–348]. This phase should last for a long enough time. This is typically measured by the number of times the scale factor increases by a factor of e , also known as *e-foldings*. In order to explain observations, inflation must last for around 60 e-foldings.

8.1.1 Field-theory description

Inflation and other subsequent processes can be generally described in the language of field theory. In many cases, it is possible to work in the *semi-classical approximation*, in which quantum corrections can be neglected due to large occupation numbers, and one can make use of classical-field-theory techniques.

To better understand this approximation we can first consider the well-known example of black-body radiation. At low temperatures, the occupation number of the different frequencies is small, and the radiation follows the quantum Planck's law. However, as temperature grows, the occupation number of low-frequency modes becomes large, and the low-frequency tail of Planck's law can be approximated by the classical Boltzmann distribution. Note, however, that this does not apply to very high-frequency modes, which still behave in a quantum regime.

An analogous situation happens in the case of certain early-universe phenomena, such as possible phase transitions, the formation of cosmic defects or the emission of GWs. The modes relevant for the process have large occupation, and thus can be described in the semiclassical approximation. This limit, in contrast, cannot be applied to modes with a low occupation number.

The starting point of any classical-field-theory model is the action of the matter fields. For the purpose of this dissertation, we consider a model consisting of a real scalar, ϕ , a complex scalar, φ , which can also be expressed in terms of two real scalars, $\varphi = (\phi_1 + i\phi_2)/\sqrt{2}$, and a U(1) Abelian gauge field, A_μ , that couples to the complex field. The techniques that we present here, nonetheless, can be generalized to include several copies of each field, scalar multiplets and non-Abelian gauge fields—see ref. [349] for a review.

For the model we consider, the action takes the form

$$S = \int d^4x \sqrt{-g} \left[\frac{1}{2} \partial_\mu \phi \partial^\mu \phi + (D_\mu \varphi)(D^\mu \varphi)^* - \frac{1}{4} F_{\mu\nu} F^{\mu\nu} - V(\phi, \varphi) \right], \quad (8.7)$$

where $g = \det(g_{\mu\nu})$ is the determinant of the FLRW metric, eq. (8.2), and Greek indices are contracted using this metric. In this equation, $V(\phi, \varphi)$ is a general potential density depending on the scalar fields, and we have defined the covariant derivative and the field-strength tensor, respectively,

$$D_\mu = \partial_\mu - ieQA_\mu, \quad F_{\mu\nu} = \partial_\mu A_\nu - \partial_\nu A_\mu, \quad (8.8)$$

where e is the gauge coupling and Q is the charge of φ under the U(1) gauge symmetry. In analogy to QCD—see eq. (1.8)—this action is invariant under local gauge transformations,

$$\begin{aligned} \phi(x) &\longrightarrow \phi(x), \\ \varphi(x) &\longrightarrow \exp[-ieQ\alpha(x)] \varphi(x), \\ A_\mu(x) &\longrightarrow A_\mu(x) - \partial_\mu \alpha(x), \end{aligned} \quad (8.9)$$

where $\alpha(x)$ is some arbitrary function. To study the dynamics of the fields, we work in the temporal gauge, in which $A_0 = 0$. Note that while A_i is still gauge-dependent, one can define gauge-independent observables: the *electric* and the *magnetic fields*, respectively,

$$E_i = F_{0i}, \quad B_i = \frac{1}{2} \epsilon_{ijk} F^{jk}, \quad (8.10)$$

with ϵ_{ijk} the Levi-Civita symbol.

The evolution of the fields is governed by the classical equations of motion. These are obtained from minimizing the action, eq. (8.7), with respect to the fields. They read

$$\phi'' + (3 - \alpha) \frac{a'}{a} \phi' - a^{-2(1-\alpha)} \partial_i \partial_i \phi = -a^{2\alpha} \frac{dV}{d\phi}, \quad (8.11)$$

$$\varphi'' + (3 - \alpha) \frac{a'}{a} \varphi' - a^{-2(1-\alpha)} D_i D_i \varphi = -a^{2\alpha} \frac{dV}{d\varphi}, \quad (8.12)$$

$$F'_{0i} + (1 - \alpha) \frac{a'}{a} F_{0i} - a^{-2(1-\alpha)} \partial_j F_{ji} = a^{2\alpha} J_i, \quad (8.13)$$

$$\partial_i F_{0i} = a^2 J_0, \quad (8.14)$$

where we define the U(1) current density,

$$J_\mu = 2eQ \text{Im}[\varphi^* D_\mu \varphi]. \quad (8.15)$$

It is worth mentioning that eq. (8.14) is the Gauss' law, which is not a dynamical equation of the fields, but rather a constraint equation.

Eqs. (8.11) to (8.13) allow one to study the dynamics of the fields in an expanding background. The evolution of the scale factor can be fixed, given by some background fluid—see eq. (8.5)—if the matter fields are treated as spectators, or be induced by the fields themselves. This latter case is known as *self-consistent expansion*, in which the second Friedmann equation, eq. (8.4), is regarded as the equation of motion of the scale factor, while the first Friedmann equation, eq. (8.3), can be treated as a constrain equation, extending energy conservation to expanding backgrounds.

In the case of self-consistent expansion, the source of the Friedmann equations are the background energy density and pressure generated by the matter fields, which are determined from volume averages. The total energy density and pressure can be decomposed into the energy-density components of the different fields,

$$\begin{aligned} \rho &= \rho_K^\phi + \rho_K^\varphi + \rho_G^\phi + \rho_G^\varphi + V + \rho_K^{\text{U}(1)} + \rho_G^{\text{U}(1)}, \\ p &= \rho_K^\phi + \rho_K^\varphi - \frac{1}{3} (\rho_G^\phi + \rho_G^\varphi) - V + \frac{1}{3} (\rho_K^{\text{U}(1)} + \rho_G^{\text{U}(1)}), \end{aligned} \quad (8.16)$$

where V is the potential energy density, and we define the kinetic, ρ_K , and gradient, ρ_G , energy densities of the scalar and gauge fields,

$$\begin{aligned} \rho_K^\phi &= \frac{1}{2a^{2\alpha}} \phi'^2, & \rho_G^\phi &= \frac{1}{2a^2} \sum_i (\partial_i \phi)^2, \\ \rho_K^\varphi &= \frac{1}{a^{2\alpha}} |\varphi'|^2, & \rho_G^\varphi &= \frac{1}{a^2} \sum_i |D_i \varphi|^2, \\ \rho_K^{\text{U}(1)} &= \frac{1}{2a^{2+2\alpha}} \sum_i F_{0i}^2, & \rho_G^{\text{U}(1)} &= \frac{1}{2a^4} \sum_{i,j < i} F_{ij}^2. \end{aligned} \quad (8.17)$$

The kinetic and gradient energy density of the Abelian field, in the last line, are also called electric, ρ_E , and magnetic, ρ_B , energy densities, respectively, since they depend on the electric and magnetic field—see eq. (8.10).

The last ingredient needed to study the classical field dynamics are some *initial conditions* from which the fields are evolved. These should be chosen to represent the physics of interest. For scalar fields and their derivatives, the initial conditions typically consist of a homogeneous mode, on top of which some fluctuations following a given spectrum are added. For example, studies of particle production at the end of inflation set some homogeneous value for the scalar field that drives the inflation, while other daughter fields are set to zero. On top of these homogeneous values, initial fluctuations are added resembling those of quantum origin. Gauge fields are generally set to zero, while the corresponding derivatives are chosen so that the Gauss constrain, eq. (8.13), is initially verified [350]. This means the initial magnetic energy is set to zero, while there is some amount of electric energy.

8.2 Classical field theory on the lattice

Analytical methods can be used to study early-universe processes when field fluctuations are small, by treating these fluctuations as small perturbations. However, this approach is not always possible. In some regimes, early-universe phenomena present large non-linearities and the only option to capture them is the use of classical-field-theory lattice simulations, performed using a discretized and dimensionless version of the equations of motion. In this section we describe how lattice techniques can be used to study the early universe. These are the basis of the work presented in chapters 9 and 10, which makes use of the `CosmoLattice` code [349, 351].

8.2.1 Lattice definition and Fourier transform

A lattice is a discretized and finite representation of space. We consider a cubic three-dimensional lattice,

$$\Lambda = \{\mathbf{n} = (n_1, n_2, n_3) \mid n_i \in \mathbb{Z}, 0 \leq n_i < N\}, \quad (8.18)$$

where N is the number of sites per dimension.¹ We define the lattice spacing, δx , as the comoving distance between consecutive sites. In the context of an FLRW universe, lattice sites have fixed comoving coordinates, $\delta x \mathbf{n}$, and physical distances are obtained multiplying the comoving ones by the

¹The same techniques presented here can be extended to any number of dimensions.

scale factor. The comoving side of the lattice is thus $L = \delta x N$. Finally, continuum functions, $f(\mathbf{x})$ are defined on the lattice as functions $f(\mathbf{n})$ so that $f(\mathbf{n}) = f(\mathbf{x})$ when $\mathbf{x} = \delta x \mathbf{n}$.² Note we work with periodic boundary conditions in all directions, meaning $f(\mathbf{n} + L\hat{\mathbf{i}}) = f(\mathbf{n})$ with $\hat{\mathbf{i}}$ a unit vector in the i direction.

The finite volume and lattice spacing limit the range of scales that can be studied on the lattice, as they set the longest and shortest distances that can be probed. To better understand this limitation, it is convenient to first introduce the *discrete Fourier transform* and the *reciprocal lattice*. Given some real function $f(\mathbf{n})$, its discrete Fourier transform is defined as

$$f(\tilde{\mathbf{n}}) = \sum_{\mathbf{n} \in \Lambda} e^{-\frac{2\pi i}{N} \tilde{\mathbf{n}} \mathbf{n}} f(\mathbf{n}), \quad (8.19)$$

which we distinguish from the original field by the tilde in its argument. Similarly, we also define the inverse Fourier transform as

$$f(\mathbf{n}) = \frac{1}{N^3} \sum_{\tilde{\mathbf{n}} \in \Lambda_R} e^{\frac{2\pi i}{N} \tilde{\mathbf{n}} \mathbf{n}} f(\tilde{\mathbf{n}}), \quad (8.20)$$

where Λ_R refers to the reciprocal lattice, defined in eq. (8.21) below. The Fourier transform of a real field is in general complex valued. However, it is also Hermitian, $f(-\tilde{\mathbf{n}}) = f^*(\tilde{\mathbf{n}})$, and so the number of independent components of $f(\tilde{\mathbf{n}})$ equals that of $f(\mathbf{n})$.

The Fourier transform of a field takes values on the so-called *reciprocal lattice*, that contains all Fourier modes of the system, this is, all wavelengths that can be captured by our lattice. It is defined as

$$\Lambda_R = \left\{ \tilde{\mathbf{n}} = (\tilde{n}_1, \tilde{n}_2, \tilde{n}_3) \mid \tilde{n}_i \in \mathbb{Z}, -\frac{N}{2} < \tilde{n}_i \leq \frac{N}{2} \right\}, \quad (8.21)$$

so that each site corresponds to a comoving momentum,

$$\mathbf{k} = \frac{2\pi}{L} \tilde{\mathbf{n}}. \quad (8.22)$$

The reciprocal lattice makes it clear the existence of a minimum momentum that can be probed. This is called the *infrared (IR) momentum*, $k_{\text{IR}} = 2\pi/L$, which represents the lattice spacing of the reciprocal lattice. Similarly, there is a maximum ultraviolet (UV) momentum that can be probed in each direction, $k_{\text{UV}} = \pi/\delta x$, and also a maximum momentum that can be captured on the full lattice, $k_{\text{max}} = \sqrt{3}\pi/\delta x$. Note that all modes with $|\mathbf{k}| \leq k_{\text{UV}}$ lie within a sphere of radius k_{UV} that fits entirely within the reciprocal lattice,

²We distinguish continuum functions, $f(\mathbf{x})$, from functions defined on the lattice, $f(\mathbf{n})$, by their argument.

and so are lattice-isotropic, i.e., isotropic up to discretization effects. This is not the case for $|\mathbf{k}| > k_{\text{UV}}$, for which the modes are not isotropically distributed.

Using the Fourier transforms of the fields, one can define their *power spectrum*. In the continuum, the power spectrum of a real field, $f(x)$, denoted as Δ_f , is defined via

$$\langle f^2(\mathbf{x}) \rangle = \int \Delta_f(k) d \log k, \quad (8.23)$$

where $f(\mathbf{k})$ is the continuum Fourier transform of $f(\mathbf{x})$, $k = |\mathbf{k}|$ and $\langle f^2(\mathbf{x}) \rangle$ denotes the ensemble average of $f^2(\mathbf{x})$, this is, the average over multiple realizations of the field. The power spectrum is related to the two-point function of the field,

$$\langle f(\mathbf{k})f^*(\mathbf{k}') \rangle = (2\pi)^3 \frac{2\pi^2}{k^3} \Delta_f(k) \delta^3(\mathbf{k} - \mathbf{k}'), \quad (8.24)$$

with f^* the complex conjugate of f .

On the lattice, the ensemble average is substituted by a volume average,

$$\langle f^2(\mathbf{n}) \rangle_V = \frac{1}{N^3} \sum_{\mathbf{n} \in \Lambda} f^2(\mathbf{n}) = \frac{1}{N^6} \sum_{\tilde{\mathbf{n}} \in \Lambda_{\mathbf{R}}} |f(\tilde{\mathbf{n}})|^2, \quad (8.25)$$

where in the second step we have used the discrete Fourier transform of the field—see eq. (8.19). The sum over Fourier modes can be decomposed in a sum over all modes within spherical shells, R_l and the sum over all shells. We define spherical shells as

$$R_l = \left\{ \tilde{\mathbf{n}} \in \Lambda_{\mathbf{R}} \mid l - \Delta\tilde{n}_l^- \leq |\tilde{\mathbf{n}}| < l + \Delta\tilde{n}_l^+ \right\}, \quad (8.26)$$

where l is the mode that labels the shell, and $\Delta\tilde{n}_l^-$ and $\Delta\tilde{n}_l^+$ are the width of the shell from l downwards and upwards, respectively. While shells need not be labeled by their mean or have all equal width, it is common to choose $\Delta\tilde{n}_l^- = \Delta\tilde{n}_l^+ = 1/2$, called the *canonical binning*. Eq. (8.25) can then be written as

$$\langle f^2(\mathbf{n}) \rangle_V = \frac{1}{N^6} \sum_l \#_l \langle |f(\tilde{\mathbf{n}})|^2 \rangle_{R_l}, \quad (8.27)$$

where $\langle \dots \rangle_{R_l}$ is the average value over the spherical shell R_l , and $\#_l$ denotes the exact number of modes within R_l . From here, the lattice power spectrum is introduced,

$$\langle f^2(\mathbf{n}) \rangle_V = \sum_l \Delta \log k(l) \Delta_f(l). \quad (8.28)$$

A common option is to define

$$\Delta_f(l) = \frac{k(l)\delta x}{2\pi N^5} \#_l \langle |f(\tilde{\mathbf{n}})|^2 \rangle_{R_l}, \quad (8.29)$$

where $k(l) = lk_{\text{IR}}$. Alternative definitions of the lattice power spectrum also exist—see ref. [352]. It is worth mentioning that the number of modes within each shell is often approximated as $\#_l \approx 4\pi l^2$. However, this is not correct for the lowest and highest modes on the lattice, for which the discretization and the finiteness of the reciprocal lattice becomes relevant, respectively, and the multiplicity significantly differs from this approximation.

Finally, we note that the substitution of the ensemble average in eq. (8.23) by a volume average in eq. (8.25) is only justified if the number of modes within each bin is large. This is true in most cases, but for very IR or UV modes it can lead to significant systematic effects, in the same sense as the cosmic variance [353]. Thus, one wants all the relevant scales of the problem to be well encompassed within the lattice.

8.2.2 A dimensionless discretized model

To numerically study the equations of motion, they must be rewritten in terms of dimensionless variables, and discretized. The first requirement is simple to achieve. In *CosmoLattice* [349, 351], the dimensionless model is defined using two physical scales: one related to a typical field amplitude, f_* , and another related to a typical frequency of the system, ω_* . We then rescale the fields, coordinates and momenta as

$$\begin{aligned} \tilde{\phi} &= \phi/f_*, & \tilde{\varphi} &= \varphi/f_*, & \tilde{A}_\mu &= A_\mu/\omega_*, \\ \tilde{x}_i &= \omega_* x_i, & \tilde{\eta} &= \omega_* \eta, & \tilde{k}_i &= k_i/\omega_*. \end{aligned} \tag{8.30}$$

Ideally, the choice of f_* and ω_* ensures that typical field values are $\mathcal{O}(1)$, minimizing the effects of numerical errors.

The second step is to discretize the equations of motion. The case of scalar fields is simple, as one can naively substitute continuum derivatives by *finite differences*. Basic options for the finite differences are, for example,

$$\begin{aligned} [\Delta_i^\pm f](\mathbf{n}) &= \frac{\pm f(\mathbf{n} \pm \hat{\mathbf{i}}) \mp f(\mathbf{n})}{\delta x}, \\ [\Delta_i^0 f](\mathbf{n}) &= \frac{f(\mathbf{n} + \hat{\mathbf{i}}) - f(\mathbf{n} - \hat{\mathbf{i}})}{2\delta x}, \end{aligned} \tag{8.31}$$

which correspond to *forward/backward* and *neutral derivatives*, respectively, evaluated on the lattice sites. These can directly be substituted into the equations of motion, although this procedure requires some caution to make sure all terms are defined at the same lattice site and time. Another possibility, in some cases, is to perform the substitution in the action, from which the discrete equations of motion are derived.

Associated to a lattice derivative, one can define a *lattice momentum*, \mathbf{k}_L , using the Fourier transform

$$[\Delta_i f](\tilde{\mathbf{n}}) = -ik_{L,i}(\tilde{\mathbf{n}})f(\tilde{\mathbf{n}}). \quad (8.32)$$

For the lattice derivatives in eq. (8.31), defined on the lattice sites, one gets,

$$\begin{aligned} k_{L,i}^\pm &= 2 \exp\left(\mp i \frac{\pi \tilde{n}_i}{N}\right) \frac{\sin(\pi \tilde{n}_i/N)}{\delta x}, \\ k_{L,i}^0 &= \frac{\sin(2\pi \tilde{n}_i/N)}{\delta x}, \end{aligned} \quad (8.33)$$

which are complex and real, respectively.

The discretization of gauge fields is a bit more cumbersome, as it needs to preserve gauge invariance. The main difference is that covariant derivatives are substituted as a whole by parallel-transported finite differences. For example, we can define the forward parallel-transported lattice derivative as

$$D_i^+ \varphi \longrightarrow \frac{U_i(\mathbf{n} + \hat{i})\varphi(\mathbf{n} + \hat{i}) - \varphi(\mathbf{n})}{\delta x}, \quad (8.34)$$

where

$$U_i(\mathbf{n}) = \exp[-ieQ\delta x A_i(\mathbf{n})], \quad (8.35)$$

is the gauge parallel transporter along the lattice link, also known as link variable, defined in analogy to the QCD case—see sec. 1.2.1. This ensures our action is invariant under discrete gauge transformations, obtained from discretizing the derivative in the gauge transformation of A_μ in eq. (8.9).

The field-strength tensor of the gauge field admits several discretizations. The simplest option is the *non-compact formulation*, in which one works with the A_μ field as the degrees of freedom, and discretizes $F_{\mu\nu}$ by substituting the continuum derivatives with finite differences.

Another option is the so-called *compact formulation*, analogous to that used in QCD—see eq. (1.32). In this case the link variables become the dynamical degrees of freedom and the field-stress tensor term of the action, $F_{\mu\nu}F^{\mu\nu}/4$ is substituted by

$$\frac{1}{2\delta x^4 e^2 Q^2} \sum_{\mu\nu} [1 - \text{Re}(\mathcal{P}_{\mu\nu})], \quad (8.36)$$

where $\mathcal{P}_{\mu\nu}$ is the *plaquette*,

$$\mathcal{P}_{\mu\nu}(\mathbf{n}) = U_\mu(\mathbf{n})U_\nu(\mathbf{n} + \hat{\mu})U_\mu^*(\mathbf{n} + \hat{\nu})U_\nu^*(\mathbf{n}). \quad (8.37)$$

When using the compact formulation, one needs to accordingly redefine the relevant energy components. In particular, the components of the stress-energy tensor are recovered from

$$F_{\mu\nu} = \frac{i}{2eQ\delta x^2}(\mathcal{P}_{\mu\nu} - \mathcal{P}_{\mu\nu}^*), \quad (8.38)$$

while the magnetic energy is

$$E_B = \frac{1}{a^4\delta x^4 e^2 Q^2} \sum_{i,j < i} [1 - \text{Re}(\mathcal{P}_{ij})]. \quad (8.39)$$

We note that, in the case of non-Abelian fields, only the non-compact formulation makes it possible to keep gauge invariance [349].

Another option for Abelian fields is a *hybrid formulation*. In this case, the action is written in terms of the links, as in the compact case, but the A_μ field is kept as the dynamical degree of freedom.

8.2.3 Solving the field dynamics

To numerically evolve the equations of motion of the fields, they need to be expressed in a way that is suited for a numerical evolution algorithm. The equations are typically a system of coupled non-linear second-order differential equations. To solve them numerically, it is convenient to rewrite the system in a Hamiltonian scheme. This requires to define some *conjugate momenta* to express each equation as a system of two first-order differential equations. While this is typically done by choosing the time derivative as the conjugate momentum, in the context of an expanding background it is convenient to include some power of the scale factor. This makes it possible to eliminate the friction terms—those proportional to derivatives of the scale factor in eqs. (8.11) to (8.13)—from the equation of motion.

We can consider, for example, a real scalar field in the continuum. Defining the conjugate momenta as $\pi_\phi = a^{3-\alpha}\phi'$, the equation of motion, eq. (8.11), becomes a system of two first-order differential equations,

$$\begin{aligned} \pi'_\phi &= -a^{3+\alpha} \frac{dV}{d\phi} + a^{1+\alpha} \partial_i \partial_i \phi, \\ \phi' &= a^{-(3-\alpha)} \pi_\phi. \end{aligned} \quad (8.40)$$

A similar result holds for complex scalars. In the case of gauge fields, on the other hand, the conjugate momentum is defined as $\pi_{A,i} = a^{1-\alpha} A'_i$, and the equation of motion in the temporal gauge becomes

$$\begin{aligned} \pi'_{A,i} &= a^{1+\alpha} J_i + a^{\alpha-1} \partial_j F_{ji}, \\ A'_i &= a^{-(1-\alpha)} \pi_{A,i}. \end{aligned} \quad (8.41)$$

In the discretized model, an analogous procedure is used.

After the dimensionless, discretized equations of motion are rewritten in the Hamiltonian scheme, they can be evolved using some numerical evolution scheme. The simplest ones suited for the systems presented in this thesis are either the *leapfrog* or the *Verlet algorithms* [354], which fall in the class of symplectic algorithms. This class of algorithms is ideal to study problems with conservative forces, as they preserve the volume of the phase space to $\mathcal{O}(\delta\eta^2)$ accuracy, with $\delta\eta$ the time step used in the numerical evolution. Mathematically, this is related to Liouville's theorem [355, 356]. In the case of non-conservative forces, one can use some non-symplectic integrator, such as the Runge-Kutta algorithms [357, 358]. Note that in all cases the time step must obey the Courant stability condition [359], this is, $\delta\eta < \delta x/\sqrt{3}$, related to the hyperbolic form of the equations of motion of the fields.

8.3 Emission of gravitational waves

Gravitational waves (GWs) are the transverse-traceless (TT) part tensor perturbations of the metric.³ They are represented by a symmetric tensor field, $h_{ij} = h_{ji}$, that depends on the coordinates of spacetime, $h_{ij} = h_{ij}(\eta, \mathbf{x})$, and is transverse and traceless, this is,

$$\partial_i h_{ij} = 0, \quad h_{ii} = 0. \quad (8.42)$$

This two properties imply GWs represent only two independent degrees of freedom. On a FLRW background, GWs are defined as

$$ds^2 = a^{2\alpha}(\eta)d\eta^2 - a^2(\eta) [\delta_{ij} + h_{ij}(\eta, \mathbf{x})] dx^i dx^j, \quad (8.43)$$

The emission of GWs by early universe processes can usually be studied in the *linearized gravity regime*, $|h_{ij}| \ll 1$. In the work presented in this dissertation, the backreaction of the GWs into the matter fields is neglected. Also, we make *passive use of gravity*, this is, we compute the emission of GWs from the matter fields, but do not subtract them from the energy budget of the source fields.

Using Einstein equations, one can obtain the equations of motion for the h_{ij} fields. This requires to separate the equation into a homogeneous background part, corresponding to the Friedmann equations, and an equation of motion for the perturbations. Moreover, one needs to evaluate the stress-energy tensor of the matter fields using the perturbed metric. The resulting equation of motion for the GWs is [361]

³See ref. [360] for an extensive introduction to the topic of GWs.

$$h''_{ij} + (3 - \alpha) \frac{a'}{a} h'_{ij} - a^{-2(1-\alpha)} \partial_k \partial_k h_{ij} = -a^{2\alpha} \frac{2}{m_p^2} \Pi_{ij}^{\text{TT}}, \quad (8.44)$$

where the source of GWs, Π_{ij}^{TT} , is the spatial-spatial part of the TT anisotropy tensor, $\Pi_{\mu\nu}$, which thus obeys

$$\partial_i \Pi_{ij}^{\text{TT}} = 0, \quad \Pi_{ii}^{\text{TT}} = 0. \quad (8.45)$$

In the context of eq. (8.7), Π_{ij}^{TT} takes the form [362]

$$\Pi_{ij}^{\text{TT}} = \left\{ \frac{1}{a^2} \partial_i \phi \partial_j \phi + \frac{2}{a^2} \text{Re} [D_i \varphi (D_j \varphi)^*] - \frac{1}{a^{2\alpha}} E_i E_j - \frac{1}{a^2} B_i B_j \right\}^{\text{TT}}, \quad (8.46)$$

where $\{\dots\}^{\text{TT}}$ indicates the TT part of the expression between the brackets, and E_i and B_i are, respectively, the components of the electric and magnetic fields, defined in eq. (8.10).

The TT part of the anisotropic tensor can be defined from an effective tensor, Π_{ij}^{eff} , containing only those terms of the full Π_{ij} that have a non-zero TT projection,

$$\Pi_{ij}^{\text{eff}} = \frac{1}{a^2} \partial_i \phi \partial_j \phi + \frac{2}{a^2} \text{Re} [D_i \varphi (D_j \varphi)^*] - \frac{1}{a^{2\alpha}} E_i E_j - \frac{1}{a^2} B_i B_j. \quad (8.47)$$

From here, the source of GWs can be recovered by projecting to the TT component. This projection is a very non-local operation in coordinate space, but becomes linear in Fourier space [363],

$$\Pi_{ij}^{\text{TT}}(\mathbf{k}) = \Lambda_{ij,lm}(\hat{\mathbf{k}}) \Pi_{lm}^{\text{eff}}(\mathbf{k}), \quad (8.48)$$

where the TT projector is

$$\Lambda_{ij,lm}(\hat{\mathbf{k}}) = P_{il}(\hat{\mathbf{k}}) P_{jm}(\hat{\mathbf{k}}) - \frac{1}{2} P_{ij}(\hat{\mathbf{k}}) P_{lm}(\hat{\mathbf{k}}), \quad (8.49)$$

with

$$P_{ij}(\hat{\mathbf{k}}) = \delta_{ij} - \hat{k}_i \hat{k}_j. \quad (8.50)$$

and $\hat{k}_i = k_i / |\mathbf{k}|$.

Note that Π_{ij}^{TT} depends on spatial derivatives of the fields, and so the production of GWs is tied to the presence of inhomogeneities in the system. In the early universe, non-linear phenomena that develop large non-linearities may lead to the production of a vast amount of GWs with a particular spectral distribution that depends on the producing process. After the source ends, these GWs propagate freely until today, redshifting their spectral features, and could be measured as a stochastic GW background [361]. Thus, a detection of a stochastic background of GWs would provide precious information of the processes emitting the GWs.

GWs detectors can probe the power spectrum of a GW background, the particular shape of which depends on the phenomena that emitted the gravitational radiation. The GW energy density can be defined from an average over a volume, V , that encompasses all the relevant scales of the problem,

$$\rho_{\text{GW}}(\eta) = \frac{m_{\text{p}}^2}{4a(\eta)^{2\alpha}} \langle h'_{ij}(\eta, \mathbf{x}) h'_{ij}(\eta, \mathbf{x}) \rangle = \int \frac{d\rho_{\text{GW}}}{d \log k} d \log k. \quad (8.51)$$

Here, we have defined the *GW energy-density power spectrum*,

$$\frac{d\rho_{\text{GW}}}{d \log k} = \frac{m_{\text{p}}^2 k^3}{8\pi^2 a(\eta)^{2\alpha} V} \int \frac{d\Omega_k}{4\pi} h'_{ij}(\eta, \mathbf{k}) h'_{ij}{}^*(\eta, \mathbf{k}), \quad (8.52)$$

where $d\Omega_k$ refers to the solid-angle measure in Fourier space. Typically, one defines the *fractional GW energy-density power spectrum*,

$$\Omega_{\text{GW}} = \frac{1}{\rho_c} \frac{d\rho_{\text{GW}}}{d \log k}, \quad (8.53)$$

where $\rho_c = 3\mathcal{H}^2 m_{\text{p}}^2$ is the critical energy density of the universe. In the case of self-consistent expansion, this is indeed the total energy density of the matter fields, $\rho_c^{\text{self-cons}} = \rho$, given in eq. (8.16). When working in Minkowski spacetime, on the contrary, no critical energy density can be defined, and one usually uses the total energy density of the matter fields.

8.3.1 Simulating the emission of GWs

The TT nature of GWs makes their study on the lattice complicated. The source of eq. (8.44) is the TT part of the anisotropic tensor, and its computation would require to go back and forth to Fourier space in every time step of the simulation. It is true that fast Fourier transform algorithms exist that allows the computation of Fourier transform in $\mathcal{O}(N^3 \log N)$ time,⁴ where N is the number of points per dimension of the lattice. However, this remains much more expensive than standard evolution steps, which scale as $\mathcal{O}(N^3)$.

In ref. [366], a workaround was proposed to overcome this limitation. The TT projection, eq. (8.48), and the equation of motion for GWs, eq. (8.44), are both linear operations on the fields. Thus, we can work with six unphysical non-TT fields, $u_{ij} = u_{ji}$, related to the h_{ij} fields as

$$h_{ij}(\mathbf{k}, \eta) = \Lambda_{ij,kl}(\hat{\mathbf{k}}) u_{kl}(\mathbf{k}, \eta), \quad (8.54)$$

⁴In *CosmoLattice* we use the FFTW [364] and PFFT [365] libraries for the computation of fast Fourier transforms.

which are sourced by the effective anisotropic tensor in eq. (8.47),

$$u''_{ij} + (3 - \alpha) \frac{a'}{a} u'_{ij} - a^{-2(1-\alpha)} \partial_k \partial_k u_{ij} = -a^{2\alpha} \frac{2}{m_p^2} \Pi_{ij}^{\text{eff}}. \quad (8.55)$$

Thus, one can evolve these u_{ij} fields without the need to TT-project the source. Only when the GW energy density needs to be determined, the fields are Fourier transformed and projected to the TT component,

$$\Omega_{\text{GW}}(\eta) = \frac{m_p^2 k^3}{8\pi^2 \rho_c a(\eta)^{2\alpha} V} \int \frac{d\Omega_k}{4\pi} u'_{ij}(\eta, \mathbf{k}) \Lambda_{ij,kl} u'_{kl}(\eta, \mathbf{k}). \quad (8.56)$$

Note that the use of this technique has a drawback, as one is forced to work with six unphysical degrees of freedom u_{ij} , instead of the two physical ones. However, the gain in computing time is notorious.

The lattice implementation of eq. (8.55) follows a similar approach to that presented in sec. 8.2 for scalar fields. The u_{ij} fields are dimensionless and we define program variables as

$$\tilde{u}_{ij} = \left(\frac{m_p}{f_\star} \right)^2 u_{ij}, \quad (8.57)$$

to eliminate the factor of m_p^2 in the right-hand side of the equation of motion, eq. (8.55). The continuum equation of motion for these fields then reads

$$\tilde{u}''_{ij} + (3 - \alpha) \frac{a'}{a} \tilde{u}'_{ij} - a^{-2(1-\alpha)} \tilde{\partial}_k \tilde{\partial}_k \tilde{u}_{ij} = -2a^{2\alpha} \tilde{\Pi}_{ij}^{\text{eff}}. \quad (8.58)$$

To solve it numerically, we rewrite it in a Hamiltonian scheme, using conjugate momentum variables $(\pi_{\tilde{u}})_{ij} = a^{3-\alpha} \tilde{u}'_{ij}$,

$$\begin{aligned} \pi'_{\tilde{u},ij} &= 2a^{1+\alpha} \tilde{\Pi}_{ij}^{\text{eff}} + a^{1+\alpha} \tilde{\partial}_k \tilde{\partial}_k \tilde{u}_{ij}, \\ \tilde{u}'_{ij} &= a^{-(3-\alpha)} \pi_{\tilde{u},ij}. \end{aligned} \quad (8.59)$$

This is then discretized by substituting the continuum derivatives by finite differences.

As we have commented above, u_{ij} fields are projected in Fourier space to the TT components to measure physical observables. However, the definition of the TT projector on the lattice carries some subtleties [367]. On the lattice, this projection leads to fields that are transverse with respect to some choice of the discrete derivative, and so the particular form of the projector depends on the choice of derivative. As the lattice momentum associated to

discrete derivatives can in general be complex—see eq. (8.34)—one defines a complex version of the projector

$$\Lambda_{ij,kl}(\hat{\mathbf{n}}) = P_{ik}(\hat{\mathbf{n}})P_{jl}^*(\hat{\mathbf{n}}) - \frac{1}{2}P_{ij}(\hat{\mathbf{n}})P_{kl}^*(\hat{\mathbf{n}}), \quad (8.60)$$

with

$$P_{ij}(\hat{\mathbf{n}}) = \delta_{ij} - \hat{k}_{L,i}^* \hat{k}_{L,j}, \quad (8.61)$$

where $\hat{k}_{L,i} = k_{L,i}/|\mathbf{k}_L|$. This projector obeys, among others, the following set of properties,

$$\begin{aligned} 1) \ k_{L,i}^\pm P_{ij}^\pm &= 0, & 2) \ (k_{L,i}^\pm)^* P_{ij}^\pm &\neq 0, \\ 3) \ k_{L,j}^\pm P_{ij}^\pm &\neq 0, & 4) \ (k_{L,j}^\pm)^* P_{ij}^\pm &= 0, \\ 5) \ P_{ij}^{\pm*} &= P_{ji}^\pm, & 6) \ P_{ij}^\pm(-\tilde{\mathbf{n}}) &= P_{ji}^\pm(\tilde{\mathbf{n}}), \\ 7) \ P_{ij}^\pm P_{jk}^\pm &= P_{ik}^\pm, & 8) \ P_{ij}^\pm P_{kj}^\pm &\neq P_{ik}^\pm. \end{aligned} \quad (8.62)$$

For example, these properties indicate that the projector is hermitian (property 5) and idempotent (property 7). For a real lattice momentum, as is the case for neutral finite differences—see eq. (8.33)—the projector becomes real and these properties simplify [11, 367].

Using the projected fields, one can measure the power spectrum of the fractional GW energy density. On the lattice, this is defined similarly to other field power spectra—see eq. (8.29). For example,

$$\Omega_{\text{GW}}(\tilde{\mathbf{n}}, \tilde{\eta}) = \frac{1}{\tilde{\rho}_c} \frac{\tilde{k}(l)}{(8\pi a^{2\alpha})} \left(\frac{\delta\tilde{x}}{N^5} \right) \left(\frac{f_*}{m_{\text{p}}} \right)^2 \#_l a^{-2(3-\alpha)} \langle \tilde{T}(\tilde{\mathbf{n}}, \tilde{\eta}) \rangle_{R(l)}, \quad (8.63)$$

with

$$\begin{aligned} T(\mathbf{n}, \eta) &= u'_{ij}(\mathbf{n}, \eta) \Lambda_{ij,kl}(\mathbf{n}) u'_{kl}{}^*(\mathbf{n}, \eta) \\ &= \text{Tr}[\mathbf{P}\mathbf{u}'\mathbf{P}\mathbf{u}'^*] - \frac{1}{2}\text{Tr}[\mathbf{P}\mathbf{u}']\text{Tr}[\mathbf{P}\mathbf{u}'^*], \end{aligned} \quad (8.64)$$

where \mathbf{P} and \mathbf{u} are matrices with entries $P_{ij}(\mathbf{n})$ and $u_{ij}(\mathbf{n}, \eta)$, respectively, and we have used eqs. (8.60) to (8.62).

The implementation of the techniques presented in this section in *CosmoLattice*, for both scalar and Abelian gauge theories, was done as part of the doctoral research presented in this dissertation [11, 12].

9 GW emission from cosmic string loops: global case

Phase transitions taking place during the early universe may lead to the formation of *cosmic defects* [368–371]. These are metastable structures in which one or more fields are trapped far from the true vacuum of a theory due to topological constraints. Defects forming in the early universe may contain a large amount of energy and leave observable cosmological imprints after decaying.

The characteristics of the defects are related to the topological structure of the vacuum manifold, \mathcal{M} , of the underlying field theory, which corresponds to the possible value the field can take in the equivalent vacua of the theory. This manifold can be identified with the coset space of the associated symmetry breaking pattern, $G \rightarrow H$, this is, $\mathcal{M} = G/H$.

One of the better-known examples of defects are *cosmic strings*. These are one-dimensional topological defects that arise in theories in which the vacuum manifold has the topology of a circle, $\mathcal{M} \cong S^1$, characterized by having a non-trivial first homotopy group, $\pi_1(S^1) = \mathbb{Z}$.

The formation of networks of cosmic strings in the early universe is predicted by a variety of field-theory and superstring early-universe scenarios [372–375]. These networks are composed of long (infinite) strings that stretch along the observable universe, and *loops*. The former are expected to decay mainly via the production of loops due to self-intersection, while loops emit particles and gravitational waves (GWs), leading to the formation of a stochastic GW background (GWB) [376–378]. This could potentially be detected by current and future GW experiments, including LIGO and VIRGO [379, 380], pulsar-timing-array collaborations, that recently announced evidence of a GWB signal [381–384], and next-generation detectors, such as LISA [385].

A correct interpretation of a positive signal of a GWB requires of accurate predictions of the hypothetical sources of GWs. In the case of strings, these predictions are typically based on the Nambu-Goto (NG) approximation [386, 387], in which strings are considered to be infinitely thin, and the decay into particles is neglected. However, the latter has been argued to be a vital decay channel for some types of string loops [388, 389], and an in-depth study requires of field-theory simulations.

In this chapter, the results from ref. [6] are presented. We use lattice simulations to study the decay of cosmic string loops in theories containing a complex singlet scalar field with a Mexican-hat-like potential, the so-called *global strings*. We consider both particle and GW emission simultaneously, for loops with an initial length up to 1700 times their core width. In sec. 9.1 we introduce global strings and present some analytical results. We also discuss the NG approximation. We then detail in Sec. 9.2 how lattice simulations of cosmic strings are performed. Sec. 9.2.1 introduces the different observables used to study the string dynamics, and secs. 9.2.2 and 9.2.3 explain the procedure we use to generate the string loops. Our results on particle and GW emission are summarized in sec. 9.3, and we finalize in sec. 9.4 with some brief conclusions.

9.1 Global cosmic strings in the early universe

The simplest model leading to the formation of cosmic strings consists of a single complex scalar field, $\varphi = (\phi_1 + i\phi_2)/\sqrt{2}$, where ϕ_1 and ϕ_2 are real scalar fields, with action

$$S = \int d^4x \sqrt{-g} [(\partial_\mu \varphi)^* \partial^\mu \varphi - V(\varphi)], \quad (9.1)$$

where $V(\varphi)$ is the potential

$$V(\varphi) = \lambda \left(|\varphi|^2 - \frac{v^2}{2} \right)^2. \quad (9.2)$$

Here, λ is a dimensionless coupling constant and v is the vacuum expectation value of the complex field. This model is invariant under a U(1) global symmetry,

$$\varphi \rightarrow e^{i\alpha} \varphi, \quad (9.3)$$

with α a constant value.

The model in eq. (9.1) presents a symmetric and a broken phase. The former is characterized by a vacuum $\langle \varphi \rangle = 0$ that realizes the U(1) symmetry,

while in the broken phase the vacuum becomes $\langle \phi_1^2 + \phi_2^2 \rangle = v^2$, spontaneously breaking the global symmetry. The vacuum manifold after symmetry breaking has the topology of a circle, $\mathcal{M} \cong S^1$, and so may lead to the formation of cosmic strings after the phase transition.

The formation of the strings may happen via the so-called *Kibble mechanism* [368]. In a thermal environment, φ does not realize the potential in eq. (9.2), but instead some finite-temperature effective potential that includes corrections depending on the temperature, T ,

$$V_{\text{eff}}(\varphi, T) = V(\varphi) - \frac{\lambda}{3} T^2. \quad (9.4)$$

At high temperatures, the minima of this effective potential corresponds to the symmetric phase, but as the temperature falls below some critical value, $T_c = \sqrt{3}v$, the field falls into the true vacuum and the global U(1) symmetry is spontaneously broken.

If this phase transition happens before the end of inflation, $\varphi(x)$ takes a homogeneous value within a significant fraction of the observable universe today. However, if the transition happens after the end of inflation, causally disconnected patches of the universe may fall into different realizations of the true vacuum. Once they get in causal contact at a later time, cosmic strings must form to ensure continuity of the complex field.

Cosmic strings are thus topologically protected from decaying. The corresponding topological invariant is the *winding number*, $k \in \mathbb{Z}$, measured over any closed path. The winding number over some path quantifies the number of times the phase of φ completes a full 2π rotation along that path. Its conservation implies that long strings can only disappear if they collide with another string. Loops, even if formed by string segments with non-zero winding number, globally have $k = 0$, and so can collapse. Note that while the winding number is conserved, the length of the strings can vary. Infinite strings can emit part of their length as small loops, and curved regions in any type of strings can be smoothen up via the emission of particles and GWs.

It is possible to study the behavior of the theory close to the true vacuum, by expanding $\varphi(x)$ in terms of a radial, $\chi(x)$, and an angular, $\theta(x)$, degrees of freedom,

$$\varphi(x) = \frac{v + \chi(x)}{\sqrt{2}} e^{i\theta(x)}. \quad (9.5)$$

In these new variables, the action takes the form

$$S = \int d^4x \sqrt{-g} \left[\frac{1}{2} \partial_\mu \chi \partial^\mu \chi + \frac{1}{2} \left(1 + \frac{\chi}{v} \right) \partial_\mu \theta \partial^\mu \theta - \lambda v^2 \chi^2 - \lambda v^3 \chi^3 - \frac{1}{4} \lambda \chi^4 \right]. \quad (9.6)$$

Thus, after spontaneous symmetry breaking, the theory becomes that of a massive scalar field with mass $m_\chi = \sqrt{2\lambda}v$, and a massless field with $m_\theta = 0$.

9.1.1 The QCD axion

One of the best-known scenarios that may lead to the formation of cosmic strings are *axion models* [390, 391]. These aim at solving the strong CP problem, introduced in sec. 1.1, but also represent a viable explanation of dark matter [39].

Axion models extend the SM by adding a complex scalar field with an anomalous $U(1)$ symmetry, known as the Peccei-Quinn symmetry [37, 38]. The potential in eq. (9.2) is the simplest example having such symmetry. In this case, the QCD axion, a , corresponds to the θ fluctuation in eq. (9.5). After spontaneous symmetry breaking of the anomalous symmetry, the QCD axion develops a coupling to the gluon topological term,

$$\mathcal{L}_{\text{axion}}[a, A] \supset \frac{g^2 a N_f}{32\pi^2 f_a} \text{tr} [F_{\mu\nu} \tilde{F}^{\mu\nu}], \quad (9.7)$$

where f_a is the axion decay constant, and N_f , g , $F_{\mu\nu}$ and $\tilde{F}^{\mu\nu}$ are the number of quark flavors, the QCD gauge coupling, the gluon field-strength tensor and its dual counterpart, respectively. This term is analogous to the theta-term from QCD—see eq. (1.10)—and so both can be combined via a redefinition of the axion field $a \rightarrow \tilde{a} = a - \theta f_a$. In addition to eq. (9.7), the axion also develops a mass $m_a = \chi_{\text{top}}/f_a^2$, with χ_{top} the topological susceptibility of QCD, as well as a potential $V[a, \theta]$ that reaches a minimum when $\tilde{a} = 0$. This justifies the small upper bound of the observed CP violation in QCD, thus solving the strong CP problem.

Furthermore, QCD axions are very weakly interacting [392–395], and so they also represent a viable dark-matter candidate [396–398]. Closely-related dark-matter models are the so-called *axion-like theories* [399, 400]. These also include an anomalous spontaneously broken $U(1)$ symmetry, but do not aim at solving the strong CP problem, and so f_a and m_a can take a wider range of values.

Both the QCD axion and axion-like models may lead to the formation of cosmic strings if the anomalous $U(1)$ symmetry is spontaneously broken

after the end of inflation. The study of the cosmological implications of cosmic strings makes it possible to impose bounds on the parameters of the theories, such as the mass of the axion [401, 402].

9.1.2 Analytical solutions for cosmic strings

Investigating the dynamics of cosmic strings requires in general of field-theory numerical computations. However, one can gain insight on the properties of the strings by analytically studying some simple configurations. Here, we consider the global version of the so-called *Nielsen-Olesen vortex* [403], which corresponds to a static infinite straight string. For simplicity, we restrict ourselves to Minkowski spacetime, with scale factor $a = 1$.

Using cylindrical coordinates, (r, θ, z) , and assuming the string lies on the z -axis, we can write the complex field as

$$\varphi_{\text{NO}} = f(r) \frac{v}{\sqrt{2}} e^{ik\theta}, \quad (9.8)$$

where $k \in \mathbb{Z}$ is the winding number of the string and $f(r)$ is its radial profile. Substituting this into the equation of motion for the complex scalar field, eq. (8.12), one obtains

$$\frac{d^2 f}{d\tilde{r}^2} + \frac{1}{\tilde{r}} \frac{df}{d\tilde{r}} + k^2 \frac{f}{\tilde{r}^2} - f(f^2 - 1) = 0, \quad (9.9)$$

where $\tilde{r} = \sqrt{\lambda}vr$. This equation has been solved numerically using relaxation methods and imposing the boundary conditions $f(0) = 0$ and $f(\infty) = 1$. The results for $k = 1$ are shown in fig. 9.1. From here, one notes that strings have a typical core radius of the order $r_c \sim m_\chi^{-1}$. This result can be generalized to a homogeneous expanding background changing $r \rightarrow ar$. This means that it is the physical width of the string which remains constant as the universe expands, rather than its comoving counterpart, $w_c = r_c/a$, which decreases.

It is interesting to study the short- and long-range behaviour of $f(r)$. At short distances, $r \ll m_h^{-1}$, the last term in eq. (9.9) can be neglected and $f(r)$ is found to grow linearly, $f(r) \propto r$. At long separation, $r \gg m_h^{-1}$, on the other hand, the field approaches the vacuum quadratically, $f(r) = 1 - \mathcal{O}(r^{-2})$.

This behavior of the field has some implications for the dynamics of global strings. The total energy density of the string is

$$\rho(r) = \frac{1}{2} \left(\frac{df}{dr} \right)^2 + \frac{\lambda}{4} (f^2 - 1)^2 + \left(\frac{kf}{r} \right)^2. \quad (9.10)$$

The string tension, μ , representing the energy of the string per unit length, is obtained from integrating this energy density over all r and θ . The first

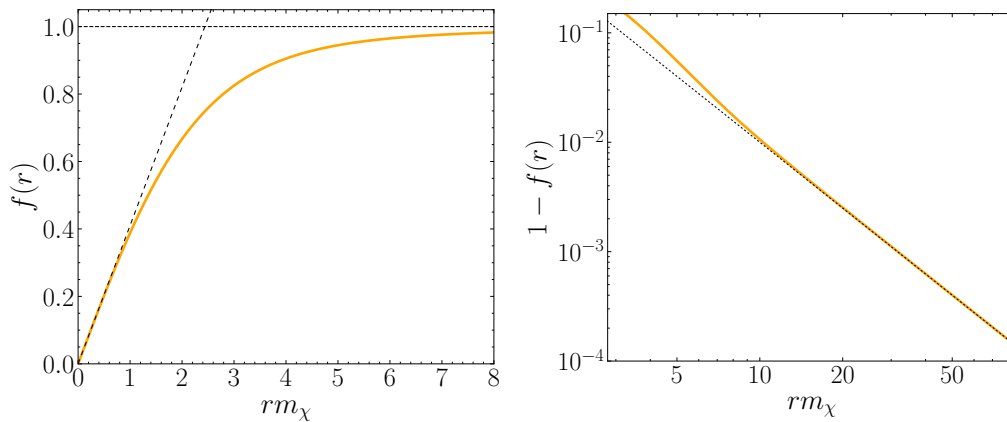


Figure 9.1. Radial profile of the global NO vortex with $k = 1$. We represent the short-range (dashed line, left panel) and the long-range (dotted line, left panel, in logarithmic scale) approximations.

two terms correspond to the gradient and potential energy of the massive field, and the result from integrating them is a finite contribution, μ_0 , that dominates up to distances of a few core radii. The last term is related to the massless field, and leads to a logarithmically divergent contribution to the tension that dominates at long distances,

$$\mu_\theta(R) \approx 2\pi \int_{r_c}^R \left(\frac{1}{r} \frac{d\varphi_{\text{NO}}}{d\theta} \right)^2 r dr = 2\pi v^2 \log \left(\frac{R}{r_c} \right), \quad (9.11)$$

where R is some cutoff scale, which in an early universe scenario would be related to the curvature of real strings or to the Hubble radius, H^{-1} . The total string tension is then

$$\mu = \mu_0 + \mu_\theta(R) \approx \mu_0 + 2\pi v^2 \log \left(\frac{R}{r_c} \right). \quad (9.12)$$

The logarithmic divergent tension implies that interactions between global strings are long-ranged, with a force that scales roughly as $\sim r^{-2}$.

Before concluding, we note that the NO solution can be used to create other string configurations. For example, one can consider a boosted NO vortex or use the *product ansatz* [371] to create a multistring solution, valid as long as the strings are sufficiently separated. However, the study of more complicated configurations requires of numerical lattice simulations.

9.1.3 The Nambu-Goto approximation

Numerical simulations of cosmic-string networks are restricted to a limited dynamical range. Cosmological string scenarios may reach a separation of scales of the order $\log(m_h/H) \sim 70$ [404], while current lattice simulations are limited to $\log(m_h/H) \lesssim 9$ [405–407], from which the results need to be extrapolated. An alternative approach to study cosmic strings is the use of an effective description, in which the strings are represented by infinitely-thin objects.

To understand this effective description, we can start by neglecting the massless modes in the theory. The dynamics of strings is then described using the Nambu-Goto action [386, 387],

$$S_{\text{NG}} = -\mu \int d^2\sigma \sqrt{-\gamma}, \quad (9.13)$$

where $\sigma = (\sigma^0, \sigma^1)$ are the coordinates of the string worldsheet and $\gamma = \det(\gamma_{ab})$, with

$$\gamma_{ab} = g_{\mu\nu} \frac{dx^\mu}{d\sigma^a} \frac{dx^\nu}{d\sigma^b}, \quad (9.14)$$

the metric on the worldsheet, being x the spacetime coordinates of the string core. The NG effective action can be recovered from field theory by integrating out the massive degrees of freedom, and remains valid as long as the curvature radius of the string is much bigger than its core width.

From this action, an equation of motion for the strings can be derived. In Minkowski spacetime one can write it in the form of a wave equation [371],

$$\ddot{x} - x'' = 0, \quad (9.15)$$

where $\dot{x} = \partial x / \partial \sigma^0$ and $x' = \partial x / \partial \sigma^1$. This equation is complemented by the gauge conditions

$$\dot{x} \cdot x' = 0, \quad \dot{x}^2 + x'^2 = 0, \quad (9.16)$$

and by setting σ_0 to be equal to the Minkowski time coordinate. A general solution can be expressed as a combination of right- and left-moving waves. This implies, for example, that the dynamics of loop have period $T = L_{\text{str}}/2$, where L_{str} is the proper length of the string,

$$L_{\text{str}} = \int d\sigma^1. \quad (9.17)$$

The traveling modes on the string may present discontinuities in x' and even infinite values. These features are typically known as *kinks* and *cusps*, respectively.

In the NG approximation, string loops can only decay via the emission of GWs. In particular they emit gravitational radiation at harmonic frequencies, $\omega_n = 2\pi n/T_{\text{NG}} = 4\pi n/L$ ($n = 1, 2, \dots$), with individual power,

$$P_n = \frac{8\pi\Gamma\mu^2}{m_{\text{p}}^2} \frac{n^{-q}}{\zeta(q)}, \quad (9.18)$$

where Γ is a dimensionless number, and q is a parameter that takes different values depending on the feature that dominates the GW emission [371, 378]: $q = 4/3$ for cusps, $q = 5/3$ for kinks and $q = 2$ for kink-kink collisions. The value of Γ can be analytically computed for some specific string configuration [408, 409], or determined from numerical simulations in more general cases. In particular, ref. [410] gets, from averaging over many simulations, that the distributions of values of Γ is peaked at $\Gamma \sim 50$. The total emission power of the loop is [411]

$$P_{\text{GW}} = \sum_{n=1}^{\infty} P_n = \frac{8\pi\Gamma\mu^2}{m_{\text{p}}^2}. \quad (9.19)$$

Note that eq. (9.18) is based on an asymptotic expansion of the tensor wave form, and so is a priori only valid for $n \gg 1$. At low n the structure of the entire loop becomes important [408]. However, the total power emitted is independent of this assumption—see ref. [371]. It is thus common to consider eq. (9.18) valid for all harmonics.

The NG approximation has been used as the basis of numerical studies of cosmic strings [412–417]. It is also the basis of other empirical approximations to string networks. This is for example the case of the *velocity-dependent one-scale (VOS) model* [418–420], which describes the statistical distribution of infinite strings and their velocities as a function two quantities: the mean string separation, ξ , and the average mean-square velocity, v_{rms}^2 .

The VOS model predicts that evolving string networks reach a stable *scaling regime* in which ξ grows linearly with conformal time and v_{rms}^2 remains constant. In the case of NG strings, this constant value is $v_{\text{rms,NG}}^2 = 1/2$, but the model has also been used to describe field-theory strings [406, 407, 421], which show smaller results for v_{rms}^2 . Note this model only describes the statistical properties of networks of infinite strings. The loss of energy from long strings via the emission of loops is encoded in some of the empirical parameters of the VOS model.

Beyond the NG model, it is also possible to construct an effective theory for the strings that includes massless modes, which is better suited to describe global strings. This is the so-called *Kalb-Ramond model* [422], in which massless modes are represented by an antisymmetric tensor field coupled to

the string. This model makes it possible to obtain the logarithmic-divergent tension in eq. (9.12). If naively we substituted this tension in eq. (9.19), the emission of GW would be enhanced at cosmological scales. However, the validity of eq. (9.19) is not clear in this case. In addition, the Kalb-Ramond model also predicts that the total emission power of loops into massless radiation takes the form,

$$P_\theta = \Gamma_\theta v^2, \quad (9.20)$$

with $\Gamma_\theta \sim 100$ [409, 423].

9.2 Lattice simulations of global strings

The zero-width approximation, presented in the previous section, disregards the internal structure of strings. The emission of massive particles is neglected, and even if massless modes are included, the effective description fails in the high curvature regions, which are those expected to dominate the radiation of particles and GWs. To fully capture the field-theory nature of cosmic strings, we need lattice simulations. While their applicability to study full networks is limited by the dynamical range, one can focus on individual strings or features. These could be, for example, oscillations of infinite strings [424, 425], kink-kink collisions [426] or the decay of isolated loops [427, 428]. In this chapter, we focus on this last case.

The use of lattice simulations to study the decay of global string loops follows the same basics as any other field-theory early-universe simulation. We describe the particular string observables that we measure in sec. 9.2.1, and present the procedure used to generate two types of loops that we study, which we call *network* and *artificial loops*, in secs. 9.2.2 and 9.2.3, respectively. We consider a Minkowski background and work in dimensionless program variables, as introduced in see sec. 8.2.2, defined with

$$f_\star = v, \quad \omega_\star = \sqrt{\lambda}v. \quad (9.21)$$

We recall that dimensionless variables are indicated by adding a tilde to its dimensional version. For example, if L denotes the string length, $\tilde{L} = \sqrt{\lambda}vL$.

9.2.1 Global-string observables

To monitor the length and the dynamics of the strings, we determine the location of the string cores from those plaquettes having a non-zero winding number. A plaquette with lattice coordinate \mathbf{n} in the ij -plane, has winding number [429, 430],

$$W_{ij}(\mathbf{n}) = \frac{1}{2\pi} \left[Y_i(\mathbf{n}) + Y_j(\mathbf{n} + \hat{\mathbf{i}}) - Y_i(\mathbf{n} + \hat{\mathbf{j}}) - Y_j(\mathbf{n}) \right], \quad (9.22)$$

where

$$Y_i(\mathbf{n}) = \left[\theta(\mathbf{n}) - \theta(\mathbf{n} + \hat{\mathbf{i}}) \right]_{\pi}, \quad (9.23)$$

is the variation of the phase along each link of the plaquette. In this equation, $[\alpha]_{\pi}$ sets the angle α in the range $-\pi < \alpha \leq \pi$. The determination of the coordinates of the string core can be refined by using the values of the field at the plaquette vertices to infer its exact location on the plaquette [424, 431], but we do not use these techniques in the work presented here.

Using the total number of pierced plaquettes, N_w , we can estimate the total comoving length of the string in the lattice frame,

$$L_w = \frac{2}{3} \delta x N_w, \quad (9.24)$$

where the 2/3 factor takes into account the Manhattan effect [431], i.e., the fact that after entering some lattice cell, strings may leave it through any of the other five faces.

In addition, the coordinates of the pierced plaquettes allow us to have real-time insight on the structure and shape of the string configuration. For example, we can use these results to determine if an isolated loop has been found. This, however, requires to reconstruct the strings from the measurement of the coordinates of the pierced plaquettes.

Knowing the sign of the winding on each plaquette, one can determine an unordered list of string segments, $s_i = \{\mathbf{n}_i^{\text{ini}}, \mathbf{n}_i^{\text{fin}}\}$. Each one starts at the center of some cell, with coordinate $\mathbf{n}_i^{\text{ini}}$, and ends at the center of one of the adjacent cells, of coordinate $\mathbf{n}_i^{\text{fin}}$. Note that both loops and infinite strings are closed in a periodic lattice, meaning that for every cell \mathbf{n} where some segment i ends, another segment j starts, $\mathbf{n}_i^{\text{fin}} = \mathbf{n}_j^{\text{ini}}$. Reconstructing the string implies identifying, for each segment s_i , the segment s_j that follows.

Naively, one would order the segments iterating over the full list and, for each segment s_i , finding the segment s_j that follows it. This algorithm, however, would have a time complexity $\mathcal{O}(N_w^2)$, representing a huge bottleneck for the simulations. To overcome this limitation, we propose an algorithm that scales as $\mathcal{O}(N_w \log N_w)$. This is explained now, complemented diagrammatically with fig. 9.2, with a simple example of a string consisting of four segments.

The first step is to order the segments according to their final coordinate, \mathbf{n}^{fin} . This can be done, for example, comparing first the x component, followed by the y component and finally the z one. The second step consists on indexing each segment with an integer number, k , that indicates their position in the current ordered list.

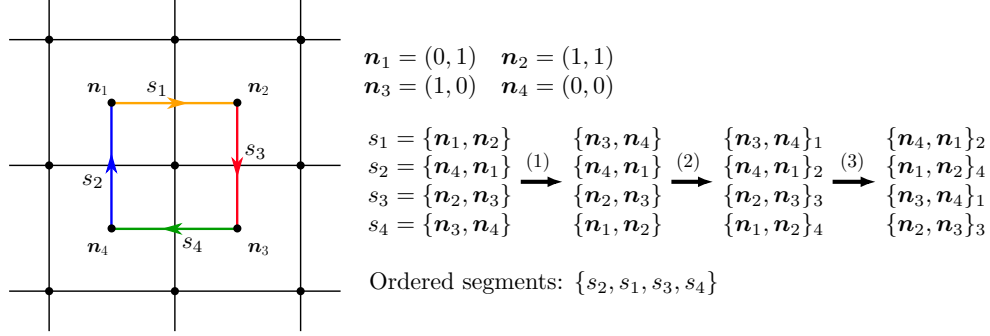


Figure 9.2. Representation of the algorithm used to join the segments of strings determined from the pierced plaquettes, in the case of a four-segment loop.

In a third step, we order again the indexed segments according to their initial coordinate, \mathbf{n}^{ini} , following the same criteria as in the first step. In this newly-ordered list, the index of each segment indicates the position, within the current list, of the next segment. In our example, for instance, the segment with initial coordinate \mathbf{n}_4 has index $k = 2$, indicating that the following string in the second in the newly-ordered list, in this case that with initial coordinate \mathbf{n}_1 . From this, one can move to the following segment in the string, until the initial segment is reached again, closing the string. Then, if there are segments that have still not been assigned to any string, one considers another of these segments and reconstructs the corresponding string and so on. Thus, using this ordered indexed list, reconstructing the strings becomes trivial.

We also measure the energy components of the strings. To avoid including free radiation and prevent issues with the logarithmically-divergent tension, we make use of a weight function, $W(\varphi)$, that is peaked at the string core. We use a weight related to the potential,

$$W(\varphi) = \frac{4V(\phi)}{\lambda v^4} \Theta \left(\frac{v^2}{2} - |\varphi|^2 \right), \quad (9.25)$$

normalized such that $W(0) = 1$. Here Θ is the Heaviside function that ensures we are not including field values with $|\varphi|^2 > v^2/2$. Using this weight, we can measure the total kinetic, gradient and potential energy component of the string. In an expanding background, with a the scale factor and working in conformal time, they take the form

$$E_{\text{K, str}} = a \int W(\varphi) |\varphi'|^2 d^3x, \quad E_{\text{G, str}} = a \sum_i \int W(\varphi) |\partial_i \varphi|^2 d^3x, \quad (9.26)$$

$$E_{\text{V, str}} = a^3 \int W(\varphi) V(\varphi) d^3x,$$

with the Minkowski results corresponding to the $a = 1$ case. The sum of all three components is the total energy of the string,

$$E_{\text{str}} = E_{\text{K,str}} + E_{\text{G,str}} + E_{\text{V,str}}. \quad (9.27)$$

The string angular momentum is also determined [428],

$$J_{\text{str},i} = -\frac{a^2}{2} \varepsilon_{ijk} \int W(\varphi) [\Delta x_j (\dot{\varphi} \partial_k \varphi^* - \dot{\varphi}^* \partial_k \varphi)] d^3x, \quad (9.28)$$

where $\Delta x_i = x_i - x_i^{\text{geom}}$ are the relative coordinates with respect to the geometric center of the string, \mathbf{x}^{geom} , that we determine using the pierced plaquettes,

$$\mathbf{x}^{\text{geom}} = \frac{\delta x}{N_w} \sum_i^{N_w} \mathbf{n}_{\text{pierced}}, \quad (9.29)$$

where $\mathbf{n}_{\text{pierced}}$ are the coordinates of the pierced plaquettes. Note that we can only reliably estimate the angular momentum of strings with a total size smaller than the lattice volume, i.e., those that do not warp around the periodic boundary, as the definition of Δx_i is otherwise ill-defined. Program variables corresponding to the string energy and angular momentum are defined, respectively, as

$$\tilde{E}_{\text{str}} = (\sqrt{\lambda}/v) E_{\text{str}}, \quad \tilde{J}_i = \lambda J_i. \quad (9.30)$$

Using the weighted energy components, it is possible to obtain estimates of the proper comoving length of the strings and its mean squared velocity [406, 407],

$$L_{\text{str}} = \frac{1}{a} \frac{E_{\text{str}} + f_V E_{\text{L,str}}}{\mu(1 + f_V)}, \quad (9.31)$$

$$v_{\text{rms}}^2 = \frac{E_{\text{str}} + E_{\text{L,str}}}{E_{\text{str}} + f_V E_{\text{L,str}}},$$

where $E_{\text{L,str}} = E_{\text{K,str}} - E_{\text{G,str}} - E_{\text{V,str}}$ is the weighted Lagrangian energy of the string and μ and f_V are the weighted tension and the fraction of weighted potential energy of the NO vortex,

$$\mu = a^2 \int W(\varphi) \left[\frac{1}{2} \left(\frac{df}{dr} \right)^2 + \frac{\lambda}{4} (f^2 - 1) + \left(\frac{kf}{r} \right)^2 \right] d^2x, \quad (9.32)$$

$$f_B = \frac{\lambda a^2}{4\mu} \int W(\varphi) (f^2 - 1)^2 d^2x,$$

with f the profile function introduced in eq. (9.8). We compute both these quantities for our choice of the weight function, eq. (9.25), finding $\mu = 1.7824v^2$ and $f_V = 0.3689$ for $k = 1$. Other independent estimators of

the mean square velocity can also be defined—see ref. [407]. We note L_{str} is approximately related to L_w in eq. (9.24) as

$$L_w = L_{\text{str}} \langle \gamma^{-1} \rangle, \quad (9.33)$$

where γ is the usual boost factor. The average of γ^{-1} , however, is in general not equal to $(1 - v_{\text{rms}}^2)^{1/2}$.

Finally, we also study the emission of massive and massless particles from the string loops. Separating the radial and the angular modes as $\varphi(x) = \rho(x)/\sqrt{2} \times \exp[i\theta(x)]$, the energy density of φ can be divided between the two,

$$\begin{aligned} \rho_\rho &= \frac{1}{2} \dot{\rho}^2 + \frac{1}{2} \partial_i \rho \partial_i \rho + \frac{\lambda}{4} (\rho^2 - v^2)^2, \\ \rho_\theta &= \frac{\rho^2}{2} \left[\dot{\theta}^2 + \partial_i \theta \partial_i \theta \right]. \end{aligned} \quad (9.34)$$

To compute the gradients and time derivatives appearing in these expressions, it is convenient to work with the full complex scalar field [424]. For example, recalling we define $\varphi = (\phi_1 + i\phi_2)/\sqrt{2}$, we can compute

$$\dot{\theta} = \frac{\phi_1 \dot{\phi}_2 - \phi_2 \dot{\phi}_1}{\sqrt{2} v |\varphi|}, \quad (9.35)$$

and similarly for $\dot{\chi}$, $\partial_i \theta$ and $\partial_i \chi$.

We also study the power spectrum of both massive and massless modes and of the associated energy components. For example, in the case of massless modes, the energy per Fourier mode is defined as [428]

$$\rho_\theta(k) = \frac{v^2}{2} \left[|\dot{\theta}(\mathbf{k})|^2 + k^2 |\theta(\mathbf{k})|^2 \right]. \quad (9.36)$$

9.2.2 Generation of network loops

We consider two types of string loops for this work. The first type are called *network loops*. They are generated from the decay of string networks that are close to the scaling regime, and are expected to have shapes and features that resemble physical configurations expected in the early universe.

The string networks that lead to the loops are generated following the procedure from refs. [406, 407]. Simulations are initialized with a random Gaussian field in Fourier space with variance given by a power spectrum,

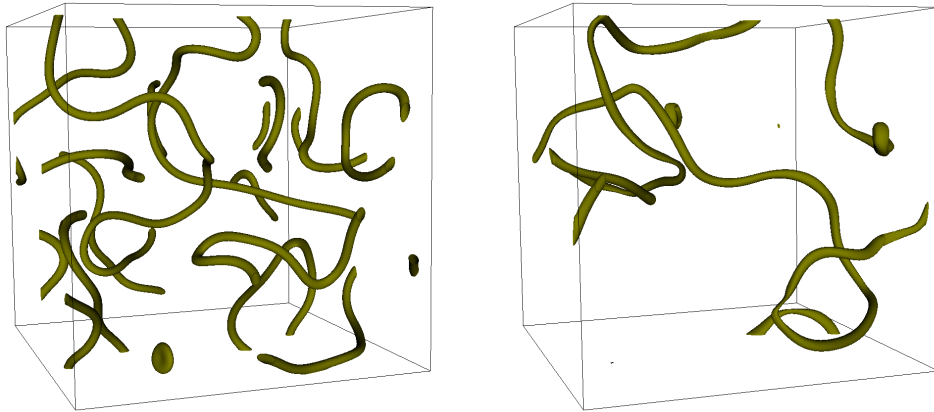
$$\Delta_{\phi_i}(k) = \frac{k^3 v^2 \ell_{\text{str}}^3}{\sqrt{2\pi}} \exp\left(-\frac{1}{2} k^2 \ell_{\text{str}}^2\right), \quad (9.37)$$

that is normalized such that $\langle \phi_1^2 \rangle + \langle \phi_2^2 \rangle = v^2$ —see eq. (8.23). Here, ℓ_{str} is a correlation length that controls the density of the network. The time derivative of the scalar field is initially set to zero.

The configuration resulting from the previous step is initially too energetic. To remove the excess energy, we evolve the complex field following a diffusion process,

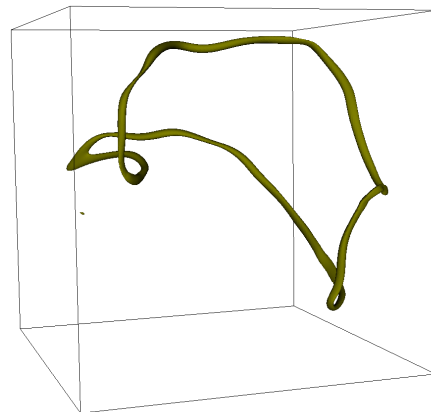
$$\sqrt{\lambda} v \phi'_i - \partial_j \partial_j \phi_i = -2\lambda \left(|\phi|^2 - \frac{v^2}{2} \right) \phi. \quad (9.38)$$

We make this period last for 20 units of program time, which we found to be enough to leave a smooth configuration. An example of the resulting network is presented in fig. 9.3a.



(a) End of diffusion.

(b) End of extra-fattening.



(c) Moment when an isolated loop is found.

Figure 9.3. Snapshots of $|\varphi^2| = 0.1v^2$ surfaces of a network loop generated with $\tilde{\ell}_{\text{str}} = 5$ in a box with $\tilde{L} = 64$, $\delta\tilde{x} = 0.25$.

After the diffusion phase, the string network is evolved in a radiation-dominated (RD) background. The equation of motion of the field, working in conformal time τ , is

$$\varphi'' + 2\frac{a'}{a}\varphi' - \partial_i\partial_i\varphi = -2a^2\lambda\left(|\varphi|^2 - \frac{v^2}{2}\right)\varphi, \quad (9.39)$$

where $\varphi' = d\varphi/d\tau$. In addition, the scale factor is fixed to evolve as $a(\tau) = \tau/\tau_0$, where we use $\tau_0 = 70/\sqrt{\lambda}v$ in our simulations. This evolution of the scale factor is the late-time approximation of eq. (8.5) in a RD universe. The background expansion is maintained for a half-box-light-crossing time, $\Delta\tau_{\text{HL}} = L/2$, with L the side of the lattice, which is the time it takes a beam of light to cross half of the lattice side.

Evolving the string network in an expanding universe, however, comes with a drawback. The string width is constant in physical units, and so the comoving width of the strings reduces with time, $w_c = r_c a^{-1}$. This means that as the universe expands, less and less lattice sites are contained inside of the string core and we loose resolution of the string structure.

To prevent this loss of resolution, we employ the resolution-preserving approach from ref. [432], known as *extra-fattening*. The idea is to perform an initial phase of evolution during which the coupling constant λ is promoted to a time-dependent parameter, $\lambda = a^{-4}\lambda_0$, with λ_0 its value at the end of diffusion, which we use to define program variables, $\omega_* = \sqrt{\lambda_0}v$. This change implies that the comoving string width grows in time, $w_c \propto a$. The extra-fattening phase is taken to last for $\Delta\tau_{\text{ef}} = \sqrt{\tau_0}(\Delta\tau_{\text{HL}} + \tau_0)$, after which standard physical evolution in a RD background follows. This guarantees that at time $\tau_0 + \Delta\tau_{\text{HL}}$ the comoving string width is equal to its value at the end of diffusion, $w_c(\tau_0 + \Delta\tau_{\text{HL}}) = w_c(\tau_0)$. An example of the evolution of the scale factor, λ parameter and string width is represented in fig. 9.4, for a simulation with $\tilde{L} = 256$ and $\delta\tilde{x} = 0.25$. We show an example of a network at the end of the extra-fattening phase in fig. 9.3b. It is worth mentioning that this approach differs from the so-called *fattening* in which $\lambda \rightarrow a^{-2}\lambda$ is kept during the whole simulation so that the comoving string radius is kept constant.

After evolving the network in an expanding background for a time $\Delta\tau_{\text{HL}}$, that includes the extra-fattening phase during the initial $\Delta\tau_{\text{ef}}$, networks are found to be close to the scaling regime. This can be seen in fig. 9.5, where we represent $\xi = (L^3/L_{\text{str}})^{1/2}$ and v_{rms}^2 averaged over 10 independent network realizations. One observe that ξ approaches a linear scaling, $\xi \propto \tau$, while v_{rms}^2 approaches a constant around $v_{\text{rms}}^2 \sim 0.4$, which is slightly smaller than the NG expectation. Note that, due to the limited size of our simulations, we are not able to completely reach the expected scaling regime—see however refs. [406, 407] for bigger simulations.

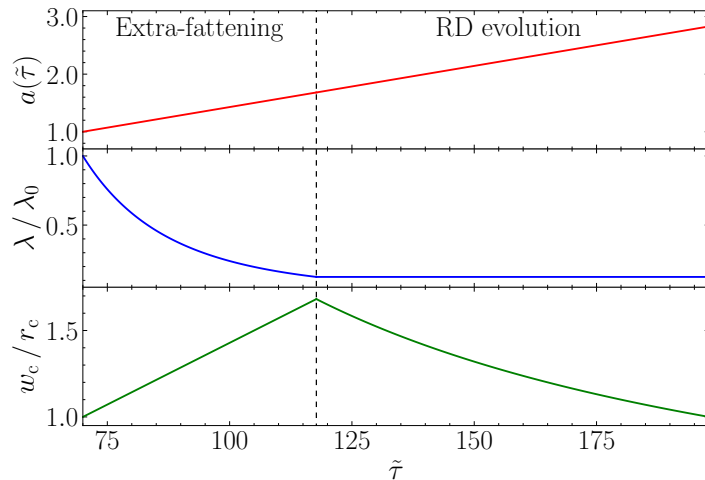


Figure 9.4. Evolution of the scale factor (top), the λ parameter (center) and the core width of the string (bottom) during the extra-fattening phase and the subsequent evolution in a RD background, separated by a vertical dashed line. Both λ and w_c are normalized by their initial values at the end of diffusion.

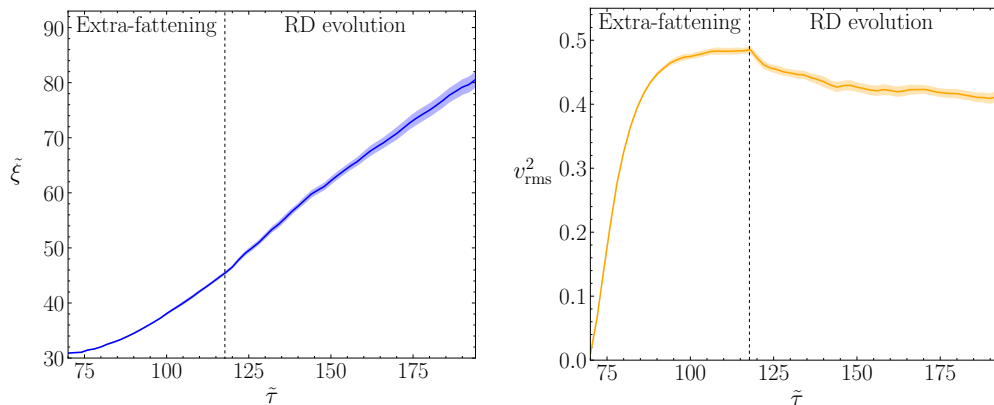


Figure 9.5. Time-evolution of the comoving mean string separation (left) and the mean-squared velocity (right) of a network of global strings averaged over 10 independent realizations. The networks are generated with $\tilde{\ell}_{\text{str}} = 15$ and simulations are performed with $\tilde{L} = 256$ and $\delta\tilde{x} = 0.25$. The vertical dotted line indicates the end of extra-fattening and the shaded region corresponds to one standard deviation.

At this point, however, the network has not had enough time to decay into a single isolated loop. We thus let it evolve longer in a Minkowski background ($a = 1, \dot{a} = 0$) for a maximum time of $\Delta\tau_{\text{HL}}/2$, which we find sufficient for the network to lead to a single loop. We find that $\sim 35\%$ of our simulations have decayed into a single loop after this time, with the remaining ones forming multiple loops or infinite strings, and hence not being suitable for our study. An example of an isolated network loop is shown in fig. 9.3c.

Once we find an isolated loop, the emission of GWs is turned on and we study the evolution of the loop, still in Minkowski background, until it disappears, this is, until the moment when no pierced plaquettes are measured during some consecutive time units. It turns out that only $\sim 40\%$ of the isolated loops could be used for this study. We discarded those that self-intersected forming infinite strings or that were much longer than the box size. Overall, only $\sim 10\%$ of the simulations of network loops were used for this study.

9.2.3 Generation of artificial loops

Artificial loops are generated from the intersection of two pairs of parallel infinite boosted strings, following the procedure in ref. [428]. This gives us control over the initial conditions at the cost of a more artificial squared shape of the loops. We consider one pair of infinite strings parallel to the z -axis and the other aligned with the x -axis. We will refer with a subscript “1” to those quantities related to the z -axis pair and with a “2” subscript to quantities related to the x -axis one.

We explain how the pair parallel to the z axis is generated—an analogous procedure applies for the other pair. The relevant quantities used to generate each pair are depicted in fig. 9.6. We start from the NO vortex solution, $\varphi_{\text{NO}}^{(k)}$, given in eq. (9.8), where $k = \pm 1$ denotes the winding number of the string.

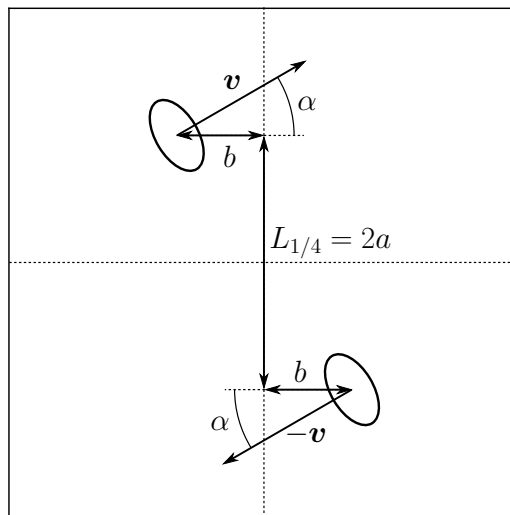


Figure 9.6. Schematic representation of the relevant variables used for the creation of a pair of parallel boosted strings. We have exaggerated b compared to the actual simulations, which use $r_c \lesssim b \ll a = L_{1/4}/2$.

The static NO solution can be boosted with velocity $\mathbf{v}_1 = v_1(\sin \alpha_1, \cos \alpha_1)$ in the (x, y) -plane, $\varphi_{\mathbf{v}_1}^{(\pm)}(x, y; t) = \varphi_{\text{NO}}^{(\pm)}(x', y')$, where

$$\begin{aligned} x' &= -\gamma_1 v_1 s_1 t + [1 + (\gamma_1 - 1)s_1^2]x + (\gamma_1 - 1)s_1 c_1 y, \\ y' &= -\gamma_1 v_1 c_1 t + (\gamma_1 - 1)s_1 c_1 x + [1 + (\gamma_1 - 1)c_1^2]y, \end{aligned} \quad (9.40)$$

with $c_1 = \cos \alpha_1$, $s_1 = \sin \alpha_1$ and $\gamma_1 = (1 - v_1^2)^{-1/2}$. Here (x', y') are the coordinates in the rest frame, where the string is static, and (x, y, t) refer to the lattice frame.

A pair of strings parallel to the z -axis is constructed using the product ansatz on two strings with opposite winding, $k = \pm 1$, and velocities, $\pm \mathbf{v}_1$,

$$\begin{aligned} \varphi_1(x, y; t) &= \frac{1}{v} \varphi_{\mathbf{v}_1}^{(+)} \left[x - \left(\frac{L}{2} + a_1 \right), y - \left(\frac{L}{2} + b_1 \right); t \right] \\ &\quad \times \varphi_{-\mathbf{v}_1}^{(-)} \left[x - \left(\frac{L}{2} - a_1 \right), y - \left(\frac{L}{2} - b_1 \right); t \right], \end{aligned} \quad (9.41)$$

where a_1 and b_1 refer, respectively, to the displacement of the string in the x and y directions with respect to the center of the box—see fig. 9.6. Note that, for this work, we consider symmetric configurations in which both strings have the same velocity magnitude and displacements.

The resulting field and its derivative, evaluated at $t = 0$, are modified following the procedure presented in ref. [428] to incorporate them in a periodic lattice. The complete initial configuration for our simulations is obtained using the product ansatz again in two perpendicular string pairs, parallel each one to the z and the x axis,

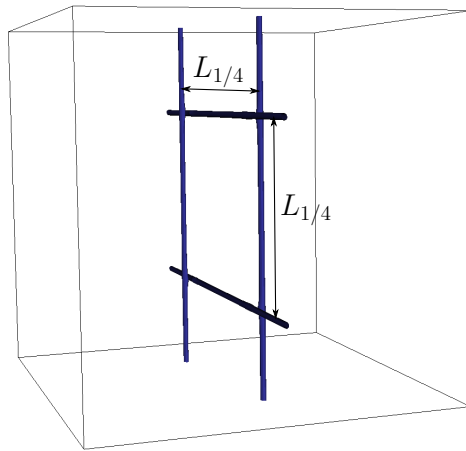
$$\varphi(x, y, z) = \varphi_1(x, y; t = 0) \times \varphi_2(z, y; t = 0). \quad (9.42)$$

An example of the resulting configuration is shown in fig. 9.7a. The time derivative of the fields can be computed as

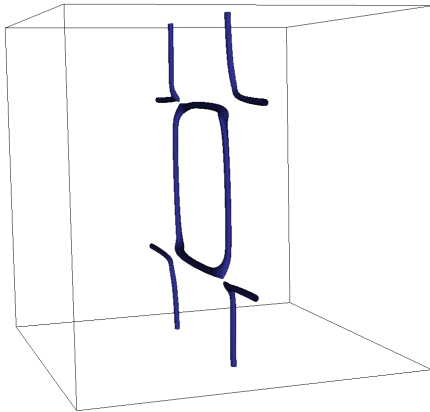
$$\dot{\varphi} = \dot{\varphi}_1 \varphi_2 + \varphi_1 \dot{\varphi}_2, \quad (9.43)$$

where $\dot{\varphi}_i$ can be determined from successive application of the chain rule.

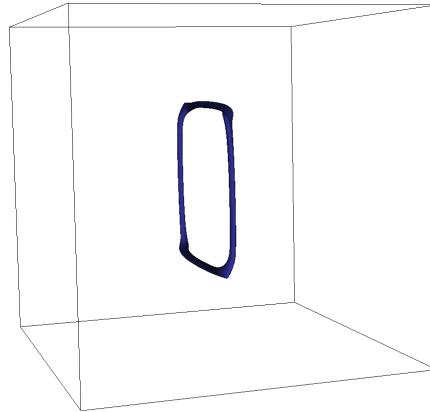
We consider, in general, boost velocities for the two pairs with different magnitude, $v_1 \neq v_2$ and $v_2 \geq v_1$, but the same angle, $\alpha_1 = \alpha_2 = \alpha$. We also take the strings to initially lie almost in the $y = L/2$ plane. We set $b_1 = 0$ and $b_2 = 2/\sqrt{\lambda}v$, so that the strings are separated enough that the product ansatz applies, but also the intersection between the strings happens soon in the simulation. In addition, we consider $a_1 = a_2$ to be a significant fraction of the box size, typically $L/4$ or $L/6$. The approximate separation of the two strings within each pair is denoted $L_{1/4} = 2a$ —see fig. 9.7a.



(a) Beginning of the simulation.



(b) Instant before isolating the inner loop.



(c) Instant after isolating the inner loop.

Figure 9.7. Snapshots of $|\varphi^2| = 0.06v^2$ surfaces of an artificial loop generated with $v_1 = 0.6$, $v_2 = 0.8$ and $\sin \alpha = 0.5$ in a box with $\tilde{L} = 64$, $\delta\tilde{x} = 0.25$.

The initial field configuration in eq. (9.42) is evolved in a Minkowski background, and the four strings soon intersect forming two square-shaped loops, an *inner loop* with initial length approximately $L_w = 4L_{1/4}$, and an *outer loop*. Initially the two loops are almost planar and the inner one has its center close to that of the lattice. Shortly after forming, the two-loops start to shrink due to particle emission and separate from each other.

We have developed a method to isolate the inner loop. After the loops form, we let them evolve until their separation is a fraction (we choose a 15%) of the radius of the inner loop, defined as the maximum distance to the center of the box from any point of the string core. We then consider a cylinder of radius R and axis parallel to the y -axis, so that it encompasses the inner loop and its surface lies midway between the two loops. The field and its derivative outside the cylinder are then substituted by a smooth field configuration

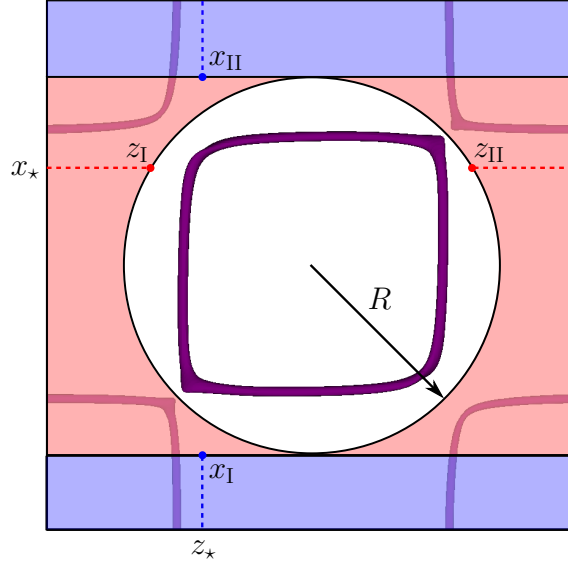


Figure 9.8. Schematic representation of the relevant variables used to isolate the inner loop in artificial-loop simulations. The red and blue regions outside the cylinder are substituted by a smooth configuration in two separate steps.

containing no loops. The cylinder and other quantities relevant for the isolation procedure, which we introduce below, are pictorially represented in fig. 9.8

This substitution is performed in two steps, repeated for each fixed value of the y coordinate, which we call y_* . First, we consider the points (x, y_*, z) outside the cylinder with $|L/2 - x| < R$, represented by the red region in fig. 9.8. Each value of $x = x_*$ defines a line that intersects the cylinder twice, at z_I and $z_{II} > z_I$. The field and its derivative outside the cylinder are substituted by a smooth field configuration: phases are linearly interpolated using the values at z_I and z_{II} , while their magnitudes are substituted by some periodic ansatz based on the long-range behavior of the NO solution,

$$|\varphi(x_*, y_*, z)| = \begin{cases} \frac{\xi_I}{(\Delta - z + z_I)^2} + \frac{\xi_{II}}{(L + z + \Delta - z_{II})^2} + \frac{v}{\sqrt{2}}, & 0 \leq z < z_I, \\ \frac{\xi_I}{(L - z + \Delta + z_I)^2} + \frac{\xi_{II}}{(\Delta + z - z_{II})^2} + \frac{v}{\sqrt{2}}, & z_{II} < z < L, \end{cases} \quad (9.44)$$

$$|\dot{\varphi}(x_\star, y_\star, z)| = \begin{cases} \frac{\pi_{\text{I}}}{(\Delta - z + z_{\text{I}})^3} + \frac{\pi_{\text{II}}}{(L + z + \Delta - z_{\text{II}})^3}, & 0 \leq z < z_{\text{I}}, \\ \frac{\pi_{\text{I}}}{(L - z + \Delta + z_{\text{I}})^3} + \frac{\pi_{\text{II}}}{(\Delta + z - z_{\text{II}})^3}, & z_{\text{II}} < z < L, \end{cases} \quad (9.45)$$

where $\xi_{\text{I,II}}$ and $\pi_{\text{I,II}}$ are constants that ensure continuity at the surface of the cylinder, and Δ is a length parameter we set to $\Delta = 2/\sqrt{\lambda v}$.

In a second step, we consider points with $|L/2 - x| \geq R$ (represented by the blue region in fig. 9.8) and proceed analogously working at fixed $z = z_\star$. Both steps are repeated for all values of y_\star . An example of a loop configuration before and after isolating the inner loop is shown in figs. 9.7b and 9.7c, respectively. After the inner loop is isolated, we turn on the emission of GWs and study the loop until it decays.

We finally remark that we have studied the effect of varying Δ , as well as the isolation time and the size of the cylinder. Our results are insensitive, within errors, to such changes, as long as, at the isolation time, both loops are enough separated from each other and the cylinder surface is kept at a distance from both loops.

9.3 Results

We now present our results on loop decay into particles and GWs. We characterize the particle emission power in sec. 9.3.1 and study in sec. 9.3.2 the spectral distribution of the massive and massless modes produced by the string. Then, we analyze the GW emission power in sec. 9.3.3. We stress that the energy radiated in form of GWs is not subtracted from the strings, since we neglect backreaction of the GWs into the matter fields. We justify this assumption self-consistently later. This implies that loops in our simulations decay only due to the emission of particles.

9.3.1 Loop decay into particles

We characterize the lifetime of the loops, Δt_{dec} , as a function of their initial size, L_0 , energy, $E_{\text{str},0}$, and angular momentum, $J_0 = |\mathbf{J}_0|$. We analyzed 23 different network loops with length-to-width ratios up to $L_0/r_c \lesssim 1700$, and 49 artificial loops with $L_0/r_c \lesssim 800$. The parameters used in the simulations of network loops are summarized in table 9.1. For artificial loops, for each set of boost parameters in table 9.2, we run simulations for all the lattices in table 9.3

\tilde{L}	$\delta\tilde{x}$	$\tilde{\ell}_{\text{str}}$	\tilde{L}_0
256	0.25	25	868.3
256	0.25	20	924.3
256	0.25	20	889.7
$320/\sqrt{2} \approx 226.3$	$0.25/\sqrt{2} \approx 0.177$	22	1162.5
$256/\sqrt{2} \approx 181.0$	$0.25/\sqrt{2} \approx 0.177$	15	1071.5
$256/\sqrt{2} \approx 181.0$	$0.25/\sqrt{2} \approx 0.177$	15	684.0
$256/\sqrt{2} \approx 181.0$	$0.25/\sqrt{2} \approx 0.177$	15	371.2
144	0.25	12	557.0
144	0.25	12	296.3
144	0.1875	12	605.0
144	0.1875	12	553.5
144	0.125	12	633.6
$192/\sqrt{2} \approx 135.8$	$0.25/\sqrt{2} \approx 0.177$	15	728.6
$192/\sqrt{2} \approx 135.8$	$0.25/\sqrt{2} \approx 0.177$	15	699.8
$192/\sqrt{2} \approx 135.8$	$0.25/\sqrt{2} \approx 0.177$	15	582.2
$192/\sqrt{2} \approx 135.8$	$0.25/\sqrt{2} \approx 0.177$	15	462.4
$192/\sqrt{2} \approx 135.8$	$0.25/\sqrt{2} \approx 0.177$	15	405.2
128	0.25	10	433.2
$128/\sqrt{2} \approx 90.5$	$0.25/\sqrt{2} \approx 0.177$	8	260.7
$128/\sqrt{2} \approx 90.5$	$0.25/\sqrt{2} \approx 0.177$	8	234.1
$128/\sqrt{2} \approx 90.5$	$0.25/\sqrt{2} \approx 0.177$	8	215.2
$128/\sqrt{2} \approx 90.5$	$0.25/\sqrt{2} \approx 0.177$	8	88.2
$128/\sqrt{2} \approx 90.5$	$0.25/\sqrt{2} \approx 0.177$	8	60.3

Table 9.1. Summary of the simulation parameters used to study the decay of network loops, together with the initial length of the isolated loops estimated from the number of pierced plaquettes—see eq. (9.24).

v_1	v_2	$\sin \alpha$
0.9	0.9	0.4
0.9	0.6	0.4
0.9	0.3	0.4
0.9	0.0	0.4
0.6	0.6	0.4
0.6	0.3	0.4
0.3	0.3	0.4

Table 9.2. Sets of boost parameters (rows) used to generate artificial loops.

\tilde{L}	$\tilde{L}_{1/4}$	$\delta\tilde{x}$
$50/\sqrt{2} \approx 35.4$	$25/\sqrt{2} \approx 17.7$	$0.25/\sqrt{2} \approx 0.177$
$100/\sqrt{2} \approx 70.7$	$50/\sqrt{2} \approx 35.4$	$0.25/\sqrt{2} \approx 0.177$
$150/\sqrt{2} \approx 106.1$	$75/\sqrt{2} \approx 53.0$	$0.25/\sqrt{2} \approx 0.177$
$200/\sqrt{2} \approx 141.4$	$100/\sqrt{2} \approx 70.7$	$0.25/\sqrt{2} \approx 0.177$
$250/\sqrt{2} \approx 176.8$	$125/\sqrt{2} \approx 88.4$	$0.25/\sqrt{2} \approx 0.177$
$300/\sqrt{2} \approx 212.1$	$150/\sqrt{2} \approx 106.1$	$0.25/\sqrt{2} \approx 0.177$
$400/\sqrt{2} \approx 282.8$	$200/\sqrt{2} \approx 141.4$	$0.25/\sqrt{2} \approx 0.177$

Table 9.3. Sets of lattice parameters used for artificial-loop simulations. For each family of boost parameters in table 9.2, a simulation is performed using each set in this table.

In fig. 9.9a, we show the decay time of network loops as a function of their initial lengths, the latter measured using the number of pierced plaquettes—see eq. (9.24). We observe that the results scale roughly linearly with L_0 , indicating a scale invariant mechanism driving the decay of the loops. Similar behavior is also observed as a function of the initial string energy, $E_{\text{str},0}$, determined using eq. (9.27) at the time when the isolated loop is found. The results of linear fits of the form $\Delta\tilde{t}_{\text{dec}} = A\tilde{L}_0 + B$ and $\Delta\tilde{t}_{\text{dec}} = C\tilde{E}_{\text{str},0} + D$ are presented in the first row of table 9.4. The latter result allows us to estimate the particle-emission power,

$$\tilde{P}_\varphi = \frac{d\tilde{E}_{\text{str}}}{d\tilde{\tau}} = \frac{1}{C} = 11.2(1.6), \quad (9.46)$$

where $\tilde{P}_\varphi = P_\varphi/v^2$.

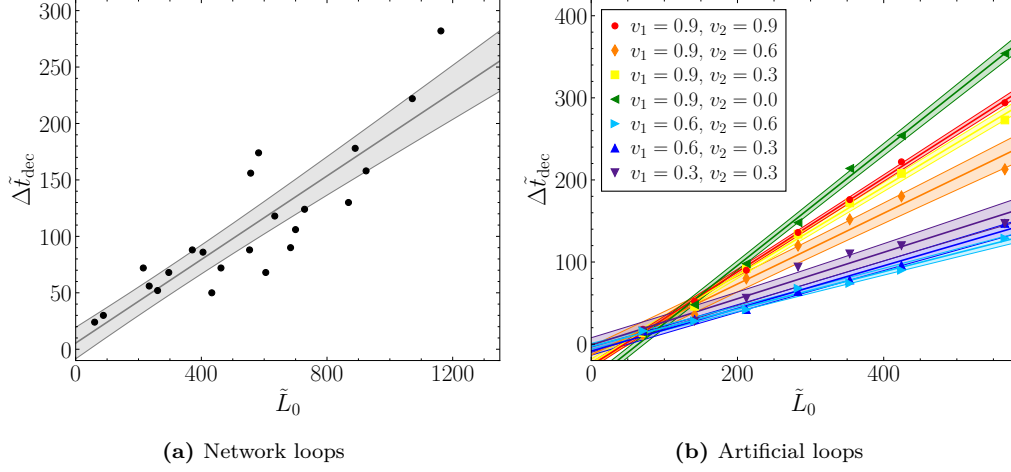


Figure 9.9. Lifetime of the network (left) and artificial loops (right) as a function of their initial length. Lines and shaded regions are the results of a linear fit.

Type of loop	$A \times 10^3$	B	$C \times 10^3$	D
Network	185(22)	5(14)	89(13)	-1(17)
Artificial, $v_1 = 0.9, v_2 = 0.9$	571(10)	-26(3)	270(9)	-22(6)
Artificial, $v_1 = 0.9, v_2 = 0.6$	430(30)	-13(11)	223(14)	-14(9)
Artificial, $v_1 = 0.9, v_2 = 0.3$	534(14)	-23(5)	269(9)	-20(6)
Artificial, $v_1 = 0.9, v_2 = 0.0$	706(19)	-45(6)	348(9)	-40(6)
Artificial, $v_1 = 0.6, v_2 = 0.6$	227(11)	-3(4)	125(5)	-1(3)
Artificial, $v_1 = 0.6, v_2 = 0.3$	260(15)	-9(5)	140(8)	-6(5)
Artificial, $v_1 = 0.3, v_2 = 0.3$	280(30)	-1(9)	154(15)	2(9)

Table 9.4. Results of linear fits $\Delta\tilde{t}_{\text{dec}} = A\tilde{L}_0 + B$ and $\Delta\tilde{t}_{\text{dec}} = C\tilde{E}_{\text{str},0} + D$, for network and artificial loops. All artificial loops are simulated with $\sin\alpha = 0.4$.

In fig. 9.9b, we present the decay time of artificial loops as a function of L_0 for different choices of initial boost velocities. Here we approximate L_0 as $4L_{1/4}$, since the use of eq. (9.24) is not appropriate as the Manhattan effect underestimates the length on straight strings. We observe that artificial loops live up to three times more than network loops of the same length depending on the initial velocities, for the range of lengths that can be compared. As before, we observe that $\Delta\tilde{t}_{\text{dec}}$ scales linearly with L_0 (and also $E_{\text{str},0}$), although the data shows a clear dependence on the velocity. The results of linear fits to each set of velocities are also presented in table 9.4, from which the particle-emission power, as defined in eq. (9.46), can be obtained, $\tilde{P}_\varphi \approx 3 - 8$, depending on the initial velocities. Note that the $v_1 = v_2 = 0.6$ case corresponds to the same setup used in ref. [428], which finds the linear regression with coefficient A to be $\sim 40\%$ bigger than ours.

In fig. 9.10, we show $\Delta\tilde{t}_{\text{dec}}$ as a function of J_0 for artificial loops. We observe all the loops follow a universal power-law dependence, that roughly scales as $\Delta\tau_{\text{dec}} \propto J_0^{3/5}$. This highlights angular momentum as one of the key ingredients affecting global loop decay. Retrospectively, this also explains the observed dispersion of the points in fig. 9.9a, since we have no control over the angular momentum for network loops.

Finally, we have performed several consistency checks to ensure the robustness of our results. We observe very small variations of $\Delta\tilde{t}_{\text{dec}}$ when changing δx , and for artificial loops we find changes smaller than 10% when varying the ratio $L/L_{1/4}$. For artificial loops, we have also observed minimal

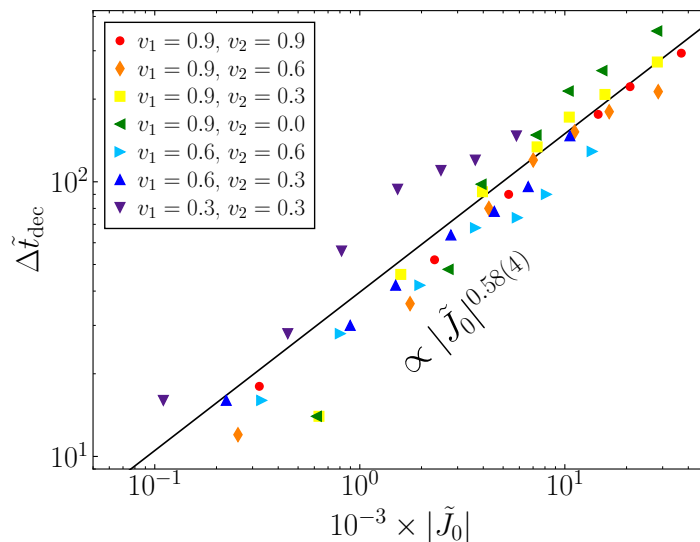


Figure 9.10. Lifetime of artificial loops with different initial velocities as a function of their initial angular momentum, measured using eq. (9.28). The line is the result of a power-law fit to all families.

dependence on $\Delta\tilde{t}_{\text{dec}}$ on the boost direction, given by the choice of α , which indicates that the long-range interactions rapidly take over any impact of this parameter, as it does not affect the total energy in the system.

9.3.2 Particle emission

We also study the distribution of massive, χ , and massless, θ , particles after the collapse of the loop, as defined in eq. (9.5). In figs. 9.11a and 9.11b we represent the power spectra of θ (left) and χ (right) at the end of the decay of an artificial loop generated with $v_1 = v_2 = 0.6$, $\sin\alpha = 0.4$ and $\tilde{L}_{1/4} = \tilde{L}/2 \approx 141$. We observe the spectrum of massless models is power-law suppressed at high modes, while the spectrum of massive excitations peaks at $\tilde{k} \sim 1$, albeit with an amplitude much smaller than that of the massless field spectrum at the same scale. Massless modes with $\tilde{k} \ll 1$ can easily be emitted, while the emission of massive particles, although also possible, is suppressed compared to the massless case.

We note that ref. [428] presents the energy spectrum of massless modes, defined from eq. (9.36), which shows a peak at a scale half that of the massive mode, $k = m_\chi/2$ (which corresponds to $\tilde{k} = \sqrt{2}/2$ in our program units). We present our results for this energy spectrum after the loop decays in red in fig. 9.12. From a power-law fit, we observe that the spectrum roughly scales as $\propto k^{-1}$, in agreement with ref. [428]. However, we detect no presence of any such peak at $k = m_\chi/2$. Interestingly, if we set the initial radius of the string to be larger than its physical value by modifying the radial profile of the NO vortices used to generate the initial strings as $f(r) \rightarrow f(2r)$, we

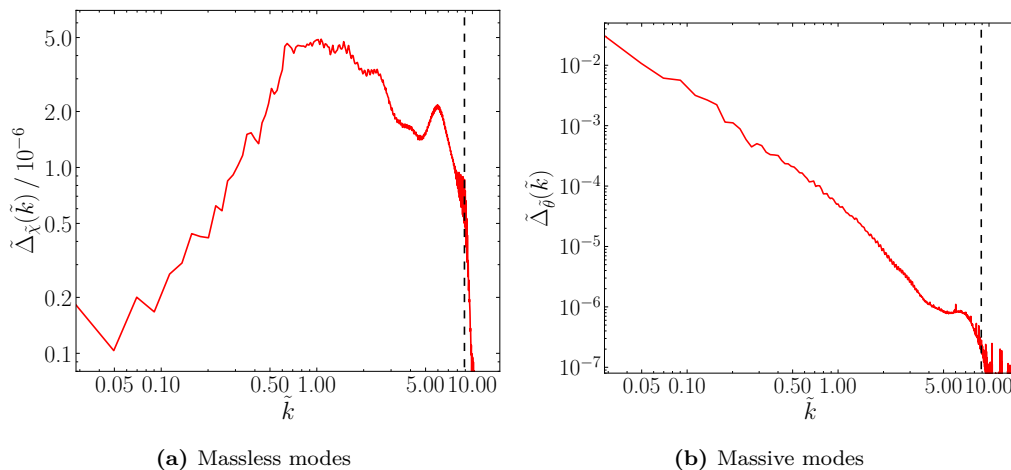


Figure 9.11. Power spectrum of massive (left) and massless (right) modes just after the collapse of an artificial loop generated with $v_1 = v_2 = 0.6$ and $\sin\alpha = 0.4$. Vertical dashed lines indicate the scale of the string core, $\tilde{k}_c = 2\pi/\tilde{r}_c \approx 9$.

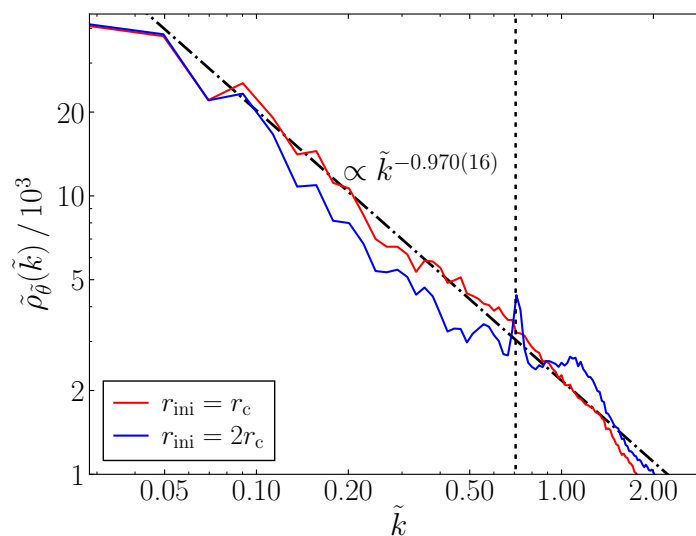


Figure 9.12. Lifetime of artificial loops with different initial velocities as a function of their initial angular momentum, measured using eq. (9.28). The vertical dashed line indicates the scale of the core radius, $\tilde{k}_c = 2\pi/\tilde{r}_c$, and the dot-dashed line is the result of a power-law fit to the $r_{\text{ini}} = r_c$ result.

observe a peak appearing at the same scale as in ref. [428]. We believe this peak is related to an excess energy in the radial mode of the string due to an excessively large core width set in the initial conditions.

9.3.3 GW emission

We study the emission of GWs from decaying loops, following the procedure outlined in sec. 8.3.1. In a Minkowski background, the equation of motion of the GWs becomes

$$\ddot{h}_{ij} - \partial_k \partial_k h_{ij} = \frac{4}{m_p^2} [\text{Re}(\partial_i \varphi \partial_j \varphi^*)]^{\text{TT}}, \quad (9.47)$$

where recall, $[...]^{\text{TT}}$ refers to the transverse-traceless component, and we are neglecting backreaction of the GWs on the loop dynamics. We define the fractional GW energy density normalizing with the total energy density of the complex scalar field, ρ_φ , which is conserved,

$$\Omega_{\text{GW}}(k, t) = \frac{1}{\rho_\varphi} \frac{d\rho_{\text{GW}}(k, t)}{d \log k}. \quad (9.48)$$

The total GW energy emitted is computed by integration,

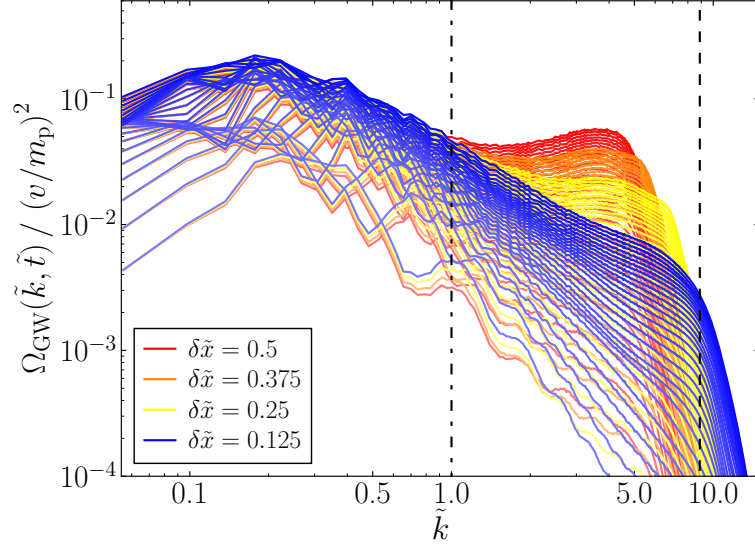
$$E_{\text{GW}} = \rho_\varphi L^3 \int \Omega_{\text{GW}}(k, t) d \log k. \quad (9.49)$$

We first analyze lattice discretization effects on the GW spectrum of a loop. For network loops, we run a high-resolution simulation with $\delta\tilde{x} = 0.125$ and save the configuration when an isolated loop is found. This is used to create new coarser configurations with $\delta\tilde{x}^{(p)} = p\delta\tilde{x}$ ($p = 2, 3, 4$), by eliminating $p - 1$ sites of every p consecutive points of the original lattice per dimension. For artificial loops, we run simulations with different $\delta\tilde{x}$, generated using equivalent initial conditions and parameters $\tilde{L} = 192$, $\tilde{L}_{1/4} = 96$, $v_1 = 0.6$, $v_2 = 0.7$ and $\sin\alpha = 0.5$.

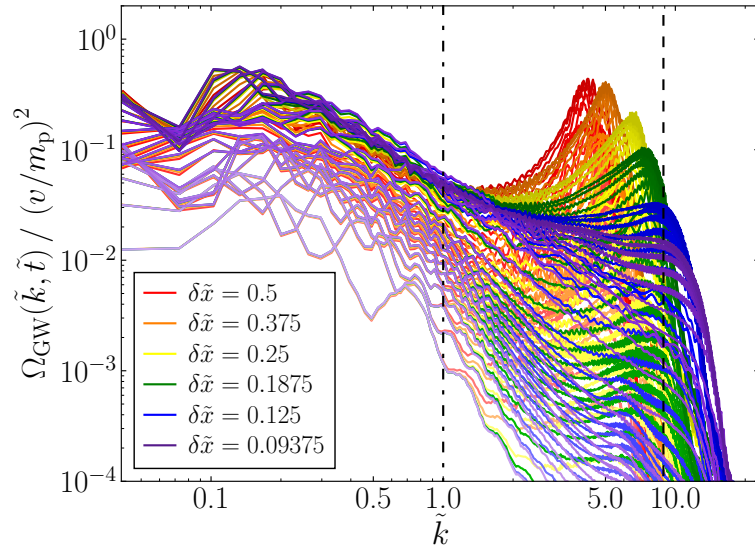
The evolution of the resulting power spectra for network and artificial loops are shown in fig. 9.13. Different lines correspond to different times, measured every four and two units of program time, respectively, with time going in general from bottom to top. In both cases, GW emission peaks at IR scales, $\tilde{k} \sim (2-6)\tilde{k}_0$, with $k_0 = 2\pi/L_0$ the scale of the initial string length, and there is good agreement between all resolutions up to $\tilde{k} \sim 0.1\tilde{k}_c$, where $k_c = 2\pi/r_c$ is the scale of the core radius. A second peak emerges at higher modes, but it is suppressed as the UV resolution is improved, indicating it is indeed a lattice artifact arising when the string core is not well resolved. In view of this, we decide to compute the total GW energy emitted by loops integrating the spectrum only up to some cutoff scale, $\tilde{k}_{\text{cut}} \sim 0.1\tilde{k}_c$. This ensures the result does not capture the unphysical UV peak.

We also study the effect of varying the IR coverage for artificial loops. We set $\tilde{L}_{1/4} = 64$, $\delta\tilde{x} = 0.25$, $v_1 = 0.6$, $v_2 = 0.7$ and $\sin\alpha = 0.5$, and vary the box size. The resulting spectra are shown in fig. 9.14, multiplied by a factor that accounts for volume dependencies. The spectra are represented every four units of program time. We observe a noticeable discrepancy at intermediate scales for the smallest box, but the spectra converges rapidly as the box size increases. We also observe that the emission of GWs is suppressed for scales larger than the initial loop length, $k < k_0$, represented with a black dotted line.

A zoomed-in version of the spectra in the largest box is shown, every two units of program time, in fig. 9.15. Here we note the presence of various peaks in the spectrum. Although the peak structure resembles the harmonic pattern expected in NG strings—see sec. 9.1.3—peak frequencies here are not in harmonic proportions, and their absolute and relative locations vary between early (purple) and late (red) times. From a fit to the UV tail of the spectrum, we observe it decays roughly as $k^{-3/2}$. This represents a steeper fall than standard NG predictions for a cusp-dominated emission, expected to be proportional to $k^{-4/3}$.



(a) Network loop



(b) Artificial loop

Figure 9.13. Evolution of the GW energy density power spectrum with varying UV resolution and fixed lattice size. The vertical dashed line indicates the scale of the string core, $\tilde{k}_c = 2\pi/\tilde{r}_c$, and the vertical dot-dashed line is the cutoff, \tilde{k}_{cut} , up to which we integrate the spectrum to compute the GW energy to prevent capturing UV artifacts. Spectra go from early to late times from bottom to top, with a separation of four and two units of program time between consecutive lines, for the top and bottom panels, respectively.

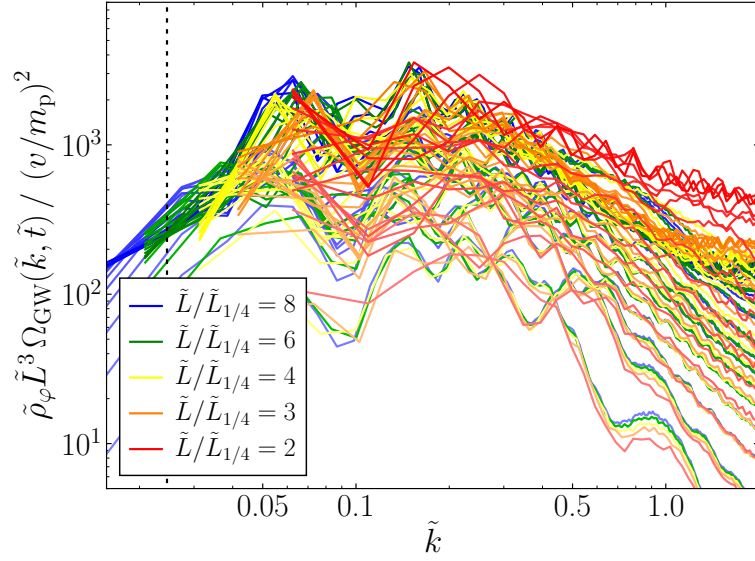


Figure 9.14. Evolution of the GW energy density power spectrum for artificial loops generated with $v_1 = 0.6$, $v_2 = 0.7$ and $\sin \alpha = 0.5$, with fixed $\delta \tilde{x} = 0.25 \tilde{L}_{1/4} = 64$ and varying L . The vertical dotted line indicates the scale of the initial length of the string, $\tilde{k}_0 = 2\pi/\tilde{L}_0$. Spectra go from early to late times from bottom to top, with a separation of four units of program time between consecutive lines.

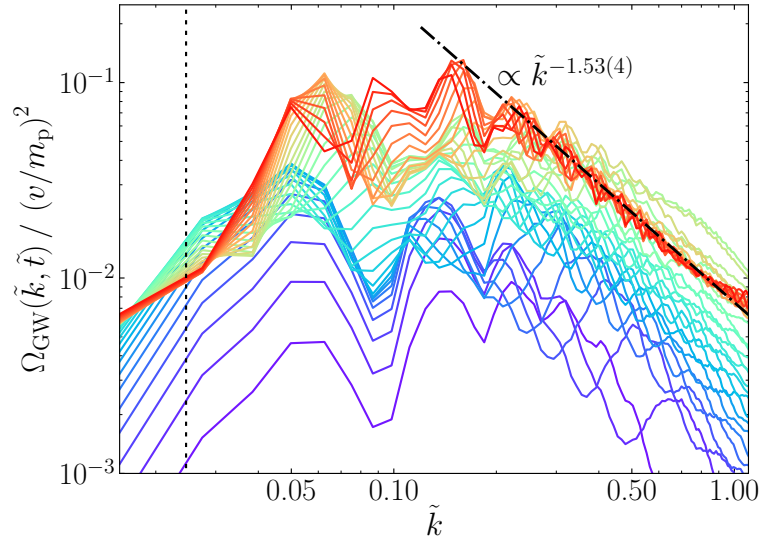


Figure 9.15. Evolution of the GW energy density power spectrum of an artificial loop with $\delta \tilde{x} = 0.25$, $\tilde{L} = 512$ and $\tilde{L}_{1/4} = 64$, generated with $v_1 = 0.6$, $v_2 = 0.7$ and $\sin \alpha = 0.5$. Each line corresponds to a different time, going from purple to red, with separation of two units of program time. The vertical dotted line indicates the scale of the initial length of the string, $\tilde{k}_0 = 2\pi/\tilde{L}_0$, and the dot-dashed line is a fit to the high-frequency tail of the final-time spectrum.

Having understood the main sources of systematic errors, we now turn our attention to the GW power emitted by a decaying loop. We define a rolling-average measurement of this quantity,

$$P_{\text{GW}}(t) \equiv \frac{L^3 \rho_\varphi}{2T} \int_{t-T}^{t+T} dt' \int_0^{k_{\text{cut}}} \dot{\Omega}_{\text{GW}}(k, t') d \log k, \quad (9.50)$$

which, in terms of program variables, is $\tilde{P}_{\text{GW}} = P_{\text{GW}}/v^2 \times (v^2/m_{\text{p}}^2)$. Our result for the GW power emitted is shown in fig. 9.16 for a number of network and artificial loops, as a function of the lifetime of the loops. The rolling-averaged GW emission power is computed using $\tilde{T} = 15$, which we observe is enough to remove rapid oscillations while still keeping features related to the string dynamics, and $k_{\text{cut}} = 1$.

The left panel corresponds to network loops with different L_0 , simulated for various δx and L , as shown in the plot legend. In all cases, we observe the power emitted does not depend on L_0 and is roughly constant in time, with fluctuations that depend on the specific details of the dynamics of each loop. At late time, the emission power drops down as the loop finally disappears. Remarkably, we do not observe evidence of any systematic variation of the GW power emission due to the shrinking of the loops. Between $\tilde{t} = 30 - 100$, the average emission of all loops is $\tilde{P}_{\text{GW}} = 240 \pm 80$ (grey dashed line and band). Although there is a priori no reason to expect this to be similar to the NG prediction, eq. (9.19), it is still instructive to

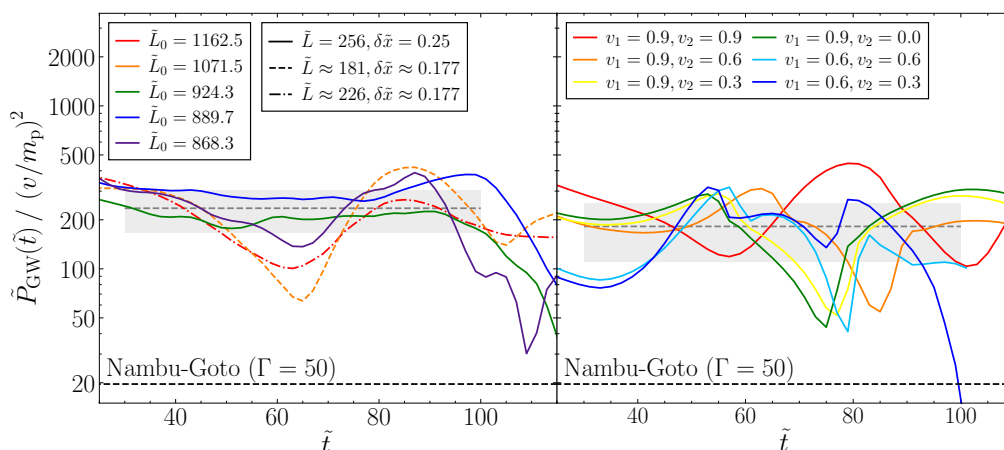


Figure 9.16. Rolling-averaged GW power emitted by network loops of several lengths (left) and artificial loops with different boost velocities (right), computed using eq. (9.50). In the case of network loops, each color corresponds to a different initial length and the linestyle indicates the lattice parameters, as indicated in the plot legends. For artificial loops, each color refers to a different pair of boost velocities. For comparison, the typical NG result (for $\mu = \pi v^2$ and $\Gamma = 50$) is shown as a horizontal dashed line. Finally, The grey bands represent the average value of the emission power in the range $\tilde{t} = 30 - 100$ for each type of loop.

make the comparison. Using $\mu = \pi v^2$ and $\Gamma = 50$, one gets $\tilde{P}_{\text{GW}} \approx 20$, roughly an order of magnitude smaller than our result.

The right panel of fig. 9.16 shows our results for artificial loops with different velocities, produced in simulations with $\tilde{L} = 450/\sqrt{2} \approx 319$ and $\delta\tilde{x} = 0.25/\sqrt{2} \approx 0.177$, with initial string separation $L_{1/4} = L/3$, chosen to reduce IR effects. For all pairs $\{v_1, v_2\}$, the GW power emission is of a similar order as for network loops. It presents an amplitude that, as for network loops, shows no significant variation as the loops shrink. The power emission also shows some fluctuations that we believe are related to the very symmetric initial configuration. For the period $\tilde{t} = 30 - 100$, the average emission is $\tilde{P}_{\text{GW}} = 190 \pm 80$.

Comparing the results for GW and particle-emission power, we obtain

$$\frac{P_{\text{GW}}}{P_\varphi} \approx \begin{cases} \frac{240(80)}{11.2(1.6)} \left(\frac{v}{m_{\text{p}}}\right)^2, & \text{Network loops,} \\ \frac{190(80)}{5.2(2.5)} \left(\frac{v}{m_{\text{p}}}\right)^2, & \text{Artificial loops,} \end{cases} \quad (9.51)$$

where P_φ for artificial loops is taken as an average over all families of initial velocities. As v cannot be arbitrarily large (e.g. CMB constraints require $v/m_{\text{p}} \leq 10^{-6}$ [433, 434]), we conclude $P_{\text{GW}}/P_\varphi \ll 1$, indicating that the GW emission from decaying global string loops is completely subdominant compared to particle emission. Note this justifies a posteriori neglecting the backreaction of GWs on the matter fields.

9.4 Conclusion

Studying the evolution and decay of cosmic strings requires the use of field-theory lattice simulations to fully capture the dynamics of the strings. In this chapter, we have reviewed the basics of cosmic strings in the early universe, and presented the results from ref. [6], where the simultaneously emission of particles and GWs from string loops was studied using lattice simulations for the first time. Our results show that the particle emission completely dominates the decay of the loops. Indeed, we observe a universal result

$$\frac{P_{\text{GW}}}{P_\varphi} \approx \mathcal{O}(10) \left(\frac{v}{m_{\text{p}}}\right)^2 \ll 1, \quad (9.52)$$

which holds with independence of the length, shape, energy and angular momentum of the loops. This conclusion is robust for loops with length-to-width ratio $L_0/r_c \lesssim 1700$, with no indication this will change for longer loops.

In particular, we observe no evidence of any logarithmic enhancement of the emission power of GWs with the length of the loops, which is sometimes assumed from combining field-theory results for the string tension—see eq. (9.12)—with the NG prediction for the GW emission—see eq. (9.19). Note, however, that there is no reason why NG results must hold in the case of global strings.

Our result opens the door to a new technique to calculate the GWB from a network of strings. Current approaches are based on lattice simulations of networks [435–437], which can only study a limited dynamical range, or the combination of field-theory and NG ingredients, usually assuming a logarithmic divergent string tension [438–441]. We propose to obtain the GWB spectrum from combining our results for the GW emission of isolated loops with predictions for the loop number density computed at cosmological scales [404, 415, 420, 442–444]. We believe this will lead to a suppression of the GWB from global string networks compared to present predictions, as we find no evidence of a logarithmically dependent GW power.

10 GW emission from cosmic string loops: local case

Chapter 9 is focused on the study of global strings, which arise, for example, in axion models, and we represented in our simulations using a complex scalar field with a Mexican-hat potential. This type of string presents long-range forces, and closed loops were found to decay mainly through particle production, with a very suppressed gravitational wave (GW) emission power. Another type of cosmic strings are *local strings*, which arise, for example, in grand unified theories [373, 374]. These are characterized by short-range interactions and are typically represented using the Abelian-Higgs model. These strings are, a priori, expected to be well described by the Nambu-Goto (NG) approximation.

Recall that the NG model, introduced in sec. 9.1.3, describes strings as infinitely thin objects that can only decay via the emission of GWs, while the production of massive particles is neglected. However, in a field-theory scenario both emission channels are available. In the work presented in this chapter we use field-theory lattice simulation to compare both decay routes simultaneously [7]. We consider both network loops, generated in a similar manner to those in ref. [389], and two types of artificial loops, produced following refs. [389, 427]. We recall that we neglect backreaction of the GWs on the strings, and so the energy emitted in form of gravitational radiation is not subtracted from the energy budget of the strings. This is an assumption that we self-consistently check a posteriori.

The decay of local string loops into particles has already been explored using classical-field-theory simulations. In ref. [427], artificial loops generated from the intersection of boosted infinite strings were studied, finding a lifetime proportional to the square of the string length, $\Delta t_{\text{dec}}^{\text{part}} \propto L^2$. Comparing these lattice results to the NG prediction for GW emission, $\Delta t_{\text{dec}}^{\text{GW}} \propto L$, this

work concluded that above some critical length, L_{crit} , the decay of local string loops occurs predominantly via GW production.

In ref. [389], loops originating from networks were investigated, finding their lifetime to be proportional to their length, $\Delta t_{\text{dec}}^{\text{part}} \propto L$. Ref. [389] also studied a new type of artificial loops originated from the intersection of static non-straight infinite strings. These were found to behave similarly to those in ref. [427]. This showed that the decay of both types of loops is dragged by fundamentally different mechanisms. These results point to the fact that, for loops originating after a phase transition in the early universe, the emission of GWs, based on NG predictions, would be suppressed compared to particle production.

In this chapter, we present lattice results on the simultaneous emission of particles and GWs from local string loops. In sec. 10.1, we introduce the Abelian-Higgs model and discuss some of the main properties of local strings. In sec. 10.2, we describe the observables we use to analyze the dynamics of the local strings, and the different types of initial conditions we consider. Results for particle and GW emission are presented in sec. 10.3, and we conclude in sec. 10.4 with a brief summary.

10.1 The Abelian-Higgs model

The Abelian-Higgs model contains a complex scalar field, $\varphi = (\phi_1 + i\phi_2)/\sqrt{2}$, with $\phi_{1,2}$ real scalar fields, and an Abelian gauge field, A_μ . It is characterized by the action,

$$S[\varphi, A] = \int d^4x \sqrt{-g} \left[(D_\mu \varphi)(D^\mu \varphi)^* - \frac{1}{4} F_{\mu\nu} F^{\mu\nu} - V(\varphi) \right], \quad (10.1)$$

where the scalar potential is the same as in the global case,

$$V(\varphi) = \lambda \left(|\varphi|^2 - \frac{v^2}{2} \right)^2. \quad (10.2)$$

Also, $D_\mu = \partial_\mu - ieA_\mu$ is the covariant derivative with e the gauge coupling, and $F_{\mu\nu} = \partial_\mu A_\nu - \partial_\nu A_\mu$ is the field-strength tensor. This model is invariant under local gauge transformations, as given in eq. (8.9).

The time evolution of the fields is controlled by the equations of motion, given by eqs. (8.12) and (8.13). We focus for our study in Minkowski background, where they take the form

$$\begin{aligned} \ddot{\varphi} - D_i D_i \varphi &= -2\lambda \left(|\varphi|^2 - \frac{v^2}{2} \right) \varphi, \\ \dot{F}_{0i} - \partial_j F_{ji} &= 2e \text{Im} [\varphi^* D_i \varphi]. \end{aligned} \quad (10.3)$$

A priori, these equations seem to depend on both λ and e separately. However, if we define dimensionless program variables using $f_\star = v$ and $\omega_\star = \sqrt{\lambda}v$, and make the rescaling $A_\mu \rightarrow A_\mu/e$, they take the form

$$\begin{aligned}\ddot{\tilde{\varphi}} - \tilde{\partial}_i \tilde{\partial}_i \tilde{\varphi} &= - \left(|\tilde{\varphi}|^2 - \frac{1}{2} \right) \tilde{\varphi}, \\ \dot{\tilde{F}}_{0i} - \tilde{\partial}_j \tilde{F}_{ji} &= 2 \frac{e^2}{\lambda} \text{Im} [\tilde{\varphi}^* \tilde{D}_i \tilde{\varphi}].\end{aligned}\tag{10.4}$$

This makes clear that the dynamics of the system only depends on the ratio $\beta = 2\lambda/e^2$. In this work, we focus on the $\beta = 1$ case.

As in the case of the model in used to represent global strings, given in eq. (9.1), the Abelian-Higgs model is characterized by the presence of two phases. In a high-temperature thermal environment, the universe lies in a symmetric phase, $\langle \varphi \rangle = 0$, in which the gauge symmetry is realized. At low temperatures, this local symmetry is spontaneously broken as the field falls into the true vacuum of the potential, $\langle \phi_1^2 + \phi_2^2 \rangle = v^2$. Similarly to the case of global strings, if the gauge symmetry is broken after the end of inflation, cosmic strings may form.

It is instructive to analyze the behaviour of the theory around the true vacuum. We can expand the complex scalar field in terms of the radial and angular excitations, as we did in chapter 9 for the global case,

$$\varphi(x) = \frac{v + \chi(x)}{\sqrt{2}} e^{i\theta(x)}.\tag{10.5}$$

Using this expression, the action can be expanded as

$$\begin{aligned}S[\chi, \theta, A_\mu] &= \int d^4x \sqrt{-g} \left[-\frac{1}{4} F_{\mu\nu} F^{\mu\nu} + \frac{1}{2} \partial_\mu \chi \partial^\mu \chi \right. \\ &\quad \left. - \lambda v^2 \chi^2 - \lambda v^3 \chi^3 - \frac{1}{4} \lambda \chi^4 + \frac{1}{2} e^2 (v + \chi)^2 \left(\frac{1}{e} \partial_\mu \theta - A_\mu \right)^2 \right].\end{aligned}\tag{10.6}$$

Working in the unitary gauge, $A'_\mu = A_\mu - \partial_\mu \theta/e$, makes evident that the massless mode θ is absorbed by the gauge field, which becomes massive. Thus, the low-energy effective theory contains two massive degrees of freedom: the vector field A'_μ , and the radial excitations, χ . Their masses are, respectively,

$$m_A = ev, \quad m_\chi = \sqrt{2\lambda}v.\tag{10.7}$$

In the $\beta = 1$ case, in which we work, both masses are equal. Note that, while these conclusions have been deduced working in the unitary gauge, they hold in general, since the theory is gauge invariant.

The inverse of these masses are the Compton lengths of each of the excitations. In the context of cosmic strings, they characterize the rate at

which the fields approach the vacuum and so the size of the string cores. This means that, in the $\beta = 1$ case, local strings have a unique core width, $r_c \sim m_\chi^{-1}$. The absence of massless degree of freedom also implies that interactions between strings are short-ranged.

Integrating out the massive modes, one can show that the dynamics of local strings can be effectively described by the NG action, discussed in sec. 9.1.3. Therefore, one a priori expects that, according to the NG picture, local strings mainly decay via the emission of GWs. Testing this assumption using field-theory lattice simulations is one of the main goals of the work presented in this chapter.

10.1.1 Infinite string solution

Before presenting our lattice results, we consider the solution of an infinite straight string, the so-called Nielsen-Olesen vortex [403]. Taking the core of string to lie on the z axis, we can work with cylindrical coordinates, (r, θ, z) . In the temporal gauge, $A_0 = 0$, we can use the following string ansatz,

$$\begin{aligned} \varphi &= f(r) \frac{v}{\sqrt{2}} e^{ik\theta}, & A_0 &= A_3 = 0. \\ A_1 &= -\frac{g(r)}{er} \sin \theta, & A_2 &= \frac{g(r)}{er} \cos \theta, \end{aligned} \quad (10.8)$$

where k is the winding number of the string, and f and g are profile functions that can be determined numerically. Substituting this ansatz in eq. (10.3), one finds the following equations for the profile functions,

$$\begin{aligned} \frac{\partial^2 f}{\partial \tilde{r}^2} + \frac{1}{\tilde{r}} \frac{\partial f}{\partial \tilde{r}} - \frac{f^2 k^2}{\tilde{r}^2} (1 - g)^2 - f(f^2 - 1) &= 0, \\ \frac{\partial^2 g}{\partial \tilde{r}^2} - \frac{1}{\tilde{r}} \frac{\partial g}{\partial \tilde{r}} + \frac{1}{2\beta} f^2 (1 - g) &= 0, \end{aligned} \quad (10.9)$$

where $\tilde{r} = \sqrt{\lambda}vr$. This equations can be solved numerically using relaxation methods and imposing the boundary conditions $f(0) = g(0) = 0$ and $f(\infty) = g(\infty) = 1$. Our results for $\beta = 1$ and $k = 1$ are shown in fig. 10.1.

Analytically, it is possible to study the behavior of $f(r)$ and $g(r)$ at short and long distances from the string core. Close to the string, $r \ll m_\chi^2$, one finds

$$f(r) \propto r, \quad g(r) \propto r^2, \quad (10.10)$$

and so $A_{1,2} \propto r$. At long distances, $r \gg m_\chi^2$,

$$f(r) = 1 - FK_0(\sqrt{2}r), \quad g(r) = 1 - GrK_1(\sqrt{2}r), \quad (10.11)$$

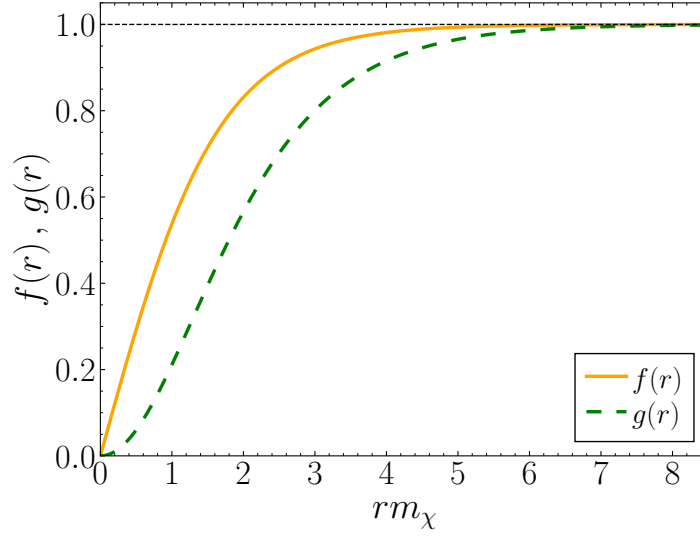


Figure 10.1. Radial profile of the NO vortex for $\beta = 1$ and $k = 1$, for the scalar and the gauge fields.

where K_0 and K_1 are modified Bessel functions of the second kind, which obey the relation $K_1 = -K_0'$, and F and G are positive constants that need to be determined from matching to the numerical solution. Asymptotically $K_0(x) \sim x^{-1/2}e^{-x}$, and so both f and g approach the vacuum exponentially fast. The full gauge field, on the other hand, only approaches zero at long distances as $A_{1,2} \propto r^{-1}$ —see eq. (10.8).

From this analytic solution, one can extract conclusions for the interactions between strings. The gradient, magnetic and potential energy density components of the infinite string are defined, respectively, as

$$\begin{aligned}\rho_G(r) &= \frac{1}{2} \left(\frac{df}{dr} \right)^2 + \left(\frac{nf}{r} \right)^2, \\ \rho_B(r) &= \frac{1}{4r^2} \left(\frac{dg}{dr} \right)^2, \\ V(r) &= \frac{\lambda}{4} (f^2 - 1)^2,\end{aligned}\tag{10.12}$$

and so the total energy density is $\rho = \rho_G + \rho_B + V$. The tension of the string—energy per unit length—can be obtained from integrating this total energy density over the whole (x, y) -plane. While the separate integrals of gradient and the magnetic components do not converge at long distances, one can prove the combined result does. Indeed, the total energy density of the fields decays exponentially at long distances. The tension of a local string takes the simple form

$$\mu = \pi v^2 B(\beta),\tag{10.13}$$

where $B(\beta)$ is a smooth function that takes the value $B(1) = 1$ [445]. The exponential fall of the energy density at long distances means that, contrary to the global case, the interactions between strings are short-ranged, mediated by the two massive degrees of freedom.

10.2 Lattice simulations of local strings

Lattice simulations fully capture the field-theory structure of local strings, and make it possible to investigate, on equal grounds, the emission of particles and GWs by the loops. We summarize the observables used to study the evolution and decay of string loops in sec. 10.2.1. Then, secs. 10.2.2 to 10.2.4 describe how the loops we use in this study are generated. In particular, we consider three types of loops, which we call *network loops* and *artificial loops* of type I and II. As in the work presented in chapter 9, we study the decay of local string loops in Minkowski background, and also focus on the $\beta = 1$ case. Program variables are defined as in the global case, using

$$f_\star = v, \quad \omega_\star = \sqrt{\lambda}v, \quad (10.14)$$

and we recall that dimensionless variables are indicated with a tilde.

10.2.1 Local-string observables

To study the dynamics and evolution of local strings, we use observables analogous to those presented in sec. 9.2.1 for the global case. We measure the location of the string cores by determining the pierced plaquettes, i.e., those with non-zero winding number. The winding number of a plaquette with lattice coordinate \mathbf{n} on the ij -plane is computed similarly to the global case,

$$W_{ij}(\mathbf{n}) = \frac{1}{2\pi} \left[Y_i(\mathbf{n}) + Y_j(\mathbf{n} + \hat{\mathbf{i}}) - Y_i(\mathbf{n} + \hat{\mathbf{j}}) - Y_j(\mathbf{n}) \right], \quad (10.15)$$

where, in this case, the contribution from each link is defined in a gauge invariant way [388, 430],

$$Y_i(\mathbf{n}) = \left[e\delta x A_i(\mathbf{n}) + \theta(\mathbf{n}) - \theta(\mathbf{n} + \hat{\mathbf{i}}) \right]_\pi - e\delta x A_i(\mathbf{n}). \quad (10.16)$$

Here, θ is the phase of the complex scalar field and $[\alpha]_\pi$ sets $-\pi < \alpha \leq \pi$. The location of the pierced plaquettes allows us to have real-time knowledge of the structure of the strings—for example, it allows us to determine if a single isolated loop is left in the simulation—and to get an estimate of the string length in the lattice frame—see eq. (9.24).

We also measure the string energy components. The kinetic, gradient, potential, electric and magnetic energy components of the strings are defined using a weight function, $W(\varphi)$. In the general case of an expanding background, working in conformal time, they take the values [388]

$$\begin{aligned} E_{\text{K,str}} &= a \int W(\varphi) |\varphi'|^2 d^3x, & E_{\text{G,str}} &= a \sum_i \int W(\varphi) |D_i \varphi|^2 d^3x, \\ E_{\text{V,str}} &= a^3 \int W(\varphi) V(\varphi) d^3x, & E_{\text{E,str}} &= \frac{a}{2} \int W(\varphi) \mathbf{E}^2 d^3x, \\ E_{\text{B,str}} &= \frac{a}{2} \int W(\varphi) \mathbf{B}^2 d^3x, \end{aligned} \quad (10.17)$$

where a is the scale factor, and the electric and magnetic fields are defined from the gauge field as $E_i = \dot{A}_i$ and $B_i = -\varepsilon_{ijk} F_{jk}/2$ —see eq. (8.10). From here, the total string energy is

$$E_{\text{str}} = E_{\text{K,str}} + E_{\text{G,str}} + E_{\text{V,str}} + E_{\text{E,str}} + E_{\text{B,str}}. \quad (10.18)$$

A priori, there is no need to use a weight function in the case of local strings, as the total string energy is convergent. However, one wants to avoid including the energy of interstring radiation. In this work, we make use of the same weight function as used in the global case in chapter 9,

$$W(\varphi) = \frac{4V(\phi)}{\lambda v^4} \Theta \left(\frac{v^2}{2} - |\varphi|^2 \right), \quad (10.19)$$

where Θ is the Heaviside function. A different weight function related to the Lagrangian has also been used in other works—see refs. [388, 389]. For such choice, however, there is no well-defined normalization of the weight function, and only the ratios between energy components have a physical meaning.

The measurements of the string energy components make it possible to obtain different estimates of the proper comoving length and mean-square velocity of the strings. For example, we can define [388],

$$L_{\text{str}} = \frac{1}{a} \frac{E_{\text{str}} - \Delta f E_{\text{L,str}}}{\mu(1 + \Delta f)}, \quad (10.20)$$

$$v^2 = \frac{E_{\text{str}} + E_{\text{L,str}}}{E_{\text{str}} - \Delta f E_{\text{L,str}}}, \quad (10.21)$$

where $E_{\text{L,str}} = E_{\text{K,str}} + E_{\text{E,str}} - E_{\text{G,str}} - E_{\text{B,str}} - E_{\text{V,str}}$ is the weighted Lagrangian energy. Other estimators of the two quantities are also available—see ref. [388]. Here μ is the weighted tension of the static string and

$\Delta f = f_B - f_V$ is the difference between the fraction of magnetic energy and the fraction of potential energy to the total energy of the static string. These are computed from the NO solution as

$$\begin{aligned}\mu &= a^2 \int W(\varphi) [\rho_G(r) + \rho_B(r) + V(r)] d^2x, \\ f_B &= \frac{a^2}{\mu} \int W(\varphi) \rho_B(r) d^2x, \\ f_V &= \frac{a^2}{\mu} \int W(\varphi) V(r) d^2x,\end{aligned}\tag{10.22}$$

where the components of the energy density of the NO vortex are defined in eq. (10.12). Using the weight function in eq. (10.19), we obtain $\mu = 1.4415v^2$, $f_B = 0.2047$ and $f_V = 0.2056$.

10.2.2 Generation of network loops

Network loops are generated from the decay of string networks in a similar fashion to the global case, outlined in sec. 9.2.2, and following the procedure in ref. [389]. They are expected to have shapes and features similar to those loops that could form after a realistic phase transition in the early universe.

Simulations are initialized with a Gaussian random realization of the scalar field in Fourier space, with the same power spectrum used for global network loops,

$$\Delta_{\phi_i}(k) = \frac{k^3 v^2 \ell_{\text{str}}^3}{\sqrt{2\pi}} \exp\left(-\frac{1}{2} k^2 \ell_{\text{str}}^2\right).\tag{10.23}$$

Recall, this depends on a correlation length, ℓ_{str} , that controls the density of the resulting network. The gauge field and the time derivatives of both fields, on the other hand, are set to zero.

The field configuration resulting from the previous step is too energetic and contains no gauge field. To get rid of the excess energy and allow the magnetic flux to form inside the strings, we evolve the configuration following diffusion equations of the form,

$$\begin{aligned}\sqrt{\lambda} v \varphi' - \partial_i \partial_i \varphi &= -2\lambda \left(|\varphi|^2 - \frac{v^2}{2} \right) \varphi, \\ \sqrt{\lambda} v F_{0i} - \partial_j F_{ji} &= 2e \text{Im} [\varphi^* D_i \varphi].\end{aligned}\tag{10.24}$$

The diffusive phase is applied for a total of 20 units of program time, which we find to be enough for our purposes.

After the diffusion process, we let the network evolve in a radiation-dominated (RD) background, with scale factor $a(\tau) = \tau/\tau_0$, where τ indicates the conformal time and $\tau_0 = 70/\sqrt{\lambda}v$ in our simulations. While it would be possible to obtain analogous results working in Minkowski background, as done in ref. [389], evolving the network in RD dissipates some of the energy radiated from its decay. Moreover, we find the networks to decay slightly faster in an expanding background compared to a flat one.

As in the case of global strings, evolving local strings in an expanding background leads to a loss of resolution of the string core. To prevent this from happening, we perform an initial phase of extra-fattening, in which the fields are evolved with equations of motion,

$$\begin{aligned} \varphi'' + 2\frac{a'}{a}\varphi' - D_i D_i \varphi &= -2a^{-2}\lambda \left(|\varphi|^2 - \frac{v^2}{2} \right) \varphi, \\ F'_{0i} + 4\frac{a'}{a}F_{0i} - a^{-4}\partial_j F_{ji} &= 2a^{-2}e\text{Im}[\varphi^* D_i \varphi]. \end{aligned} \quad (10.25)$$

This phase is set to last for a total of $\Delta\tau_{\text{ef}} = \sqrt{\tau_0(\Delta\tau_{\text{HL}} + \tau_0)}$, where $\Delta\tau_{\text{HL}} = L/2$ is the half-box-light-crossing time of the lattice. After this, the fields are evolved normally in a RD background, with equations of motion

$$\begin{aligned} \varphi'' + 2\frac{a'}{a}\varphi' - D_i D_i \varphi &= -2a^2\lambda \left(|\varphi|^2 - \frac{v^2}{2} \right) \varphi, \\ F'_{0i} - \partial_j F_{ji} &= 2a^2e\text{Im}[\varphi^* D_i \varphi]. \end{aligned} \quad (10.26)$$

for an additional time $\Delta\tau_{\text{RD}} = \Delta\tau_{\text{HL}} - \Delta\tau_{\text{ef}}$. The initial extra-fattening phase ensures that, after this additional time, the width of the string is equal to that at the end of diffusion.

We note that the extra-fattening evolution can be regarded, after redefining $A'_\mu = A_\mu/e$, as promoting the couplings to time-dependent variables, $\lambda \rightarrow a^{-4}\lambda$ and $e^2 \rightarrow a^{-4}e^2$. This implies the mass of both massive modes decreases with time, so that string width grows. Naively substituting the couplings without redefining A_μ would instead break gauge invariance of the action. Note that Gauss' law is conserved during the extra-fattening, but needs to be redefined accordingly,

$$\partial_i F_{0i} = 2a^{-2}e\text{Im}[\varphi^* \dot{\varphi}]. \quad (10.27)$$

By the end of the evolution in a RD background, the string network is close to the scaling regime, with the comoving mean string separation, $\xi = (L^3/L_{\text{str}})^{1/2}$, linearly increasing, $\xi \propto \tau$, and an almost constant mean square velocity, v_{str}^2 . In fig. 10.2 we represent the time evolution of these two

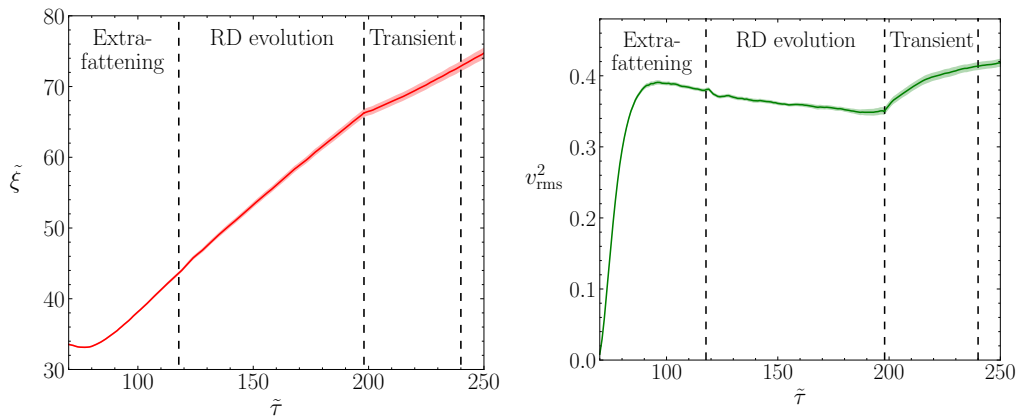


Figure 10.2. Time evolution of the mean string separation and the mean-squared velocity of a network of local strings averaged over 20 independent realizations. Networks are generated with $\tilde{\ell}_{\text{str}} = 15$ and simulations are performed with $\tilde{L} = 256$ and $\delta\tilde{x} = 0.25$. The vertical lines corresponding to the end of the extra-fattening, RD evolution and the transient phases, as indicated. The time coordinate corresponds to comoving time during the first two phases, while it is the standard time coordinate in Minkowski spacetime. Bands indicate one standard deviation.

quantities from the end of diffusion, averaged over 20 network realizations simulated with $\tilde{L} = 256$, $\delta\tilde{x} = 0.25$ and $\tilde{\ell}_{\text{str}} = 15$, for which the end of the evolution in RD corresponds to $\tilde{\tau} = 198$.

In most cases, however, the network has not yet decayed into a single loop at the end of the evolution in RD. We subsequently evolve the resulting network in a Minkowski background, for a maximum time of $2\Delta\tau_{\text{HL}}$, which we found enough to typically have one isolated string remaining. Note this is much longer than the period $\Delta\tau_{\text{HL}}/2$ used in the case of global networks, since we find local networks to decay slower.

Note that, when changing from RD to a Minkowski background, the network undergoes a transition period to adapt to the new background. This is clearly visible in fig. 10.2, where after $\tilde{\tau} = 198$ the evolution of the mean square separation and the mean squared velocity changes from the previous regime. This is related to the fact that the characteristics of the scaling regime depend on the background metric. After changing to Minkowski, we wait for $\Delta\tau_{\text{HL}}/2$ after analyzing any loops, which we call a *transient phase*. We believe this minimizes the impact of the sudden change of background. Even if a loop forms during this phase, we do not study its dynamics and GW emission until a time $\Delta\tau_{\text{HL}}/2$ has passed from the end of RD evolution.

After the transient period and if an isolated loop is found before a time $2\Delta\tau_{\text{HL}}$ has passed since the end of the evolution in RD, we turn on the emission of GWs and study the evolution of the loop until it disappears.

Approximately, $\sim 20\%$ of our simulations lead to isolated loops, of which $\sim 80\%$ can be used for our study. We discard those loops that self intersect forming several loops of similar size or infinite strings. Altogether, only $\sim 16\%$ of the simulations are suitable for this study.

10.2.3 Generation of artificial loops of type I

Local artificial loops of type I are generated from the intersection of two pairs of parallel infinite boosted strings. We follow the procedure used in ref. [427], similar in spirit to that presented for global artificial loops in sec. 9.2.3. Note, however, that we do not isolate local strings loops, as was done in the global case. We have found that a naive generalization of the technique presented in sec. 9.2.3 breaks Gauss' law. Instead, we choose the initial configuration so that one of the two loops resulting from the intersection of infinite strings is much larger than the other one, and wait for the smaller one to decay before starting our study of the longer loop. We now describe the initialization procedure in detail. As in sec. 9.2.3, we consider one pair parallel to the z -axis and the other parallel to the x -axis, and we refer to each of them with subscripts "1" and "2", respectively, which should not be confused with the component index of the gauge field, $\mu = 0, 1, 2, 3$.

We first explain how the pair of strings parallel to the z -axis is generated. The starting point is the solution for the NO vortex in the temporal gauge, given in eq. (10.8). We refer to this solution as $\varphi_{\text{NO}}^{(k)}$ and $A_{\text{NO},\mu}^{(k)}$, where $k = \pm 1$ indicates the winding number of the string.

The static NO configuration can be boosted in the (x, y) -plane with velocity $\mathbf{v}_1 = v_1(\sin \alpha_1, \cos \alpha_1)$, resulting in

$$\begin{aligned}\bar{\varphi}_{\mathbf{v}_1}^{(\pm)}(x, y; t) &= \varphi_{\text{NO}}^{(\pm)}(x', y'), \\ \bar{A}_{\mathbf{v}_1,0}^{(\pm)}(x, y; t) &= -\gamma_1 s_1 v_1 A_{\text{NO},1}^{(\pm)}(x', y') - \gamma_1 c_1 v_1 A_{\text{NO},2}^{(\pm)}(x', y'), \\ \bar{A}_{\mathbf{v}_1,1}^{(\pm)}(x, y; t) &= [1 + (\gamma_1 - 1)s_1^2] A_{\text{NO},1}^{(\pm)}(x', y') + (\gamma_1 - 1)s_1 c_1 A_{\text{NO},2}^{(\pm)}(x', y'), \\ \bar{A}_{\mathbf{v}_1,2}^{(\pm)}(x, y; t) &= (\gamma_1 - 1)s_1 c_1 A_{\text{NO},1}^{(\pm)}(x', y') + [1 + (\gamma_1 - 1)c_1^2] A_{\text{NO},2}^{(\pm)}(x', y'),\end{aligned}\tag{10.28}$$

where we define $s_1 = \sin \alpha_1$, $c_1 = \cos \alpha_1$ and $\gamma_1 = (1 - v_1^2)^{-1/2}$. Here (x', y') are the coordinates in the rest frame of the string and (t, x, y) are the coordinates in the boosted frame, related by

$$\begin{aligned}
x' &= -\gamma_1 v_1 s_1 t + [1 + (\gamma_1 - 1)s_1^2]x + (\gamma_1 - 1)s_1 c_1 y, \\
y' &= -\gamma_1 v_1 c_1 t + (\gamma_1 - 1)s_1 c_1 x + [1 + (\gamma_1 - 1)c_1^2]y.
\end{aligned} \tag{10.29}$$

The relativistic boost produces an undesired time component of the gauge field. To go back to the temporal gauge, we perform a gauge transformation,

$$\varphi = e^{i\xi} \bar{\varphi}, \quad A_\mu = \bar{A}_\mu - \partial_\mu \xi, \tag{10.30}$$

where ξ is a function chosen so that $A_0 = 0$ in the boosted frame,

$$\dot{\xi} = \bar{A}_0 \longrightarrow \xi = \int_0^t A_0 dt. \tag{10.31}$$

As we evaluate the initial configuration at $t = 0$, we can set $\xi = 0$. However, $\dot{\xi} = \bar{A}_0$, which we need to take into account to compute the time derivatives of the fields,

$$\begin{aligned}
\dot{\varphi} &= \dot{\bar{\varphi}} - ie \bar{A}_0 \bar{\varphi}, \\
\dot{A}_i &= \dot{\bar{A}}_i - \partial_i \bar{A}_0.
\end{aligned} \tag{10.32}$$

The product ansatz can then be used to generate a pair of parallel boosted strings. The complex fields for both strings, evaluated at $t = 0$, are multiplied, while the gauge fields are summed,

$$\begin{aligned}
\varphi_1(x, y; t) &= \frac{1}{v} \varphi_{v_1}^{(+)} \left[x - \left(\frac{L}{2} + a_1 \right), y - \left(\frac{L}{2} + b_1 \right); t \right] \\
&\quad \times \varphi_{-v_1}^{(-)} \left[x - \left(\frac{L}{2} - a_1 \right), y - \left(\frac{L}{2} - b_1 \right); t \right], \tag{10.33}
\end{aligned}$$

$$\begin{aligned}
A_{1,\mu}(x, y; t) &= A_{v_1,\mu}^{(+)} \left[x - \left(\frac{L}{2} + a_1 \right), y - \left(\frac{L}{2} + b_1 \right); t \right] \\
&\quad + A_{-v_1,\mu}^{(-)} \left[x - \left(\frac{L}{2} - a_1 \right), y - \left(\frac{L}{2} - b_1 \right); t \right], \tag{10.34}
\end{aligned}$$

where a_1 and b_1 indicate the distance of each string to the center of the lattice, in analogy to the variables of the same name defined in the local case—see fig. 9.6. The corresponding time derivatives are straightforward to evaluate.

The resulting configuration is then modified to fit in a periodic lattice, using a similar approach that that in ref. [427]. We do not modify the gauge field, as we observe its long-distance energy contribution to be negligible. The scalar field approaches the vacuum exponentially fast far from the string, and we only need to change its phase,

$$\varphi_1 = |\varphi_1| e^{i\theta_1} \rightarrow \varphi_1^{\text{per}} = |\varphi_1| e^{ih(x,y)\theta_1}, \tag{10.35}$$

which also affects the time-derivative of the field. The filter function $h(x, y)$ is chosen so that the phase changes smoothly close to the boundary towards zero. We opt to use

$$h(x, y) = \begin{cases} \frac{L/2 - |x_L|}{L/2 - L_h}, & |x_L| > L_h \text{ and } |x_L| \geq |y_L|, \\ \frac{L/2 - |y_L|}{L/2 - L_h}, & |y_L| > L_h \text{ and } |x_L| < |y_L|, \\ 1, & \text{otherwise,} \end{cases} \quad (10.36)$$

where we denote $x_L = x - L/2$ and $y_L = y - L/2$. This differs from the choice in ref. [427], which we find leaves some residual energy close to the $(x = 0, L, y = L/2)$ boundaries that leads to instabilities at late times in the simulations. We use $\tilde{L}_h = \tilde{L}/2 - 16$ in our simulations, independently of the size of the lattice. We observe that varying L_h up to a factor of four has a negligible effect on the final results.

Finally, we use again the product ansatz on two perpendicular string pairs and generate the initial conditions for our simulations,

$$\begin{aligned} \varphi(x, y, z) &= \varphi_1^{\text{per}}(x, y; t = 0) \times \varphi_2^{\text{per}}(z, y; t = 0), \\ A_\mu(x, y, z) &= A_{1,\mu}(x, y; t = 0) + A_{2,\mu}(z, y; t = 0). \end{aligned} \quad (10.37)$$

The time derivatives of the fields are computed by successive differentiation, taking into account the gauge transformations in eq. (10.32) and the use of the filter function in eq. (10.35).

In this work, we consider different boost velocities for the two pairs, $v_1 \neq v_2$ and set $\alpha_1 = -\alpha_2 = \alpha$, as we observe this leads to longer-lived strings. More concretely, we have found that other choices of the boost direction, such as $\alpha_1 = \alpha_2$, lead rapidly to a *double-line collapse* event, this is, a string configuration in which two antiparallel segments of the string approach each other, completely annihilating. We also consider $b_1, b_2 \ll L$, so that the strings intersect rapidly after the start of the simulation. Finally, we set $a_1 = a_2$ to be a small fraction of the box size, which we justify below.

The initial configuration is evolved in a Minkoski background using eq. (10.3), and the four strings soon intersect forming two loops. Taking advantage of the absence of long-range interactions between the strings, we opt to set $a_1 = a_2$ small compared to the box size, so that the inner loop is much smaller than the outer one and collapses rapidly after the start of the simulation. After this happens, we start to measure the emission of particles and GWs from the loop.

The reason why we focus on the outer loop, rather than the inner one, is to keep the initial infinite strings in each pair far from the region modified by the filter in eq. (10.36). Note some parts of the strings of each pair still lie on top of the modified region of the opposite pair. The size of this region depends on the choice of L_h and, as discussed above, we observe no effect on the dynamics of the loops from changing this parameter. Thus, we believe the effect of the chosen filter function on the loop to be negligible

10.2.4 Generation of artificial loops of type II

Artificial loops of type II are generated following the procedure introduced in refs. [388, 389]. This is based on initializing static strings of arbitrary shape by setting some magnetic flux on the plaquettes pierced by the initial strings. We note that this technique relies on the use of the hybrid or the compact formulation of the gauge theory, introduced in sec. 8.2.2. For our study, we use the hybrid formulation.

Given some shape of the desired one-dimensional strings, one can determine a set of plaquettes pierced by the string. The idea is to set the magnetic flux through these plaquettes to $\pm 2\pi$, depending on the direction from which it is pierced by the string. This is achieved by setting the gauge variables on the links to

$$A_\mu(\mathbf{n}) = \pm \frac{\pi}{2\delta x e}, \quad (10.38)$$

where the sign depends on the orientation of link. The complex scalar field is set to be equal to the vacuum expectation value, $\varphi = v$, everywhere. A diagrammatic representation for one plaquette is presented in fig. 10.3, pierced by a string going out of the plane of the paper.

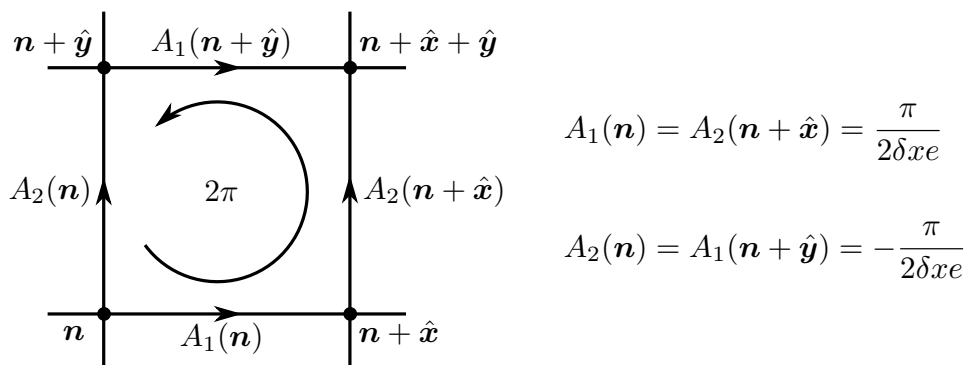


Figure 10.3. Representation of a single plaquette in the (x, y) -plane pierced by a string going in the z direction (out of the paper). We indicate the initial values to which the different links are set. The scalar field is fixed to $\varphi = v$ everywhere.

The initial configuration is then diffused for five units of program time, using eq. (10.24), which leads to the formation of strings with the expected radius, $r_c \sim m_\chi^{-1}$. Note that in the hybrid formulation the $\partial_j F_{ji}$ term in eq. (10.24) needs to be discretized using the plaquette,

$$\partial_j F_{ji}|_{\text{hybrid}} = \frac{1}{\delta x^2 e} \Delta_j^+ \sin [\delta x e \mathcal{C}_{ji}(\mathbf{n})] , \quad (10.39)$$

where Δ_j^+ denotes the forward finite difference—see eq. (8.31)—and $\mathcal{C}_{ij}(\mathbf{n})$ is the circulation of the gauge field on the plaquette,

$$\mathcal{C}_{ij}(\mathbf{n}) = [A_i(\mathbf{n}) + A_j(\mathbf{n} + \hat{\mathbf{i}}) - A_i(\mathbf{n} + \hat{\mathbf{j}}) - A_j(\mathbf{n})] . \quad (10.40)$$

The remaining terms in the diffusion equation can be naively discretized.

For our study, we use an initial configuration composed by four non-straight static strings, following ref. [389], which intersect soon after the start of the simulation forming two loops. We consider two strings at $y = L/10$ and $y = 9L/10$ with sinusoidal form. The coordinates of the string core are given by

$$x = \pm A \cos(2\pi z/L) , \quad (10.41)$$

with each sign corresponding to a different value of y . Also, we set $A = 0.075L$. The other two strings have fixed z with a sawtooth form,

$$x = \begin{cases} \pm B \left[\frac{y}{L/4} - 1 \right] , & 0 \leq y \leq L/2 , \\ \mp B \left[\frac{y}{L/4} - 3 \right] , & L/2 < y < L , \end{cases} \quad (10.42)$$

with $z = L/10$ and $z = 9L/10$, for each string, and $B = L/2$. The signs, again, corresponds to each possible value of z . A representation of the resulting configuration, at the end the diffusion period, is shown in fig. 10.4a.

After the diffusive phase, the strings are let to evolve in Minkoski space-time. This is performed using a discretized version of eq. (10.3) consistent with the hybrid formulation, using the discretization for the $\partial_j F_{ji}$ term in eq. (10.39). The four infinite strings start to move as a result of their non-straight form, and they eventually intersect, forming two loops. Due to the initial position of the infinite strings, the outer one is much smaller than the inner one. Thus, we wait until the outer loop disappears and study the inner one afterwards. An example of the resulting isolated loop is presented in fig. 10.4b.

A drawback of this initialization method is that there remains a magnetic flux frozen on the initialized plaquettes. When measuring the winding number on these plaquettes using eq. (10.16), one finds a non-zero results,

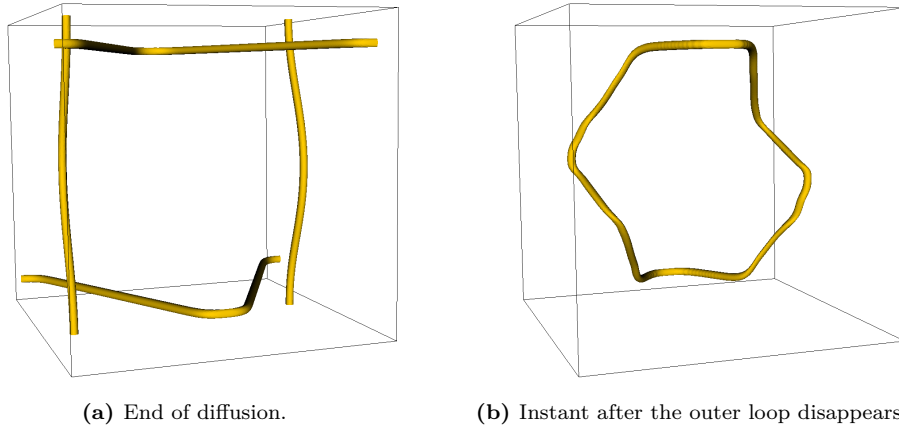


Figure 10.4. Three-dimensional snapshots of $|\varphi|^2 = 0.2v^2$ surfaces of the simulation of an artificial loop of type II.

which is associated to a *ghost* string [388]. This is an unphysical consequence of this particular procedure, since these ghost strings neither contain energy, nor affect the dynamics of the physical strings. When measuring the length of artificial strings of type II from the number of pierced plaquettes, we subtract the number of initialized plaquettes. For our loops, the number of plaquettes belonging simultaneously to both the real and the ghost string is negligible compared to the total number of plaquettes, and so this does not affect our ability to measure the length of the loops.

10.3 Results

We now present our results on the emission of particles and GWs from local string loops. In secs. 10.3.1 and 10.3.2 we characterize the lifetime of network and artificial loops, respectively, as a function of their length and energy, and determine the emission power of particles. Then, sec. 10.3.3 presents results on the GW emission from network and artificial loops of type I. We recall that we are neglecting backreaction of the GWs on the matter fields, an assumption that we check self-consistently later.

10.3.1 Particle emission from network loops

We study the evolution of network loops and characterize their lifetime, Δt_{dec} , as a function of their initial length, L_0 , and energy, $E_{\text{str},0}$. In total, we

study 41 different network loops with length-to-width ratios up to $L_0/r_c \lesssim 3500$, using $\delta\tilde{x} = 0.25$ in our simulations, as we justify later.

Network loops behave very similarly to their global counterparts, with their length decreasing almost linearly with time. An example of the time evolution of the length of a network loop, generated in a lattice with $\tilde{L} = 256$ using $\tilde{\ell}_\varphi = 15$, is shown in fig. 10.5a. In general, network loops do not oscillate, having a lifetime smaller of their NG period, $T_{\text{NG}} = L_{\text{str}}/2$.

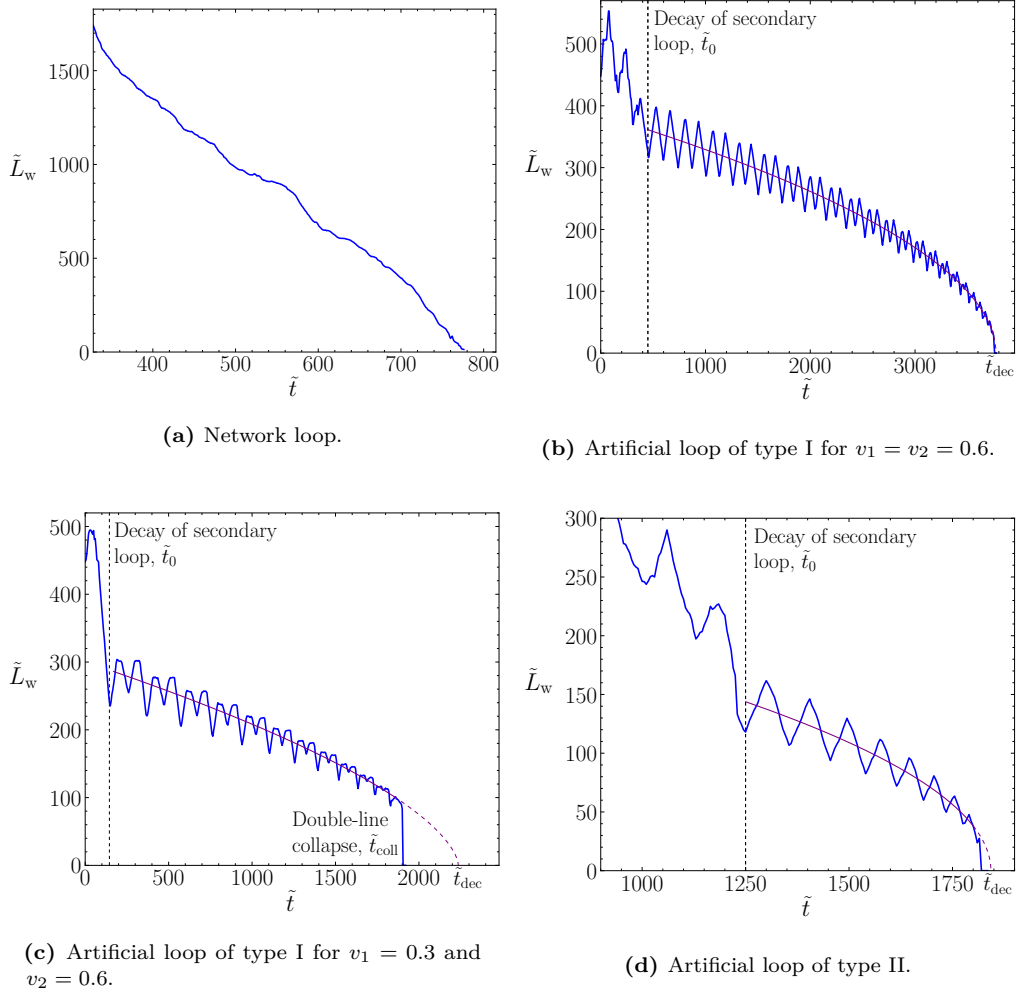


Figure 10.5. Example of the time evolution of the length of a network loop (top left) and artificial loops of type I (top right and bottom left) and type II (bottom right), measured from the number of pierced plaquettes. In the case of artificial loops, we indicate the time at which the secondary loop decays with a vertical dashed line. For these loops we also show the result from a fit to eq. (10.44). This is used to estimate the decay time in the absence of double-line collapse, which is observed to occur in the last stages of the loop evolution for some initial configurations, as shown, for example, in the bottom left panel.

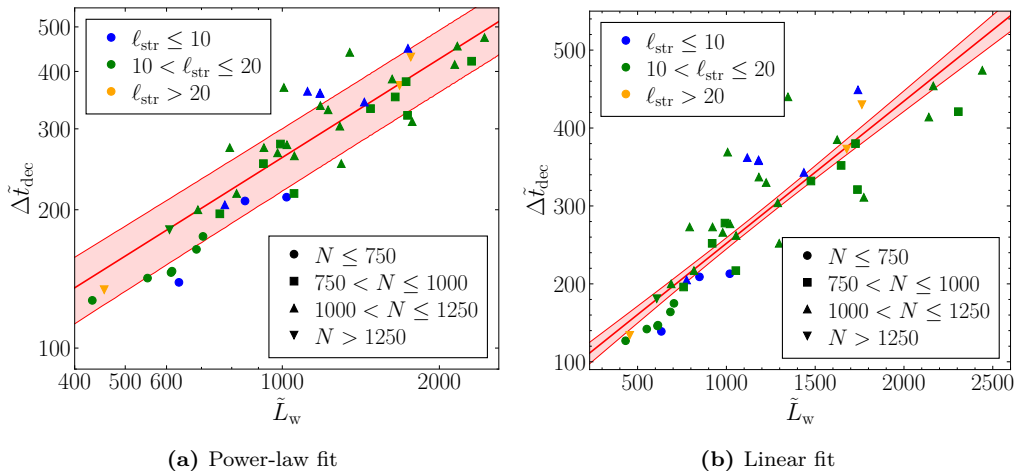


Figure 10.6. Decay time of network loops as a function of their initial lengths. Lines and bands represent the best-fit result to a power law, $\Delta\tilde{t}_{\text{dec}} = A\tilde{L}_0^\alpha$ (left, in logarithmic scale), and a linear dependence, $\Delta\tilde{t}_{\text{dec}} = c_1\tilde{L}_0 + c_2$ (right, in linear scale). All simulations are performed with $\delta\tilde{x} = 0.25$.

In fig. 10.6a, we show the decay time of all the studied network loops as a function of their initial lengths, measured from the number of pierced plaquettes—see eq. (9.24). From a two-parameter fit of the form $\Delta\tilde{t}_{\text{dec}} = A\tilde{L}_0^\alpha$, we find that network loops decay slightly faster than linearly with their length, with $\alpha = 0.71(5)$ and $A = 1.9(0.7)$. The result of this fit is also presented in fig. 10.6. A similar relation is also obtained from the string energies, measured using eq. (10.18). Fitting to $\Delta\tilde{t}_{\text{dec}} = B\tilde{E}_{\text{str},0}^\beta$, we obtain $\beta = 0.73(6)$ and $B = 1.0(0.5)$.

Note this has very important implications in the evolution of the strings. In particular, we can determine the particle emission power,

$$\tilde{P}_\varphi = \frac{d\tilde{E}_{\text{str}}}{d\tilde{t}} \propto \tilde{L}^\gamma, \quad (10.43)$$

where $\gamma = \alpha(1 - \beta)/\beta$ and the power in program units is $\tilde{P}_\varphi = P_\varphi/v^2$. From these results, we find that the emission power from network loops seems to increase slightly with the string length, with $\gamma = 0.26(8)$. If GW emission power is independent of the length, as we show in sec. 10.3.3 and is predicted by NG, this implies that strings originating from phase transitions in the early universe would decay mainly via the emission of particles, with a very suppressed production of GWs.

It is worth commenting about systematic effects that could affect our results. We have studied the sensitivity of network loops to the UV resolution. We use a coarse graining procedure to generate low-resolution loop configurations from one with $\delta\tilde{x} = 0.125$, finding that the dependence on $\delta\tilde{x}$

is be small for network loops. For the choice $\delta\tilde{x} = 0.25$ used in this work, we estimate the systematic error to remain only of a few percents.

Finite-volume effects can also play a role. In some cases, we study loops that are several times longer than the box size. This could imply a higher curvature than typically expected in loops of the same size, if they were not constrained to fit in our lattices. Our loops may thus radiate faster than would be expected for loops of their size. However, we do not observe evidence of this effect for the loop sizes studied, and so we expect that finite-volume effect on α and β for network loops to be small. Even for a relative errors of $\sim 30\%$ size, we would still obtain $\gamma \gtrsim 0$, meaning that the emission of particle radiation is, at most, independent of the size of the loops.

Given this observation, it is instructive to also analyze our results assuming a linear dependence. The results to a fit of the form $\Delta\tilde{t}_{\text{dec}} = c_1\tilde{L}_0 + c_2$ is presented in fig. 10.6b, which is observed to be compatible with our data. From the fit we obtain $c_1 = 0.182(13)$ and $c_2 = 69(16)$. A similar fit to $\Delta\tilde{t}_{\text{dec}} = d_1\tilde{E}_{\text{str},0} + d_2$ yields $d_1 = 0.097(7)$ and $d_2 = 63(18)$. If we assume this linear relation, we find that the emission power is independent of the length of the strings, with a power $\tilde{P}_\varphi^{\text{linear}} = 10.3(7)$, which is almost equal to that obtained for global loops—see eq. (9.46). As we discuss in sec. 10.3.3, even in this case, the decay of the loops would still be dominated by particle emission, with a suppression of GW production proportional to v^2/m_{p}^2 .

10.3.2 Particle emission from artificial strings

We study the decay time of 14 artificial loops of type I and 6 loops of type II, with length to width ratios up to $L_0/r_c \lesssim 640$, as a function of their initial length and energy. We use simulations with $\delta\tilde{x} = 0.1875$ and $\delta\tilde{x} = 0.125$, which we justify below. Local artificial loops present a qualitatively very different dynamics than network loops, since they oscillate multiple times before they decay. Their lifetimes are thus much longer than that of network loops of the same size. As an example, we represent in fig. 10.7 the evolution of a loop of type I generated with $v_1 = v_2 = 0.6$ and $\sin\alpha = 0.4$, simulated in a box with $\tilde{L} = 64$ and $\delta\tilde{x} = 0.25$.¹ Notoriously, we find that even for a simulation of this reduced size, the loop oscillates multiple times before decaying.

¹We use a lattice of reduced size for the representation due to the size of the three-dimensional distribution savefiles, which becomes very large (tens of gigabytes) for bigger lattices.

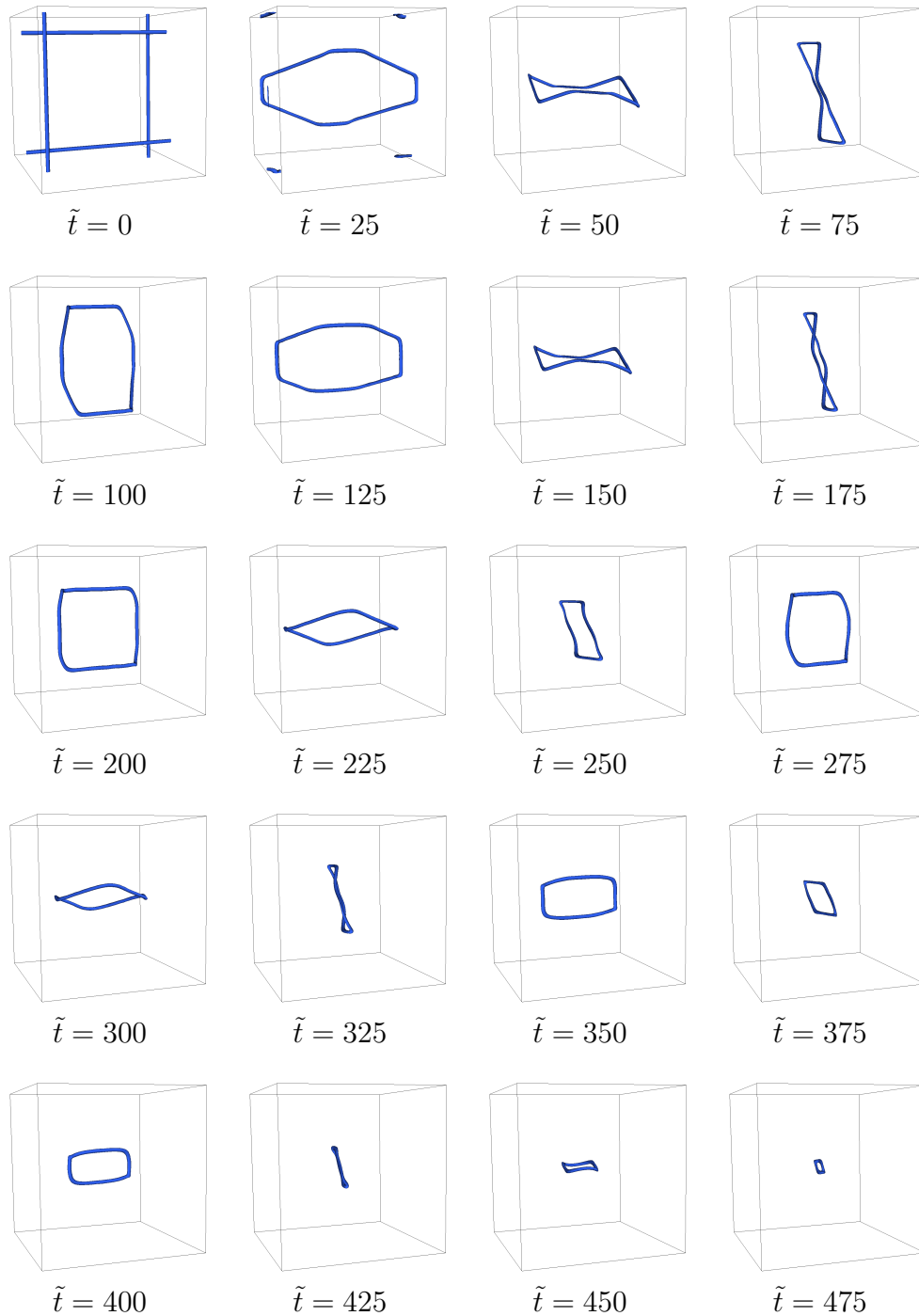


Figure 10.7. Three-dimensional snapshots of $|\varphi|^2 = 0.2v^2$ surfaces of different moments of the evolution of an artificial loop of type I, simulated with $\tilde{L} = 64$, $\delta\tilde{x} = 0.25$, $v_1 = v_2 = 0.25$ and $\sin\alpha = 0.4$. The secondary loop has already vanished at $\tilde{t} = 50$, while the other one oscillates several times before decaying. The field has been periodically shifted by $L/2$ in the x and z directions so that the outer loop is centered in the figures.

Due to their long-lasting behaviour, the study of the decay time of artificial loops as a function of their initial length is more complicated than for network loops. Examples of the evolution of the strings length are presented in fig. 10.5 for three artificial loops. In fig. 10.5b, we represent the case of an artificial loop of type I, generated with $v_1 = v_2 = 0.6$ and $\sin \alpha = 0.4$, in a box with $\tilde{L} = 168$ and $\delta\tilde{x} = 0.1875$. In this case, we observe that after the inner loop disappears at $\tilde{t}_0 \approx 450$ (vertical dotted line), the length of the outer loop begins to decay slowly while oscillating, until it smoothly disappears at $\tilde{t}_{\text{dec}} \approx 3800$. We observe this behavior is very similar to that of an artificial loop of type II, presented in fig. 10.5d for a simulation with $\tilde{L} = 336$ and $\delta\tilde{x} = 0.1875$.

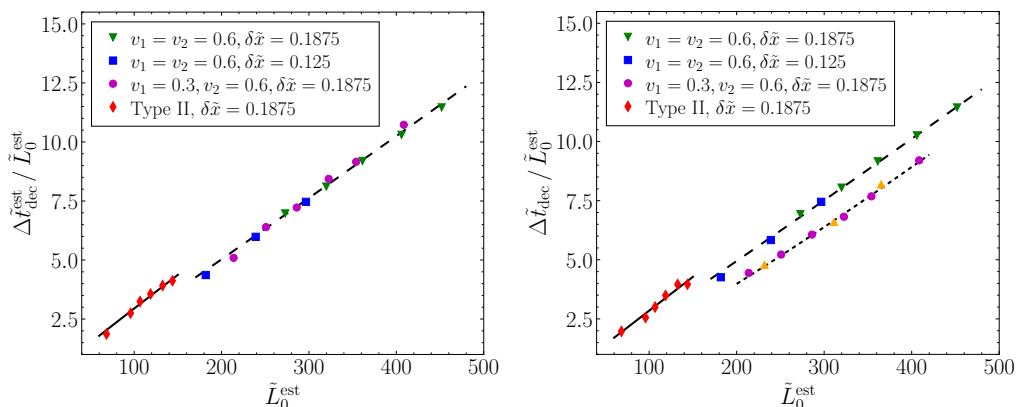
A bit different is the evolution of the artificial loop of type I shown in fig. 10.5c, generated with $v_1 = 0.3$, $v_2 = 0.6$ and $\sin \alpha = 0.4$, in a box with $\tilde{L} = 168$ and $\delta\tilde{x} = 0.1875$. In this case, after oscillating a number of times, the loop disappears almost instantly. This is related to a double-line collapse event. Due to the initial square configuration, the loop eventually reaches a point in which two parallel segments approach each other, completely annihilating.

Since the double-line collapse is a result of the artificial initial conditions, we opt to focus on the rate of decay while the loop oscillates. For all artificial loops of both types considered, we fit the time evolution of the length of the string to the following function

$$\tilde{L}_w = A(\tilde{t} - \tilde{t}_{\text{dec}})^p, \quad (10.44)$$

where A , t_{dec} and p are the fit parameters. The fits are performed between the time the secondary loop disappears, t_0 , and the time at which the loop collapses. The result of this fit is also presented in figs. 10.5b to 10.5d, from which we obtain an estimate of the decay time of the loop, t_{dec} , if no double-line collapse happened. From this fit, we can get estimates of the initial length of the string, L_0^{est} , evaluating eq. (10.44) at t_0 , which averages over the loop oscillation, and the lifetime of the loop if no double-line collapse happened, $\Delta\tilde{t}_{\text{dec}}^{\text{est}} = \tilde{t}_{\text{min}} - \tilde{t}_{\text{dec}}$. We note that in the cases in which no double-line collapse occurs—see figs. 10.5b and 10.5d—this is very close to the measured lifetime of the loop.

The results for the estimated initial length of the string as a function of the estimated decay time, are represented in fig. 10.8a for several artificial loops of type I and II. We observe that the results for artificial loops of type I present a very similar behavior independently of the initial velocities, at least for the initial conditions considered in this work. The results can be simultaneously fitted to $\Delta\tilde{t}_{\text{dec}} = A(\tilde{L}_0^{\text{est}})^\alpha$, finding, $A = 21(3) \times 10^{-3}$ and $\alpha = 2.027(25)$. A similar result is obtained for artificial loops of



(a) Estimated lifetime without double-line collapse (b) Measured lifetime with double-line collapse

Figure 10.8. Decay time of artificial loops, as a function of their initial lengths, with lifetime computed with (left) and without (right) extrapolating the decay time to remove the effect of a double-line collapse. All loops of type I are generated with $\sin \alpha = 0.4$. Lines represent the best-fit result to a power law, and the initial length is estimated from fitting the evolution of the string length, as explained in the main text. We note that the effect of the double-line collapse is only notorious for those loops generated with $v_1 = 0.3$ and $v_2 = 0.6$ (magenta dots), which we fit separately from the other loops of type I in the right panel.

type II, $A = 33(12) \times 10^{-3}$ and $\alpha = 1.97(7)$. These results indicate that the mechanism underlying the decay of artificial loops is similar for both types, with $\alpha \approx 2$, and different from that of network loops, which have $\alpha \approx 0.7$.

Note that this conclusions are not affected if the measured collapse time is used to compute the lifetime of the loops instead of the extrapolated \tilde{t}_{dec} —see fig. 10.8b. In this case, we obtain significant differences for those loops generated with $v_1 = 0.3$ and $v_2 = 0.6$, which present a notorious double-line collapse event at the end of their decay. Although a universal behavior is no longer observed, loops with $v_1 = 0.3$ and $v_2 = 0.6$ still decay with an exponent $\alpha = 2.16(3)$, close to that obtained in above.

A similar approach can be taken to study the lifetime of the loops as a function of their initial energy. We fit the evolution of the loop energy to

$$\tilde{E}_{\text{str}} = B(\tilde{t} - \tilde{t}_{\text{dec}})^a, \quad (10.45)$$

on the same range as for the previous analysis. Using the results, we can also determine an estimate of the initial string energy, $\tilde{E}_{\text{str},0}^{\text{est}}$. The results are fitted to $\Delta \tilde{t}_{\text{dec}} = B \left(\tilde{E}_{\text{str},0}^{\text{est}} \right)^\beta$, obtaining in this case $B = 5.4(1.0) \times 10^{-3}$ and $\beta = 1.988(26)$ for type I, and $B = 3.4(2.5) \times 10^{-3}$ and $\beta = 2.08(13)$ for type II. Again, both exponents are compatible with $\beta \approx 2$.

Using these results and eq. (10.43), we can compute an estimate for the particle emission power. Assuming $\alpha, \beta \approx 2$, we obtain that the power is inversely proportional to the length of the strings,

$$P_\varphi = \frac{1}{2\sqrt{AB}} L^{-1}, \quad (10.46)$$

in agreement with the results from refs. [389, 427] for artificial loops. This implies that particle emission from these type of loops would be suppressed for longer loops. In particular, for a constant emission power of GWs, as predicted by NG and as we demonstrate in the next section, there would be some critical length, L_{crit} , above which the emission power of GWs will be higher to that of particles, in agreement to ref. [427].

We also study possible discretization systematic effects on our results for artificial strings. We analyze the dynamics of the loops varying the UV resolution, by generating an equivalent initial configuration for several δx . The time evolution of the string length of artificial loops of type I, for different δx , is presented in fig. 10.9. We observe a large dependence of the results on the resolution, with convergence only being reached for $\delta \tilde{x} \lesssim 0.1$. In particular, all simulations evolve similarly until the loop starts to oscillate, when it becomes clear that low resolutions vastly overshoots the decay rate. This justifies using $\delta \tilde{x} = 0.1875$ in general for our study, as we observe systematic errors not bigger than 10%. This is also confirmed by our results in fig. 10.8, where no noticeable discrepancy can be found between loops with $\delta \tilde{x} = 0.1875$ and $\delta \tilde{x} = 0.125$.

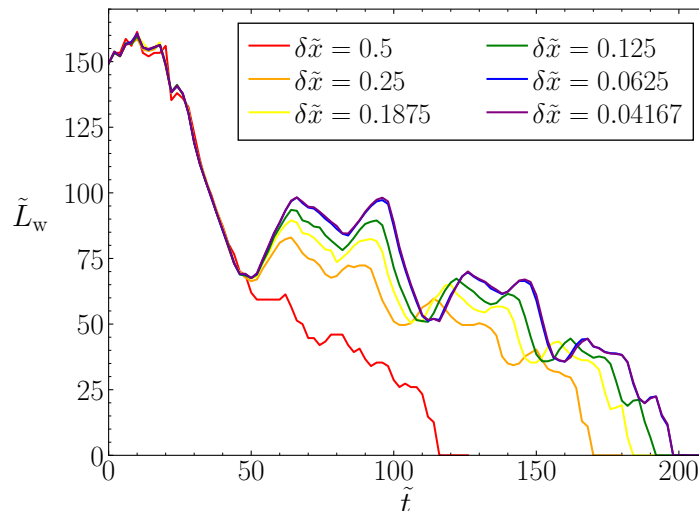


Figure 10.9. Time evolution of the length of an artificial loop of type I, generated with $v_1 = 0.3, v_2 = 0.6$ and $\sin \alpha = 0.5$, in a lattice of size $\tilde{L} = 56$, for varying UV resolution. The length is measured from the number of pierced plaquettes.

10.3.3 GW emission

We now study the emission of GWs from network and artificial loops of type I. The production of GWs is simulated following the procedure in sec. 8.3.1. For the model under study in a flat background, the equations of motion of GWs are

$$\ddot{h}_{ij} - \partial_k \partial_k h_{ij} = \frac{2}{m_{\text{p}}^2} \{2\text{Re}[D_i \varphi (D_j \varphi)^*] - E_i E_j - B_i B_j\}^{\text{TT}}. \quad (10.47)$$

We define the fractional energy density of gravitational waves as

$$\Omega_{\text{GW}}(k, t) = \frac{1}{\rho_{\text{m}}} \frac{d\rho_{\text{GW}}(k, t)}{d \log k}, \quad (10.48)$$

where we normalize with the total energy of the gauge and scalar fields, $\rho_{\text{m}} = \rho_{\varphi} + \rho_{\text{U}(1)}$. We also define the total energy of GWs by integrating over the whole spectrum,

$$E_{\text{GW}} = \rho_{\text{m}} L^3 \int \Omega_{\text{GW}}(k, t) d \log k. \quad (10.49)$$

We stress, again, that we are not considering backreaction of the GWs on the matter fields, which we justify below.

Given the UV dependence observed for the GW emission of global loops—see sec. 9.3.3—and for the dynamics of local ones as discussed at the end of the previous section, we first study discretizations effects on the GW emission from local artificial loops. We make use of the same artificial loops presented in fig. 10.9. The evolution of the power spectra is shown, for several values of $\delta \tilde{x}$, in fig. 10.10, with early and late times represented in purple and red, respectively. We observe how the overall amplitude of the spectrum is suppressed for coarser lattices, as a result of the shorter lifetime of loops simulated with bad UV resolution.

For all resolutions, furthermore, we observe the presence of a peak at IR scales, $\tilde{k} \sim 0.4 - 0.5$. A second peak emerges in the UV for large δx close to the scale of the core radius, $k_{\text{c}} = 2\pi/r_{\text{c}}$, represented by a vertical dashed line. This peak, however, vanishes as the resolution is increased, indicating it is a lattice artifact. Deeper in the UV, the amplitude is exponentially suppressed. Overall, we observe that simulations with $\delta \tilde{x} \lesssim 0.1875$ agree up to scales $\tilde{k}_{\text{cut}} \sim 2.5$. We perform our study with $\delta \tilde{x} = 0.1875$, and opt to compute the total energy density of GWs integrating up to this cutoff, as the contribution from the UV is very suppressed in this case, and even further suppressed for finer lattices. This cutoff will be used for both network and artificial loops.

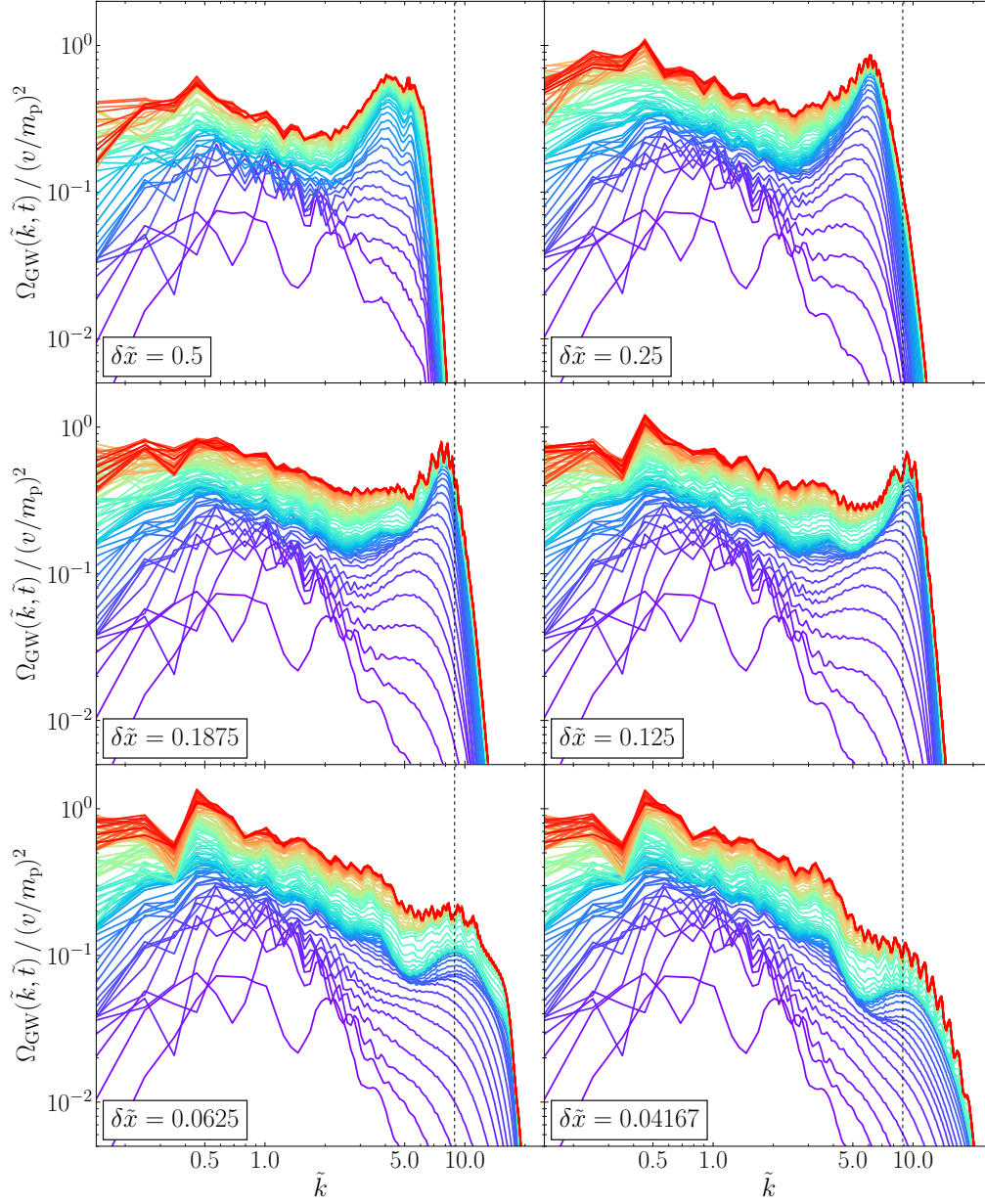


Figure 10.10. GW power spectra produced by an artificial loop of type I, generated with $v_1 = 0.3$, $v_2 = 0.6$ and $\sin \alpha = 0.5$, in a lattice of size $\tilde{L} = 56$ for varying UV resolution. The vertical dashed line indicates the scale of the string core, $\tilde{k} = 2\pi/\tilde{r}_c$. Spectra are represented every unit of program time, going from early (purple) to late (red) times.

Regarding the IR coverage of the lattices, the spectra in fig. 10.10 seem to start decreasing for small scales, at $k \sim 0.3$. Ideally one would like to have better IR coverage. However, we are limited in this aspect by our simulation procedures. Network loops are typically of a length larger than the lattice size, and artificial loops are constructed to have a size similar to that of the lattice, since we want the secondary loop to vanish rapidly. Thus, our techniques do not allow us to easily increase the size of the lattice while keeping the strings of fixed length. We hope to come back to this point in the early future.

We now present our result for the GW emission power of isolated loops. In the case of network loops, we follow the procedure used for global strings, and compute a rolling average of the total GW emission power, given in eq. (9.50), using a window width $\tilde{T} = 20$. We find this choice of \tilde{T} to cancel fast oscillations, with very minor variations of the results if the window width is increased. Our results for network loops of different length are presented in the left panel of fig. 10.11 as a function of the time since we started measuring the GWs, normalized by the lifetime of each loop. In all cases, the emission power is roughly constant in time, with fluctuations that depend on the particular dynamics of the loops, and a minor decreasing trend during the life of the loop. At late times, the emission power rapidly drops down as the loop finally disappears.

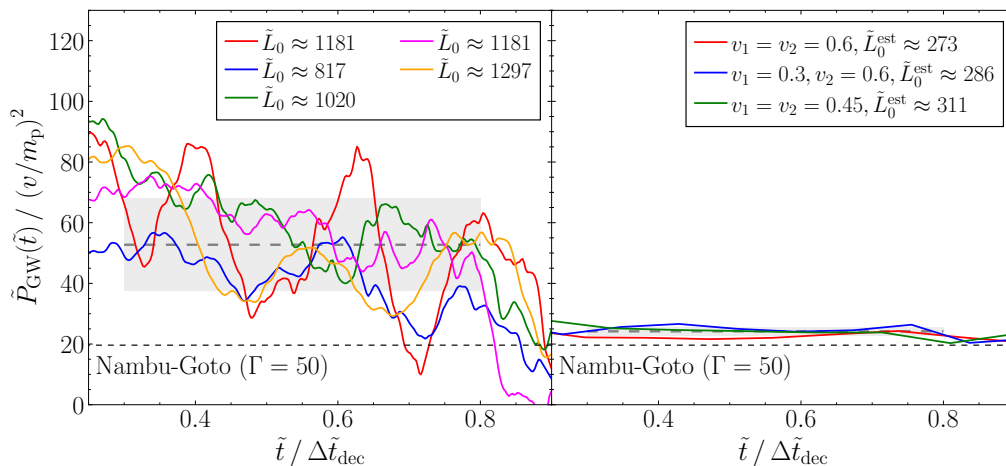


Figure 10.11. GW emission power for both network (left) and artificial loops of type I (right), computed using eq. (9.50) and eq. (10.50), respectively. The grey band and line represents an average of the emission power, and we compare the NG predictions (horizontal dashed line), estimated with $\Gamma = 50$ and $\mu = \pi v^2$. The power is represented as a function of the time since the emission of GWs started, normalized by the total decay time of each loop. Network and artificial loops are simulated with $\delta\tilde{x} = 0.25$ and $\delta\tilde{x} = 0.1875$, respectively.

From these results, we can obtain an average value of the emission power. In the range $\tilde{t}/\Delta\tilde{t}_{\text{dec}} \in [0.3, 0.8]$, we obtain $P_{\text{GW}} = 53(15)$ for network loops. This result is around five times smaller than the one obtained for global network loops. Comparing to NG expectations, $\tilde{P}_{\text{GW}}^{\text{NG}} \approx 20$, we observe that our result is still more than two times larger.

The study of the GW emission power from artificial loops is more complicated. The main reason is the longer lifetimes of these loops, which can be dozens of times larger than the half-box-light-crossing time of the lattice. For example, for the simulation presented in figs. 10.9 and 10.10, $\Delta\tilde{t}_{\text{HL}} = 27$, while the string lives almost 500 units of program time. This may have a severe impact in the study of GWs, since gravitational radiation propagates at the speed of light and can present interferences around the box. Indeed, we believe this to be the origin of the oscillations observed in the spectra in fig. 10.10 at late times.

To prevent said self-interferences, we take a different approach to obtain the GW emission power from artificial loops. We initialize the GWs to zero when the secondary loop disappears, and evolve them normally for a period of time ΔT_{GW} , after which we measure the GW power spectrum. We then reset the GWs to zero and repeat the procedure until the loop decays. The average emission power of GWs during each of these intervals is computed as

$$P_{\text{GW}} = \frac{L^3 \rho_{\text{m}}}{\Delta T_{\text{GW}}} \int_0^{k_{\text{cut}}} \Omega_{\text{GW}}(k, t) \, d \log k. \quad (10.50)$$

The duration of the interval should be taken long enough to ensure all relevant frequencies of the system are captured, but small enough so that the emission power remains mostly constant and finite-volume effects are small. We find that using $\Delta\tilde{T}_{\text{GW}} = 80 - 200$ leads to stable results, with discrepancies smaller than 10% from varying this quantity, and choose to use $\Delta\tilde{T}_{\text{GW}} = 160$ in this work. We also focus only on artificial loops of type I, since those of type II have much shorter lifetimes.

The results for the GW emission of artificial loops of type I is presented in the right panel of fig. 10.11. As in the case of network loops, the emission power remains mostly constant, with minor variations related to the oscillations of the loops. Averaging our results over the range $\tilde{t}/\Delta\tilde{t}_{\text{dec}} \in [0.3, 0.8]$, we obtain $\tilde{P}_{\text{GW}} = 24.2(1.4)$, which is very close to NG predictions.

We can finally compare these results to the particle emission power obtained in secs. 10.3.1 and 10.3.2. We find that GW are emitted with a constant power that is independent of the length of the strings, both for network and artificial loops, although with different emission power. Particle emission, on the other hand, shows a dependence on the length of the loops, which is very different between the two types of loops.

For network loops, our results from a power-law fit indicate the the emission of particles increases slightly with the size of the loop, and so the emission of GWs is completely subdominant at large scales. Even if we assume a linear relation, which is also well reproduced by our data, we obtain, for reasonable values of v ,

$$\frac{P_{\text{GW}}}{P_{\varphi}^{\text{linear}}} = \frac{53(15)}{10.3(7)} \left(\frac{v}{m_{\text{p}}} \right)^2 = 5.1(1.5) \left(\frac{v}{m_{\text{p}}} \right)^2. \quad (10.51)$$

Therefore, the emission of GWs is very suppressed compared to particle production for reasonable values of the vacuum expectation value, $v/m_{\text{p}} \lesssim 3 \times 10^{-5}$ (obtained using $\mu = \pi v^2$ combined with constrains of the string tension from the GWB²). These results justify neglecting the backreaction of GWs on the strings.

The opposite situation happens for artificial loops, for which particle emission depends roughly on the inverse of the length of the strings, $P_{\varphi} \propto L^{-1}$, and so it is suppressed compared to GW radiation for long enough loops. Combining our results for the GW emission power and those for particle productions presented in sec. 10.3.2—see eq. (10.46)—it is possible to obtain an estimate of the critical length at which the emission power of particles equals that of GWs, $P_{\varphi} = P_{\text{GW}}$. We find

$$L_{\text{crit}} = 2.8(3) \times \frac{m_{\text{p}}^2}{\sqrt{\lambda} v^3} \sim \mathcal{O}(1) r_{\text{c}} \left(\frac{v}{m_{\text{p}}} \right)^{-2}. \quad (10.52)$$

Given present constrains on the vacuum expectation values, $v/m_{\text{p}} \lesssim 3 \times 10^{-5}$ [446], the emission of GWs dominates for loops of a length-to-width ratio higher than $\sim 10^9$. For smaller loops, $L < L_{\text{crit}}$, particle emission is the main decay channel. For artificial loops with $L < L_{\text{crit}}$ neglecting the backreaction of the GWs is justified.

To summarize, we find that it is possible to create local loops (the artificial ones) for which the emission of GWs is the main decay route at cosmological scales. However, such loops are not observed to originate from a phase transition. For realistic loops forming in the early universe (network loops) our results indicate that the emission of GWs from string loops forming in the early universe is very suppressed compared to particle production at all scales.

²Constrains from the CMB require $v/m_{\text{p}} \lesssim 10^{-3}$ [447–449] [446].

10.4 Conclusions

In this chapter, we have presented results on a lattice study of the decay of local string loops into particles and GWs [7]. We perform this study for two types of loops: network loops generated from the decay of string networks, with length-to-width ratios up to $L_0/r_c \lesssim 3500$, and artificial loops that form from the intersection of infinite strings, with $L_0/r_c \lesssim 640$. In both cases, we have found that the emission power of gravitational radiation is roughly constant in time, independently of the string length. This time-independent emission is in agreement with NG expectations, although with different magnitude, being around three times larger for network loops than for artificial ones.

The emission of particles, on the other hand, shows two different dependencies on the string length for each type of loops. In the case of network loops, the results from a power-law fit indicate a residual positive length dependence, meaning that the emission of particles from network loops increases with their length. Our data, however, is also compatible with a linear fit, in which case the emission power of particles would be constant. In both cases, anyways, the production of GWs from loops is highly suppressed compared to particle emission at large scales. By contrast particle emission is inversely proportional to the length for artificial loops, $P_\varphi \propto L^{-1}$, meaning that GW production dominates for loops longer than a critical length, $L_{\text{crit}} \sim \mathcal{O}(1)r_c(v/m_p)^{-2}$.

Our results have important consequences for the predicted GW background from a network of local strings. Studies of local loops are commonly based on the NG approximation, assuming that particle emission is absent at cosmological scales and the decay is dominated by GW emission. We have found that it is possible to fabricate loops for which this remains the case, as we have seen for artificial loops. However, this is not true for loops originating from phase transition. Our results for network loops clearly indicate that particle emission is not suppressed, but instead is the primary decay route for local string loops of cosmological size.

As a next step, we plan to use the results presented in this chapter for the GW emission from local loops to obtain an estimate of the GW background generated from a network of local strings, by combining the results with predictions for the loop number density computed at cosmological scales from NG simulations [404, 415, 420, 442–444]. We expect this to have an impact in suppressing the prediction for the GW background for local string networks, compared to estimations that ignore particle production, as we have found that the production of GWs is subdominant for realistic loops.

Conclusions and outlook

The use of lattice techniques to study field-theory phenomena that cannot be captured by perturbative methods has become widespread during the last decades, tied to the development of large supercomputing facilities. Lattice computations have been successfully applied to study the strong interactions at low energies, for which perturbative approaches fail due to the phenomena of asymptotic freedom and confinement, and also to investigate non-linear processes taking place during the early universe, for which fluctuations of the fields cannot be treated as small perturbations. The work presented in this doctoral thesis is focused on the application of lattice techniques, complemented by other analytical approaches, to study two very different physical situations: hadron interactions in quantum chromodynamics (QCD), and the dynamics and emission of particles and gravitational waves (GWs) from cosmic string loops that could arise in the early universe.

Hadron interactions from lattice QCD

Lattice QCD simulations allow one to study two- and three-particle scattering using the so-called quantization conditions, which relate the finite-volume energies of multiparticle states to infinite-volume scattering observables. Numerical computations can moreover be complemented by other analytical approaches, such as chiral perturbation theory (ChPT) or the limit of large number of colors, N_c . Part I of this dissertation focuses on the study of hadron interactions, with special emphasis on the synergy between lattice QCD, ChPT and the large N_c limit.

Chapters 3 and 4 are devoted to the study of the interactions between two mesons as a function of N_c . Chapter 3 presents the results from refs. [1, 8], in which pion-pion interactions near threshold are investigated. We performed lattice simulations with $N_c = 3 - 6$ in a theory with four

degenerate quark flavors, $N_f = 4$. We focused on two scattering channels: the SS channel, which is analogous to the isospin-two channel of two-flavor QCD, and the AA channel, which only exists for $N_f \geq 4$. We used the two-particle quantization condition to match our results of the finite-volume energies to ChPT predictions including the η' particle, and constrained the N_c scaling of the relevant low-energy constants. The results from this fit are presented in fig. 3.10. We found that the leading N_c contribution is unnaturally small compared to subleading N_c corrections.

In addition, the AA channel was found to have attractive interactions. This, together with its flavor quantum number makes it a candidate to contain a tetraquark resonance. This is supported by recent experimental discoveries at LHBb [30–33], which found tetraquark particles that would have the quantum numbers of the AA channel in a theory with $N_f = 4$ degenerate flavors. All this motivated us to extend the study of meson-meson interactions to higher energies, with the main goal of shedding light on the nature of tetraquarks at large N_c [2, 10]. In chapter 4, we have present results of this ongoing work in which we have studied the scattering of two mesons as a function of N_c . We have managed to characterize the scattering process of two pions as a function of N_c for both the SS and the AA channels, as shown in figs. 4.8 and 4.9. While we have found no clear evidence of a tetraquark resonance in the AA channel, the presence of a virtual bound state for $N_c = 3$ cannot be discarded and needs to be further investigated. We have also analyzed meson interactions in the AS channel, which contains odd partial waves, finding that interactions are very weak in this channel.

Following this work, the study of the N_c dependence of other scattering processes is compelling. One possibility is the case of the interactions of two pions in the isospin-one channel, well-known to contain the $\rho(770)$ resonance. This investigation would allow us to constrain the N_c dependence of the decay width of this particle, Γ , expected to scale as $\Gamma \sim 1/N_c$. This work would open the door to use the large N_c dependence to characterize the nature of other resonances, such as the $\sigma(550)$, which has been proposed to be a tetraquark state [450].

Chapters 5 and 6 are devoted to the study of three pion interactions in ChPT. Early lattice studies of three pions in the isospin-three channel found large discrepancies against leading-order (LO) ChPT predictions for the three-particle divergence-free K -matrix, $\mathcal{K}_{\text{df},3}$. This is an intermediate scheme-dependent quantity that appears in the relativistic-field-theory (RFT) three-particle quantization condition and is related to the scattering amplitude via some integral equations. In chapters 5 and 6, results for $\mathcal{K}_{\text{df},3}$ at next-to-leading order (NLO) in ChPT are presented.

Chapter 5 presents the results from ref. [3], in which $\mathcal{K}_{\text{df},3}$ was determined at NLO in ChPT for the isospin-three channel. We found that, when working at NLO in ChPT, the relation between $\mathcal{K}_{\text{df},3}$ and the three-pion scattering amplitude, \mathcal{M}_3 , is reduced to a simple algebraic equation. We also developed a series of techniques to determine the various contributions to $\mathcal{K}_{\text{df},3}$ from different parts of amplitude and from subtractions. Our results showed that NLO corrections are indeed large, and help to reconcile ChPT predictions and lattice results—see fig. 5.4. The results, however, could also indicate that ChPT fails to converge in the range of pion masses studied. We also analyzed the convergence of the threshold expansion of $\mathcal{K}_{\text{df},3}$, which is typically the parametrization of $\mathcal{K}_{\text{df},3}$ used when fitting to lattice results. We found that, for energies in the three-pion elastic regime, the difference between the threshold-expanded and the exact result is smaller than 20%.

Following this work, chapter 6 discusses the results from ref. [4], in which we determined the three-pion K -matrix up to NLO in ChPT for all isospin channels. As in the case of isospin three, we found that NLO corrections to LO are in general large. Our results for $\mathcal{K}_{\text{df},3}$ are depicted in fig. 6.2, and provide insight on the convergence of the chiral expansion for three-particle quantities. They will be useful to compare against future lattice studies of three-pions at non-maximal isospin, and also to parametrize $\mathcal{K}_{\text{df},3}$ around threshold. Note, however, that the presence of resonances in these channels limits the range of validity of ChPT.

The work presented in chapters 5 and 6 paves the path to computing $\mathcal{K}_{\text{df},3}$ in ChPT for more complicated systems. A notorious example is the scattering of pions and kaons, or that of three kaons, which have already been studied on the lattice at maximal isospin [301, 302]. However, the determination of the corresponding scattering amplitudes at NLO in ChPT is yet not available.

Part I of this dissertation is completed by chapter 7. This chapter presents ongoing work [5] on the study of two- and three-particle scattering in the (1+1)-dimensional $O(3)$ non-linear sigma model. This model is commonly used as a toy model of QCD, as both theories share many qualitative features, such as asymptotic freedom or the existence of a low-lying spectrum of isospin-one particles. Moreover, the S -matrix of the $O(3)$ model is known analytically, making the model ideal to test different formalisms. Our ultimate goal is to test the RFT three-particle formalism by performing a direct comparison between analytical predictions and lattice computations, to ensure that the different approximations made in the derivation of the formalism do not have a large numerical impact.

With the work presented in chapter 7, we take a first step in this direction. We have developed a three-particle generalization of the cluster algorithm,

with which we have determined the finite-volume energy spectra of the isospin-two and -one channels for two particles, and the isospin-three, -two and -one channels for three particles. These energies have been extrapolated to the continuum using lattices with different lattice spacing and finely tuned physical volume. The results for two particles were compared against exact analytical predictions, finding good agreement to analytical results, raising the confidence in our simulating procedure.

Results for three-particles, on the other hand, have been compared against analytical predictions made under the assumption that $\mathcal{K}_{\text{df},3} = 0$, computed using an adapted version of the the RFT formalism to 1+1 dimensions that we have developed. These predictions, together with our lattice results, are presented in figs. 7.12 to 7.14. We have observed a discrepancy between the analytical predictions and the lattice results, indicating that $\mathcal{K}_{\text{df},3}$ is indeed non-zero. This work has also allowed us to gain insight on the intricacies of the RFT formalism, especially in relation to the role of the cutoff function and possible numerical instabilities. The future plan is to use our lattice results to constrain $\mathcal{K}_{\text{df},3}$, and eventually compare them to an analytical prediction made from the factorizable S -matrix. This last point, however, would first require to adapt the integral equations that relate $\mathcal{K}_{\text{df},3}$ to \mathcal{M}_3 to the (1+1)-dimensional world.

Beyond the $O(3)$ model, the knowledge gained about the study of three-particle systems and the application of the RFT formalism opens the door to investigate more complicated systems in QCD. Of particular interest are, for example, systems of three-pions at non-maximal isospin, which could allow one to characterize the nature of different resonances, such as the $\omega(782)$ resonance in the isospin-zero channel. Other states of three mesons are also relevant, such as the $DD\pi$ system [451], expected to contain the $T_{cc}(3875)$ tetraquark. Finally, the application of lattice techniques to study light nuclei, such as the tritium or helium-3, is also very compelling.

Cosmic string loops from lattice simulations

The second part of my doctoral research has been presented in part II. This is focused on the application of classical-field-theory lattice techniques to study non-linear dynamics in an expanding background. In particular, this part of the thesis is devoted to analyzing the evolution of cosmic string loops using lattice simulations, capturing simultaneously the emission of particles and GWs. Cosmic strings are one-dimensional topological defects predicted to originate in the early universe by many theories beyond the Standard Model. For example, global strings that present long-range interactions

are expected to form in axion and dark matter scenarios [39], while local strings, having short-range interactions, are predicted by some grand unified theories [373, 374]. Cosmic strings are expected to emit GWs which could potentially be detected by current and future GWs experiments. The numerical studies of string loops presented in this dissertation have been performed using the *CosmoLattice* package. As part of my doctoral work, I have contributed to the development of this software [11, 12].

Chapter 9 presents the results from ref. [6]. This chapter focuses on cosmic string loops of global type, which are captured by a model containing a single complex scalar field with a Mexican-hat potential. Using field-theory lattice simulations, we studied the decay of this type of string loops into particles and GWs. Our results showed that, independently of the shape and length of the loops, and of the initial conditions used to generate the loops, the emission power of particles and GWs is approximately constant. This can be seen in fig. 9.9, where we showed that the lifetime of the loops depends linearly on their size, and in fig. 9.16. We found that the emission power of GWs is suppressed compared to particle radiation, $P_{\text{GW}}/P_\varphi \approx \mathcal{O}(10)(v/m_p)^2$, with $m_p \approx 2.44 \times 10^{18}$ GeV the reduced Planck mass and v the vacuum expectation value of the scalar field, constrained by experimental observations to values $v/m_p \leq 10^{-6}$ [433, 434].

In chapter 10 we present results for local string loops [7], which we capture using the Abelian-Higgs model. Our conclusions are very different from the case of global strings. We found that the emission of particles from the strings depends on their shape and features. Loops originating from the decay of string networks, which are expected to possess features similar to loops arising in the early universe, have a particle emission power that seems to depend slightly on the size of the loops. This can be seen from fig. 10.6, where we showed that the lifetime of the loops scales roughly as $\Delta t_{\text{dec}} \propto L^{-0.7}$ with their initial length, meaning that particle emission increases with the loop size. On the contrary, loops that are generated from the intersection of infinite strings have a lifetime that roughly scales quadratically with their initial length—see fig. 10.8—so that the emission of particles is suppressed for longer loops. In both cases we found that the emission of GWs is mostly independent of the size of the loops, as shown in fig. 10.11. This means that it is possible to fabricate loops for which the emission of GWs is the main decay route at cosmological scales. However, these were not found to form from networks, and loops that originate naturally in the early universe after a phase transition decay mainly into particles, with a negligible emission of GWs.

The work presented in these two chapters represents a first step in the determination of the GW background (GWB) from a network of strings,

which is of vital importance to properly interpret future experimental detections. Combining our results with predictions for the loop number density in the early universe [404, 415, 420, 442–444] will make it possible to determine the expected GWB emitted by a network of string loops, without relying on effective predictions of the GW emission. In addition, predictions for the GWB from a network of local strings could also be compared to the results from a full lattice simulation of the network dynamics that incorporates the emission of GWs, which has not been performed before.

Final remarks

Numerical lattice simulations are one of the main tools to address problems in high-energy physics from first principles. These include, for example, the use of lattice QCD to investigate the hadron spectrum, or the application of classical-field-theory lattice techniques to predict the GW emission from hypothetical early-universe phenomena. Throughout this dissertation, work in these two different topics has been presented. On the QCD side, two- and three-particle interactions have been investigated using numerical techniques complemented by other approaches such as ChPT and the large N_c limit. The results presented contribute to the understanding of the non-perturbative regime of QCD, especially in relation to meson interactions and the possible existence of exotic resonances, such as tetraquarks. They also represent a starting point to study more complex systems, such as resonant three-meson systems and, eventually, light nuclei. The cosmology side of this dissertation, on the other hand, has been focused on analyzing the emission of particles and GWs from cosmic string loops using field-theory simulations. We have found that, for the type of the string loops that may form in the early universe, the production of GWs is very suppressed compared to particle emission. We leave for future work a prediction of the GWB, which we believe will be suppressed compared to present estimates.

Resumen

La teoría de campos es el marco con que se describen la gran mayoría de fenómenos físicos a altas energías. Es el caso del modelo estándar de partículas, basado en la mecánica cuántica y la relatividad especial, y del modelo cosmológico estándar, que nace del principio cosmológico y la teoría de la relatividad general. En muchos casos, es posible realizar predicciones precisas mediante el uso de métodos perturbativos. Estas técnicas permiten, por ejemplo, estudiar en detalle procesos electromagnéticos en el modelo estándar, los cuales se pueden describir como una serie de potencias en la constante de estructura fina. Del mismo modo, ciertos fenómenos del universo primigenio, pueden analizarse mediante métodos perturbativos, tratando las fluctuaciones de los campos de materia y de la métrica como pequeños frente a un valor promedio homogéneo.

En otros contextos, sin embargo, no es posible aplicar métodos perturbativos. Uno de los ejemplos más conocidos es el estudio de las interacciones fuertes a baja energía mediante la cromodinámica cuántica (QCD, por sus siglas en inglés). A bajas escalas, debido al fenómeno de libertad asintótica, la constante de interacción fuerte crece, invalidando el uso de la aproximación basada en una serie de potencias de esta constante. En el universo primigenio, asimismo, muchos fenómenos están caracterizados por grandes fluctuaciones y no linealidades, que impiden el uso de métodos perturbativos. Algunos ejemplos son la producción de partículas durante y tras el fin de la época inflacionaria, o la emisión consiguiente de ondas gravitacionales (GW).

El uso de simulaciones numéricas en el retículo (o *lattice*, en inglés), es una de las técnicas más extendidas para estudiar regímenes no perturbativos y/o no lineales. En el caso de QCD, la formulación en la *lattice*, conocida como *lattice QCD*, permite resolver la integral de camino mediante técnicas Monte Carlo. Por otro lado, utilizando simulaciones de campos clásicos

es posible estudiar la evolución temporal de los campos de materia y la producción de GW durante los primeros instantes del universo.

Esta tesis doctoral se centra en la aplicación de técnicas de *lattice* al estudio de dos temas tan dispares como son la física hadrónica y el universo primigenio. En relación con el primero de estos temas, el trabajo presentado en la primera parte de la tesis se centra en el estudio de las interacciones entre dos y tres partículas, utilizando simulaciones de *lattice* QCD junto a otros métodos como son las teorías efectivas—más concretamente la teoría quiral de perturbaciones—y el límite de gran número de colores. En la segunda parte de esta tesis, el trabajo presentado versa sobre la evolución y emisión de GW por parte de cuerdas cósmicas, estructuras unidimensionales que podrían formarse en el universo primigenio de acuerdo con diversas extensiones del modelo estándar.

Parte 1. Interacciones entre hadrones mediante técnicas de *lattice*

QCD a baja energía

La cromodinámica cuántica es la teoría cuántica que describe las interacciones fuertes entre quarks y gluones [27]. Esta fuerza es responsable de mantener protones y neutrones unidos en núcleos atómicos, así como de la existencia de otros muchos hadrones inestables, con tiempos de vida media de tan solo una fracción de segundo. La teoría se basa en el grupo no abeliano $SU(N_c)$, donde N_c es el número de colores, siendo $N_c = 3$ en el mundo real. La teoría contiene N_f sabores de quarks, representados por campos fermiónicos, y los mediadores de la fuerza fuerte, llamados gluones, dados por el campo *gauge*.

Una de las características distintivas de QCD es la propiedad de libertad asintótica [40, 41]. A bajas energías, la constante de interacción fuerte crece sin límite. Esto impide la aplicación de métodos perturbativos a energías por debajo de la escala de QCD, Λ_{QCD} , pero tiene otras consecuencias de interés. La más importante es el fenómeno de confinamiento. A baja energía los quarks y gluones no se encuentran aislados en la naturaleza, sino que se hallan confinados formando hadrones. La mayor parte de los hadrones conocidos son mesones, formados por un quark y un antiquark, o bariones, formados por tres quarks [34]. Durante las últimas décadas, no obstante, otros estados con una composición más exótica han sido descubiertos experimentalmente, como los llamados tetraquarks, formados por dos quarks y dos antiquarks [28–34].

Junto con la libertad asintótica y el confinamiento de quarks y gluones a bajas energías, otra de las propiedades características de QCD es la ruptura espontánea de la simetría quiral. En ausencia de masa, la acción de QCD es invariante bajo transformaciones globales del grupo de simetría,

$$G = \text{SU}(N_f)_V \times \text{SU}(N_f)_A \times \text{U}(1)_V \times \text{U}(1)_A .$$

A bajas energías, sin embargo, el vacío de QCD no respeta esta simetría, sino solo la parte vectorial, $H = \text{SU}(N_f)_V \times \text{U}(1)_V$, que se corresponde con la simetría de isospín y el número bariónico. Los hadrones se pueden clasificar en representaciones irreducibles del grupo de isospín. El mejor ejemplo es el conocido *eightfold way* [18, 19], que explica las similitudes observadas entre mesones pseudoescalares. Estos patrones se mantienen incluso en presencia de masa de los quarks, siempre que estas sean más pequeñas que Λ_{QCD} .

Al mismo tiempo, la simetría $\text{U}(1)_A$ está adicionalmente rota por efectos cuánticos, es decir, es anómala. Esto implica que el mesón singlete, la η' , tiene una masa mucho mayor que el resto de mesones pseudoescalares. La relación entre las masas viene dada por la fórmula de Witten-Veneziano [56, 57].

Debido a estas propiedades de QCD, su estudio analítico a bajas energías es especialmente complejo. Uno de los métodos más exitosos es la formulación de QCD en la *lattice* [59, 60], basada en el cálculo mediante técnicas de Monte Carlo de la integral de camino de QCD en un volumen finito y tiempo Euclídeo, utilizando una discretización del espacio-tiempo.

Lattice QCD permite calcular funciones de correlación entre distintos operadores, a partir de las cuales se puede extraer información sobre observables de QCD. En particular, las funciones de correlación a dos puntos permiten extraer las energías de estados de una o más partículas con los números cuánticos del operador en cuestión. Por ejemplo, las energías de los estados de dos o más partículas permiten extraer información sobre sus propiedades de dispersión.

Complementando las técnicas de *lattice*, existen otras alternativas que permiten estudiar las interacciones fuertes a baja energía. Una de ellas es el límite de gran número de colores, o límite de 't Hooft [120], en el cual N_c se hace tender a infinito, manteniendo N_f constante. En este límite, QCD se simplifica manteniendo muchas de sus propiedades no perturbativas, como la libertad asintótica y la ruptura espontánea de la simetría quiral.

Mediante el estudio de diagramas de Feynman en este límite, es posible caracterizar la dependencia con N_c y N_f de numerosos observables. Por ejemplo, se puede demostrar que las interacciones entre varios mesones están suprimidas a medida que N_c crece, y que QCD se convierte en una teoría de resonancias libres [120, 122, 123]. Sin embargo, estimar las correcciones

subdominantes al límite de gran N_c es muy complicado analíticamente. Las técnicas de *lattice*, por otro lado, nos permiten cuantificarlas directamente, simulando a diferentes N_c . Estas técnicas también nos permiten explorar otras preguntas abiertas en el límite de gran N_c , como la posible existencia de hadrones exóticos, alrededor de la cual ha habido bastante polémica recientemente [122, 123, 137].

Otra alternativa que permite el estudio analítico de QCD a baja energía es el uso de teorías efectivas [141], en particular la paradigmática teoría quiral de perturbaciones (ChPT) [141, 145–147], que describe el régimen no perturbativo de QCD utilizando los mesones pseudoescalares como grados de libertad. La acción que describe las interacciones entre ellos contiene todos los términos compatibles con las simetrías de QCD, que dependen de ciertos parámetros, L_i , llamadas constantes de baja energía, cuyo valor ha de ser determinado experimentalmente o a partir de simulaciones *lattice*. ChPT permite la realización de predicciones analíticas en potencias de M_π^2/F_π^2 o p^2/F_π^2 , donde M_π y F_π son la masa y la constante de decaimiento del pion, respectivamente, y p indica su momento.

ChPT también permite estudiar el límite de gran N_c [147, 159–165], aunque requiere de ciertas modificaciones. En particular, es necesario incluir el mesón singlete η' junto al resto de mesones, ya que esta vuelve degenerada con el resto de mesones pseudoescalares a gran N_c , e incluir el número de colores en el conteo de potencias de la expansión quiral.

Interacciones entre hadrones

Los quarks y los gluones no se observan aislados en la naturaleza, sino formando estados compuestos llamados hadrones, cientos de los cuales han sido observados experimentalmente [34]. La gran mayoría de estas partículas son inestables, con tiempos de vida medio tan pequeños como 10^{-22} segundos. Estos estados no pueden observarse directamente, sino que sus propiedades se infieren a partir de los productos de su decaimiento.

En general, se define un proceso de dispersión (o *scattering*, en inglés), como aquel en que las partículas de un estado asintótico inicial, separadas inicialmente por distancias macroscópicas, se aproximan e interaccionan, dando lugar a un estado final generalmente diferente. La probabilidad de transición entre dos estados cualesquiera viene caracterizada por la amplitud de dispersión, \mathcal{M} .

En el caso de dos partículas, dicha amplitud tiene una estructura analítica bien definida. En particular, contiene una serie de cortes para valores reales de la energía, relativos a los diferentes umbrales en los que diferentes estados

finales de varias partículas aparecen. La dependencia de estos cortes con la energía viene caracterizada por las propiedades cinemáticas del sistema, y pueden sustraerse analíticamente. La parte restante de la amplitud se conoce como matriz K , \mathcal{K}_2 , la cual es una función meromorfa de las variables cinemáticas. La ubicación de polos en \mathcal{K}_2 indica la presencia de estados intermedios en el proceso de dispersión. Polos en el eje real por debajo del umbral de dos partículas se corresponden con estados ligados de estas partículas, mientras que polos en el semiplano inferior en la segunda hoja de Riemann indican la presencia de resonancias.

El caso de tres partículas es más complejo, ya que las interacciones están dadas no solo por interacciones de corto alcance de tres cuerpos, sino también por interacciones sucesivas de dos partículas. Al igual que en el caso anterior, es posible definir una matriz K que contiene información únicamente sobre las interacciones de corto alcance de las tres partículas. Dadas \mathcal{M}_2 y \mathcal{M}_3 , la matriz K se obtiene resolviendo ciertas ecuaciones integrales, las cuales sustraen divergencias relacionadas con procesos intermedios de dos partículas. La matriz K resultante, no obstante, depende de la regularización utilizada para tratar las dichas divergencias. El trabajo presentado en esta tesis utiliza una definición de la matriz K propuesta en el contexto del formalismo de teoría de campos relativista (RFT) de tres partículas [172, 173], llamada matriz K libre de divergencias o $\mathcal{K}_{\text{df},3}$.

En QCD, los procesos de interacción de dos y tres partículas pueden clasificarse en diferentes canales de isospín. En el caso de piones, partículas de isospín uno, las interacciones de dos partículas pueden ocurrir en tres canales de isospín ($I_{\pi\pi} = 2, 1, 0$) mientras que interacciones de tres piones tienen lugar en cuatro canales diferentes ($I_{\pi\pi\pi} = 3, 2, 1, 0$). En este último caso, algunos de los canales tienen multiplicidad mayor a uno, correspondiéndose con los posibles canales en que interacciones intermedias entre dos pions pueden ocurrir. Por ejemplo, en el canal de $I_{\pi\pi\pi} = 2$, dos pions pueden interactuar con $I_{\pi\pi} = 2$ ó $I_{\pi\pi} = 1$.

Una opción para describir las interacciones entre varios piones es el uso de ChPT. En el caso de dos piones con isospin dos, las predicciones para la amplitud de dispersión se conocen hasta segundo orden (*next-to-next-to-leading order*, NNLO) [141, 146, 184]. A orden cero (*leading-order*, LO), estas reproducen los resultados experimentales de forma muy precisa, indicando un buen comportamiento de la expansión. En el caso de tres piones en isospín tres, la situación es muy diferente. La matriz K de tres piones puede determinarse en ChPT a LO a partir de la amplitud de dispersión [194–196] mediante relaciones algebraicas obtenidas a partir de las ecuaciones integrales. Sin embargo, se observan grandes discrepancias con resultados obtenidos

en la *lattice* [194, 301], indicando posiblemente correcciones importantes procedentes de órdenes superiores en ChPT.

Otra posibilidad para analizar las interacciones de varias partículas en QCD es el uso de simulaciones *lattice*. El estudio directo de procesos de dispersión no es posible en la *lattice*, ya que estos ocurren en tiempo real y no se pueden definir estados asintóticos en volumen finito. Sin embargo, las propiedades de dispersión en volumen infinito se pueden determinar en la *lattice* a partir del espectro de energía en volumen finito, usando las llamadas condiciones de cuantización.

En el caso de dos partículas, la condición de cuantización de Lüscher [197, 198] relaciona \mathcal{K}_2 con un factor geométrico que depende de las características de la *lattice*, pero es independiente de las propiedades de dispersión del proceso. En el caso de tres partículas se han propuesto varias alternativas [172, 173, 226–229]. Esta tesis se centra en el formalismo RFT [172, 173], el cual relaciona $\mathcal{K}_{\text{df},3}$ con un factor geométrico de tres partículas que depende de las características de la *lattice*, y también de las interacciones entre pares de partículas.

Dispersión de mesones en el límite de gran N_c

Los capítulos 3 y 4 de esta tesis se centran en el estudio de la interacciones de dos mesones como función del número de colores, utilizando simulaciones *lattice* en una teoría con $N_f = 4$ quarks degenerados. En este modelo, las interacciones de dos mesones ocurren en siete canales diferentes, correspondientes con las representaciones irreducibles del grupo de isospín, $SU(4)$ en este caso.

En el capítulo 3 se presentan los resultados de las refs. [1, 8], centrados en el estudio de las interacciones entre dos mesones pseudoescalares cerca del umbral. En particular, se analizaron dos canales diferentes: el canal SS , equivalente al canal de isospín dos en QCD con dos sabores, y el canal AA , el cual solo existe en teorías con cuatro o más sabores degenerados. Las interacciones en estos canales se estudiaron utilizando el límite de gran N_c y la teoría quiral de perturbaciones incluyendo la η' . Se determinó por primera vez la amplitud para ambos canales en ChPT con la η' a NNLO. Las amplitudes para cada canal dependen de combinaciones lineales de las LECs, llamadas L_{SS} y L_{AA} . En el límite de gran N_c , se espera que ambas tomen el mismo valor.

Para estudiar la dependencia de estas LECs con N_c se usaron simulaciones *lattice* con $N_c = 3 - 6$ y diferentes valores de M_π , utilizando el software HiRep [263, 264]. Las simulaciones permitieron determinar las energías en

volumen finito de dos piones en el estado de mínima energía. Comparando dos discretizaciones diferentes de los fermiones de valencia y distintos espaciados de la *lattice* se estudiaron también los efectos de discretización presentes en el canal AA . Finalmente, se usó el formalismo de Lüscher para determinar L_{SS} y L_{AA} a partir de las predicciones de ChPT. A partir de un ajuste simultáneo a ambos canales y todos los valores de N_c y M_π , se obtuvo,

$$\frac{L_{SS,AA}}{N_c} \times 10^3 = -0.02(8) - 0.01(5) \frac{N_f}{N_c} \mp 1.76(20) \frac{1}{N_c} + \mathcal{O}(N_c^{-2}).$$

donde el signo superior/inferior se corresponde con el canal SS/AA . Este resultado muestra que el valor de las variables en el límite de gran N_c es despreciable respecto a las correcciones subdominantes, que dominan a bajos valores de N_c . Cabe notar que, si bien parece que una de las contribuciones subdominantes es mucho mayor que la otra, estas dependen de la escala de regularización (no así el término dominante).

Una de las observaciones más interesantes del trabajo expuesto en el capítulo 3 es el hecho que el canal AA presenta interacciones atractivas cerca del umbral. Esto, unido al hecho que contiene estados con cuatro sabores abiertos, hacen de este canal un candidato idóneo para explorar la existencia de tetraquarks y su dependencia con N_c . La posible presencia de un tetraquark en el canal AA podría estar relacionada con ciertos estados exóticos recientemente hallados en el LHCb [30–33], los cuales tendrían los números cuánticos del canal AA en una teoría con cuatro sabores.

El capítulo 4 presenta resultados de un trabajo en progreso sobre las interacciones entre mesones como función de la energía a N_c variable [2, 10], con el objetivo principal de estudiar la existencia de tetraquarks. En particular, se realizaron simulaciones *lattice* con $N_c = 3 - 6$ para $M_\pi = 590$ MeV y espaciado fijo, centradas en el estudio de los canales SS y AA , así como del canal AS que contiene ondas parciales impares. Para ello, se utilizó una base de operadores formada por operadores de dos partículas, tanto dos piones como dos mesones vectoriales, así como de operadores locales con forma de tetraquark.

Usando la condición de cuantización de Lüscher, se determinó la amplitud de dispersión para estos canales. En el caso de los canales SS y AA , un ajuste de los resultados a N_c fijo permitió hallar la longitud de dispersión y el rango efectivo de ambos canales, los cuales se utilizaron para realizar una extrapolación a gran N_c . Aunque no se ha observado la existencia de resonancias en el canal AA , los resultados para $N_c = 3$ sugieren la presencia de un estado ligado con una energía $E_{\text{lig}}/M_\pi = 1.741(13)$. Para el canal AS , se observaron interacciones muy suprimidas, en la línea de lo esperado de acuerdo con ChPT, que predice una amplitud de dispersión nula a LO. En el futuro, sería de interés estudiar más en detalle el estado observado en

el canal AA para $N_c = 3$, en particular su dependencia con la masa de los piones y su posible relación con las resonancias observadas.

Con este trabajo se da un paso más en la caracterización de la dependencia en N_c de observables de dispersión y se prepara el camino para el análisis de otros procesos de interés. Un ejemplo sería el estudio de resonancias, como la $\rho(770)$, que aparece en el canal de isospín uno, o la $\sigma(550)$, en el canal de isospín cero. En particular, el análisis de la dependencia de esta última con N_c podría proveer información sobre su naturaleza, y sobre si se trata de una resonancia mesónica o tiene una composición más exótica [191–193].

Matriz K de tres piones a primer orden en ChPT

Los capítulos 5 y 6 presentan los resultados de las refs. [3, 4], centrados en la determinación de $\mathcal{K}_{\text{df},3}$ para tres piones a primer orden en ChPT (*next-to-leading-order*, NLO). Recientemente se observó que los resultados a LO en ChPT para la matriz K de tres piones en el canal de isospín tres muestran una gran discrepancia con resultados *lattice* para esta cantidad [194, 301]. El trabajo presentado en estos capítulos busca determinar si esta diferencia se puede explicar debido a correcciones de gran tamaño a NLO.

En el capítulo 5 se presentan los resultados de la ref. [3], centrados en el caso de isospín máximo. Al igual que a LO, las ecuaciones integrales que relacionan la amplitud de dispersión con $\mathcal{K}_{\text{df},3}$ se reducen a una simple ecuación algebraica a NLO en ChPT, $\text{Re}\mathcal{M}_{\text{df},3} = \mathcal{K}_{\text{df},3}$, donde $\mathcal{M}_{\text{df},3}$ es la amplitud libre de divergencias, obtenida tras sustraer posibles divergencias relacionadas con interacciones sucesivas de dos partículas.

El cálculo de $\mathcal{K}_{\text{df},3}$ a este orden, partiendo de los resultados para \mathcal{M}_3 de las refs. [195, 196], se puede dividir en tres partes, cada una de las cuales se trató con técnicas ligeramente distintas. La primera de ellas es la contribución proveniente de diagramas que contienen el intercambio de una partícula (OPE), justo con la sustracción de posibles divergencias que surgen cuando el cuadrimomento de dicha partícula obedece la condición de dispersión relativista, es decir, está *on-shell*. Las otras dos contribuciones a $\mathcal{K}_{\text{df},3}$ son la llamada amplitud no OPE, asociada con el resto de la amplitud, y la sustracción correspondiente. En este caso, al contrario que para la parte OPE, ambas contribuciones pueden calcularse independientemente, ya que su parte real es siempre convergente.

Los resultados de esta trabajo demuestran que las correcciones a NLO para los términos constante y lineal de una expansión de $\mathcal{K}_{\text{df},3}$ alrededor del umbral representan grandes correcciones respecto al resultado a LO. Aunque esto puede indicar una mala convergencia de la expansión quiral

para observables de tres piones, también es posible que la corrección a NLO sea anómalamente grande, y otras correcciones a órdenes superiores sean de menor tamaño.

En el capítulo 6 se resumen los resultados de la ref. [4], en la cual se extendió el trabajo realizado para el canal de isospín tres al resto de canales de tres piones, determinando $\mathcal{K}_{df,3}$ a LO y NLO en ChPT. Este cálculo sigue las mismas líneas que el capítulo 5, con ciertas novedades. Estas son, entre otros, la presencia de una nueva contribución en el canal de isospín uno, relacionada con diagramas en los que una partícula se intercambia en el canal s , o la existencia de diferentes estructuras cinemáticas para los diferentes canales de isospín.

Al igual que el canal de isospín tres, el resto de canales también presentan grandes correcciones a NLO en ChPT. Esto proporciona valiosa información sobre la convergencia de la expansión quiral para observables de tres partículas. Además, los resultados obtenidos en este capítulo pueden ser de gran relevancia en el futuro, ya que podrán ser comparados con resultados *lattice* o usados para parametrizar la dependencia quiral de $\mathcal{K}_{df,3}$ cerca del umbral.

Siguiendo las líneas de este trabajo, el cálculo de $\mathcal{K}_{df,3}$ para otros procesos puede ser de interés. En particular, sistemas de piones y kaones con isospín máximo ya han sido estudiados en la *lattice* [301, 302]. Sin embargo, las correspondientes amplitudes de dispersión a NLO en ChPT, necesarias para el cálculo de $\mathcal{K}_{df,3}$, aún no han sido calculadas.

Interacciones de dos y tres partículas en el modelo O(3)

El capítulo 7 cierra la primera parte de esta tesis doctoral. Está centrado en el estudio de la dispersión de dos y tres partículas en el modelo O(3) sigma no lineal en 1+1 dimensiones [5, 9]. Este modelo es comúnmente usado para probar distintos formalismos [114, 317], antes de aplicarlos a QCD, ya que ambos comparten muchas propiedades, como la libertad asintótica o la existencia de un espectro de tres partículas con isospín uno. Además, el modelo O(3) es integrable, es decir, es posible obtener resultados exactos para su amplitud de dispersión [323, 324]. El trabajo presentado en este capítulo tiene como fin último utilizar este modelo para estudiar el formalismo RFT de tres partículas, comparando resultados *lattice* con predicciones analíticas obtenidas a partir de la amplitud de dispersión.

Como primer paso en esta dirección, se determinaron los espectros de energía de dos y tres partículas, y comparado con predicciones analíticas hechas bajo la suposición de una matrix $\mathcal{K}_{df,3}$ nula. Se realizaron simulaciones *lattice* para cuatro valores del volumen, con tres espaciados cada uno, usando una

generalización a tres *clusters* del algoritmo de actualización de *cluster* [334]. Se trata de un algoritmo colectivo que permite reducir la correlación entre configuraciones y el ruido al medir funciones de correlación. Los resultados para las energías de volumen finito se extrapolaron directamente al continuo utilizando las simulaciones realizadas a igual volumen y diferente espaciado.

En el sector de dos partículas, se estudiaron los canales de isospín dos y uno. El espectro de energías se comparó directamente con una predicción analítica, observando muy buena concordancia entre ambos. En el caso de tres partículas, se estudiaron los canales de isospín tres, dos y cero. Los resultados de las energías de volumen finito se compararon con predicciones obtenidas con una versión adaptada del formalismo RFT al caso de una dimensión espacial y asumiendo $\mathcal{K}_{df,3} = 0$. Se observaron discrepancias significativas, indicando que la matriz K de tres partículas es en realidad no nula. Este estudio, además, permitió ganar conocimiento acerca de las complejidades de la condición de cuantización, como la posible existencia de inestabilidades numéricas o el rol de la función de *cutoff* usada en el formalismo.

Siguiendo el camino marcado por este trabajo, el espectro de energías de tres partículas puede utilizarse para determinar $\mathcal{K}_{df,3}$. Posteriormente, estos resultados pueden compararse con predicciones analíticas para esta cantidad. Dicha comparación requerirá reformular las ecuaciones integrales que relacionan la amplitud de dispersión con $\mathcal{K}_{df,3}$ en una dimensión espacial. Más allá del modelo $O(3)$, este trabajo prepara el camino para el estudio de sistemas de tres partículas en QCD más allá de sistemas de tres mesones con isospín máximo, en que se han centrado la gran mayoría de estudios *lattice* hasta ahora [194, 268, 294–302]. Por ejemplo, un caso interesante es el estudio de tres piones en isospín no máximo, ya que alguno canales de isospín contienen resonancias de interés, como la $\omega(782)$ para el canal de isospín cero [34].

Parte 2. Cuerdas cósmicas mediante simulaciones de *lattice*

El universo primigenio

El modelo cosmológico estándar está construido a partir de las bases de la relatividad general y el principio cosmológico. De acuerdo con este último, el universo es isótropo y homogéneo, es decir, idéntico en todas las direcciones y para cualquier observador independientemente de la posición

en que se halle. Esto se traduce en la métrica de Friedman-Lemaître-Robertson-Walker (FLRW) [342], caracterizada por el factor de escala, $a(t)$, que determina el ratio de expansión del universo. La evolución temporal del dicho factor de escala, a su vez, está determinada por la densidad de energía y la presión de la materia que llena el universo, de acuerdo con las ecuaciones de Friedman [343].

Durante los primeros instantes del universo tras el fin de inflación, es probable que se alcanzaran energías muy por encima de las cotas alcanzables por aceleradores. Esto implica que, mediante el análisis experimental del universo primigenio, sería posible estudiar física más allá del modelo estándar.

La descripción de ciertos fenómenos que tienen lugar durante el primer segundo del universo puede realizarse en el marco de la teoría de campos. Más concretamente, debido a los altos números de ocupación, es posible describir la dinámica del sistema utilizando métodos de teoría clásica de campos, basados en el estudio de la evolución de los campos de acuerdo con sus ecuaciones de movimiento.

En ciertas ocasiones esta evolución temporal se puede estudiar analíticamente, tratando las fluctuaciones como pequeñas perturbaciones. Sin embargo, en muchos casos el sistema puede desarrollar contribuciones no lineales de gran tamaño y la única opción es usar simulaciones numéricas en la *lattice*. Las simulaciones de campos clásicos se basan en la resolución numérica de las ecuaciones de movimiento de dichos campos, partiendo de unas condiciones iniciales dadas. Para ello se utiliza una versión discretizada de las ecuaciones de movimiento. Para la realización de simulaciones *lattice* en los trabajos presentados en esta tesis doctoral se utilizó el software *CosmoLattice* [349, 351].

El uso de técnicas de *lattice* permite estudiar también la emisión de GW en el universo primigenio [360, 361]. Una vez cesa la fuente que las genera, estas ondas viajan libremente hasta el día de hoy, y mediante una detección experimental sería posible determinar las características de los fenómenos que las producen. Sin embargo, una interpretación correcta de una potencial detección requiere de predicciones teóricas precisas.

La simulación de GW en la *lattice* es especialmente compleja. La fuente de GW es la parte transversa y de traza nula (TT) del tensor anisótropo, y su cálculo en espacio real es una operación no local que requiere conocer el valor de los campos en todo el espacio. En espacio de Fourier, en cambio, la proyección al la componente TT es local, pero requiere transformar los campos a dicho espacio en cada paso temporal. Numéricamente, es más conveniente utilizar seis campos no físicos, u_{ij} , generados por un tensor anisótropo efectivo que no es TT [366], evitando la necesidad de calcular

transformadas de Fourier en cada paso de la evolución temporal. Solo cuando se desea medir el espectro de energía de las GW es necesario proyectar los campos u_{ij} a su parte TT, que se corresponde con los campos de GW. La implementación de estas técnicas en *CosmoLattice* ha representado una parte del trabajo de esta tesis doctoral [11, 12].

Emisión de partículas y GWs por *loops* cósmicos

Las cuerdas cósmicas son defectos topológicos unidimensionales que podrían formarse en el universo primigenio tras una transición de fase, de acuerdo con ciertas extensiones del modelo estándar [372–375]. Se trata de defectos topológicos que se originan en teorías con un vacío no simplemente conexo. Un ejemplo son los modelos de gran unificación, que predicen la formación de cuerdas con interacciones de corto alcance, llamadas locales. Otro ejemplo de interés son los modelos de axiones [37, 38], los cuales incluyen una simetría U(1) anómala, la simetría de Peccei-Quin, que se rompe espontáneamente a bajas energías. Si esta ruptura de simetría ocurre tras el final de inflación, se podrían originar *networks* de cuerdas cósmicas de tipo global, que interactúan a larga distancia.

Las *networks* de cuerdas están formadas por cuerdas infinitas, que se extienden a lo largo de todo el universo, y cuerdas cerradas de tamaño subhorizonte, llamadas *loops*. Típicamente, la evolución de las cuerdas se ha descrito utilizando la acción de Nambu-Goto (NG), en la cual se aproximan las cuerdas como objetos infinitamente finos [386, 387]. En esta aproximación, las cuerdas infinitas decaen emitiendo *loops*, mientras que estos últimos radían GW, dando lugar a un fondo estocástico de GW.

Una interpretación correcta de una hipotética detección del fondo de GW depende de predicciones teóricas precisas. En particular, una posibilidad es que los *loops* decaigan mediante la emisión de partículas, la cual es despreciada por la aproximación de NG. Una comparativa entre ambas rutas de decaimiento requiere estudiar los dos canales simultáneamente y un estudio en detalle que capture la estructura interna de las cuerdas solo es posible mediante el uso de simulaciones *lattice*.

Los capítulos 9 y 10 de esta tesis se centran en el estudio de la emisión de partículas y GW por parte de cuerdas cósmicas. Cada capítulo se centra en una teoría diferente. El capítulo 9 presenta los resultados de la ref. [6]. Este trabajo trata el caso de cuerdas globales, las cuales se representan con una teoría cuyo contenido es únicamente un campo escalar complejo, con un potencial con forma $V(\varphi) = \lambda(|\varphi|^2 - v^2/2)$ siendo v el valor de expectación del vacío y λ un parámetro adimensional que regula las interacciones del campo escalar. Las cuerdas de este tipo decaen emitiendo radiación tanto

masiva como sin masa. El capítulo 10, por otro lado, está centrado en el caso de cuerdas locales [7], las cuales se simulan utilizando el modelo Higgs abeliano, que contiene un campo *gauge* $U(1)$ y un campo escalar complejo. Al contrario que las cuerdas globales, las cuerdas locales solo pueden emitir partículas masivas.

En sendos capítulos se presentan resultados relativos al estudio en la *lattice* de la emisión de partículas y GW por parte de *loops* globales y locales, respectivamente. En ambos casos, se analizan dos tipos de *loops*. El primer tipo, referido como *network loops*, se genera tras el decaimiento de una *network* de cuerdas, y se espera que presente características similares a aquellos *loops* que se podrían formar en el universo primigenio [389, 406, 407]. El segundo tipo son los llamados *loops* artificiales, que se originan a partir de la intersección de cuerdas infinitas [427, 428] y permiten controlar las condiciones iniciales.

En el caso de las cuerdas globales, se encontró que ambos tipos de *loops* se comportan de forma similar, emitiendo partículas con una potencia aproximadamente constante, con independencia de su longitud. Respecto a la emisión de GW, también se halló que ambos tipos de *loops* emiten con una potencia similar y constante, independiente de su longitud. Comparando los dos canales, se observó que potencia de la emisión de GW, P_{GW} , está muy suprimida comparado con la de partículas, P_φ ,

$$\frac{P_{\text{GW}}}{P_\varphi} \approx \mathcal{O}(10) \left(\frac{v}{m_p} \right)^2 \ll 1,$$

teniendo en cuenta que medidas experimentales del fondo cósmico de microondas restringen $v/m_p \lesssim 10^{-6}$ [433, 434].

Para cuerdas locales, los resultados obtenidos fueron distintos. La potencia de emisión de partículas en este caso puede depender de la longitud de las cuerdas. Sin embargo, lo hace de forma muy distinta para cada tipo de *loop*. Mientras que nuestros resultados indican que la potencia de emisión de los *network loops* aumenta débilmente con su longitud (siendo los datos también consistentes con una emisión independiente de la longitud), los *loops* artificiales emiten partículas más lentamente a mayor tamaño. Por otro lado, la emisión de GW parece ser independiente de la longitud para ambos tipos de *loops*, aunque presenta mayor potencia para los *network loops*. Cabe notar que el resultado obtenido para *loops* artificiales es muy próximo a la predicción de NG, siendo un factor tres veces más grande para los *network loops*.

Extrapolados a escalas cosmológicas, estos resultados tienen consecuencias relevantes. Si *loops* locales con características similares a los artificiales se hubieran formado en el universo primigenio, decaerían principalmente

emitiendo GW, dando lugar a un fondo de GW de gran amplitud. Sin embargo, no observamos que dicho tipo de *loops* se forme a partir de *networks* de cuerdas locales. Los *network loops*, que sí se esperan en el universo temprano, decaen principalmente emitiendo partículas, y la producción de GW está muy suprimida.

En el futuro, planeamos utilizar nuestros resultados sobre el decaimiento de *loops* aislados, combinados con predicciones sobre la densidad de *loops* en el universo primigenio, para determinar el fondo de GW emitido por una red de cuerdas cósmicas. Una predicción realizada de esta forma tendría la ventaja de no depender de predicciones de NG sobre la emisión de GW, ni de grandes extrapolaciones hechas a partir de resultados *lattice* para redes de cuerdas cósmicas. Tanto para *loops* globales como para locales, es de esperar que estos cálculos supriman la amplitud del fondo de GW respecto a predicciones actuales.

Comentarios finales

Esta tesis doctoral está centrada en el uso de técnicas de *lattice* para estudiar dos temas tan dispares como son las interacciones entre hadrones y el decaimiento y emisión de GW por cuerdas cósmicas. El trabajo presentado en la primera parte de esta tesis se centra en el estudio de interacciones entre dos y tres partículas, haciendo uso de simulaciones de *lattice* QCD, junto con otros métodos como el límite de gran N_c y la teoría quiral de perturbaciones. Los resultados obtenidos representan un paso en la comprensión del régimen no perturbativo de QCD, en particular sobre la existencia de resonancias exóticas con cuatro quarks y las interacciones de tres mesones, y abren la puerta a estudiar sistemas más complejos.

La segunda parte de la tesis se centra en la evolución y decaimiento de *loops* cósmicos, con especial énfasis en la emisión de partículas y GW. Los resultados presentados muestran que para *loops* globales, la emisión de GW está universalmente suprimida comparada con la producción de partículas, con independencia del tamaño, forma o momento angular del *loop*. Para *loops* locales, por contra, es posible construir configuraciones para las cuales la emisión de GW podría dominar. Sin embargo, para *loops* locales realistas que pudieran formarse en el universo primigenio, la ruta principal de decaimiento es la emisión de partículas, con una producción de GW muy suprimida. Combinando los resultados obtenidos con predicciones de la densidad de *loops*, planeamos calcular una predicción para el fondo de GW. En vista de nuestro resultados, esperamos que dicho fondo esté muy suprimido, comparado con las predicciones actuales.

Bibliography

- [1] J. Baeza-Ballesteros, P. Hernández and F. Romero-López, *A lattice study of $\pi\pi$ scattering at large N_c* , JHEP 06 (2022) 049.
- [2] J. Baeza-Ballesteros, P. Hernández and F. Romero-López, *Meson-meson scattering at large N_c* , 2024 (in preparation).
- [3] J. Baeza-Ballesteros, J. Bijnens, T. Husek, F. Romero-López, S. R. Sharpe and M. Sjö, *The isospin-3 three-particle K -matrix at NLO in ChPT*, JHEP 05 (2023) 187.
- [4] J. Baeza-Ballesteros, J. Bijnens, T. Husek, F. Romero-López, S. R. Sharpe and M. Sjö, *The three-pion K -matrix at NLO in ChPT*, JHEP 03 (2024) 048.
- [5] J. Baeza-Ballesteros and M. T. Hansen, *Two- and three-particle scattering in the (1+1)-dimensional $O(3)$ non-linear sigma model*, 2024 (in preparation).
- [6] J. Baeza-Ballesteros, E. J. Copeland, D. G. Figueroa and J. Lizarraga, *Gravitational wave emission from a cosmic string loop: Global case*, Phys. Rev. D 110 (2024) 043522.
- [7] J. Baeza-Ballesteros, E. J. Copeland, D. G. Figueroa and J. Lizarraga, *Gravitational Wave Emission from a Cosmic String Loop, II: Local Case*, 2024 (submitted to Phys. Rev. Lett.).
- [8] J. Baeza-Ballesteros, P. Hernández and F. Romero-López, *$\pi\pi$ scattering at Large N_c* , PoS LATTICE2021 (2022) 309.
- [9] J. Baeza-Ballesteros and M. T. Hansen, *Two- and three-particle scattering in the (1+1)-dimensional $O(3)$ non-linear sigma model*, PoS LATTICE2022 (2023) 050.

-
- [10] J. Baeza-Ballesteros, P. Hernández and F. Romero-López, *Progress in meson-meson scattering at large N_c* , PoS LATTICE2023 (2024) 059.
- [11] J. Baeza-Ballesteros, D. G. Figueroa, A. Florio and N. Loayza Romero, *CosmoLattice Technical Note II: Gravitational Waves*, 2022.
- [12] J. Baeza-Ballesteros, D. G. Figueroa and N. Loayza Romero, *CosmoLattice Technical Note III: Gravitational Waves from $U(1)$ gauge theories*, 2023.
- [13] J. Baeza-Ballesteros, A. Donini and S. Nadal-Gisbert, *Dynamical measurements of deviations from Newton's $1/r^2$ law*, Eur. Phys. J. C 82 (2022) 154.
- [14] J. Baeza-Ballesteros, A. Donini, G. Molina-Terriza, F. Monrabal and A. Simón, *Towards a realistic setup for a dynamical measurement of deviations from Newton's $1/r^2$ law: the impact of air viscosity*, Eur. Phys. J. C 84 (2024) 596.
- [15] D. J. Griffiths, *Introduction to elementary particles; 2nd rev. version*. Physics textbook. Wiley, New York, NY, 2008.
- [16] H. Yukawa, *On the Interaction of Elementary Particles I*, Proc. Phys. Math. Soc. Jap. 17 (1935) 48–57.
- [17] C. M. G. Lattes, H. Muirhead, G. P. S. Occhialini and C. F. Powell, *Processes Involving Charged Mesons*, Nature 159 (1947) 694–697.
- [18] M. Gell-Mann, *The Eightfold Way: A Theory of strong interaction symmetry*, 1961.
- [19] Y. Ne'eman, *Derivation of strong interactions from a gauge invariance*, Nuclear Physics 26 (1961) 222–229.
- [20] M. Gell-Mann, *A Schematic Model of Baryons and Mesons*, Phys. Lett. 8 (1964) 214–215.
- [21] G. Zweig, *An SU_3 model for strong interaction symmetry and its breaking; Version 2*, 1964.
- [22] M. Gell-Mann, *Isotopic Spin and New Unstable Particles*, Phys. Rev. 92 (1953) 833–834.
- [23] V. E. Barnes et al., *Observation of a Hyperon with Strangeness Minus Three*, Phys. Rev. Lett. 12 (1964) 204–206.

- [24] O. W. Greenberg, *Spin and Unitary Spin Independence in a Paraquark Model of Baryons and Mesons*, Phys. Rev. Lett. 13 (1964) 598–602.
- [25] D. B. Lichtenberg, *Unitary symmetry and elementary particles*, 1978.
- [26] S. L. Glashow, *Quarks with color and flavor*, Scientific American 233 (1975) 38–51.
- [27] H. Fritzsch, M. Gell-Mann and H. Leutwyler, *Advantages of the Color Octet Gluon Picture*, Phys. Lett. B 47 (1973) 365–368.
- [28] BELLE COLLABORATION collaboration, S.-K. Choi, S. L. Olsen, K. Abe, T. Abe, I. Adachi, B. S. Ahn et al., *Observation of a narrow charmoniumlike state in exclusive $B^\pm \rightarrow K^\pm \pi^+ \pi^- J/\psi$ decays*, Phys. Rev. Lett. 91 (Dec, 2003) 262001.
- [29] L. Maiani, F. Piccinini, A. D. Polosa and V. Riquer, *Diquark-antidiquarks with hidden or open charm and the nature of $X(3872)$* , Phys. Rev. D 71 (2005) 014028.
- [30] LHCb collaboration, R. Aaij et al., *A model-independent study of resonant structure in $B^+ \rightarrow D^+ D^- K^+$ decays*, Phys. Rev. Lett. 125 (2020) 242001.
- [31] LHCb collaboration, R. Aaij et al., *Amplitude analysis of the $B^+ \rightarrow D^+ D^- K^+$ decay*, Phys. Rev. D 102 (2020) 112003.
- [32] LHCb collaboration, R. Aaij et al., *First Observation of a Doubly Charged Tetraquark and Its Neutral Partner*, Phys. Rev. Lett. 131 (2023) 041902.
- [33] LHCb COLLABORATION collaboration, R. Aaij, A. S. W. Abdelmotteleb, C. Abellan Beteta, F. Abudinén, T. Ackernley, B. Adeva et al., *Amplitude analysis of $B^0 \rightarrow \bar{d}^0 D_s^+ \pi^-$ and $B^+ \rightarrow D^- D_s^+ \pi^+$ decays*, Phys. Rev. D 108 (Jul, 2023) 012017.
- [34] P. D. Group, P. A. Zyla, R. M. Barnett, J. Beringer, O. Dahl, D. A. Dwyer et al., *Review of Particle Physics*, Progress of Theoretical and Experimental Physics 2020 (08, 2020) 083C01.
- [35] C. A. Baker et al., *An Improved experimental limit on the electric dipole moment of the neutron*, Phys. Rev. Lett. 97 (2006) 131801.
- [36] T. Chupp, P. Fierlinger, M. Ramsey-Musolf and J. Singh, *Electric dipole moments of atoms, molecules, nuclei, and particles*, Rev. Mod. Phys. 91 (2019) 015001.

- [37] R. D. Peccei and H. R. Quinn, *CP Conservation in the Presence of Instantons*, Phys. Rev. Lett. 38 (1977) 1440–1443.
- [38] R. D. Peccei and H. R. Quinn, *Constraints Imposed by CP Conservation in the Presence of Instantons*, Phys. Rev. D 16 (1977) 1791–1797.
- [39] L. Hui, *Wave Dark Matter*, Ann. Rev. Astron. Astrophys. 59 (2021) 247–289.
- [40] D. J. Gross and F. Wilczek, *Ultraviolet Behavior of Nonabelian Gauge Theories*, Phys. Rev. Lett. 30 (1973) 1343–1346.
- [41] H. D. Politzer, *Reliable Perturbative Results for Strong Interactions?*, Phys. Rev. Lett. 30 (1973) 1346–1349.
- [42] T. van Ritbergen, J. A. M. Vermaseren and S. A. Larin, *The Four loop beta function in quantum chromodynamics*, Phys. Lett. B 400 (1997) 379–384.
- [43] T. Luthe, A. Maier, P. Marquard and Y. Schroder, *The five-loop Beta function for a general gauge group and anomalous dimensions beyond Feynman gauge*, JHEP 10 (2017) 166.
- [44] J. Letessier and J. Rafelski, *Hadrons and Quark–Gluon Plasma*. Cambridge Monographs on Particle Physics, Nuclear Physics and Cosmology. Cambridge University Press, 2002.
- [45] A. M. Jaffe and E. Witten, *Quantum Yang-Mills theory*, 2000.
- [46] Y. Nambu, *Quasi-particles and gauge invariance in the theory of superconductivity*, Phys. Rev. 117 (Feb, 1960) 648–663.
- [47] J. Goldstone, *Field Theories with Superconductor Solutions*, Nuovo Cim. 19 (1961) 154–164.
- [48] J. Goldstone, A. Salam and S. Weinberg, *Broken symmetries*, Phys. Rev. 127 (Aug, 1962) 965–970.
- [49] S. L. Adler, *Axial-vector vertex in spinor electrodynamics*, Phys. Rev. 177 (Jan, 1969) 2426–2438.
- [50] J. S. Bell and R. Jackiw, *A PCAC puzzle: $\pi^0 \rightarrow \gamma\gamma$ in the σ model*, Nuovo Cim. A 60 (1969) 47–61.
- [51] G. 't Hooft, *Computation of the Quantum Effects Due to a Four-Dimensional Pseudoparticle*, Phys. Rev. D 14 (1976) 3432–3450.

- [52] C. Callan, R. Dashen and D. Gross, *The structure of the gauge theory vacuum*, Physics Letters B 63 (1976) 334–340.
- [53] R. Jackiw and C. Rebbi, *Vacuum periodicity in a yang-mills quantum theory*, Phys. Rev. Lett. 37 (Jul, 1976) 172–175.
- [54] K. Fujikawa, *Path Integral Measure for Gauge Invariant Fermion Theories*, Phys. Rev. Lett. 42 (1979) 1195–1198.
- [55] G. 't Hooft, *Symmetry Breaking Through Bell-Jackiw Anomalies*, Phys. Rev. Lett. 37 (1976) 8–11.
- [56] E. Witten, *Current Algebra Theorems for the $U(1)$ Goldstone Boson*, Nucl. Phys. B 156 (1979) 269–283.
- [57] G. Veneziano, *$U(1)$ Without Instantons*, Nucl. Phys. B 159 (1979) 213–224.
- [58] R. P. Feynman, *Space-time approach to non-relativistic quantum mechanics*, Rev. Mod. Phys. 20 (Apr, 1948) 367–387.
- [59] K. G. Wilson, *Confinement of Quarks*, Phys. Rev. D 10 (1974) 2445–2459.
- [60] K. G. Wilson, *Quarks and Strings on a Lattice*, in *13th International School of Subnuclear Physics: New Phenomena in Subnuclear Physics*, 11, 1975.
- [61] C. Gattringer and C. B. Lang, *Quantum chromodynamics on the lattice*, vol. 788. Springer, Berlin, 2010.
- [62] V. Neumann, *Various techniques used in connection with random digits*, Notes by GE Forsythe (1951) 36–38.
- [63] N. Metropolis and S. Ulam, *The monte carlo method*, Journal of the American Statistical Association 44 (1949) 335–341.
- [64] S. Duane, A. Kennedy, B. J. Pendleton and D. Roweth, *Hybrid monte carlo*, Physics Letters B 195 (1987) 216–222.
- [65] L. Susskind, *Lattice Fermions*, Phys. Rev. D 16 (1977) 3031–3039.
- [66] H. B. Nielsen and M. Ninomiya, *Absence of Neutrinos on a Lattice. 1. Proof by Homotopy Theory*, Nucl. Phys. B 185 (1981) 20.
- [67] H. B. Nielsen and M. Ninomiya, *Absence of Neutrinos on a Lattice. 2. Intuitive Topological Proof*, Nucl. Phys. B 193 (1981) 173–194.

- [68] J. B. Kogut and L. Susskind, *Hamiltonian Formulation of Wilson's Lattice Gauge Theories*, Phys. Rev. D 11 (1975) 395–408.
- [69] D. B. Kaplan, *A Method for simulating chiral fermions on the lattice*, Phys. Lett. B 288 (1992) 342–347.
- [70] H. Neuberger, *Exactly massless quarks on the lattice*, Phys. Lett. B 417 (1998) 141–144.
- [71] K. Symanzik, *Continuum Limit and Improved Action in Lattice Theories. 1. Principles and φ^4 Theory*, Nucl. Phys. B 226 (1983) 187–204.
- [72] K. Symanzik, *Continuum Limit and Improved Action in Lattice Theories. 2. $O(N)$ Nonlinear Sigma Model in Perturbation Theory*, Nucl. Phys. B 226 (1983) 205–227.
- [73] B. Sheikholeslami and R. Wohlert, *Improved Continuum Limit Lattice Action for QCD with Wilson Fermions*, Nucl. Phys. B 259 (1985) 572.
- [74] M. Luscher, S. Sint, R. Sommer and P. Weisz, *Chiral symmetry and $O(a)$ improvement in lattice QCD*, Nucl. Phys. B 478 (1996) 365–400.
- [75] S. Aoki and Y. Kuramashi, *Determination of the improvement coefficient c_{sw} up to one-loop order with conventional perturbation theory*, Phys. Rev. D 68 (2003) 094019.
- [76] M. Luscher, S. Sint, R. Sommer, P. Weisz and U. Wolff, *Nonperturbative $O(a)$ improvement of lattice QCD*, Nucl. Phys. B 491 (1997) 323–343.
- [77] M. Luscher and P. Weisz, *$O(a)$ improvement of the axial current in lattice QCD to one loop order of perturbation theory*, Nucl. Phys. B 479 (1996) 429–458.
- [78] ALPHA collaboration, K. Jansen and R. Sommer, *$O(a)$ improvement of lattice QCD with two flavors of Wilson quarks*, Nucl. Phys. B 530 (1998) 185–203.
- [79] T. Bhattacharya, R. Gupta, W. Lee, S. R. Sharpe and J. M. S. Wu, *Improved bilinears in lattice QCD with non-degenerate quarks*, Phys. Rev. D 73 (2006) 034504.
- [80] M. Luscher and P. Weisz, *On-shell improved lattice gauge theories*, Commun. Math. Phys. 98 (1985) 433.

- [81] Y. Iwasaki, *Renormalization group analysis of lattice theories and improved lattice action: Two-dimensional non-linear $O(N)$ sigma model*, Nucl. Phys. B 258 (1985) 141–156.
- [82] Y. Iwasaki, *Renormalization Group Analysis of Lattice Theories and Improved Lattice Action. II. Four-dimensional non-Abelian $SU(N)$ gauge model*, 1983.
- [83] ALPHA collaboration, R. Frezzotti, P. A. Grassi, S. Sint and P. Weisz, *Lattice QCD with a chirally twisted mass term*, JHEP 08 (2001) 058.
- [84] A. Shindler, *Twisted mass lattice QCD*, Phys. Rept. 461 (2008) 37–110.
- [85] R. Frezzotti and G. C. Rossi, *Chirally improving Wilson fermions. 1. $O(a)$ improvement*, JHEP 08 (2004) 007.
- [86] M. I. Buchoff, J.-W. Chen and A. Walker-Loud, *$\pi\pi$ scattering in twisted mass chiral perturbation theory*, Phys. Rev. D 79 (2009) 074503.
- [87] Z. T. Draper and S. R. Sharpe, *$\pi\pi$ scattering in partially-quenched twisted-mass chiral perturbation theory*, Phys. Rev. D 105 (2022) 034508.
- [88] D. Becirevic, P. Boucaud, V. Lubicz, G. Martinelli, F. Mescia, S. Simula et al., *Exploring twisted mass lattice QCD with the Clover term*, Phys. Rev. D 74 (2006) 034501.
- [89] ALPHA collaboration, U. Wolff, *Monte Carlo errors with less errors*, Comput. Phys. Commun. 156 (2004) 143–153.
- [90] B. Efron, *Bootstrap Methods: Another Look at the Jackknife*, The Annals of Statistics 7 (1979) 1 – 26.
- [91] H. L. Jones, *Jackknife estimation of functions of stratum means*, Biometrika 61 (1974) 343–348.
- [92] G. C. Wick, *The Evaluation of the Collision Matrix*, Phys. Rev. 80 (1950) 268–272.
- [93] B. F. Smith, *Domain Decomposition Methods for Partial Differential Equations*, pp. 225–243. Springer Netherlands, Dordrecht, 1997. 10.1007/978-94-011-5412-3_8.
- [94] M. Luscher, *Solution of the Dirac equation in lattice QCD using a domain decomposition method*, Comput. Phys. Commun. 156 (2004) 209–220.

- [95] Y. Saad and M. H. Schultz, *Gmres: A generalized minimal residual algorithm for solving nonsymmetric linear systems*, SIAM Journal on Scientific and Statistical Computing 7 (1986) 856–869.
- [96] M. R. Hestenes and E. Stiefel, *Methods of conjugate gradients for solving linear systems*, Journal of research of the National Bureau of Standards 49 (1952) 409–435.
- [97] A. Frommer, K. Kahl, S. Krieg, B. Leder and M. Rottmann, *Adaptive aggregation-based domain decomposition multigrid for the lattice wilson–dirac operator*, SIAM Journal on Scientific Computing 36 (2014) A1581–A1608.
- [98] W. Detmold, D. J. Murphy, A. V. Pochinsky, M. J. Savage, P. E. Shanahan and M. L. Wagman, *Sparsening algorithm for multihadron lattice QCD correlation functions*, Phys. Rev. D 104 (2021) 034502.
- [99] S.-J. Dong and K.-F. Liu, *Stochastic estimation with $Z(2)$ noise*, Phys. Lett. B 328 (1994) 130–136.
- [100] W. Wilcox, *Noise methods for flavor singlet quantities*, in *Interdisciplinary Workshop on Numerical Challenges in Lattice QCD*, pp. 127–141, 8, 1999.
- [101] J. Foley, K. Jimmy Juge, A. O’Cais, M. Peardon, S. M. Ryan and J.-I. Skullerud, *Practical all-to-all propagators for lattice QCD*, Comput. Phys. Commun. 172 (2005) 145–162.
- [102] S. Gusken, U. Low, K. H. Mutter, R. Sommer, A. Patel and K. Schilling, *Nonsinglet Axial Vector Couplings of the Baryon Octet in Lattice QCD*, Phys. Lett. B 227 (1989) 266–269.
- [103] C. Alexandrou, F. Jegerlehner, S. Güsken, K. Schilling and R. Sommer, *B-meson properties from lattice qcd*, Physics Letters B 256 (1991) 60–67.
- [104] UKQCD collaboration, C. R. Allton et al., *Gauge invariant smearing and matrix correlators using Wilson fermions at Beta = 6.2*, Phys. Rev. D 47 (1993) 5128–5137.
- [105] HADRON SPECTRUM collaboration, M. Peardon, J. Bulava, J. Foley, C. Morningstar, J. Dudek, R. G. Edwards et al., *A Novel quark-field creation operator construction for hadronic physics in lattice QCD*, Phys. Rev. D 80 (2009) 054506.

- [106] C. Morningstar, J. Bulava, J. Foley, K. J. Juge, D. Lenkner, M. Peardon et al., *Improved stochastic estimation of quark propagation with Laplacian Heaviside smearing in lattice QCD*, Phys. Rev. D 83 (2011) 114505.
- [107] G. Parisi, *The strategy for computing the hadronic mass spectrum*, Physics Reports 103 (1984) 203–211.
- [108] G. P. Lepage, *The Analysis of Algorithms for Lattice Field Theory*, in *Theoretical Advanced Study Institute in Elementary Particle Physics*, 6, 1989.
- [109] W. I. Jay and E. T. Neil, *Bayesian model averaging for analysis of lattice field theory results*, Phys. Rev. D 103 (2021) 114502.
- [110] E. T. Neil and J. W. Sitison, *Improved information criteria for Bayesian model averaging in lattice field theory*, Phys. Rev. D 109 (2024) 014510.
- [111] J. Frison, *Towards fully bayesian analyses in Lattice QCD*, 2023.
- [112] J. J. Dudek, R. G. Edwards and C. E. Thomas, *S and D-wave phase shifts in isospin-2 pi pi scattering from lattice QCD*, Phys. Rev. D 86 (2012) 034031.
- [113] C. Morningstar, J. Bulava, B. Fahy, J. Foley, Y. C. Jhang, K. J. Juge et al., *Extended hadron and two-hadron operators of definite momentum for spectrum calculations in lattice QCD*, Phys. Rev. D 88 (2013) 014511.
- [114] M. Luscher and U. Wolff, *How to Calculate the Elastic Scattering Matrix in Two-dimensional Quantum Field Theories by Numerical Simulation*, Nucl. Phys. B 339 (1990) 222–252.
- [115] B. Blossier, M. Della Morte, G. von Hippel, T. Mendes and R. Sommer, *On the generalized eigenvalue method for energies and matrix elements in lattice field theory*, JHEP 04 (2009) 094.
- [116] M. Luscher, *Volume Dependence of the Energy Spectrum in Massive Quantum Field Theories. 1. Stable Particle States*, Commun. Math. Phys. 104 (1986) 177.
- [117] J. Gasser and H. Leutwyler, *Thermodynamics of Chiral Symmetry*, Phys. Lett. B 188 (1987) 477–481.
- [118] G. Colangelo, S. Durr and C. Haefeli, *Finite volume effects for meson masses and decay constants*, Nucl. Phys. B 721 (2005) 136–174.

- [119] G. Colangelo and C. Haefeli, *An Asymptotic formula for the pion decay constant in a large volume*, Phys. Lett. B 590 (2004) 258–264.
- [120] G. 't Hooft, *A Planar Diagram Theory for Strong Interactions*, Nucl. Phys. B 72 (1974) 461.
- [121] A. V. Manohar, *Large N QCD*, in *Les Houches Summer School in Theoretical Physics, Session 68: Probing the Standard Model of Particle Interactions*, pp. 1091–1169, 2, 1998.
- [122] E. Witten, *Baryons in the $1/n$ Expansion*, Nucl. Phys. B 160 (1979) 57–115.
- [123] S. R. Coleman, *$1/N$* , in *17th International School of Subnuclear Physics: Pointlike Structures Inside and Outside Hadrons*, 3, 1980.
- [124] P. Hernández and F. Romero-López, *The large N_c limit of QCD on the lattice*, Eur. Phys. J. A 57 (2021) 52.
- [125] E. Corrigan and P. Ramond, *A Note on the Quark Content of Large Color Groups*, Phys. Lett. B 87 (1979) 73–74.
- [126] A. Armoni, M. Shifman and G. Veneziano, *Exact results in non-supersymmetric large N orientifold field theories*, Nucl. Phys. B 667 (2003) 170–182.
- [127] A. Armoni, M. Shifman and G. Veneziano, *SUSY relics in one flavor QCD from a new $1/N$ expansion*, Phys. Rev. Lett. 91 (2003) 191601.
- [128] A. Armoni, G. Shore and G. Veneziano, *Quark condensate in massless QCD from planar equivalence*, Nucl. Phys. B 740 (2006) 23–35.
- [129] C. Angelantonj and A. Armoni, *Nontachyonic type 0B orientifolds, nonsupersymmetric gauge theories and cosmological RG flow*, Nucl. Phys. B 578 (2000) 239–258.
- [130] A. Armoni and B. Kol, *Nonsupersymmetric large N gauge theories from type 0 brane configurations*, JHEP 07 (1999) 011.
- [131] G. 't Hooft, *A Two-Dimensional Model for Mesons*, Nucl. Phys. B 75 (1974) 461–470.
- [132] R. F. Dashen, E. E. Jenkins and A. V. Manohar, *$1/n_c$ expansion for baryons*, Phys. Rev. D 49 (1994) 4713.
- [133] E. E. Jenkins, *Baryon hyperfine mass splittings in large N QCD*, Phys. Lett. B 315 (1993) 441–446.

-
- [134] C. Carone, H. Georgi and S. Osofsky, *On spin independence in large N_c baryons*, Phys. Lett. B 322 (1994) 227–232.
- [135] R. F. Dashen, E. E. Jenkins and A. V. Manohar, *Spin flavor structure of large N_c baryons*, Phys. Rev. D 51 (1995) 3697–3727.
- [136] J. Dai, R. F. Dashen, E. E. Jenkins and A. V. Manohar, *Flavor symmetry breaking in the $1/N_c$ expansion*, Phys. Rev. D 53 (1996) 273–282.
- [137] S. Weinberg, *Tetraquark mesons in large- n quantum chromodynamics*, Phys. Rev. Lett. 110 (Jun, 2013) 261601.
- [138] M. Knecht and S. Peris, *Narrow Tetraquarks at Large N* , Phys. Rev. D 88 (2013) 036016.
- [139] T. D. Cohen and R. F. Lebed, *Are There Tetraquarks at Large N_c in $QCD(F)$?*, Phys. Rev. D 90 (2014) 016001.
- [140] T. D. Cohen and R. F. Lebed, *Tetraquarks with exotic flavor quantum numbers at large N_c in $QCD(AS)$* , Phys. Rev. D 89 (2014) 054018.
- [141] S. Weinberg, *Phenomenological Lagrangians*, Physica A 96 (1979) 327–340.
- [142] E. Fermi, *An attempt of a theory of beta radiation. 1.*, Z. Phys. 88 (1934) 161–177.
- [143] W. Heisenberg and H. Euler, *Consequences of dirac theory of the positron*, 2006.
- [144] I. Brivio and M. Trott, *The Standard Model as an Effective Field Theory*, Phys. Rept. 793 (2019) 1–98.
- [145] S. Weinberg, *Pion scattering lengths*, Phys. Rev. Lett. 17 (1966) 616–621.
- [146] J. Gasser and H. Leutwyler, *Chiral Perturbation Theory to One Loop*, Annals Phys. 158 (1984) 142.
- [147] J. Gasser and H. Leutwyler, *Chiral Perturbation Theory: Expansions in the Mass of the Strange Quark*, Nucl. Phys. B 250 (1985) 465–516.
- [148] A. Pich, *Chiral perturbation theory*, Rept. Prog. Phys. 58 (1995) 563–610.
- [149] S. Scherer, *Introduction to chiral perturbation theory*, Adv. Nucl. Phys. 27 (2003) 277.

-
- [150] E. Jenkins and A. V. Manohar, *Baryon chiral perturbation theory using a heavy fermion lagrangian*, Physics Letters B 255 (1991) 558–562.
- [151] V. Bernard, N. Kaiser and U.-G. Meissner, *Chiral dynamics in nucleons and nuclei*, Int. J. Mod. Phys. E 4 (1995) 193–346.
- [152] G. Burdman and J. F. Donoghue, *Union of chiral and heavy quark symmetries*, Phys. Lett. B 280 (1992) 287–291.
- [153] G. Munster, C. Schmidt and E. E. Scholz, *Chiral perturbation theory for twisted mass QCD*, Nucl. Phys. B Proc. Suppl. 140 (2005) 320–322.
- [154] S. R. Sharpe and J. M. S. Wu, *Twisted mass chiral perturbation theory at next-to-leading order*, Phys. Rev. D 71 (2005) 074501.
- [155] S. Weinberg, *The Quantum Theory of Fields*. Cambridge University Press, 1995.
- [156] W. R. Hamilton, *Lectures on Quaternions*. Hodges and Smith, 1853.
- [157] A. Cayley, *A Memoir on the Theory of Matrices*, p. 475–496. Cambridge Library Collection - Mathematics. Cambridge University Press, 2009.
- [158] G. Frobenius, *Ueber lineare substitutionen und bilineare formen.*, Journal für die reine und angewandte Mathematik 84 (1877) 1–63.
- [159] P. Di Vecchia and G. Veneziano, *Chiral Dynamics in the Large n Limit*, Nucl. Phys. B 171 (1980) 253–272.
- [160] C. Rosenzweig, J. Schechter and C. G. Trahern, *Is the Effective Lagrangian for QCD a Sigma Model?*, Phys. Rev. D 21 (1980) 3388.
- [161] E. Witten, *Large N Chiral Dynamics*, Annals Phys. 128 (1980) 363.
- [162] K. Kawarabayashi and N. Ohta, *The Problem of η in the Large N Limit: Effective Lagrangian Approach*, Nucl. Phys. B 175 (1980) 477–492.
- [163] H. Leutwyler, *Bounds on the light quark masses*, Phys. Lett. B 374 (1996) 163–168.
- [164] P. Herrera-Siklody, J. I. Latorre, P. Pascual and J. Taron, *Chiral effective Lagrangian in the large N_c limit: The Nonet case*, Nucl. Phys. B 497 (1997) 345–386.

- [165] R. Kaiser and H. Leutwyler, *Large N_c in chiral perturbation theory*, Eur. Phys. J. C 17 (2000) 623–649.
- [166] G. Ecker, J. Gasser, A. Pich and E. de Rafael, *The Role of Resonances in Chiral Perturbation Theory*, Nucl. Phys. B 321 (1989) 311–342.
- [167] S. Peris and E. de Rafael, *On the large N_c behavior of the L_7 coupling in χPT* , Phys. Lett. B 348 (1995) 539–542.
- [168] P. Herrera-Siklody, *Matching of $U_L(3) \times U_R(3)$ and $SU_3(3) \times SU_R(3)$ chiral perturbation theories*, Phys. Lett. B 442 (1998) 359–368.
- [169] R. Eden, P. Landshoff, D. Olive and J. Polkinghorne, *The Analytic S-Matrix*. Cambridge University Press, 2002.
- [170] S. Weinberg, *Evidence That the Deuteron Is Not an Elementary Particle*, Phys. Rev. 137 (1965) B672–B678.
- [171] I. Matuschek, V. Baru, F.-K. Guo and C. Hanhart, *On the nature of near-threshold bound and virtual states*, Eur. Phys. J. A 57 (2021) 101.
- [172] M. T. Hansen and S. R. Sharpe, *Relativistic, model-independent, three-particle quantization condition*, Phys. Rev. D 90 (2014) 116003.
- [173] M. T. Hansen and S. R. Sharpe, *Expressing the three-particle finite-volume spectrum in terms of the three-to-three scattering amplitude*, Phys. Rev. D 92 (2015) 114509.
- [174] M. Rubin, R. Sugar and G. Tiktopoulos, *Dispersion Relations for Three-Particle Scattering Amplitudes. I*, Phys. Rev. 146 (1966) 1130–1149.
- [175] D. D. Brayshaw, *Off- and on-shell analyticity of three-particle scattering amplitudes*, Phys. Rev. 176 (1968) 1855–1870.
- [176] V. S. Potapov and J. R. Taylor, *Three-particle scattering rates and singularities of the t matrix. i.*, Phys. Rev. A 16 (Dec, 1977) 2264–2275.
- [177] V. S. Potapov and J. R. Taylor, *Three-particle scattering rates and singularities of the t matrix. ii.*, Phys. Rev. A 16 (Dec, 1977) 2276–2287.
- [178] A. W. Jackura, R. A. Briceño, S. M. Dawid, M. H. E. Islam and C. McCarty, *Solving relativistic three-body integral equations in the presence of bound states*, Phys. Rev. D 104 (2021) 014507.

- [179] S. M. Dawid, M. H. E. Islam and R. A. Briceño, *Analytic continuation of the relativistic three-particle scattering amplitudes*, Phys. Rev. D 108 (2023) 034016.
- [180] S. M. Dawid, M. H. E. Islam, R. A. Briceno and A. W. Jackura, *Evolution of Efimov states*, Phys. Rev. A 109 (2024) 043325.
- [181] T. D. Blanton, F. Romero-López and S. R. Sharpe, *Implementing the three-particle quantization condition including higher partial waves*, JHEP 03 (2019) 106.
- [182] M. T. Hansen, F. Romero-López and S. R. Sharpe, *Generalizing the relativistic quantization condition to include all three-pion isospin channels*, JHEP 07 (2020) 047.
- [183] FLAVOUR LATTICE AVERAGING GROUP (FLAG) collaboration, Y. Aoki et al., *FLAG Review 2021*, Eur. Phys. J. C 82 (2022) 869.
- [184] J. Bijnens, G. Colangelo, G. Ecker, J. Gasser and M. E. Sainio, *Elastic π π scattering to two loops*, Phys. Lett. B 374 (1996) 210–216.
- [185] G. Ecker, J. Gasser, H. Leutwyler, A. Pich and E. de Rafael, *Chiral Lagrangians for Massive Spin 1 Fields*, Phys. Lett. B 223 (1989) 425–432.
- [186] T. N. Truong, *Chiral Perturbation Theory and Final State Theorem*, Phys. Rev. Lett. 61 (1988) 2526.
- [187] A. Dobado, M. J. Herrero and T. N. Truong, *Unitarized Chiral Perturbation Theory for Elastic Pion-Pion Scattering*, Phys. Lett. B 235 (1990) 134–140.
- [188] A. Dobado and J. R. Pelaez, *Global fit of $\pi\pi$ and πk elastic scattering in chiral perturbation theory with dispersion relations*, Phys. Rev. D 47 (1993) 4883–4888.
- [189] T. Hannah, *Unitarity, chiral perturbation theory, and K_{l4} decays*, Phys. Rev. D 51 (1995) 103–110.
- [190] A. Dobado and J. R. Pelaez, *The Inverse amplitude method in chiral perturbation theory*, Phys. Rev. D 56 (1997) 3057–3073.
- [191] J. R. Pelaez, *Recent progress on the light meson resonance description from unitarized chiral perturbation theory and large N_c* , AIP Conf. Proc. 688 (2003) 45–60.

- [192] J. R. Pelaez, *Light scalar and vector mesons in the large N_c limit from unitarized chiral perturbation theory*, AIP Conf. Proc. 814 (2006) 670–674.
- [193] J. R. Pelaez and G. Rios, *Nature of the $f_0(600)$ from its N_c dependence at two loops in unitarized Chiral Perturbation Theory*, Phys. Rev. Lett. 97 (2006) 242002.
- [194] T. D. Blanton, F. Romero-López and S. R. Sharpe, *$I = 3$ Three-Pion Scattering Amplitude from Lattice QCD*, Phys. Rev. Lett. 124 (2020) 032001.
- [195] J. Bijnens and T. Husek, *Six-pion amplitude*, Phys. Rev. D 104 (2021) 054046.
- [196] J. Bijnens, T. Husek and M. Sjö, *Six-meson amplitude in QCD-like theories*, Phys. Rev. D 106 (2022) 054021.
- [197] M. Luscher, *Volume Dependence of the Energy Spectrum in Massive Quantum Field Theories. 2. Scattering States*, Commun. Math. Phys. 105 (1986) 153–188.
- [198] M. Luscher, *Two particle states on a torus and their relation to the scattering matrix*, Nucl. Phys. B 354 (1991) 531–578.
- [199] N. Ishii, S. Aoki and T. Hatsuda, *The Nuclear Force from Lattice QCD*, Phys. Rev. Lett. 99 (2007) 022001.
- [200] S. Aoki, T. Hatsuda and N. Ishii, *Nuclear Force from Monte Carlo Simulations of Lattice Quantum Chromodynamics*, Comput. Sci. Dis. 1 (2008) 015009.
- [201] S. Aoki, T. Hatsuda and N. Ishii, *Theoretical Foundation of the Nuclear Force in QCD and its applications to Central and Tensor Forces in Quenched Lattice QCD Simulations*, Prog. Theor. Phys. 123 (2010) 89–128.
- [202] HAL QCD collaboration, S. Aoki, T. Doi, T. Hatsuda, Y. Ikeda, T. Inoue, N. Ishii et al., *Lattice QCD approach to Nuclear Physics*, PTEP 2012 (2012) 01A105.
- [203] M. Bruno and M. T. Hansen, *Variations on the Maiani-Testa approach and the inverse problem*, JHEP 06 (2021) 043.
- [204] M. Luscher, *Signatures of unstable particles in finite volume*, Nucl. Phys. B 364 (1991) 237–251.

- [205] K. Rummukainen and S. A. Gottlieb, *Resonance scattering phase shifts on a nonrest frame lattice*, Nucl. Phys. B 450 (1995) 397–436.
- [206] C. h. Kim, C. T. Sachrajda and S. R. Sharpe, *Finite-volume effects for two-hadron states in moving frames*, Nucl. Phys. B 727 (2005) 218–243.
- [207] S. He, X. Feng and C. Liu, *Two particle states and the S-matrix elements in multi-channel scattering*, JHEP 07 (2005) 011.
- [208] V. Bernard, M. Lage, U.-G. Meissner and A. Rusetsky, *Resonance properties from the finite-volume energy spectrum*, JHEP 08 (2008) 024.
- [209] T. Luu and M. J. Savage, *Extracting Scattering Phase-Shifts in Higher Partial-Waves from Lattice QCD Calculations*, Phys. Rev. D 83 (2011) 114508.
- [210] R. A. Briceno and Z. Davoudi, *Moving multichannel systems in a finite volume with application to proton-proton fusion*, Phys. Rev. D 88 (2013) 094507.
- [211] R. A. Briceno, *Two-particle multichannel systems in a finite volume with arbitrary spin*, Phys. Rev. D 89 (2014) 074507.
- [212] M. Gockeler, R. Horsley, M. Lage, U. G. Meissner, P. E. L. Rakow, A. Rusetsky et al., *Scattering phases for meson and baryon resonances on general moving-frame lattices*, Phys. Rev. D 86 (2012) 094513.
- [213] I. M. Gelfand, G. E. Shilov, M. I. Graev, N. Y. Vilenkin and I. I. Pyatetskii-Shapiro, *Generalized functions*. AMS Chelsea Publishing. Academic Press, New York, NY, 1964.
- [214] K. t. r. Davies, M. I. Glasser, V. Protopopescu and F. Tabakin, *The Mathematics of Principal Value Integrals and Applications to Nuclear Physics, Transport Theory, and Condensed Matter Physics*, Math. Models Methods Appl. Sci. 6 (1996) 833–885.
- [215] C. Morningstar, J. Bulava, B. Singha, R. Brett, J. Fallica, A. Hanlon et al., *Estimating the two-particle K-matrix for multiple partial waves and decay channels from finite-volume energies*, Nucl. Phys. B 924 (2017) 477–507.
- [216] A. B. a. Raposo and M. T. Hansen, *Finite-volume scattering on the left-hand cut*, JHEP 08 (2024) 075.

- [217] L. Meng, V. Baru, E. Epelbaum, A. A. Filin and A. M. Gasparyan, *Solving the left-hand cut problem in lattice QCD: $T_{cc}(3875)^+$ from finite volume energy levels*, Phys. Rev. D 109 (2024) L071506.
- [218] R. Bubna, H.-W. Hammer, F. Müller, J.-Y. Pang, A. Rusetsky and J.-J. Wu, *Lüscher equation with long-range forces*, JHEP 05 (2024) 168.
- [219] S. R. Beane, W. Detmold and M. J. Savage, *n -Boson Energies at Finite Volume and Three-Boson Interactions*, Phys. Rev. D 76 (2007) 074507.
- [220] K. Huang and C. N. Yang, *Quantum-mechanical many-body problem with hard-sphere interaction*, Phys. Rev. 105 (Feb, 1957) 767–775.
- [221] M. T. Hansen and S. R. Sharpe, *Perturbative results for two and three particle threshold energies in finite volume*, Phys. Rev. D 93 (2016) 014506.
- [222] S. R. Beane, W. Detmold, T. C. Luu, K. Orginos, M. J. Savage and A. Torok, *Multi-Pion Systems in Lattice QCD and the Three-Pion Interaction*, Phys. Rev. Lett. 100 (2008) 082004.
- [223] F. Romero-López, A. Rusetsky, N. Schlage and C. Urbach, *Relativistic N -particle energy shift in finite volume*, JHEP 02 (2021) 060.
- [224] J.-Y. Pang, J.-J. Wu, H. W. Hammer, U.-G. Meißner and A. Rusetsky, *Energy shift of the three-particle system in a finite volume*, Phys. Rev. D 99 (2019) 074513.
- [225] F. Müller, T. Yu and A. Rusetsky, *Finite-volume energy shift of the three-pion ground state*, Phys. Rev. D 103 (2021) 054506.
- [226] M. Mai, B. Hu, M. Doring, A. Pilloni and A. Szczepaniak, *Three-body Unitarity with Isobars Revisited*, Eur. Phys. J. A 53 (2017) 177.
- [227] M. Mai and M. Döring, *Three-body Unitarity in the Finite Volume*, Eur. Phys. J. A 53 (2017) 240.
- [228] H.-W. Hammer, J.-Y. Pang and A. Rusetsky, *Three-particle quantization condition in a finite volume: 1. The role of the three-particle force*, JHEP 09 (2017) 109.
- [229] H. W. Hammer, J. Y. Pang and A. Rusetsky, *Three particle quantization condition in a finite volume: 2. general formalism and the analysis of data*, JHEP 10 (2017) 115.

- [230] R. A. Briceño, M. T. Hansen and S. R. Sharpe, *Relating the finite-volume spectrum and the two-and-three-particle S matrix for relativistic systems of identical scalar particles*, Phys. Rev. D 95 (2017) 074510.
- [231] R. A. Briceño, M. T. Hansen and S. R. Sharpe, *Three-particle systems with resonant subprocesses in a finite volume*, Phys. Rev. D 99 (2019) 014516.
- [232] T. D. Blanton and S. R. Sharpe, *Relativistic three-particle quantization condition for nondegenerate scalars*, Phys. Rev. D 103 (2021) 054503.
- [233] T. D. Blanton and S. R. Sharpe, *Three-particle finite-volume formalism for $\pi^+\pi^+K^+$ and related systems*, Phys. Rev. D 104 (2021) 034509.
- [234] M. T. Hansen, F. Romero-López and S. R. Sharpe, *Incorporating $DD\pi$ effects and left-hand cuts in lattice QCD studies of the $T_{cc}(3875)^+$* , JHEP 06 (2024) 051.
- [235] Z. T. Draper, M. T. Hansen, F. Romero-López and S. R. Sharpe, *Three relativistic neutrons in a finite volume*, JHEP 07 (2023) 226.
- [236] Z. T. Draper and S. R. Sharpe, *Three-particle formalism for multiple channels: the $\eta\pi\pi + K\bar{K}\pi$ system in isosymmetric QCD*, JHEP 07 (2024) 083.
- [237] A. W. Jackura, S. M. Dawid, C. Fernández-Ramírez, V. Mathieu, M. Mikhasenko, A. Pilloni et al., *Equivalence of three-particle scattering formalisms*, Phys. Rev. D 100 (2019) 034508.
- [238] T. D. Blanton and S. R. Sharpe, *Equivalence of relativistic three-particle quantization conditions*, Phys. Rev. D 102 (2020) 054515.
- [239] T. D. Blanton and S. R. Sharpe, *Alternative derivation of the relativistic three-particle quantization condition*, Phys. Rev. D 102 (2020) 054520.
- [240] R. A. Briceño, M. T. Hansen and S. R. Sharpe, *Numerical study of the relativistic three-body quantization condition in the isotropic approximation*, Phys. Rev. D 98 (2018) 014506.
- [241] M. T. Hansen and S. R. Sharpe, *Threshold expansion of the three-particle quantization condition*, Phys. Rev. D 93 (2016) 096006.

- [242] S. R. Sharpe, *Testing the threshold expansion for three-particle energies at fourth order in ϕ^4 theory*, Phys. Rev. D 96 (2017) 054515.
- [243] M. Fukugita, T. Inami, N. Sakai and S. Yazaki, *Nonleptonic decays of kaons in the $1nc$ expansion*, Physics Letters B 72 (1977) 237–239.
- [244] R. S. Chivukula, J. M. Flynn and H. Georgi, *Polychromatic Penguins Don't Fly*, Phys. Lett. B 171 (1986) 453–458.
- [245] W. A. Bardeen, A. J. Buras and J. M. Gerard, *A consistent analysis of the $\Delta I = 1/2$ rule for K decays*, Phys. Lett. B 192 (1987) 138–144.
- [246] W. A. Bardeen, A. Buras and J.-M. Gérard, *The $\Delta I = 1/2$ rule in the large- N limit*, Physics Letters B 180 (1986) 133–140.
- [247] W. A. Bardeen, A. J. Buras and J. M. Gerard, *The $K \rightarrow \pi\pi$ Decays in the Large N Limit: Quark Evolution*, Nucl. Phys. B 293 (1987) 787–811.
- [248] S. R. Sharpe, *On the Contribution of Electromagnetic Penguins to ϵ'* , Phys. Lett. B 194 (1987) 551–556.
- [249] A. Pich and E. de Rafael, *Weak K amplitudes in the chiral and $1/N_c$ expansions*, Phys. Lett. B 374 (1996) 186–192.
- [250] G. S. Bali, F. Bursa, L. Castagnini, S. Collins, L. Del Debbio, B. Lucini et al., *Mesons in large- N QCD*, JHEP 06 (2013) 071.
- [251] A. C. Cordón, T. DeGrand and J. L. Goity, *N_c dependencies of baryon masses: Analysis with lattice QCD and effective theory*, Phys. Rev. D 90 (2014) 014505.
- [252] T. DeGrand and Y. Liu, *Lattice study of large N_c QCD*, Phys. Rev. D 94 (2016) 034506.
- [253] T. DeGrand, *Simple chromatic properties of gradient flow*, Phys. Rev. D 95 (2017) 114512.
- [254] T. DeGrand, *Topological susceptibility in QCD with two flavors and 3-5 colors: a pilot study*, Phys. Rev. D 101 (2020) 114509.
- [255] T. DeGrand, *Finite temperature properties of QCD with two flavors and three, four and five colors*, Phys. Rev. D 103 (2021) 094513.
- [256] A. Athenodorou and M. Teper, *$SU(N)$ gauge theories in $3+1$ dimensions: glueball spectrum, string tensions and topology*, JHEP 12 (2021) 082.

- [257] A. Donini, P. Hernández, C. Pena and F. Romero-López, *Nonleptonic kaon decays at large N_c* , Phys. Rev. D 94 (2016) 114511.
- [258] P. Hernández, C. Pena and F. Romero-López, *Large N_c scaling of meson masses and decay constants*, Eur. Phys. J. C 79 (2019) 865.
- [259] A. Donini, P. Hernández, C. Pena and F. Romero-López, *Dissecting the $\Delta I = 1/2$ rule at large N_c* , Eur. Phys. J. C 80 (2020) 638.
- [260] M. G. Pérez, A. González-Arroyo and M. Okawa, *Meson spectrum in the large N limit*, JHEP 04 (2021) 230.
- [261] J. Bijnens and J. Lu, *Meson-meson Scattering in QCD-like Theories*, JHEP 03 (2011) 028.
- [262] G. Passarino and M. J. G. Veltman, *One Loop Corrections for e^+e^- Annihilation Into $\mu^+\mu^-$ in the Weinberg Model*, Nucl. Phys. B 160 (1979) 151–207.
- [263] L. Del Debbio, A. Patella and C. Pica, *Higher representations on the lattice: Numerical simulations. $SU(2)$ with adjoint fermions*, Phys. Rev. D 81 (2010) 094503.
- [264] L. Del Debbio, B. Lucini, A. Patella, C. Pica and A. Rago, *Conformal versus confining scenario in $SU(2)$ with adjoint fermions*, Phys. Rev. D 80 (2009) 074507.
- [265] O. Bar, G. Rupak and N. Shores, *Simulations with different lattice Dirac operators for valence and sea quarks*, Phys. Rev. D 67 (2003) 114505.
- [266] T. Umeda, *A Constant contribution in meson correlators at finite temperature*, Phys. Rev. D 75 (2007) 094502.
- [267] X. Feng, K. Jansen and D. B. Renner, *The $\pi^+\pi^+$ scattering length from maximally twisted mass lattice QCD*, Phys. Lett. B 684 (2010) 268–274.
- [268] M. Fischer, B. Kostrzewa, L. Liu, F. Romero-López, M. Ueding and C. Urbach, *Scattering of two and three physical pions at maximal isospin from lattice QCD*, Eur. Phys. J. C 81 (2021) 436.
- [269] J. Bulava, A. D. Hanlon, B. Hörz, C. Morningstar, A. Nicholson, F. Romero-López et al., *Elastic nucleon-pion scattering at $m_\pi = 200$ MeV from lattice QCD*, Nucl. Phys. B 987 (2023) 116105.

- [270] ETM collaboration, C. Helmes, C. Jost, B. Knippschild, C. Liu, J. Liu, L. Liu et al., *Hadron-hadron interactions from $N_f = 2 + 1 + 1$ lattice QCD: isospin-2 $\pi\pi$ scattering length*, JHEP 09 (2015) 109.
- [271] J. R. Green, A. D. Hanlon, P. M. Junnarkar and H. Wittig, *Weakly bound H dibaryon from $SU(3)$ -flavor-symmetric QCD*, Phys. Rev. Lett. 127 (2021) 242003.
- [272] M. Cè, M. García Vera, L. Giusti and S. Schaefer, *The topological susceptibility in the large- N limit of $SU(N)$ Yang–Mills theory*, Phys. Lett. B 762 (2016) 232–236.
- [273] NPLQCD collaboration, S. R. Beane, E. Chang, W. Detmold, H. W. Lin, T. C. Luu, K. Orginos et al., *The $I=2$ $\pi\pi$ S -wave Scattering Phase Shift from Lattice QCD*, Phys. Rev. D 85 (2012) 034505.
- [274] B. Knippschild, *Computation of luescher’s zeta function*, 2014 (Available at <https://github.com/knippsch/LueschersZetaFunction>).
- [275] D. York, N. M. Evensen, M. L. Martínez and J. De Basabe Delgado, *Unified equations for the slope, intercept, and standard errors of the best straight line*, American Journal of Physics 72 (2004) 367–375.
- [276] T. Ledwig, J. Nieves, A. Pich, E. Ruiz Arriola and J. Ruiz de Elvira, *Large- N_c naturalness in coupled-channel meson-meson scattering*, Phys. Rev. D 90 (2014) 114020.
- [277] A. Pich, *Colorless mesons in a polychromatic world*, in *The Phenomenology of Large N_c QCD*, pp. 239–258, 5, 2002.
- [278] J. Bijnens and J. Lu, *Technicolor and other QCD-like theories at next-to-next-to-leading order*, JHEP 11 (2009) 116.
- [279] J. Bijnens and G. Ecker, *Mesonic low-energy constants*, Ann. Rev. Nucl. Part. Sci. 64 (2014) 149–174.
- [280] R. Molina and E. Oset, *$T_{c\bar{s}}(2900)$ as a threshold effect from the interaction of the D^*K^* , $D_s^*\rho$ channels*, Phys. Rev. D 107 (2023) 056015.
- [281] HADRON SPECTRUM collaboration, J. J. Dudek, R. G. Edwards and C. E. Thomas, *Energy dependence of the ρ resonance in $\pi\pi$ elastic scattering from lattice QCD*, Phys. Rev. D 87 (2013) 034505.
- [282] BARYON SCATTERING (BASC) collaboration, J. Bulava et al., *Two-Pole Nature of the $\Lambda(1405)$ resonance from Lattice QCD*, Phys. Rev. Lett. 132 (2024) 051901.

- [283] BARYON SCATTERING (BASC) collaboration, J. Bulava et al., *Lattice qcd study of $\pi\Sigma - \bar{K}n$ scattering and the $\Lambda(1405)$ resonance*, Phys. Rev. D 109 (2024) 014511.
- [284] J. Bulava, B. Fahy, B. Hörz, K. J. Juge, C. Morningstar and C. H. Wong, *$I = 1$ and $I = 2$ $\pi - \pi$ scattering phase shifts from $N_f = 2 + 1$ lattice QCD*, Nucl. Phys. B 910 (2016) 842–867.
- [285] C. Alexandrou, L. Leskovec, S. Meinel, J. Negele, S. Paul, M. Petschlies et al., *P-wave $\pi\pi$ scattering and the ρ resonance from lattice QCD*, Phys. Rev. D 96 (2017) 034525.
- [286] F. J. Yndurain, *Low-energy pion physics*, 2002.
- [287] J. R. Pelaez, A. Rodas and J. Ruiz De Elvira, *Global parameterization of $\pi\pi$ scattering up to 2 GeV*, Eur. Phys. J. C 79 (2019) 1008.
- [288] S. L. Adler, *Consistency conditions on the strong interactions implied by a partially conserved axial-vector current*, Phys. Rev. 137 (Feb, 1965) B1022–B1033.
- [289] S. L. Adler, *Consistency conditions on the strong interactions implied by a partially conserved axial-vector current. ii*, Phys. Rev. 139 (Sep, 1965) B1638–B1643.
- [290] R. A. Briceno, J. J. Dudek and R. D. Young, *Scattering processes and resonances from lattice QCD*, Rev. Mod. Phys. 90 (2018) 025001.
- [291] M. T. Hansen and S. R. Sharpe, *Lattice QCD and Three-particle Decays of Resonances*, Ann. Rev. Nucl. Part. Sci. 69 (2019) 65–107.
- [292] M. Mai, M. Döring and A. Rusetsky, *Multi-particle systems on the lattice and chiral extrapolations: a brief review*, Eur. Phys. J. ST 230 (2021) 1623–1643.
- [293] M. Mai, U.-G. Meißner and C. Urbach, *Towards a theory of hadron resonances*, Phys. Rept. 1001 (2023) 1–66.
- [294] M. Mai and M. Doring, *Finite-Volume Spectrum of $\pi^+\pi^+$ and $\pi^+\pi^+\pi^+$ Systems*, Phys. Rev. Lett. 122 (2019) 062503.
- [295] B. Hörz and A. Hanlon, *Two- and three-pion finite-volume spectra at maximal isospin from lattice QCD*, Phys. Rev. Lett. 123 (2019) 142002.
- [296] M. Mai, M. Döring, C. Culver and A. Alexandru, *Three-body unitarity versus finite-volume $\pi^+\pi^+\pi^+$ spectrum from lattice QCD*, Phys. Rev. D 101 (2020) 054510.

- [297] C. Culver, M. Mai, R. Brett, A. Alexandru and M. Döring, *Three pion spectrum in the $I = 3$ channel from lattice QCD*, Phys. Rev. D 101 (2020) 114507.
- [298] HADRON SPECTRUM collaboration, M. T. Hansen, R. A. Briceño, R. G. Edwards, C. E. Thomas and D. J. Wilson, *Energy-Dependent $\pi^+\pi^+\pi^+$ Scattering Amplitude from QCD*, Phys. Rev. Lett. 126 (2021) 012001.
- [299] A. Alexandru, R. Brett, C. Culver, M. Döring, D. Guo, F. X. Lee et al., *Finite-volume energy spectrum of the $K^-K^-K^-$ system*, Phys. Rev. D 102 (2020) 114523.
- [300] R. Brett, C. Culver, M. Mai, A. Alexandru, M. Döring and F. X. Lee, *Three-body interactions from the finite-volume QCD spectrum*, Phys. Rev. D 104 (2021) 014501.
- [301] T. D. Blanton, A. D. Hanlon, B. Hörz, C. Morningstar, F. Romero-López and S. R. Sharpe, *Interactions of two and three mesons including higher partial waves from lattice QCD*, JHEP 10 (2021) 023.
- [302] Z. T. Draper, A. D. Hanlon, B. Hörz, C. Morningstar, F. Romero-López and S. R. Sharpe, *Interactions of πK , $\pi\pi K$ and $KK\pi$ systems at maximal isospin from lattice QCD*, JHEP 05 (2023) 137.
- [303] M. Mai, C. Culver, A. Alexandru, M. Döring and F. X. Lee, *Cross-channel study of pion scattering from lattice QCD*, Phys. Rev. D 100 (2019) 114514.
- [304] Z. Fu and X. Chen, *$I = 0$ $\pi\pi$ s -wave scattering length from lattice QCD*, Phys. Rev. D 98 (2018) 014514.
- [305] G. B. Arfken and H. J. Weber, *Mathematical methods for physicists; 4th ed.* Academic Press, San Diego, CA, 1995.
- [306] K. T. R. Davies, M. L. Glasser, V. Protopopescu and F. Tabakin, *The mathematics of principal value integrals and applications to nuclear physics, transport theory, and condensed matter physics*, Mathematical Models and Methods in Applied Sciences 06 (1996) 833–885.
- [307] J. Hadamard, *Lectures on Cauchy's Problem in Linear Partial Differential Equations*. Dover phoenix editions. Dover Publications, 2003.

- [308] O. Costin and H. M. Friedman, *Foundational aspects of singular integrals*, 2014.
- [309] G. Colangelo, J. Gasser and H. Leutwyler, $\pi\pi$ scattering, Nucl. Phys. B 603 (2001) 125–179.
- [310] MILC collaboration, A. Bazavov et al., *Results for light pseudoscalar mesons*, PoS LATTICE2010 (2010) 074.
- [311] S. R. Beane, W. Detmold, P. M. Junnarkar, T. C. Luu, K. Orginos, A. Parreno et al., *$SU(2)$ Low-Energy Constants from Mixed-Action Lattice QCD*, Phys. Rev. D 86 (2012) 094509.
- [312] S. Borsanyi, S. Durr, Z. Fodor, S. Krieg, A. Schafer, E. E. Scholz et al., *$SU(2)$ chiral perturbation theory low-energy constants from 2+1 flavor staggered lattice simulations*, Phys. Rev. D 88 (2013) 014513.
- [313] BMW collaboration, S. Dürer et al., *Lattice QCD at the physical point meets $SU(2)$ chiral perturbation theory*, Phys. Rev. D 90 (2014) 114504.
- [314] P. A. Boyle et al., *Low energy constants of $SU(2)$ partially quenched chiral perturbation theory from $N_f=2+1$ domain wall QCD*, Phys. Rev. D 93 (2016) 054502.
- [315] K. Yu, Y. Li, J.-J. Wu, D. B. Leinweber and A. W. Thomas, *Study of the pion-mass dependence of ρ -meson properties in lattice QCD*, Phys. Rev. D 109 (2024) 034505.
- [316] M. Garofalo, M. Mai, F. Romero-López, A. Rusetsky and C. Urbach, *Three-body resonances in the φ^4 theory*, JHEP 02 (2023) 252.
- [317] J. Bulava, M. T. Hansen, M. W. Hansen, A. Patella and N. Tantalo, *Inclusive rates from smeared spectral densities in the two-dimensional $O(3)$ non-linear σ -model*, JHEP 07 (2022) 034.
- [318] M. Karowski, H. J. Thun, T. T. Truong and P. H. Weisz, *On the uniqueness of a purely elastic S -matrix in $(1+1)$ -dimensions*, Phys. Lett. B 67 (1977) 321–322.
- [319] A. A. Belavin, A. M. Polyakov, A. S. Schwartz and Y. S. Tyupkin, *Pseudoparticle Solutions of the Yang-Mills Equations*, Phys. Lett. B 59 (1975) 85–87.
- [320] W. A. Bardeen, B. W. Lee and R. E. Shrock, *Phase Transition in the Nonlinear σ Model in $2 + \epsilon$ Dimensional Continuum*, Phys. Rev. D 14 (1976) 985.

- [321] E. Brezin and J. Zinn-Justin, *Spontaneous Breakdown of Continuous Symmetries Near Two-Dimensions*, Phys. Rev. B 14 (1976) 3110.
- [322] A. M. Polyakov, *Hidden Symmetry of the Two-Dimensional Chiral Fields*, Phys. Lett. B 72 (1977) 224–226.
- [323] A. B. Zamolodchikov and A. B. Zamolodchikov, *Relativistic factorized S-matrix in two dimensions having $O(N)$ isotopic symmetry*, JETP Lett. 26 (1977) 457.
- [324] A. B. Zamolodchikov and A. B. Zamolodchikov, *Factorized S-matrices in two dimensions as the exact solutions of certain relativistic quantum field models*, Annals Phys. 120 (1979) 253–291.
- [325] M. Luscher, *Quantum Nonlocal Charges and Absence of Particle Production in the Two-Dimensional Nonlinear Sigma Model*, Nucl. Phys. B 135 (1978) 1–19.
- [326] D. Buchholz and J. T. Lopuszanski, *Nonlocal Charges: A New Concept in Quantum Field Theory*, Lett. Math. Phys. 3 (1979) 175–180.
- [327] D. Buchholz, J. T. Lopuszanski and S. Rabsztyn, *Nonlocal Charges in Local Quantum Field Theory*, Nucl. Phys. B 263 (1986) 155–172.
- [328] J. B. McGuire, *Study of Exactly Soluble One-Dimensional N-Body Problems*, J. Math. Phys. 5 (1964) 622–636.
- [329] C.-N. Yang, *Some exact results for the many-body problems in one dimension with repulsive delta-function interaction*, Phys. Rev. Lett. 19 (1967) 1312–1314.
- [330] L. Castillejo, R. H. Dalitz and F. J. Dyson, *Low's scattering equation for the charged and neutral scalar theories*, Phys. Rev. 101 (1956) 453–458.
- [331] D. J. Gross and A. Neveu, *Dynamical symmetry breaking in asymptotically free field theories*, Phys. Rev. D 10 (Nov, 1974) 3235–3253.
- [332] R. A. Briceño, M. A. Carrillo, J. V. Guerrero, M. T. Hansen and A. M. Sturzu, *Accessing scattering amplitudes using quantum computers*, PoS LATTICE2021 (2022) 315.
- [333] R. H. Swendsen and J.-S. Wang, *Nonuniversal critical dynamics in monte carlo simulations*, Phys. Rev. Lett. 58 (1987) 86–88.

-
- [334] U. Wolff, *Collective monte carlo updating for spin systems*, Phys. Rev. Lett. 62 (1989) 361–364.
- [335] U. Wolff, *Collective Monte Carlo Updating in a High Precision Study of the x - y Model*, Nucl. Phys. B 322 (1989) 759–774.
- [336] U. Wolff, *Continuum behavior in the lattice $O(3)$ sigma model*, Physics Letters B 222 (1989) 473–475.
- [337] U. Wolff, *Asymptotic freedom and mass generation in the $O(3)$ nonlinear σ -model*, Nuclear Physics B 334 (1990) 581–610.
- [338] U. Wolff, *Comparison between cluster monte carlo algorithms in the ising model*, Physics Letters B 228 (1989) 379–382.
- [339] J. Bulava. Private communication, 2022.
- [340] J. Balog, F. Niedermayer and P. Weisz, *Logarithmic corrections to $O(a^2)$ lattice artifacts*, Phys. Lett. B 676 (2009) 188–192.
- [341] J. Balog, F. Niedermayer and P. Weisz, *The Puzzle of apparent linear lattice artifacts in the 2d non-linear sigma-model and Symanzik’s solution*, Nucl. Phys. B 824 (2010) 563–615.
- [342] H. P. Robertson, *Kinematics and World-Structure*, Astrophys. J. 82 (1935) 284–301.
- [343] A. Friedmann, *Über die krümmung des raumes*, Zeitschrift für Physik 10 (1922) 377–386.
- [344] A. H. Guth, *The Inflationary Universe: A Possible Solution to the Horizon and Flatness Problems*, Phys. Rev. D 23 (1981) 347–356.
- [345] D. Kazanas, *Dynamics of the Universe and Spontaneous Symmetry Breaking*, Astrophys. J. Lett. 241 (1980) L59–L63.
- [346] A. A. Starobinsky, *A New Type of Isotropic Cosmological Models Without Singularity*, Phys. Lett. B 91 (1980) 99–102.
- [347] K. Sato, *First Order Phase Transition of a Vacuum and Expansion of the Universe*, Mon. Not. Roy. Astron. Soc. 195 (1981) 467–479.
- [348] A. D. Linde, *A New Inflationary Universe Scenario: A Possible Solution of the Horizon, Flatness, Homogeneity, Isotropy and Primordial Monopole Problems*, Phys. Lett. B 108 (1982) 389–393.
- [349] D. G. Figueroa, A. Florio, F. Torrenti and W. Valkenburg, *The art of simulating the early Universe – Part I*, JCAP 04 (2021) 035.

- [350] D. G. Figueroa, J. Garcia-Bellido and F. Torrenti, *Decay of the standard model Higgs field after inflation*, Phys. Rev. D 92 (2015) 083511.
- [351] D. G. Figueroa, A. Florio, F. Torrenti and W. Valkenburg, *CosmoLattice: A modern code for lattice simulations of scalar and gauge field dynamics in an expanding universe*, Comput. Phys. Commun. 283 (2023) 108586.
- [352] D. G. Figueroa and A. Florio, *CosmoLattice Technical Note I: Power spectra*, 2022.
- [353] R. S. Somerville, K. Lee, H. C. Ferguson, J. P. Gardner, L. A. Moustakas and M. Giavalisco, *Cosmic variance in the great observatories origins deep survey*, Astrophys. J. Lett. 600 (2004) L171.
- [354] L. Verlet, *Computer "Experiments" on Classical Fluids. I. Thermodynamical Properties of Lennard-Jones Molecules*, Phys. Rev. 159 (1967) 98–103.
- [355] J. Liouville, *Note sur la théorie de la variation des constantes arbitraires.*, Journal de Mathématiques Pures et Appliquées (1838) 342–349.
- [356] J. W. Gibbs, *Elementary principles in statistical mechanics: developed with especial reference to the rational foundations of thermodynamics*. C. Scribner's sons, 1902.
- [357] C. Runge, *Ueber die numerische auflösung von differentialgleichungen.*, Mathematische Annalen 46 (1895) 167–178.
- [358] W. Kutta, *Beitrag zur näherungsweise Integration totaler Differentialgleichungen*, Zeit. Math. Phys. 46 (1901) 435–53.
- [359] R. Courant, K. Friedrichs and H. Lewy, *Über die partiellen Differenzgleichungen der mathematischen Physik*, Math. Ann. 100 (1928) 32–74.
- [360] M. Maggiore, *Gravitational Waves. Vol. 1: Theory and Experiments*. Oxford University Press, 2007.
- [361] C. Caprini and D. G. Figueroa, *Cosmological Backgrounds of Gravitational Waves*, Class. Quant. Grav. 35 (2018) 163001.
- [362] D. G. Figueroa, *Phenomenology and theoretical aspects of reheating*. PhD thesis, Universidad Autónoma de Madrid, 2010.

- [363] C. W. Misner, K. S. Thorne and J. A. Wheeler, *Gravitation*. W. H. Freeman, San Francisco, 1973.
- [364] M. Frigo and S. Johnson, *The Design and Implementation of FFTW3*, Proceedings of the IEEE 93 (2005) 216–231.
- [365] M. Pippig, *Pfft: An extension of fftw to massively parallel architectures*, SIAM Journal on Scientific Computing 35 (2013) C213–C236.
- [366] J. Garcia-Bellido, D. G. Figueroa and A. Sastre, *A Gravitational Wave Background from Reheating after Hybrid Inflation*, Phys. Rev. D 77 (2008) 043517.
- [367] D. G. Figueroa, J. Garcia-Bellido and A. Rajantie, *On the Transverse-Traceless Projection in Lattice Simulations of Gravitational Wave Production*, JCAP 11 (2011) 015.
- [368] T. W. B. Kibble, *Topology of Cosmic Domains and Strings*, J. Phys. A 9 (1976) 1387–1398.
- [369] T. W. B. Kibble, *Some Implications of a Cosmological Phase Transition*, Phys. Rept. 67 (1980) 183.
- [370] A. Vilenkin, *Cosmic Strings and Domain Walls*, Phys. Rept. 121 (1985) 263–315.
- [371] A. Vilenkin and E. P. S. Shellard, *Cosmic Strings and Other Topological Defects*. Cambridge University Press, 7, 2000.
- [372] M. B. Hindmarsh and T. W. B. Kibble, *Cosmic strings*, Rept. Prog. Phys. 58 (1995) 477–562.
- [373] E. J. Copeland and T. W. B. Kibble, *Cosmic Strings and Superstrings*, Proc. Roy. Soc. Lond. A 466 (2010) 623–657.
- [374] E. J. Copeland, L. Pogosian and T. Vachaspati, *Seeking String Theory in the Cosmos*, Class. Quant. Grav. 28 (2011) 204009.
- [375] T. Vachaspati, L. Pogosian and D. Steer, *Cosmic Strings*, Scholarpedia 10 (2015) 31682.
- [376] A. Vilenkin, *Gravitational radiation from cosmic strings*, Phys. Lett. B 107 (1981) 47–50.
- [377] C. J. Hogan and M. J. Rees, *Gravitational interactions of cosmic strings*, Nature 311 (1984) 109–113.

- [378] T. Vachaspati and A. Vilenkin, *Gravitational Radiation from Cosmic Strings*, Phys. Rev. D 31 (1985) 3052.
- [379] LIGO SCIENTIFIC, VIRGO collaboration, B. P. Abbott et al., *Constraints on cosmic strings using data from the first Advanced LIGO observing run*, Phys. Rev. D 97 (2018) 102002.
- [380] LIGO SCIENTIFIC, VIRGO, KAGRA collaboration, R. Abbott et al., *Constraints on Cosmic Strings Using Data from the Third Advanced LIGO–Virgo Observing Run*, Phys. Rev. Lett. 126 (2021) 241102.
- [381] NANOGrav collaboration, G. Agazie et al., *The NANOGrav 15 yr Data Set: Evidence for a Gravitational-wave Background*, Astrophys. J. Lett. 951 (2023) L8.
- [382] EPTA, INPTA: collaboration, J. Antoniadis et al., *The second data release from the European Pulsar Timing Array - III. Search for gravitational wave signals*, Astron. Astrophys. 678 (2023) A50.
- [383] D. J. Reardon et al., *Search for an Isotropic Gravitational-wave Background with the Parkes Pulsar Timing Array*, Astrophys. J. Lett. 951 (2023) L6.
- [384] H. Xu et al., *Searching for the Nano-Hertz Stochastic Gravitational Wave Background with the Chinese Pulsar Timing Array Data Release I*, Res. Astron. Astrophys. 23 (2023) 075024.
- [385] LISA collaboration, P. Amaro-Seoane et al., *Laser Interferometer Space Antenna*, 2017.
- [386] Y. Nambu, *Lectures at the copenhagen symposium (1970).; t. goto*, Prog. Theor. Phys 46 (1971) 174.
- [387] T. Goto, *Relativistic quantum mechanics of one-dimensional mechanical continuum and subsidiary condition of dual resonance model*, Prog. Theor. Phys. 46 (1971) 1560–1569.
- [388] M. Hindmarsh, J. Lizarraga, J. Urrestilla, D. Daverio and M. Kunz, *Scaling from gauge and scalar radiation in Abelian Higgs string networks*, Phys. Rev. D 96 (2017) 023525.
- [389] M. Hindmarsh, J. Lizarraga, A. Urrio and J. Urrestilla, *Loop decay in Abelian-Higgs string networks*, Phys. Rev. D 104 (2021) 043519.
- [390] S. Weinberg, *A New Light Boson?*, Phys. Rev. Lett. 40 (1978) 223–226.

- [391] F. Wilczek, *Problem of Strong P and T Invariance in the Presence of Instantons*, Phys. Rev. Lett. 40 (1978) 279–282.
- [392] J. E. Kim, *Weak Interaction Singlet and Strong CP Invariance*, Phys. Rev. Lett. 43 (1979) 103.
- [393] M. A. Shifman, A. I. Vainshtein and V. I. Zakharov, *Can Confinement Ensure Natural CP Invariance of Strong Interactions?*, Nucl. Phys. B 166 (1980) 493–506.
- [394] A. R. Zhitnitsky, *On Possible Suppression of the Axion Hadron Interactions.*, Sov. J. Nucl. Phys. 31 (1980) 260.
- [395] M. Dine, W. Fischler and M. Srednicki, *A Simple Solution to the Strong CP Problem with a Harmless Axion*, Phys. Lett. B 104 (1981) 199–202.
- [396] J. Preskill, M. B. Wise and F. Wilczek, *Cosmology of the Invisible Axion*, Phys. Lett. B 120 (1983) 127–132.
- [397] L. F. Abbott and P. Sikivie, *A Cosmological Bound on the Invisible Axion*, Phys. Lett. B 120 (1983) 133–136.
- [398] M. Dine and W. Fischler, *The Not So Harmless Axion*, Phys. Lett. B 120 (1983) 137–141.
- [399] P. Svrcek and E. Witten, *Axions In String Theory*, JHEP 06 (2006) 051.
- [400] A. Arvanitaki, S. Dimopoulos, S. Dubovsky, N. Kaloper and J. March-Russell, *String Axiverse*, Phys. Rev. D 81 (2010) 123530.
- [401] M. Gorghetto, E. Hardy and G. Villadoro, *More axions from strings*, SciPost Phys. 10 (2021) 050.
- [402] M. Buschmann, J. W. Foster, A. Hook, A. Peterson, D. E. Willcox, W. Zhang et al., *Dark matter from axion strings with adaptive mesh refinement*, Nature Commun. 13 (2022) 1049.
- [403] H. Nielsen and P. Olesen, *Vortex-line models for dual strings*, Nuclear Physics B 61 (1973) 45–61.
- [404] V. B. Klaer and G. D. Moore, *How to simulate global cosmic strings with large string tension*, JCAP 10 (2017) 043.
- [405] M. Gorghetto, E. Hardy and G. Villadoro, *Axions from Strings: the Attractive Solution*, JHEP 07 (2018) 151.

-
- [406] M. Hindmarsh, J. Lizarraga, A. Lopez-Eiguren and J. Urrestilla, *Scaling Density of Axion Strings*, Phys. Rev. Lett. 124 (2020) 021301.
- [407] M. Hindmarsh, J. Lizarraga, A. Lopez-Eiguren and J. Urrestilla, *Approach to scaling in axion string networks*, Phys. Rev. D 103 (2021) 103534.
- [408] C. J. Burden, *Gravitational Radiation From a Particular Class of Cosmic Strings*, Phys. Lett. B 164 (1985) 277–281.
- [409] D. Garfinkle and T. Vachaspati, *Radiation From Kinky, Cuspless Cosmic Loops*, Phys. Rev. D 36 (1987) 2229.
- [410] J. J. Blanco-Pillado and K. D. Olum, *Stochastic gravitational wave background from smoothed cosmic string loops*, Phys. Rev. D 96 (2017) 104046.
- [411] S. Weinberg, *Gravitation and Cosmology: Principles and Applications of the General Theory of Relativity*. John Wiley and Sons, New York, 1972.
- [412] B. Allen and E. P. S. Shellard, *Cosmic string evolution: a numerical simulation*, Phys. Rev. Lett. 64 (1990) 119–122.
- [413] V. Vanchurin, K. D. Olum and A. Vilenkin, *Scaling of cosmic string loops*, Phys. Rev. D 74 (2006) 063527.
- [414] V. Vanchurin, K. Olum and A. Vilenkin, *Cosmic string scaling in flat space*, Phys. Rev. D 72 (2005) 063514.
- [415] C. Ringeval, M. Sakellariadou and F. Bouchet, *Cosmological evolution of cosmic string loops*, JCAP 02 (2007) 023.
- [416] K. D. Olum and V. Vanchurin, *Cosmic string loops in the expanding Universe*, Phys. Rev. D 75 (2007) 063521.
- [417] J. J. Blanco-Pillado, K. D. Olum and B. Shlaer, *Large parallel cosmic string simulations: New results on loop production*, Phys. Rev. D 83 (2011) 083514.
- [418] C. J. A. P. Martins and E. P. S. Shellard, *Quantitative string evolution*, Phys. Rev. D 54 (1996) 2535–2556.
- [419] C. J. A. P. Martins and E. P. S. Shellard, *Extending the velocity dependent one scale string evolution model*, Phys. Rev. D 65 (2002) 043514.

- [420] C. J. A. P. Martins, *Scaling properties of cosmological axion strings*, Phys. Lett. B 788 (2019) 147–151.
- [421] J. R. C. C. Correia and C. J. A. P. Martins, *Extending and Calibrating the Velocity dependent One-Scale model for Cosmic Strings with One Thousand Field Theory Simulations*, Phys. Rev. D 100 (2019) 103517.
- [422] M. Kalb and P. Ramond, *Classical direct interstring action*, Phys. Rev. D 9 (Apr, 1974) 2273–2284.
- [423] A. Vilenkin and T. Vachaspati, *Radiation of goldstone bosons from cosmic strings*, Phys. Rev. D 35 (Feb, 1987) 1138–1140.
- [424] A. Drew and E. P. S. Shellard, *Radiation from global topological strings using adaptive mesh refinement: Methodology and massless modes*, Phys. Rev. D 105 (2022) 063517.
- [425] A. Drew and E. P. S. Shellard, *Radiation from global topological strings using adaptive mesh refinement: Massive modes*, Phys. Rev. D 107 (2023) 043507.
- [426] A. Drew, T. Kinowski and E. P. S. Shellard, *Axion string source modeling*, Phys. Rev. D 110 (2024) 043513.
- [427] D. Matsunami, L. Pogosian, A. Saurabh and T. Vachaspati, *Decay of Cosmic String Loops Due to Particle Radiation*, Phys. Rev. Lett. 122 (2019) 201301.
- [428] A. Saurabh, T. Vachaspati and L. Pogosian, *Decay of Cosmic Global String Loops*, Phys. Rev. D 101 (2020) 083522.
- [429] T. Vachaspati and A. Vilenkin, *Formation and Evolution of Cosmic Strings*, Phys. Rev. D 30 (1984) 2036.
- [430] K. Kajantie, M. Karjalainen, M. Laine, J. Peisa and A. Rajantie, *Thermodynamics of gauge invariant $U(1)$ vortices from lattice Monte Carlo simulations*, Phys. Lett. B 428 (1998) 334–341.
- [431] L. Fleury and G. D. Moore, *Axion dark matter: strings and their cores*, JCAP 01 (2016) 004.
- [432] W. H. Press, B. S. Ryden and D. N. Spergel, *Dynamical Evolution of Domain Walls in an Expanding Universe*, Astrophys. J. 347 (1989) 590–604.

- [433] A. Lopez-Eiguren, J. Lizarraga, M. Hindmarsh and J. Urrestilla, *Cosmic Microwave Background constraints for global strings and global monopoles*, JCAP 07 (2017) 026.
- [434] J. N. Benabou, M. Buschmann, S. Kumar, Y. Park and B. R. Safdi, *Signatures of primordial energy injection from axion strings*, Phys. Rev. D 109 (2024) 055005.
- [435] D. G. Figueroa, M. Hindmarsh and J. Urrestilla, *Exact Scale-Invariant Background of Gravitational Waves from Cosmic Defects*, Phys. Rev. Lett. 110 (2013) 101302.
- [436] D. G. Figueroa, M. Hindmarsh, J. Lizarraga and J. Urrestilla, *Irreducible background of gravitational waves from a cosmic defect network: update and comparison of numerical techniques*, Phys. Rev. D 102 (2020) 103516.
- [437] M. Gorghetto, E. Hardy and H. Nicolaescu, *Observing invisible axions with gravitational waves*, JCAP 06 (2021) 034.
- [438] Y. Gouttenoire, G. Servant and P. Simakachorn, *Beyond the Standard Models with Cosmic Strings*, JCAP 07 (2020) 032.
- [439] C.-F. Chang and Y. Cui, *Stochastic Gravitational Wave Background from Global Cosmic Strings*, Phys. Dark Univ. 29 (2020) 100604.
- [440] C.-F. Chang and Y. Cui, *Gravitational waves from global cosmic strings and cosmic archaeology*, JHEP 03 (2022) 114.
- [441] Y. Gouttenoire, G. Servant and P. Simakachorn, *Kination cosmology from scalar fields and gravitational-wave signatures*, 2021.
- [442] J. J. Blanco-Pillado, K. D. Olum and B. Shlaer, *The number of cosmic string loops*, Phys. Rev. D 89 (2014) 023512.
- [443] P. Auclair, C. Ringeval, M. Sakellariadou and D. Steer, *Cosmic string loop production functions*, JCAP 06 (2019) 015.
- [444] P. Auclair, K. Leyde and D. A. Steer, *A window for cosmic strings*, JCAP 04 (2023) 005.
- [445] C. T. Hill, H. M. Hodges and M. S. Turner, *Bosonic superconducting cosmic strings*, Phys. Rev. D 37 (Jan, 1988) 263–282.
- [446] D. G. Figueroa, M. Pieroni, A. Ricciardone and P. Simakachorn, *Cosmological Background Interpretation of Pulsar Timing Array Data*, Phys. Rev. Lett. 132 (2024) 171002.

-
- [447] PLANCK collaboration, P. A. R. Ade et al., *Planck 2013 results. XXV. Searches for cosmic strings and other topological defects*, *Astron. Astrophys.* 571 (2014) A25.
- [448] A. Lazanu and P. Shellard, *Constraints on the Nambu-Goto cosmic string contribution to the CMB power spectrum in light of new temperature and polarisation data*, *JCAP* 02 (2015) 024.
- [449] J. Lizarraga, J. Urrestilla, D. Daverio, M. Hindmarsh and M. Kunz, *New CMB constraints for Abelian Higgs cosmic strings*, *JCAP* 10 (2016) 042.
- [450] L. Maiani, F. Piccinini, A. D. Polosa and V. Riquer, *A New look at scalar mesons*, *Phys. Rev. Lett.* 93 (2004) 212002.
- [451] LHCb collaboration, R. Aaij et al., *Study of the doubly charmed tetraquark T_{cc}^+* , *Nature Commun.* 13 (2022) 3351.